INSTITUTE *of* TECHNOLOGY SLIGO

An Investigation of Geosynthetic Reinforced Piled Embankments with Particular Reference to Embankment Extremities

Keith Jennings

This project is submitted in fulfilment of Quality and Qualifications Ireland requirements for the Degree of Doctor of Philosophy

Supervisor: Dr. Patrick J. Naughton

Submitted to Institute of Technology Sligo, November 2013

ABSTRACT

The design of reinforced piled embankments is a complex soil-structure interaction problem involving embankment fill, geosynthetic reinforcement, a pile group and the soft underlying soil. In designing a reinforced piled embankment both vertical and horizontal equilibrium must be achieved. Lateral outward forces exist at the outer extremities of reinforced piled embankments and in order to achieve structural stability, this destabilizing force must be restrained to maintain equilibrium within the embankment and to limit excessive deformations.

In this study, plane strain physical models of a reinforced piled embankment were investigated in a geotechnical centrifuge at up to 60 times Earth's gravity (*g*). The centrifuge model facilitated the capturing of photographic images in-flight to allow the deformational response of the piled embankment to be assessed. Numerical analyses, using Plaxis 2D, replicated the centrifuge model testing to allow further assessment of the deformational response, the stress along the geosynthetic and stress in the embankment fill above the reinforcement. Direct comparison of the data from the physical and numerical models largely validated Plaxis 2D for use in the analysis of reinforced piled embankment.

The analysis indicates that significant horizontal and vertical deformations occur in the reinforcement under the side slopes of reinforced piled embankments. Significant bending moments and pile head deflections were observed in the outer row of piles. Bending moments and deflections were present in all piles within the pile group. The analysis indicates that the pile group should extend for a greater distance towards the toe of the embankment than that currently recommended in BS 8006 (2010). The analysis indicated that an increase in the pile bending moment correlated to an increase of the horizontal and vertical deformation of the reinforcement and a decrease in the pile group efficacy. Significant axial tensions were recorded in the reinforcement and were seen to increase from near the crest of the embankment approximately linearly until dropping shapely to zero at the toe of the embankment.

ACKNOWLEDGEMENTS

Dr. Patrick Naughton offered me the opportunity of postgraduate study at the Institute of Technology Sligo. I would like to thank my supervisor Dr. Patrick Naughton very much for this outstanding initiative. I had opportunity to obtain insights into geotechnical engineering and contribute to the research project on reinforced piled embankments on soft soil which resulted in this thesis. During this time, Dr. Patrick Naughton encouraged me to present my work at many workshops and conferences all over the world. For his encouragement and truly generous attitude I would like to thank Dr. Patrick Naughton very much.

Special thanks to the technical team at the Institute. To David Lally, for his patience and assistance in designing and testing of materials for the geotechnical centrifuge models. To Dr. Cathal Colreavy, Dr. Anthony Blake and Raymond Grennan for their assistance in constructing the geotechnical centrifuge equipment, getting it running and their continuous support during the modelling process. Special thanks also goes to all those colleagues and friends who are not named explicitly in here, but who supported me a lot during the preparation of this thesis.

A special thanks to my internal and external examiners Dr. Tomas O Flaherty and Dr. Edward Ellis, thank you for your patience in reading, examining and correcting such a long document, I know it wasn't easy.

I am greatly indebted to the financial support provided by the Technological Sector Research: Strand I Programme. This great support enabled me concentrate on the research and provided me with many opportunities to extend my knowledge and experience.

Last, but not least, I particularly would like to thank my family for their encouragement and mental support throughout the years. My parents, Colm and Madeleine Jennings, have been a constant source of support emotional and of course financial support during my postgraduate years, and this thesis would certainly not have been possible without them.

Table of Contents

LIST OF TABLES VIII
LIST OF FIGURES IX
NOTATION XXVI

CHAPTER

1 Introduction 1

1.1 Background 1
1.2 Statement of the problem 4
1.3 Research options 5
1.4 Aims and objectives 7
1.5 Layout of thesis 8

2 Literature review 10

2.1 Introduction 10
2.2 Lateral forces within the embankment 10
2.3 Geosynthetic reinforcement 13
2.3.1 Horizontal loading on geosynthetic reinforcement 13
2.3.2 Vertical loading on geosynthetic reinforcement 14
2.3.3 Design of geosynthetic reinforcement 16
2.4 Lateral loading on the piles 17
2.4.1 Loading exerted on the pile 17
2.4.2 Failure mode of piles 21
2.4.3 Design of laterally loaded piles 22
2.4.3.1 Simple static method 22
2.4.3.2 Subgrade reaction method 22
2.4.3.3 Goh et al. (1997) 23
2.4.3.4 Elastic continuum method 24
2.4.3.5 Characteristic load method 25
2.4.3.6 Hybrid solutions 26

2.4.3.7 Empirical stiffness distribution method 26
2.4.4 Pile group efficacy 27
2.5 BS 8006 (2010) Design Code 27
2.5.1 Vertically distributed load 28
2.5.2 Tension in the reinforcement 31
2.5.3 Tension in the reinforcement due to lateral sliding 33
2.5.4 Pile group design 34
2.5.5 Pile group extent 35
2.5.6 Lateral deflection of the pile head and bending moments 36
2.5.7 Slope Stability Analysis 37
2.6 Finite element analyses 38
2.6.1 Finite element analysis techniques 39
2.6.2 Finite element modelling approaches 40
2.6.2.1 Plane strain models 40
2.6.2.2 Axisymmetric models 40
2.6.3 Two dimensional analyses of a GRPE 41
2.7 Centrifuge modelling 41
2.8 Summary 46

3 Methodology 47

3.1 Introduction 47
3.2 Centrifuge modelling – Equipment and experimentation procedures 48
3.2.1 Centrifuge model testing procedure 48
3.2.2 Beam rotor centrifuge 49
3.2.3 Centrifuge strongbox 53
3.2.4 Centrifuge camera 53
3.2.4.1 Data extrapolation 55
3.2.4.2 Centrifuge model refraction error 55
3.2.5 Centrifuge prototype model 59
3.2.6 Centrifuge prototype model materials 60
3.2.6.1 Embankment fill 60

3.2.6.2 Sand material characteristics used to model embankment fill 61
3.2.6.3 Sand particle size distribution 61
3.2.6.4 Particle density 62
3.2.6.5 Maximum and dry density 63
3.2.6.6 Shear strength 63
3.2.6.7 Pile group 66
3.2.6.8 Soft subsoil 67
3.2.6.9 Geosynthetic reinforcement 70
3.2.7 Centrifuge modelling potential source of errors 73
3.3 Numerical modelling 75
3.3.1 Finite element analysis 76
3.3.1.1 Soft Soil Model 76
3.3.1.2 Embankment fill 80
3.3.1.3 Geosynthetic reinforcement 80
3.3.1.4 Pile model 81
3.3.2 Finite model boundary conditions 81
3.3.2.1 Mesh generation 82
3.3.2.2 Generation of initial stresses 84
3.3.3 Plastic analysis 86
3.3.4 Model construction phase 86
3.3.5 Tolerated error 86
3.3.6 Post validation finite element model parametric analyses 87
3.3.7 Factor of safety on global stability 89
3.4 Summary 90

4 Centrifuge modelling and validation of numerical analysis 92

4.1 Introduction 92
4.2 Centrifuge testing 95
4.2.1 Centrifuge Test Series 1 96
4.2.1.1 Pile group deformations 97

4.2.1.2 Geosynthetic reinforcement deformations 101
4.2.1.3 Embankment surface mean settlements 104
4.2.2 Centrifuge Test Series 2 108
4.2.2.1 Pile group deformations 109
4.2.2.2 Geosynthetic reinforcement deformations 113
4.2.2.3 Embankment surface mean settlements 114
4.3 Plaxis 2D analysis 116
4.3.1 Plaxis Test Series 1 116
4.3.1.1 Pile group deformations 116
4.3.1.2 Geosynthetic reinforcement deformations 119
4.3.1.3 Embankment surface mean settlements 122
4.3.2 Plaxis Test Series 2 125
4.3.2.1 Pile group deformations 126
4.3.2.2 Geosynthetic reinforcement deformations 129
4.3.2.3 Embankment surface mean settlements 131
4.4 Centrifuge modelling summary 131
4.5 Plaxis 2D and Centrifuge modelling comparative analysis summary....132

5.0 FEM modelling – Presentation of analysis data.....134

5.1 Introduction.....134
5.2 Influence of Pile Spacing.....141
5.3 Influence of Pile Cap Size 152
5.4 Influence of Outer Pile Rake Angle.....163
5.5 Influence of Geosynthetic Reinforcement Stiffness.....174
5.6 Influence of Depth of Soft Soil Layer.....184
5.7 Influence of Soft Soil Stiffness 193
5.8 Influence of Embankment Height.....203
5.9 Influence of Embankment Side Slope.....214
5.10 Influence of Outer pile row location ratio 222
5.11 Summary.....230

6.0 Discussion of Results 231

6.1 Introduction 231
6.2 Comparison of centrifuge modelling and Plaxis analyses 232
6.2.1 Pile group deformations 232
6.2.2 Geosynthetic reinforcement deformations 235
6.2.3 Embankment mean surface deformations 238
6.2.4 Summary 242
6.3 Finite element analysis of reinforced piled embankments 242
6.3.1 Outer pile row deformations 242
6.3.2 Geosynthetic reinforcement deformations 244
6.3.3 Geosynthetic reinforcement axial tension 246
6.3.4 Factor of safety on global stability 248
6.3.5 Strain Compatibility Ratio (SCR) 250
6.4 Implications for design 252
6.5 Summary 256

7.0 Conclusions 259

7.1 Introduction 259
7.2 Project Summary 259
7.3 Results of Physical and Numerical Modelling 261
7.4 Conclusions 266
7.5 Recommendations for further research 267

8.0 References 270

Appendix A: Methodology analysis

Appendix B: Reinforced concrete pile and pile cap design

Appendix C: Plane strain model test results

Appendix D: Centrifuge and Plaxis 2D model

LIST OF TABLES

Table 2.1 Centrifuge scaling relationships 43

Table 2.2 Centrifuge scale factors, Viswanadham & Konig (2008) 44

Table 3.1 Centrifuge specifications 52

Table 3.2 Grading characteristics 62

Table 3.3 Particle density test results 62

Table 3.4 Maximum and minimum dry densities and max and min void ratio 63

Table 3.5 Density index range for shearbox samples 64

Table 3.6 Peak and constant volume shear strength and dilation angle of loose sand 64

Table 3.7 Summary angles of friction and dilation for the test sand 64

Table 3.8 Sand classification and properties of the sand used in this study 64

Table 3.9 Young's modulus (E) of perspex piles 67

Table 3.10 R_{inter} parameter for interface between loose sand and geosynthetic 71

Table 3.11 Mohr Coulomb parameters of loose sand 80

Table 3.12 Material parameters for pile model from Appendix B Section B.2 88

Table 3.13 Material parameters for pile cap model from Appendix B Section B.4 88

Table 3.14 Generic plane strain model parameters 89

Table 4.1 Summary of Test Series 1 model geometry and properties 96

Table 4.2 Summary of Test Series 2 model geometry and properties 109

Table 5.1 Plaxis 2D model tests 1 - 32 138

Table 5.2 Plaxis 2D model tests 33 - 66 139

Table 5.3 Plaxis 2D model tests 67 - 76 140

LIST OF FIGURES

Figure 1.1 Various forms of pile embankment system 3
Figure 1.2 Lateral thrust within a reinforced embankment 4
Figure 2.1 Illustration of the lateral forces within an embankment 11
Figure 2.2 Rendulic's approximation (1938) for lateral earth pressure 12
Figure 2.3 Tensile forces in the reinforcement under embankment of medium dense soil (Jones et al. (1990)) 16
Figure 2.4 Illustration of reduction in lateral pile resistance due to pile-pile interface 21
Figure 2.5 Failure modes for laterally loaded piles (*Fleming et al*. 1985) 21
Figure 2.6 (a) Dimensionless plot of M^* versus (q/c_u), (b) Values of λ and β 24
Figure 2.7 Variables used in the determination of T_{rp} (after BS8006, 2010) 32
Figure 2.8 Lateral sliding stability at the interface of the fill/reinforcement (after BS8006, 2010) 34
Figure 2.9 Outer limit of pile caps (after BS8006, 2010). 36
Figure 2.10 Variables used in analysis of overall stability of basal reinforced piled embankments (after BS8006, 2010) 38
Figure 2.11 Element discretization for (a) FDM and (b) FEM 40
Figure 2.12 Inertial stress in centrifuge model and corresponding prototype gravitational stress (Taylor, 1995) 42
Figure 3.1 Centrifuge prototype model cross section 49
Figure 3.2 Vertical stress vs depth in centrifuge model and corresponding prototype 50
Figure 3.3 General centrifuge layout 51
Figure 3.4 The IT Sligo 9*g*-tonne geotechnical centrifuge 51
Figure 3.5 Sectional arrangement of centrifuge. 52
Figure 3.6 (a) & (b) Plane strain strongbox with camera bracket mounted. 54
Figure 3.7 Error due to refraction in horizontal plane. 57

Figure 3.8 Error due to refraction in horizontal plane. 58
Figure 3.9 Particle size distribution 62
Figure 3.10 Shear stress vs. horizontal displacement for loose sand (I_D = 44.8 – 62.0 %) 65
Figure 3.11 Vertical vs. horizontal displacement for loose sand (I_D = 44.8 – 62.0 %). 65
Figure 3.12 Normal stress v shear stress for loose sand (I_D = 44.8 – 62.0 %). 65
Figure 3.13 Fixed end beam-deflection test results on Perspex 66
Figure 3.14 Cantilever beam-deflection test results on Perspex 67
Figure 3.15 Load – deformational response of synthetic sponge used in this test programme. 68
Figure 3.16 Load – deformational response of EPS used in this test programme 68
Figure 3.17 Normal stress v shear stress for loose sand 71
Figure 3.18 Shear stress vs. horizontal displacement for sand geosynthetic interface for loose sand (I_D = 46.2 – 66.6 %). 72
Figure 3.19 Normal stress vs. shear stress for sand geosynthetic interface for loose sand (I_D = 46.2 – 66.6 %). 72
Figure 3.20 Effective radius influence on centrifugal acceleration. 74
Figure 3.21 Plaxis 2D plane strain geosynthetic reinforced piled embankment model 75
Figure 3.22 Volumetric strain vs. *ln*(p') for subsoil A. 79
Figure 3.23 Volumetric strain vs. *ln*(p') for subsoil B. 79
Figure 3.24 Illustration of vertical pre-consolidation stress in relation to the in-situ vertical effective stress (after Plaxis 2010) 85
Figure 4.1 Typical pile group lateral deformation, geosynthetic reinforcement and embankment surface deformation profile (Piles are labelled to P1 to P7). 93
Figure 4.2 Photographic image of in-flight model at 60*g* showing superimposed lines from AutoCAD 94

Figure 4.3 Photographic image of in-flight model at 60g showing superimposed lines from AutoCAD of embankment surface vertical deformation. 94
Figure 4.4 Photographic image of in-flight model at 60g showing superimposed lines from AutoCAD of pile head lateral deformation. 95
Figure 4.5 Photographic image of in-flight model at 60g showing superimposed lines from AutoCAD of geosynthetic reinforcement vertical deformation. 95
Figure 4.6 Relationship of outer row pile deflection with g –level..... 97
Figure 4.7 Lateral deflection (mm) in pile group for physical modelling (Centrifuge) in Test No. 3. 98
Figure 4.8 Lateral deflection (mm) of outer row pile for a range of embankment geometric ratios (H/(s-a)) in Test Nos. 1 - 4 and 9 - 12. 99
Figure 4.9 Lateral deflection (mm) of outer row pile for a range of embankment side slopes in Test Nos. 1 – 3. 100
Figure 4.10 Lateral deflection (mm) of outer row pile for a range of subsoil stiffness in Test Nos. 1 – 8. 100
Figure 4.11 Vertical deformation in reinforcement in Test No. 3. 102
Figure 4.12 Maximum vertical deformation in reinforcement for a range of geometric ratios (H/(s-a)) in Test Nos. 1 – 4 and 9 – 12. 102
Figure 4.13 Maximum vertical deformation in reinforcement for a range of side slope steepness (1V:XH) in Tests Nos. 3, 11 and 13. 103
Figure 4.14 Maximum vertical deformation in reinforcement for a range of subsoil stiffness in Test Nos. 1 – 8. 104
Figure 4.15 Embankment mean surface deformations for a range of embankment geometric ratios (H/(s-a)) in Test Nos. 1 – 4 and 9 – 12. 105
Figure 4.16 Embankment mean surface deformations for a range of embankment geometric ratios (H/(s-a)) in Test Nos. 3, 11, 13. 106
Figure 4.17 Embankment mean surface deformations for a range of subsoil stiffness in Test Nos. 1 – 8. 107
Figure 4.18 Embankment crest deformations for a range of embankment side slope steepness (1V:XH) in Test Nos. 1 – 8. 108

Figure 4.19 Outer row pile lateral deflections for a range of ORPLR and soil stiffness in Test Nos. 14 – 23. 110
Figure 4.20 Outer row pile lateral deflections for a range of ORPLR and side slope steepness (1V:XH) in Test Nos. 14 – 18 and 24 – 28.....111
Figure 4.21 Pile group lateral deformations for a range of ORPLR in Test Nos. 14 – 18.....112
Figure 4.22 Pile group lateral strain (%) for a range of ORPLR in Test Nos. 14 – 18. 113
Figure 4.23 Vertical deformational response of reinforcement for a range of ORPLR in Test Nos. 14 – 23.....114
Figure 4.24 Vertical deformational response of reinforcement for a range of ORPLR in Test Nos. 14 – 18 and 24 – 28. 115
Figure 4.25 Embankment mean surface deformations for a range of ORPLR in Test Nos. 14 – 23. 115
Figure 4.26 Lateral deflection (mm) in pile group for physical modelling (Centrifuge) in Test No. 3.....117
Figure 4.27 Lateral deflection (mm) of outer row pile for a range of embankment geometric ratios (H/(s-a)) in Test Nos. 1 - 4 and 9 - 12. 118
Figure 4.28 Lateral deflection (mm) of outer row pile for a range of embankment side slopes in Test Nos. 1 – 3. 118
Figure 4.29 Lateral deflection (mm) of outer row pile for a range of subsoil stiffness in Test Nos. 1 – 8.....119
Figure 4.30 Vertical deformation in reinforcement in Test No. 3. 120
Figure 4.31 Maximum vertical deformation in reinforcement for a range of geometric ratios (H/(s-a)) in Test Nos. 1 – 4 and 9 – 12. 121
Figure 4.32 Maximum vertical deformation in reinforcement for a range of side slope steepness (1V:XH) in Tests Nos. 3, 11 and 13. 121
Figure 4.33 Maximum vertical deformation in reinforcement for a range of subsoil stiffness in Test Nos. 1 – 8.....122

Figure 4.34 Embankment mean surface deformations for a range of embankment geometric ratios (H/(s-a)) in Test Nos. 1 – 4 and 9 – 12. 123
Figure 4.35 Embankment mean surface deformations for a range of embankment geometric ratios (H/(s-a)) in Test Nos. 3, 11, 13. 124
Figure 4.36 Embankment mean surface deformations for a range of subsoil stiffness in Test Nos. 1 – 8....124
Figure 4.37 Embankment crest deformations for a range of embankment side slope steepness (1V:XH) in Test Nos. 1 – 8. 125
Figure 4.38 Outer row pile lateral deflections for a range of ORPLR and soil stiffness in Test Nos. 14 – 23. 127
Figure 4.39 Outer row pile lateral deflections for a range of ORPLR and side slope steepness (1V:XH) in Test Nos. 14 – 18 and 24 – 28. 127
Figure 4.40 Pile group lateral deformations for a range of ORPLR in Test Nos. 14 – 18. 128
Figure 4.41 Pile group lateral strain (%) for a range of ORPLR in Test Nos. 14 – 18 129
Figure 4.42 Vertical deformational response of reinforcement for a range of ORPLR in Test Nos. 14 – 23....130
Figure 4.43 Vertical deformational response of reinforcement for a range of ORPLR in Test Nos. 14 – 18 and 24 – 28. 130
Figure 4.44 Embankment mean surface deformations for a range of ORPLR in Test Nos. 14 – 23. 131
Figure 5.1 Geometric layout of generic case model of a reinforced piled embankment on soft soil....135
Figure 5.2 Surface deformations (mm) at the embankment crest for a range of pile spacing (m)....136
Figure 5.3 Strain compatibility ratio (SCR) plot for a parametric range (%)....137
Figure 5.4 Surface deformation (mm) at the embankment crest for a range of pile spacing (m), (H = 4.0m, J_{re} = 500kN/m and a = 1.0m)....141

Figure 5.5 Vertical deformation (m) under the side slope between the embankment toe and outer row pile for a range of pile spacing (m) (H = 4.0m, J_{re} = 500kN/m and a = 1.0m) 142
Figure 5.6 Lateral Deformation (LD) (m) within the side slope above the outer row pile centre line for a range of pile spacing (m) for (a) a side slope of 1V:2H and (b) a side slope of 1V:3H (H = 4.0m, J_{re} = 500kN/m and a = 1.0m).....143
Figure 5.7 Vertical deformation of the geosynthetic reinforcement for a range of pile spacing (H = 4.0m, J_{re} = 500kN/m and a = 1.0m) 144
Figure 5.8 Horizontal deformation of geosynthetic reinforcement for a range of pile spacing (m) (H = 4.0m, J_{re} = 500kN/m and a = 1.0m).....145
Figure 5.9 Axial tension in the reinforcement for a range of pile spacing (m) (H = 4.0m, J_{re} = 500kN/m and a = 1.0m).....147
Figure 5.10 Axial loading (kN) on pile group under reinforced piled embankment for a range of pile spacing (m) (H = 4.0m, J_{re} = 500kN/m and a = 1.0m) 148
Figure 5.11 Lateral deflection (mm) at the pile head within a pile group under a reinforced piled embankment for a range of pile spacing (m) (H = 4.0m, J_{re} = 500kN/m and a = 1.0m).....148
Figure 5.12 Bending moments (kNm) within a pile group for a range of pile spacing (m) (H = 4.0m, J_{re} = 500kN/m and a = 1.0m) 149
Figure 5.13 Pile group efficacy (%) for a range of pile spacing (m) (H = 4.0m, J_{re} = 500kN/m and a = 1.0m) 150
Figure 5.14 Strain in reinforcement and outer row pile and piled embankment Strain Compatibility Ratio (SCR) (%) for a range of pile spacing (m) for a 1V:2H side slope (H = 4.0m, J_{re} = 500kN/m and a = 1.0m).....151
Figure 5.15 Safety factor at failure for a range of pile spacing.....152
Figure 5.16 Surface deformations (mm) at the embankment crest for a range of pile cap sizes (m) (H = 4.0m, J_{re} = 500kN/m and s = 3.0m).....153

Figure 5.17 Vertical deformation (m) under the side slope between the embankment toe and outer row pile for a range of pile cap sizes (m) (H = 4.0m, J_{re} = 500kN/m and s = 3.0m) 154
Figure 5.18 Lateral Deformation (LD) (m) within the side slope above the outer row pile centre line for a range of pile cap sizes (m) for (a) a side slope of 1V:2H and (b) a side slope of 1V:3H (H = 4.0m, J_{re} = 500kN/m and s = 3.0m) 155
Figure 5.19 Vertical deformation of the geosynthetic reinforcement for a range of pile cap size (H = 4.0m, J_{re} = 500kN/m and s = 3.0m) 156
Figure 5.20 Horizontal deformation of geosynthetic reinforcement for a range of pile cap size (m) (H = 4.0m, J_{re} = 500kN/m and s = 3.0m) 158
Figure 5.21 Axial tension in the reinforcement for a range of pile cap size (m) (H = 4.0m, J_{re} = 500kN/m and s = 3.0m) 158
Figure 5.22 Axial loading (kN) on pile group under reinforced piled embankment for a range of pile cap size (m) (H = 4.0m, J_{re} = 500kN/m and s = 3.0m) 159
Figure 5.23 Lateral deflections (mm) at the pile head within a pile group under a reinforced piled embankment for a range of pile spacing (m) (H = 4.0m, J_{re} = 500kN/m and s = 3.0m) 160
Figure 5.24 Bending moments (kNm) within a pile group for a range of pile cap size (m) (H = 4.0m, J_{re} = 500kN/m and s = 3.0m) 160
Figure 5.25 Pile group efficacy (%) for a range of pile cap size (m) (H = 4.0m, J_{re} = 500kN/m and s = 3.0m) 161
Figure 5.26 Strain in reinforcement and outer row pile and piled embankment Strain Compatibility Ratio (SCR) (%) for a range of pile cap size (m) for a 1V:2H side slope (H = 4.0m, J_{re} = 500kN/m and s = 3.0m) 162
Figure 5.27 Safety factor at failure for a range of pile cap size 163
Figure 5.28 Surface deformations (mm) at the embankment crest for a range of outer pile rake angle (Degree (°)) (H = 4.0m, J_{re} = 500kN/m and s = 3.0m) 164

Figure 5.29 Vertical deformation (m) under the side slope between the embankment toe and outer row pile for a range of outer pile rake angle (Degree (°)) (H = 4.0m, J_{re} = 500kN/m and s = 3.0m).....165
Figure 5.30 Lateral Deformation (LD) (m) within the side slope above the outer row pile centre line for a range of outer pile rake angle (Degree (°)) for (a) a side slope of 1V:2H and (b) a side slope of 1V:3H (H = 4.0m, J_{re} = 500kN/m and s = 3.0m) 166
Figure 5.31 Vertical deformation of the geosynthetic reinforcement for a range of outer pile rake angle (Degree (°)) (H = 4.0m, J_{re} = 500kN/m and s = 3.0m).....167
Figure 5.32 Horizontal deformations (mm) of geosynthetic reinforcement for a range of outer pile rake angle (Degree (°)) (H = 4.0m, J_{re} = 500kN/m and s = 3.0m) 168
Figure 5.33 Axial tensions (kN/m) in the reinforcement for a range of outer pile rake angle (Degree (°)) (H = 4.0m, J_{re} = 500kN/m and s = 3.0m) 169
Figure 5.34 Axial loading (kN) on pile group under reinforced piled embankment for a range of outer pile rake angle (Degree (°)) (H = 4.0m, J_{re} = 500kN/m and s = 3.0m) 169
Figure 5.35 Lateral deflections (mm) at the pile head within a pile group under a reinforced piled embankment for a range of outer pile rake angle (Degree (°)) 170
Figure 5.36 Bending moments (kNm) within a pile group for a range of outer pile rake angle (Degree (°)) (H = 4.0m, J_{re} = 500kN/m and s = 3.0m) 171
Figure 5.37 Pile group efficacy (%) for a range of outer pile rake angle (Degree (°)) (H = 4.0m, J_{re} = 500kN/m and s = 3.0m).....171

Figure 5.38 Strain in reinforcement and outer row pile and piled embankment Strain Compatibility Ratio (SCR) (%) for a range of outer pile rake angle (Degree (°)) for a 1V:2H side slope (H = 4.0m, J_{re} = 500kN/m and s = 3.0m) 172
Figure 5.39 Safety factor at failure for a range of outer pile rake angle 173
Figure 5.40 Surface deformations (mm) at the embankment crest for a range of geosynthetic reinforcement stiffness (H = 4.0m, J_{re} = 500kN/m and s = 3.0m) 174
Figure 5.41 Vertical deformation (m) under the side slope between the embankment toe and outer row pile for a range of geosynthetic reinforcement stiffness (H = 4.0m, J_{re} = 500kN/m and s = 3.0m) 175
Figure 5.42 Lateral Deformation (LD) (m) within the side slope above the outer row pile centre line for a range of geosynthetic reinforcement stiffness for (a) a side slope of 1V:2H and (b) a side slope of 1V:3H (H = 4.0m, J_{re} = 500kN/m and s = 3.0m) 176
Figure 5.43 Vertical deformation of the geosynthetic reinforcement for a range of geosynthetic reinforcement stiffness (H = 4.0m, J_{re} = 500kN/m and s = 3.0m) 177
Figure 5.44 Horizontal deformations (mm) of geosynthetic reinforcement for a range of geosynthetic reinforcement stiffness (H = 4.0m, J_{re} = 500kN/m and s = 3.0m 178
Figure 5.45 Axial tensions (kN/m) in the reinforcement for a range of geosynthetic reinforcement stiffness (H = 4.0m, J_{re} = 500kN/m and s = 3.0m) 179
Figure 5.46 Axial loading (kN) on pile group under reinforced piled embankment for a range of geosynthetic reinforcement stiffness (H = 4.0m, J_{re} = 500kN/m and s = 3.0m) 180
Figure 5.47 Lateral deflection (mm) at the pile head within a pile group under a reinforced piled embankment for a range of geosynthetic reinforcement stiffness (H = 4.0m, J_{re} = 500kN/m and s = 3.0m) 181

Figure 5.48 Bending moments (kNm) within a pile group for a range of geosynthetic reinforcement stiffness (H = 4.0m, J_{re} = 500kN/m and s = 3.0m) 181
Figure 5.49 Pile group efficacy (%) for a range of geosynthetic reinforcement stiffnesses (H = 4.0m, J_{re} = 500kN/m and s = 3.0m) 182
Figure 5.50 Strain in reinforcement and outer row pile and piled embankment Strain Compatibility Ratio (SCR) (%) for a range of geosynthetic reinforcement stiffness for a 1V:2H side slope (H = 4.0m, J_{re} = 500kN/m and s = 3.0m)..... 183
Figure 5.51 Safety factor at failure for a range of geosynthetic reinforcement stiffness 184
Figure 5.52 Surface deformations (mm) at the embankment crest for a range of soft soil layer depth (m) (H = 4.0m, J_{re} = 500kN/m and s = 3.0m)..... 185
Figure 5.53 Vertical deformation (m) under the side slope between the embankment toe and outer row pile for a range of soft soil layer depth (m) (H = 4.0m, J_{re} = 500kN/m and s = 3.0m) 186
Figure 5.54 Lateral Deformation (LD) (m) within the side slope above the outer row pile centre line for a range of soft soil layer depth (m) for (a) a side slope of 1V:2H and (b) a side slope of 1V:3H (H = 4.0m, J_{re} = 500kN/m and s = 3.0m)..... 187
Figure 5.55 Vertical deformation of the geosynthetic reinforcement for a range of soft soil layer depth (m) (H = 4.0m, J_{re} = 500kN/m and s = 3.0m) .. 187
Figure 5.56 Horizontal deformations (mm) of geosynthetic reinforcement for a range of soft soil layer depth (m) (H = 4.0m, J_{re} = 500kN/m and s = 3.0m)..... 188
Figure 5.57 Axial tensions (kN/m) in the reinforcement for a range of soft soil layer depth (m) (H = 4.0m, J_{re} = 500kN/m and s = 3.0m)..... 188

Figure 5.58 Axial loading (kN) on pile group under reinforced piled embankment for a range of soft soil layer depth (m) (H = 4.0m, J_{re} = 500kN/m and s = 3.0m) 189
Figure 5.59 Lateral deflection (mm) at the pile head within a pile group under a reinforced piled embankment for a range of soft soil layer depth (m) (H = 4.0m, J_{re} = 500kN/m and s = 3.0m) 190
Figure 5.60 Bending moments (kNm) within a pile group for a range of soft soil layer depth (m) (H = 4.0m, J_{re} = 500kN/m and s = 3.0m) 190
Figure 5.61 Pile group efficacy (%) for a range of soft soil layer depth (m) (H = 4.0m, J_{re} = 500kN/m and s = 3.0m) 191
Figure 5.62 Strain in reinforcement and outer row pile and piled embankment Strain Compatibility Ratio (SCR) (%) for a range of soft soil layer depth (m) for a 1V:2H side slope (H = 4.0m, J_{re} = 500kN/m and s = 3.0m) 192
Figure 5.63 Safety factor at failure for a range of soft soil layer depth (m) 193
Figure 5.64 Surface deformations (mm) at the embankment crest for a range of soft soil stiffness *E* (kN/m^2) (H = 4.0m, J_{re} = 500kN/m and s = 3.0m) 194
Figure 5.65 Vertical deformation (m) under the side slope between the embankment toe and outer row pile for a range of soft soil stiffness *E* (kN/m^2) (H = 4.0m, J_{re} = 500kN/m and s = 3.0m) 195
Figure 5.66 Lateral Deformation (LD) (m) within the side slope above the outer row pile centre line for a range of soft soil stiffness *E* (kN/m^2) for (a) a side slope of 1V:2H and (b) a side slope of 1V:3H (H = 4.0m, J_{re} = 500kN/m and s = 3.0m) 195
Figure 5.67 Vertical deformation of the geosynthetic reinforcement for a range of soft soil stiffness *E* (kN/m^2) (H = 4.0m, J_{re} = 500kN/m and s = 3.0m) 196

Figure 5.68 Horizontal deformations (mm) of geosynthetic reinforcement for a range of soft soil stiffness *E* (kN/m^2) (H = 4.0m, J_{re} = 500kN/m and s = 3.0m) 197
Figure 5.69 Axial tensions (kN/m) in the reinforcement for a range of soft soil stiffness *E* (kN/m^2) (H = 4.0m, J_{re} = 500kN/m and s = 3.0m) 198
Figure 5.70 Axial loading (kN) on pile group under reinforced piled embankment for a range of soft soil stiffness *E* (kN/m^2) (H = 4.0m, J_{re} = 500kN/m and s = 3.0m) 199
Figure 5.71 Lateral deflection (mm) at the pile head within a pile group under a reinforced piled embankment for a range of soft soil stiffness *E* (kN/m^2) (H = 4.0m, J_{re} = 500kN/m and s = 3.0m).....200
Figure 5.72 Bending moments (kNm) within a pile group for a range of soft soil stiffness *E* (kN/m^2) (H = 4.0m, J_{re} = 500kN/m and s = 3.0m) 200
Figure 5.73 Pile group efficacy (%) for a range of soft soil stiffness *E* (kN/m^2) (H = 4.0m, J_{re} = 500kN/m and s = 3.0m) 201
Figure 5.74 Strain in reinforcement and outer row pile and piled embankment Strain Compatibility Ratio (SCR) (%) for a range of soft soil stiffness *E* (kN/m^2) for a 1V:2H side slope (H = 4.0m, J_{re} = 500kN/m and s = 3.0m).....202
Figure 5.75 Safety factor at failure for a range of soft soil stiffness 202
Figure 5.76 Surface deformations (mm) at the embankment crest for a range of embankment height (m) (a = 1.0m, J_{re} = 500kN/m and s = 3.0m).....204
Figure 5.77 Vertical deformation (m) under the side slope between the embankment toe and outer row pile for a range of embankment height (m) (a = 1.0m, J_{re} = 500kN/m and s = 3.0m) 204
Figure 5.78 Lateral Deformation (LD) (m) within the side slope above the outer row pile centre line for a range of embankment height (m) for (a) a side slope of 1V:2H and (b) a side slope of 1V:3H (a = 1.0m, J_{re} = 500kN/m and s = 3.0m) 205

Figure 5.79 Vertical deformation of the geosynthetic reinforcement for a range Of embankment height (m) (a = 1.0m, J_{re} = 500kN/m and s = 3.0m) 206
Figure 5.80 Horizontal deformations (mm) of geosynthetic reinforcement for a range of embankment height (m) (a = 1.0m, J_{re} = 500kN/m and s = 3.0m).....208
Figure 5.81 Axial tensions (kN/m) in the reinforcement for a range of embankment height (m) (a = 1.0m, J_{re} = 500kN/m and s = 3.0m).....208
Figure 5.82 Axial loading (kN) on pile group under reinforced piled embankment for a range of embankment height (m) (a = 1.0m, J_{re} = 500kN/m and s = 3.0m).....209
Figure 5.83 Lateral deflections (mm) at the pile head within a pile group under a reinforced piled embankment for a range of embankment height (m) (a = 1.0m, J_{re} = 500kN/m and s = 3.0m).....210
Figure 5.84 Bending moments (kNm) within a pile group for a range of embankment height (m) (a = 1.0m, J_{re} = 500kN/m and s = 3.0m).....211
Figure 5.85 Pile group efficiencies (%) for a range of embankment height (m) (a = 1.0m, J_{re} = 500kN/m and s = 3.0m).....211
Figure 5.86 Strain in reinforcement and outer row pile and piled embankment Strain Compatibility Ratio (SCR) (%) for a range of embankment height (m) for a 1V:2H side slope (a = 1.0m, J_{re} = 500kN/m and s = 3.0m) 212
Figure 5.87 Safety factor at failure for a range embankment height (m) 213
Figure 5.88 Vertical deformation of the geosynthetic reinforcement for a range of side slopes (H = 4.0m, J_{re} = 500kN/m and s = 3.0m).....215
Figure 5.89 Horizontal deformations (mm) of geosynthetic reinforcement for a range of side slopes (H = 4.0m, J_{re} = 500kN/m and s = 3.0m) 215
Figure 5.90 Axial tensions (kN/m) in the reinforcement for a range of side slopes (H = 4.0m, J_{re} = 500kN/m and s = 3.0m) 216

Figure 5.91 Axial loading (kN) on pile group under reinforced piled embankment for a range of side slopes (H = 4.0m, J_{re} = 500kN/m and s = 3.0m) ...217
Figure 5.92 Lateral deflections (mm) at the pile head within a pile group under a reinforced piled embankment for a range of side slopes (H = 4.0m, J_{re} = 500kN/m and s = 3.0m) 218
Figure 5.93 Bending moments (kNm) within a pile group for a range of side slopes (H = 4.0m, J_{re} = 500kN/m and s = 3.0m) 219
Figure 5.94 Pile group efficiencies (%) for a range of side slopes (H = 4.0m, J_{re} = 500kN/m and s = 3.0m) 220
Figure 5.95 Strain in reinforcement and outer row pile and piled embankment Strain Compatibility Ratio (SCR) (%) for a range of side slopes (H = 4.0m, J_{re} = 500kN/m and s = 3.0m) 221
Figure 5.96 Safety factor at failure for a range of side slope steepness 222
Figure 5.97 Vertical deformation under the side slope between the embankment toe and outer pile row for a range of ORPLR (H = 4.0m, J_{re} = 500kN/m and s = 3.0m) 223
Figure 5.98 Vertical deformation of the geosynthetic reinforcement for a range of side slopes (H = 4.0m, J_{re} = 500kN/m and s = 3.0m)....224
Figure 5.99 Horizontal deformations (mm) of geosynthetic reinforcement for a range of ORPLR (H = 4.0m, J_{re} = 500kN/m and s = 3.0m)....225
Figure 5.100 Axial tensions (kN/m) in the reinforcement for a range of ORPLR (H = 4.0m, J_{re} = 500kN/m and s = 3.0m) 226
Figure 5.101 Axial loading (kN) on pile group under reinforced piled embankment for a range of ORPLR (H = 4.0m, J_{re} = 500kN/m and s = 3.0m)....227
Figure 5.102 Lateral deflections (mm) at the pile head within a pile group under a reinforced piled embankment for a range of ORPLR (H = 4.0m, J_{re} = 500kN/m and s = 3.0m) 227
Figure 5.103 Bending moments (kNm) within a pile group for a range of ORPLR (H = 4.0m, J_{re} = 500kN/m and s = 3.0m) 228

Figure 5.104 Pile group efficiencies (%) for a range of ORPLR (H = 4.0m, J_{re} = 500kN/m and s = 3.0m) 228
Figure 5.105 Strain in reinforcement and outer row pile and piled embankment Strain Compatibility Ratio (SCR) (%) for a range of ORPLR (H = 4.0m, J_{re} = 500kN/m and s = 3.0m) 229
Figure 5.106 Safety factor at failure for a range of ORPLR 230
Figure 6.1 Relationship of centrifuge and Plaxis 2D modelling of the lateral deformational response of the outer pile row. 233
Figure 6.2 Relationship of centrifuge and Plaxis 2D modelling of the lateral deformational response of the outer pile row for both Subsoil A and B. 234
Figure 6.3 Relationship of centrifuge and Plaxis 2D modelling of the lateral deformational response of the outer pile row for a range of side slope steepness. 234
Figure 6.4 Relationship of centrifuge and Plaxis 2D modelling of the lateral deformational response of the outer pile row for a range of ORPLR. 235
Figure 6.5 Relationship of centrifuge and Plaxis 2D modelling of the vertical deformational response of the geosynthetic reinforcement near the embankment toe. 236
Figure 6.6 Relationship of centrifuge and Plaxis 2D modelling of the vertical deformational response of the geosynthetic reinforcement for a range of side slope steepness. 237
Figure 6.7 Relationship of centrifuge and Plaxis 2D modelling of the vertical deformational response of the geosynthetic reinforcement for a variation of subsoil stiffness. 238
Figure 6.8 Relationship of centrifuge and Plaxis 2D modelling of the mean embankment surface deformational response of the geosynthetic reinforcement for a variation of ORPLR. 239

Figure 6.9 Relationship of centrifuge and Plaxis 2D modelling of the mean embankment surface deformational response of the geosynthetic reinforcement for a variation of Subsoil stiffness.....240
Figure 6.10 Relationship of centrifuge and Plaxis 2D modelling of the mean embankment surface deformational response of the geosynthetic reinforcement for a variation of ORPLR.....241
Figure 6.11 Lateral deformational response of the outer pile row for a range of parametric variations.....243
Figure 6.12 Lateral deformational response of the outer pile row for a range of parametric variations.....244
Figure 6.13 Vertical deformational response of the geosynthetic reinforcement for a range of parametric variations.....245
Figure 6.14 Vertical deformational response of the geosynthetic reinforcement for a range of parametric variations.....245
Figure 6.15 Maximum axial tension in the geosynthetic reinforcement for a range of parametric variations.....246
Figure 6.16 Maximum axial tension in the geosynthetic reinforcement for a range of parametric variations with H/(s-a) held constant.....247
Figure 6.17 Factor of safety of the overall GRPE for a range of parametric variations with H/(s-a) held constant.....248
Figure 6.18 Factor of safety of the overall GRPE for a range of parametric variations with H/(s-a) held constant.....249
Figure 6.19 Strain Compatibility Ratio (SCR) of the overall GRPE for a variation of H/(s-a) ratio.....251
Figure 6.20 Strain Compatibility Ratio (SCR) of the overall GRPE for a range of parametric variations with H/(s-a) held constant.....251
Figure 6.21 Strain Compatibility condition between reinforcement and pile group.....254
Figure 6.22 Tension developed in reinforcement for a range of embankment heights for Plaxis 2D and BS 8006 (2010) T_{ds} & T_{rp}.....255

Figure 6.23 Tension developed in reinforcement for a range of pile spacing (s) for Plaxis 2D and BS 8006 (2010) T_{ds} & T_{rp} 255
Figure 6.24 Tension developed in reinforcement for a range of pile cap size (a) for Plaxis 2D and BS 8006 (2010) T_{ds} & T_{rp} 256

NOTATION

Symbol	Meaning (common units)
a	Pile cap size (m)
a'_1	the interaction coefficient relating the soil/reinforcement bond angle to $tan\ \varphi'_{cv1}$ on one side of the reinforcement (-)
a'_2	is the interaction coefficient relating the soil/reinforcement bond angle to $tan\ \varphi'_{cv2}$ on the opposite side of the reinforcement (-)
A_c	Area of concrete (mm^2)
A_{sc}	Area of steel reinforcement (mm^2)
b	Width of the pile (m)
B	Maximum length of unsupported side slope past the outer pile row (m)
c	Soil cohesion (kN/m^2)
C_c	BS 8006 (2010) arching coefficient (-)
C_u	Coefficient of uniformity (-)
c_u	Undrained strength of the soft soil (kPa)
C_z	Coefficient of curvature (-)
d	Distance from the neutral axis (mm)
d	Width of the pile (m)
D	Depth below the ground level which the footing is founded (m)
e	Void ratio (-)
E	Young's modulus (kN/m^2)
E	Pile group efficacy (%)
E_{50}	Confining stress dependent stiffness modulus for primary loading

EA	Axial stiffness (kN)
E_c	Young's modulus of concrete (30 kN/mm^2)
E_{cap}	Efficacy at the pile cap (%)
E_{crown}	Efficacy at the crown of an arch (%)
EI	Flexural stiffness (kNm^2)
e_{max}	Maximum void ratio (-)
E_{min}	Minimum pile load efficacy (%)
e_{min}	Minimum void ratio (-)
E_p	Pile modulus of elasticity (kN/m^2)
EPS	Expanded polystyrene
E_s	Young's modulus of steel (kN/m^2)
E_{ur}	Elastic strain (%)
F	Factor of safety (-)
f_{cu}	Concrete cube strength at 28 days (N/m^2)
FDM	Finite Difference Method
FEM	Finite Element Method
f_{fs}	Partial load factor applied to the unit weight of soil (-)
f_{ms}	Partial material factor applied to tan φ'_{cv} (-)
f_{ms}	Partial load factor for applied external loads (-)
f_n	Partial factor for reinforcement sliding resistance (-)
f_p	Partial factor applied to the pull-out resistance of the reinforcement (-)
f_q	Partial load factor for the application of external loads (-)

f_s	Partial factor for reinforcement sliding resistance (-)
f_{sc}	Characteristic strength of reinforcement (N/mm^2)
g	Earth's gravity (m/s^2)
H	Height of the embankment (m)
h	Average height of the embankment fill above the reinforcement length L_e (m)
h_2	Pile half length (m)
I	Second moment of area (m^4)
I_p	Second moment of pile area (m^4)
J	Stiffness of the reinforcement (kN/m)
K	Maximum bending moment of a pile (kNm)
K_0	Coefficient of earth presure at rest (-)
K_a	Rankine's active earth pressure coefficient (-)
K_p	Rankine's coefficient of passive earth pressure (-)
K_R	Relative pile-soil stiffness ratio (-)
L_b	Reinforcement bond length needed beyond the outer row of piles across the width of the embankment (m)
l_e	Average element size (Plaxis 2D)
L_e	Minimum reinforcement bond length (m)
*M**	Bending moment acting on the pile (kNm)
M_c	Characteristic moment (kNm)
M_D	Factored distributing moment along the base of the embankment (kNm)
M_{max}	Maximum bending moment that the pile could resist (kNm)

$M_{recorded}$	Bending moment that the pile was subjected (kNm)
M_{RP}	Restoring moment due to the axial load in the piles (kNm)
M_{RR}	Restoring moment due to reinforcement (kNm)
M_{RS}	Restoring moment due to the soil (kNm)
n	Embankment side slope steepness (1 in n)
n	Modular ratio (-)
OCR	Over consolidation ratio (-)
p'	Mean effective stress (kN/m^2)
p'_0	Initial effective confining stress (kN/m^2)
P_a	Lateral earth pressure (kN/m^2)
P_c	Characteristic load (kN)
POP	Pre overburden pressure (kN/m^2)
q	Total load from the embankment (kN)
q_f	Ultimate bearing capacity (kN)
q_n	Net bearing pressure (kN/m^2)
q_o	Surcharge pressure acting on the soil surface (kN/m^2)
Q_p	Allowable load carrying capacity of each pile in the pile group (kN)
r	Effective radius of centrifuge model (m) (Taylor 1995)
r	Radius (m)
r'	Effective unit weight of sand, reinforcement (kN/m^3)
R_I	Moment of inertia ratio=ratio of moment of inertia of the pile to the moment of inertia on a solid circular cross section (-)
R_{inter}	Interface influence factor (-)

s	Centre to centre spacing of the pile (m)
S	Maximum pile spacing (m)
S_{3D}	Stress reduction ratio (-)
SCR	Strain Compatibility Ratio (-)
SL	Pile spacing in the longitudinal direction (m)
S_u	Undrained shear strength of clay (kN/m^2)
T	Tension in the reinforcement (kN/m)
T_{ds}	Tension in the reinforcement due to lateral sliding (kN/m)
T_{rp}	Tension in the reinforcement due to vertical loading (kN/m)
T_{Total}	Total load required to be resisted by the reinforcement (kN/m)
w_s	Uniformly distributed surcharge loading (kN/m^2)
W_T	Vertically distributed loading acting on the reinforcement (kN/m)
$x_{corrected}$	Correction applied to the horizontal measurement (-)
$y1$	Depth to the centre of the area from the top of the pile section (m)
$y_{corrected}$	Correction applied to the vertical measurement (-)
z	Vertical depth to earth pressure location (m)
β	Dimensionless parameter (-)
γ	Unit weight of soft soil (kN/m^3)
ε_{GG}	*Strain* in the reinforcement (%)
λ^*	Modified compression index (-)
v_{ur}	Poisson's ratio for unloading/reloading (default: v_{ur} = 0.15)
ρ_s	Particle density (kg/m^3)

$\sigma'_{h,o}$	Inital horizontal effective stress (kN/m^2)
σ_s	Pressure acting at the surface of the hemispherical dome (kN/m^2)
$\sigma'_{v,o}$	Initial vertical effective stress (kN/m^2)
$\varphi`_{cv}$	Largest strain angle of friction of the embankment fill under effective stress conditions (°)
φ'	Effective stress friction angle for sand (°)
κ^*	Modified swelling index (-)
α	Interaction coefficient relating the embankment fill/reinforcement bond angle to *tan* φ'_{cv} (-)
ν_c	Shear stress (N/mm^2)
K_0^{nc}	K_0 value associated with normally consolidated states of stress (-)
L_p	Horizontal distance between the outer edge of the pile cap (m)
$p`_c$	Vertical stress on the pile caps (kN/m^2)
ν_{ur}	Poisson's ratio (-)
ε_v	Volumetric strain (%)
ε_{vo}	Initial volumetric strain (%)
θ_p	Angle to the vertical between the shoulder of the embankment and the outer edge of the outer pile cap (°)
$\sigma`_v$	Average vertical stress at the base of the embankment (kN/m^2)
σ_{yy}^0	In-situ vertical effective stress (kN/m^2)
φ_{cv}	Critical state friction angle of the embankment fill (°)

Chapter 1

Introduction

1.1 Background

The presence of weak foundation soil poses a significant challenge to Geotechnical Engineers. The challenges encountered in the design of road/rail projects on weak foundations consist of bearing capacity, slope stability, consolidation, lateral pressures and differential settlements that require careful attention at the design stage.

Techniques such as deep mixing columns, stone columns, usage of lightweight fill (Rowe and Soderman,1985), lime stabilization and soil replacement are commonly used in challenging subsoil conditions (Gangakhedkar, 2004, Magnan, 2004). Whilst these techniques will enhance the weak foundation, their usage can be time consuming, expensive and in certain cases impractical. A piled embankment consists of piles, usually in a square grid (Kempfert, 2004), driven through the unsuitable foundation soil to a firm-bearing stratum (Farag, 2008), under the foot print of the embankment (Rowe & Li, 2002). Concrete pile caps are usually

constructed on top of the pile head. The benefits of a piled embankment structure are as follows:

- Construction of structures in a single stage without excessive waiting times (Han & Gabr, 2002)
- Reduction in earth pressures by the structure (Farag, 2008)
- Reduction in total and differential settlements (Han & Gabr, 2002)
- Avoid the need for soil excavation and refill (Love and Milligan, 2003)

The conventional pile supported system, Figure 1.1(a), requires large pile caps (Han, 1999) and very closely spaced piles, these two characteristics are essential to ensure the embankment load is carried by the piles and large differential settlements between the pile caps are avoided (Rathmayer, 1975). The conventional supported pile system also requires raked (inclined) piles at the outer row of pile to resist the lateral spreading force from the centreline of the embankment (Gangakhedkar, 2004).

Piled embankments that consist of a solid concrete slab, Figure 1.1(b), across the cross sectional width of the embankment upon the pile heads are the most successful in transferring all the embankment loads to the pile heads (Gangakhedkar, 2004). Such structures require large amounts of steel as reinforcement or very thick concrete slabs thus making such structures uneconomical and rarely used in practice.

Geosynthetic reinforced piled embankments (GRPS), Figure 1.1(c), are becoming increasingly popular. The GRPS system utilizes geosynthetic reinforcement with high tensile properties, to span the clear distance between adjacent pile caps and results in an increase in the efficiency of the load transfer from the soil to the pile cap. The high tensile properties of the reinforcement enables the piles to be moderately spaced apart in a square grid pattern whilst the embankment load is still transferred to the pile caps without the presence of excessive differential settlements (Kempfert et al., 1997). The geosynthetic reinforcement also provides lateral restraint to the embankment fill above the reinforcement (Rowe and Li, 2002).

The geosynthetic reinforced piled embankment does not require excessively large pile cap sizes and closely spaced piles or an expensive solid concrete slab (Han, 1999). The GPRS system enables the construction and life span performance advantages of a pile embankment to be achieved with the most efficient usage of materials, labour and time.

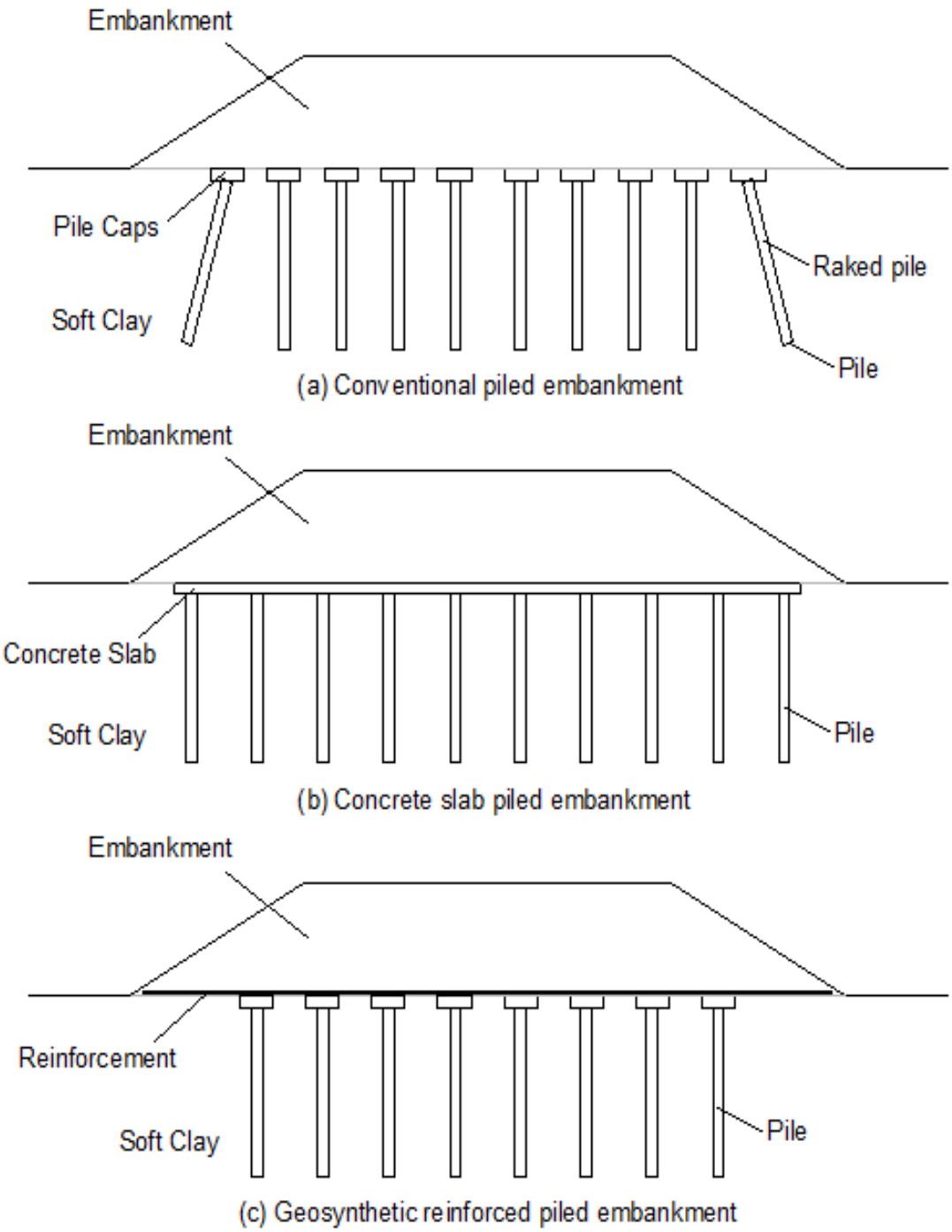

Figure 1.1 Various forms of pile embankment system

1.2 Statement of the problem

The design of piled embankments is a complex soil-structure interaction problem involving embankment fill, geosynthetic reinforcement, a pile group and the soft underlying soil (Love & Milligan, 2003).

Underneath the side slope of an embankment, the embankment fill is subjected to lateral stresses due to the horizontal spreading effect of the slope (Rowe & Li, 2002), Figure 1.2. The magnitude of the spreading effect is assumed equal to the active earth pressure at the bottom of the embankment height directly underneath the crest of the embankment. The lateral thrust influences the stability of the structure and may possibly exert a lateral load on the pile cap resulting in a lateral deflection at the pile head (Farag, 2008).

In designing a piled embankment both vertical and horizontal equilibrium must be achieved. The internal horizontal (lateral) forces from the embankment fill acting outwards needs to be balanced by a combination of tension in the horizontal geosynthetic reinforcement, lateral loads on the pile group and resistance from the soft soil. In addition to equilibrium considerations, strain compatibility between the displacement of the geosynthetic reinforcement, the pile group and the soft soil must be achieved (Love & Milligan, 2003).

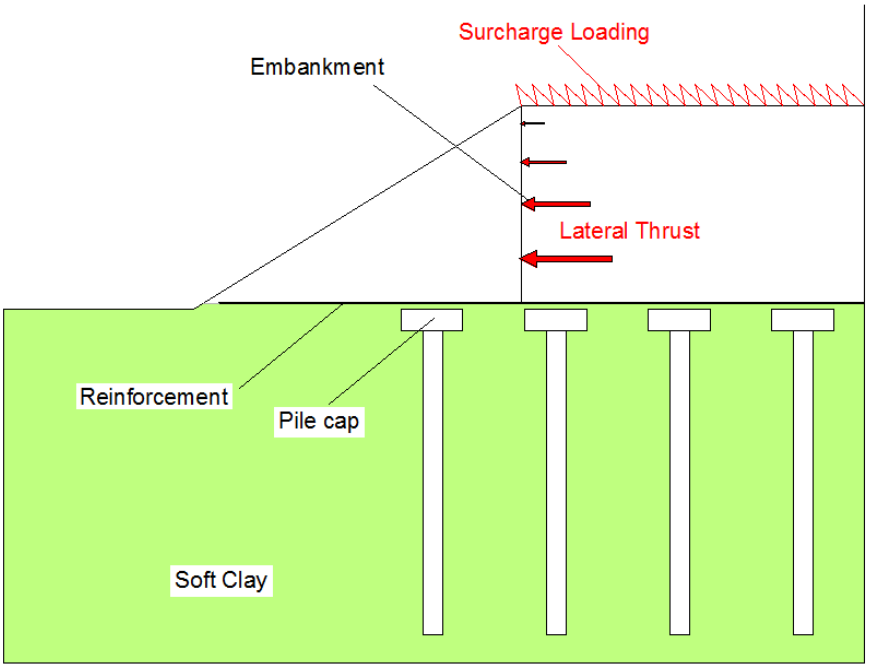

Figure 1.2 Lateral thrust within a reinforced embankment

Current design approaches (BS 8006, 2010; Russell et al*.,* 2003; Kempfert *et al.* 2004), while identifying the problem of lateral loadings at the outer extremities of the embankment, do not suggest methods for quantifying either the magnitude of horizontal equilibrium or strain compatibility under the embankment.

BS 8006 (2010) assumes that the lateral thrust is resisted solely by the geosynthetic reinforcement placed at the base of the embankment directly over the pile caps. The BS 8006 (2010) limit equilibrium approach requires that strain compatibility is achieved between the deformations of the geosynthetic, movement of the embankment fill and deflection of the pile cap.

This study examined the performance of geosynthetic reinforced piled embankments, through a numerical and physical analysis approach. The effects of certain pertinent factors; the pile spacing, pile cap size, stiffness of the geosynthetic reinforcement, height of the embankment and the effect of the soft soil layer under the embankment were investigated.

1.3 Research options

Earlier research (Han, 2002; Low et al., 1994; van Eekelen et al., 2010; Chen, 2008a & b; Ellis and Aslam, 2009a & b; Britton & Naughton, 2008a & b) in the area of reinforced piled embankments have been focused to understand arching, load transfer and differential settlements at the pile head elevation and the embankment surface. The research consisted of both numerical and physical analyses.

Previous numerical research on reinforced piled embankments focused on the mechanisms, deformations and loadings present at the embankment centre (Han, 2002; Kempton et al, 1998). Conditions at the outer extremities of the reinforced piled embankment with specific reference to the effects of the lateral thrust from the embankment fill were not discussed in previous studies. Previous research investigated the effects of lateral loading on stone encased columns (Farag 2008) using finite element modelling. Whilst the study examined the effect of lateral thrust from the embankment on the stone encased columns, the scope of the study is dissimilar to the problem examined here as the behaviour of stone columns is considerably different to rigid concrete piles.

Numerical ‘‘experiments’’ or simulations by means of appropriate methods such as finite-element (FE) or finite-difference (FD) techniques (e.g. Ho and Rowe, 1994) is essentially required. In general, two-dimensional (2D) analysis can be categorized into two types: (1) 2D plane stress which is usually applied to the stress analysis of a thin plate structure by assuming the stress in the direction perpendicular to the plate is equal to zero and (2) 2D plane strain which is defined as the strain state in the direction perpendicular to the plane being equal to zero. Most researches assumed plane strain condition for numerical simulations of reinforced earth structures (Chai, 1992, Chai and Bergado, 1993a & b; Bergado et al., 1995, 2003; Karpurapu and Bathurst, 1995; Alfaro et al., 1997; Chai et al., 1997; Rowe and Ho, 1998; Rowe and Li, 2002; Zdravkovic et al., 2002; Hinchberger and Rowe, 2003).

Many studies attempted to conduct 3D FE analyses while investigating the behaviour of embankments (Bergado & Teerwattanasuk, 2007; Smith and Su, 1997; Briaud and Lim, 1999; Auvinet and Gonzalez, 2000; Smith and Su, 1997) summarized that the 3D FE analysis can be used successfully to model the reinforced soil embankment under service loading and at collapse successfully. Auvinet and Gonzalez (2000) recommended that a 3D analysis must be considered under the following conditions: (a) in the case of short slopes of which boundary conditions cannot be ignored, such as earth dams built in a narrow valley or embankment at the bridge approach, (b) when soil properties vary significantly along the longitudinal direction of the slope or embankment, (c) when the slope is subjected to concentrated loading and (d) when the potential failure is irregular.

Previous research workers have used physical models or full scale field tests (Ellis and Aslam, 2009a & b; van Eekelen, 2010). The behaviour of the physical models was monitored to reveal the various behavioural mechanisms which enabled suitable design guidance to be codified. To date there has been no full scale field study of the particular problem modelled here, mainly due to the additional constraints of construction within tight budgets and schedules. Since a large variation in field conditions is common, it is more practical to have a controlled study in which foundation geometry, pile spacing and the pile group effects may be varied within the framework of a known stress history with more predicable estimates of soil strength.

While this can be accomplished at model scale in a conventional laboratory, where the testing procedure is relatively quick and cheap there are anomalies (Springman, 1989). The behaviour of a soil is stress dependent and as such it is not possible to account properly for the in-situ stress conditions.

Centrifuge modelling, in which scaled down replicas simulate the same stress strain conditions of a full scale prototype is an attractive research option. The advantage of this technique is that small 1/*n* scale samples may be rotated at sufficient speed in a centrifuge facility to impose an enhanced gravitational field, *ng*, on the sample. The imposition of an enhanced gravity field recreates the field conditions of stress and strain expected in full scale prototype tests (Taylor, 1995). It is important to achieve correct modelling similarity when dealing with the interaction of the complex strain fields surrounding a pile which is actively loaded by the soil. Also, consolidation time is reduced by n^2 with the advantage of saving time and money (Taylor, 1995).

Soil models with similar properties, strengths and stress histories may be reproduced and greater control may be exerted during the entire test. The fixing of piles and the geometry of the foundation may be predetermined to suit the problem under investigation. Models may be prepared at a considerable lower cost than in the field, and they may be tested to the limit without the full scale consequences of danger to life and facilities (Taylor, 1995).

Appropriate adjustments may be made, in stages, to the design of the centrifuge model tests to isolate particular areas of interest in a complex problem, so that a complete understanding of the mechanism may be reached (Taylor, 1995). Inevitably there are some disadvantages, and the errors induced by testing in this way (scaling and model installation errors).

1.4 Aims and Objectives

The foremost aim of the research reported in this dissertation was to study the effects of lateral loading on pile embankments specifically near the side slopes constructed on a layer of soft subsoil. The research determines the pertinent factors that influence the lateral loading mechanism within a piled embankment to combat

the lack of knowledge on the influence of lateral loading on pile groups under geosynthetic reinforced piled embankments.

The principle aims and objectives of this study were to:

i.) Design and conduct centrifuge model tests of piled embankments, giving scaled up data for an equivalent prototype with various foundation geometries, embankment heights, side slope steepness and soft subsoil stiffnesses.

ii.) Calibrate the centrifuge model test performance by equivalent site specific finite element analysis and to yield more information about the pile-soil-embankment lateral loading specific interaction.

iii.) Assess the horizontal equilibrium and strain compatibility at the extremities of a piled embankment.

iv.) Assess the lateral load on piles groups and the resistance required to prevent excessive deformations or excessive loading of the piles.

v.) Conduct numerical analysis of the stress and displacements of pile groups at the extremities of a piled embankment.

vi.) Examine the relationship between the geosynthetic reinforcement and lateral disturbing forces in the embankment under a variation of structural morphology.

vii.) Analysis of the stability of the reinforced piled embankments system.

viii.) Characterize the subsoil properties, pile types and geometry, geosynthetic reinforcement properties and the embankment geometry typically encountered in piled embankments.

1.5 Layout of thesis

In Chapter 2 a review of the literature and state of the art on piled embankments is presented. Particular attention was focused on the lateral loading conditions in some of the key piled embankment physical and numerical modelling studies.

Chapter 3 explains the methodology of the centrifuge testing and numerical analyses undertaken in this study. The engineering properties of the materials used in the experimental and numerical studies are also presented.

The results of the centrifuge testing and numerical analyses are presented in Chapter 4, with some preliminary analysis and discussion.

The results of additional numerical analyses are presented in Chapter 5 with some preliminary analyses and discussion.

The significance of the results of this study are discussed in Chapter 6 and conclusions of the study and recommendations for further research are presented in Chapter 7.

Chapter 2

Literature review

2.1 Introduction

At the extremities of the embankment both horizontal equilibrium and strain compatibility between the different components; the embankment fill, the geosynthetic reinforcement, the pile group and the soft soil, must be achieved (Love & Milligan, 2003). This chapter presents the current knowledge of the lateral loading on piled embankments by examination of the lateral loading effects on each of the reinforced piled embankments in the following sequence:

1. Lateral forces within the embankment
2. Geosynthetic reinforcement
3. Lateral loading on the pile group

2.2 Lateral forces within the embankment

The embankment fill is subjected to vertical and horizontal loading. The horizontal component of the loading is a combination of the spreading effect of the partial transfer of the surcharge loading effect from the trafficked loads and the horizontal

earth pressure from the fill material itself (Figure 2.1). The lateral thrust results in horizontal deformation within the embankment structure in the direction towards the toe of the embankment. Excessive horizontal deformation will result in vertical deformation at the surface of the embankment which may lead to serviceability concerns of the structure (Jennings and Naughton, 2010).

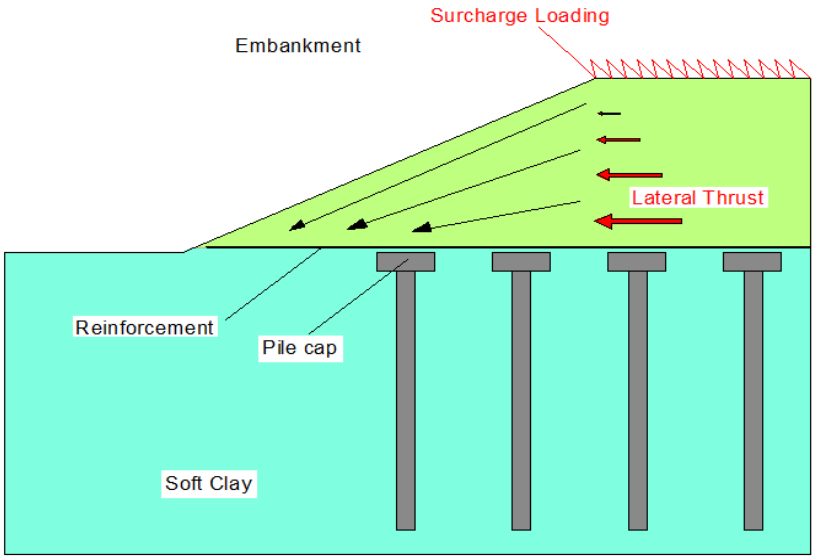

Figure 2.1 Illustration of the lateral forces within an embankment

Kempfert et al (1997) and Love and Milligan (2003) concluded the lateral forces must be transferred to the geosynthetic reinforcement at the base of the embankment where the reinforcement/pile/soil interaction would provide resistance against the embankment sliding. The lateral thrust acting outward within the embankment structure develops shear stresses at the embankment base (Rowe and Li, 2002). The inclusion of geosynthetic reinforcement at the base of the embankment resists the lateral thrust and prevents horizontal displacement within the structure.

The estimation of the lateral earth pressures is possible by a number of methods. The German recommendation EBGEO (2007) defines the lateral spreading effect as the lateral force resulting from the horizontal active pressure that acts from the surface of the embankment to the top of the reinforcement (i.e. height above reinforcement). The German EBGEO (2007) active earth pressure estimation is a function of the height of the embankment and the active earth pressure coefficient K_{ah}. The British Standard BS8006 (2010) considers the lateral force as an ultimate limit state and thus applies partial load factors to the calculation. BS 8006 (2010)

stated that the bond between the fill material and the geosynthetic reinforcement must be adequate to generate the limit state tensile force in order to prevent horizontal sliding/deformation.

Methods such as Rendulic (1938) can be used in the estimation of the active earth pressure for cohesionless soils and the method specified by Rankine (1857) for cohesive soils. According to Rendulic (1938) the lateral earth pressure at any depth z (Figure 2.2) can be given as:

$$P_a = Kz\gamma - \frac{3}{2H}(K - K_a)z^2\gamma \qquad \text{Equation 2.1}$$

where

P_a is the lateral earth pressure

K is the maximum bending moment of a pile

γ the unit weight of the soil

z is the vertical depth to earth pressure location

K_a Rankine's active earth pressure coefficient = $\tan^2(45 - \varphi/2)$

The total horizontal active earth pressure (similar to Rankine's) can be approximated by:

$$P_a = \frac{1}{2}K_a\gamma H^2 \qquad \text{Equation 2.2}$$

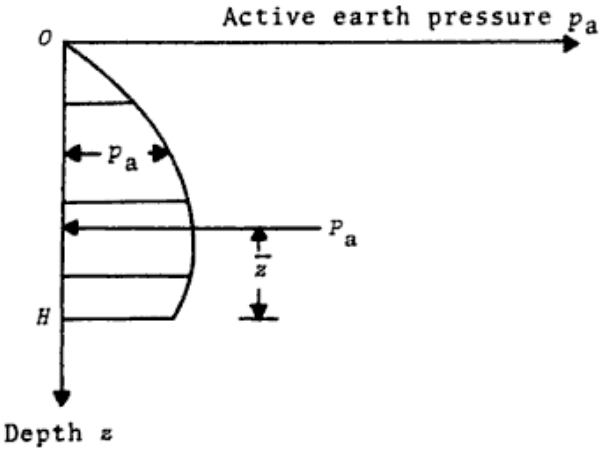

Figure 2.2 Rendulic's approximation (1938) for lateral earth pressure

The spreading forces generated at the base of the embankment in the slope zone are related to the horizontal pressures. For the Rankine case the active earth pressure force acts parallel to the base of the embankment. The active earth pressure force due to cohesion c' is developed by Rankine as:

$$\sigma_h' = \left(\sigma_v' K_a - 2c'\sqrt{K_a}\right) \qquad \text{Equation 2.3}$$

$$P_a = \left(\sigma_v' K_a - 2c'\sqrt{K_a}\right)H \qquad \text{Equation 2.4}$$

2.3 Geosynthetic reinforcement

The primary purpose of the geosynthetic reinforcement is to resist the lateral sliding of the embankment fill and transfer the vertical embankment and surcharge loads to the pile. The precise mechanism by which load is transferred to the reinforcement remains poorly understood (Love and Milligan, 2003). The geosynthetic reinforcement is required to resist/transfer loading in two components;

1. Horizontal loading on geosynthetic reinforcement
2. Vertical loading on geosynthetic reinforcement

The tension developed in the geosynthetic reinforcement due to the spreading effect and the membrane or arching effect in the reinforcement has been examined by a number of studies (Farag, 2008; Gangakhedkar, 2004). The design approach adopted by BS8006 (2010) and EBGEO (2007) are the most commonly used in design.

2.3.1 Horizontal loading on geosynthetic reinforcement

The reinforcement must resist the horizontal force due to lateral sliding (spreading effect). To resist this horizontal force the geosynthetic reinforcement must generate the tensile load, $T_{ds,}$ (Figure 2.8) over a minimum reinforcement length, $L_{e,}$ (bond length, Figure 2.8). By having a minimum bond length the reinforcement has an adequate length to develop the shear stresses within the embankment fill to generate the required tension T_{ds} to prevent sliding. This tensile force must achieve

strain compatibility with allowable lateral pile movements. Enabling the reinforcement to transfer some of the lateral loading to the pile heads eliminates the need for raked piles at the outer extremities of the pile group.

The reinforcement develops the required tensile force, by mobilizing shear stresses between the reinforcement and the base of the fill from the lateral force from the embankment fill due to active earth pressure (Rowe and Li, 2002). The influence on the interaction of the soil and the geosynthetic reinforcement is generally dependent on two components, bond and sliding resistance. The more important of these is the bond between the reinforcement and the soil, which is reliant upon the friction between the reinforcement and the soil, and is greatly influenced by particularly wide structures (Terram, 2000). An adequacy check for bond is required for a structure that has a potential failure surface intersecting the reinforcement plane. A check on the sliding resistance is required when the failure surface coincides with the reinforcement. The inclusion of a layer of geosynthetic reinforcement in a soil structure effectively leads to a reduction in the overall resistance to the soil spreading outwards from the centreline of the embankment structure and thus an improvement in stability (Terram, 2000).

According to EBGEO (2007) the membrane force in the reinforcement depends mainly on the parameters of the foundation soil such as the stiffness and the depth of the soft underlying soil. The horizontal outward thrust of the embankment fill is resisted by the reinforcement and the base friction between the subsoil and the reinforcement which mainly depends on the friction parameters of the subsoil (c, φ). The horizontal active earth pressure at the slope crest causes a tensile force in the geosynthetic and is added to the membrane force. According to EBGEO (2007) the total tensile force in the geosynthetic reinforcement is defined as the force at the limit state that includes the tensile force due to the membrane effect and spreading effect. Love et al. (2003) recommended taking one or the other of these forces, whichever is biggest.

2.3.2 Vertical loading on geosynthetic reinforcement

The vertical loading on the geosynthetic (membrane effect) is directly due to the embankment weight and surcharge loading above the reinforcement. The

magnitude of loading on the reinforcement reduces as the effectiveness of arching increases within the embankment for a given height.

During and particularly after construction of the reinforced piled embankment, the soft soil underneath the embankment structure consolidates, resulting in differential settlements between the top of the pile cap and the fill material above the clear span between the piles. These differential settlements mobilise shear stresses within the embankment fill and transfer the vertical loading from the embankment fill onto the pile caps. The transfer of vertical loads to the pile caps by this mechanism is known as arching (McNulty, 1965).

The theoretical loading carried by the geosynthetic reinforcement is the magnitude of the total loading from the embankment weight and surcharge loading minus the loading transferred by the arching mechanism. This theory in BS8006 (2010) is based on the assumption that the geosynthetic reinforcement receives no supported from the soft soil. The degree of arching will increase within the embankment after completion of the construction stage (unless staged construction is undertaken) (van Eekelen *et al.*, 2010).

Most current reinforced piled embankments design methods are based on the assumption that the soft soil underlying the foundation offers no support to the structure, however, EBGEO (2007) does allow soft soil support. Ignoring soft soil support results in a conservative design (Kempton et al., 1996; Russell et al., 2003; Jennings & Naughton, 2010; van Eekelen et al., 2010). BS8006 (2010) states that any subsoil support to be considered needs to be available for the design life of the structure, which is typically 120 years.

The soft soil layer beneath the embankment, although deficient in its ability to provide significant structural support, will in practice provide some support to the geosynthetic reinforcement (Love & Milligan, 2003). This may significantly reduce the magnitude of the tension in the reinforcement. Previous studies (Reid and Buchman, 1984; Russell and Pierpoint, 1997) found that the soft soil offers support to the underside of the reinforcement approximately equal to $0.18\gamma H$ where γ is the unit weight of the soil and H is the height of the embankment fill. A similar study (John, 1987, after Han, 2003) found the soil resistance to be $0.15\gamma H$. Finite element analysis by Jones et al (1990), Figure 2.3, showed that the tension

developed in the reinforcement due to the vertical loading was reduced as the support of the soft soil increased. In the construction of a reinforced piled embankment on very soft soil where the settlement/consolidation of the soft soil below the reinforcement results in a separation of the underside of the reinforcement and the top of the soft soil/piling platform, it seems reasonable to consider a cavity below the structure, which is the approach used in BS8006 (2010).

Ellis and Aslam (2008 and 2009) suggested large differential settlements and low efficacy values were observed at lower embankment height to clear spacing between piles ratio indicating a poor arch formation, whereas higher ratios yielded higher efficacy values with the fill surface remaining relatively even for both the reinforced and unreinforced case.

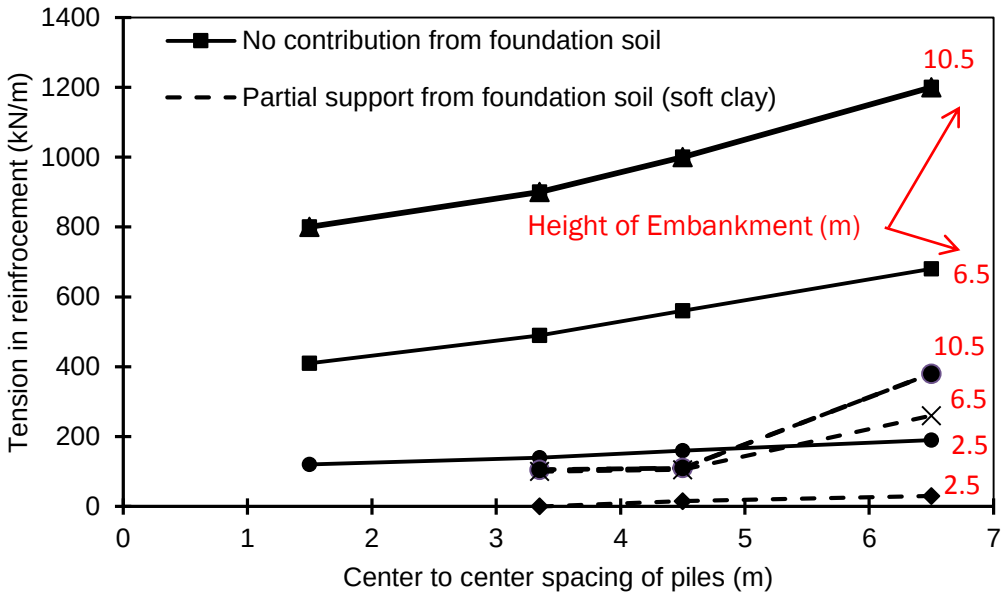

Figure 2.3 Tensile forces in the reinforcement under embankment of medium dense soil (Jones et al., 1990)

2.3.3 Design of geosynthetic reinforcement

The total load required to be resisted by the reinforcement (T_{Total}) is defined by BS 8006 (2010) as the sum of the reinforcement due to lateral sliding (T_{ds}) and the tension due to vertical loading (T_{rp}).

$$T_{Total} = T_{ds} + T_{rp} \qquad \text{Equation 2.5}$$

Love and Milligan (2003) suggested the reinforcement should be designed for whichever tension is greater (T_{rp} or T_{ds}), but not the summation of the forces. Love and Milligan (2003) also stated that the system will adjust by the piles moving to reach horizontal equilibrium. If the tension to resist sliding is greater and is used for design, this will result in the piles moving laterally outwards from the centreline of the embankment, resulting in the geosynthetic reinforcement being pulled outward and tightening of the membrane between the piles will occur.

Love and Milligan (2003) also suggested that the piles should be spaced a sufficient distance apart to ensure the piles deflect as little as possible to resist the lateral thrust of the embankment. This would enable the required tension in the reinforcement to be developed by the vertical sagging of the reinforcement rather than being mobilised by the lateral sliding force of the embankment above.

2.4 Lateral loading on the piles

The primary objective of the inclusion of piles in the reinforced piled embankment structure is to transfer the loading from the embankment to the firm bearing stratum under the soft soil layer. The piles must however also withstand any bending stresses induced by the lateral earth pressure of the embankment and provide stability to the structure.

2.4.1 Loading exerted on the piles

Lateral loading is described as “active” when it is applied to a pile by an external means, causing the pile to load the soil. “Passive” loading is exerted when movement of the soil subjects the pile to a lateral thrust and the associated bending stresses. In the context of this study, active loading is applied to the pile from the lateral thrust of the embankment fill. Passive loading can be exerted on the pile due to the deformation of the soil between adjacent piles.

The lateral thrust due to the active earth pressure results in lateral deflections at the pile head, inducing possible bending moments within the pile. The magnitude of the bending moment induced is directly related to the support offered by the soil along the shaft length of the pile. The greater the stiffness of the pile soil interaction, the lower the magnitude of the bending moment induced in the pile (Jennings and Naughton, 2010).

The vertical loading from the embankment is transferred on to the pile head at the pile cap. Han (1999) found that the percentage coverage for a conventional piled embankment of pile caps over the total foundation area is 60-70%, whereas for a reinforced piled embankment the percentage area drops to 10-20% (Rathmayer, 1975; Lin and Wong, 1999; Tsukada, *et al*., 1993). The ability to use smaller pile caps offers a significant economic advantage.

The load carrying capacity of the pile is required to ensure the structural stability of the embankment structure is not undermined. The maximum allowable pile spacing between adjacent piles is determined from the maximum axial load capacity of a single pile. To determine the maximum allowable pile spacing, the approach adopted by BS8006 (2010), consists of multiplying the loading from the embankment weight and adding it to the surcharge load divided by the axial load capacity of a single pile.

BS8006 (2010) states that the lateral thrust of the embankment should not result in excessive settlement/deformations within the side slopes of reinforced piled embankments; the piles are required to extend a distance to resist these disturbing forces and to ensure that differential movement/settlement or instability of the fill at the outer extremities does not affect the embankment crest. This distance is called the pile group extent (L_p) in BS8006 (2010).

Typically, a pile group refers to a group of piles that are connected at the pile head by a single large concrete pile cap which offers fixity against rotation at the pie head. The pile group considered in this study, consists of a number of piles with pile caps that are not interconnected (no moment restraint at the pile head) Figure 2.5. BS 8006 (2010) actually refers to the collection of piles with pile caps that are not interconnected as a ''pile group''. The studies presented in this section on pile group interaction effects are based on pile groups with a single pile cap spanning across the whole pile group extents. Currently, there is a lack of information on the interaction effects between closely spaced piles that are not connected together at the pile head. Therefore, established observations regarding ''group effects'' may not be directly applicable.

Lateral movements of the piles are seen when an embankment load is applied (Jennings and Naughton, 2010). Significant lateral deflection is undesirable for the

piles in the GRPS system as it can result in excessive settlements in the system and can prove to be more critical than vertical settlements. The foundations or structures in the adjacent areas can be greatly affected by these resultant lateral movements. Current design methods (BS 8006, 2010 and EBGEO, 2007) do not provide suitable procedures to estimate the lateral movement of geosynthetic reinforced pile supported embankments. Initial predictive methods should be used to determine lateral ground movements. The design method used will depend on the sensitivity of the structure to the soil movements. Seaman (1994) (after Li et al., 2002) investigated the effects of various factors on lateral movements. The following factors tend to increase the lateral movements in piled embankments:

- Vertical stress applied on the soil due to the embankment fill
- Length of the embankment
- Width of the embankment
- Embankment slope
- Poisson's ratio of the soil

Seaman (1994) also states that increases of certain structural characteristic factors tend to decrease the lateral movements were:

- Thickness and stiffness of the fill
- The distance from the embankment toe
- Stiffness of the soil
- Strength of the soil
- Adhesion between the soil and the fill

Since the pile is always found within a group, interaction effects between each pile within the pile group becomes important on the overall performance of the pile group (Zhang et al., 1999; Patra & Pise, 2001; Zhang, 2003; Ashour *et al.*. 2004; Rollins *et al.,* 2005 & 2006 and Chandrasekaran et al., 2009). As the closely spaced piles move laterally due to active loading from the embankment structure, the failure zones for front or trailing rows piles overlap with leading row piles and

decrease lateral resistance as shown in Figure 2.4. The tendency for a pile in a trailing row to exhibit less lateral resistance due to location behind another pile is commonly referred to as pile-soil-pile interaction or the group interaction effect (shadowing) (Abbas, 2010). Group interaction effects would be expected to become less significant as the spacing between piles increased as the overlapping of adjacent pile stress zones diminishes (Abbas, 2010).

Rollins et al. (2006) commented that due to the high cost and logistical difficulty of conducting lateral load tests on pile groups, relatively few full-scale load test results are available that show the distribution of load within a pile group (Brown et al, 1987; Brown et al, 1988; Meimon et al, 1986; Rollins et al, 1998; Ruesta and Townsend, 1997). The results from these studies indicate that the average load for a pile in a closely spaced group (spacing of 3 pile diameters) will be substantially less than that for a single isolated pile at the same deflection and that leading row piles in the group will carry significantly higher loads than trailing row piles at the same deflection.

The piles in trailing rows are thought to exhibit less lateral resistance because of interference (shadowing) with the failure surface of the row of piles in front of them. This shadowing or group interaction effect is expected to become less significant as the spacing between piles increases because there is less overlap between adjacent failure planes. Unfortunately, there is currently significant variation in the recommendations from various agencies and researchers as to the appropriate adjustment factors to account for this reduction in resistance with variation in pile spacing (AASHTO, 2000; US Army, 1993; Reese and Van Impe, 2001).

In addition, there is uncertainty about whether the reduction factors for group interaction developed from tests on pile groups with three or less rows will be appropriate for subsequent rows in a large pile group or whether the reduction factors will continue to gradually decrease with each additional trailing row as observed for the second and third rows (Abbas, 2010). Recent centrifuge test results in sands (McVay et al, 1998) suggest that reduction factors may stabilize for greater numbers of rows; however, no test results are yet available for clays. Soft clays are most often the foundation soil for piled embankments.

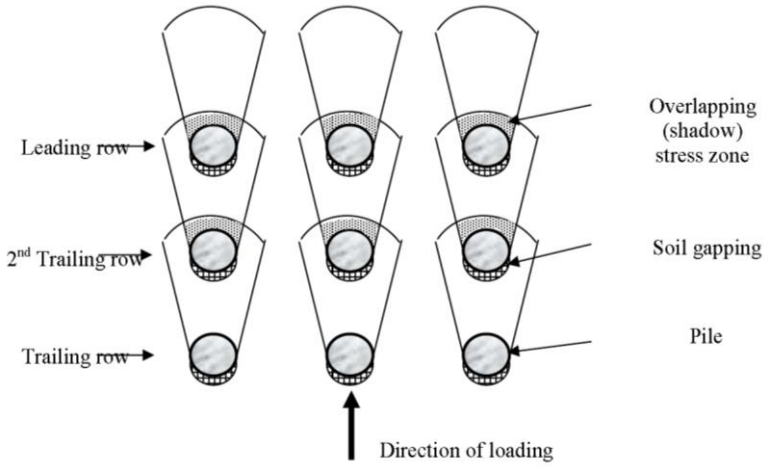

Figure 2.4: Illustrated of reduction in lateral pile resistance due to pile-pile interface under active loading conditions (Rollins et al. 1998 and Ashour et al. 2004, after Abbas et al. 2010)

2.4.2 Failure mode of piles

The failure mode of a pile subjected to active lateral loading is conditioned by the relative pile soil stiffness and the length of the pile. Since laterally loaded piles are transversely loaded, the pile may rotate, bend or translate (Fleming et al. 1992, Salgado 2008). For piles that are short in length, the pile will rotate about a point of zero deflection, Figure 2.5(a), or undergo translation, Figure 2.5(c). For long flexible piles in relatively soft soil, either a pile hinge will develop at the depth of the maximum bending moment or the soil will fail in front of (active loading) or around the pile (passive loading), Figure 2.5b, d & e.

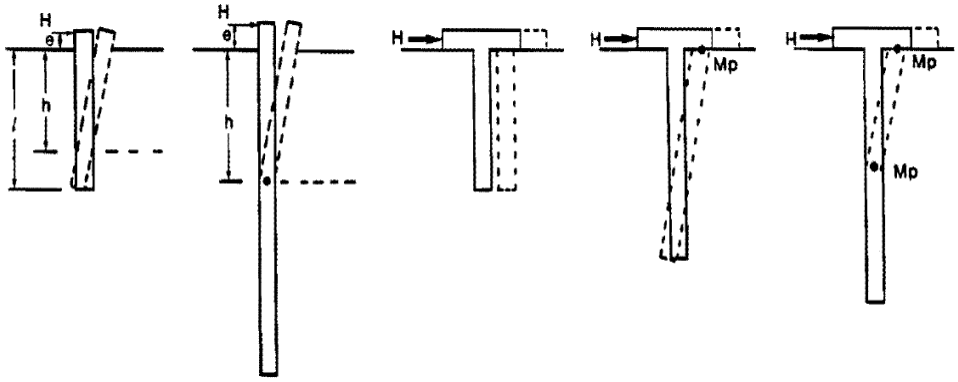

Free headed Fixed headed

(a) Short pile (b) Long pile (c) No hinge (d) 1 hinge (e) 2 hinges

Figure 2.5: Failure modes for laterally loaded piles (Fleming et al, 1985)

2.4.3 Design of laterally loaded piles

Whilst none of the existing design methods for pile group design can be considered well established, the main restraint has been the lack of reliable data from instrumented full scale trials in which to compare the proposed methods. The methods discussed (Winkler, 1867; Goh et al, 1997; Poulos, 1971; Evans and Duncan, 1982; Focht & Koch, 1973; O'Neill and Dunnavant, 1985) in this section range from the simple static design to comprehensive analytical methods which take account of soil structure interaction.

2.4.3.1 Simple static method

For simple cases of identical piles and structure minor in size and loading, where lateral loads are small, a straightforward resolution of the forces within the structure may be adequate (Springman, 1989). Despite the lack of sophistication of the method, it is normally limited to cases where the actual lateral load is less than 10% of the vertical load (Springman, 1989). The piles are assumed to be simple in-jointed at the pile cap, and to act as axially loaded columns. The forces in individual piles are calculated by resolving forces or by constructing polygon forces. Simple statics cannot be used if the group contains more than three rows of piles with different rakes. It is vital that the deformation of the group is within acceptable limits (Springman, 1989). The allowable load on each pile must not be exceeded. These methods do not take into account the lateral restraint offered by the soil. Consequently, calculated deformations of the pile group cannot be expected to be accurate.

2.4.3.2 Subgrade reaction method

One of the original ways in which the response of piles to lateral loads was modelled was described by Winkler (1867). Winkler replaced the horizontal resistance of the soil by a series of springs of appropriate stiffness, where $p=ky$, with subgrade reaction modulus, k, and the lateral pile movement y. Matlock & Reese (1960) developed the methods to give the bending moment, shear force and deflection down the pile for constant k with depth.

Experience and empirical correlations are readily available for the subgrade reaction method and so it remains popular (Rollins et al, 1998). Non-linearities in foundation strength, stiffness and composition are adjusted for by changing the

value or gradient of k with depth. Transfer of shear stress between the soil and the pile is not possible and the discrete springs fail to allow for additional displacements caused by stress cycling elsewhere

2.4.3.3 Goh et al. (1997)

The preliminary empirical estimation of the bending moment of a single pile was developed by Goh et al (1997) to study the behaviour of the lateral movement of a single pile. The piles are represented by beams to study the bending moments and the lateral movement. Hyperbolic soil springs are used to denote the soil-pile interaction. Goh et al (1997) developed charts from experimental data, Figure 2.6. Empirical relations can be used for preliminary estimation of the bending moment induced in the piles located near the toe of the embankment and restrained from rotating at the pile head. The equations developed to calculate the bending moment were as follows:

$$M^* = \frac{M_{max}}{c_u d h_2^2} \qquad \text{Equation 2.6}$$

$$\text{Or} \quad M^* = \lambda exp\left[\beta\left(\frac{q}{c_u}\right)\right] \qquad \text{Equation 2.7}$$

where

M_{max} is the maximum bending moment of a pile

M^* is the bending moment acting on the pile

d is the width of the pile

c_u the undrained strength of the soft soil

q the total load from the embankment

λ dimensionless parameter

β dimensionless parameter

h_2 pile half length

λ and β are constants depending on the relative pile-soil stiffness ratio K_R as shown in Figure 2.6 (a) and (b) below.

$$\lambda = 1.88(K_R)^{0.5} \qquad \text{Equation 2.8}$$

$$\beta = 0.18(K_R)^{-0.1} \qquad \text{Equation 2.9}$$

$$K_R = \frac{E_p I_p}{E_{50} h_2^4} \qquad \text{Equation 2.10}$$

where

E_p modulus of elasticity of pile

I_p second moment of pile area

E_{50} confining stress dependent stiffness modulus for primary loading

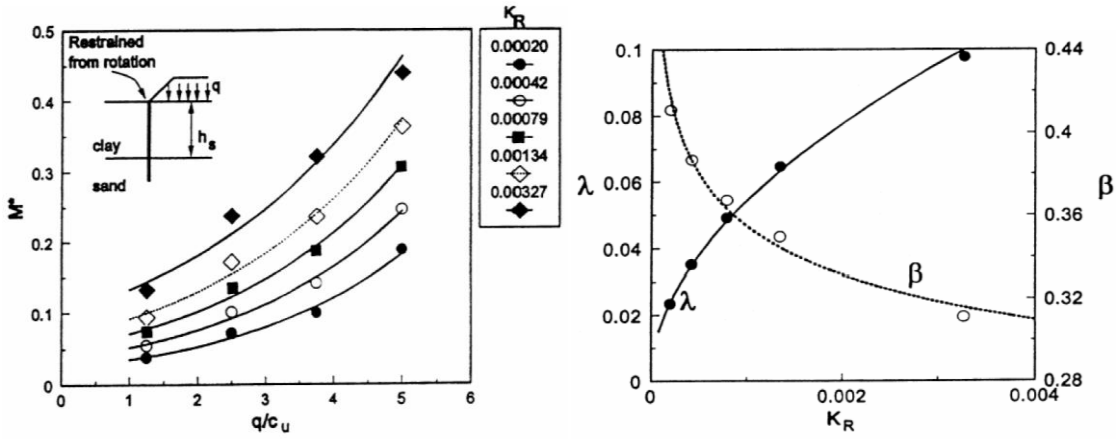

(a) (b)

Figure 2.6 (a) Dimensionless plot of M versus (q/c_u), (b) Values of λ and β*

2.4.3.4 Elastic continuum method

The elastic continuum method offers an approach which can be modified for group effects Poulos (1971), battered piles and yielding of the soil at a specified limit pressure. The soil modulus may be varied with depth to achieve a complete picture of the pile behaviour. The ability to vary the soil modulus is particularly useful for

cases in which the stress range may be described as elastic and for which an appropriate secant modulus can be selected.

Poulos (1971) described a method in which the horizontal displacements in an isotropic elastic continuum created by a horizontal point load are calculated according to Mindlins (1936) solution. The piles are modelled in elements as thin strips of constant stiffness, and the resulting integral equations based on the flexural bending of a thin beam are solved numerically for the relevant boundary conditions using finite difference techniques.

Banjerjee & Driscoll (1976) proposed a development of the boundary element model by adding a uniform distribution of shear stress around the pile for homogeneous soils. Banjerjee & Davies (1978) constructed an approximate point force solution for non-homogeneous soils in which soil modulus increases linearly with depth.

2.4.3.5 Characteristic load method

Evans and Duncan (1982) and Duncan et al. (1992) proposed characteristic load method (CLM), which closely approximates the results of nonlinear p-y analyses, and this method obtains results more quickly. This method can be used to determine ground-line deflections due to lateral load, ground-line deflections due to moments applied at the ground line, maximum moments, and the location of maximum moments. The characteristic load and moment can be calculated by using the following equations;

For clay $$P_c = 7.34D^2(E_P R_I)\left[\frac{S_u}{E_P R_I}\right]^{0.68}$$ Equation 2.11

For sand $$P_c = 1.57D^2(E_P R_I)\left[\frac{\gamma' D\varphi K_P}{E_P R_I}\right]^{0.68}$$ Equation 2.12

For clay $$M_c = 3.86D^3(E_P R_I)\left[\frac{S_u}{E_P R_I}\right]^{0.4}$$ Equation 2.13

For sand $$M_c = 1.33D^3(E_P R_I)\left[\frac{\gamma' D\varphi K_P}{E_P R_I}\right]^{0.4}$$ Equation 2.14

where

P_c characteristic load

M_c characteristic moment

D pile width or diameter,

E_p pile modulus of elasticity

R_I moment of inertia ratio=ratio of moment of inertia of the pile to the moment of inertia on a solid circular cross section

r' effective unit weight of sand,

S_u undrained shear strength of clay

φ' effective stress friction angle for sand

K_p Rankine's coefficient of passive earth pressure

2.4.3.6 Hybrid solutions

Hybrid solutions use p-y curves to model soil interaction and use Mindlins equations to approximate the effects of the pile-soil-pile interaction, Mindlins (1936). Mindlins equations generally are used to define stretching or densing factors for the displacement terms in the load transfer relations. Peak soil reactions often are not modified for group effects. The original hybrid solution is the Focht & Koch (1973) procedure in which elasticity based α-factor charts and equations for evaluating group deflection and pile load distribution (Poulos, 1971b) are used to incorporate the pile-soil-pile interaction. A single y-multiplier is applied to stretch all p-y curves along the pile. Reese et al. (1984) proposed a modification to the method, in which elastic deflections used in the group deflection equations are estimated using the result of p-y analyses performed at load levels at which pile load deflection behaviour is essentially linear.

2.4.3.7 Empirical stiffness distribution method

The empirical stiffness distribution method was developed estimating shear distribution among piles in a group (O'Neill and Dunnavant, 1985). The method is based upon observed reductions in pile head lateral translational stiffness in pile groups, relative to isolated pile stiffness, as a function of the ratio of centre to centre pile spacing to pile diameter (s/d) and whether a pile is in a leading or

trailing position within the pile group. The data for the method was obtained from Cox et al. (1984) from tests of a 25.4mm steel piles in very soft clay configured in line and side by side. The method introduced shadowing into the calculations of the performance of pile groups.

2.4.4 Pile group efficacy

The efficacy of the pile group under the embankment structure is also of interest. The efficacy of the pile group is the ratio of the total axial load acting on the pile group to the theoretical loading from the entire embankment structure above the pile caps. Methods used to estimate efficacy was for arching only (conditions near the embankment centre) and do not consider bending moments in the piles (conditions at the outer extremities of the embankment). One particular method to estimate the pile efficacy (Hewlett and Randolph 1988) is as follows:

$$E = 1 - \delta\left[1 - \frac{s}{2H}\right](1 - \delta)^{(K_p - 1)} \qquad \text{Equation 2.15}$$

where

$$\delta = \frac{b}{s}$$

H is the height of the embankment

s centre to centre spacing of the pile

b the width of the pile

K_p Rankine's earth pressure

2.5 BS 8006 (2010) Design Code

The British Standard 8006 (2010) is the current method adhered to in the design of basally reinforced piled embankments on soft soils. The current adopted design approach is the most commonly used and is considered to be overly conservative in terms of the estimation of tension to be developed (Jennings & Naughton 2010; van Eekelen, 2010; Farag, 2008; Hewlett and Randolph 1988).

2.5.1 Vertically distributed load

The sequential design process of the geosynthetic reinforcement initially calculates the vertically distributed loading (W_T) (BS 8006:2010) acting on the reinforcement. Two equations are presented; the first considered the case where the embankment is sufficiently high relative to clear spacing between adjacent piles that full arching is mobilised, Equation 2.17, while the second considers only partial arching when the embankment height is less than 1.4 times the clear spacing between adjacent piles, Equation 2.18. In all cases BS 8006 (2010) requires that the height of the embankment is a minimum of 0.7 times the clear spacing between adjacent piles.

For H>1.4(s-a)

$$W_T = \frac{1.4sf_{fs}\gamma(s-a)}{s^2-a^2}\left[s^2 - a^2\left(\frac{p_c}{\sigma_v}\right)\right] \qquad \text{Equation 2.16}$$

For 0.7(s-a)≤H≤1.4(s-a)

$$W_T = \frac{s\times(f_{fs}\gamma H + f_q w_s)}{s^2-a^2}\left[s^2-a^2\left(\frac{\grave{p}_c}{\grave{\sigma}_v}\right)\right] \qquad \text{Equation 2.17}$$

$$\text{But } W_T = 0 \text{ if } \frac{s^2}{a^2} \leq \frac{\grave{p}_c}{\grave{\sigma}_v} \qquad \text{Equation 2.18}$$

where

w_s the uniformly distributed surcharge loading

a the size of the pile caps

$\grave{\sigma}_v$ the average vertical stress at the base of the embankment

$\grave{p}_c$ the vertical stress on the pile caps

$$\grave{\sigma}_v = f_{fs}\gamma H + f_q w_s \qquad \text{Equation 2.19}$$

where

f_q the partial load factor for the application of external loads

f_{fs} the partial load factor applied to the unit weight of soil

The BS8006 (2010) method was developed from the analysis of buried conduits. The method (Equation 2.21) is based on Marston's formula for positive projecting subsurface conduits (Love and Milligan, 2003). Marston's original equation was intended for loading on an infinitely long pipe in a plain strain situation as opposed to a three dimensional structure.

$$p`_c = \sigma'_v \left[\frac{c_c a}{H}\right]^2 \qquad \text{Equation 2.20}$$

BS8006 (2010) developed equations for the calculation of the arching coefficient (C_c) for different pile group support conditions (end bearing piles/shaft friction).

$$C_c = 1.95\frac{H}{a} - 0.18 \quad \text{for end bearing piles (unyielding)} \qquad \text{Equation 2.21}$$

$$C_c = 1.5\frac{H}{a} - 0.07 \quad \text{for friction and other piles} \qquad \text{Equation 2.22}$$

The distributed load W_T carried by the reinforcement between adjacent pile caps may be determined from:

For H > 1.4(s-a);

$$W_T = \frac{1.4 s f_{fs} \gamma (s-a)}{s^2 - a^2}\left[s^2 - a^2\left(\frac{p'}{\sigma'_v}\right)\right] \qquad \text{Equation 2.23}$$

For 0.7(s-a) ≤ H ≤ 1.4 (s-a);

$$W_T = \frac{s(f_{fs}\gamma H + f_{q\omega s})}{s^2 - a^2}\left[s^2 - a^2\left(\frac{p'_c}{\sigma'_v}\right)\right] \qquad \text{Equation 2.24}$$

But

$W_T = 0$ if $s^2/a^2 \leq p'_c/\sigma'_v$

where

W_T the distributed vertical loading on the reinforcement between adjacent pile caps

The stress reduction ratio (S_{3D}) is defined as the ratio of the average vertical stress acting on the geosynthetic reinforcement to the total overburden stress of the embankment. The stress reduction ratio based on the above equations computes as follows:

$$S_{3D} = \frac{2.8s}{(s+a)^2 H}\left[s^2 - a^2\left[\frac{p_c}{\gamma H}\right]\right] \qquad \text{Equation 2.25}$$

BS 8006 (2010) suggested an alternative theoretical solution based on Hewlett and Randolph (1988) to determine the vertical load acting across the reinforcement. This method was based on the observed mechanism from model tests and considers a series of hemispherical domes. The efficacy at the crown of an arch can be determined from:

$$E_{crown} = 1 - \frac{(s^2 - a^2)}{s^2 \gamma H}\left[\sigma_S + \gamma(s-a)/\sqrt{2}\right] \qquad \text{Equation 2.26}$$

where:

- s — is the pile spacing between adjacent piles
- σ_s — is the pressure acting at the surface of the hemispherical dome
- $\frac{\gamma(s-a)}{\sqrt{2}}$ — is the weight of the soil beneath the hemispherical dome
- γ — is the unit weight of the embankment fill
- H — is the height of the embankment
- a — is the pile cap size

Hence E_{crown} may be written as:

$$E_{crown} = \left[1 - \left(\frac{a}{s}\right)^2\right][A - AB + C] \qquad \text{Equation 2.27}$$

Where A, B and C are calculations coefficients given by:

$$A = \left(1 - \left(\frac{a}{s}\right)\right)^{2(k_p - 1)} \qquad \text{Equation 2.28}$$

$$B = \frac{s}{\sqrt{2H}}\left[\frac{2K_P - 2}{2K_P - 3}\right] \qquad \text{Equation 2.29}$$

$$C = \frac{s-a}{\sqrt{2H}}\left(\frac{2K_P-2}{2K_P-3}\right)$$ Equation 2.30

Efficacy at the pile cap E_{cap} may be taken as:

$$E_{cap} = \frac{\beta}{1+\beta}$$ Equation 2.31

Where β is a coefficient given by:

$$\beta = \frac{2K_P}{(K_P+1)\left(1+\frac{a}{s}\right)}\left[\left(1-\frac{a}{s}\right)^{-K_p} - \left(1+K_P\frac{a}{s}\right)\right]$$ Equation 2.32

The minimum pile load efficacy $E_{\min}$, the minimum proportion of embankment loading acting on the piles should be used in the subsequent formulation to determine the maximum distributed load W_T carried by the reinforcement between adjacent pile caps:

$$W_T = \frac{s(f_{fs}\gamma H+f_q\omega_s)}{(s^2-a^2)}(1-E_{min})s^2$$ Equation 2.33

The pile cap punching capacity is not considered by BS8006 (2010). The pile caps can punch through the embankment fill if the height of the embankment is relatively low and results in a low stress concentration over the pile caps. The inclusion of the geosynthetic reinforcement to the structure aides in the distribution of the stress onto the pile caps thus reducing the probability of a punching failure of the pile caps.

2.5.2 Tension in the reinforcement

The tensile load T_{rp} per metre "run" generated in the reinforcement resulting from the distributed load W_T defined by BS 8006 (2010) is, Figure 2.7:

$$T_{rp} = \frac{W_T(s-a)}{2a}\sqrt{1+\frac{1}{6\varepsilon}}$$ Equation 2.34

where

T_{rp} the tension in the geosynthetic reinforcement

ε the strain in the reinforcement (%)

The calculation of the tension present in the reinforcement is problematic due to the presence of two unknowns (the tension and the strain in the reinforcement). For the calculation of the tension present, a strain value and geosynthetic reinforcement stiffness is assumed and Equation 2.34 iterated to convergence.

BS8006 (2010) stipulates a maximum limit of 6% strain (ε) should not be exceeded during design to ensure the transfer of the clear span loading to the pile caps. The upper limit of the allowable strain should be reduced for a lower range of embankment heights to prevent excessive differential settlement at the surface of the embankment. In shallow embankments, the degree of soil arching might be relatively low depending upon the pile spacing, thus a greater proportion of the loading will be transferred to the reinforcement over the clear span between the adjacent pile caps. If the maximum allowable strain in the reinforcement is not adjusted to take account of such conditions, excessive deformation at the embankment surface may occur. BS8006 (2010) advises the examination of the load/strain relationship at design stage for different load levels. A maximum creep strain of 2% is permitted over the design life of the reinforcement (BS8006, 2010).

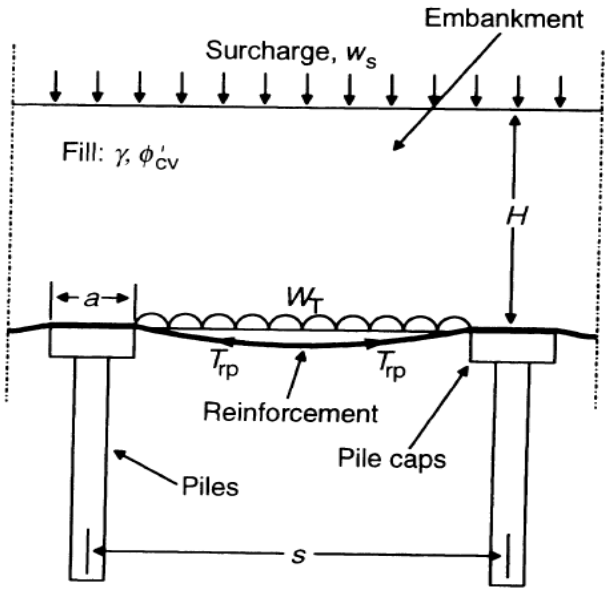

Figure 2.7 Variables used in the determination of T_{rp} (after BS8006, 2010)

2.5.3 Tension in the reinforcement due to lateral sliding

The tensile load T_{ds} per metre "run" generated in the reinforcement resulting from lateral thrust is defined by BS 8006 (2010) as:

$$T_{ds} = 0.5K_a\left(f_{fs}\gamma H + 2f_q w_s\right)H \qquad \text{Equation 2.35}$$

where

K_a the active earth pressure coefficient (= $tan^2\left(45^\circ - \varphi_{cv}/2\right)$

To achieve the required magnitude of tensile load in the reinforcement in order to resist lateral sliding of the embankment fill, the reinforcement must have a minimum length of bond (L_e). BS8006 (2010) requires that the bond length should be (Figure 2.8):

$$L_e \geq \frac{0.5K_aH\left(f_{fs}\gamma H+2f_q w_s\right)f_s f_n}{\gamma H\frac{\alpha tan(\varphi)c}{f_{ms}}} \qquad \text{Equation 2.36}$$

where

f_s the partial factor for reinforcement sliding resistance

f_n the partial factor for reinforcement sliding resistance

h the average height of the embankment fill above the reinforcement length L_e

α the interaction coefficient relating the embankment fill and reinforcement bond angle to $tan\ \varphi'_{cv}$

φ'_{cv} the large strain angle of friction of the embankment fill under effective stress conditions

f_{ms} the partial load factor for applied external loads

To generate the maximum limit state loads across the width of the embankment and also along its length, the reinforcement is required to extend a distance past the outer row of pile, this distance is defined as the bond length L_b (Figure 2.8).

$$L_b \geq \frac{f_n f_p\left(T_{rp}+T_{ds}\right)}{\gamma h\left[\frac{\alpha'_1 tan\varphi'_{cv1}}{f_{ms}}+\frac{\alpha'_2 tan\varphi'_{cv2}}{f_{ms}}\right]} \qquad \text{Equation 2.37}$$

where

L_b is the reinforcement bond length needed beyond the outer row of piles across the width of the embankment

f_p is the partial factor applied to the pull-out resistance of the reinforcement

a'_1 is the interaction coefficient relating the soil/reinforcement bond angle to $tan\ \varphi'_{cv1}$ on one side of the reinforcement;

a'_2 is the interaction coefficient relating the soil/reinforcement bond angle to $tan\ \varphi'_{cv2}$ on the opposite side of the reinforcement;

f_{ms} is the partial material factor applied to $\tan \varphi'_{cv}$

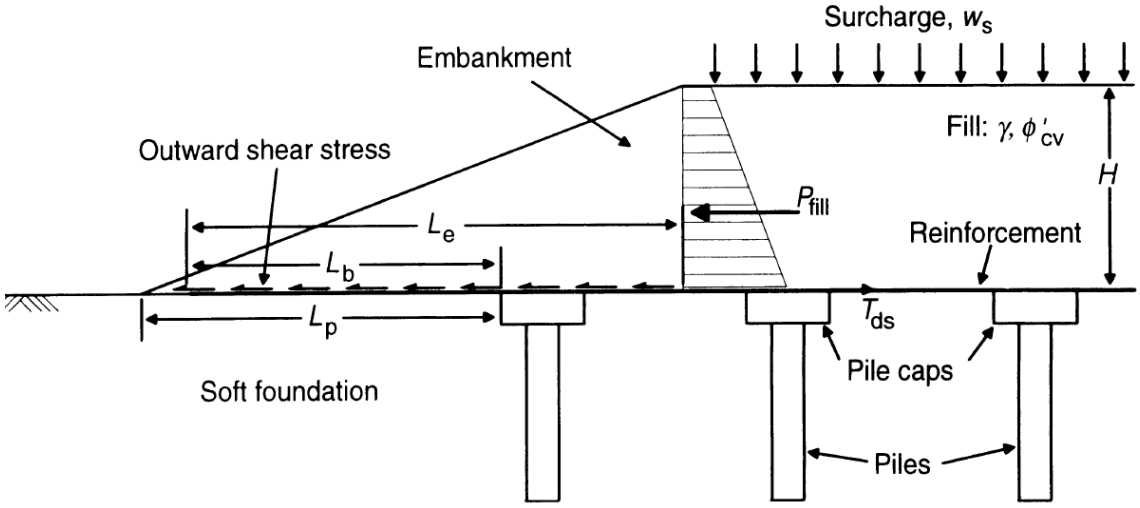

Figure 2.8 Lateral sliding stability at the interface of the fill/reinforcement (after BS8006, 2010)

2.5.4 Pile group design

The piles in the basally reinforced piled embankment are installed in a square grid. BS8006 (2010) recommends that the maximum spacing between the piles is limited to:

$$s = \sqrt{\frac{Q_p}{(f_{fs}\gamma H + f_q w_s)}} \qquad \text{Equation 2.38}$$

where

Q_p allowable load carrying capacity of each pile in the pile group

2.5.5 Pile group extent

The piled area is required to extend a distance beyond the shoulder of the embankment to ensure that any differential settlement or instability outside the piled area will not affect the embankment crest. The calculation is based on Rankine's active earth pressure theorem, the equation relates the position of the outer row pile within a sufficient distance from the embankment crest to ensure stability near the slope Figure 2.9. The magnitude of the required extension is defined by BS8006 (2010) as:

$$L_p = H(n - tan\theta_p) \qquad \text{Equation 2.39}$$

where

L_p the horizontal distance between the outer edge of the pile cap

H the height of the embankment fill

n the side slope of the embankment

θ_p the angle to the vertical between the shoulder of the embankment and the outer edge of the outer pile cap

$$\theta_p = 45^\circ - \frac{\varphi'_{cv}}{2} \qquad \text{Equation 2.40}$$

where

φ_{cv} the angle of internal friction of the embankment fill

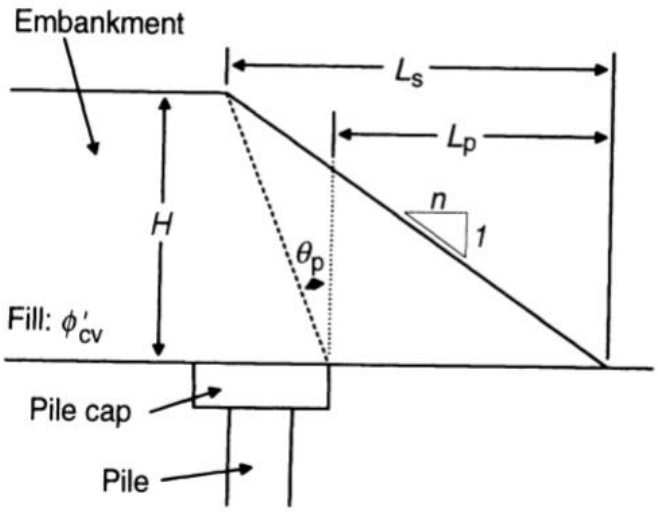

Figure 2.9 Outer limit of pile caps (after BS8006, 2010)

2.5.6 Lateral deflection of the pile head and bending moments

BS8006 (2010) does not provide a method of calculating the lateral deflection of the pile head and the resulting bending moment in the pile based on a range of structural morphology. BS 8006 (2010) states that "the design of laterally loaded piles is outside the scope of the document". The design code principle is based upon the theory that the stiffened embankment platform resists the lateral forces acting towards the extremities of the embankment in full and transfers the loading from the embankment in the vertical component only on to the top of the pile caps. The underlying principle of the design code is that the soft soil does not provide support in either component (vertical/horizontal) and thus, the pile group supports the structure entirely.

The underlying soft soil does provide support to the pile itself. The soft soil negates to some degree the force exerted from the pile to move in the horizontal direction whilst being subject to a lateral force from the embankment structure above. The pile/soil interaction is complex and is sensitive to the following variables:

- Length of pile
- Pile stiffness modulus
- Pile diameter
- Pile group spacing
- Strength of soil

- Lateral restraint provided by deeper soil layers
- Water table condition

Lateral deformation of the pile occurs when the embankment loading is applied onto the piles. When the magnitude of the loading is large, significant lateral deformations of the pile can occur (Jennings and Naughton, 2010). Large lateral deformations of the pile can often prove to be more problematic than vertical settlements within the structure. Whilst the lateral deflection and the resulting bending moment within the piles cannot be calculated using the BS8006 (2010) design code, the magnitudes of the two can be calculated using finite element analysis (van Eekelen, 2010).

2.5.7 Slope Stability Analysis

The rotational stability of the reinforced piled embankment is required to be checked as specified by BS8006 (2010) using conventional slip circle methods. The procedure involves a slip surface analysis search along the base of the embankment to determine the profile of the tensile load in the reinforcement which is necessary to provide an adequate margin of stability (Figure 2.10). To ensure stability of the structure has been achieved, the sum of the disturbing forces at any location within the structure must be less than the sum of the restoring forces (due to piles, reinforcement and soft soil support).

$$M_D \leq M_{RS} + M_{RP} + M_{RR} \qquad \text{Equation 2.41}$$

where

M_D the factored distributing moment along the base of the embankment

M_{RS} the restoring moment due to the soil

M_{RP} the restoring moment due to the axial load in the piles

M_{RR} the restoring moment due to reinforcement

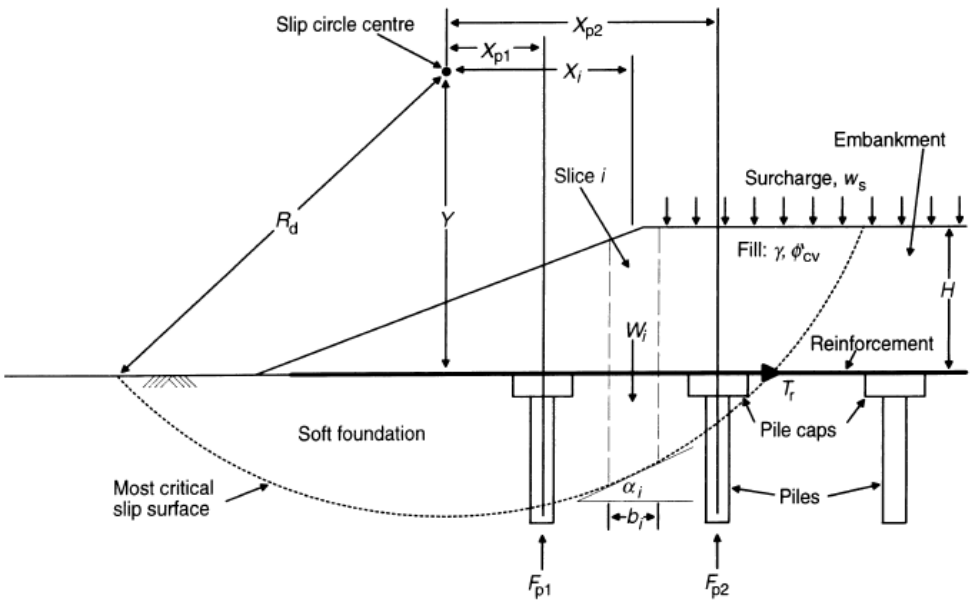

Disturbing moment due to soil and loading:

$$M_D = \left[\sum \left(f_{fs} W_i + f_q b_i w_{si}\right) \sin \alpha_i\right] R_d$$

Restoring moment due to soil:

$$M_{RS} = \left[\sum \left\{ \frac{c_i'}{f_{ms}} b_i \sec \alpha_i + \left((W_i + b_i w_{si}) \cos \alpha_i - u_i b_i \sec \alpha_i\right) \frac{\tan \phi'_{cvi}}{f_{ms}} \right\}\right] R_d$$

Restoring moment due to piles:

$$M_{RP} = F_{p1} X_{p1} + F_{p2} X_{p2}$$

Restoring moment due to reinforcement:

$$M_{RR} = T_r Y$$

Figure 2.10 Variables used in analysis of overall stability of basal reinforced piled embankments (after BS8006, 2010)

2.6 Finite element analyses

Finite element methods are typically employed by more ambitious analytical approaches to discretize the problem and aim to apply an appropriate stress strain law to the models constitutive elements. It is possible in some cases to identify new mechanisms and behavioural models are discovered. Application of sophisticated numerical modelling improves both the reliability and the economy of engineering design (Krishna, 2006).

2.6.1 Finite element analysis techniques

There are numerous types of numerical methods of simulating geosynthetic reinforced piled embankments, two of the most common modes of analysis are Finite Element Method (FEM) and the Finite Difference Method (FDM).

The principle of FEM is to discretize the region, body or structure being analyzed into a large number of finite interconnected elements. In principle there are an infinite number of points in the region which corresponds to an infinite number of stresses to be determined. By discretizing the region into interconnected elements, a closed-form analytical solution with finite elements exists (Krishna, 2006). The FEM uses interpolating polynomials to describe the field variable (displacement, tension, stress and loading etc.) within an element (Frank, 1985).

FDM can be used to solve problems with the same degree of complexity as FEM. Both methods require discretization of the region into finite elements. The FDM approach is fundamentally different. FDM discretization is achieved by dividing the region into a finite number of lumps (Frank, 1985).

Figure 2.11 illustrates the discretization methods of both FEM and FDM approaches. In the FDM approach, each element is assumed to have a constant field value in contrast to the FEM approach where each node (FEM element has node at each corner, FDM has node at the center of each element) has a different field value. The nodes in both approaches are where field variables are to be interpolated. In FDM one can only use squares or cubes as the basic elements, whereas in FEM one can use arbitrary basic elements, the sides don’t have to be straight. If one is dependent on using lumps (cubes) as the only element, this leads automatically to a bad approximation of the geometry, technical objects aren't usually designed purely rectangular. The FEM approach can meet this problem by making a local refinement of the element mesh. Refinement of the FDM element mesh is not possible locally, thus requiring a refinement throughout the whole region which necessitates greater amounts of computing capacity (FLAC, 1995).

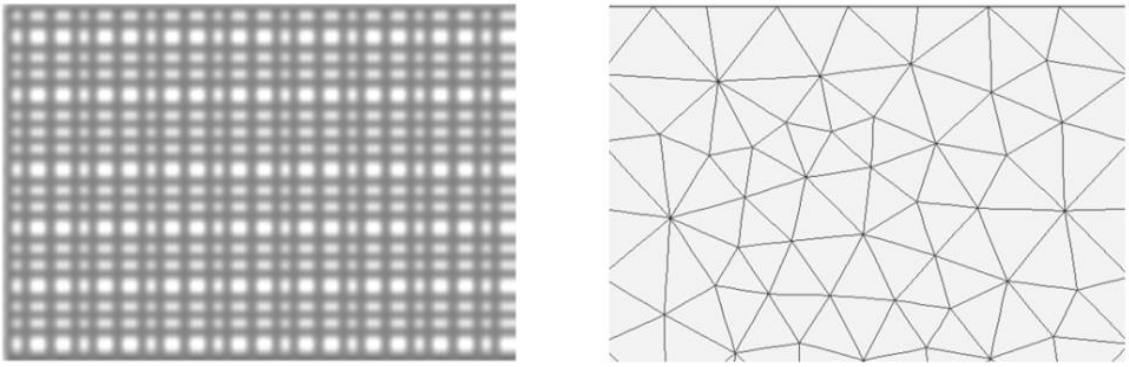

Figure 2.11: Element discretization for (a) FDM and (b) FEM

Jennings & Naughton (2012b) suggested that the coupled FEM and FDM numerical analyses approaches were in good agreement for the numerical modelling of a geosynthetic reinforced piled embankment. Similitude conditions exist in both the numerical analysis techniques to consistently develop the response of structural and soil elements in their behaviour.

2.6.2 Finite element modelling approaches

2.6.2.1 Plane strain models

Plane strain modelling idealizes a 3D problem as a 2D model with homogeneous material characteristics and infinite length in the longitudinal direction. A plane strain model is used for geometries with uniform cross section and corresponding stress state and loads over certain length perpendicular to the cross section.

2.6.2.2 Axisymmetric models

Axisymmetric modelling is the idealization of a model as having cylindrical symmetry. A three dimensional analyses of a single pile is possible using this technique. However, the approach is only suitable for the simulation of a single pile at the centre of a pile group where the loading conditions are uniform around the pile (Han and Gabr, 2002). Numerous studies have used the axisymmetric model to analyse the arching condition at the pile head. Axisymmetric models are used for circular structures with a uniform radial cross section and loads around a central axis. Axisymmetric modelling was deemed unsuitable to adequately simulate the behaviour of the geosynthetic reinforced piled embankment structure (Han and Gabr 2002).

2.6.3 Two dimensional analyses of a GRPE

A geosynthetic reinforced piled embankment (GRPE) is a complex three dimensional problem (van Duijen and Kwast, 2003; Laurent et al., 2003 and Kempton et al., 1998). Studies by Bergado and Teerawattanasuk (2008) concluded that the simulation of a reinforced embankment by 2D numerical analysis was in good agreement with 3D analyses of the problem. The inclusion of the pile group to the structure and the complex pile-soil complex interaction warrants consideration adopting 3D analysis over a simple plain strain or axisymmetric technique. Farag (2008) concluded that 3D analysis recorded significantly lower tensions and strains in the reinforcement in comparison to 2D FEM analysis of a GRPE.

Satibi (2009) suggested plane strain geometry cannot be used to model soil arching, because soil arching instability can occur by punching failure. Slaats (2008) found that the results of 2D plane strain and 3D geometry do correspond. Studies by Kempton et al. (1998), Krishna (2006) and Kalla (2010) showed that the results of 2D plane strain and 3D geometry have the tendency to be in agreement, however, the stress reduction ratio is much lower in 3D analysis compared to 2D analysis. Analysis of a 3D geosynthetic reinforced piled embankment structure by 2D finite element analysis and the limits of resultant expressions developed is constrained by the arbitrary restrictions of the 2D models predictive limits.

2.7 Centrifuge modelling

Geotechnical centrifuge modelling is a well-established means of providing insight into geotechnical engineering problems. Typically a 1/*n*th scale model of the problem is constructed and subjected to an inertial acceleration field of *n* times earth's gravity (*g*). This produces a stress similarity between the model and the full-scale prototype, for example the stresses produced beneath a 5 m embankment in earth's gravity are identical to those beneath a 50 mm model embankment spun at a centrifugal acceleration of 100*g* (Taylor, 1995). Some of the common scaling relationships that exist between the model and prototype are given in Table 2.1.

A wide range of geotechnical problems can be evaluated with centrifuge physical modelling techniques (Corte, 1988: Ko & McLean, 1991; Leung *et al*., 1994).

Centrifuge testing provides a tool for geotechnical modelling in which prototype structures can be studied as scaled-down models while preserving the stress states (Avgherinos & Schofield 1969).

The inertial acceleration field created by rotating the model in a centrifuge is given by $\omega^2 r$ where ω is the angular velocity of the centrifuge in radians per second and r is the effective radius of the model. The acceleration field creates a non-linear vertical stress distribution in the model which differs slightly from the vertical stress distribution in the prototype, Figure 2.12. This error, however, is kept to a minimum by measuring the effective radius as the distance between the axis of rotation and one-third of the model depth (Taylor 1995).

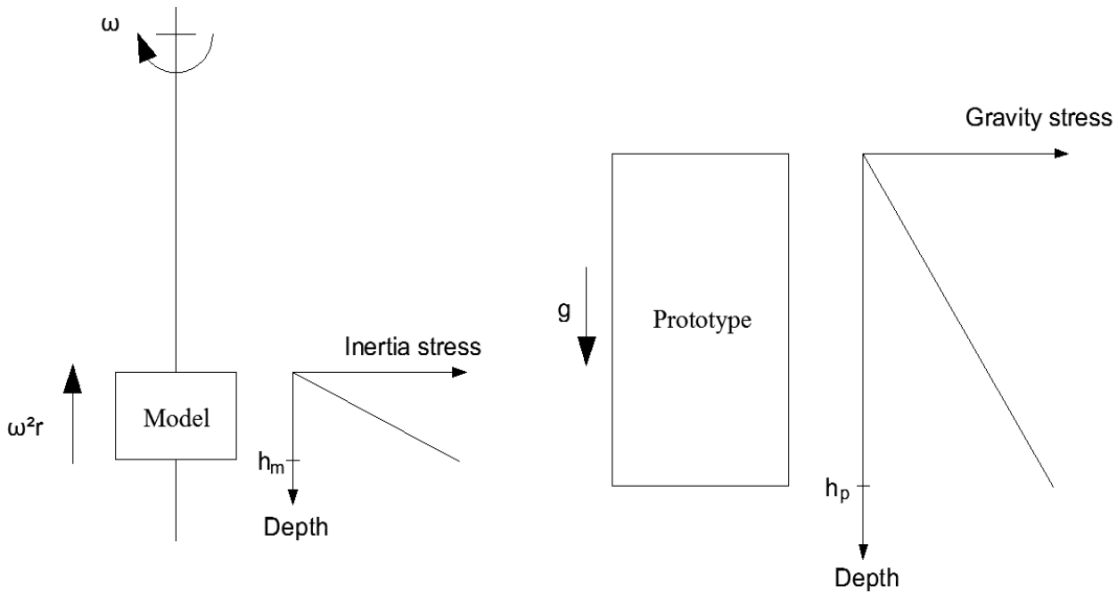

Figure 2.12 Inertial stress in centrifuge model and corresponding prototype gravitational stress (Taylor 1995)

Table 2.1 Centrifuge scaling relationships

Description	Units	Scaling relationships Model:Prototype
Gravity	m/s^2	n
Length	m	1/n
Area	m^2	$1/n^2$
Volume	m^3	$1/n^3$
Density	kg/m^3	1
Mass	kg	$1/n^3$
Stress	kPa	1
Strain	%	1
Force	N	$1/n^2$
Deflection	m	1/n
Bending moments	Nm	$1/n^3$

The scaling down of geosynthetic materials is essential in small-scale physical modelling studies in order to obtain the correct response of prototype structure. Viswanadham & Konig (2004) found it difficult to select appropriate materials to represent geogrid in a geotechnical centrifuge. Contrary to soils, the similitude condition does not allow the use of identical geosynthetic materials in model and prototype studies. Viswanadham & Konig (2004), presented the relevant scale factors for modelling of geosynthetic materials for both 1*g* and *ng* tests, Table 2.2, and also noted that the influence of base material on the tensile strength - strain behaviour of the geogrid cannot be ruled out.

Table 2.2.Centrifuge scale factors, Viswanadham & Konig (2004)

Parameters Scale factors	Scale Factors	
	1*g*	*ng*
Tensile strength T_g (kN/m)	$1/n^2$	$1/n^c$
Secant modulus J_g (kN/m)	$1/n^2$	1/n
Soil–geosynthetic friction angle (deg)	1	1
Cross-section area of rib/unit length A (m)	1/n	1/n

[c] = Cross sectional area of rib (model)/cross sectional area of rib (prototype).

Previous studies on the phenomenon of soil arching in piled embankments conducted using a geotechnical centrifuge include that of Bujang & Faisal (2005) and Ellis & Aslam (2008). Bujang & Faisal (2005) reported a series of tests on a 1/100 scale model and examined the influence of parameters such as fill height, pile area ratio and fill properties on arch formation. Large differential settlements and low efficacy (proportion of embankment weight carried by piles) values were observed at lower embankment height (H) / spacing (s) ratios indicating a poor arch formation, whereas higher H/s ratios yielded higher efficacy values with the fill surface remaining relatively even. It was also concluded that high quality fill with high strength and stiffness and high pile area ratios result in a more efficient arching mechanism Bujang & Faisal (2005).

Ellis & Aslam (2008) compared the results of centrifuge tests investigating the performance of unreinforced piled embankments constructed over soft soil with current piled embankment design approaches (Low *et al.* 1994; Love & Mulligan, 2003; BS8006, 2010; Hewlett & Randolph, 1988; Kempfert *et al.,* 2004). The foundation soil was modelled using expanded polystyrene styro-foam and the model piles were constructed from 25 mm diameter aluminium tubes. It was concluded that the Hewlett and Randolph (1988) method appeared to be the most rational design approach as it considers all geotechnical parameters, soil strength and punching shear failure at the pile caps. The possibility of using a ground reaction curve (GRC) in the design process was also examined by Ellis and Aslam (2008). A GRC is a plot of the stress reduction ratio (σs / γHe) vs. the ratio of uniform surface settlement to the pile cap clear spacing (δ/(s-a)) for a series of g-levels (1*g* to 60*g*). It was concluded, that with further research, GRCs could potentially be used in

design to form interaction diagrams to examine whether the response of the subsoil and any geosynthetic reinforcement would be sufficient for a particular embankment.

The majority of centrifuge analyses carried out on piles have focussed on the performance of single piles. Ilyas et al. (2004) performed centrifuge analysis on pile groups and their response to lateral loads. Ilyas concluded the average lateral load per pile decreases with increasing number of piles in the group. In line with the findings of Brown et al. (1988) and Rollins et al. (1998), the shadowing effect of lead piles over trailing piles is observed and such effect increases with increasing number of piles in a group. This results in a higher lateral load for the lead row piles as compared to that on the trailing piles. The shadowing effect is most significant for the lead row piles and less significant on subsequent rows of trailing piles.

Installation of the model pile group at 1*g* before the prototype soft soil does not replicate the exact stress strain conditions experienced in the field, Craig (1983). Craig (1983) reported variations approaching 50% in the measured axial capacity of single displacement model piles pushed into medium dense sand at 1*g* and later tested under a higher gravity field. Craig (1983) also reported that the lateral capacity varied less than 10% for piles installed at 1*g* and loaded at 52*g* in the centrifuge. During lateral loading, the region of high strain at the top of the pile governs pile behaviour and there is less variation between stresses at installation at 1*g* and under enhanced gravity whereas axial capacity is more dependent on soil conditions at depth. Numnez, *et al*. (1988) suggested that unintentional lateral movement of the pile between installation and testing has a potential for a greater disturbance and ultimate reduction of the soil stiffness. Care was taken to minimize the disturbance to the model under construction and installation in the centrifuge. Numnez, *et al*. (1988) reported the influence of the previously mentioned disturbance on an actual soil, the prototype soft soil model employed was synthetic homogeneous single elements, localized disturbances to the stiffness of the material due to the lateral movement of the piles was deemed insignificant.

2.8 Summary

A large number of design methods (Low *et al.* 1994; Love & Mulligan, 2003; BS8006, 2010; Hewlett & Randolph, 1988; Kempfert *et al.,* 2004), based on experimental and numerical models are available to design reinforced piled embankments. Studies comparing the various methods (Ellis & Aslam, 2008; Love & Mulligan, 2003), have found that they give differing results and are significantly controlled by parameters such as the shear strength of the fill, the ratio of clear spacing to height of fill and the strength and stiffness of the geosynthetic. In design both vertical and horizontal equilibrium must be achieved. In addition to equilibrium considerations, strain compatibility between deformation of the geosynthetic, pile group and soft soil must be achieved.

Many of the design methods neglect the stiffness of the subsoil and the performance of the pile group underlying the reinforced piled embankment. There have been numerous past studies on the performance of single pile and pile groups by both numerical and physical modelling (Brown et al, 1987; Brown et al, 1988; Meimon et al., 1986; Rollins et al., 1998; Ruesta and Townsend, 1997; Rollins et al, 1998; Winkler, 1867; Goh et al, 1997; Poulos, 1971; Evans and Duncan, 1982; Focht & Koch, 1973; O'Neill and Dunnavant, 1985). However, limited research has been conducted on the lateral deformational response of a pile group under the reinforced embankment. In consideration of the importance of achieving strain compatibility partly through pile group deformations, the ability to quantify the lateral support offered to the embankment structure is of critical importance.

The lateral thrust acting outwards from the embankment centre has a significant effect on all the GRPE structural components (embankment, geosynthetic reinforcement and pile group). The lateral forces within the embankment fill are a function of the active earth pressure of the fill material. At the outer extremities of the embankment, an excessively large lateral thrust acting outwards from within the embankment will result in excessively large deformations at the surface of the embankment fill that may lead to serviceability concerns of the structure. At present, there is a lack of informative literature available on conditions at the extremities of reinforced piled embankments.

Chapter 3

METHODOLOGY

3.1 Introduction

The objective of this study was to investigate the effects of lateral loading of the piles at the extremities of geosynthetic reinforced piled embankments. The study was split into three main parts.

The first stage of the study involved the construction of a scaled 2D plane strain geosynthetic reinforced piled embankment in the IT Sligo geotechnical centrifuge. Plane strain analysis longitudinally models the cross section of the GRPE as a homogenous continuum longitudinally. Consideration of pile spacing in the longitudinal direction and its resultant effect on load and stress distribution within the model structure were outside the scope of this study. Conclusions may be developed with respect to the trend of deformations, loads and stresses with the discrepancies of the computed absolute values of the field variables acknowledged. The scaled geosynthetic reinforced piled embankment centrifuge model was sized in accordance with BS 8006 (2010). The centrifuge testing consisted of a variation of the embankment height, side slope steepness, the stiffness of the soft subsoil layer and location of the outer row pile along the embankment side slope. Due to

the size of the centrifuge maximum allowable sample size, variation of some structural parameters (pile spacing, pile cap size, soft soil depth and stiffness of the geosynthetic reinforcement) was not permissible.

The second stage comprised of numerical analysis using the finite element analysis code Plaxis 2D 2010 to replicate the centrifuge testing. The dimensions of the geosynthetic reinforced piled embankment was equivalent to those of the centrifuge model at 60 times gravity. The material characteristic parameters of the structural components (piles, geosynthetic and soil models) were equivalent to those determined during the centrifuge testing stage. The numerical analysis replicated the parametric variation of the centrifuge modelling. A comparative analysis of the centrifuge and the numerical analysis was performed to validate the finite element analysis software code Plaxis 2D 2010 and its ability to predict the deformational response of the geosynthetic reinforced piled embankment structure.

The third and final stage of the study consisted of expanding the numerical analysis of the geosynthetic reinforced piled embankment model to determine the influence of the parameters (pile spacing, pile cap size, geosynthetic reinforcement stiffness, embankment height, side slope steepness, subsoil stiffness, outer pile rake angle and location of the outer pile row) not possible during the centrifuge modelling.

The test procedures employed to achieve these objectives are discussed in this chapter.

3.2 Centrifuge modelling – Equipment and experimental procedures

A description of the methodology, equipment and materials used in the centrifuge modelling of the prototype reinforced piled embankment models is presented. The aim of the centrifuge testing was to validate the Plaxis 2D numerical model results.

3.2.1 Centrifuge model testing procedure

The centrifuge model tests were carried out under a centrifugal acceleration of 60g at a radius of 0.57m. The centrifuge prototype model was subjected to a parametric variation, Figure 3.1. The embankment height, side slope steepness, subsoil

stiffness and the location of the outer pile row along the embankment side slope were varied.

The embankment height was ranged from low to relatively high embankments, 0.428 – 3.428m in height at 60g. The variation of the embankment heights gave a range of embankment height to clear spacing between the piles ratio of 0.5, 1.0 and 2.0. The side slope steepness was ranged from 1V:1.5H →1V:2H →1V:3H →1V:4H. The outer pile row was moved in increments of 0.25 × (plan length of side slope) from directly under the embankment crest until reaching the embankment toe.

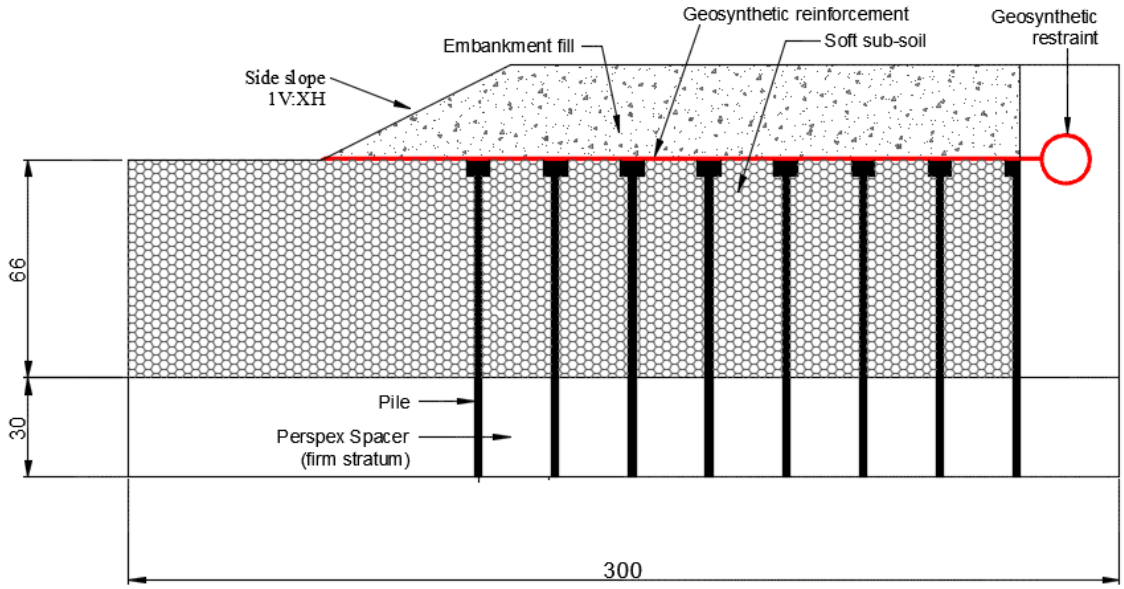

Figure 3.1 Centrifuge prototype model cross section

3.2.2 Beam rotor centrifuge

The Institute of Technology Sligo (ITS) geotechnical centrifuge is a 9 *g*-tonne beam centrifuge, with two strongboxes at either end of a 0.75 m beam rotor. A substantial steel casing with an outer diameter of 1.7 m surrounds the rotating assembly; the wall thickness of the casing is 12 mm and is sufficient to contain the debris should the strongbox be overloaded such that it breaks free in flight. The centrifuge is designed such that a strongbox rather than a swinging platform is suspended from pivots at either end of the beam rotor.

The maximum rotational speed is 638 rpm, equivalent to an acceleration level of 259 *g* at the top of a soil sample (at radius = 0.57 m), 341 *g* at the base (at radius = 0.75 m) and 300 g at the effective radius of the sample = 0.66 m. This corresponds to a maximum over stress of ~12% at the surface of the sample and ~14% at the base of the sample Figure 3.2. Schematics and photographs of the IT Sligo geotechnical centrifuge are provided in Figures 3.3, 3.4 and 3.5 and further specifications are provided in Table 3.1.

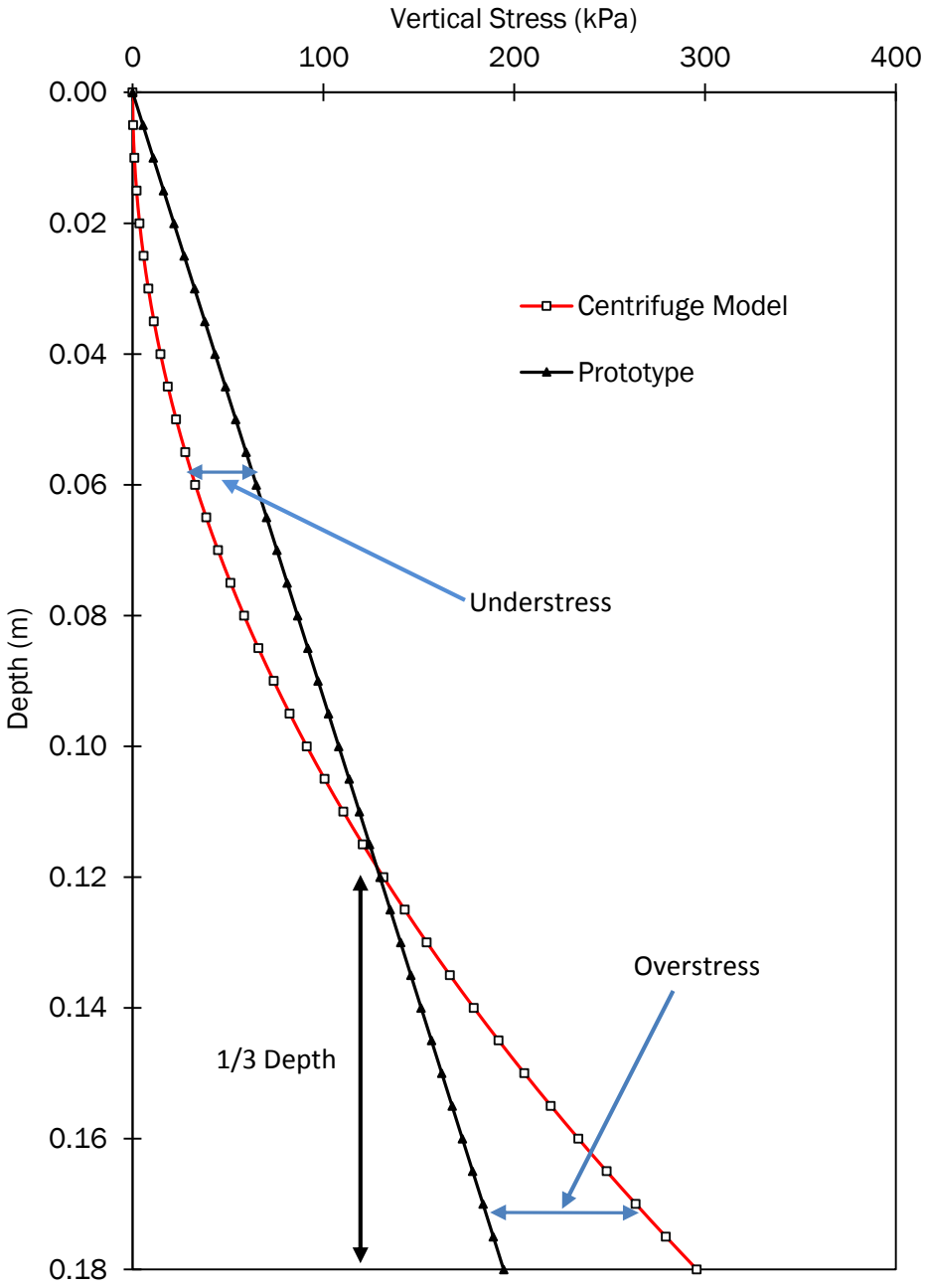

Figure 3.2 Vertical stress vs depth in centrifuge model and corresponding prototype

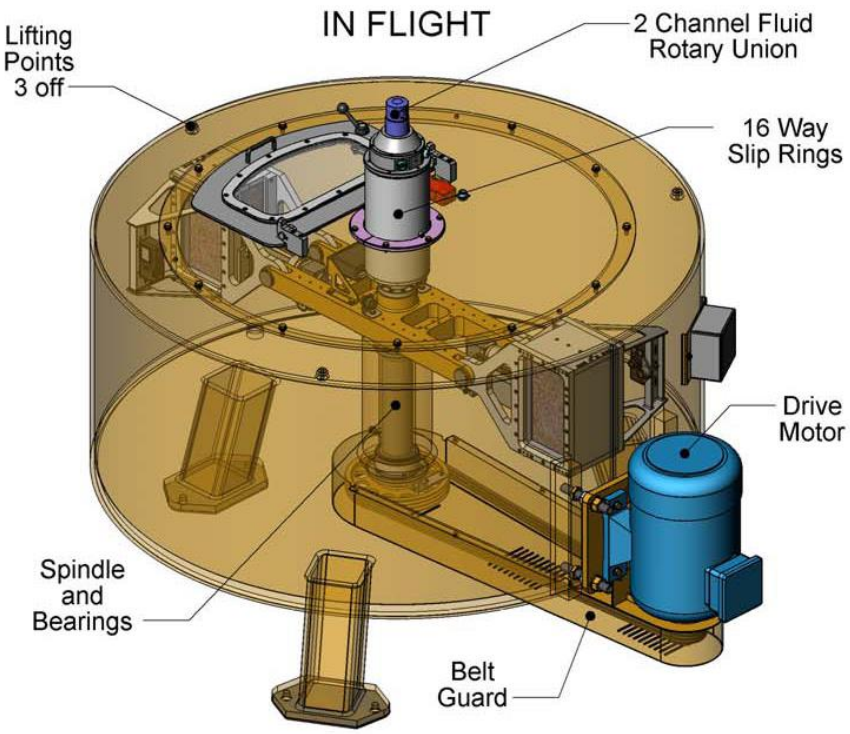

Figure 3.3 General centrifuge layout

Figure 3.4 The IT Sligo 9g-tonne geotechnical centrifuge

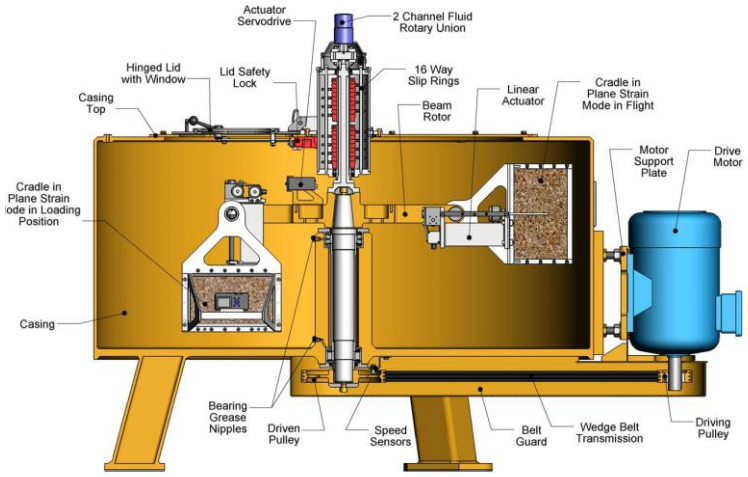

Figure 3.5 Sectional arrangement of centrifuge

Table 3.1: Centrifuge specifications

Strongbox base radius	0.750 m
Effective radius	0.660 m
Pivot radius	0.350 m
Maximum rotational speed	638 rpm
Maximum acceleration	300 g at effective radius (0.66 m) 341 g at base of strongbox (0.75 m)
Maximum size of payload	W = 0.170 m (circumferential in flight) L = 0.300 m (vertical in flight) H = 0.150 m (radial in flight)
Maximum payload at each end of beam	9 *g*-tonne (30 kg at 300 *g*)
Maximum unbalance	0.45 *g*-tonne (1.5 kg at 300 *g*)

3.2.3 Centrifuge strongbox

The strongboxes used in this study were plane strain boxes with internal (sample) dimensions of 300 × 170 × 150 mm. Each strongbox acts as a counterweight to the other. Although the centrifuge is rated to 9 *g*-tonne, the current strongboxes are designed for a safe working payload of 6 *g*-tonne. The strongboxes can be easily removed through a hinged hatch on the casing lid. Alternatively the entire casing lid can be removed using either a portable crane or overhead gantry.

Allowing for the thickness of the perspex windows, the width of the allowable sample in the strongbox is 110mm. The maximum height of sample allowable is constrained by the maximum vertical height of sample viewable through the perspex window which is approximately 160mm, Figure 3.1.

3.2.4 Centrifuge Camera

The camera utilized to obtain photographic records of the deformational response of the centrifuge model was a Canon PowerShot S80 8 megapixel digital camera. The camera was located on the centrifuge strongboxes inside the centrifuge, Figure 3.6(a & b). A control box outside the centrifuge linked to the camera by means of a circuit breaker which passed through a junction box, the centrifuge slip rings and a second junction box and finally connecting to the camera through the shutter button. This mechanism enabled the control of the cameras shutter button by remote access.

Continuous shooting mode was utilized to shoot successive frames while the shutter button was fully pressed. Recording ceases when the shutter button was released. Continuous shooting had a speed of approximately 1.8 shots per second. The centrifuge loading was increased in increments of 5*g* per minute until the maximum *g*-level required under testing conditions was reached. At each g-level increment, continuous shooting of approximately 15 seconds was recorded to enable accurate photography of the deformational response of the sample at that particular *g*-level. The internal camera clock was calibrated with a separate control clock. Knowledge of the images time stamp enabled the g level on the model to be determined.

(a) (b)

Figure 3.6: (a) & (b) Plane strain strongbox with camera bracket mounted

The photo display selected was large with a resolution of 3264 x 2448 pixels, a superfine compression was selected to enable to capture higher quality images. The photo effects were set to vivid to emphasize the contrast and colour saturation to record bold colours, the result of which would improve the efficiency of data interpolation to be measured from the photographs. The camera flash was disabled, as earlier testing conducted with the camera flash enabled produced photos poor in quality with glare on the perspex windows heavily prevalent rendering extrapolation of deformations of the model impossible. An additional light source attached to the centrifuge box focussed onto the box windows provided sufficient light to ensure consistent quality of the recorded images. A maximum ISO speed of 200 was selected to ensure the images were not vulnerable to vibrations from the centrifuge when rotating at high gravitational loads and adverse lighting conditions. The ISO speed which is defined by the International Organization for Standardization's is the numeric representation of the cameras sensitivity to light.

Shooting a wide scale image can sometimes throw the background out of focus. Enabling the macro function on the camera allows shooting at maximum wide angle allows the camera to bring the entire image into focus.

3.2.4.1 Data extraction

The extensive image database recorded during the centrifuge testing was transferred to a PC by means of a SD memory card. The individual images were imported as a raster image into an AutoCAD file. For each individual gravitational loading increment, the image of best quality was imported into the AutoCAD file. The real scale dimensions of the grid pattern on the centrifuge perspex window was known, by comparing the known dimension and the dimension as measured in AutoCAD, an appropriate scaling factor to be applied to the imported image to scale to the correct size.

The structures deformational response was measured within AutoCAD using the linear dimension tool to measure the vertical and horizontal scalar deformations. All measurements of the deformations of the structural components (piles, geosynthetic and embankment fill) were measured relative to the grid pattern superimposed on the perspex centrifuge strongbox windows, this would enable consistency in the measurement of the deformations magnitude.

The scaled GRPE model constructed within the centrifuge strong boxes spanned almost the entire length of the centrifuge window, as such the deformations to be measured were located over a wide range along the centrifuge strongbox perspex window. The camera and the scaled model were positioned on the opposite sides of the perspex window. Measurements of deformations from the imported images were accurate to 0.05mm, which was the equivalent of 3mm at 60g.

3.2.4.2 Centrifuge model refraction error

The strongbox mounted camera and the scaled model are positioned on the opposite sides of the perspex window. To measure deformations at the extremities of the field of view, the line of vision is at an angle to the 35mm thick centrifuge perspex window. The occurrence of which can lead to the possibility of an error due to refraction.

Deformations were required to be measured at locations that were offset in the horizontal and vertical planes on the centrifuge perspex windows from the cameras line of sight normal to the window. The measurement of the lateral deformation

occurring within the structure was focussed on the piles. The pile group contained eight piles, six of these piles were located to the right of the centreline of the camera line of sight and the remaining two piles to the left of the camera centreline. Piles to the right of the camera line of sight were required to have the recorded magnitude of lateral pile deformation to be reduced, Figure 3.7. Conversely, the piles to the left of the camera centreline of sight required a correction factor to increase the magnitude of lateral pile deformation recorded due to the error of refraction, Figure 3.7. The magnitude of the correction due to refraction is a function of the distance from the centreline of the camera sightline normal to the strongbox window. All measurements were taken from the camera centreline, Figure 3.7 and 3.7. The correction applied to the horizontal deformations ranged from 12% to 14% dependent on the distance of the location of measurement from the centreline of camera sight, Figure 3.7. The actual correction, $x_{corrected}$, applied to the horizontal measurement was determined using Equation 3.1:

$$x_{corrected} = -0.0001x^2 + 2 \times 10^{-5}x + 14.026 \qquad \text{Equation 3.1}$$

where x is the measured value.

The vertical deformations occurring within the structure required to be recorded were focussed on the deformations of the geosynthetic reinforcement. Correction due to refraction error was deemed necessary to ensure the accurate measurement of the magnitude of vertical deformations, Figure 3.8. The correction, $y_{corrected}$, applied to the vertical measurement was calculated using Equation 3.2:

$$y_{corrected} = -0.0001x^2 + 9 \times 10^{-5}X + 14.07 \qquad \text{Equation 3.2}$$

where y is the measured value.

For both the horizontal ($x_{corrected}$, Equation 3.1) and vertical corrections ($y_{corrected}$, Equation 3.2), the error is zero for x = 0.

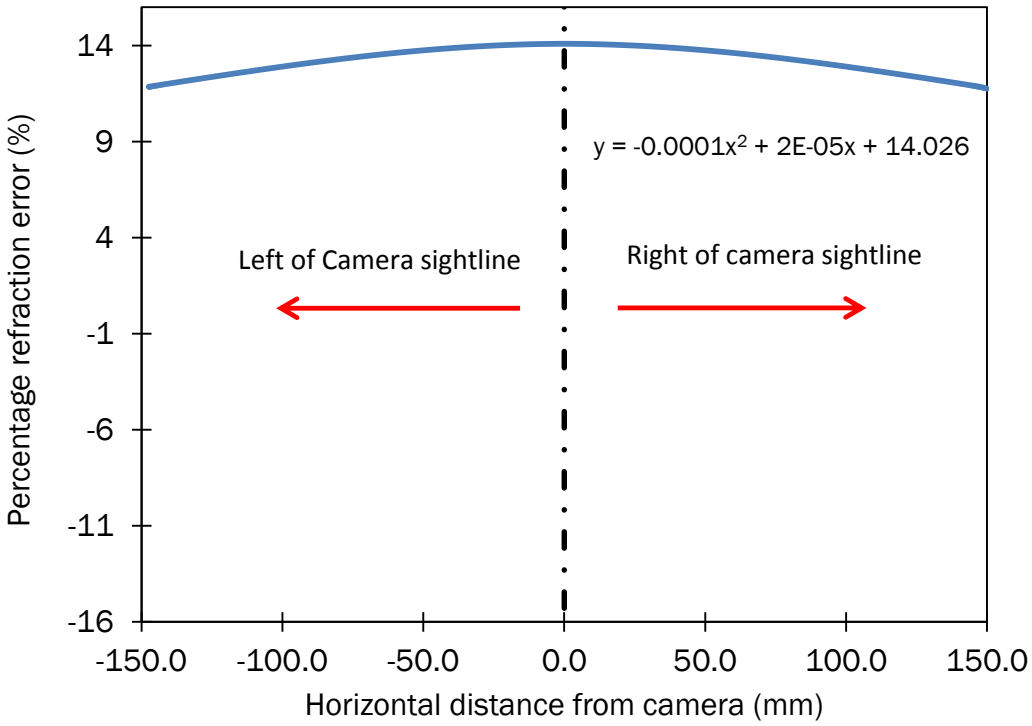

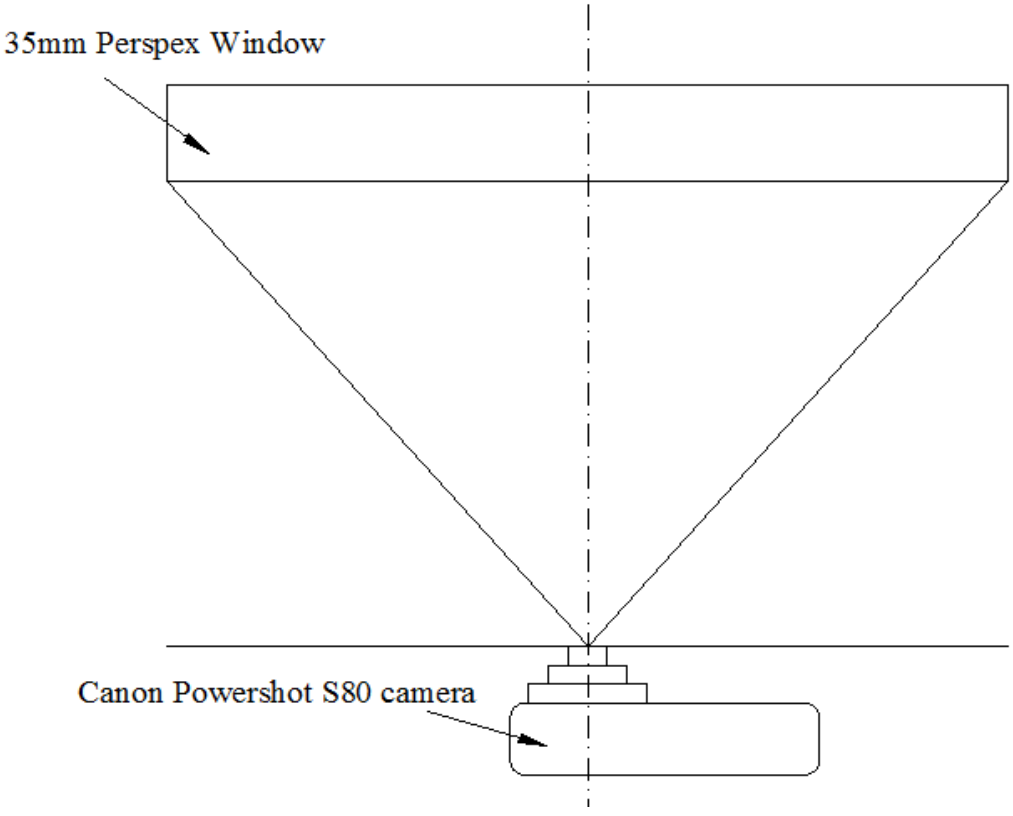

Figure 3.7 Error due to refraction in horizontal plane

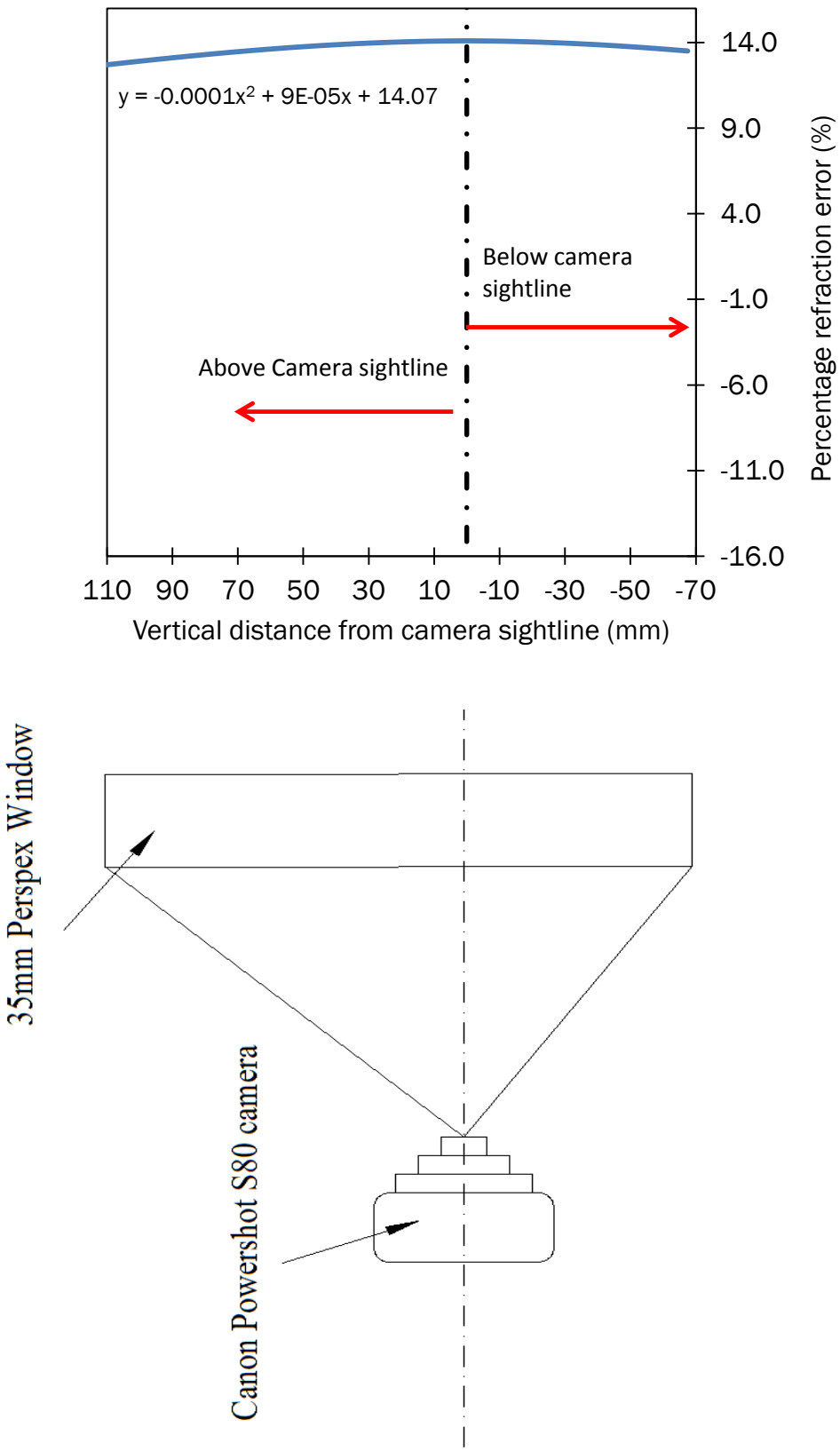

Figure 3.8 Error due to refraction in vertical plane

3.2.5 Centrifuge prototype model

The model making procedures were the same for all tests performed on the prototype geosynthetic reinforced piled embankment model. The modelling of a drained sample expedited the model making process in comparison to a consolidation analysis.

The plane strain piled embankment model, illustrated in Figure 3.1, was designed for the centrifuge strongbox which has internal plan dimensions of 300 x 100 mm and a height of 180 mm. The model incorporated eight piles with a clear spacing between piles (s-a) of 14.28 mm, equivalent to 0.856 m at 60*g*, Figure 3.1.

Each pile within the pile group was modelled as a 2D plane strain pile wall. The piles were held firmly in place at the base by a fixing mechanism consisting of a series of Perspex spacers and threaded steel bars, which passed through the piles and the spacer blocks fixing them rigidly together at the base of the model, Figure 3.1 and Appendix D Figures D1, D2 and D3.

To ensure friction effects of the pile against the perspex centrifuge window was negated, a minute gap between the window and the pile was constructed. Care was taken to ensure that the gap between the perspex windows was big enough to enable the free movement of the pile horizontally but small enough to ensure no embankment fill or soft soil material could lodge itself between the pile and the perspex window restraining the pile against movement.

Pile caps were included as the 2mm thick piles were deemed too small and punching shear through the geosynthetic reinforcement could be a problem. The pile caps were 5mm wide and were constructed of the same material as that of the piles. The perspex pile caps were attached to the top of the pile heads using high strength epoxy adhesive.

Synthetic materials were used as the subsoil between the piles. This allowed for consistency in properties and also facilitated fabrication of the model. The prototype soft soil was cut to ensure a flush finish with the top of the pile caps whilst ensuring pressure from the soft soil prototype to the strongbox window was minimized.

Geosynthetic reinforcement was placed directly over the top of both the piles and subsoil and was custom cut to 300mm in length and 100mm in width.

Approximately 120mm of the geosynthetic reinforcement model was wrapped around a 20mm diameter cylinder. The cylinder was placed in the custom made restraint, Figure 3.1 and Appendix D Figures D4, D5, D6 and D7. A perspex clamp was secured with bolts over the top of the geosynthetic restraint, Figure 3.1. The remaining length of geosynthetic reinforcement prototype was continued over the top of the pile caps and synthetic subsoil until it reached the embankment toe location.

The embankment fill was constructed using a uniform, slightly silty, medium sand. To achieve a homogeneous sample, the sand was poured at a constant rate and height of 50mm above the embankment for the loose samples. In reality, compacted dense samples of embankment fill are typically encountered in the field. Medium and dense sand samples were not tested, compaction of these samples was found to disturb the model and result in sand particles lodging between the pile and the perspex window, consequently restraining the perspex pile wall against lateral movement. No surcharge was applied to the top of the embankment surface. The embankment side slope was built from the embankment toe inwards. The side slope was gently shaped to a smooth finish taking to the required steepness with care to not apply a surcharge load and avoid a localized densification of the sand sample.

The height of the embankment, steepness of the side slope and stiffness of the soft soil (synthetic material soil representative) was varied during testing. The behaviour of the system was assessed by photographing the deformations in the model using the camera mounted on the strongbox as discussed in Section 3.2.4.1.

3.2.6 Centrifuge prototype model materials

The embankment fill, piles and soft sub soil were required to be modelled. Presented here is an explanation of the materials selected, their characteristics and a description of the methods employed to determine their pertinent characteristics.

3.2.6.1 Embankment fill

The embankment fill was modelled using sand. Suitability of sand for centrifuge modelling in the replication of a coarse granular fill was deemed possible by Taylor

(1980) as the scaling effects of the material under loading greater than 1*g* does not alter the stress strain characteristics of the material. Taylor (1980) suggested there could be a problem if an attempt was made to model at high acceleration and hence at a very small scale, an event in a prototype soil consisting mainly of a coarse soil (gravel). In that case, the soil grain size would be significant when compared to model dimensions and it is unlikely that the model would mobilise the same stress-strain curve in the soil as would be the case in the prototype. Local effects of the soil grains would influence the behaviour rather than the soil appearing like a continuum as would be the case in the prototype.

3.2.6.2 Sand material characteristics used to model embankment fill

A uniform, slightly silty, medium sand, was retrieved from a beach at Ballyshannon, Co. Donegal and was used as the embankment fill in the physical models. The sand was tested to determine its engineering characteristics, in accordance with BS 1377 (1990).

3.2.6.3 Sand particle size distribution

The particle size distribution was determined to classify the test sand. The particle size distribution, Figure 3.9, was determined using the dry sieving method in accordance with BS 1377-2 (1990).

The particle sizes corresponding to the 10 %, 30 % and 60 % particle factors, D_{10}, D_{30} and D_{60}, and the coefficients of uniformity C_U and curvature C_Z for the test sand examined in this study are presented in Table 3.2. The coefficients of uniformity C_U and curvature C_Z were defined using Equation 3.3 and 3.4 respectively.

$$C_U = \frac{D_{60}}{D_{10}} \qquad \text{Equation 3.3}$$

$$C_Z = \frac{(D_{30})^2}{D_{60}D_{10}} \qquad \text{Equation 3.4}$$

The sand was classified as a uniform, slightly silty, medium sand using BS 5930 (1999) and consisted of 99.1% coarse material (98.9% sand and 0.2% gravel) and 0.9% fines, Table 3.2.

Table 3.2: Grading characteristics

D_{10} (mm)	D_{30} (mm)	D_{60} (mm)	C_z	C_u
0.17	0.22	0.26	1.1	1.53

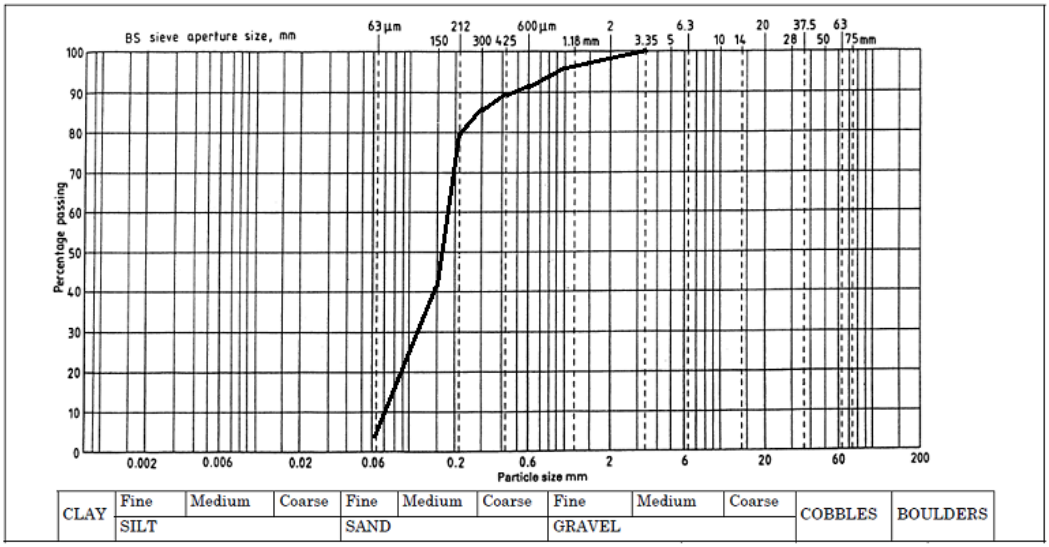

Figure 3.9 Particle size distribution

3.2.6.4 Particle density

The particle density (ρ_s) of the sand was determined using the small and large pyknometer methods in accordance with BS 1377-2 (1990) and was found to have an average value of 2.621 Mg/m^3, Table 3.3.

Table 3.3: Particle density test results

Test	Particle density ρ_s (Mg/m^3)
Large pyknometer: Test 1	2.597
Large pyknometer: Test 2	2.645
Small pyknometer: Test 1	2.634
Small pyknometer: Test 2	2.637
Average value	2.621

3.2.6.5 Maximum and minimum dry density

The density index (I_D) of the sand was computed by means of the maximum ($\rho_{d,max}$) and minimum dry ($\rho_{d,min}$) densities of the material. The magnitude of the density index (I_D) is an expression of level of compaction of the material and is calculated using Equation 3.5.

$$I_D = \left(\frac{\rho_d - \rho_{d,min}}{\rho_{d,max} - \rho_{d,min}}\right)\left(\frac{\rho_{d,min}}{\rho_d}\right) \qquad \text{Equation 3.5}$$

The maximum and minimum dry density tests were determined using BS 1377-4 (1990). To determine the maximum dry density, a sample was compacted under water in three equal layers, in a 1 litre mould using a rammer consisting of a 2.5 kg mass falling freely through 300 mm, thus forming a very dense sample. The minimum dry density was determined by dry shaking the test sand in a glass cylinder and allowing it to fall freely allowing the sand to adopt its loosest state. The maximum and minimum dry densities and corresponding minimum and maximum void ratios for the sand are presented in Table 3.4.

Table 3.4: Maximum and minimum dry densities and max and min void ratio

$\rho_{d,max}$. (Mg/m^3)	$\rho_{d,min}$. (Mg/m^3)	e_{max}	e_{min}
1.75	1.35	0.941	0.498

3.2.6.6 Shear Strength

The shear strength parameters of the sand were determined using the direct shear method (small shearbox apparatus) set out in BS 1377-7 (1990). Shearbox tests were conducted on loose samples of the sand type at normal stresses of 25, 62.5, 125, 250 and 375 kPa. Loose samples were prepared by pouring the sand directly into the assembled shearbox from a height of 50 mm. The specimen was then consolidated by applying the appropriate normal stress and sheared to failure at a constant rate of horizontal displacement of 2 mm/min. The shear force and vertical and horizontal displacements were measured using dial gauges with resolutions of 0.002 mm, 0.002 mm and 0.01 mm respectively. The ranges of values obtained for the density index (I_D) of the shearbox samples are given in Table 3.5.

Table 3.5: Density index range for shearbox samples

	Loose sample
Density Index (%)	44.8 – 62.0

The strength values presented in Table 3.6 were determined from shearbox tests on the loose samples of the test sand. The maximum shear strength was determined from the relationships between shear stress and horizontal displacement, Figure 3.10. The sand samples did not dilate, Figure 3.11. The angle of internal friction was determined from the relationship between the shear and normal stresses for the test sand, Figure 3.12, and is summarised in Table 3.7.

Table 3.6: Maximum shear stress and angle of dilation for the loose sand

Normal Stress (kPa)	25	62.5	125	250	375
C.V. Shear Stress (kPa)	6	31	60	150	230
Max. dilation angle (degrees)	0	0	0	0	0

Table 3.7: Summary of angles of friction and dilation for the test sand

	I_D (%)	φ_{cv}	Ψ
Loose	44.8-62.0	29.8	0

Table 3.8: Sand classification and properties of the sand used in this study

Classification	Uniform, slightly silty, medium SAND.
C_z	1.1
C_u	1.53
ρ_s (Mg/m3)	2.621
ρ_d,max. (Mg/m3)	1.75
φ_{cv}	29.8°
Ψ (I_D 44.8 - 62%)	0

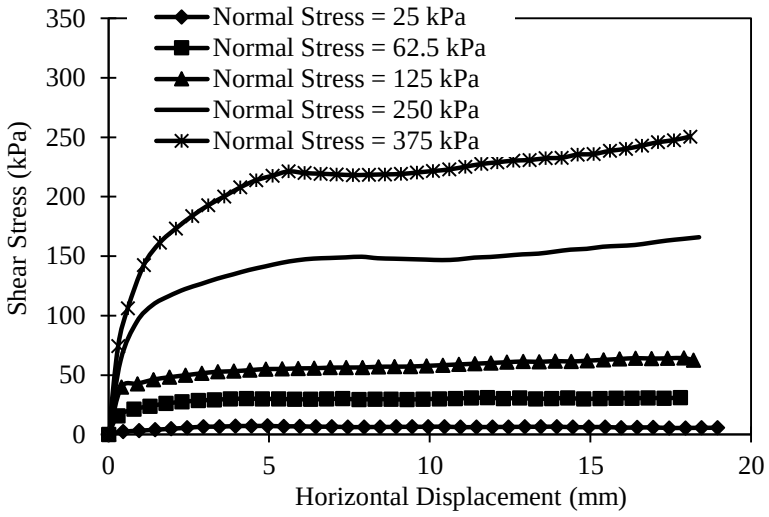

Figure 3.10 Shear stress vs. horizontal displacement for loose sand (I_D = 44.8 – 62.0 %)

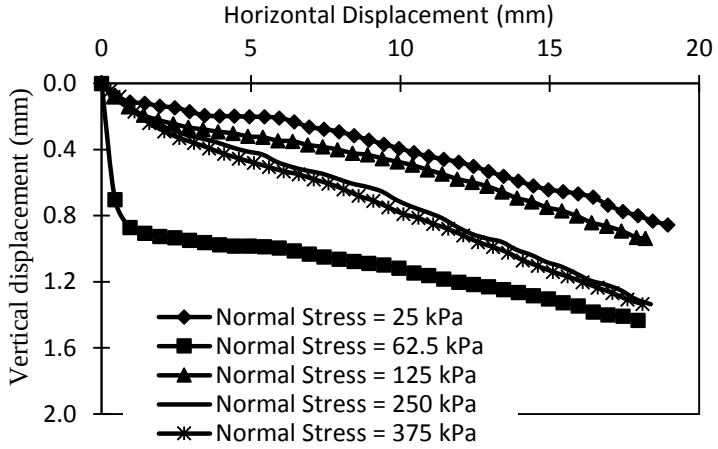

Figure 3.11 Vertical vs. horizontal displacement for loose sand (I_D = 44.8 – 62.0 %)

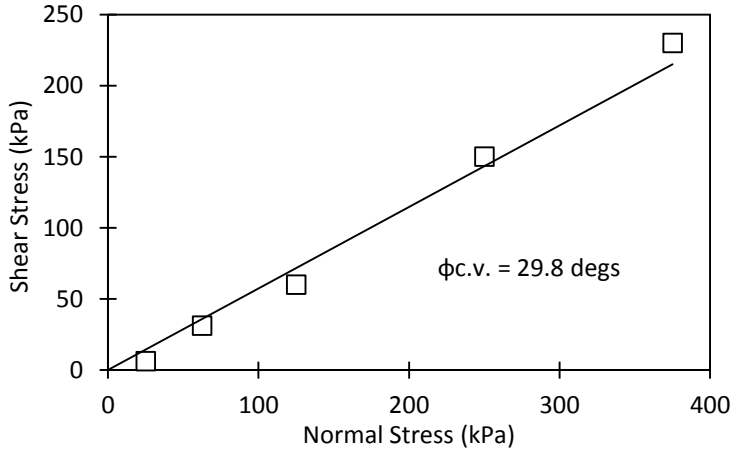

Figure 3.12 Normal stress v shear stress for loose sand (I_D = 44.8 – 62.0 %)

3.2.6.7 Pile group

Normally aluminium would be used to model piles in a centrifuge test. The bending stiffness of an aluminium pile would be extremely stiff. Preliminary centrifuge testing of suitable materials to model the pile wall revealed the aluminium and materials of similar stiffness's experienced relatively low magnitudes of lateral deformations that were difficult to accurately measure using the camera. To achieve lateral deformations of the piles that could be accurately measured from the cameras photos, a more flexible pile material in the form of perspex was selected.

Each pile within the pile group was manufactured from perspex sheets with plan dimensions of 100mm x 2mm and a height of 71.42mm. A beam deflection procedure was used to determine the stiffness characteristics of the piles. The beam-deflection test sample had a width of approximately 24 mm and height of 2 mm and was clamped at one (cantilever) or both ends (fixed-ends) to prevent movement. Point load increments that produced 0.25 mm deflection were applied to the material at the free end (cantilever) or midpoint of the beam (fixed-ends), to produce ultimate deflections of 10 and 5 mm respectively. The load required to produce each 0.25 mm deflection increment was recorded. The load-deflection relationships for the fixed-end and cantilever beam-deflection testing are illustrated in Figures 3.12 and 3.13. Beam deflection testing of the perspex was used to calculate the Young's modulus of the material as 1.9 GPa, giving an average axial stiffness of 0.9 MN which was equivalent to 3.24 GN at 60g, Table 3.9.

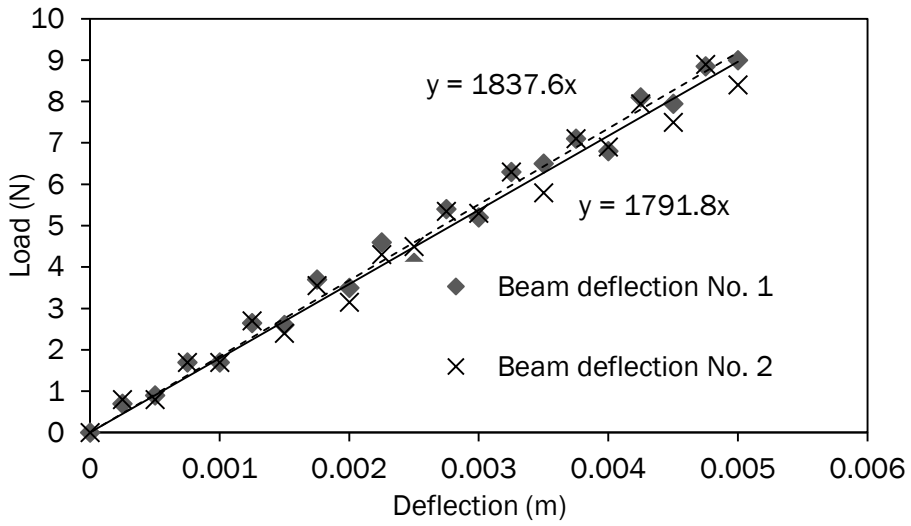

Figure 3.13: Fixed end beam-deflection test results on Perspex

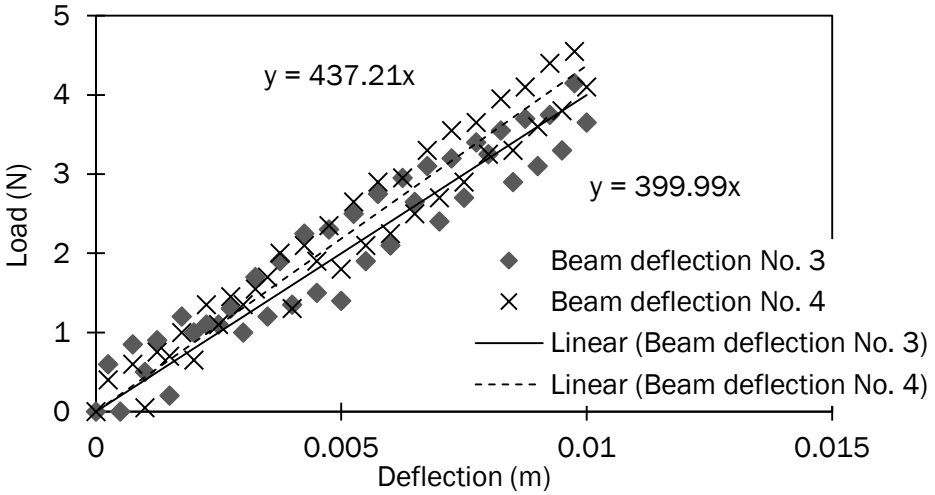

Figure 3.14: Cantilever beam-deflection test results on Perspex

Table 3.9: Young's modulus (*E*) of perspex piles

	Fixed-end *E* (GPa)	Cantilever *E* (GPa)
Beam-deflection Test No. 1	1.95	
Beam-deflection Test No. 2	1.93	
Beam-deflection Test No. 3		1.85
Beam-deflection Test No. 4		1.88
Average (based on Test No. 1-4)	1.9	

3.2.6.8 Properties of the soft subsoil

Typically, a range of sands and clays would be used to model soft soil in centrifuge tests. A geosynthetic reinforced piled embankment will have a considerable stiffness differential between the soft soil layer and the piles. In consideration of the flexible perspex sheets used to model the pile wall and consequently, the lower stiffness of the perspex pile wall, a corresponding reduction in the stiffness of the soft soil material to achieve a similar stiffness differential between the pile and the soft soil was required. Typical sands and clays used are not sufficiently low in stiffness to be considered here.

The soft subsoil was modelled using two different materials, a synthetic sponge and expanded polystyrene (EPS), Appendix D Figures D8 and D9. A variation of the soft soil prototype stiffness would enable the determination of the soil stiffness effect on

the performance of the geosynthetic reinforced piled embankment with specific reference to the effect of lateral deformation at or near the extremities of the structure. The lateral displacement of the soil will not be properly simulated by the synthetic sponge and EPS materials, a typical soil may develop shear planes in failure, this was not possible with the two materials selected. The selection of the materials was based on their stiffnesses.

The stiffness of the synthetic sponge and EPS used in the models as the soft soil was determined in a modified oedometer apparatus. The test samples were cut to fit snugly into a consolidation ring, which rigidly supported and confined the specimen laterally. This was then placed on the bed of the loading apparatus and stress increments of approximately 0.4 to 1 kPa were applied to the specimen. The deformation of the sample under each stress increment was recorded. The dial gauge used to record the vertical deformation had a resolution of 0.001 mm. The strain was defined as the change in height normalised by the initial height of the sample ($\Delta H/H_0$). The stiffness of the sample was determined by measuring the slope of the initial linear portion of the stress-strain curve and found to be approximately 54 kPa and 240 kPa for the sponge and EPS respectively, Figures 3.14 and 3.15, corresponding to stiffness's of 54 kPa and 240 kPa, respectively, at 60*g*.

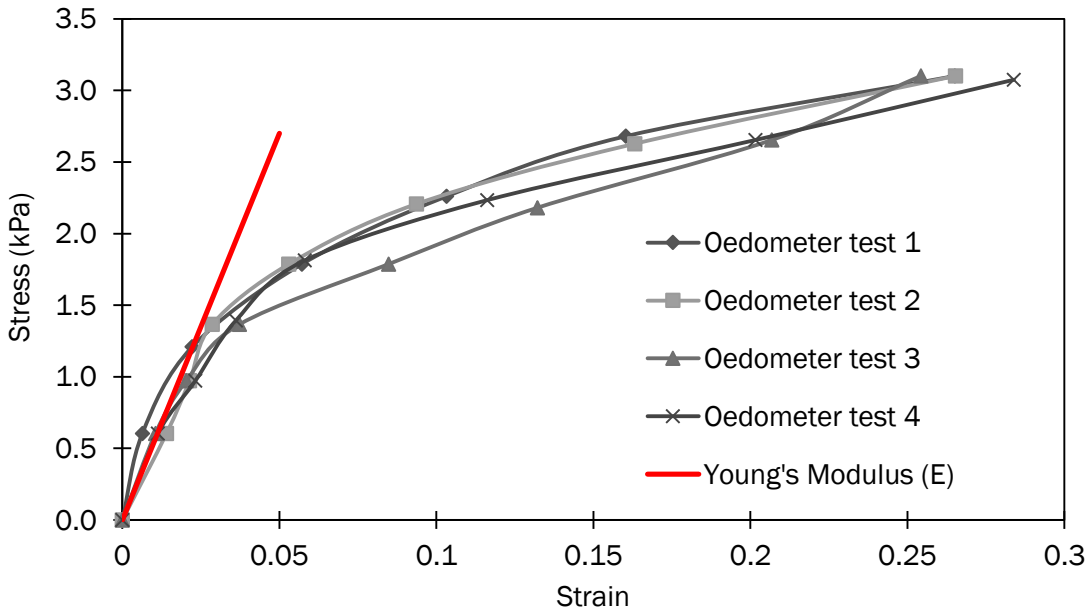

Figure 3.15: Load – deformational response of synthetic sponge used in this test programme

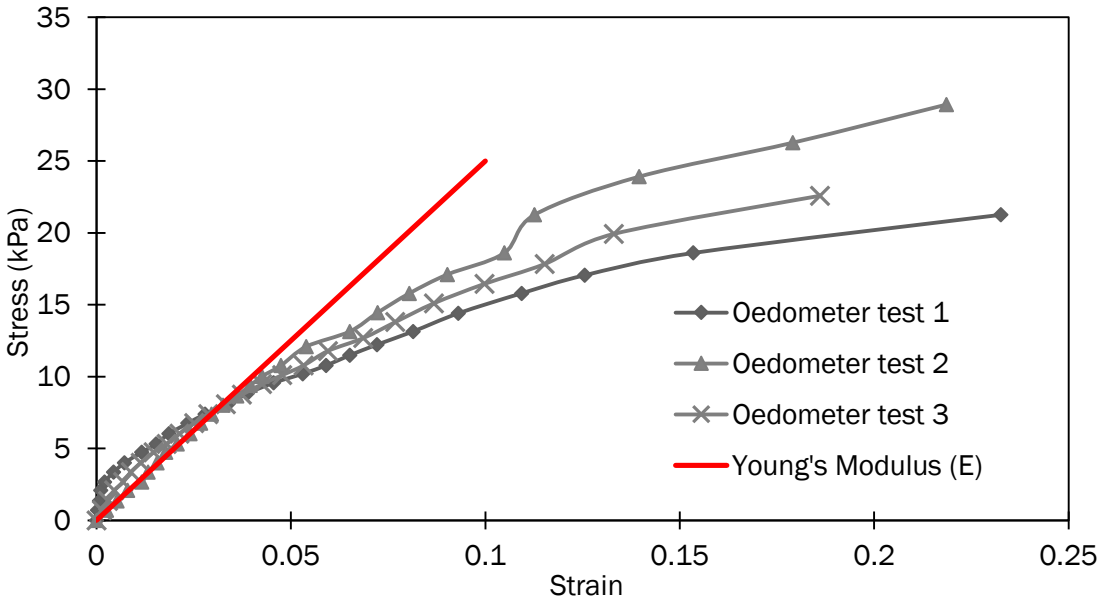

Figure 3.16: Load – deformational response of EPS used in this test programme

To ensure friction effects of the soft subsoil model against the perspex centrifuge window was negated, a slight gap between the prototype sub-soil models and the perspex strongbox windows ensured that no confining pressure from the windows would enhance the soil elements resistance to lateral/vertical deformation. The slight gap between the soil model material and the perspex window would have closed as the g level increased. The closing of the gap between the soil model material and the perspex window increased the friction effects along the perspex window. Lubrication alone in the form of grease, oils or silicones had little or no effect in reducing the friction angle between the soil model materials and the perspex window which ranged from 22° to 25°. The best intervening layer system consisted of a thin layer of silicone lubricant applied to the window and covered with very thin polyethylene sheet, this system reduced the friction angle between the soil model materials to 6.1° to 8.2°. This system was also used to negate friction effects between the embankment fill and the perspex window.

It was not possible to determine the strength characteristics of either the sponge or EPS material using conventional geotechnical engineering apparatus. Attempts to determine the strength characteristics with shear box testing were unsuccessful, a φ value of 25.0° for the Sponge and EPS was assumed. The synthetic sponge and the EPS were modelled using a preconsoildation pressure of 1.45 kN/m^2 and 8.2

kN/m^2 respectively. An assumed interface influence factor, R_{inter} of 0.95 was taken for both materials.

3.2.6.9 Properties of the geosynthetic reinforcement

The geosynthetic reinforcement was modeled in the centrifuge prototype model using polyethylene sheets. The polyethylene sheets are normally used as refuse bin liners, Appendix D Figures D10 and D11. The sheets were fully restrained along one side of the model (parallel to the piles) and free at the other.

Tensile testing of the polyethylene sheets was carried out to determine the tensile stiffness. The test sample had a width of 100 mm and length of 300 mm and was clamped at either end to prevent slippage. Load increments of approximately 2 to 4 N were applied to the material at one end while the other end was fixed. The change in length and width of the sample at the mid length of the sample under each known load increment were recorded. The relationship between tensile load per meter width (corrected for reduction in width during the test) and strain for the samples are presented in Figure 3.17. The stiffness of the sample (J_{re}) was determined by measuring the slope of the initial linear portion of the curve and found to be 4.7 kN/m respectively, corresponding to stiffness of 282 kN/m at 60g.

The interface influence factor (R_{inter}) between the soil and geosynthetic reinforcement was determined using the shearbox apparatus. A block of wood (custom cut to fit snugly into shearbox) wrapped with polyethylene sheeting (geosynthetic) was placed into the lower half of the shearbox, with the top surface of the wood flush with the shearbox shear plane. The top half of the shearbox was then attached and filled with sand. Shearbox tests were conducted using loose sand at normal stresses of 62.5 or 90, 125, 250 and 375 kPa.

Loose samples were prepared by pouring the sand directly into the assembled shearbox from a height of 50 mm. The specimen was then consolidated by applying the appropriate normal stress and sheared to failure at a rate of 2 mm/min. The shear force and horizontal displacements were measured using dial gauges with resolutions of 0.002 mm and 0.01 mm respectively. The ranges of density index (I_D) for the shearbox samples are given in Table 3.5.

The maximum shear strength was determined from the relationships between shear stress and horizontal displacement, Figure 3.18. The angle of internal friction at the interface was determined from Figure 3.19, and is summarised in Table 3.10.

The interface influence factor (R_{inter}) between the soil-geosynthetic was determined using Equation 3.6. In this study an average interface influence factor of 0.79 was used in the analyses, Table 3.10.

$$R_{inter} = \frac{\tan \varphi(geo)}{\tan \varphi(sand)} \qquad \text{Equation 3.6}$$

Table 3.10: R_{inter} parameter for interface between loose sand and geosynthetic

		Angle of internal friction for sand	Angle of friction for sand geosynthetic interface	R_{inter}
Loose sand	$\varphi_{c.v.}$	29.8°	24.4°	0.79

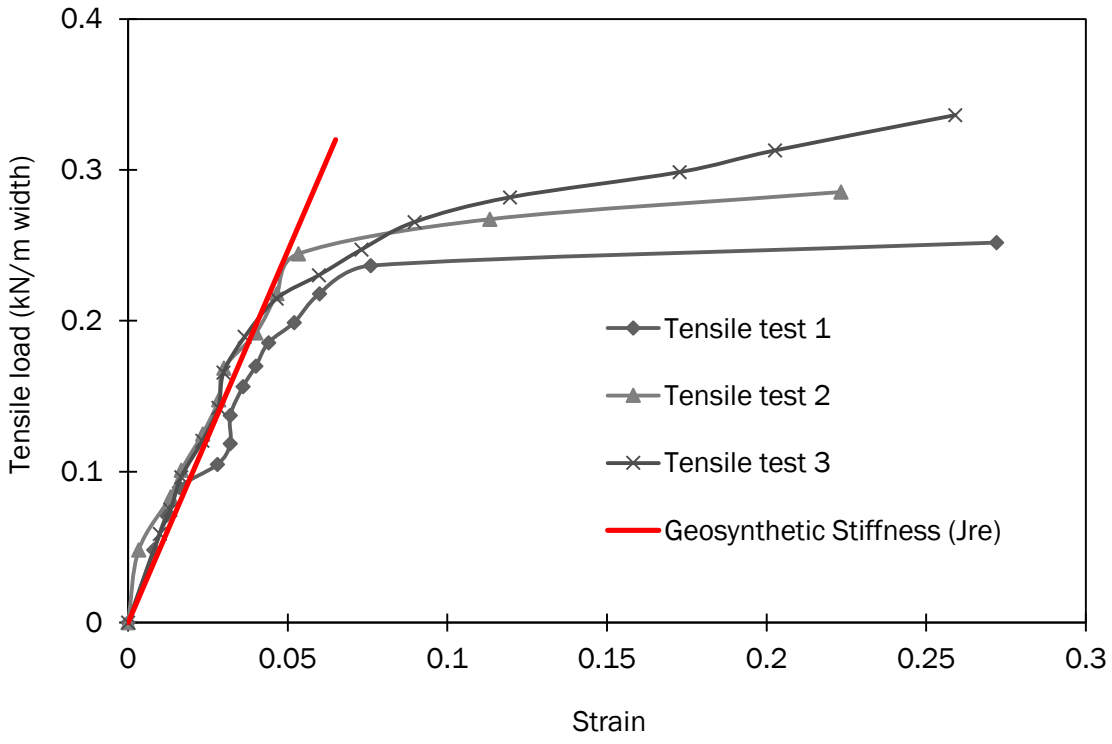

Figure 3.17 Normal stress v shear stress for loose sand

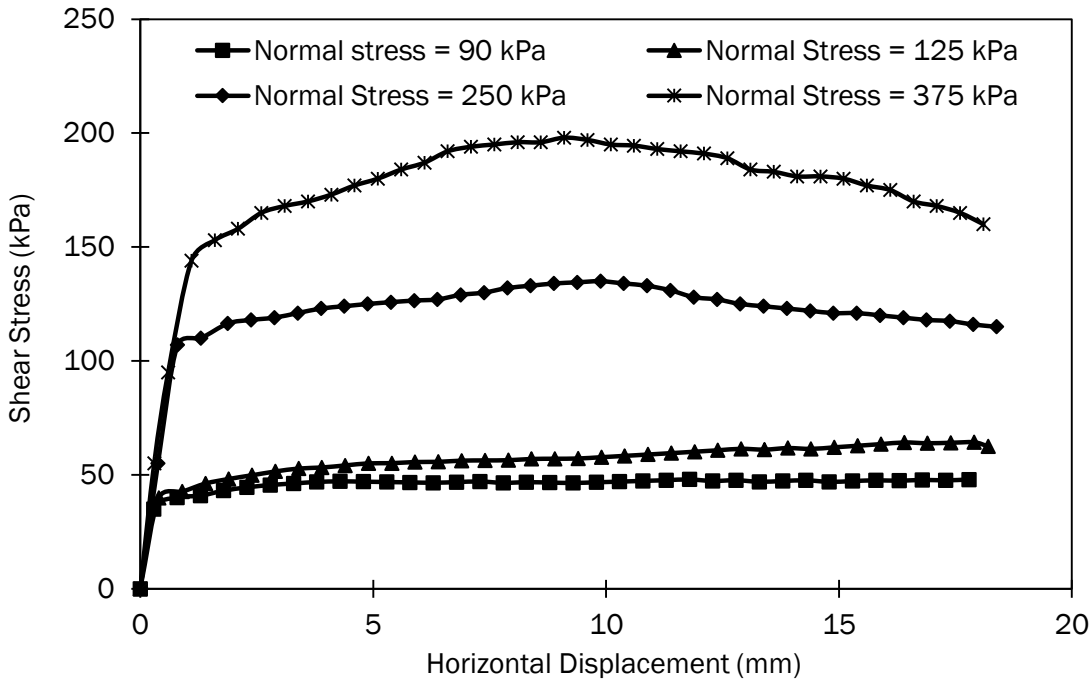

Figure 3.18 Shear stress vs. horizontal displacement for sand geosynthetic interface for loose sand (I_D = 46.2 – 66.6 %)

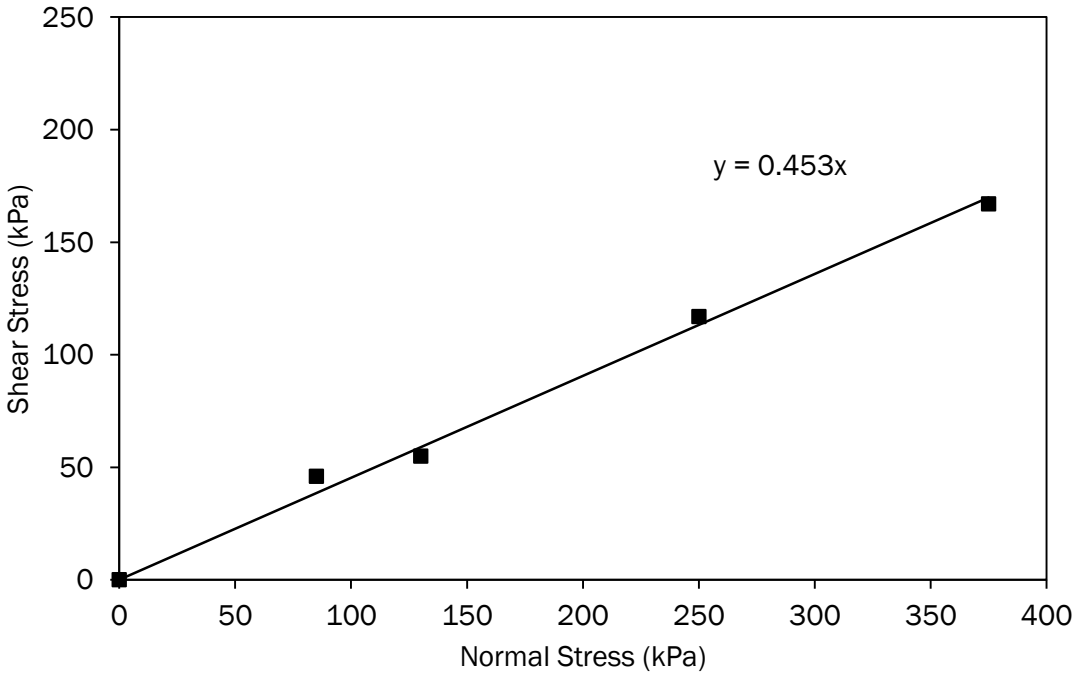

Figure 3.19 Normal stress vs. shear stress for sand geosynthetic interface for loose sand (I_D = 46.2 – 66.6 %)

3.2.7 Centrifuge modelling potential source of errors

One of the few criticisms leveled at centrifuge modelling is having significant errors due to the non-uniform acceleration field and also the difficulty representing sufficient detail of the problem in a small scale model.

The earth's gravity is uniform in the practical range of soil depths encountered in civil engineering. There is a slight variation in acceleration through the centrifuge model because the inertial acceleration field is given by $\omega^2 r$ where ω is the angular rotational speed of the centrifuge and r is the radius to any element in the soil model. The problem can be minimized if care is taken to select the radius at which the gravity scale factor *n* is determined and limit the height of the model relative to the nominal radius.

The inertial radial acceleration is proportional to the radius which leads to a variation with depth. When the depth of the model is ignored by assuming a constant radius, there is a difference between the calculated and the actual centrifuge stress field, Figure 3.20. The effective radius of the beam centrifuge used in this study was 660mm which equates to 90mm above the base of the strong box. The effective radius was approximately 16mm below the top of the pile caps/geosynthetic reinforcement, Figure 3.20. The radius of the IT Sligo geotechnical centrifuge was relatively small in comparison to the strongbox width. The result of which can lead to areas of activity at the boundary of the model container. Taylor (1995) advised that it is good practice to ensure that major events occur in the central region of the model where the error due to the radial nature of the acceleration field is small.

Another potential source of inaccuracy is due to the curvature of the stress field. The radial direction of centrifuge acceleration is aligned with the vertical axis of the model only at the centre. The related velocities of the piles and soil offset from the center of the model, were very small and inaccuracies due to the Coriolis effects are considered to be negligible, Taylor (1995).

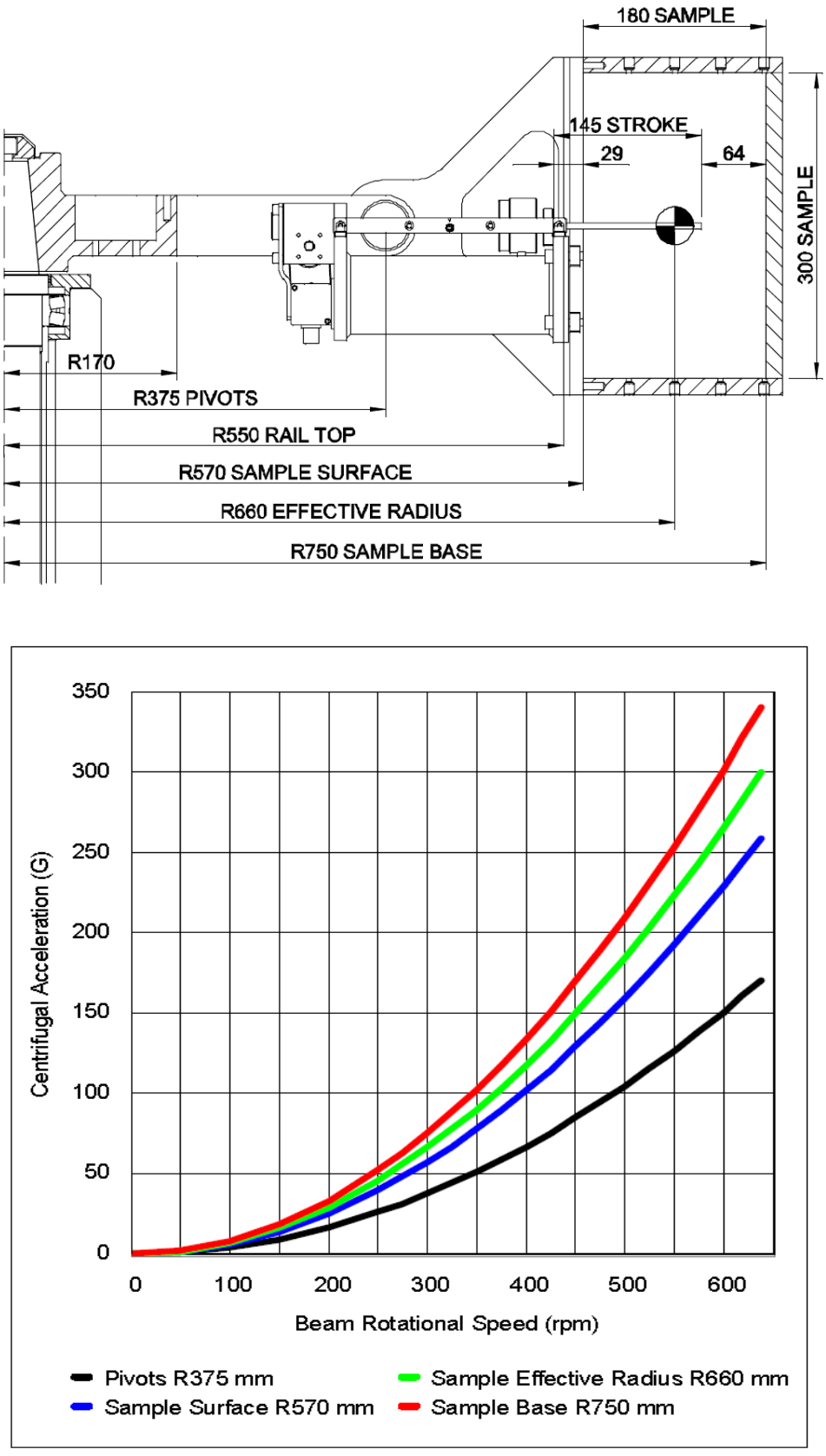

Figure 3.20 Effective radius influence on centrifugal acceleration (Thomas Broadbent and Sons Limited centrifuge manual)

3.3 Numerical modelling

Numerical analyses using finite element techniques have been particularly popular in recent years for verifying or refining design procedures. Based on the method described by Zienkiewicz (1977), a variety of finite element computer programs are available with different facilities to suit a number of needs. Finite element modelling of the reinforced piled embankment structure was performed using Plaxis 2D 2010. Plaxis 2D is a two-dimensional finite element package for analysis of deformation and stability in geotechnical engineering.

The Plaxis 2D 2010 full scale plane strain model both replicated the testing carried out by the geotechnical centrifuge and extended the analysis to investigate other parametric variations. The dimensions and material characteristics of the full scale numerical model were equivalent to that of the centrifuge geosynthetic reinforced piled embankment model at 60 times gravity. The geometric layout of the Plaxis 2D model replicated the layout of the centrifuge model that was sized in accordance with BS 8006 (2010), Figure 3.21.

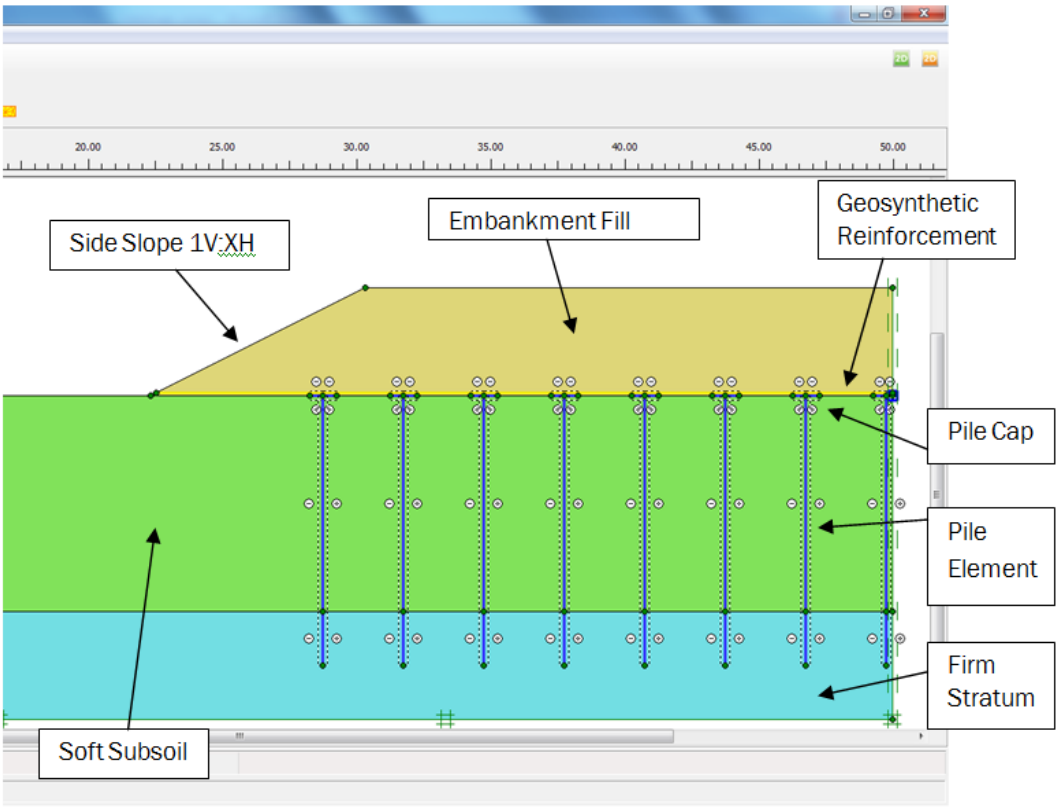

Figure 3.21 Plaxis 2D plane strain geosynthetic reinforced piled embankment model

A parametric study of the plane strain model similar to centrifuge modelling was undertaken with particular attention to the deformations and forces developed of both the geosynthetic reinforcement and the piles within the pile group at the outer extremities of the embankments.

For analyses using critical state models, Philips (1986) and Kusakabe (1982) have shown that provided the mesh is fine enough in the areas of high strain gradient, and the loading increments were small enough, good agreement has been reached between numerical and experimental results.

A comparative analysis between the physical centrifuge testing and finite element analysis would enable the effect of the lateral thrust within the embankment fill to be assessed.

3.3.1 Finite Element Analysis

Plane strain finite element modelling of the reinforced piled embankment structure was performed using Plaxis 2D (2010). Idiosyncratic differences between the two modelling methods (centrifuge and numerical) are stated and the means to minimize potential sources of error are justified. In the study the soft subsoil was modelled using the soft soil model, the embankment fill using the Mohr-Coulomb model, the piles using the plate model and the geosynthetic reinforcement as an elastic geogrid.

3.3.1.1 Soft Soil Model

The soft soil underlying the embankment structure was modelled using the Soft Soil model in Plaxis 2D. The Soft Soil model is based on the modified Cam-Clay isotropic soil model. In the soft soil model, strains are composed of elastic (reversible) strains and plastic (irreversible) strains. The soft soil model is very useful to simulate the behaviour of normally consolidated clays and peat in primary loading, as long as time aspects are of minor importance (Plaxis 2D, 2010; Neher et al, 2001). In the soft soil model, it is assumed that there is a logarithmic relationship between the volumetric strain $\varepsilon_{v,}$ and the mean effective stress p', which can be formulated as:

$$\varepsilon_{\upsilon} - \varepsilon_{\upsilon 0} = \lambda^{*}.\ln\left(\frac{p\prime}{p\prime_0}\right) \quad \text{(For isotropic virgin compression)} \qquad \text{Equation 3.7}$$

where:

ε_v the volumetric strain

ε_{vo} the initial volumetric strain

λ^* the modified compression index

p' mean effective stress

p'_0 initial effective confining stress

During isotropic unloading and reloading a different path is followed, which can be formulated as:

$$\varepsilon_{\upsilon}^{e} - \varepsilon_{\upsilon 0}^{e} = \kappa^{*}.\ln\left(\frac{p\prime}{p\prime_0}\right) \quad \text{(For isotropic unloading/reloading)} \qquad \text{Equation 3.8}$$

where:

ε_v^e the volumetric strain

ε_{vo}^e the initial volumetric strain

κ^* the modified swelling index

The parameter κ* is the swelling index which determines soil behaviour during unloading and reloading. This behaviour is assumed to be elastic. The elastic strain is defined as the following:

$$E_{ur} = 3(1 - 2\upsilon_{ur}).\frac{p\prime}{\kappa^{*}} \qquad \text{Equation 3.9}$$

where:

v_{ur} Poisson's ratio for unloading/reloading (default: v_{ur} = 0.15)

The modified compression and swelling index differ from the normal compression and swelling index used in the original Cam Clay model as they are defined in terms of the void ratio e instead of the volumetric strain ε_v.

Two soft soil models were utilized with the parameters replicating those of the materials used in the centrifuge modelling test programme (Synthetic sponge and EPS). The direct shear method was not suitable for characterising the strength characteristics of the synthetic materials. To determine strength parameters for the model a parametric study investigating the significance of angle of friction, angle of dilation and cohesion was conducted. Parametric studies on a low to medium height embankment using Plaxis confirmed that the friction angles had a marginal effect on deformations within the embankment respectively, Appendix A Figure A1 and A2. A friction angle of 25° was assumed, lower values of friction yielded greater magnitudes of lateral deformations at the outer pile row and vertical deformations of the reinforcement near the embankment toe. Variation of the dilation angles had a negligible effect on deformations within the structure, Figure A3, A4 in Appendix A. The soil cohesion however was found to have a significant effect on deformations, Appendix A Figure A5 and A6. A cohesion of 3 kPa, was chosen for the Plaxis analyses because values higher than this may have resulted in a model that overestimated the subsoil support and hence underestimated the stresses and deformations in the geosynthetic reinforcement at the base of the embankment and support offered to the pile group. An R_{inter} value of 0.95 was assumed, values lower than 0.95 yielded a marginal increase in pile lateral deformations and the vertical deformations near the toe remained constant, Appendix A Figure A7 and A8.

The modified compression index determines the compressibility of the material in primary loading and was determined from the logarithmic relationship between volumetric strain and mean stress (p'). The modified compression index for sub-soils A (sponge) and B (EPS) was determined using the results acquired from the stiffness testing in the modified oedometer apparatus, outlined in Section 3.2.6.8. The modified compression index was determined by measuring the slope of the logarithmic stress-strain curve over a mean stress range of 2.7 to 20 kPa. This stress range was typical of that encountered in the subsoil immediately beneath the geosynthetic reinforcement in a full scale embankment. The modified compression index was found to be approximately 0.585 and 0.045 for sub-soils A and B respectively, Figures 3.21 and 3.22.

The modified swelling index was held constant, as it was assumed that the idealized finite element model was subjected to primary loading only and consequently did not undergo unloading reloading.

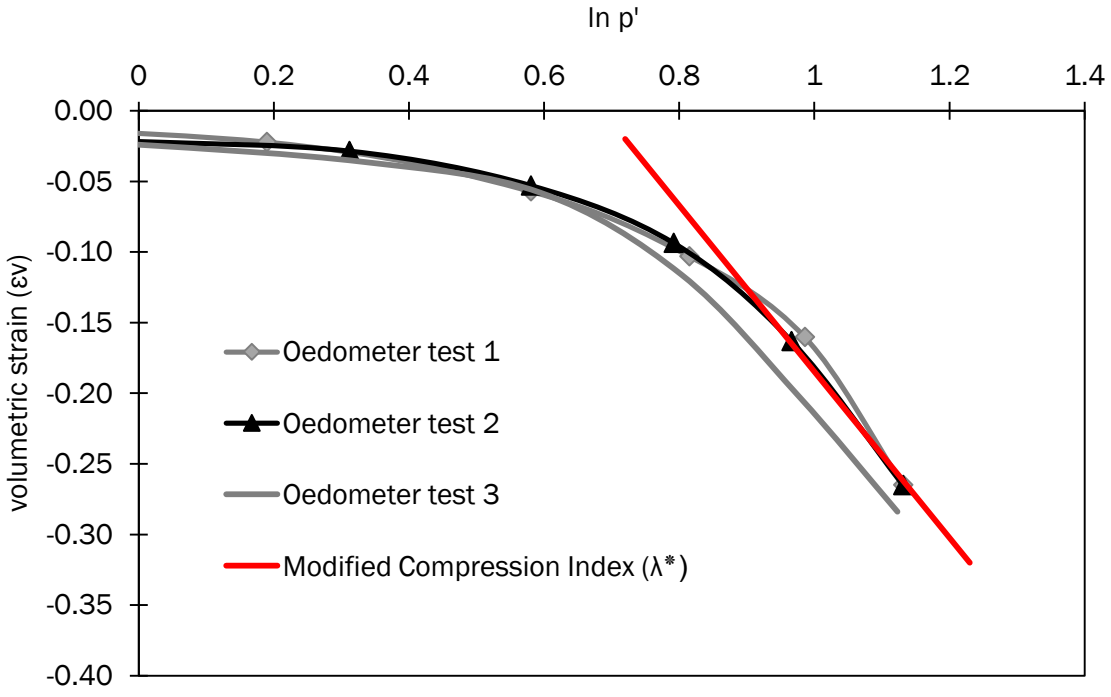

Figure 3.22 Volumetric strain vs. ln(p') for subsoil A

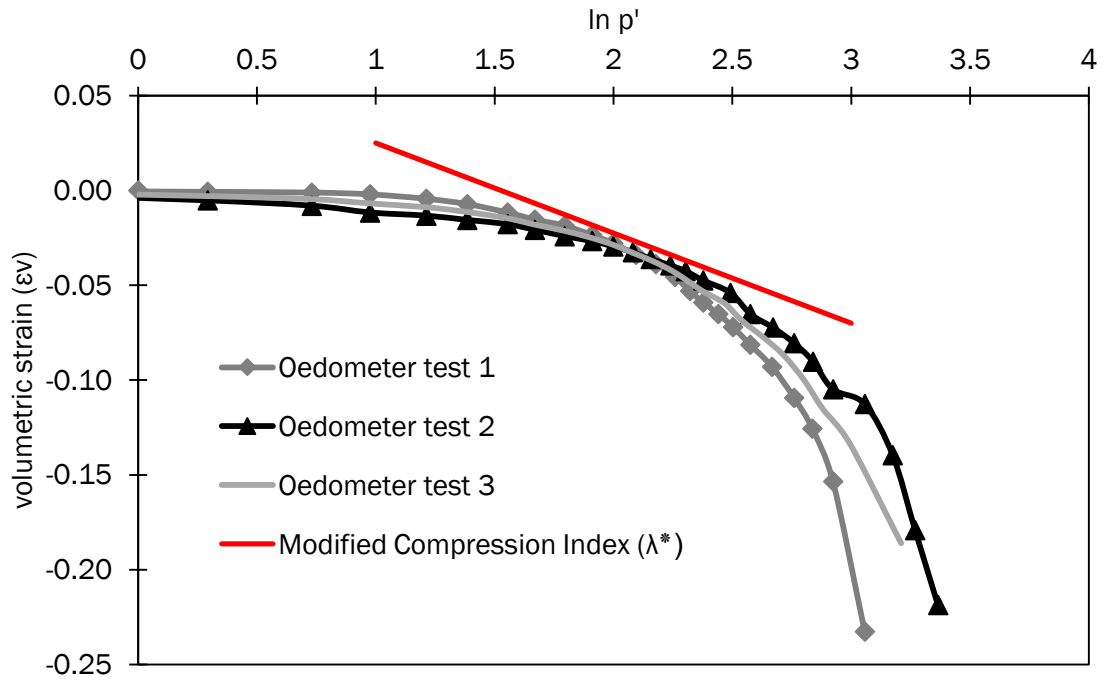

Figure 3.23 Volumetric strain vs. ln(p') for subsoil B

3.3.1.2 Embankment Fill

A Mohr-Coulomb (*MC*) linear-elastic perfectly plastic soil model was utilized to model the embankment material fill. The Mohr-Coulomb model, is suitable where soil parameters are not known with great certainty (Plaxis 2D, 2010). This model requires five basic soil input parameters, namely Young's modulus (E) or shear modulus (G), poisson's ratio (ν), cohesion (c), friction angle (φ) and dilatancy angle (ψ).

The material characteristics of the slightly silty medium sand used during the centrifuge testing program was adopted, Table 3.11. The primary disadvantage of a MC model is that it only gives a first order approximation of deformations. However, the MC model is used extensively, primarily as the required parameters can be readily determined. The unit weight of the fill and the initial void ratio were calculated based on the average dry density of the embankment fill encountered during centrifuge testing. This was calculated by measuring the mass of sand required to construct the embankment. The Young's Modulus and Poisson's ratio were calculated as 20 MPa and 0.2, respectively during testing.

Table 3.11: Mohr Coulomb parameters of loose sand

	Loose sand
Friction angle (°)	30
Angle of dilation (°)	6.5
Cohesion (kPa)	0.0
Saturated unit weight (kN/m^3)	18.16
Unsaturated unit weight (kN/m^3)	15.15
Initial void ratio	0.698
Young's Modulus (*MPa*)	20
Poisson's Ratio	0.2

* Britton (2012).

3.3.1.3 Geosynthetic Reinforcement

Plaxis 2D suggests geosynthetic reinforcement should be modelled as an elastic geogrid with an axial stiffness equivalent to the polyethylene sheets used in the centrifuge modelling of 282kN/m. The axial stiffness (J_{re}) of the geosynthetic

reinforcement was held constant. A single layer of geogrid reinforcement was placed 100mm above the pile caps. The tensile stiffness of the geosynthetic reinforcement utilized was based on the equivalent of stiffness of the centrifuge model at 60*g*, Section 3.2.6.9. An interface interaction value R_{inter} of 0.79 was used for the interface between the reinforcement and the fill.

3.3.1.4 Pile Model

Plaxis 2D (2010) recommends pile elements should be modelled using a plate model with a linear elastic material set applied, Table 3.9. The pile was embedded into a stiff bearing layer to replicate a fixed restraint at the lower extremity. The influence of the interface was reduced when the deformations are very small. The Young's modulus of the thermoplastic co-polyester pile material was measured as 1.9GPa. The pile had a thickness of 0.120m, which corresponded to the centrifuge pile dimension at 60g. The pile cap size was held constant at 0.428m with a thickness of 0.214m. It is important to model the inter-face between the geosynthetic-soil and the pile-soil (Plaxis 2D, 2010). An assumed interface factor between the subsoil and the piles of 0.95 was used in this study.

The real interface thickness (δ_{inter}) is a parameter that represents the real thickness of a shear zone between a structure and a soil. Plaxis suggests that the value of δ_{inter} is only of importance when the hardening soil model is employed. Thus for this study using the soft soil model the real interface thickness (δ_{inter}) was left at the default value of 0.1. The real interface thickness is expressed in length and is generally of the order of a few times the average grain size. This parameter is used to calculate the change in void ratio in interfaces for the dilatancy cut-off point.

3.3.2 Finite model boundary conditions

The boundary conditions chosen for the Plaxis 2D finite element model were intended to represent those imposed by the rigid centrifuge strongbox with frictionless internal surfaces. The overall geometry of the finite element model was equivalent to that of the centrifuge strongboxes at 60g.

The finite element model was created using the geometry line, plate elements (pile and pile cap), geogrid (geosynthetic reinforcement) and interface features and all

material sets were created and applied to the relevant areas, Figure 3.21 and Appendix D Figure D12. The soil and tip of the pile were restrained in all directions at the base of the model which replicated the centrifuge modelling. The piles were penetrated into a very stiff layer ensuring the piles were fully fixed.

Standard fixities option was selected for the boundary conditions during analysis, Plaxis suggests standard fixities is suitable for most geotechnical applications (Plaxis 2010). The boundary conditions for standard fixities are generated under the following rules:

- Vertical geometry lines which the x-coordinate is equal to the lowest or highest x-coordinate in the model obtain a horizontal fixity ($U_x = 0$).
- Horizontal geometry lines for which the y-coordinate is equal to the lowest y-coordinate in the model obtain a full fixity ($U_x = U_y = 0$).
- Plates that extend to the boundary of the geometry model obtain a fixed rotation in the point at the boundary ($U_z = 0$) if at least one of the displacement directions of that point is fixed.

3.3.2.1 Mesh generation

To model soil layers and other clusters, a 15-node or 6-node triangular elements may be used. A 15-node element provides fourth order interpolation for the variable field (displacements) and the numerical integration involves twelve Gauss points also known as stress points. However, for a 6-node element, order of interpolation is two and numerical integration involves three Gauss points. A 15-node triangular element is preferred over a 6-node element for its very accurate and high quality stress results. In addition, it has been observed that the 6-node element over predicts the failure loads and safety factors (Nag Rao, 2006). A beam and a geotextile (structural element) are 5-node and 3-node elements, which is compatible with the 15-node or 6-node soil elements. Since the failure due to excessive settlement is a concern in this analysis, a 15-node triangular element was considered.

The geometry has to be divided into finite elements in Plaxis 2D to perform finite element analyses. Division of geometry is automatically done when all the material properties and the structural elements are defined in the model. The mesh

generator requires a meshing parameter which represents the average element size l_e. The meshing parameter is dependent on the geometry dimensions of the model and the coarseness factor called n_c. The relation between the average element size, meshing parameter, and the coarseness factor is shown below (Plaxis, 2010):

$$l_e = \sqrt{\frac{(x_{max}-x_{min})(y_{max}-y_{min})}{n_c}} \qquad \text{Equation 3.10}$$

Where x_{max}, x_{min}, y_{max} and y_{min} are the outer geometry dimensions and n_c is given by:

Very coarse	n_c =25	Around 75 elements
Coarse	n_c =50	Around 150 elements
Medium	n_c =100	Around 300 elements
Fine	n_c =200	Around 600 elements
Very fine	n_c =400	Around 1200 elements

A very fine mesh discretization was selected with a local refinement around the pile group selected, Appendix D Figure D13. In conventional finite element analysis, the influence of the geometry change of the mesh on the equilibrium conditions is neglected. This is usually a good approximation when the deformations are relatively small as is the case for most engineering structures, Plaxis (2010). However, there are circumstances under which it is necessary to take this influence into account. Typical applications where updated mesh analyses may be necessary include the analysis of reinforced soil structures, the analysis of large offshore footing collapse problems and the study of problems where soils are soft and large deformations occur. When large deformation theory is included in a finite element program some special features need to be considered. Firstly, it is necessary to include additional terms in the structure stiffness matrix to model the effects of large structural distortions on the finite element equations. Secondly, it is necessary to include a procedure to model correctly the stress changes that occur when finite material rotations occur, Plaxis (2010). Updated mesh was selected in this study to consider the influence of change in the geometry of the model caused by large deformation of the soft soils.

3.3.2.2 Generation of initial stresses

The staged construction loading input was selected with three construction phases; initial phase, pile and geosynthetic reinforcement installation, and embankment construction. In Plaxis 2D, the initial stresses in the soil can be generated by either the K_0 modelling procedure or by using gravity loading. Plaxis suggests the K_0 procedure should only be used in cases with a horizontal surface and all soil layers and pheatric layers parallel to the surface, for all other cases, gravity loading should be used. The inital stresses in the soil in a soil body are influenced by the weight of the material and the history of its formation. The stress state in the soil body is usually characterised by an initial vertical effective stress ($\sigma'_{v,o}$). The inital horizontal effective stress $\sigma'_{h,o}$ is related to the initial vertical effective stress by the coefficient of lateral earth presure K_0 ($\sigma'_{h,o} = K_0 \times \sigma'_{v,o}$).

The K_0 procedure is a special calculation method availiable in Plaxis to define the inital stresses for the model taking into account the loading history of the soil. For advanced soil models (hardening soil model, HSM with small strain stiffness, soft soil model, SS creep model and the modified cam clay model) the default value is influenced by the over consolidation ratio (OCR) and the pre overburden pressure (POP) in the following way (Plaxis 2010), Figure 3.24:

$$K_{OX} = K_0^{nc} OCR - \frac{v_{ur}}{1-v_{ur}}(OCR - 1) + \frac{K_0^{nc} - \frac{v_{ur}}{1-v_{ur}} POP}{|\sigma_{yy}^0|} \qquad \text{Equation 3.11}$$

Where the default value K_0 value is then in principal based on Jaky's formula:

$$K_0 = 1 - \sin\varphi \qquad \text{Equation 3.12}$$

Where K_0^{nc} is the K_0 value associated with normally consolidated states of stress, which is an input parameter for the advanced soil models. The default parameter setting is such that:

$$K_0^{nc} \approx 1 - \sin\varphi \qquad \text{Equation 3.13}$$

where:

v_{ur} = Poisson's Ratio

σ_{yy}^{0} = insitu vertical effective stress

OCR = over consolidation ratio

POP = pre overburden pressure

It is also possible to specify the initial stress using the pro overburden pressure (POP) as an alternative to prescribing the over-consolidation ratio. The pre overburden pressure is defined by:

$$POP = \left|\sigma_P - \sigma'^{0}_{yy}\right| \qquad \text{Equation 3.14}$$

These two ways of specifying the vertical pre-consolidation stress are illustrated in Figure 3.24. The centrifuge soil material models were normally consolidated soils subjected to primary loading, to replicate this, the over consolidation ratio of the soft soil model used to model the soft subsoil was selected as 1.0 and the pre overburden pressure was selected as zero.

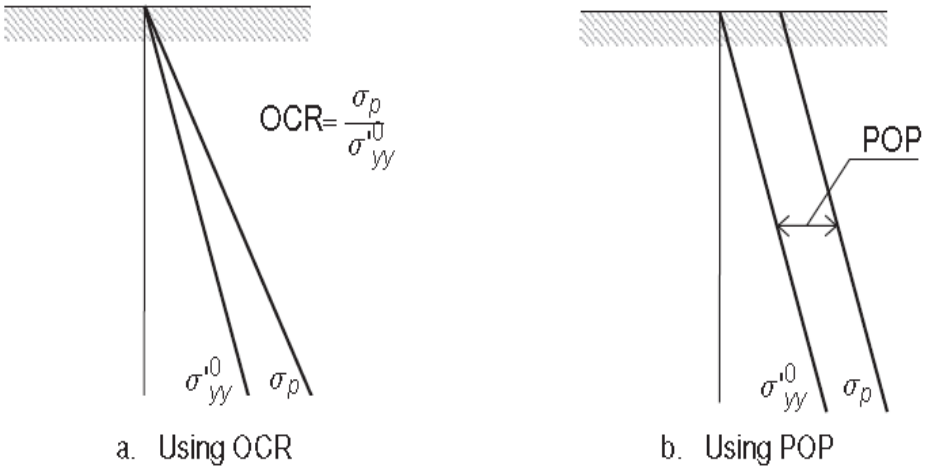

Figure 3.24 Illustration of vertical pre-consolidation stress in relation to the in-situ vertical effective stress (after Plaxis 2010)

3.3.3 Plastic analysis

The centrifuge analysis was performed using a drained analysis. To replicate the centrifuge modelling, a drained analysis was selected during the finite element modelling process. A plastic drained calculation was used to carry out an elastic plastic deformation analysis where undrained behaviour is ignored. The stiffness of the water within the matrix was not taken into account. As a plastic analysis was performed, consolidation was not a consideration and the time dependent construction process was ignored. Performing a fully drained analysis can access the long term deformational response of the model.

3.3.4 Model construction phase

The construction of the Plaxis 2D geosynthetic reinforced piled embankment consisted of the following three phases:

- The generation of the initial stresses within the soil body.
- Installation of the pile group within the soil and a layer of geogrid on top of the pile caps from the centre of the embankment to the toe at the side slope.
- The construction of the embankment on top of the geogrid/pile group.

As the analysis was not time dependent, the time (*t*) for the phase to be constructed was zero.

3.3.5 Tolerated error

In any nonlinear analysis where a finite number of calculation steps are used there will be some drift from the exact solution. The purpose of a solution is to ensure that any errors remain within acceptable bounds. Within each load step, the calculation program continues to carry out iterations until the calculated errors are smaller than the specified value. Plaxis suggests the standard error setting of 0.01 is suitable for most calculations but for failure load calculations it may be more practical to use an increased value of 0.03 or even 0.05.

In this study the tolerated error was kept to a minimum in all cases to ensure that deformations were not underestimated. A total of 22 finite element models were

constructed to replicate the centrifuge analyses. For 90% of the finite analysis, the tolerated error was lower than 0.02. The highest tolerated error of 0.3 was required for only 5% of the testing.

3.3.6 Post validation finite element model parametric analyses

The third element of the study was to perform a parametric variation on full scale geosynthetic reinforced piled embankments. The influence of pile spacing, pile cap size, stiffness of the geosynthetic reinforcement and soft subsoil depth was performed using Plaxis 2D (post centrifuge/Plaxis 2D validation). Structural geometries and material characteristics representative of in the field conditions were chosen to ameliorate the incomplete understanding of the GRPE born by the inadequacies of the centrifuge modelling to investigate these parameters. The analysis of the results is presented in Chapter 5.

The geometric layout (location of outer row pile) of the reinforced piled embankment examined using the Plaxis 2D (2010) software was determined by the BS 8006 (2010) design code. The generic model consisted of an embankment 4.0m in height with a 1V:2H side slope. The 300mm × 300m concrete piles, 10 m in length, were at 3.0m centres with a 1.0m wide pile cap. The pile was modelled as an end bearing pile that was driven 2.0m into a stiffer bearing layer to satisfy the simplifying assumption of a fixed ended pile.

The concrete pile had a bending capacity of 201 kNm at an axial load of 959 kN, Appendix B Section B.1. The 1.0m square pile cap was also designed to resist the vertical loads and the resultant bending moments, Appendix B Section B.3. The axial stiffness (*EA*) and bending stiffness (*EI*) were calculated for both the concrete pile and pile cap, Table 3.12 and 3.13 and Appendix B Section B.2 and B.4. In order to replicate the reduction of the lateral resistance of the pile group for an increase of the pile spacing in the longitudinal direction, the bending and axial stiffness characteristics of the Plaxis 2D pile wall were modified accordingly, Table 3.12.

Table 3.12: Material parameters for pile model from Appendix B Section B.2

	For single 300 × 300mm pile		Plaxis 2D pile wall	
Pile Spacing m	EA kN	EI kNm^2	EA kN/m	EI kNm^2/m
1.5	3521100	26901	2347400	17934
3.0	3521100	26901	1173700	8967
4.5	3521100	26901	782467	5978

Table 3.13: Material parameters for pile cap model from Appendix B Section B.4

For single 1000 × 1000mm square 700mm thickness pile cap		Plaxis 2D pile cap wall	
EA kN	EI kNm^2	EA kN/m	EI kNm^2/m
21192100	871377	21192100	871377

The geosynthetic reinforcement had a stiffness of 500kN/m and was placed 100mm above the pile cap. The underlying soft soil depth was 10.0m. The surcharge loading at the top of the embankment was 10kN/m as commonly used in practice for trafficked loads (Han & Gabr, 2002).

The generic model was subjected to numerable variations of its properties. The embankment height was varied from 2.0m to 10.0m, the steepness of the side slope from 1V:2H to 1V:3H, the pile spacing from 1.5m-3.0m-4.5m, the pile cap size from 0.3m (i.e. no pile cap) to 2.0m, the soft soil depth from 8.0m to 15.0m and the stiffness of the geosynthetic reinforcement from 0kN/m (unreinforced case) to 4000kN/m and Young's modulus of the piles were held constant at 30,000MPa (Table 3.14) and the outer edge pile rake ranged from 0°to 30° in 5° increments.

In general, the bond coefficient between the dry sandy soils and the geosynthetics reinforcement (geogrids) ranges from 0.85 to 1.00, and the higher soil-geosynthetics friction angles are measured when the surface has significantly sized apertures (geogrids), or allows the penetration of soil particles into the geosynthetics. The main factors affecting the development of shear in the interface

are the roughness of contact face, grain size of reinforced soil and loading (Chenggang, 2005). An interface friction value (R_{inter}) of 0.85 was chosen for the embankment fill, Table 3.14. Appendix A Table A1 represents the friction coefficient for different types of geotextiles and geogrids.

Table 3.14: Generic plane strain model parameters

	E (kN/m²)	v	c (kN/m²)	φ Deg (°)	ψ (°)	γ_{unsat} (kN/m³)	γ_{sat} (kN/m³)	R_{inter} -
Embankment Fill[1]	20000	0.2	0	35	0	19	20	0.85
Pile[2]	3.00E+07							
	λ^* -	κ^* -	φ Deg (°)	c (kN/m²)	ψ (°)	γ_{unsat} (kN/m³)	γ_{sat} (kN/m³)	R_{inter} -
Soft Soil (SSM 1)[3]	0.12	0.04	15	5	0	12	12	0.65
Soft Soil (SSM 2)[3]	0.03	0.01	25	1	0	19.5	19.5	0.7
	EA (kN/m)							
Geosynthetic Reinf[4]	500							

Note: (1) Laurent et al, 2003 (2) Han and Gabr, 2002 (3) Farag, 2008 (4) Gangakhedkar, 2004.

3.3.7 Factor of safety on global stability

Structural stability must be achieved through equilibrium and strain compatibility considerations without having a detrimental effect on the serviceability of the structure. The stability of a structure is expressed in terms of its factor of safety. The stability of the structure may be calculated by utilizing limit equilibrium (LE) or finite element analysis (FE).

The conventional limit equilibrium methods of slope stability analysis used in geotechnical practice investigate the equilibrium of a soil mass tending to move downslope under the influence of gravity (Anon, 2003). A comparison is made between forces, moments, or stresses tending to cause instability of the mass, and those that resist instability (BS 8006, 2010; Aryal, 2006).

Slope stability analysis by the finite element method use similar failure definitions as the limit equilibrium method for the soil mass but offer many advantages over limit equilibrium methods (Griffiths & Lane, 1999), such as the ability to develop the

critical failure surface automatically with fewer assumptions (Kiousis et al., 2010). The FE method is particularly useful for soil-structure interaction problems (Aryal, 2008) in which structural members interact with a soil mass. The simplifying assumptions of the limit equilibrium approach hinder its ability to adequately model the complete geosynthetic-pile-soil interaction (Rowe & Soderman, 1985) in comparison to finite element analysis. The finite element method is most widely used to perform the analysis of piles under different types of loading (Chik et al, 2009).

Embankments require the use of the soil mechanics definition of a safety factor, which is the ratio of the available shear strength to the minimum shear strength needed for equilibrium (Plaxis 2D, 2010). Plaxis 2D finite element analysis computes this factor of safety using a phi-c reduction procedure. Examination of the degree of structural stability offered by the pile geometric characteristics, embankment characteristics, geosynthetic reinforcement and the underlying soft soil to the structure was performed.

3.4 Summary

A detailed description of the test methods used to carry out this study was presented concerning two distinctly different methods. The first was the design, construction and testing of a piled embankment model in the IT Sligo geotechnical centrifuge and the second was the development of a numerical model in Plaxis 2D to replicate the centrifuge test results.

The centrifuge model consisted of piles constructed from Perspex sheets, subsoil modelled with synthetic sponge and expanded polystyrene and geosynthetic reinforcement modelled with polyethylene sheets. The suitability of the materials for use in the centrifuge model was assessed and key physical properties were determined. The centrifuge testing investigated the effect of variation of parameters such as embankment height to clear spacing H/(s−a) ratio, subsoil stiffness, side slope steepness and the location of the outer pile row along the side slope.

The numerical model was developed using the finite element modelling software Plaxis 2D. The numerical modelling performed a drained plane strain analysis of the

reinforced piled embankment. The soft subsoil was modelled using the soft soil model. The embankment fill was modelled using a Mohr-Coulomb model. A linear elastic plate model simulated the piles within the pile group and a geogrid material modelled the geosynthetic reinforcement.

Chapter 4

Centrifuge modelling and validation of numerical analysis

4.1 Introduction

The aim of this chapter is to present the centrifuge test data determined in this study, compare the centrifuge data with comparable Plaxis 2D model predictions, with the ultimate aim of validating the Plaxis 2D model against the centrifuge model.

Centrifuge model testing was carried out to investigate the lateral loading mechanism within basally reinforced piled embankments. The centrifuge testing was divided into two test series to examine the significance of parameters such as embankment height to clear spacing ratio (H/(s−a)), subsoil stiffness, embankment side slope steepness and the effect of the location of the outer row pile along the embankment side slope.

Priority was given to the data from the pile deformations and the geosynthetic reinforcement. The treatment of each pile within the pile groups lateral

deformations, which were derived from observed lateral deformations of the piles and also the vertical deformations of the geosynthetic reinforcement.

The behaviour of the system was assessed by recording the surface settlement at the top of the model embankment, lateral deformation at the pile head and vertical deformation of the geosynthetic reinforcement near the toe, Figure 4.1.

The embankment surface settlements (d_s) were determined by measuring the average embankment settlement along the embankment surface (embankment centre to crest location), Figure 4.2 and 4.3. Lateral deformations of the pile head, at the level of the geosynthetic and the embankment surface were determined by importing the photographs obtained during testing directly into AutoCAD, Figures 4.2 and 4.3, for analysis and measurement of deformations.

The lateral deformations of the pile (d_p) were measured at the top of the pile cap edge, the magnitude of the lateral deformation was the differential between the pile cap location at 1*g* and 60*g*, Figure 4.4.

The vertical deformation of the geosynthetic reinforcement (d_g) was measured at the clear span between the outer row pile and the embankment toe, Figure 4.5.

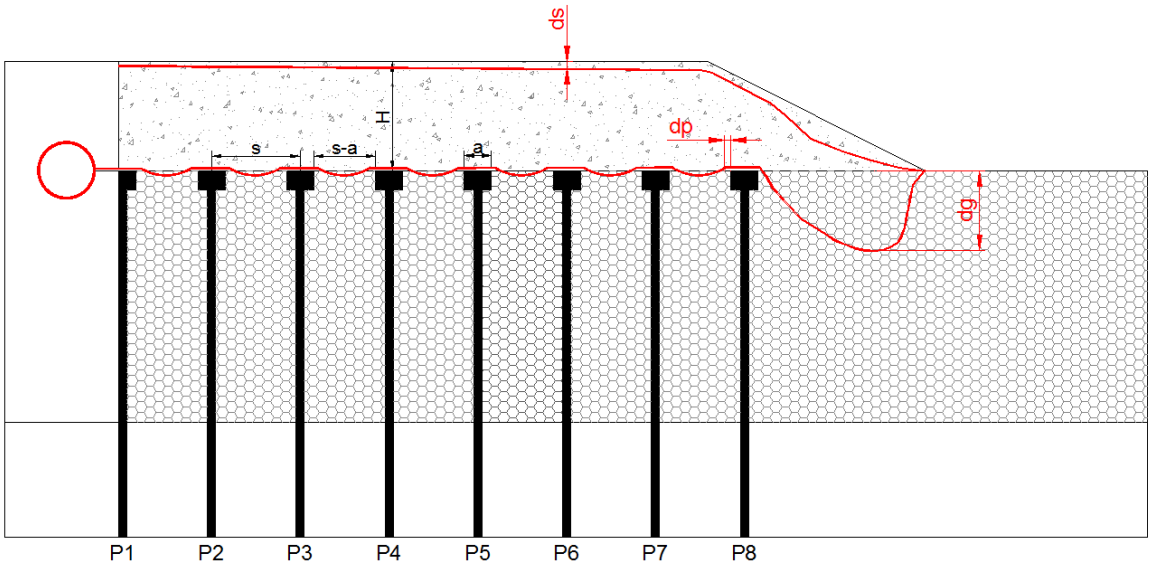

Figure 4.1: Typical pile group lateral deformation, geosynthetic reinforcement and embankment surface deformation profile (Piles are labelled to P1 to P7)

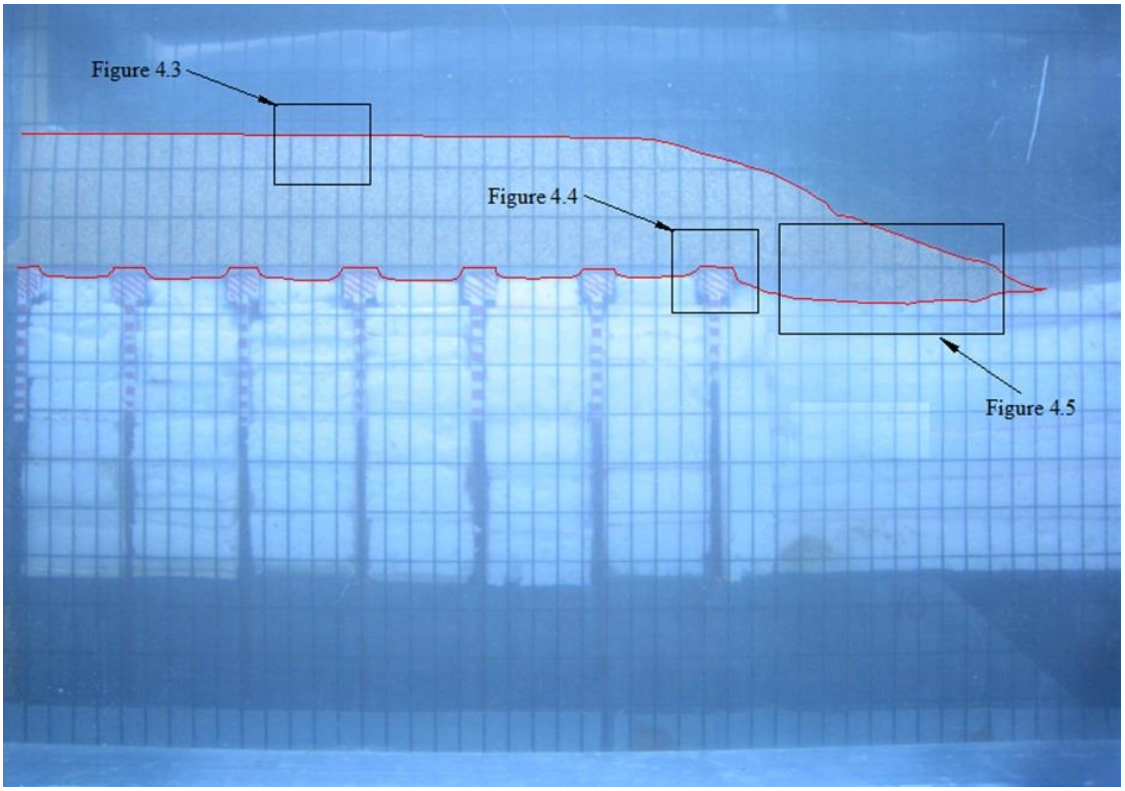

Figure 4.2: Photographic image of in-flight model at 60g showing superimposed lines from AutoCAD

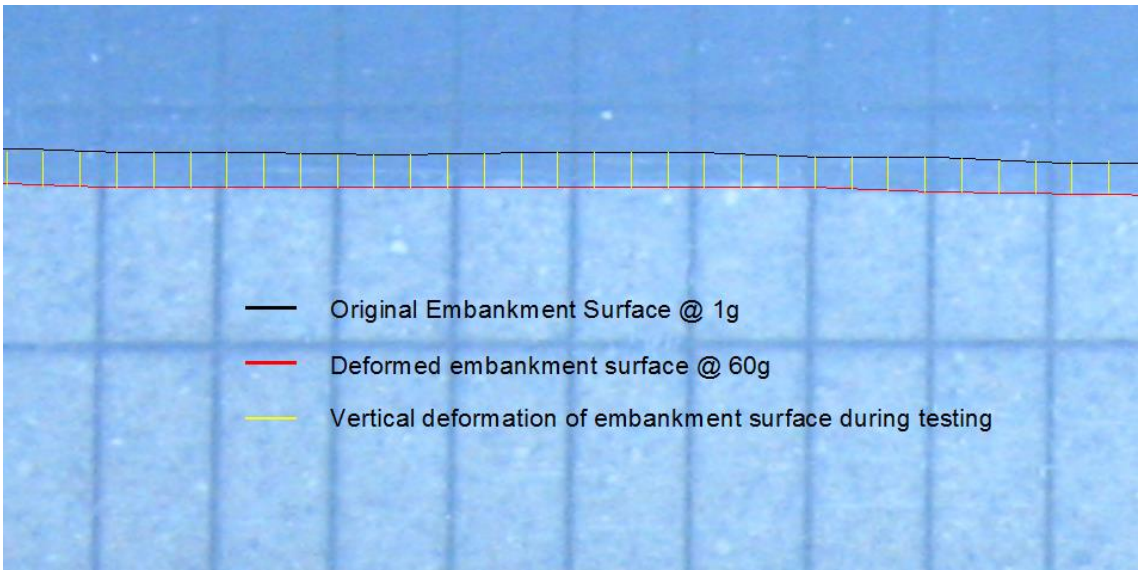

Figure 4.3: Photographic image of in-flight model at 60g showing superimposed lines from AutoCAD of embankment surface vertical deformation

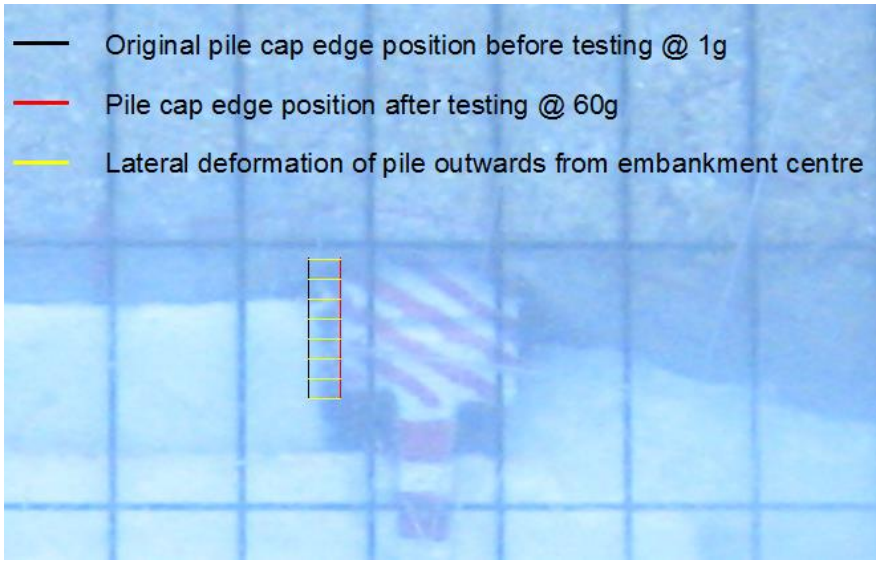

Figure 4.4: Photographic image of in-flight model at 60g showing superimposed lines from AutoCAD of pile head lateral deformation

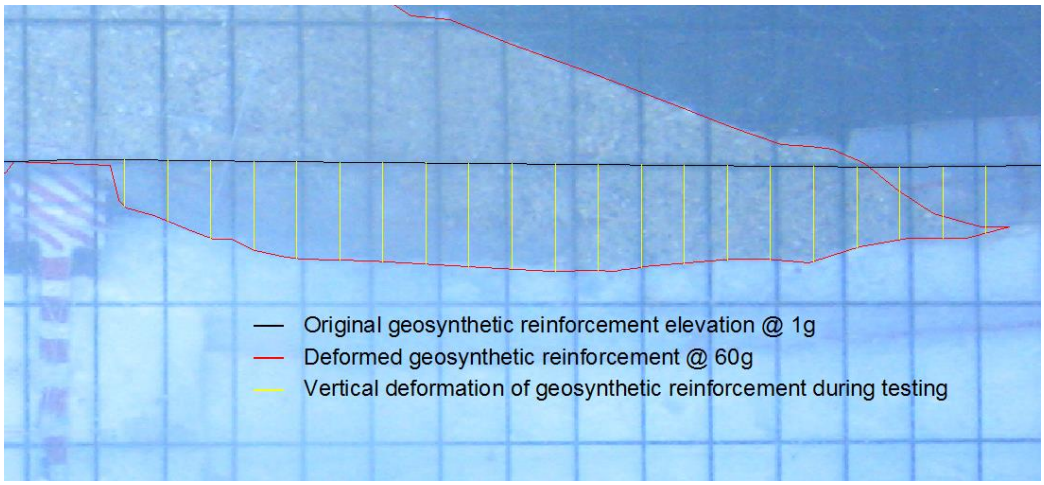

Figure 4.5: Photographic image of in-flight model at 60g showing superimposed lines from AutoCAD of geosynthetic reinforcement vertical deformation

4.2 Centrifuge testing

The centrifuge testing was divided into two test series. The results from each test series together with some preliminary analysis are presented in this section. Data for a range of geometries was produced with embankment height, subsoil stiffness and side slope steepness. However, for any one test, the H/(s−a) ratio remained constant, therefore a number of tests were conducted incorporating different embankment heights to investigate the effect of the H/(s−a) ratio on the lateral loading conditions within the embankment fill. The dry density of the fill was

determined by measuring the mass and volume of sand required to construct the embankment in the model.

4.2.1 Centrifuge Test Series 1

Centrifuge Test Series 1 examined the performance of the geosynthetic reinforced piled embankment structure for a variation in H/(s-a), subsoil stiffness and side slope steepness. The location of the most outer row pile within the pile group extent was in accordance with BS 8006 (2010).

Subsoils A and B and the geosynthetic were incorporated into the model in Test Series 1. Subsoils A and B had stiffnesses of 54 kPa and 240 kPa respectively, and the geosynthetic had a tensile stiffness of 4.7 kN/m. The H/(s−a) ratio was varied from 0.5, corresponding to a very low embankment to 4.0, corresponding to a high embankment for both subsoil A and B. The tests conducted in this test series are summarized in Table 4.1. The dry density of the embankment fill used was relatively consistent through Test Nos. 1-13, Table 4.1 and had a mean value of 1.592 Mg/m³.

Table 4.1. Summary of Test Series 1 model geometry and properties

Test No.	Density	Subsoil Type	Height (mm)	Height @ 60g (mm)	H/(s-a) ratio	Side Slope ratio	Dry Density of fill (Mg/m³)
1	Loose	A	7.14	428.4	0.5	1:2	1.576
2	Loose	A	14.28	856.8	1.0	1:2	1.554
3	Loose	A	28.57	1714.2	2.0	1:2	1.565
4	Loose	A	57.14	3428.4	4.0	1:2	1.669
5	Loose	B	7.14	428.4	0.5	1:2	1.570
6	Loose	B	14.28	856.8	1.0	1:2	1.564
7	Loose	B	28.57	1714.2	2.0	1:2	1.578
8	Loose	B	57.14	3428.4	4.0	1:2	1.643
9	Loose	A	7.14	428.4	0.5	1:3	1.621
10	Loose	A	14.28	856.8	1.0	1:3	1.575
11	Loose	A	28.57	1714.2	2.0	1:3	1.595
12	Loose	A	57.14	3428.4	4.0	1:3	1.586
13	Loose	A	28.57	1714.2	2.0	1:4	1.601

4.2.1.1 Pile group deformations

The model was accelerated in 5*g* increments from 1*g* to 60*g*, thus producing data for a range of geometries with embankment height, subsoil thickness, pile width (a) and pile spacing increasing directly proportional to the *g* - level. A preliminary examination of the lateral deformational response of the outer pile row was conducted to investigate the scalability of the lateral deformational response of the pile with g-level by accelerating the model to 160*g*, Figure 4.6. The data showed a linear increase of lateral pile deformation with *g*-level, Figure 4.6, correlation between the linear increase of lateral deformation with *g* – level suggests the scalability of the pile deformation with *g* – level was possible.

Figure 4.7 illustrates the lateral deformation within the pile group as measured from the centrifuge analysis at 60*g* from Test No. 3. A maximum lateral pile head deflection localized to the outer row pile was recorded, Figure 4.7. The centrifuge modelling recorded an exponential increase in the magnitude of lateral pile head deflection for a linear increase in distance from the embankment centre-line, Figure 4.7. All piles within the pile group deflected laterally under the influence of the lateral loading from the embankment fill. All plots of the centrifuge data presented in this chapter, with the exception of Figure 4.6, are of the scaled prototype deformations (deformations scaled by multiplication by *g*-level).

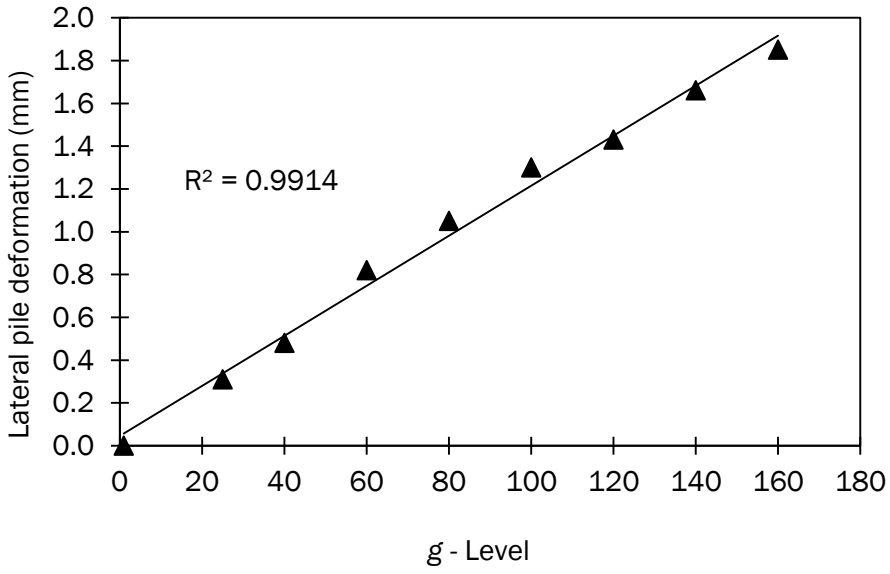

Figure 4.6 Preliminary investigation of relationship of outer row pile deflection with g – level

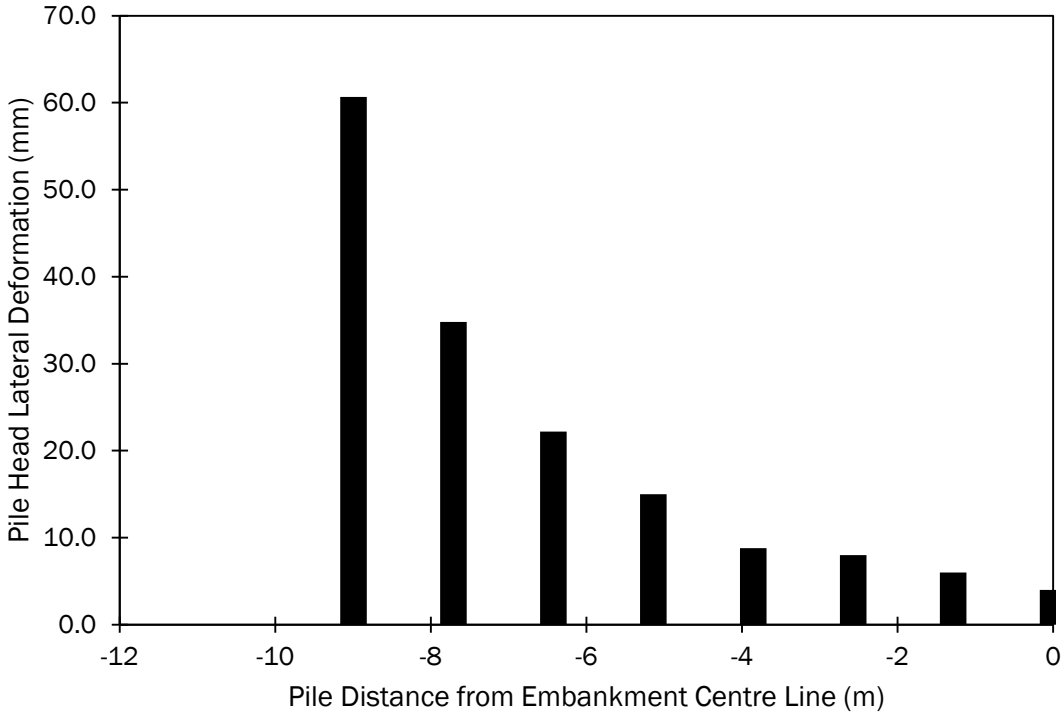

Figure 4.7 Lateral deflection (mm) in pile group for physical modelling (Centrifuge) in Test No. 3

The range of outer row pile lateral deflections from Test Nos. 1 – 4 and 9 – 12 are illustrated in Figure 4.8. The lateral deflection of the outer row pile head increased for an increase in the embankment geometric ratio (H/(s-a)), Figure 4.8. Similar conditions existed for the characteristic trend of the lateral response of the outer row pile for an increase of embankment height for a range of side slopes (increase of the H/(s-a) ratio), Figure 4.8. The centrifuge analyses recorded lateral deformations of the 1V:2H side slope consistently greater than the 1V:3H side slopes. The centrifuge modelling produced a divergence between the 1V:2H and 1V:3H side slope for an increase in the embankment height (increase of the H/(s-a) ratio), Figure 4.8. An increase of the H/(s-a) ratio from 0.5 to 2.0 yielded an increase of 484% and 339% in the magnitude of the outer row pile lateral deformation recorded for the 1V:2H and 1V:3H side slopes, respectively, Figure 4.8. For both side slope steepness, the greatest rate of outer row pile deformations occurred when the H/(s-a) ratio increased from 2.0 to 4.0, Figure 4.8.

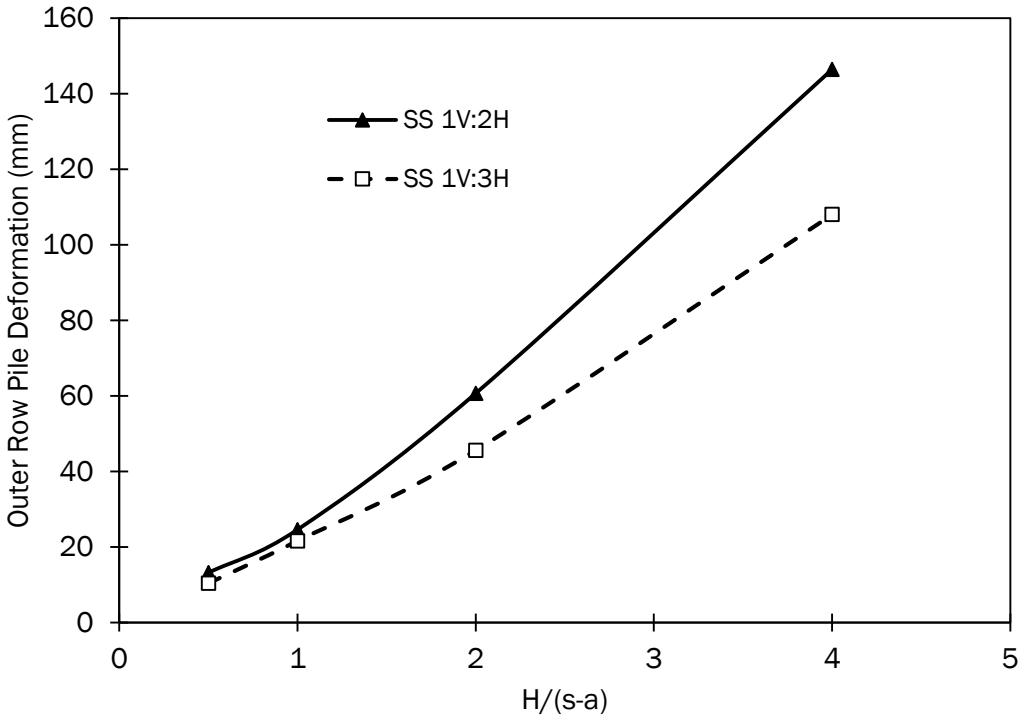

Figure 4.8 Lateral deflection (mm) of outer row pile for a range of embankment geometric ratios (H/(s-a)) in Test Nos. 1 - 4 and 9 - 12

The range of outer row pile lateral deflections from Test Nos. 3, 11 and 13 illustrate the deformational response of the pile to a range of side slope steepness, Figure 4.9. An increase in the embankment side slope steepness yielded a linear increase in magnitude of the outer row pile lateral deformation, Figure 4.9. An increase in the side slope steepness from 1V:4H to 1V:2H yielded a linear increase of 83.8% respectively at 60g.

Test Nos. 1 – 8 enabled the response of the reinforced piled embankment structure for a variation of soft soil stiffness to be investigated. Subsoils A and B with stiffness of 54 kPa and 240 kPa respectively were selected. Figure 4.10 illustrates the outer row piles response to a variation of the subsoil stiffness. Subsoil B, with material properties stiffer than subsoil A, yielded lower magnitudes of deflections than the equivalent for subsoil A for all H/(s-a) ratios. A divergence of the differential between the pile deformations for subsoil A and B occurred for an increase of the embankment height, Figure 4.10. The magnitude of the lateral deformation increased for both subsoils A and B for an increase of the H/(s-a) ratio, Figure 4.10.

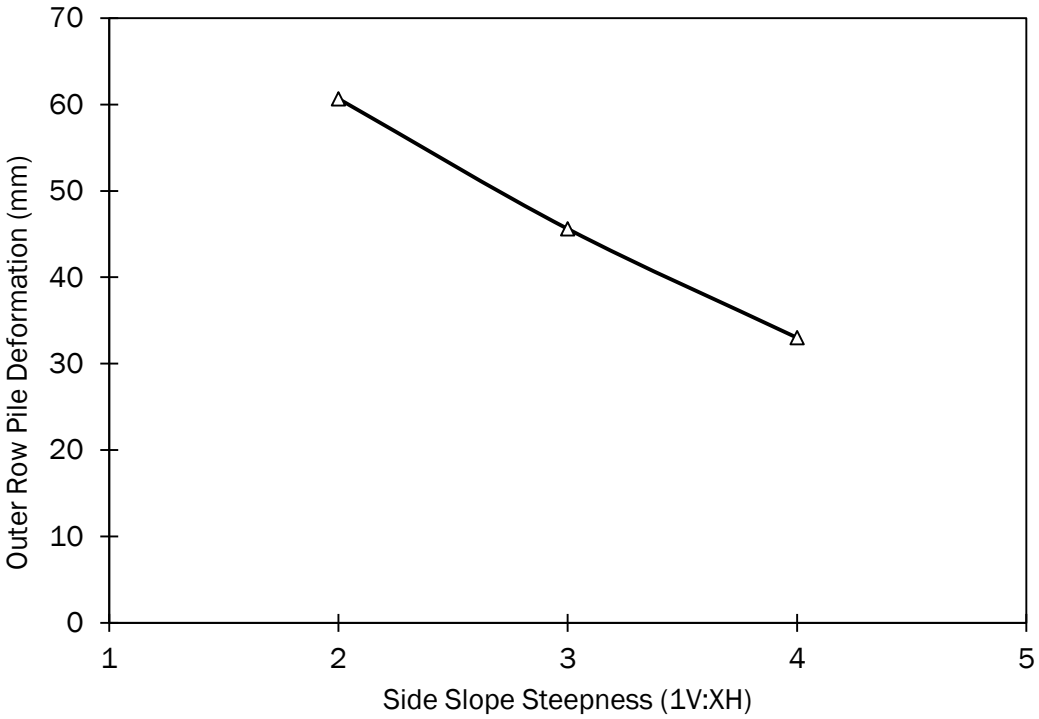

Figure 4.9 Lateral deflection (mm) of outer row pile for a range of embankment side slopes in Test Nos. 1 – 3, H/(s-a) = 2.0

Figure 4.10 Lateral deflection (mm) of outer row pile for a range of subsoil stiffness in Test Nos. 1 – 8

4.2.1.2 Geosynthetic reinforcement deformations

The measured vertical deformation of the reinforcement followed a similar, catenary type shape between adjacent pile caps, from the centre line of the embankment to the outer row of piles for all geometries examined, Figure 4.11. A vertical deformation maximum was recorded outside the outer row pile near the embankment toe for all centrifuge models, Figure 4.11. The magnitudes of the vertical deformations recorded between adjacent pile caps remained relatively consistent (+/- 5% approximately) for the centrifuge model at 60g. As the reinforcement protruded past the embankment crest, the magnitudes of the vertical deformation in between adjacent pile caps increased with an increase in distance from the embankment crest, Figure 4.11. An increase in the vertical deformations at the clear span between adjacent pile caps as the reinforcement approached the outer row of pile was observed for all centrifuge tests, Figure 4.11. At the outer row of piles the deflection at the pile head increased, Figure 4.8. This was attributed to the deflection of the pile head effectively increasing the clear span between adjacent pile caps. The reinforcement was required to support a greater span/loading and thus was subjected to greater deformation the greater the distance from the embankment centerline, Figure 4.11.

Test Nos. 1- 4 and 9 – 13 revealed that the reinforcement recorded a maximum vertical deformation for all cases outside the outer row pile. The vertical deformation of the reinforcement near the embankment toe increased for an increase in embankment height (increase of H/(s-a) ratio), Figure 4.12. The characteristic trend of the vertical deformational response of the reinforcement was to remain relatively constant for an initial increase in embankment height (increase of H/(s-a) from 0.5 to 1.0) for both side slopes, Figure 4.12. A further increase in the embankment height (1.0 to 2.0 H/(s-a) ratio) produced a significant increase in vertical deformation, Figure 4.12.

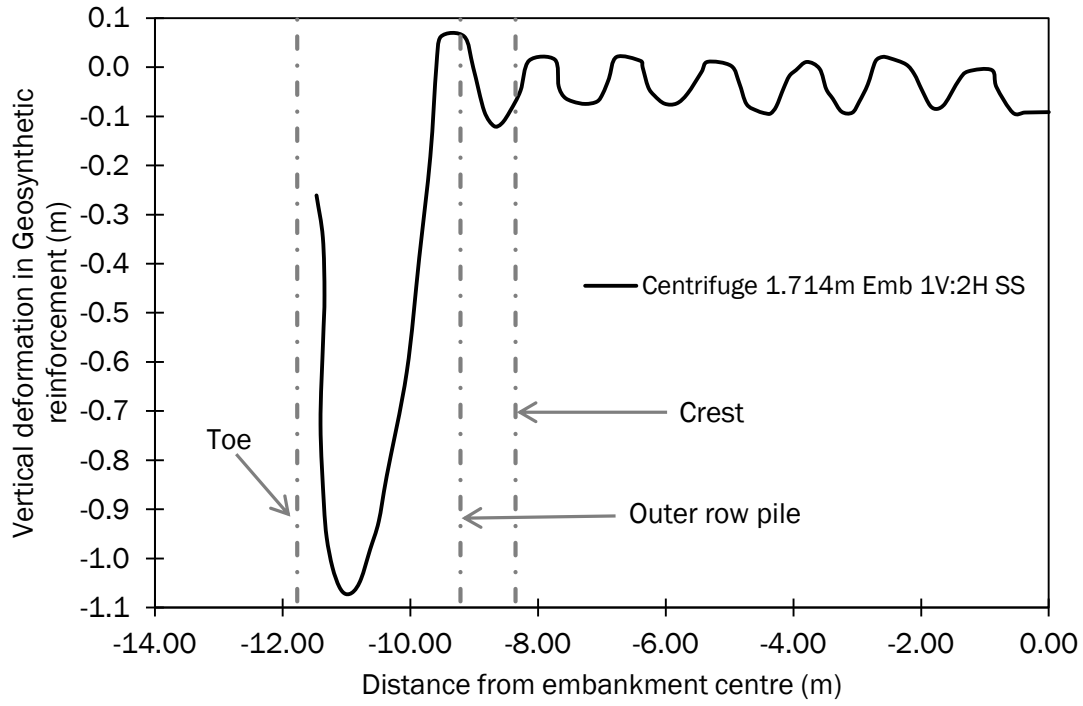

Figure 4.11 Vertical deformation in reinforcement in Test No. 3

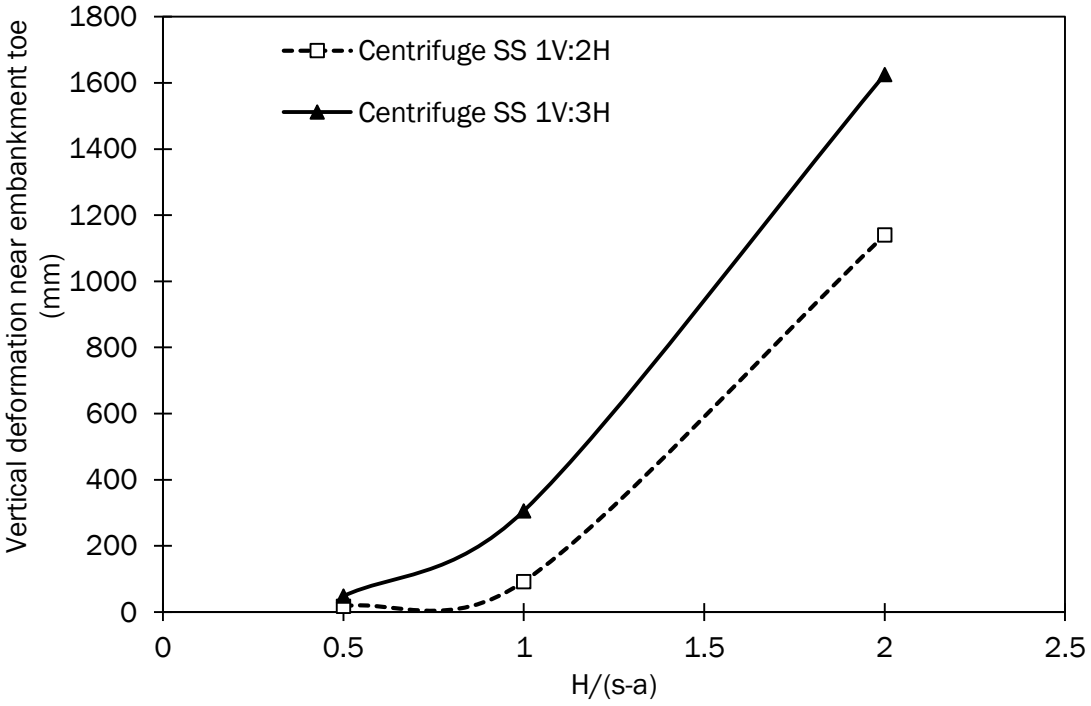

Figure 4.12 Maximum vertical deformation in reinforcement for a range of geometric ratios (H/(s-a)) in Test Nos. 1 – 4 and 9 – 12

The range of outer row pile lateral deflections from Test Nos. 3, 11 and 13 illustrate the deformational response of the pile to a range of side slope steepness, Figure 4.13. The magnitude of the vertical deformation of the reinforcement increased for a decrease in the side slope steepness, Figure 4.13. The characteristic response of the vertical deformation in the reinforcement was an initial increase (42%) for a reduction in the side slope steepness from 1V:2H to 1V:3H, Figure 4.13. A further reduction of side slope steepness (1V:3H to 1V:4H) yielded a significant reduction in the rate of vertical deformation increase, Figure 4.13.

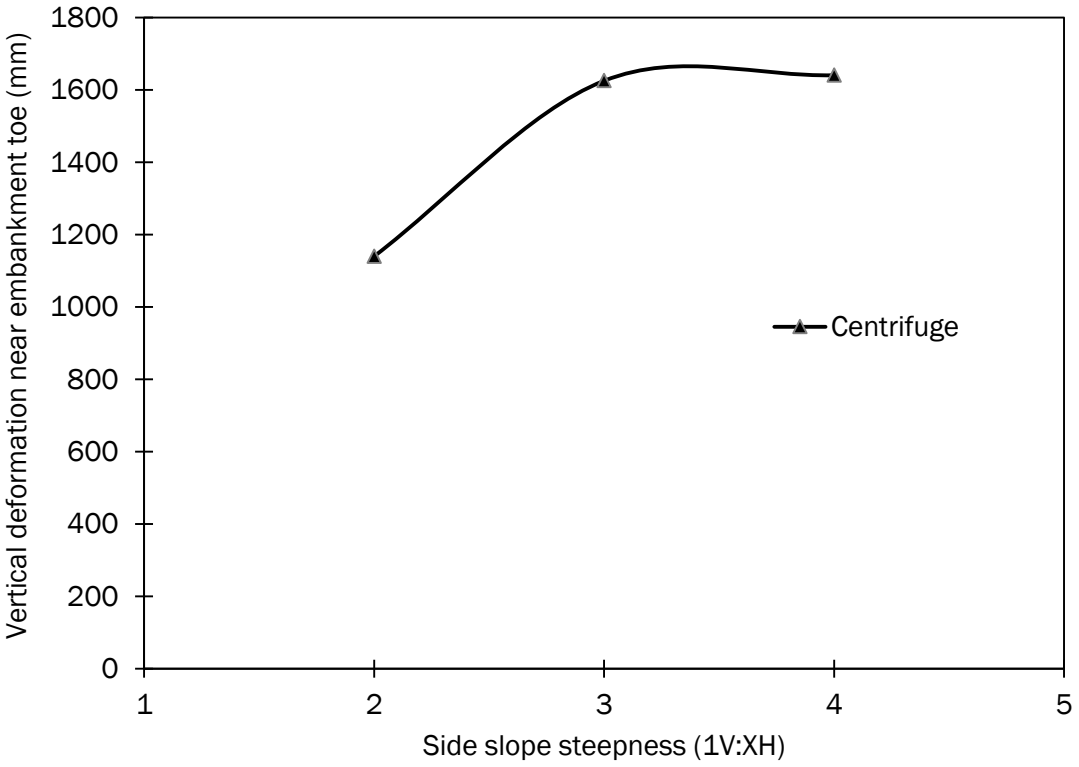

Figure 4.13 Maximum vertical deformation in reinforcement for a range of side slope steepness (1V:XH) in Tests Nos. 3, 11 and 13

The vertical deformations of the reinforcement observed in Test Nos. 1 - 8 are illustrated in Figure 4.14. The results indicate that the maximum vertical deformation in the reinforcement near the embankment toe were consistently and significantly greater for subsoil A than the stiffer subsoil B, Figure 4.14. The deformational response of the reinforcement for the stiffer subsoil B was linear for an increase of the H/(s-a) ratio, Figure 4.14. For low embankment ratios (0.5 to 1.0 H/(s-a)), the magnitude of vertical deformations were relatively low for subsoil A,

Figure 4.14. Increasing the geometric ratio greater than 1.0 H/(s-a) yielded a significant increase of the vertical deformation, Figure 4.14. A divergence in magnitudes of the differential between the two subsoils was observed for an increase of the geometric ratio (H/(s-a)), Figure 4.14.

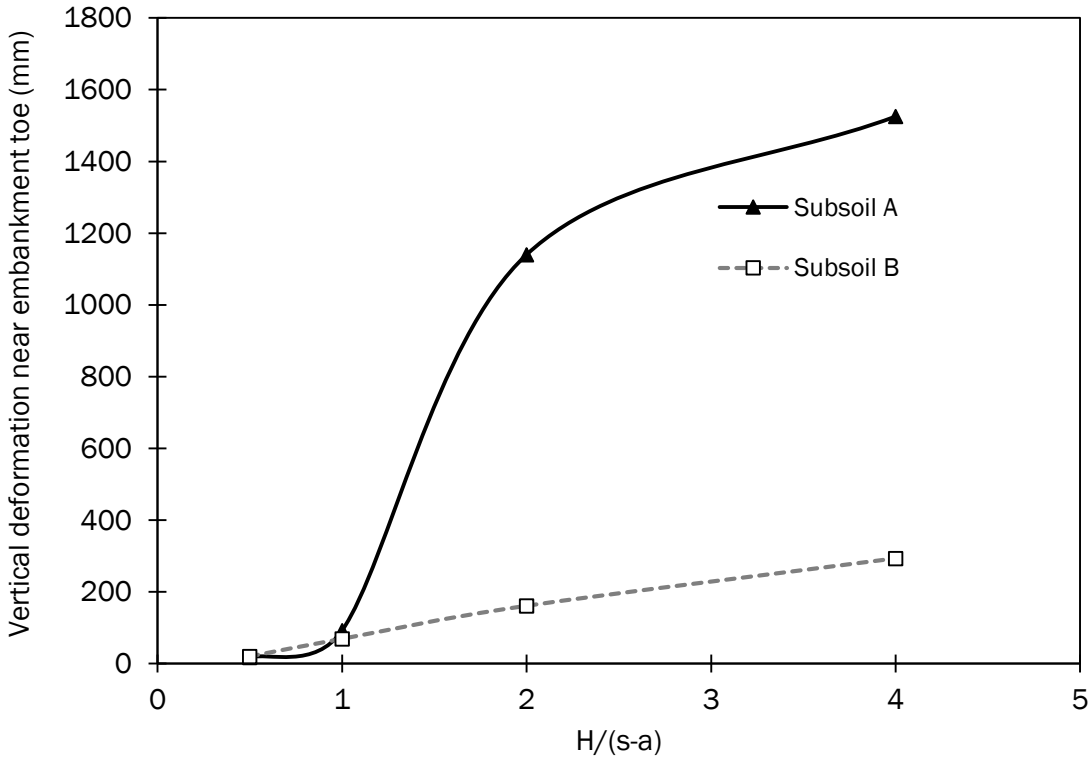

Figure 4.14 Maximum vertical deformation in reinforcement for a range of subsoil stiffness in Test Nos. 1 – 8

4.2.1.3 Embankment surface mean settlements

The embankment surface mean settlements observed in Test Nos. 1 - 13 are illustrated in Figures 4.15 – 4.18 respectively. Analysis of the deformed embankment structure itself focused on two primary locations, the embankment surface settlement and secondly the deformations at the embankment crest. The embankment surface settlement was determined by calculating the mean vertical deformation across the embankment surface (from the embankment centre to the crest). The results indicate the magnitude of vertical deformation at the embankment surface increased with embankment height (increase of H/(s-a) ratio), Figure 4.15. The deformational response of the embankment fill yielded a

consistent differential in magnitudes for a range of embankment heights (range of embankment geometric ratios) for both side slope steepness, Figure 4.15. The characteristic trend of the mean deformational response of the embankment surface was to remain relatively constant for an initial embankment height increase (increase of H/(s-a) from 0.5 to 1.0) for both side slope steepness, Figure 4.15. A further increase in the embankment height (1.0 to 2.0 H/(s-a) ratio) produced a significant increase in mean surface deformation, Figure 4.15.

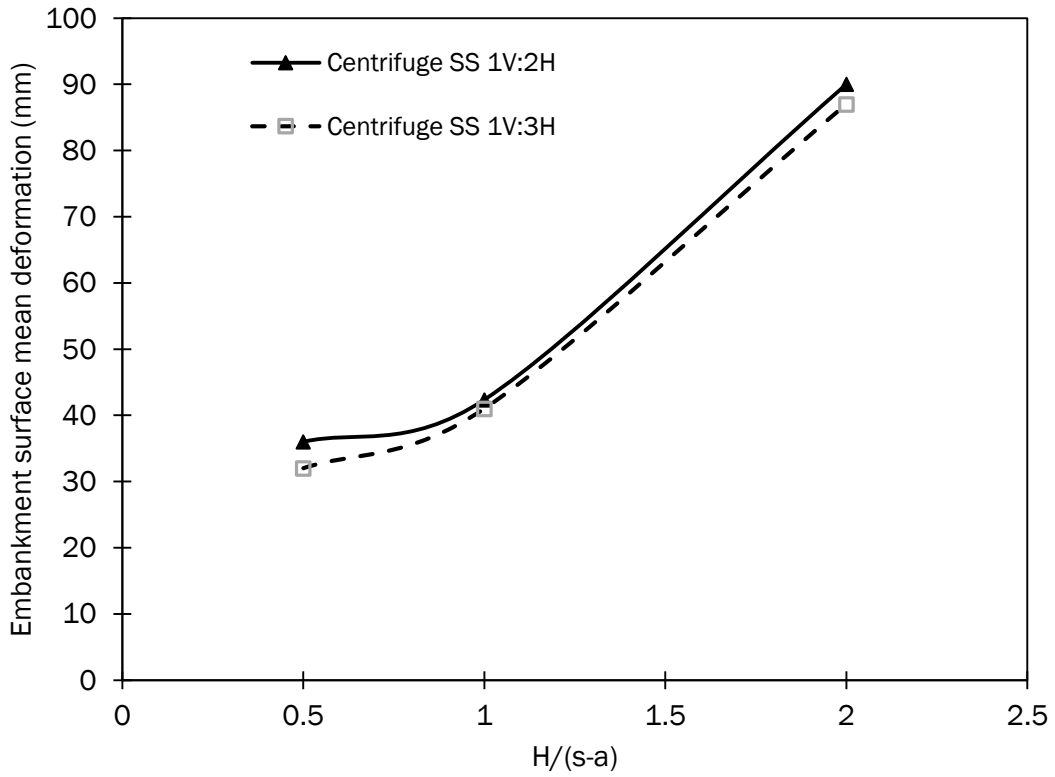

Figure 4.15 Embankment mean surface deformations for a range of embankment geometric ratios (H/(s-a)) in Test Nos. 1 – 4 and 9 – 12

The deformational response of the embankment surface was observed from tests varying the side slope steepness from 1V:4H to a maximum of 1V:2H, Figure 4.16. The results indicate increasing the steepness of the embankment side slope had a relatively insignificant influence on the overall deformation of the surface. The centrifuge analyses yielded a small reduction in magnitude of the embankment surface mean settlement for a decrease in the side slope steepness (a reduction of 4.9% respectively), Figure 4.16.

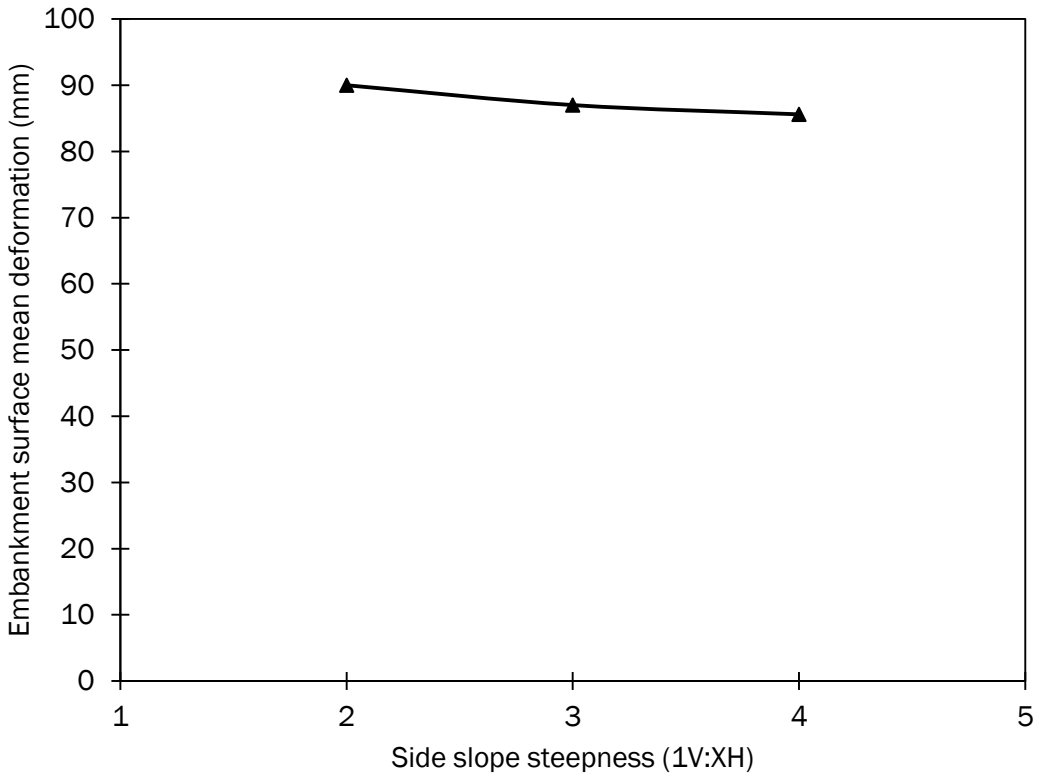

Figure 4.16 Embankment mean surface deformations for a range of embankment geometric ratios (H/(s-a)) in Test Nos. 3, 11, 13

Test Nos. 3 and 7 enabled the deformational response of the mean settlements on the embankment surface to be observed. The results indicate that for both subsoil A and B, the magnitudes of deformations increased proportional to H/(s-a) ratio, Figure 4.17. For H/(s-a) ratios, subsoil A (stiffness of 54 kPa) recorded deformations of greater magnitude than subsoil B (stiffness of 240 kPa), Figure 4.17. The characteristic trend of the mean deformational response of the embankment surface for both subsoil A and B was to remain relatively constant for an initial embankment height increase (increase of H/(s-a) from 0.5 to 1.0), Figure 4.17. A further increase in the embankment height (1.0 to 4.0 H/(s-a)) produced a significant increase in mean surface deformation, Figure 4.17. A divergence of the differential between Subsoil A and Subsoil B was observed as the embankment geometric ratio increased greater than 1.0 H/(s-a), Figure 4.17. Both subsoil cases yielded a linear increase with H/(s-a) ratio for ratios greater than 1.0 H/(s-a), Figure 4.17.

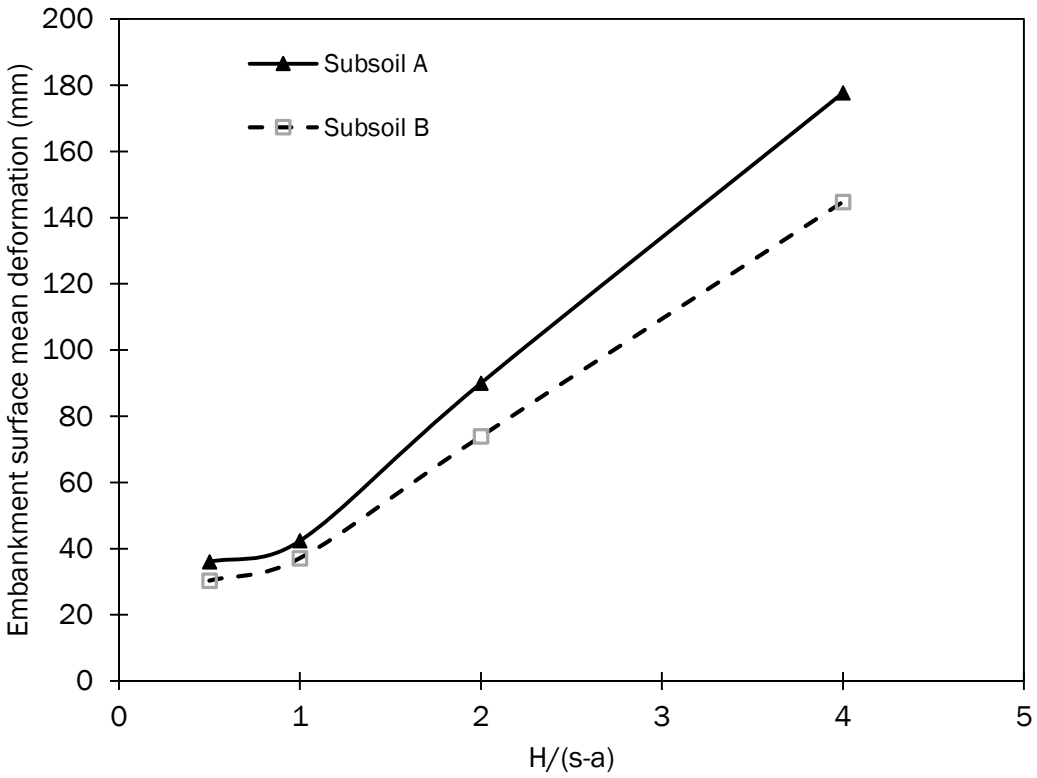

Figure 4.17 Embankment mean surface deformations for a range of subsoil stiffness in Test Nos. 1 – 8

Deformations occurring at the embankment crest location were examined in Tests Nos. 3 and 11, Figure 4.18. The deformation at the crest of the embankment was examined in terms of its vertical and horizontal component, Figure 4.18. The ratio of improvement with regard to horizontal versus vertical deformation was linear and almost proportional to an increase in the stiffness of the geosynthetic reinforcement and a decrease in the depth of the underlying soft soil. A reduction in the steepness of the side slope yielded a notable reduction in the horizontal deformation whilst having an insignificant influence on the vertical deformation, Figure 4.18. Observations of the deformational response indicated that a variation of the embankment height has a more pronounced effect on the horizontal deformation at the crest than the vertical deformation, Figure 4.18. The centrifuge analysis yielded a consistent differential between both side slope cases (1V:2H and 1V:3H) for a range of embankment heights, Figure 4.18.

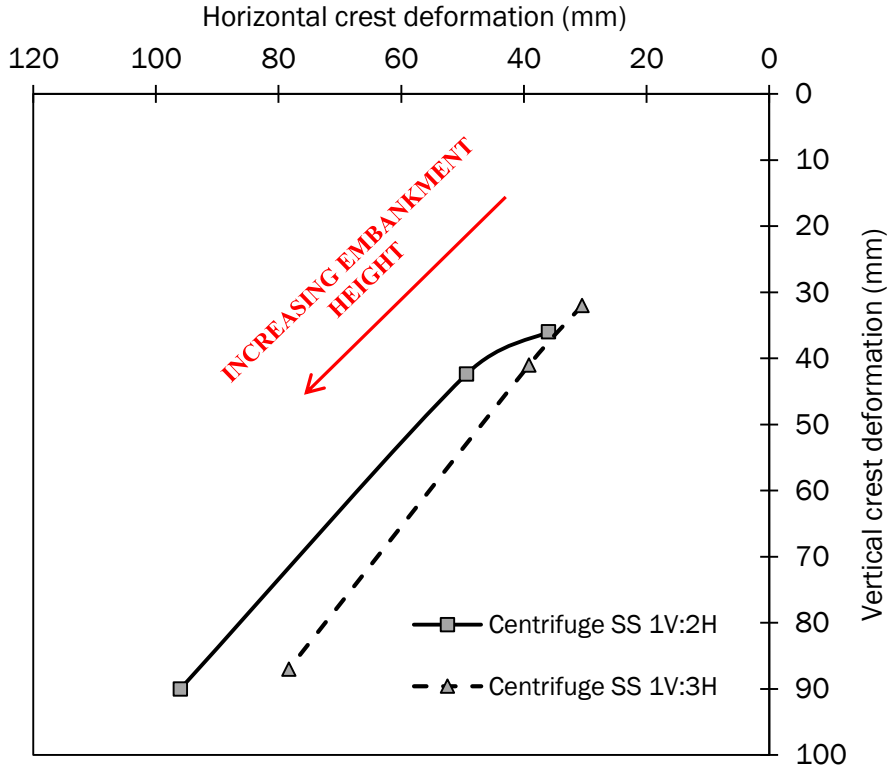

Figure 4.18 Embankment crest deformations for a range of embankment side slope steepness (1V:XH) in Test Nos. 1 – 8

4.2.2 Centrifuge Test Series 2

Centrifuge Test Series 2 examined the performance of the geosynthetic reinforced piled embankment structure for a variation in location of the most outer row pile along the side slope length. The location of the most outer row pile within the pile group extent was expressed using the outer row pile location ratio (ORPLR). The ORPLR was defined in this study as the horizontal distance from the initial embankment crest to the initial center of the outer row pile. The outer row pile was ranged from 0 (directly under the crest) to 1.0 (directly under the embankment side slope toe) in 0.25 increments.

Subsoil A and B and the geosynthetic were incorporated into the model in Test Series 2. H/(s−a) was held constant at 2.0. Side slope steepness's of 1V:2H and 1V:3H were examined. The tests conducted are summarized in Table 4.2, the mean dry density of the sand used was 1.598 Mg/m³.

Table 4.2. Summary of Test Series 2 model geometry and properties

Test No.	ORPLR	Density	Subsoil Type	Height (mm)	Height @ 60g (mm)	H/(s-a) ratio	Side slope	Dry Density of fill (Mg/m³)
14	0.00	Loose	A	28.57	1714.2	2	1:2	1.642
15	0.25	Loose	A	28.57	1714.2	2	1:2	1.586
16	0.50	Loose	A	28.57	1714.2	2	1:2	1.545
17	0.75	Loose	A	28.57	1714.2	2	1:2	1.604
18	1.00	Loose	A	28.57	1714.2	2	1:2	1.594
19	0.00	Loose	B	28.57	1714.2	2	1:2	1.566
20	0.25	Loose	B	28.57	1714.2	2	1:2	1.564
21	0.50	Loose	B	28.57	1714.2	2	1:2	1.664
22	0.75	Loose	B	28.57	1714.2	2	1:2	1.643
23	1.00	Loose	B	28.57	1714.2	2	1:2	1.613
24	0.00	Loose	A	28.57	1714.2	2	1:3	1.579
25	0.25	Loose	A	28.57	1714.2	2	1:3	1.553
26	0.50	Loose	A	28.57	1714.2	2	1:3	1.595
27	0.75	Loose	A	28.57	1714.2	2	1:3	1.590
28	1.00	Loose	A	28.57	1714.2	2	1:3	1.635

4.2.2.1 Pile group deformations

The range of outer row pile lateral deflections from Test Nos. 14 – 23 conducted at 60g are illustrated in Figure 4.19 – 4.22. The lateral deflection of the outer row pile head increased for an increase in the outer row pile location ratio (ORPLR) Figure 4.19. The analyses recorded lateral deformations for subsoil A consistently greater than for subsoil B. The centrifuge modelling produced a convergence of pile deformation for subsoil A and B for an increase in the ORPLR ratio, Figure 4.19. Convergence of the differential between the deformations recorded for the outer pile row between both subsoils indicated that as the outer row pile approached the embankment toe the influence of the subsoil stiffness was less significant. An outer row pile lateral deformation maximum was observed directly under the embankment crest (ORPLR of 0) whilst a minimum was located at the embankment toe for both soil stiffness's, Figure 4.19. The results indicate that the movement of the outer row pile outward toward the embankment toe significantly lowered the pile head deformations, Figure 4.19, the lower the stiffness of the subsoil the

greater the rate of reduction of pile head lateral deformations as the outer pile row location moved along the side slope towards the toe.

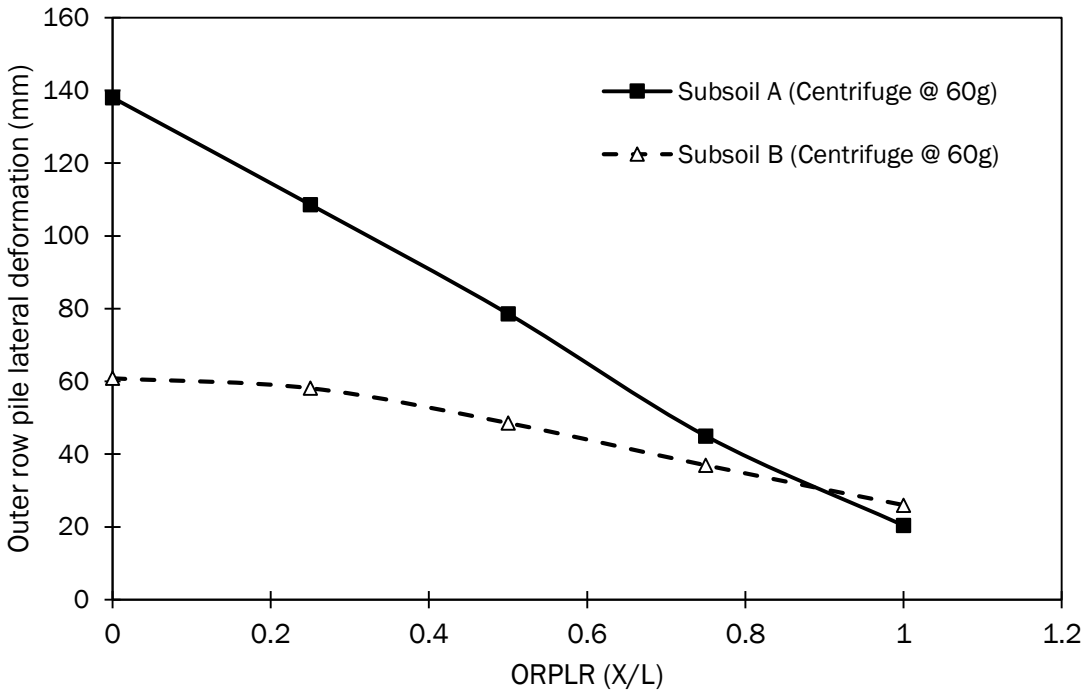

Figure 4.19 Outer row pile lateral deflections for a range of ORPLR and soil stiffness in Test Nos. 14 – 23

The range of outer row pile lateral deflections from Test Nos. 14 – 18 and 24 - 28 illustrate the deformational response of the pile to a range of ORPLR and side slope steepness, Figure 4.20. Outer row pile lateral deformations reduced in magnitude for both cases of side slope steepness (1V:2H and 1V:3H) examined; almost linearly as the pile moved toward the embankment toe, Figure 4.20. Observations of the deformational response of the pile indicated the side slope with the greatest steepness (1V:2H) yielded the greatest rate of reduction of pile lateral deformations, Figure 4.20. Similar to the response of the outer row pile response to a variation of subsoil stiffness (Figure 4.19), convergence of the pile deformation differential between both side slope steepness cases was observed as the pile moved toward the toe (ORPLR approached 1.0). The analysis suggests the rate of improvement of the outer row pile loading conditions as the pile group extent moves toward the toe was a function of the side slope steepness and the subsoil stiffness.

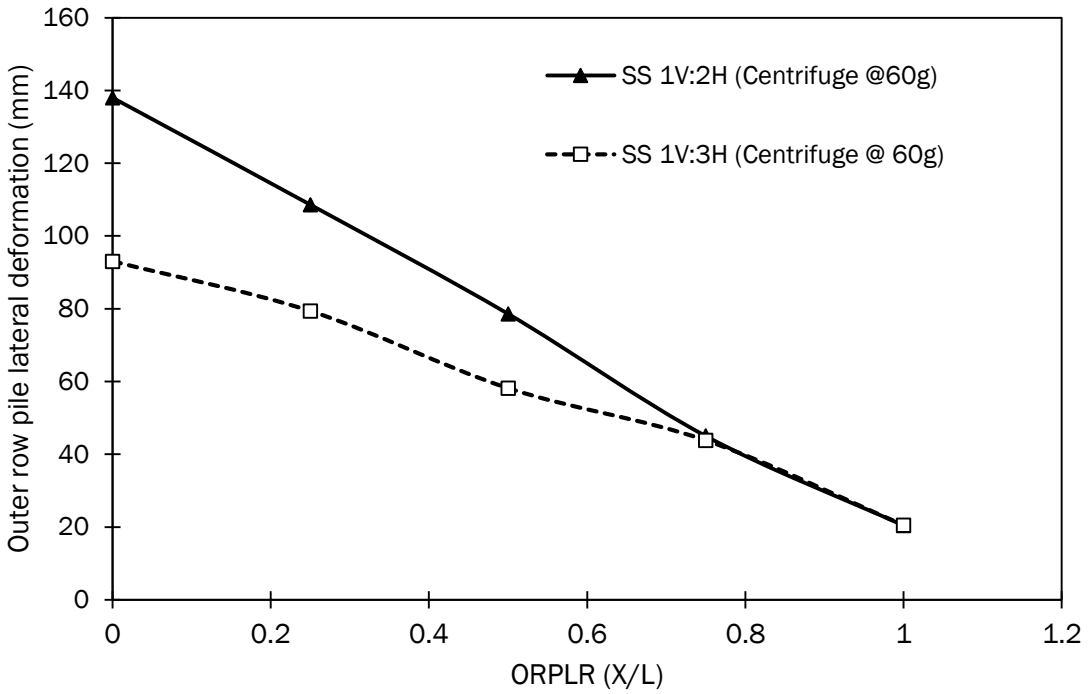

Figure 4.20 Outer row pile lateral deflections for a range of ORPLR and side slope steepness (1V:XH) in Test Nos. 14 – 18 and 24 – 28

Reduction of lateral deformations as the pile moved toward the embankment toe was not isolated to the outer row pile of the pile group. The data suggested that as the outer row pile moved toward the embankment toe all piles within the confines of the pile group were subjected to lower magnitudes of lateral deformations at each pile location, Figure 4.21. Extending the outer pile row to the embankment toe (ORPLR 1.0) significantly reduced the deformations within the pile group but did not reduce deformations to zero at the embankment centre.

Presentation of the combined lateral deformations at each pile head within the pile group as an average strain is illustrated in Figure 4.22. The strain between adjacent piles was determined as the increase in pile spacing due to the lateral deformation of the pile divided by the pile centre to centre spacing. The average of each strain was then computed along the pile group extent, which enabled the response of the pile group as a whole to a variation of ORPLR to be observed. The data suggests that increasing the ORPLR from 0 to approximately 0.8 yielded a significant linear reduction in pile group lateral mobility, Figure 4.22.

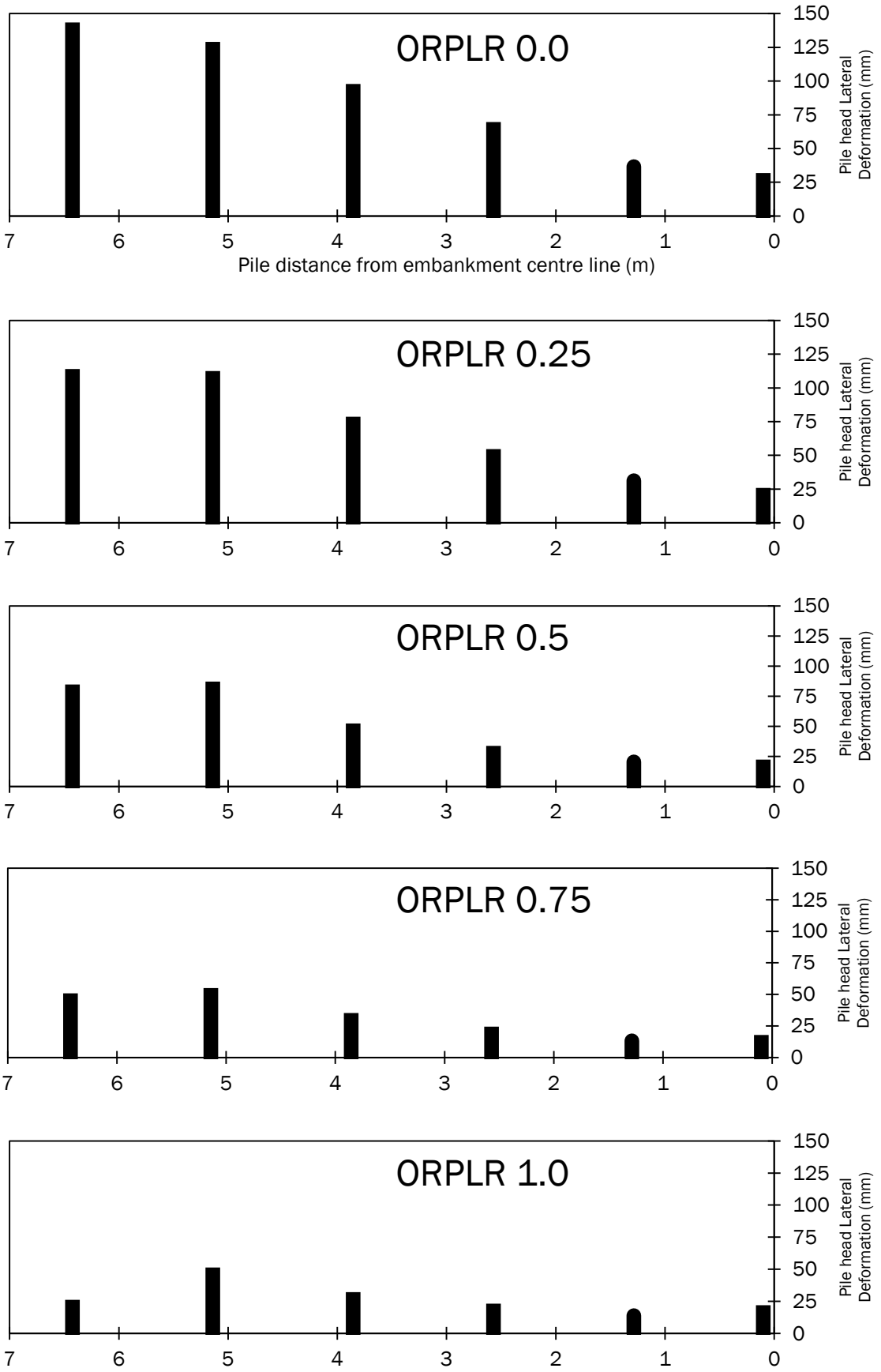

Figure 4.21 Pile group lateral deformations for a range of ORPLR in Test Nos. 14 – 18

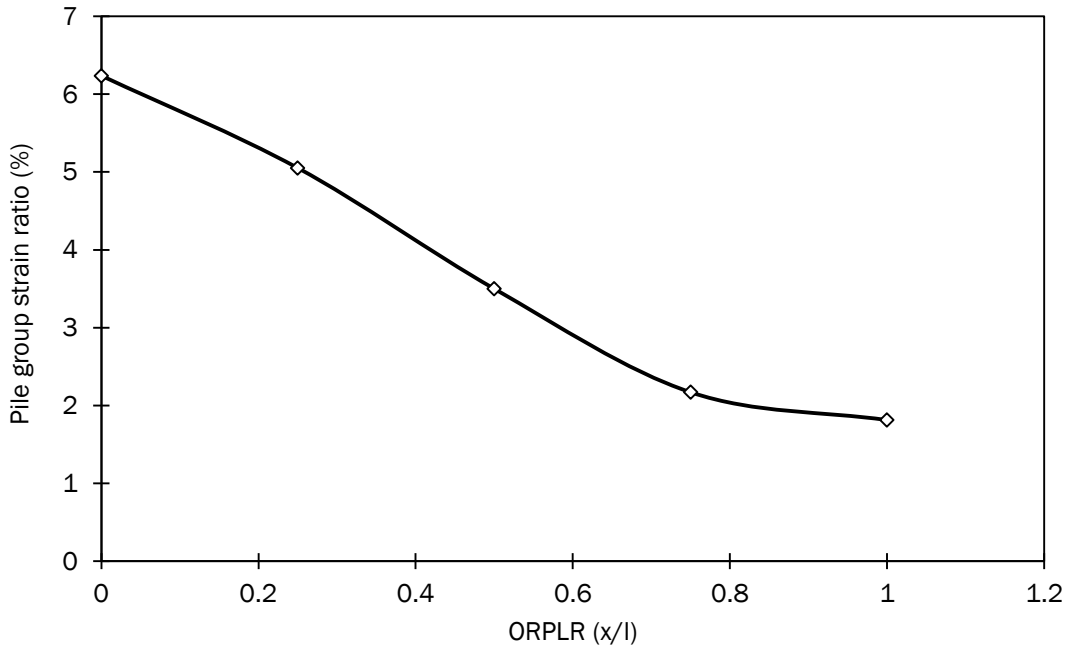

Figure 4.22 Pile group lateral strain (%) for a range of ORPLR in Test Nos. 14 – 18

4.2.2.2 Reinforcement vertical deformations

The vertical deformations of the geosynthetic reinforcement observed in Test Nos. 14 - 23 are illustrated in Figure 4.23. The results indicate that the maximum vertical deformation in the reinforcement near the embankment toe were consistently greater for subsoil A than for the stiffer subsoil B, Figure 4.23. The deformational response of the reinforcement for the stiffer subsoil B was an almost linear reduction in deformation for a linear increase of the ORPLR ratio, Figure 4.23. The subsoil A case yielded a non-linear response with ORPLR. The reinforcement vertical deformations decreased significantly (69%) for an initial increase of ORPLR from 0.0 – 0.5. Moving the outer pile row location further towards the embankment toe resulted in a lower rate of reinforcement vertical deformation, Figure 4.23. Convergence of the differential in magnitudes between vertical deformations for both subsoils was observed for an increase of ORPLR. The characteristic trend of the convergence for the vertical deformation of the reinforcement was similar to the response of the outer row pile, convergence of the differential was observed until ORPLR approached 0.8 approximately, Figure 4.23.

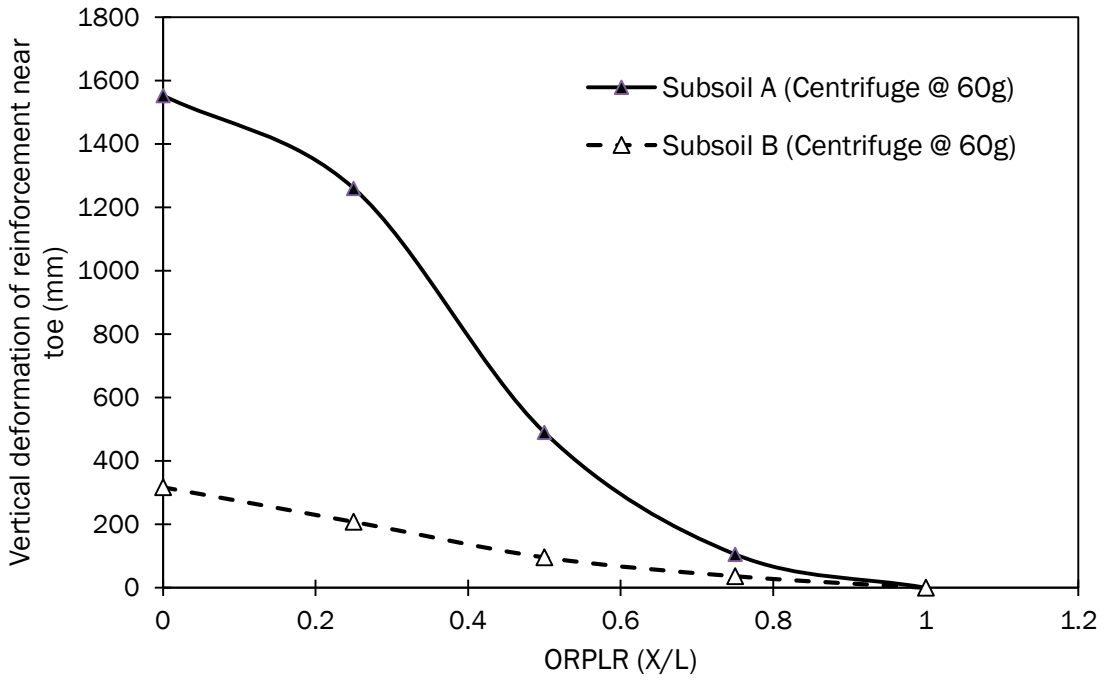

Figure 4.23 Vertical deformational response of reinforcement for a range of ORPLR in Test Nos. 14 – 23

Test Nos. 14- 18 and 24 – 28 revealed that the reinforcement recorded a maximum vertical deformation for all cases outside the outer pile row, Figure 4.24. The vertical deformation of the reinforcement near the embankment toe decreased significantly for an increase of ORPLR, Figure 4.24. The reinforcement vertical deformations decreased significantly (69% and 73%) for an initial increase of ORPLR (0.0 – 0.5) for the side slope cases 1V:2H and 1V:3H respectively. Moving the outer pile row location further towards the embankment toe, a lower rate of reinforcement vertical deformation reduction was observed, Figure 4.24. Convergence of the differential in magnitudes between both side slope cases was observed for an increase of ORPLR. Convergence of the differential in vertical deformation was observed until ORPLR approached 0.8 approximately, Figure 4.23.

4.2.2.3 Embankment mean surface deformations

Test Nos. 14 - 28 enabled the deformational response of the mean settlements on the embankment surface to be observed. The results indicate that for both subsoil A and B, the magnitudes of deformations decreased slightly with an increase in ORPLR, Figure 4.25. Subsoil A (stiffness of 54 kPa) recorded improvements equal in magnitude to the subsoil B case (stiffness of 240 kPa), Figure 4.25, although the initial magnitude of the deformation were significantly different.

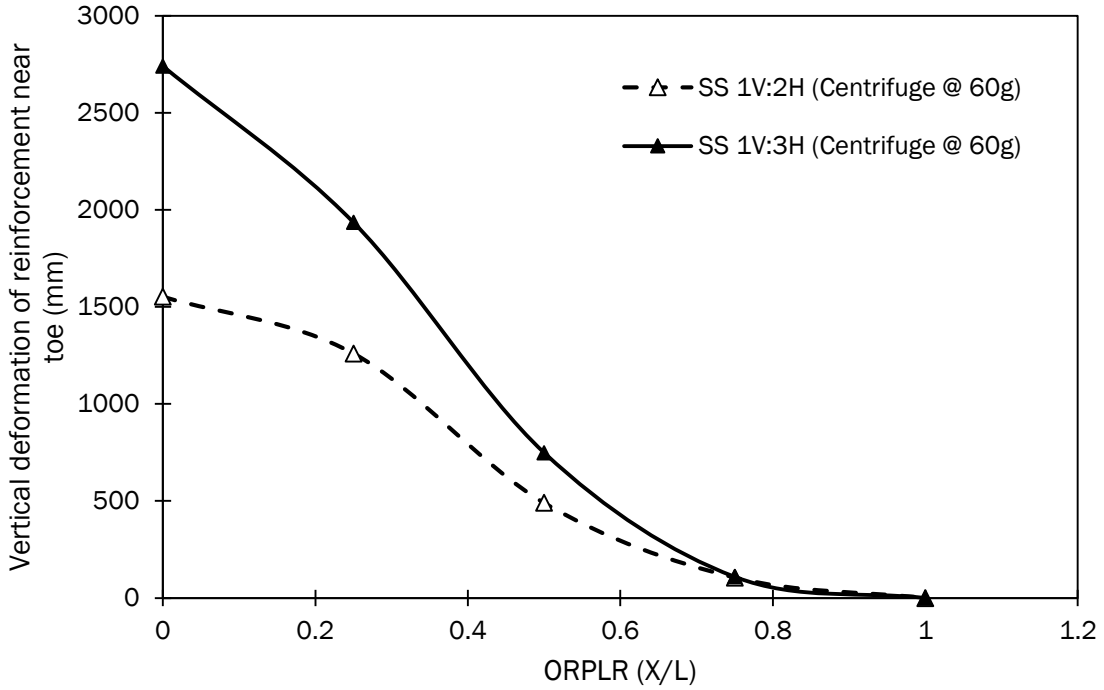

Figure 4.24 Vertical deformational response of reinforcement for a range of ORPLR in Test Nos. 14 – 18 and 24 – 28

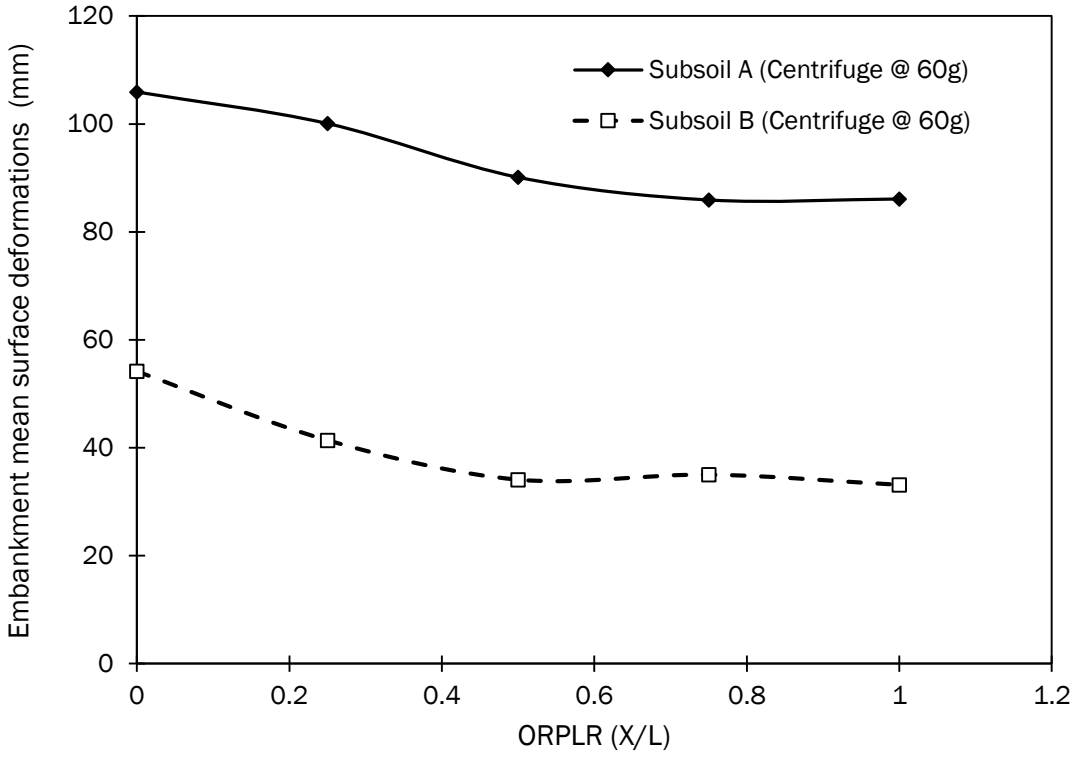

Figure 4.25 Embankment mean surface deformations for a range of ORPLR in Test Nos. 14 – 23

4.3 Plaxis 2D analysis

The numerical analysis reported in this section replicated each of the tests performed in the centrifuge test series. The dimensions and material properties were based on the experimental model subjected to a centrifugal acceleration of 60g. This section presents the pile group and geosynthetic deformations observed in the numerical modelling. Preliminary analysis of the data is also presented.

4.3.1 Plaxis Test Series 1

Plaxis Test Series 1 replicated the Centrifuge Test Series 1 modelling presented in Section 4.2.1. Material characteristics and geometric dimensions were equivalent to the centrifuge model at 60g. The tests conducted are summarized in Table 4.1, the fill density of the embankment fill was the mean density measured in the centrifuge model.

4.3.1.1 Pile group deformations

Figure 4.26 illustrates the comparison of the lateral deformation within the pile group as predicted by Plaxis 2D and measured from the Centrifuge Test No. 3. Both sets of data recorded a maximum lateral pile head deflection localized to the outer row pile for all parametric variations, Figure 4.26. Plaxis 2D and the centrifuge testing recorded an exponential increase in the magnitude of lateral pile head deflection for a linear increase in distance from the embankment centre-line, Figure 4.26. The Plaxis 2D analysis predicted lateral pile head deformations consistently greater in magnitude within the pile group in comparison to the centrifuge modelling, Figure 4.26. The magnitude of the lateral deformations increased at a greater rate approaching the outer row pile in the centrifuge test than the Plaxis 2D modelling. Figure 4.26 suggests that the response of piles near the embankment centre modelled by Plaxis 2D were more sensitive to lateral loading than the centrifuge testing. The analysis suggests the magnitudes and characteristic trend of the response of the pile group to lateral loading from Plaxis 2D and centrifuge modelling are in relatively good agreement, Figure 4.26.

The lateral deflection of the outer row pile head increased for an increase in the H/(s-a) ratio, Figure 4.27, Plaxis Test Nos. 1 - 4 and 9 - 12. Similar conditions existed for the characteristic trend of the lateral response of the outer row pile for

an increase of embankment height (increase of embankment geometric ratio), Figure 4.27. The Plaxis 2D and centrifuge modelling recorded lateral deformations of the 1V:2H side slope steepness cases consistently greater than the 1V:3H side slopes. Both the Plaxis 2D and centrifuge modelling produced a divergence between the 1V:2H and 1V:3H side slope cases for an increase in the embankment height (increase of the H/(s-a) ratio), Figure 4.27. An increase of the geometric ratio from 0.5 to 2.0 (H/(s-a)) yielded an increase of 342% and 354% in the magnitude of the outer row pile lateral deformation recorded by both the Plaxis 2D and the centrifuge modelling.

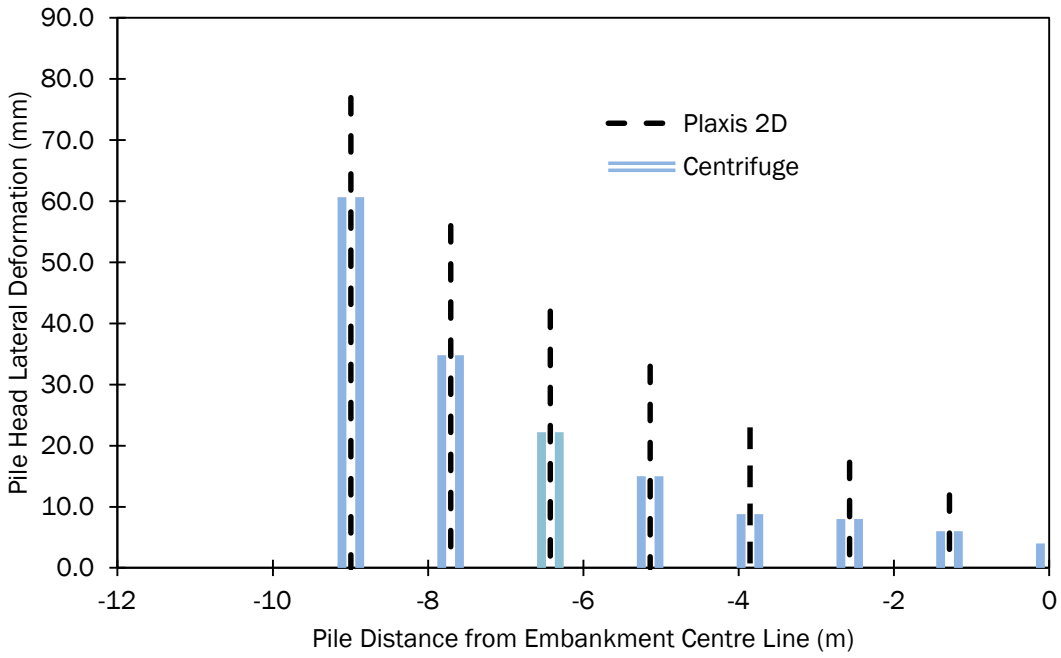

Figure 4.26 Lateral deflection (mm) in pile group for physical modelling (Centrifuge) in Test No. 3

Similar conditions exist with the deformational response of the outer pile row for a variation of the embankment side slope steepness. An increase in the embankment side slope steepness yielded an increase in the outer row pile lateral deformation for both the Plaxis 2D and centrifuge modelling, Figure 4.28, Test Nos. 1 - 4. An increase in the side slope steepness from 1V:4H to 1V:2H yielded an increase of 87% and 81% respectively for the Plaxis 2D and centrifuge modelling. The centrifuge pile group mobilised lower magnitudes of lateral deformation at the outer row pile in comparison to the Plaxis 2D case.

Figure 4.29 presents the deformational response of the outer row pile for a variation of the soft soil stiffness from Test Nos. 1 – 8. Plaxis 2D modelling consistently recorded higher magnitudes of outer row pile lateral deformations than the centrifuge modelling. The differential in magnitudes of deformations between the Plaxis 2D and centrifuge modelling decreased for an increase of embankment height, for both subsoils, Figure 4.29.

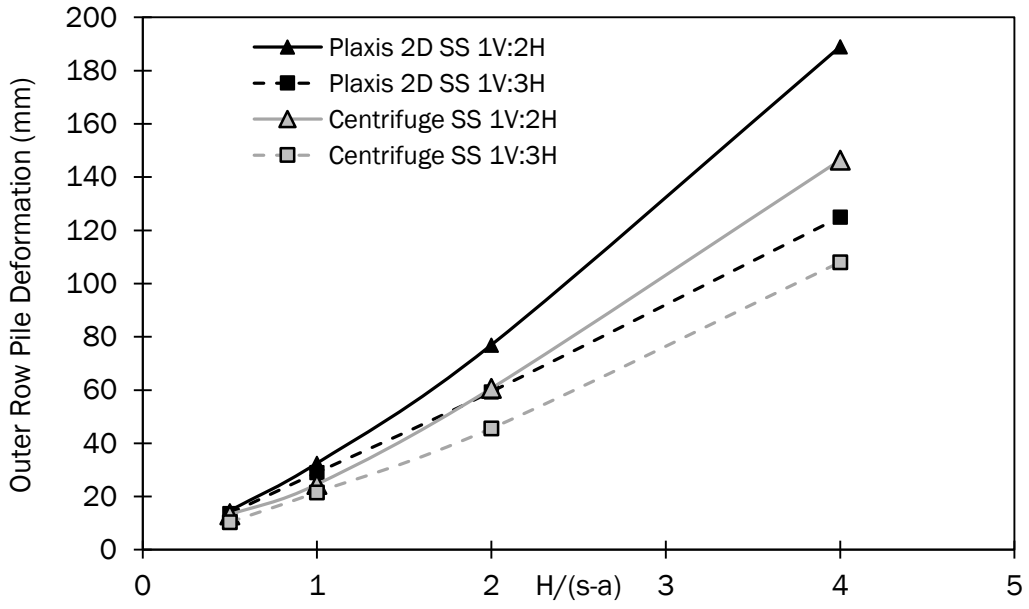

Figure 4.27 Lateral deflection (mm) of outer row pile for a range of embankment geometric ratios (H/(s-a)) in Test Nos. 1 - 4 and 9 - 12

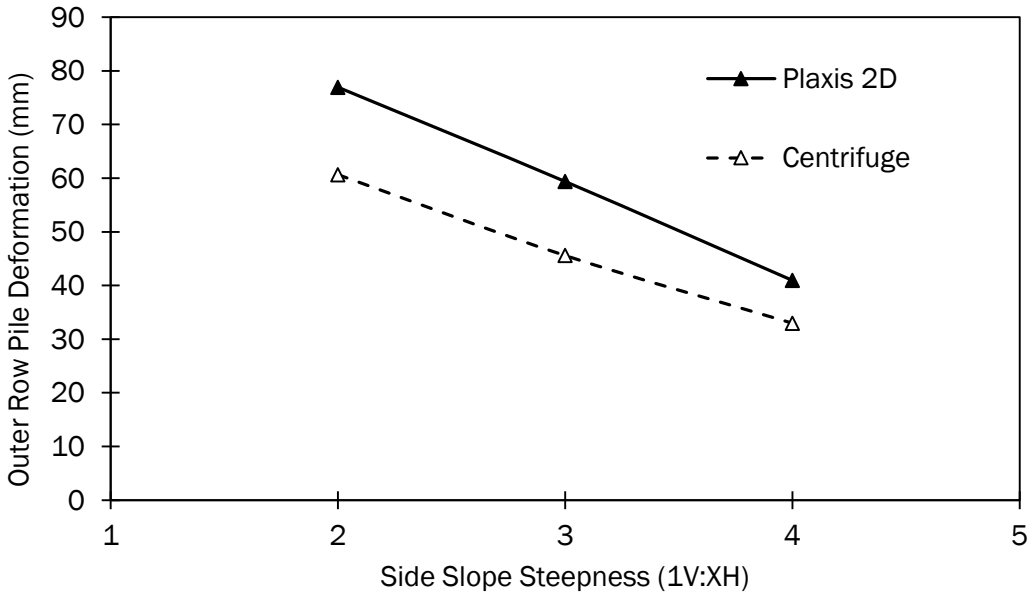

Figure 4.28 Lateral deflection (mm) of outer row pile for a range of embankment side slopes in Test Nos. 1 – 3

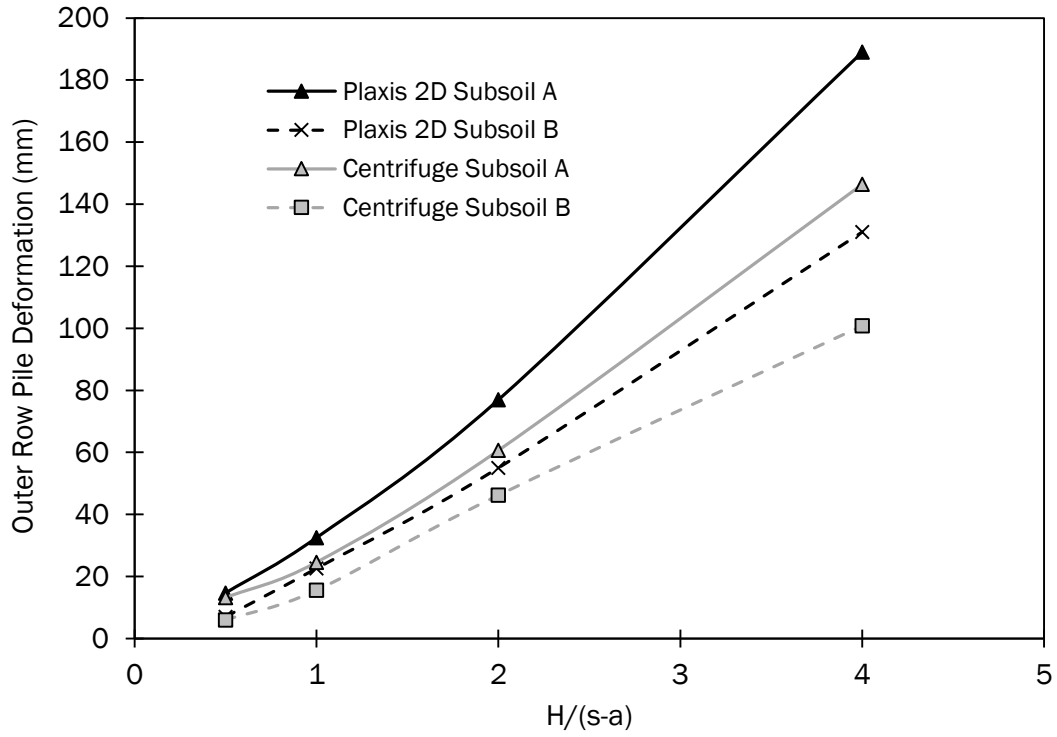

Figure 4.29 Lateral deflection (mm) of outer row pile for a range of subsoil stiffness in Test Nos. 1 – 8

4.3.1.2 Geosynthetic reinforcement deformations

The vertical deformation of the reinforcement followed a similar, catenary type shape between adjacent pile caps, from the centre line of the embankment to the outer row of piles for all geometries examined, Figure 4.30. A vertical deformation maximum was recorded outside the outer row pile near the embankment toe for both Plaxis 2D and centrifuge modelling, Figure 4.30. The magnitudes of the vertical deformations predicted by Plaxis 2D in between the adjacent pile caps within the pile group were greater in magnitude in comparison to similar centrifuge models, Figure 4.30. The magnitudes of the vertical deformations recorded between adjacent pile caps remained relatively consistent (+/- 5% approximately) for both Plaxis 2D and centrifuge modelling. As the reinforcement protruded past the embankment crest, the magnitudes of the vertical deformation in between adjacent pile caps increased with an increase in distance from the embankment crest for both Plaxis 2D and centrifuge modelling, Figure 4.30.

The vertical deformation of the reinforcement near the embankment toe increased for an increase in embankment height (increase of H/(s-a)), Figure 4.31. The

characteristic trend of the vertical deformational response of the reinforcement was to remain relatively constant for an initial increase in embankment height (increase of H/(s-a) from 0.5 to 1.0) for both Plaxis 2D and centrifuge modelling for all cases of side slope steepness, Figure 4.31. A further increase in the embankment height (1.0 to 2.0 H/(s-a)) produced a significant increase in vertical deformation, Figure 4.31. For both embankment side slope steepness 1V:2H and 1V:3H, the Plaxis 2D and centrifuge modelling were in relatively good agreement in both characteristic trend and the absolute magnitude of deformations.

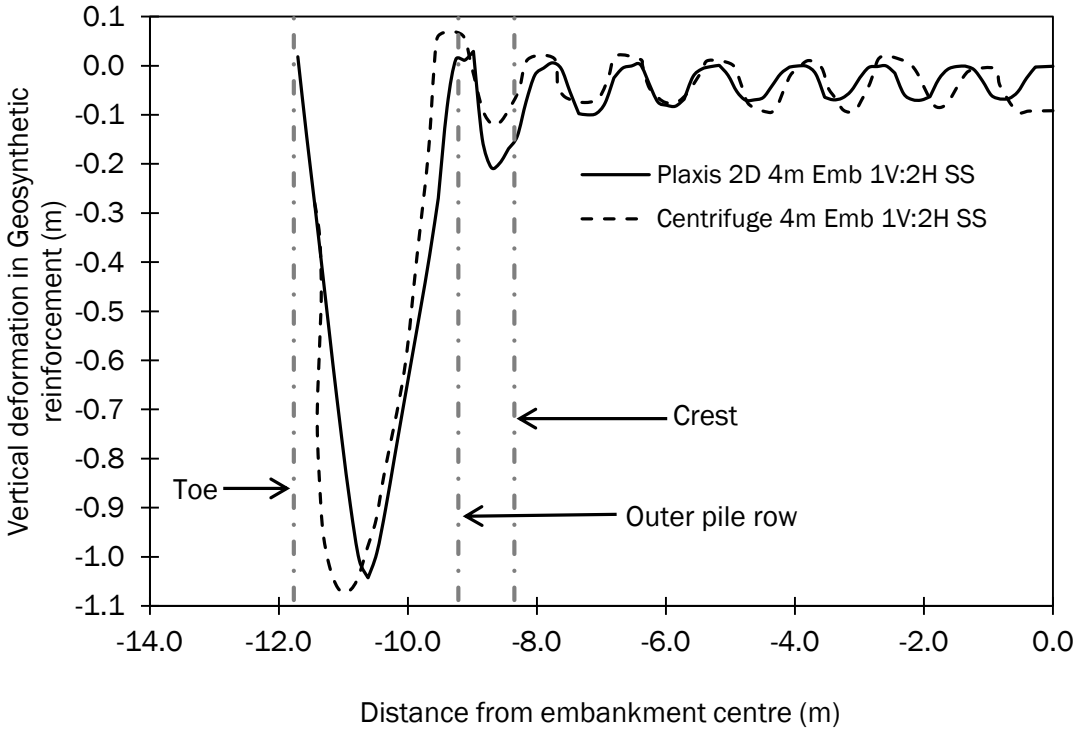

Figure 4.30 Vertical deformation in reinforcement in Test No. 3

The magnitude of the vertical deformation of the reinforcement increased for a decrease in the side slope steepness, Figure 4.32, Plaxis Test Nos. 3, 11 and 13. The characteristic response of the vertical deformation in the reinforcement was an initial increase (35%, Plaxis 2D and 42% for centrifuge) for a reduction in the side slope steepness from 1V:2H to 1V:3H, Figure 4.32. A further reduction of the embankment side slope steepness (1V:3H to 1V:4H) yielded a significant reduction in the rate of vertical deformation increase, Figure 4.32. The reduction in the rate of increase in vertical deformation was most pronounced for the Plaxis 2D case, Figure 4.32. For all cases of side slope steepness, the Plaxis 2D modelling yielded lower magnitudes of vertical deformation in the reinforcement near the embankment toe.

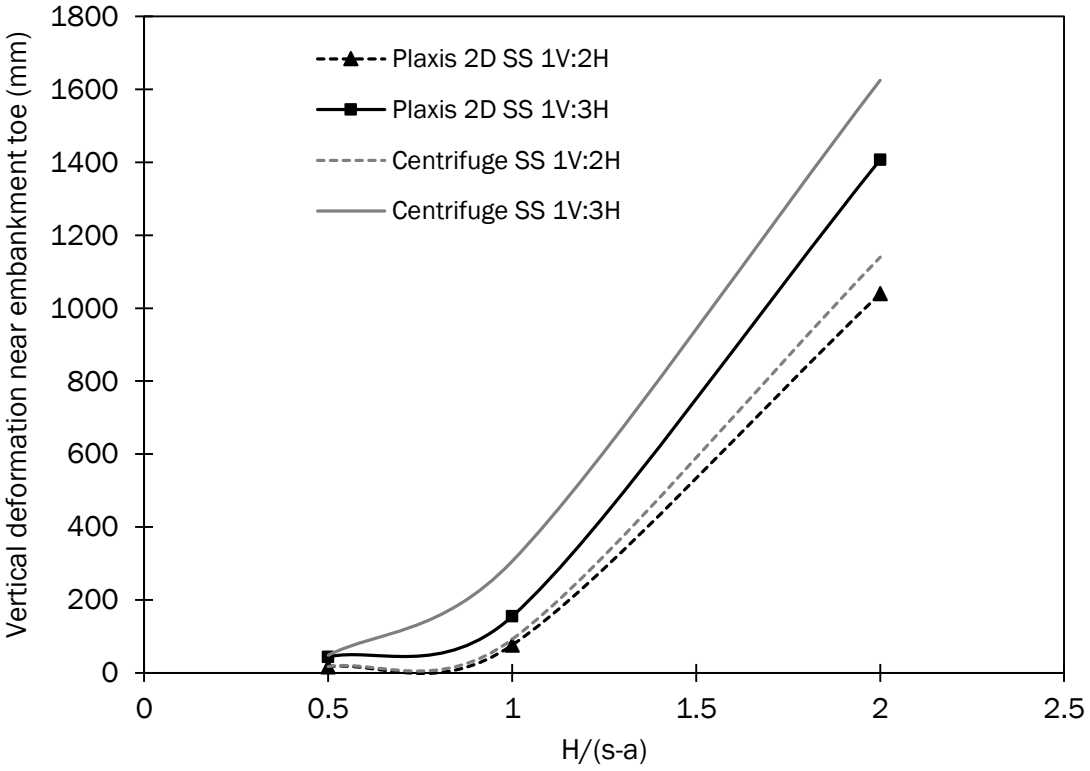

Figure 4.31 Maximum vertical deformation in reinforcement for a range of geometric ratios (H/(s-a)) in Test Nos. 1 – 4 and 9 – 12

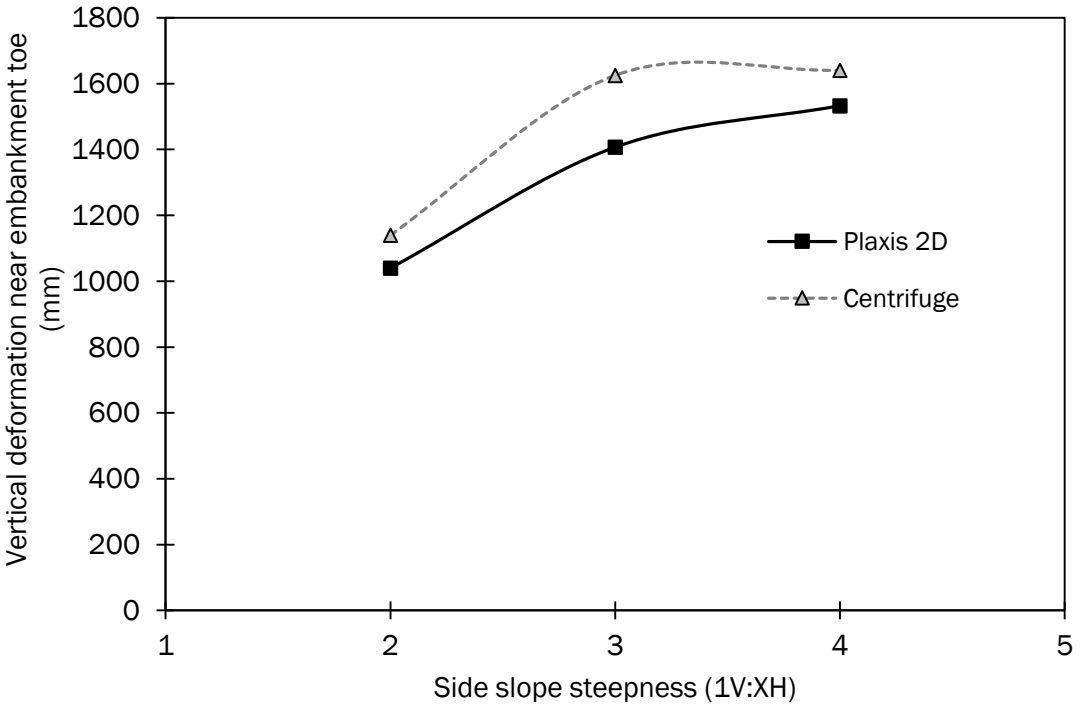

Figure 4.32 Maximum vertical deformation in reinforcement for a range of side slope steepness (1V:XH) in Tests Nos. 3, 11 and 13

Test Nos. 1 – 8 investigated the influence of a variation of the subsoil stiffness on the vertical deformations near the embankment toe, see Figure 4.33. Vertical deformations increased with H/(s-a) ratio for all subsoil stiffness in both modelling techniques. The differential between the Plaxis 2D and the centrifuge modelling deformations diverged as the H/(s-a) ratio increased. Both subsoils and modelling techniques yielded the greatest rate of increase for a H/(s-a) ratio increase from 1 – 2, Figure 4.33. The centrifuge modelling consistently recorded greater magnitudes of vertical deformations in comparison to Plaxis 2D.

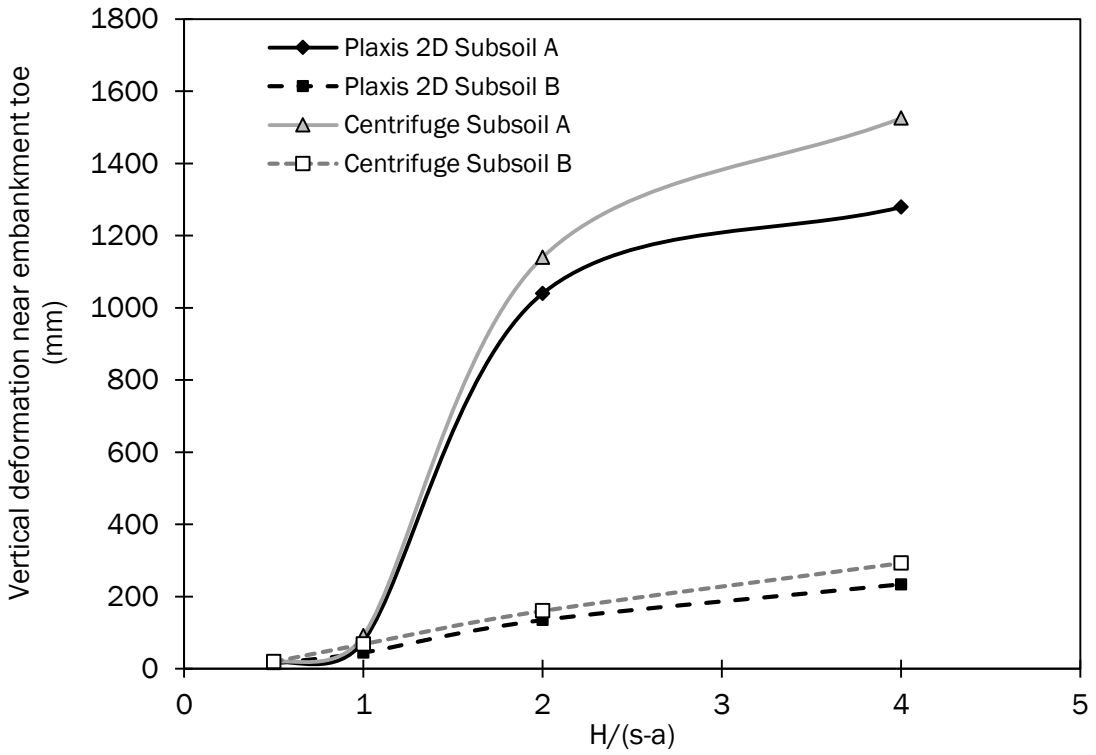

Figure 4.33 Maximum vertical deformation in reinforcement for a range of subsoil stiffness in Test Nos. 1 – 8

4.3.1.3 Embankment mean surface deformations

The magnitude of vertical deformation at the embankment surface increased for an increase in embankment height (increase of embankment geometric ratio, H/(s-a)), Figure 4.34, Plaxis Test Nos. 1 – 4 and 9 - 12. Plaxis 2D consistently predicted embankment surface settlements of lower magnitude than those measured in similar centrifuge models. The deformational response of the embankment fill yielded a consistent differential in magnitude of the Plaxis 2D and centrifuge models for a range of embankment heights (range of embankment geometric

ratios) for both side slope steepness, Figure 4.34. Plaxis 2D was consistently approximately 25mm lower in magnitude than the centrifuge model, Figure 4.34. This could be attributed to the variation of fill density in the centrifuge testing, Figure 4.34.

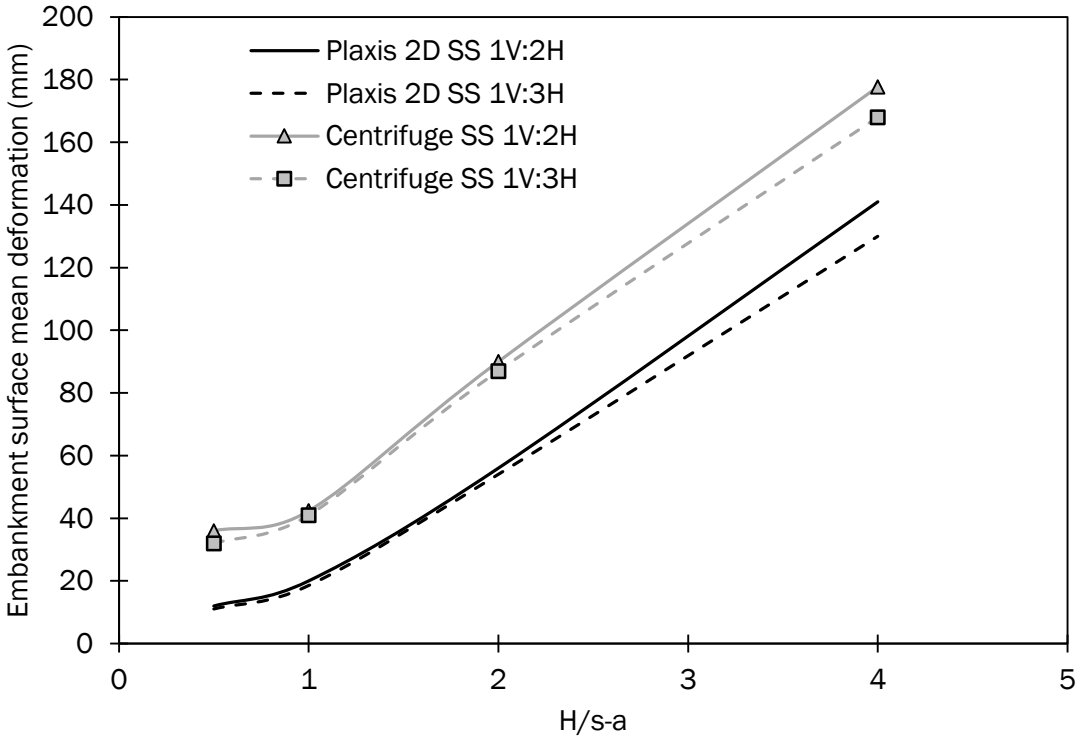

Figure 4.34 Embankment mean surface deformations for a range of embankment geometric ratios (H/(s-a)) in Test Nos. 1 – 4 and 9 – 12

Test Nos. 3, 11 and 13 indicate that an increase in the steepness of the embankment side slope had a relatively insignificant influence on the overall deformation of the surface. Both the Plaxis 2D and centrifuge modelling yielded a small reduction in magnitude of the embankment surface settlement for a decrease in the side slope steepness (a reduction of 5.4% and 4.9% for Plaxis 2D and the centrifuge respectively), Figure 4.35.

Figure 4.36 illustrates the embankment mean surface deformational response of the model for a range of subsoil stiffness and H/(s-a) ratios, Test Nos. 1 – 8. Embankment mean surface deformations increased for subsoil in both the Plaxis 2D and centrifuge modelling, Figure 4.36. Consistently greater magnitudes of embankment mean surface deformations were measured in the centrifuge model compared to those predicted by Plaxis 2D.

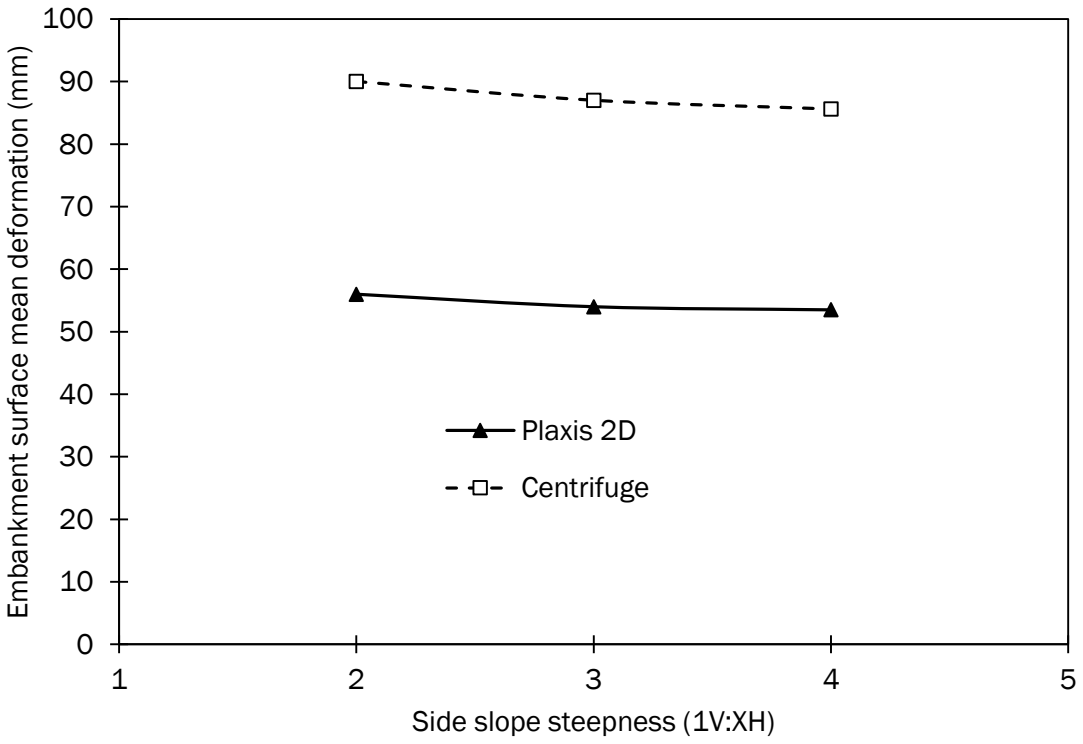

Figure 4.35 Embankment mean surface deformations for a range of embankment geometric ratios (H/(s-a)) in Test Nos. 3, 11, 13

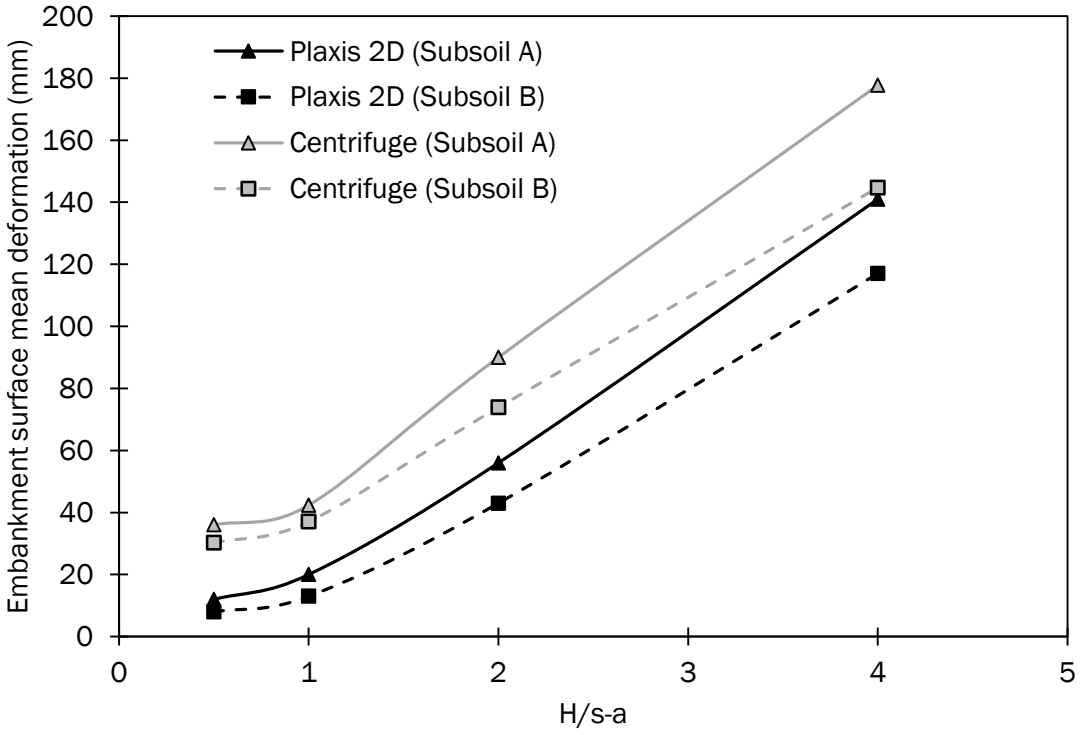

Figure 4.36 Embankment mean surface deformations for a range of subsoil stiffness in Test Nos. 1 – 8

The deformation at the crest of the embankment was examined in terms of its vertical and horizontal component, Figure 4.37, Test Nos. 1 - 8. The ratio of improvement with regard to horizontal versus vertical deformation was linear and almost proportional for an increase in the stiffness of the geosynthetic reinforcement and a decrease in the depth of the underlying soft soil. A reduction in the steepness of the side slope yielded a notable improvement in the horizontal deformation whilst having an insignificant influence on the vertical deformation, Figure 4.35. For an increase in the embankment height, the Plaxis 2D modelling predicted a convergence of the deformational response of the two side slope steepness whilst the centrifuge modelling yielded a consistent differential for a range of embankment heights, Figure 4.37.

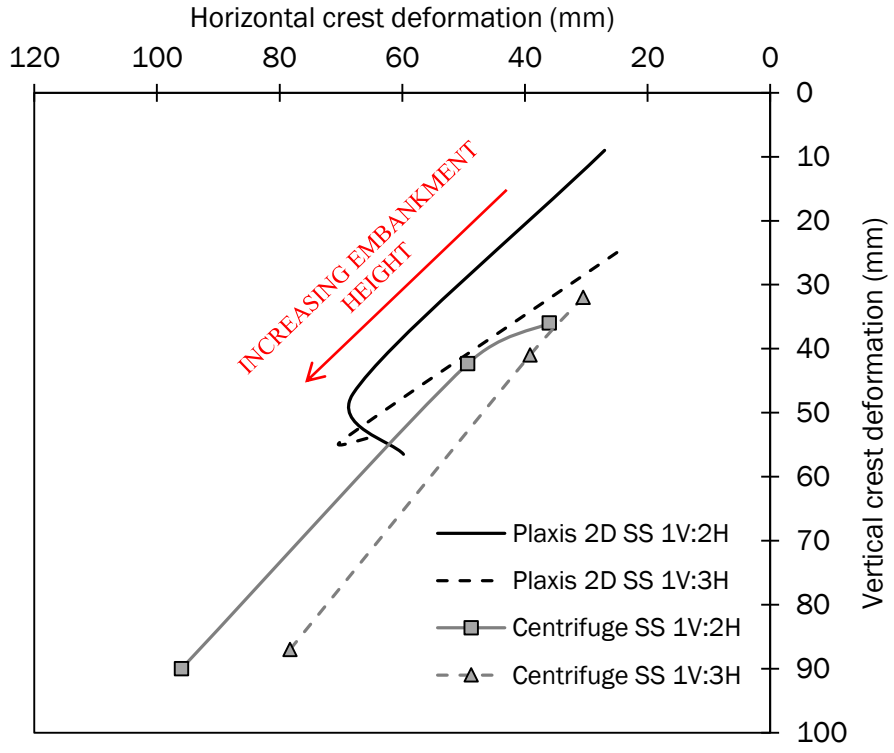

Figure 4.37 Embankment crest deformations for a range of embankment side slope steepness (1V:XH) in Test Nos. 1 – 8

4.3.2 Plaxis Test Series 2

Plaxis Test Series 2 replicated the Centrifuge Test Series 2 modelling of the outer row pile location ratio (ORPLR) presented in Section 4.2.2. Material characteristics and geometric dimensions were equivalent to the centrifuge model at 60g. The

tests conducted are summarized in Table 4.2, the embankment fill density used during modelling was the mean fill density from the centrifuge modelling.

4.3.2.1 Pile group deformations

Plaxis Test Nos. 14 – 23 examined the influence of the subsoil stiffness on the deformational response of the outer pile row for a range of ORPLR, Figure 4.38. The deformational response of the outer pile row for a variation of ORPLR was in relatively good agreement between the Plaxis 2D and the centrifuge modelling. The outer pile row lateral deformation differential between the Plaxis 2D and centrifuge modelling converged for an increase of ORPLR for subsoil A but not for subsoil B, Figure 4.38.

Figure 4.39 illustrates the deformational response of the outer row pile for different side slope steepness, Plaxis Test Nos. 14 – 18 and 24 – 28. Similar conditions exist between the deformational response of the outer pile row with different side slope steepness and a range of ORPLR in both Plaxis and centrifuge modelling, Figure 4.39. Plaxis 2D consistently predicted greater magnitudes of lateral pile head deformations at the outer row pile head in comparison to the measured values from the centrifuge for all side slope cases, Figure 4.39.

The deformational response of the pile group for a range of ORPLR is illustrated in Figure 4.40 from Test Nos. 14 – 18. Both the Plaxis 2D and centrifuge modelling suggest that the magnitudes of lateral deformations at each pile within the pile group increased as the pile location moved from the embankment centre line to near the crest, Figure 4.40. Plaxis 2D consistently predicted greater magnitudes of lateral pile head deformation in comparison to the centrifuge model.

Figure 4.41 illustrates the relationship of the pile group strain with ORPLR from Test Nos. 14 – 18. Increasing the ORPLR from 0 to 1.0 consistently decreased the pile group strain in both the Plaxis 2D and the centrifuge models, Figure 4.41. The analysis suggests that both the Plaxis 2D and centrifuge model pile groups were subjected to lower lateral deformations as the outer row pile location neared the embankment toe (ORPLR = 1.0).

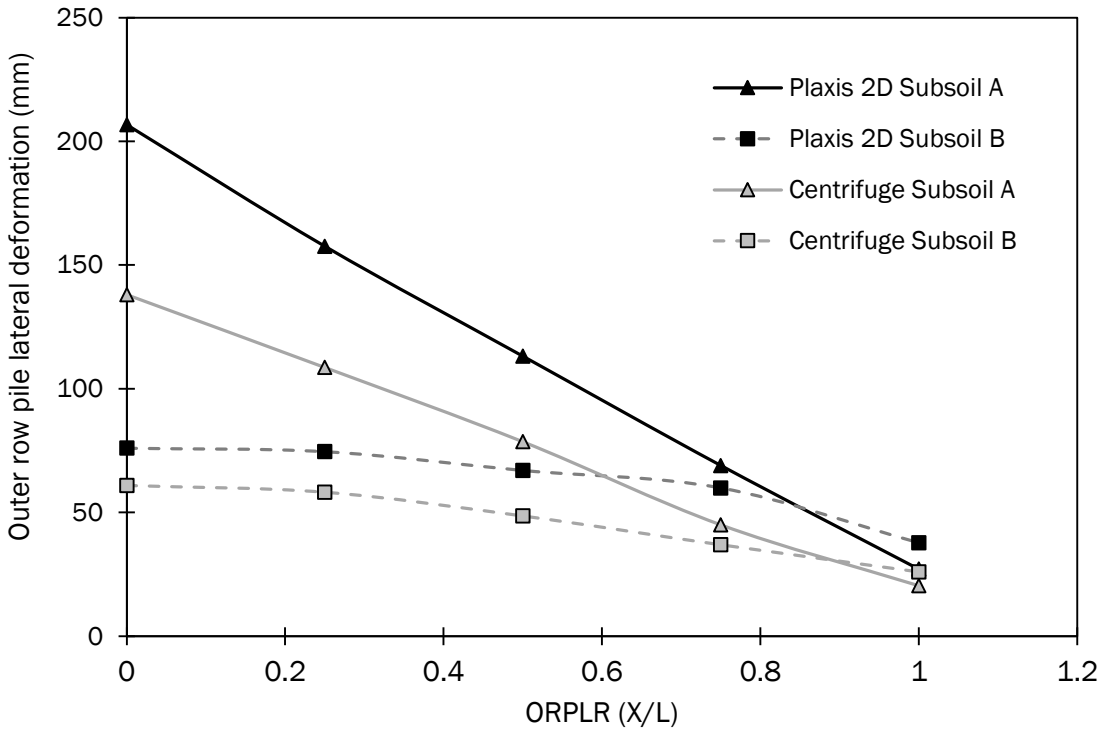

Figure 4.38 Outer row pile lateral deflections for a range of ORPLR and soil stiffness in Test Nos. 14 – 23

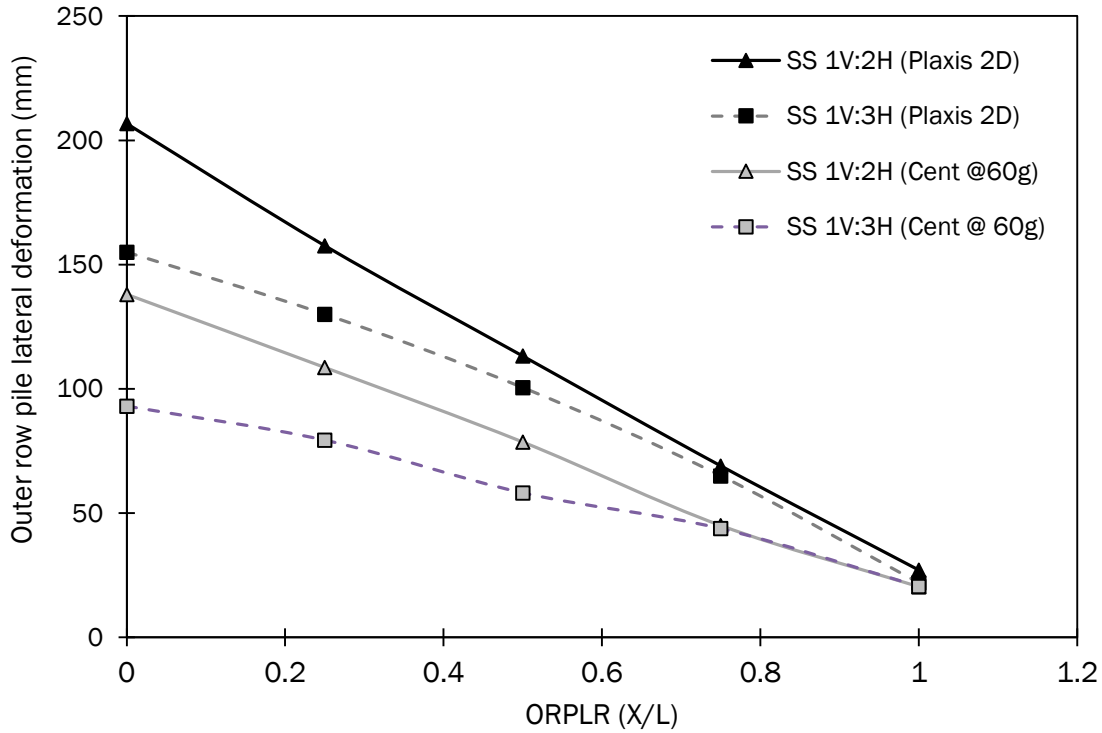

Figure 4.39 Outer row pile lateral deflections for a range of ORPLR and side slope steepness (1V:XH) in Test Nos. 14 – 18 and 24 – 28

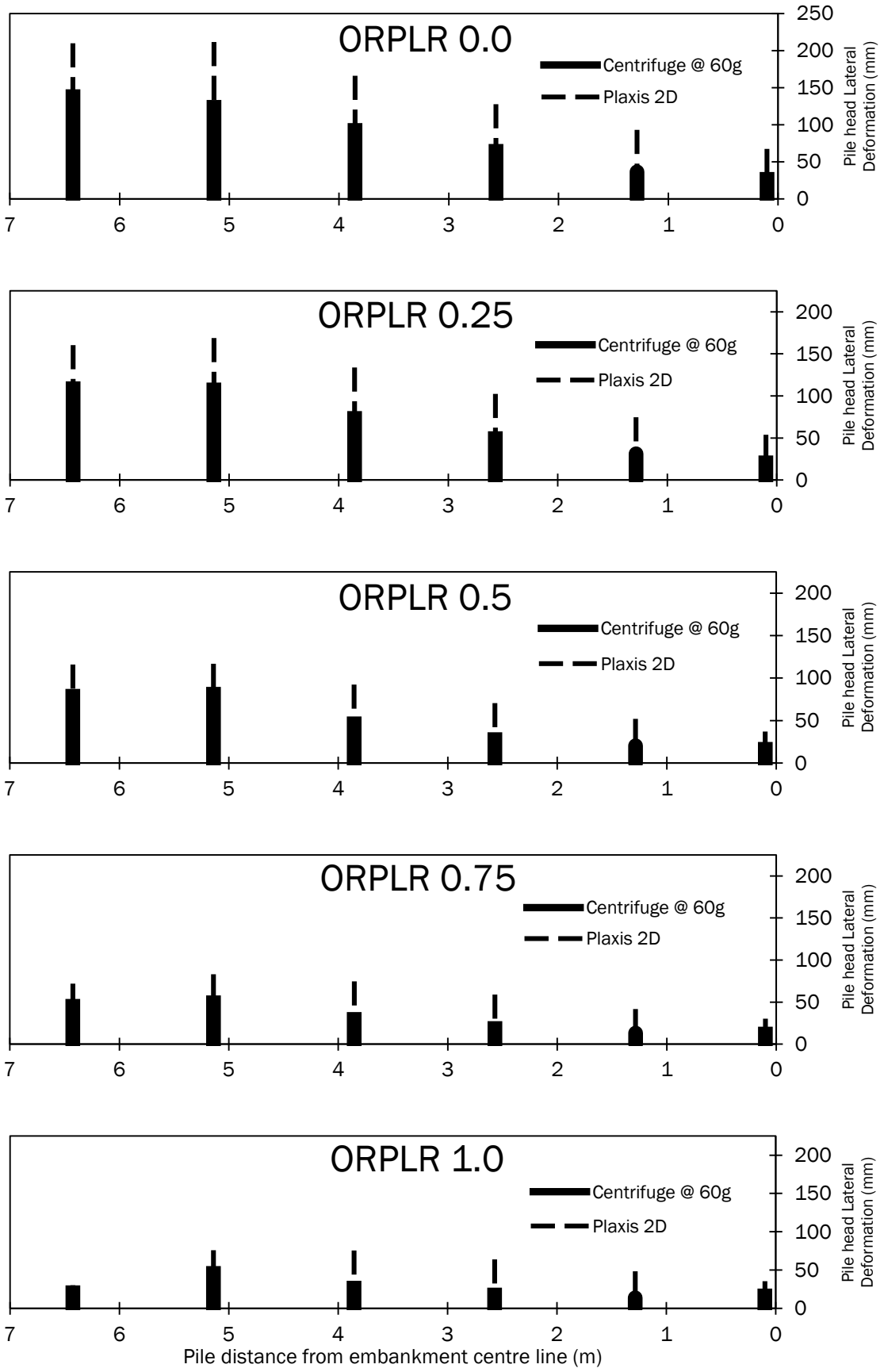

Figure 4.40 Pile group lateral deformations for a range of ORPLR in Test Nos. 14 – 18

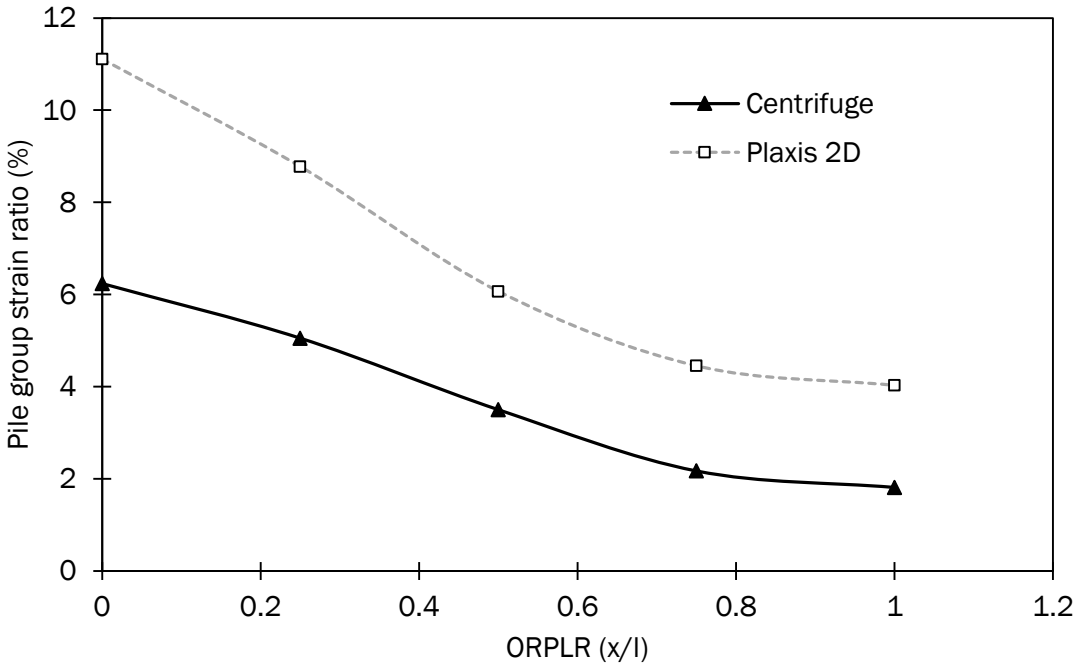

Figure 4.41 Pile group lateral strain (%) for a range of ORPLR in Test Nos. 14 – 18

4.3.2.2 Geosynthetic reinforcement deformations

Test Nos. 14 – 28 examined the vertical deformational response of the geosynthetic reinforcement near the embankment toe for two different subsoil stiffnesses and a range of ORPLR, Figure 4.42. Similitude conditions existed between the Plaxis 2D and centrifuge models in the deformational response of the geosynthetic reinforcement for both subsoil cases, Figure 4.42. Both modelling techniques recorded a significant reduction in vertical deformations as the outer row pile moved toward the embankment toe (ORPLR approached 1.0) for both subsoils.

Figure 4.43 illustrates the vertical deformational response of the geosynthetic reinforcement for a range of side slope steepness from Test Nos. 14 – 18 and 24 – 28. Both Plaxis 2D and the centrifuge model analysis recorded consistently greater magnitudes of vertical deformation for the 1V:3H case for a range of ORPLR, Figure 4.43. Both modelling techniques recorded a significant reduction in vertical deformations as the outer row pile location approached the embankment toe (ORPLR from 0 to 1.0), Figure 4.43. The vertical deformational response of both modelling techniques for both side slope case was to reduce to 0 mm as the pile location approached the embankment toe.

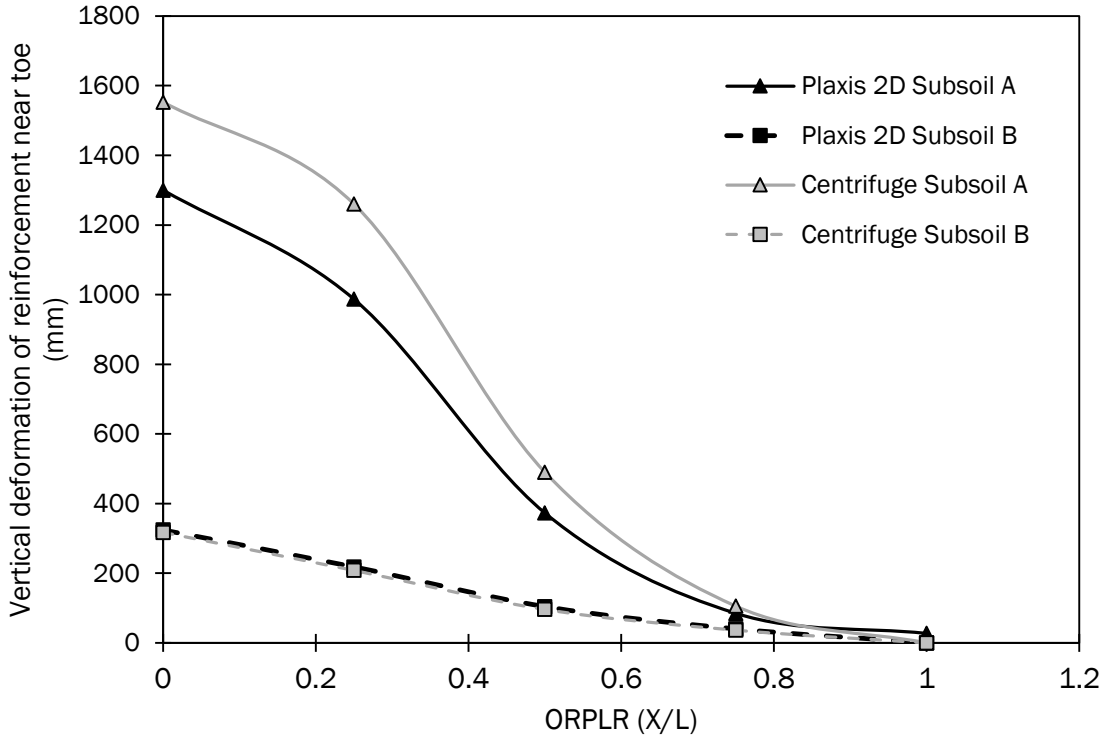

Figure 4.42 Vertical deformational response of reinforcement for a range of ORPLR in Test Nos. 14 – 23

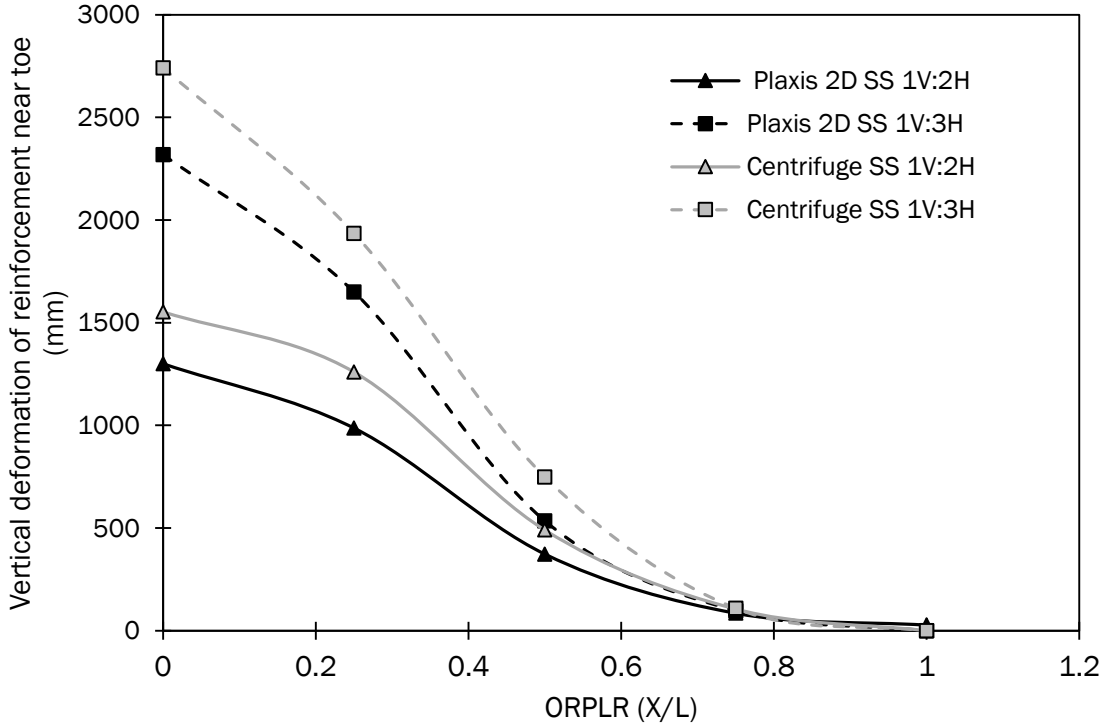

Figure 4.43 Vertical deformational response of reinforcement for a range of ORPLR in Test Nos. 14 – 18 and 24 – 28

4.3.2.3 Embankment mean surface deformations

The embankment mean surface deformations in Test Nos. 14 – 23 are illustrated in Figure 4.44. The magnitude of mean surface deformations decreased as the outer row pile location approached the embankment toe for both modelling techniques, Figure 4.44. Agreement between the Plaxis 2D and centrifuge modelling in the deformational response of the mean embankment surface with ORPLR was observed. The centrifuge testing consistently yielded greater magnitudes of deformation in comparison to those predicted by Plaxis 2D for both subsoils, Figure 4.44. Greater differentials between the Plaxis 2D and the centrifuge modelling was observed for subsoil A in comparison to subsoil B, Figure 4.44.

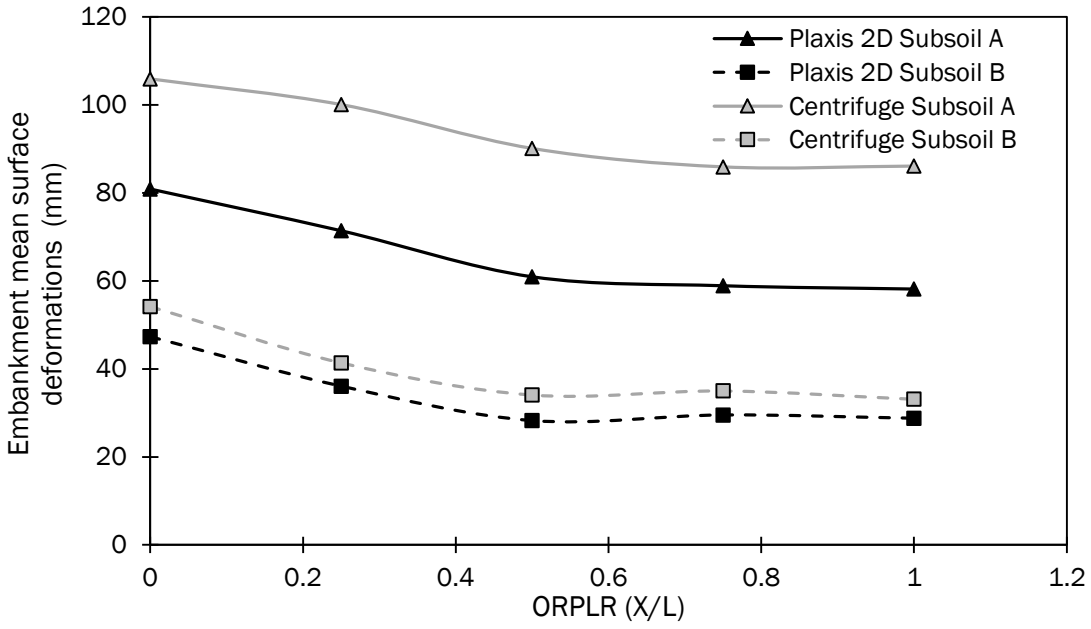

Figure 4.44 Embankment mean surface deformations for a range of ORPLR in Test Nos. 14 – 23

4.4 Centrifuge modelling summary

The pile group lateral deformations, geosynthetic reinforcement vertical deformations and embankment surface mean settlements measured in Centrifuge Test Series 1 and 2 have been presented, with some preliminary analysis and discussion. The centrifuge testing was divided into two test series. In Test Series 1, a variation of the side slope steepness, embankment height and the subsoil stiffness was performed. Test Series 2 examined the effects of the outer row pile location along the side slope length on the performance of the structure.

Analysis of the centrifuge pile group deformations suggest that each pile within the pile group is subjected to lateral deformations. Lateral deformation at each pile head within the pile group increased as the pile location approached the embankment crest. The centrifuge analysis consistently recorded a lateral pile deformation maximum located to the most outer row pile. Lateral deformation of the outer row pile increased with side slope steepness, H/(s-a) and a reduction of subsoil stiffness. The magnitude of lateral deformations within the pile group decreased as the outer row pile location approached the embankment toe (ORPLR 0 to 1.0). The overall lateral strain that the pile group was reduced significantly in a linear fashion as the outer row pile location moved toward the embankment toe.

The vertical deformation of the geosynthetic reinforcement followed a catenary type deformation shape between adjacent pile caps, from the centre line of the embankment to the outer row pile for all parametric variations. A vertical deformation recorded a maximum outside the outer row pile near the embankment toe. Maximum vertical deformations increased with H/(s-a), a reduction of side slope steepness and subsoil stiffness. Vertical deformations past the outer row pile decreased as to zero as the pile moved toward the toe.

Embankment mean surface deformations increased almost linearly with embankment height. A reduction of the subsoil stiffness (subsoil B to A) yielded a moderate increase in magnitude of mean surface deformations. A minor linear decrease in mean surface deformations was observed with a reduction of side slope steepness. Mean surface deformations decreased slightly as the outer row pile moved toward the embankment toe.

The embankment mean surface vertical deformational response of the centrifuge model suggested that the model was most sensitive to an increase of embankment height (increased H/(s-a) ratio).

4.5 Plaxis 2D and Centrifuge modelling comparative analysis summary

Similitude conditions exist between the numerical and physical modelling of the deformational response of both the pile group as a whole and the outer row pile. Both Plaxis 2D and the centrifuge modelling indicated an increase in magnitude of the lateral deformation at the pile head with an increase in distance from the

embankment center line. Both Plaxis 2D and the centrifuge modelling recorded a maximum lateral pile head deformation at the outer most pile.

The comparative analysis indicated that significant vertical deformation occurred in the reinforcement under the side slopes of piled embankments. The magnitude of the vertical deformation between adjacent piles increased for an increase in the embankment height and steepness of the side slope. Plaxis 2D and the centrifuge modelling produced a similar deformational response of the reinforcement across the width of the embankment. The vertical deformation increased significantly from the outer row pile towards the toe of the embankment. For all cases of side slope steepness, Plaxis 2D predicted lower magnitudes of vertical deformation than similar centrifuge modelling in reinforcement near the embankment toe. Plaxis 2D predicted consistently lower magnitudes of deformations at both the embankment surface and crest locations. Both Plaxis 2D and the centrifuge modelling showed that a variation of the side slope steepness had negligible effect on the deformational response of the embankment surface but a more pronounced influence on the deformation at the embankment crest location.

Moving the location of the outer row pile towards the embankment toe reduced lateral deformations at each pile location within the pile group significantly for both side slope and subsoil cases. The maximum vertical deformation of the geosynthetic reinforcement decreased almost linearly to zero as the pile moved toward the embankment toe.

The analysis suggests that the Plaxis 2D and centrifuge modelling approaches were in overall good agreement for the simulation of a geosynthetic reinforced piled embankment. Similar conditions exist in both the modelling techniques to consistently simulate the response of structural and soil elements in their behaviour. Plaxis 2D and centrifuge modelling developed characteristic trends under a variation of embankment height and side slope steepness that can be considered agreeable in nature (trends) but for some parameters slightly divergent in their absolute values.

Chapter 5

FEM modelling – Presentation of analysis data

5.1 Introduction

Plane strain analyses using Plaxis 2D 2010 were undertaken at the extremities of a geosynthetic reinforced piled embankment. The detailed examination of the relationship between geometric and material parametric variations allowed a comprehensive exploration of the behaviour of the various deformations and forces within the structure. Investigation of the effects of piles spacing, pile cap size, outer pile rake angle, geosynthetic reinforcement stiffness, depth of soft soil layer, soft soil stiffness, embankment height, side slope steepness and the outer pile row location ratio on the performance of the GRPE was performed.

The generic case model of the piled embankment, Figure 5.1, consisted of the following geometric characteristics: Embankment height (H) of 4.0m, pile spacing (s) of 3.0m, pile cap size (a) of 1.0m, soft soil depth (D) of 8.0m, a side slope of 1V:2H and finally a geosynthetic stiffness of 500kN/m as discussed in Section

3.3.6. Table 3.14 contained the material properties of the piles. The geosynthetic reinforcement had the following stiffness: 2000 kN/m and 500kN/m and 0kN/m (unreinforced case). The bending stiffness and the axial load capacity of the pile were based on that of a 300mm × 300mm square pile. A surcharge loading of 10.0kN/m^2 was applied from the embankment centre up to 1.0m from the embankment crest to simulate trafficked loading, Figure 5.1.

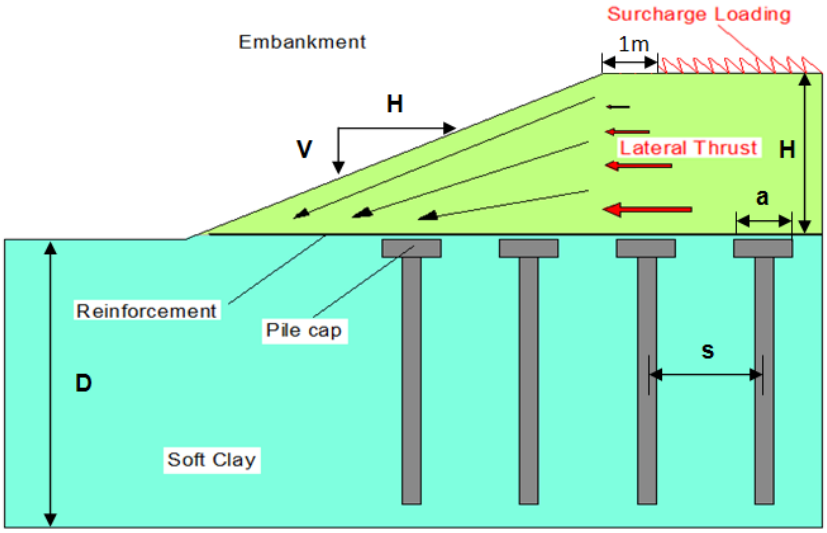

Figure 5.1 Geometric layout of generic case model of a reinforced pile embankment on soft soil

An examination of the deformations and forces within the embankment was conducted. Suitable locations where the deformations could be consistently monitored and compared under a sequence of parameter variations to enable an accurate comparison where chosen. In this study the following locations (Figure 5.2) were selected:

1. Deformation of embankment fill material
2. Deformation and loading exerted on geosynthetic reinforcement
3. Deformation and loading exerted on pile group

The magnitude of the deformations at the exact crest location (crest origin, Figure 5.2), the total deformations were converted into their respective deformational vectors (horizontal and vertical). Monitoring of the lateral deformation that occurred in the side slope above the centreline of the outer row pile would enable the monitoring of the embankment fill deformations due to the lateral thrust during the

parametric variation. The deformation localized to the clear span between the embankment toe and the outer row pile was also monitored.

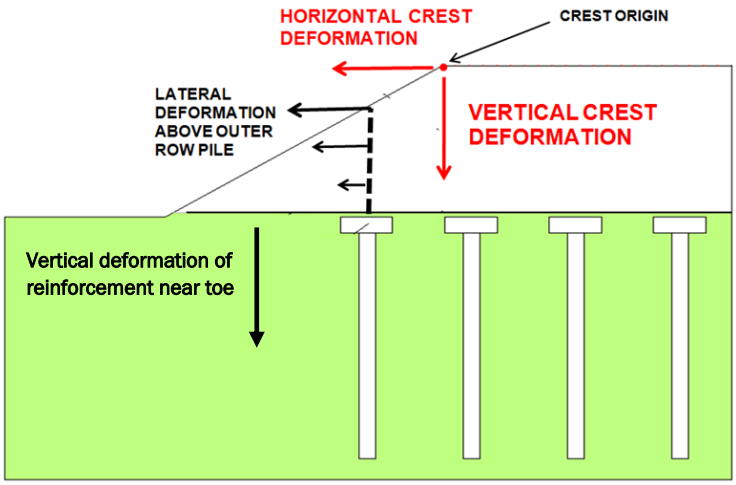

Figure 5.2 Deformations within the geosynthetic reinforced piled embankment structure

The horizontal and vertical deformation that occurred within the geosynthetic reinforcement membrane were recorded, Figure 5.2. The axial tension within the reinforcement was also examined during the analysis. The pile head deflection at each pile within the pile group was recorded along with the corresponding axial load and bending moments. Horizontal deformation of both the pile and the geosynthetic reinforcement was considered positive for deformations away from the embankment centre. Vertical deformations downwards were considered positive for the embankment surface and negative for the geosynthetic reinforcement. The theoretical pile group efficacy was calculated from the axial loads determined from the analysis.

Strain compatibility must be achieved within the structure between the deformations in the reinforcement and the pile. The strain compatibility condition was monitored through a dimensionless Strain Compatibility Ratio (SCR) which was developed as part of this study. The Strain Compatibility Ratio was defined as the ratio of the pile group strain to the geosynthetic reinforcement strain. The strain ε_{GG} (%) in the reinforcement (*GG*) was calculated using the following expression:

$$\varepsilon_{GG}\ (\%) = \frac{\text{Tension in Reinforcement } (T)}{\text{Stiffness of reinforcement } (J)} \qquad \text{Equation 5.1}$$

The pile was subjected to a bending moment ($M_{recorded}$) due to the pile head deflection. The strain in each pile was calculated by determining the maximum bending moment that the pile could resist (M_{max}) due to the steel reinforcement in the tension side of the pile. The pile bending moment was extracted from the predicted Plaxis 2D plate element data. The strain in the pile was then computed using the following expression:

$$\varepsilon_p(\%) = \frac{M_{recorded}}{M_{max}} \qquad \text{Equation 5.2}$$

The strain compatibility ratio (SCR) was defined by the following expression:

$$\text{SCR} = \frac{\text{Pile Group Strain } \varepsilon_P\ (\%)}{\text{GG Strain } \varepsilon_{GG}\ (\%)} \qquad \text{Equation 5.3}$$

A plot of the strain compatibility ratio (SCR) under a parametric variation would have the following format, Figure 5.3. A downward trend (solid line, Figure 5.3) would suggest that the reinforcement was increasingly supporting a greater proportion of the structures loading for an increase in the relevant parameter. Likewise, an upward trend (dotted line, Figure 5.3) would suggest that the pile was supporting a greater degree of loading in comparison to the reinforcement for an increase in the relevant parameter.

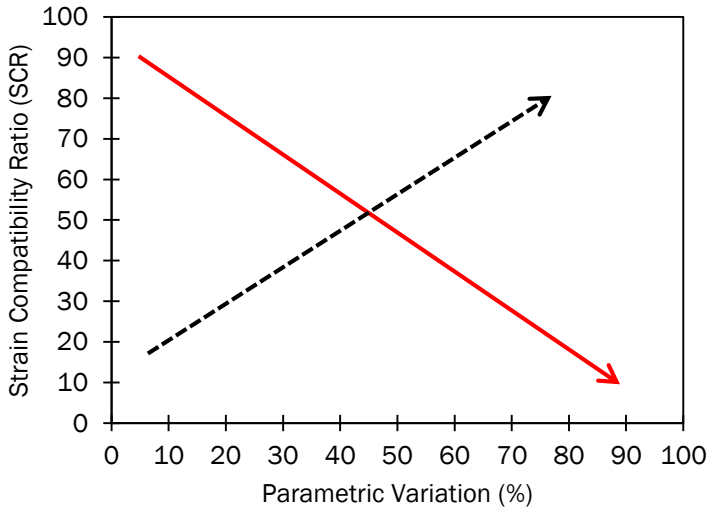

Figure 5.3 Strain compatibility ratio (SCR) plot for a parametric range (%)

Chapter 5 contains a considerable amount of data and data plots. To minimize the quantity of plots presented in Chapter 5, data from the piles and geosynthetic reinforcement were focused on and presented Chapter 5. The remaining data plots

are located in Appendix C. Tables 5.1, 5.2 and 5.3 contain a comprehensive list of the parameters varied during each Plaxis 2D model test.

Table 5.1 Plaxis 2D model tests 1 – 32

Test No.	Pile Spacing (m)	Pile Cap (m)	Outer Row Pile Rake (°)	Geogrid Stiffness kN/m	Soft Soil Depth (m)	Soft Soil Stiffness kN/m²	Emb Height (m)	Side Slope Steepness 1 in (n)	ORPLR -
1	1.5	0.30	0	500	10	800	4	1 in 2	-
2	3.0	0.30	0	500	10	800	4	1 in 2	-
3	4.5	0.30	0	500	10	800	4	1 in 2	-
4	1.5	0.30	0	500	10	800	4	1 in 3	-
5	3.0	0.30	0	500	10	800	4	1 in 3	-
6	4.5	0.30	0	500	10	800	4	1 in 3	-
7	3.0	0.30	0	500	10	800	4	1 in 2	-
8	3.0	0.50	0	500	10	800	4	1 in 2	-
9	3.0	0.75	0	500	10	800	4	1 in 2	-
10	3.0	1.00	0	500	10	800	4	1 in 2	-
11	3.0	1.50	0	500	10	800	4	1 in 2	-
12	3.0	2.00	0	500	10	800	4	1 in 2	-
13	3.0	0.30	0	500	10	800	4	1 in 3	-
14	3.0	0.50	0	500	10	800	4	1 in 3	-
15	3.0	0.75	0	500	10	800	4	1 in 3	-
16	3.0	1.00	0	500	10	800	4	1 in 3	-
17	3.0	1.50	0	500	10	800	4	1 in 3	-
18	3.0	2.00	0	500	10	800	4	1 in 3	-
19	3.0	1.00	0	500	10	800	4	1 in 2	-
20	3.0	1.00	5	500	10	800	4	1 in 2	-
21	3.0	1.00	10	500	10	800	4	1 in 2	-
22	3.0	1.00	15	500	10	800	4	1 in 2	-
23	3.0	1.00	20	500	10	800	4	1 in 2	-
24	3.0	1.00	25	500	10	800	4	1 in 2	-
25	3.0	1.00	30	500	10	800	4	1 in 2	-
26	3.0	1.00	0	500	10	800	4	1 in 3	-
27	3.0	1.00	5	500	10	800	4	1 in 3	-
28	3.0	1.00	10	500	10	800	4	1 in 3	-
29	3.0	1.00	15	500	10	800	4	1 in 3	-
30	3.0	1.00	20	500	10	800	4	1 in 3	-
31	3.0	1.00	25	500	10	800	4	1 in 3	-
32	3.0	1.00	30	500	10	800	4	1 in 3	-

Table 5.2 Plaxis 2D model tests 33 – 66

Test No.	Pile Spacing (m)	Pile Cap (m)	Outer Row Pile Rake (°)	Geogrid Stiffness kN/m	Soft Soil Depth (m)	Soft Soil Stiffness kN/m²	Emb Height (m)	Side Slope Steepness 1 in (n)	ORPLR -
33	3	1	0	0	10	800	4	1 in 2	-
34	3	1	0	500	10	800	4	1 in 2	-
35	3	1	0	2000	10	800	4	1 in 2	-
36	3	1	0	4000	10	800	4	1 in 2	-
37	3	1	0	0	10	800	4	1 in 3	-
38	3	1	0	500	10	800	4	1 in 3	-
39	3	1	0	2000	10	800	4	1 in 3	-
40	3	1	0	4000	10	800	4	1 in 3	-
41	3	1	0	500	8	800	4	1 in 2	-
42	3	1	0	500	10	800	4	1 in 2	-
43	3	1	0	500	15	800	4	1 in 2	-
44	3	1	0	500	8	800	4	1 in 3	-
45	3	1	0	500	10	800	4	1 in 3	-
46	3	1	0	500	15	800	4	1 in 3	-
47	3	1	0	500	10	800	4	1 in 2	-
48	3	1	0	500	10	1856	4	1 in 2	-
49	3	1	0	500	10	3333	4	1 in 2	-
50	3	1	0	500	10	800	4	1 in 3	-
51	3	1	0	500	10	1856	4	1 in 3	-
52	3	1	0	500	10	3333	4	1 in 3	-
53	3	1	0	500	10	800	1	1 in 2	-
54	3	1	0	500	10	800	2	1 in 2	-
55	3	1	0	500	10	800	4	1 in 2	-
56	3	1	0	500	10	800	8	1 in 2	-
57	3	1	0	500	10	800	1	1 in 3	-
58	3	1	0	500	10	800	2	1 in 3	-
59	3	1	0	500	10	800	4	1 in 3	-
60	3	1	0	500	10	800	8	1 in 3	-
61	3	1	0	500	10	800	4	1 in 1	-
62	3	1	0	500	10	800	4	1 in 2	-
63	3	1	0	500	10	800	4	1 in 3	-
64	3	1	0	500	10	800	4	1 in 4	-
65	3	1	0	500	10	800	4	1 in 5	-
66	3	1	0	500	10	800	4	1 in 6	-

Table 5.3 Plaxis 2D model tests 67 – 76

Test No.	Pile Spacing (m)	Pile Cap (m)	Outer Row Pile Rake (°)	Geogrid Stiffness kN/m	Soft Soil Depth (m)	Soft Soil Stiffness kN/m²	Emb Height (m)	Side Slope Steepness 1 in (n)	ORPLR -
67	3	1	0	500	10	800	4	1 in 2	0.00
68	3	1	0	500	10	800	4	1 in 2	0.25
69	3	1	0	500	10	800	4	1 in 2	0.50
70	3	1	0	500	10	800	4	1 in 2	0.75
71	3	1	0	500	10	800	4	1 in 2	1.00
72	3	1	0	500	10	800	4	1 in 3	0.00
73	3	1	0	500	10	800	4	1 in 3	0.25
74	3	1	0	500	10	800	4	1 in 3	0.50
75	3	1	0	500	10	800	4	1 in 3	0.75
76	3	1	0	500	10	800	4	1 in 3	1.00

5.2 Influence of Pile Spacing

Piles centre to centre spacing of 1.5m, 3.0m and 4.5m were investigated. An initial increase of the pile spacing from 1.5m to 3.0m for a piled embankment with a 1V:2H side slope yielded an increase in the horizontal deformation at the embankment crest (26%) whilst the vertical deformation remained relatively constant, Figure 5.4. A further increase of the pile spacing from 3.0m to 4.5m resulted in a further increase (39%) in the horizontal deformation at the crest whilst mobilizing a rapid increase (157%) in the vertical deformation. For an embankment side slope of 1V:3H, Figure 5.4, the magnitude of the crest deformations for relatively low pile spacing (1.5m) was significantly lower than the 1V:2H side slope, thus suggesting that the steepness of the side slope had a significant effect on the deformation at the crest. For the side slope of 1V:3H, an initial increase in the pile spacing from 1.5m to 3.0m corresponded to an almost linear increase in magnitude of the deformation (both horizontal and vertical deformation) at the crest. The horizontal deformation was subjected to an almost linear increase in the magnitude of the deformations for a linear increase in the pile spacing. The vertical deformation yielded an increase in the rate of deformation mobilization as the pile spacing increased.

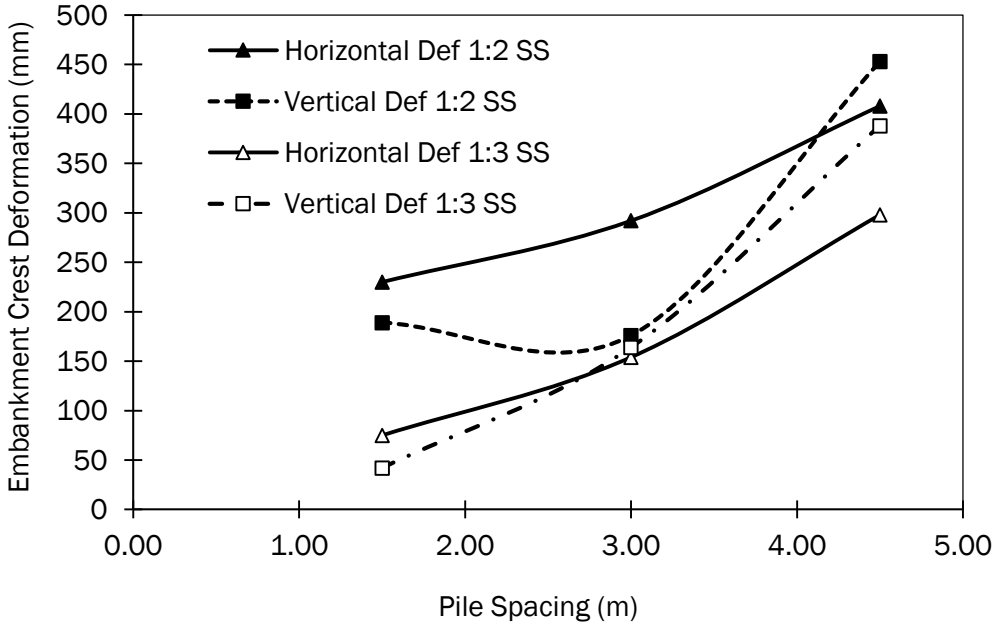

Figure 5.4 Surface deformation (mm) at the embankment crest for a range of pile spacing (m) (H = 4.0m, J_{re} = 500kN/m and a = 1.0m)

The deformation under the side slope of the piled embankment between the clear span from the toe of the embankment to the outer row pile remained relatively constant (approximately 0.54m) for the embankment with a side slope of 1V:2H for an increase of the pile spacing, Figure 5.5. The magnitude of the deformation for the 1V:3H side slope recorded greater deformations and yielded a minor increase (7%) in the deformation for an increase in the pile spacing greater than 3.0m. Pile spacing greater than 3.0m mobilised an increase in disturbing force within the embankment structure yielded an increase of the spreading force (lateral thrust), which mobilised an increased magnitude of horizontal deformation of the embankment material fill outwards from the embankment centre due to a decrease in the slope stability. This mobilised an increase in horizontal deformation of embankment fill towards the clear span between the outer pile and the embankment toe. The greater magnitude of material volume within the clear span to be supported yielded an increase in deformation near the toe of the embankment.

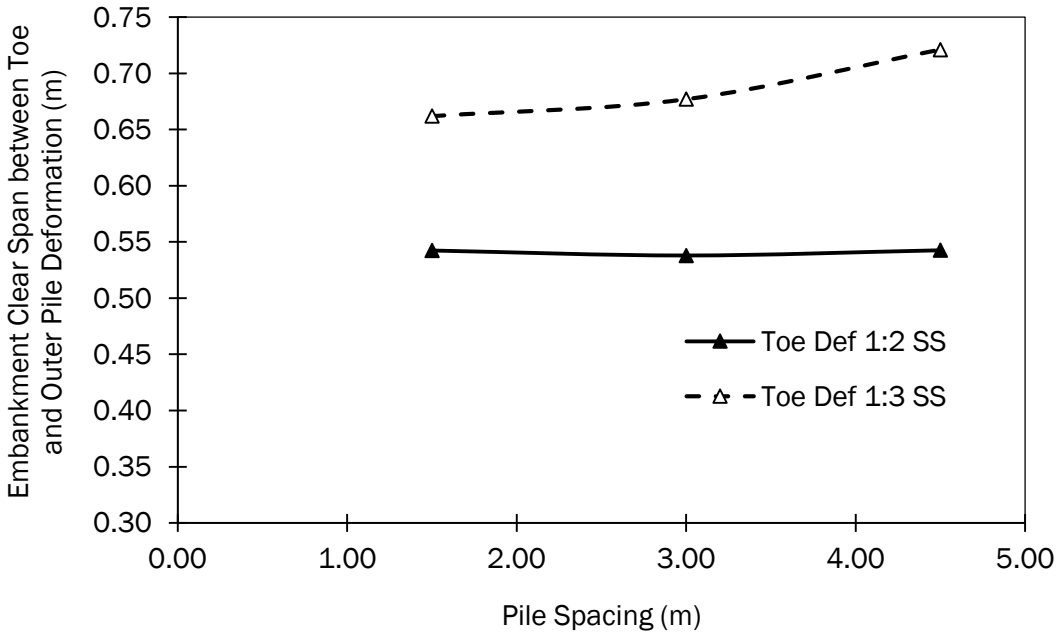

Figure 5.5 Vertical deformation (m) under the side slope between the embankment toe and outer row pile for a range of pile spacing (m) (H = 4.0m, J_{re} = 500kN/m and a = 1.0m)

The lateral deformation within the side slope above the centre line of the outer row pile was recorded. An increase in the centre to centre spacing between the piles

resulted in an increase in the lateral deformation above the outer row pile for all side slopes investigated, Figure 5.6 (a) & (b) and Appendix C Figure C1. The steeper the side slope of the embankment the greater the magnitude of the lateral deformation of the fill material above the outer row pile, Figure 5.6. The increase in magnitude of lateral deformation was consistent throughout the depth of the fill as opposed to a localized increase for an increase in the pile spacing. The consequence of an increase in volumetric lateral deformation of fill material past the outer row pile resulted in an increased volume of fill material requiring support by the soft soil near the toe of the embankment and yielded an increase in the magnitude of deformation at the toe of the embankment, Figure 5.5 (1V:3H Side Slope). The increase of volumetric deformation for a side slope of 1V:3H was consistent for an increase in pile spacing. For a side slope of 1V:3H the maximum lateral deformation recorded increased by approximately 50% as the pile spacing increased from 1.5m to 3.0m. A further increase in the pile spacing from 3.0m to 4.5m yielded a further increase of 16%.

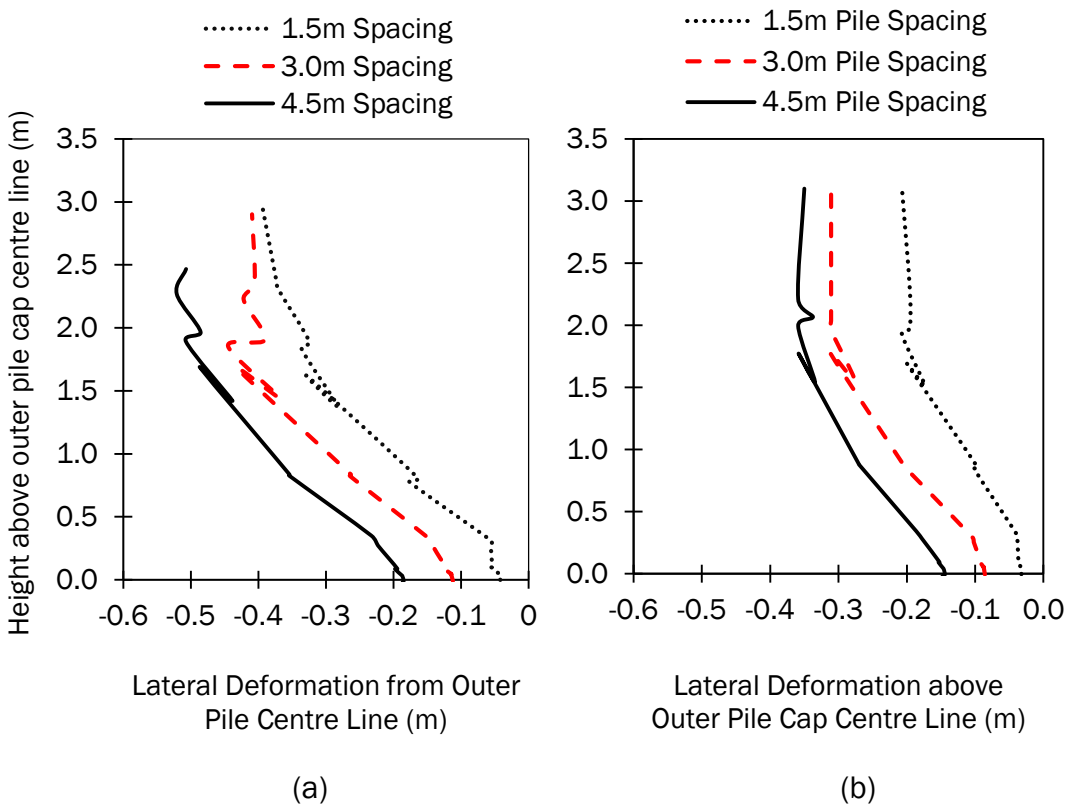

Figure 5.6 Lateral Deformation (LD) (m) within the side slope above the outer row pile centre line for a range of pile spacing (m) for (a) a side slope of 1V:2H and (b) a side slope of 1V:3H (H = 4.0m, J_{re} = 500kN/m and a = 1.0m)

The vertical and horizontal deformation of the geosynthetic reinforcement was influenced by the pile spacing. The magnitude of the vertical deformation in the reinforcement increased for an increase in the pile spacing, Figure 5.7. As the pile spacing increased, the clear span between adjacent pile caps increased and the reinforcement was required to support a greater load resulting in larger deformations. An increase of the pile spacing from 3.0m to 4.5m (50%) resulted in an increase in the vertical deformation of approximately 145%. For all cases the vertical deformation remained relatively consistent at the centre of the embankment structure. As the reinforcement neared the crest of the embankment, the deformation at the centre of the clear span between adjacent piles increased until reaching a maximum past the outer row pile near the embankment toe, where the reinforcement was no longer supported by the piles. The vertical deformation increased as the reinforcement moved away from the centreline towards the crest of the embankment due to the differential lateral pile deflection. The deflection at the pile head increased the further the piles were away from the embankment centreline. The differential in the pile head deflection was proportional to the clear span between adjacent piles. The increase in the clear span supported by the reinforcement resulted in greater deformations as the reinforcement approached the outer row pile, Figure 5.7.

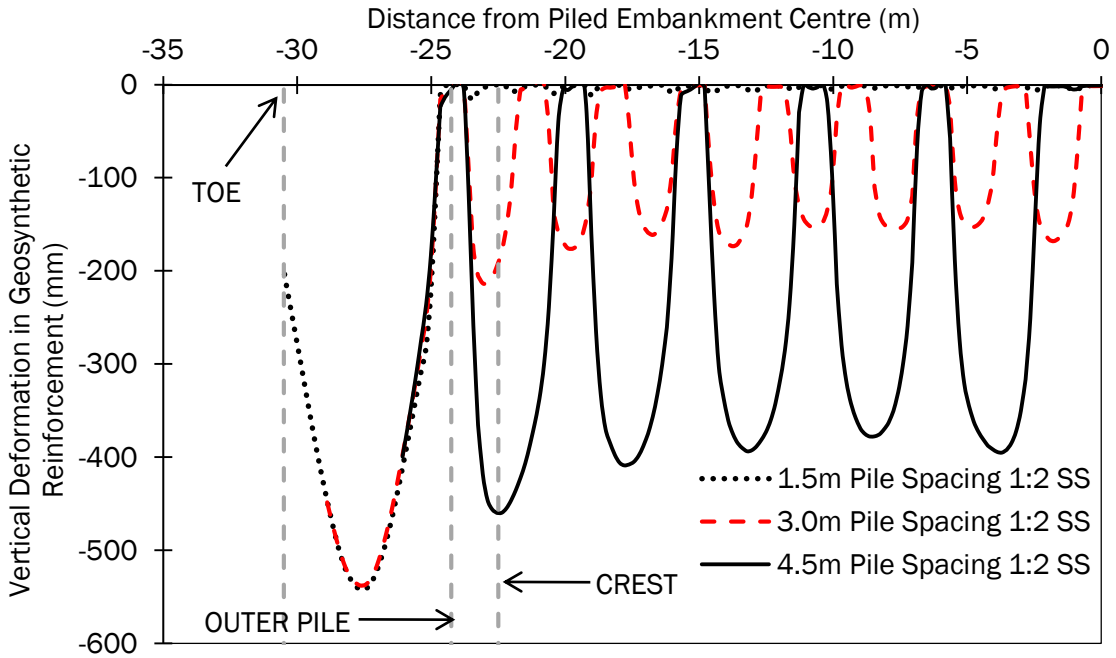

Figure 5.7 Vertical deformation of the geosynthetic reinforcement for a range of pile spacing (H = 4.0m, J_{re} = 500kN/m and a = 1.0m)

The horizontal deformation of the reinforcement increased for an increase in the pile spacing, Figure 5.8. For all cases the horizontal deformation of the reinforcement increased from a minimum at the embankment centreline until it reached a maximum value between the outer row pile and the embankment toe. The location of the maximum horizontal deformation in the reinforcement was constant for all pile spacing, whilst the magnitude of the maximum horizontal deformation increased for an increase in the pile spacing. Resistance to the outward lateral thrust from the embankment was from the pile group and the reinforcement. An increase in the spacing of the piles resulted in a decrease in the resistance of the pile group to lateral deformation. The horizontal deformation of the reinforcement, Figure 5.8, consisted of a whipsaw effect until the reinforcement protruded past the outer pile row due to the pulling effect/deformation around the pile caps at each pile location. The horizontal deformation of the reinforcement increased significantly in the clear span between the outer pile row and the toe.

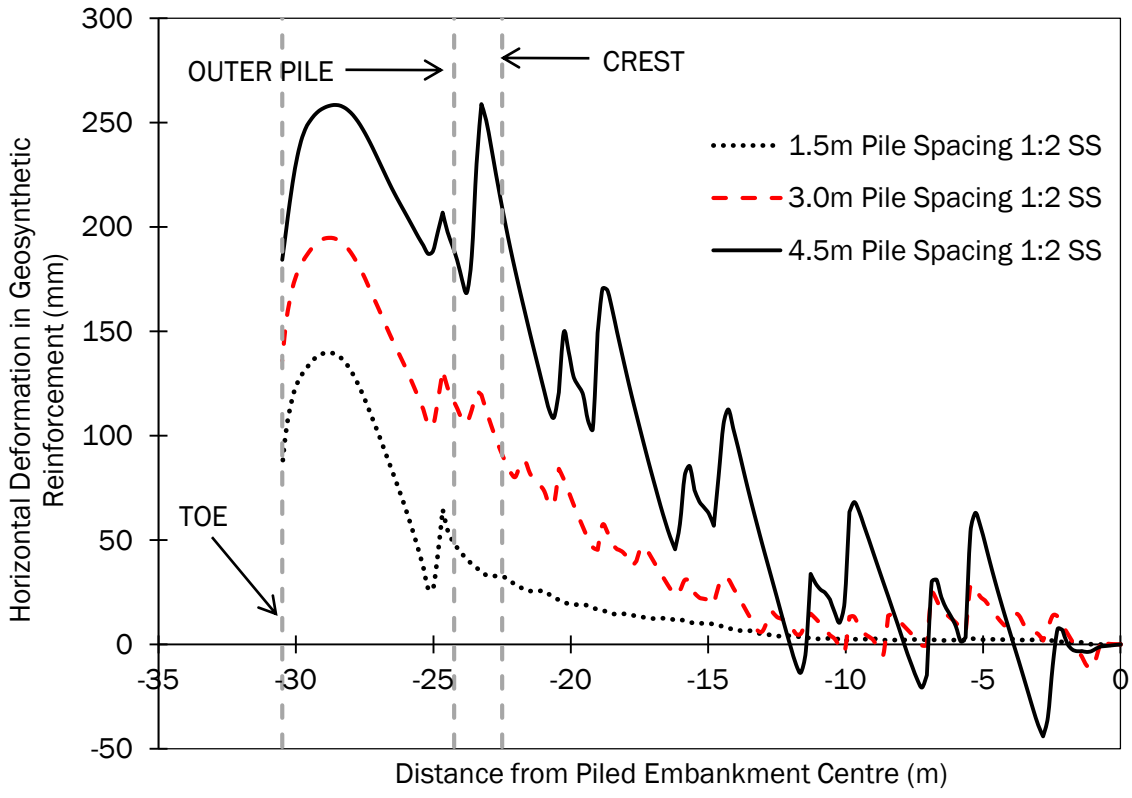

Figure 5.8 Horizontal deformation of geosynthetic reinforcement for a range of pile spacing (m) (H = 4.0m, J_{re} = 500kN/m and a = 1.0m)

The axial tension in the reinforcement increased for an increase in the pile spacing, Figure 5.9 and Appendix C Figure C2. The axial tension in the reinforcement was a minimum at or near the centreline of the embankment, Figure 5.9. Han & Gabr (2002) found that the axial tension at the centre of the clear span based on the analysis of an axisymmetric single pile model (also validated with plane strain analysis) that the tension in the reinforcement sharply reduced to zero near the centre of the reinforcement span between adjacent piles, Appendix C Figure C3. The Plaxis 2D model and Han and Gabr (2002) generated significant reinforcement tension peaks at the pile cap edge, Figure 5.9 and Appendix C Figure C3. Further investigation to examine whether these tension peaks are realistic or a product of FEM analyses is required.

Figure 5.9 suggested that the axial tension in the reinforcement did not reduce to zero at the centre of the clear span between adjacent piles due to the outward horizontal force mobilised by the embankment lateral thrust. For a relatively small pile spacing (1.5m) where the horizontal deformation close to the centre of the embankment was virtually zero, Figure 5.9, the corresponding axial tension, Figure 5.9, at the centre of the clear span reduced to zero between adjacent piles. For a pile spacing that yielded significant horizontal deformation (4.5m pile spacing, Figure 5.8), the axial tension did not reduce to zero at the centre of the reinforcement span, a significant portion of the tension developed at the edge of the pile cap was retained at the centre of the reinforcement span, Figure 5.9, for the 4.5m pile spacing.

The pile group supporting the reinforced embankment structure is required to support the vertical loading from the embankment weight and surcharge loading and partially resist the lateral thrust from the embankment. The capacity of the pile group to resist both the vertical and lateral disturbing forces is a combination of the sum of each individual pile axial load carrying capacity and bending moment resistance capacity. Figure 5.10 presents the axial loads exerted on each pile within the structure for a range of pile spacing. As the spacing of the piles increased, the axial load carried by each individual pile increased as each pile was required to support a greater portion of embankment loading, Appendix C Figure C4. The magnitude of the axial loading exerted on each pile remained constant within the centre of the embankment structure. The axial load remained constant until under

the side slope where a gradual reduction in axial load occurred. The greater the spacing of the piles, the greater the rate of decrease in the axial load on the piles as the location of the pile nears the toe.

Figure 5.11 presents the lateral deflection at the pile head within the structure. At the outer extremities an increase in the mobilised lateral thrust acting outward promoted the partial conversion of vertical load into lateral thrust. An increase in the lateral thrust resulted in a corresponding increase in the pile head deflection, as the pile spacing increased further, Figure 5.11, & Appendix C Figure C5. The magnitude of the deflection at each pile location increased exponentially as the pile location neared the embankment toe, Figure 5.11.

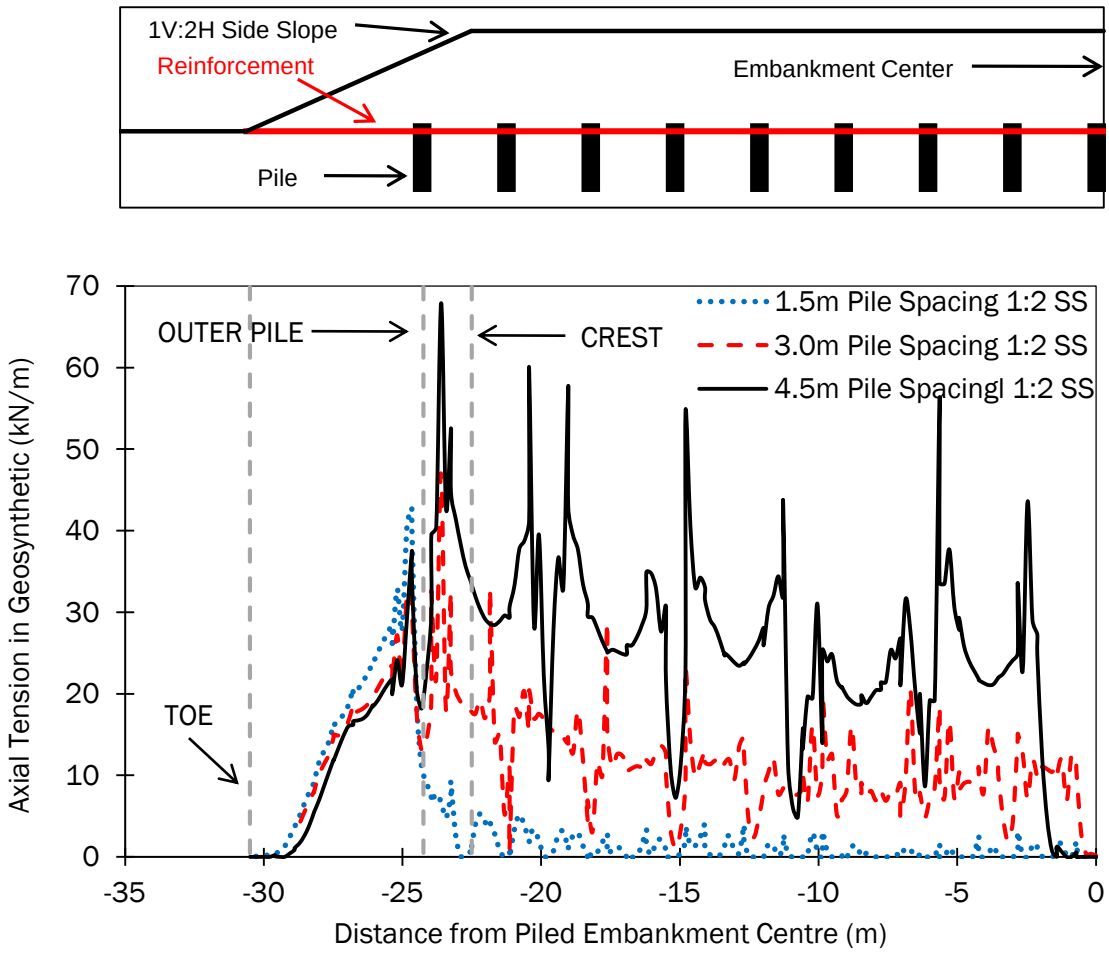

Figure 5.9 Axial tension in the reinforcement for a range of pile spacing (m) (H = 4.0m, J_{re} = 500kN/m and a = 1.0m)

The bending moment within a pile, Figure 5.12, followed the same characteristic pattern as that for pile head deflection, Figure 5.11 and Appendix C Figure C6. The

maximum bending moment was recorded in the outer row pile, the bending moments reduced significantly for piles under the main embankment.

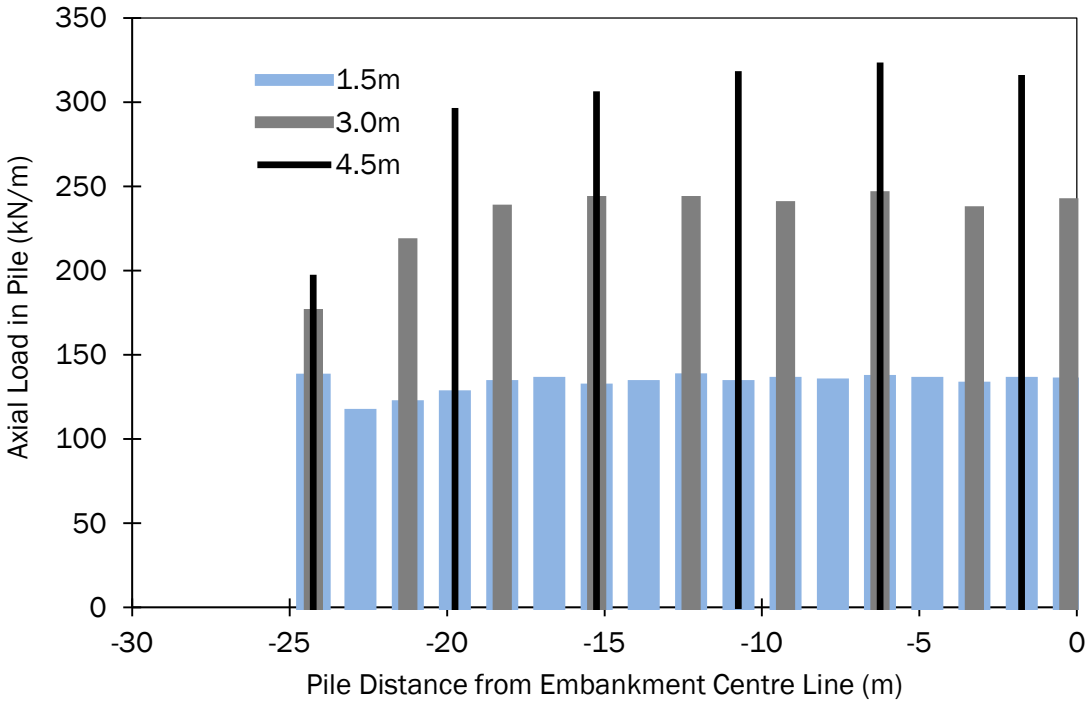

Figure 5.10 Axial loading (kN) on pile group under reinforced piled embankment for a range of pile spacing (m) (H = 4.0m, J_{re} = 500kN/m and a = 1.0m)

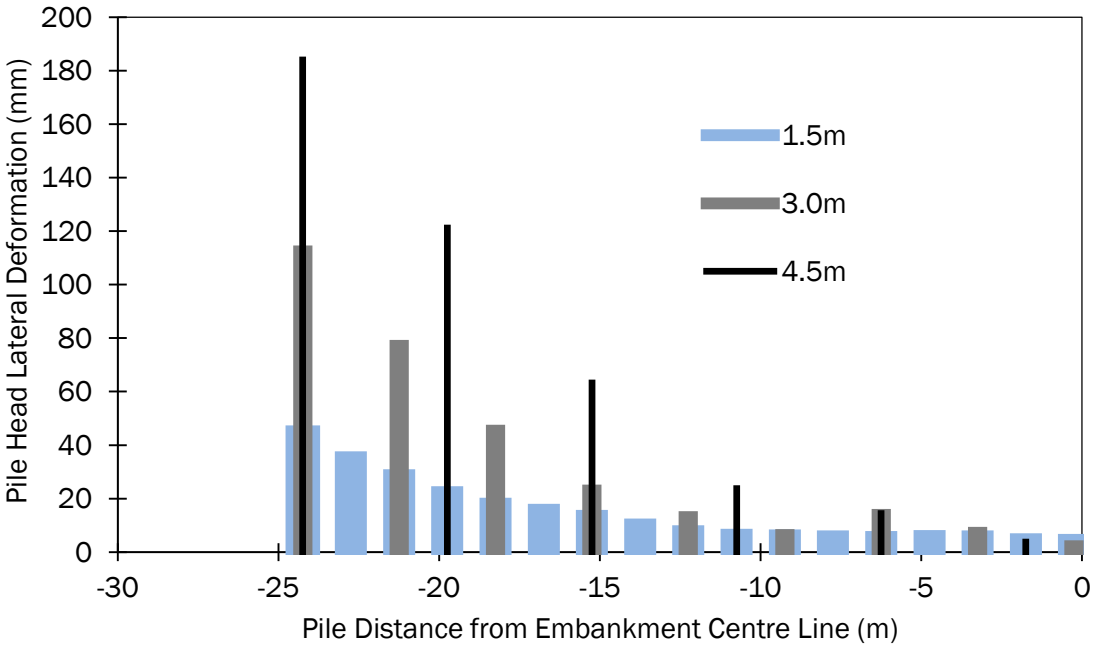

Figure 5.11 Lateral deflection (mm) at the pile head within a pile group under a reinforced piled embankment for a range of pile spacing (m) (H = 4.0m, J_{re} = 500kN/m and a = 1.0m)

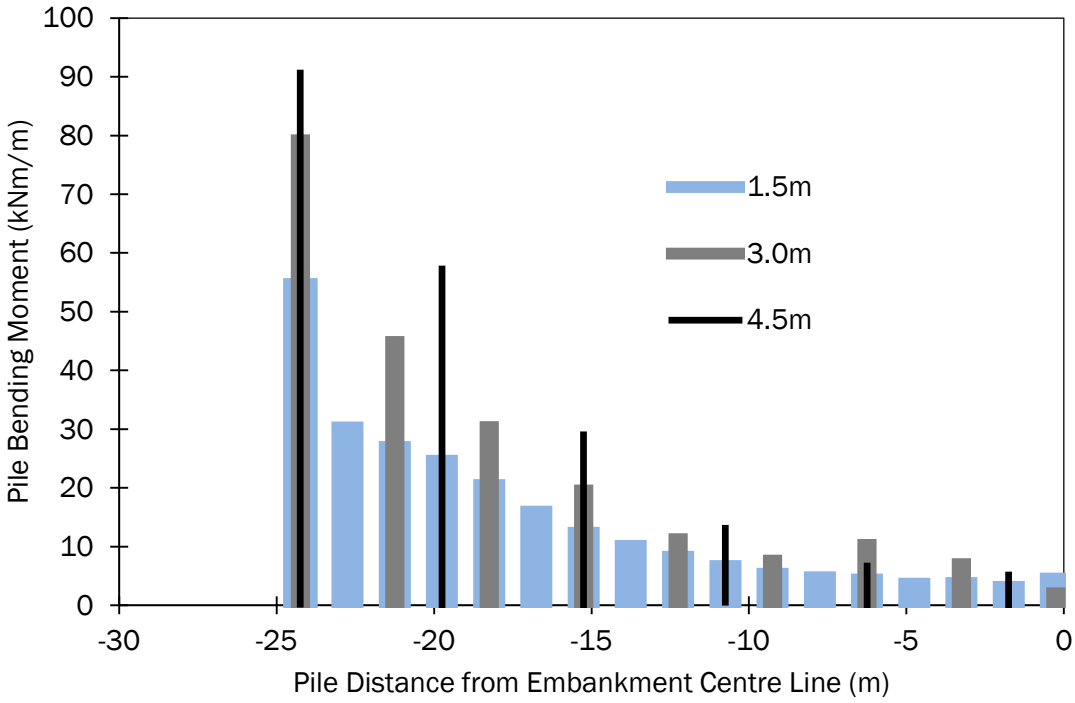

Figure 5.12 Bending moments (kNm) within a pile group for a range of pile spacing (m) (H = 4.0m, J_{re} = 500kN/m and a = 1.0m)

The bending moment at the outer row pile increased linearly with an increase in the pile spacing (Appendix C Figure C6). The pile group efficacy (%) was taken as the summation of the axial loads exerted on each pile within the pile group divided by the theoretical loading from the embankment structure and the surcharge loading. The efficacy of the pile group decreased (88% → 74%) almost linearly for an increase in the pile spacing (1.5m → 4.5m), Figure 5.13. The decrease in the pile group efficacy was a function of two factors:

1. The mobilization of the lateral thrust within the embankment structure
2. Support offered by the soft soil between adjacent piles.

As the pile spacing increased, the lateral thrust and the resulting lateral deformation within the side slope of the embankment structure increased, corresponding to an overall increase in slope deformations. Slippage occurred within the side slope fill material, which was initially supported by the piles, but was subsequently transferred onto the largely unsupported span between the embankment toe and the outer row pile resulting in a decrease in axial loading exerted on the piles located at or near the outer row pile. Increasing the pile spacing

also corresponds to a reduction in the effectiveness of arching on the load transfer mechanism within the structure.

An increase in the pile spacing resulted in the increase in the clear span to be supported by the reinforcement. As the reinforcement was subjected to a greater magnitude of load, the reinforcement underwent greater deformation and thus continued to deform until the soft soil offered some degree of support. As the soft soil was subjected to an increase in load as the pile spacing increased, the load required to be supported by the reinforcement and the pile reduced resulting in a decrease in pile group efficacy, Figure 5.13.

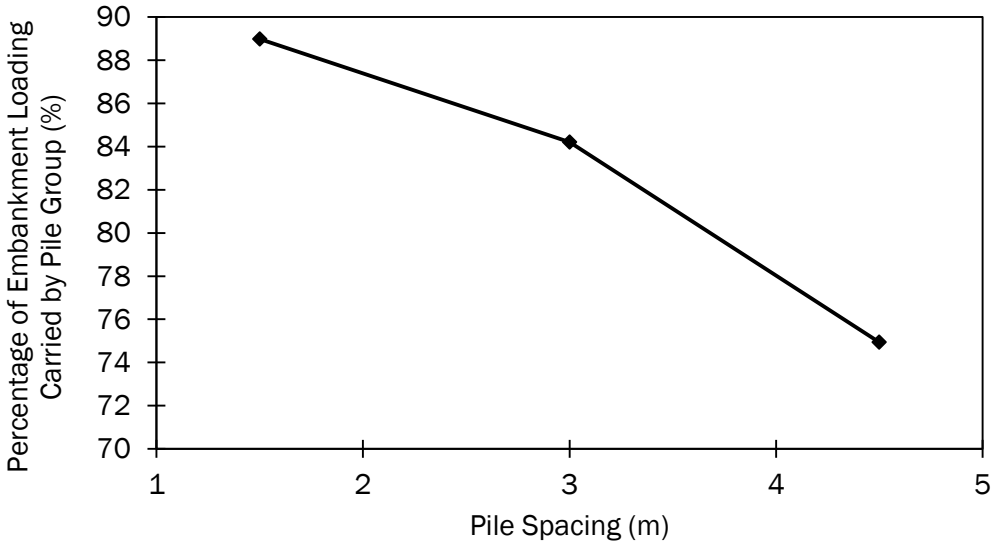

Figure 5.13 Pile group efficacy (%) for a range of pile spacing (m) (H = 4.0m, J_{re} = 500kN/m and a = 1.0m)

With an increase in the pile spacing from 1.5m to 3.0m the strain in the reinforcement increased significantly (approximately 191%, Figure 5.14). A further increase in the pile spacing resulted in an increase in the reinforcement strain, the strain increased by 92% for a 50% increase in pile spacing (3.0m to 4.5m). The characteristic shape of the reinforcement strain relationship was consistent with the increase reinforcement tension with pile spacing. The strain in the pile increased significantly for an increase in pile spacing (389% increase in strain for a 200% increase in pile spacing) which was consistent with the increase in bending moment for an increase in pile spacing, Appendix C Figure C6. For an initial increase (1.5m to 3.0m) in the pile spacing, the pile attracted a slightly lower portion of the

load than the reinforcement to satisfy the strain compatibility condition. An increase of the pile spacing from 3.0m to 4.5m mobilised an increase in the magnitude of strain attracted by the pile and yielded an increase in the SCR ratio (25% increase). Overall, for an increase of the pile spacing the portion of loading carried by the pile group decreased slightly (SCR decreased by 13%), Figure 5.14. As the pile spacing increased, the lateral load resistance capacity of the pile group decreased due to fewer piles utilized within the structure. The reduction in pile group capacity to resist lateral loads led to an increase in both the pile and reinforcement strains.

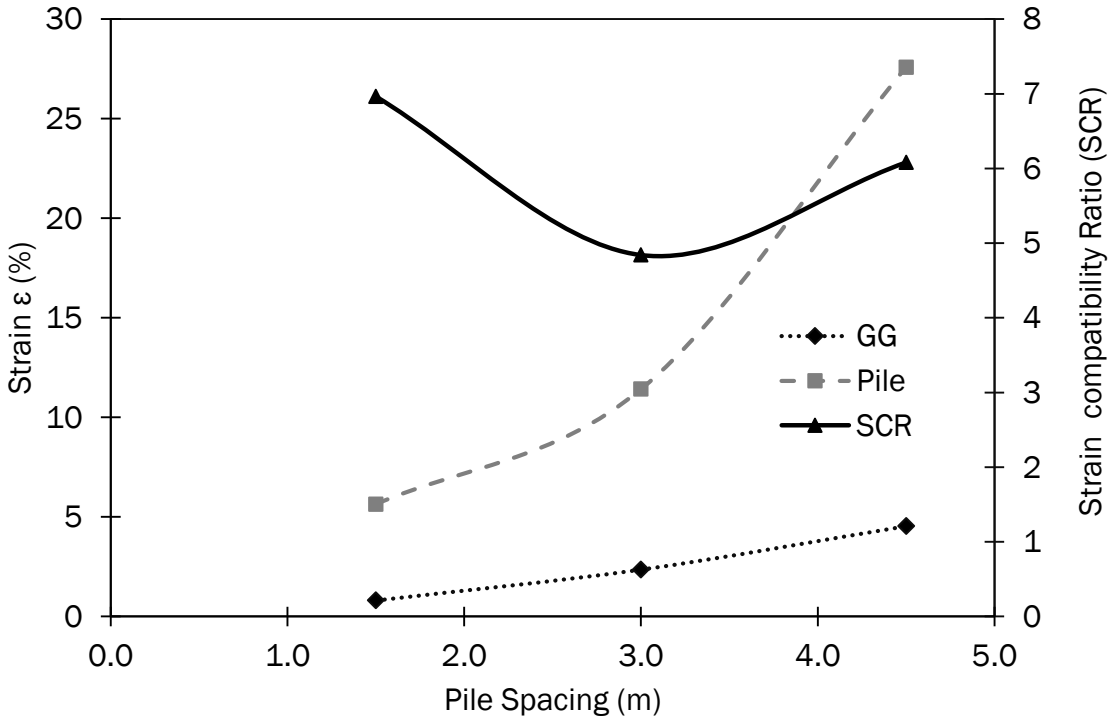

Figure 5.14 Strain in reinforcement and outer row pile and piled embankment Strain Compatibility Ratio (SCR) (%) for a range of pile spacing (m) for a 1V:2H side slope (H = 4.0m, J_{re} = 500kN/m and a = 1.0m)

Increasing pile centre to centre spacing had a significant effect on structural stability for the 1V:3H side slope only, Figure 5.15. The resistance of the pile group to lateral load is the sum of the individual piles lateral load capacities. An increase in pile spacing reduced the number of piles contained within the pile group extent, thus reducing the total lateral load resistance capacity of the group, which corresponded to an increase in pile head deflections and bending moments.

For the 1V:3H side slope, increasing the pile spacing from 1.5m to 3.0m yielded a 0.253 (11%) reduction in the safety factor. Increasing the pile spacing from 3.0m to 4.5m yielded a further 0.393 (20%) reduction in stability, Figure 5.15. The stability of the 1V:2H side slope was largely immune to a variation of pile spacing as the destabilizing active earth pressure present within the side slope far outweighs the stabilizing influence of a decrease in the pile centre to centre spacing.

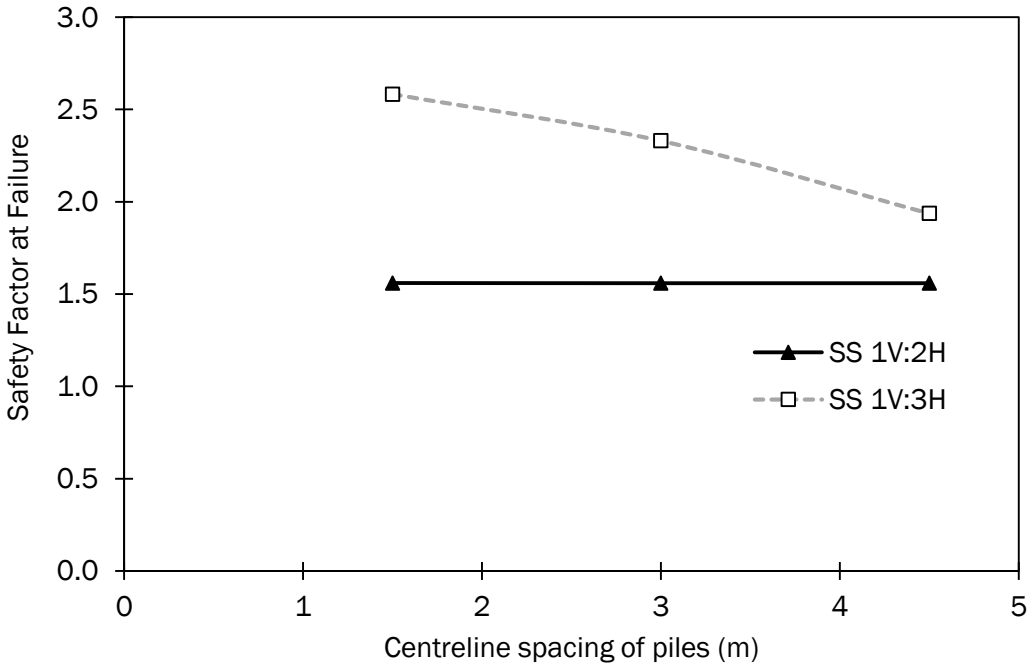

Figure 5.15 Safety factor at failure for a range of pile spacing

5.3 Influence of Pile Cap Size

The pile cap sizes examined in this study ranged from 0.3m to 2.0m with the pile spacing fixed at 3.0m. A pile cap size of 0.3m represented a pile with no pile cap as the pile head size dimension was 300mm square. An increase in the pile cap size resulted in a reduction of deformation at the embankment crest, Figure 5.16. An increase of the pile cap size from 0.3m to 1.0m (233% increase) for the 1V:2H side slope case resulted in a 25% decrease in the horizontal deformation and a 46% reduction in the vertical deformation. A further increase in the pile cap size resulted in a linear reduction of both the horizontal and vertical deformation, Figure 5.16. An increase of the pile cap size reduced the clear span between adjacent piles. The

magnitude of the vertical deformation was almost independent of the side slope and entirely a function of the clear span between the adjacent pile caps. The horizontal deformation was greatly influenced by both the side slope and the pile cap size. For a pile cap size greater than 1.0m the steeper of the two side slopes (1V:2H) resulted in a consistent differential in the horizontal deformation of approximately 100mm.

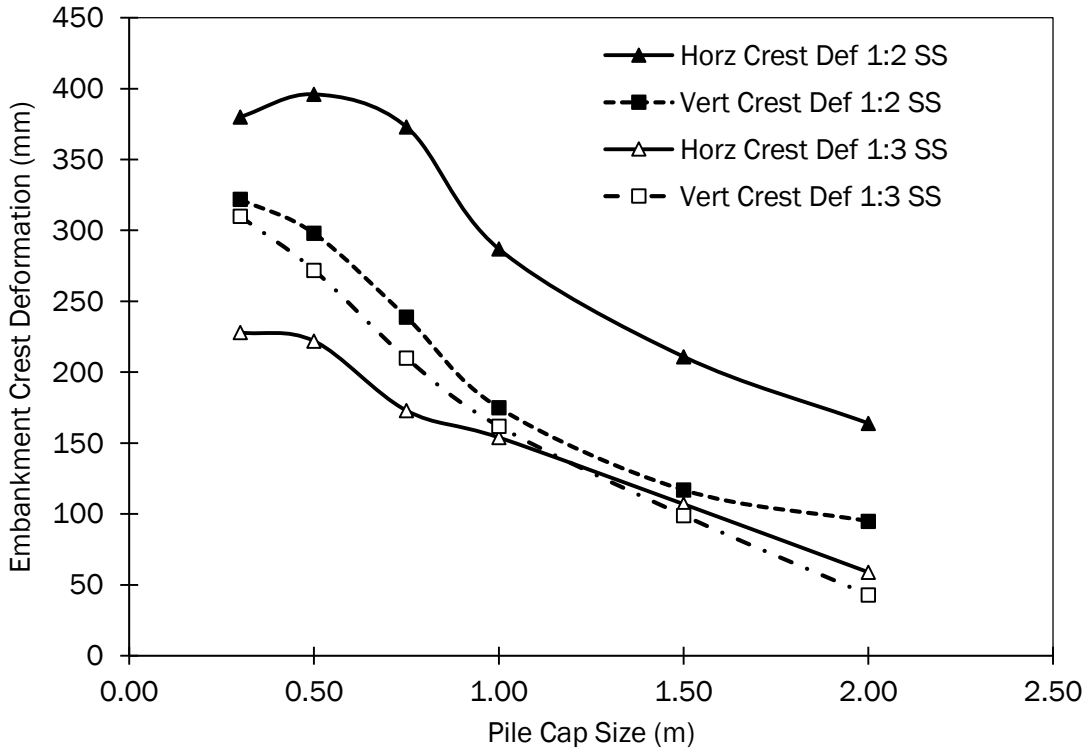

Figure 5.16 Surface deformations (mm) at the embankment crest for a range of pile cap sizes (m) (H = 4.0m, J_{re} = 500kN/m and s = 3.0m)

The vertical deformation within the slope near the toe of the embankment decreased in an almost linear fashion for an increase in the pile cap size, Figure 5.17. The deformation within the clear span between the toe of the embankment and the outer pile row was a function of the load on the geosynthetic reinforcement. An increase of the pile cap size lead to a reduction in the deformation at the crest (Figure 5.16) and above the outer row pile (Figure 5.18), therefore an increase in the pile cap size increased the stability of the side slope and as a result reduced the horizontal deformation in the side slope. A reduction in the horizontal deformation of the embankment fill reduced the volume of material transferred onto the clear unsupported span between the toe and the outer pile row. The 1V:3H side slope

consistently recorded magnitudes of vertical deformation at the toe of the embankment 145mm greater than those of the 1V:2H side slope, Figure 5.17.

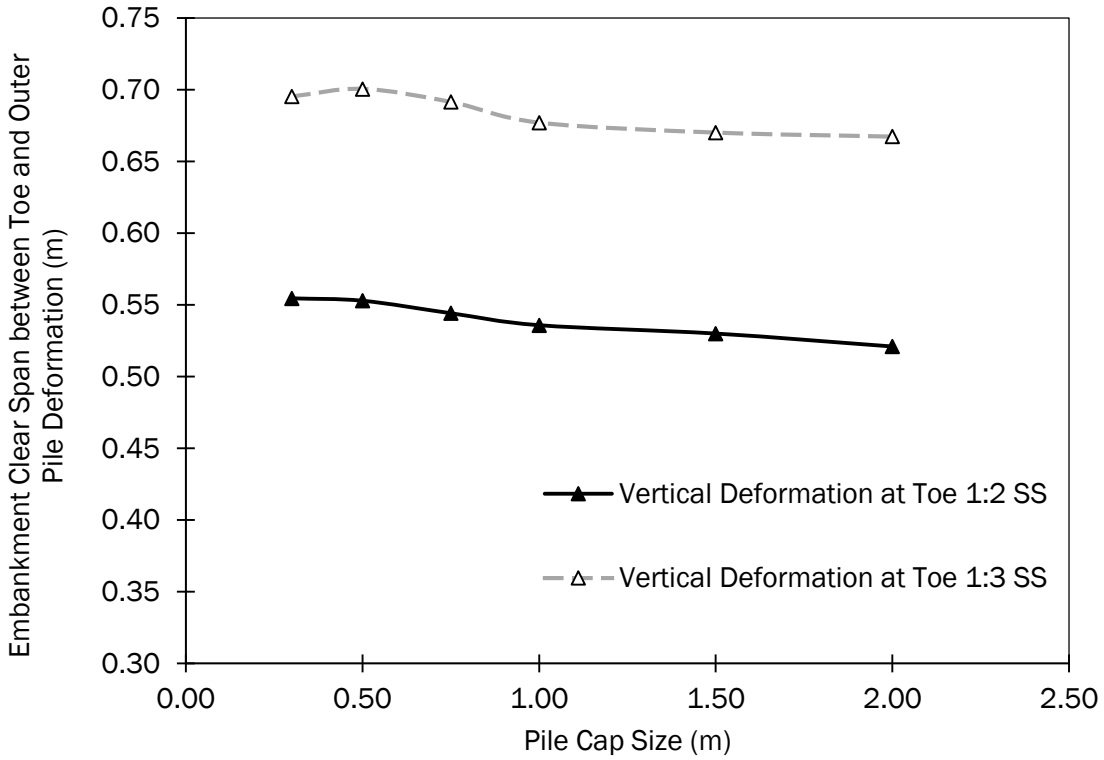

Figure 5.17 Vertical deformation (m) under the side slope between the embankment toe and outer row pile for a range of pile cap sizes (m) (H = 4.0m, J_{re} = 500kN/m and s = 3.0m)

The lateral deformation within the side slope above the centreline of the outer row pile decreased for an increase in the pile cap size, Figure 5.18 (a) & (b). The lateral volumetric deformation (LVD), horizontal deformation of fill material, Appendix C, Figure C7, for a 1V:2H side slope recorded the same characteristic relationship as that observed for horizontal deformation, Figure 5.16. The initial increase in pile cap size from 0.3m to 0.75m produced little influence on the magnitude of the horizontal deformation above the pile cap and at the embankment crest (Figure 5.16, Horizontal Crest Deformation, 1V:2H SS). An initial increase in the pile cap size from 0.3m to 0.75m reduced the lateral volumetric deformation within the embankment by 2%. A further increase in the pile cap size from 0.75m to a maximum of 2.0m (166%) yielded a linear decrease (29%) in the LVD, Appendix C Figure C7. The 1V:2H side slope recorded lateral deformations above the outer row pile greater than that of the 1V:3H side slope, Figure 5.18 (a) and (b).

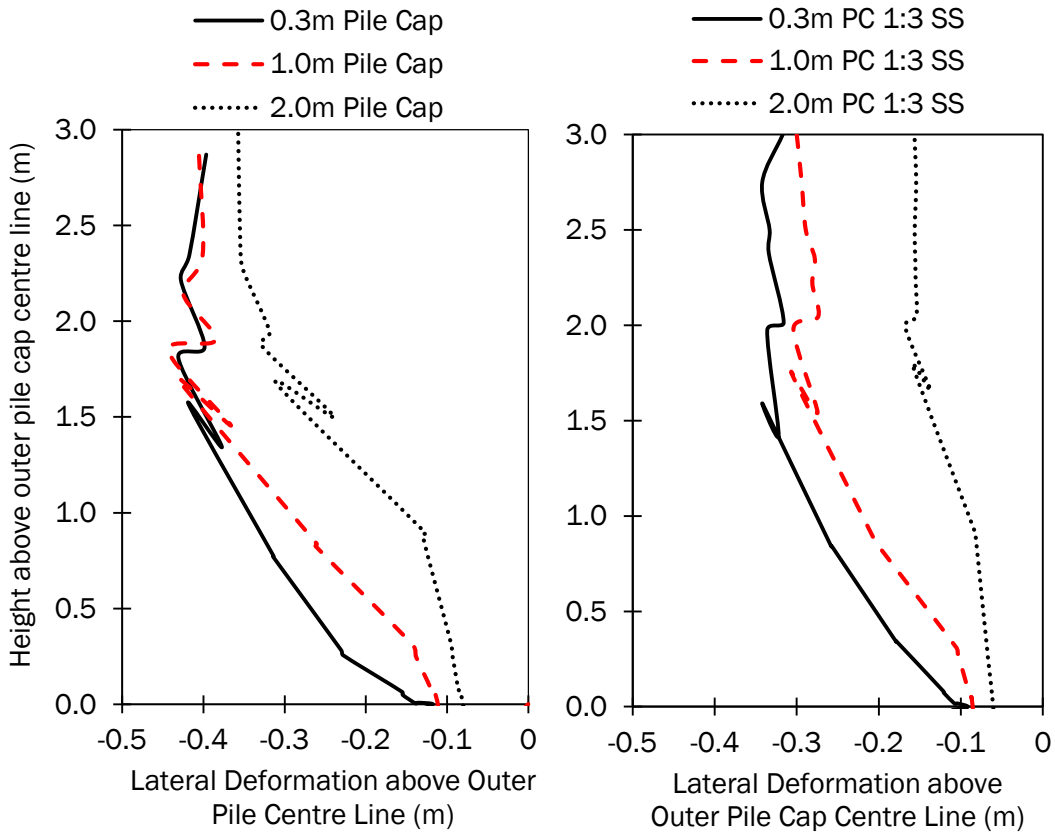

(a) (b)

Figure 5.18 Lateral Deformation (LD) (m) within the side slope above the outer row pile centre line for a range of pile cap sizes (m) for (a) a side slope of 1V:2H and (b) a side slope of 1V:3H (H = 4.0m, J_{re} = 500kN/m and s = 3.0m)

The vertical and horizontal deformation of the geosynthetic reinforcement was influenced by the pile cap size. The magnitude of the vertical deformation in the reinforcement decreased for an increase in the pile cap size, Figure 5.19. A decrease in the pile cap size corresponded to an increase in the clear span between adjacent pile cap edges, resulting in greater deformations. An increase in the pile cap size from 0.3m to 1.0m (266%) yielded a decrease in the vertical deformation between the adjacent pile caps within the main structure of the embankment of approximately 50%. The magnitudes of the vertical deformation between the adjacent piles caps remained relatively consistent across the width of the main embankment. The vertical deformations increased slightly approaching the outer row pile due to the differential pile head deflections increasing the span between adjacent pile cap edges. A maximum vertical deformation occurred at the clear span between the outer pile row and the embankment toe.

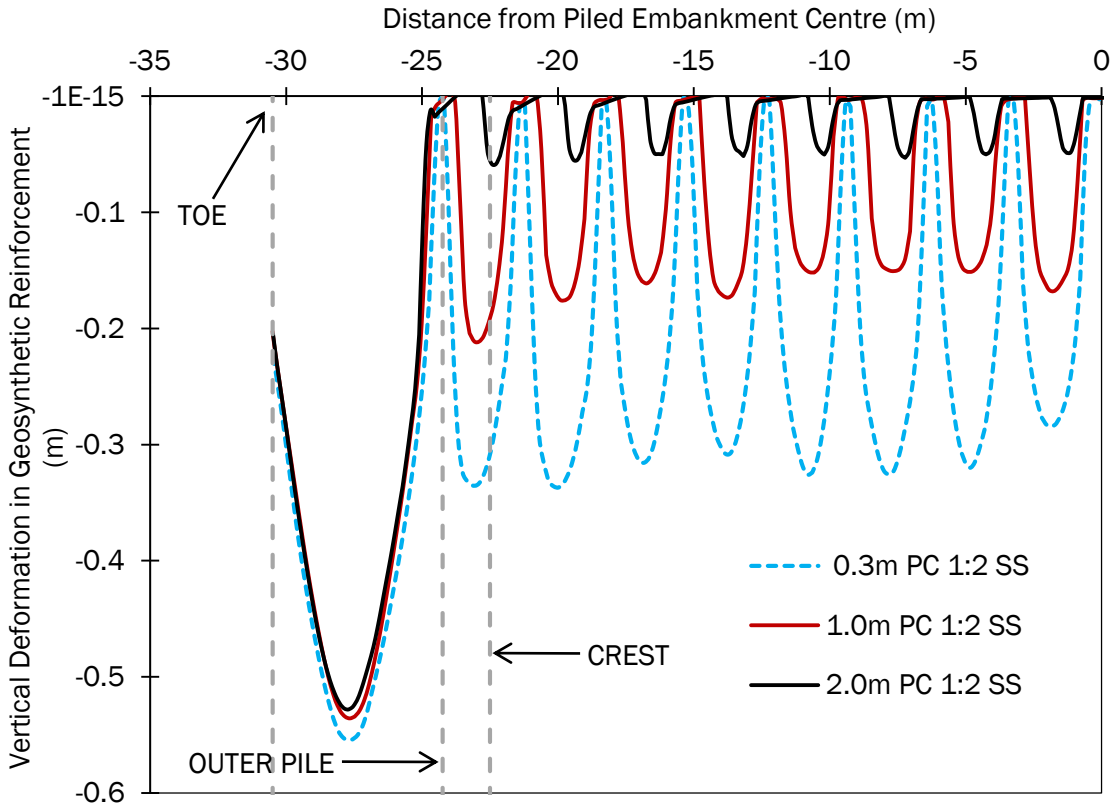

Figure 5.19 Vertical deformation of the geosynthetic reinforcement for a range of pile cap size (H = 4.0m, J_{re} = 500kN/m and s = 3.0m)

The horizontal deformation in the reinforcement decreased for an increase in the pile cap size, Figure 5.20. The horizontal deformation was approximately zero at the centre of the embankment structure. The outward lateral thrust mobilised the horizontal component of the deformation. Horizontal deformation for all pile cap sizes increased until the reinforcement reached the outer most extremities of the side slope and recorded a maximum in the clear span between the outer row pile cap edge and the embankment toe. The location of the maximum horizontal deformation in the reinforcement was consistent for all pile cap sizes whilst the magnitude of the maximum horizontal deformation increased for a decrease in the pile cap size. Resistance to the outward lateral thrust was from the lateral resistance of the pile and the reinforcement. An increase in pile cap size resulted in a decrease of side slope deformations, Figure 5.20.

The axial tension in the reinforcement decreased for an increase in the pile cap size, Figure 5.21 and Appendix C Figure C8. The maximum pile cap size examined (2.0m), the resultant clear span between the pile cap edges recorded a minimum and as a result the tension recorded at their lowest. The axial tension in the reinforcement for a 2.0m pile cap size case, close to the centre line of the embankment were insignificant as the lateral disturbing force due to embankment instability had not mobilised significant tensions in the reinforcement. As the pile cap size decreased, the deformations of the embankment structure increased and the both the maximum axial tension and the tensions developed along the reinforcement increased. An increase in the pile cap size from 0.3m to 2.0m (566% increase) yielded a 33% decrease in the maximum axial tension recorded but an approximate 90% reduction in the tension developed at the centre of the clear span between adjacent piles near the centre of the embankment structure, Figure 5.21. The pile cap size had a more prominent effect on the axial tensions developed in the reinforcement due to the vertical loading on the clear span between the adjacent pile cap edges than the tensions developed due to the lateral thrust.

The magnitude of the axial load on each pile within the pile group increased for an increase in the pile cap size, Figure 5.22 and Appendix C Figure C9. The axial load recorded at the outer pile row was approximately 27% less than that found close to the embankment centre for a 0.3m pile cap size, and 21% less for a 1.5m pile cap size.

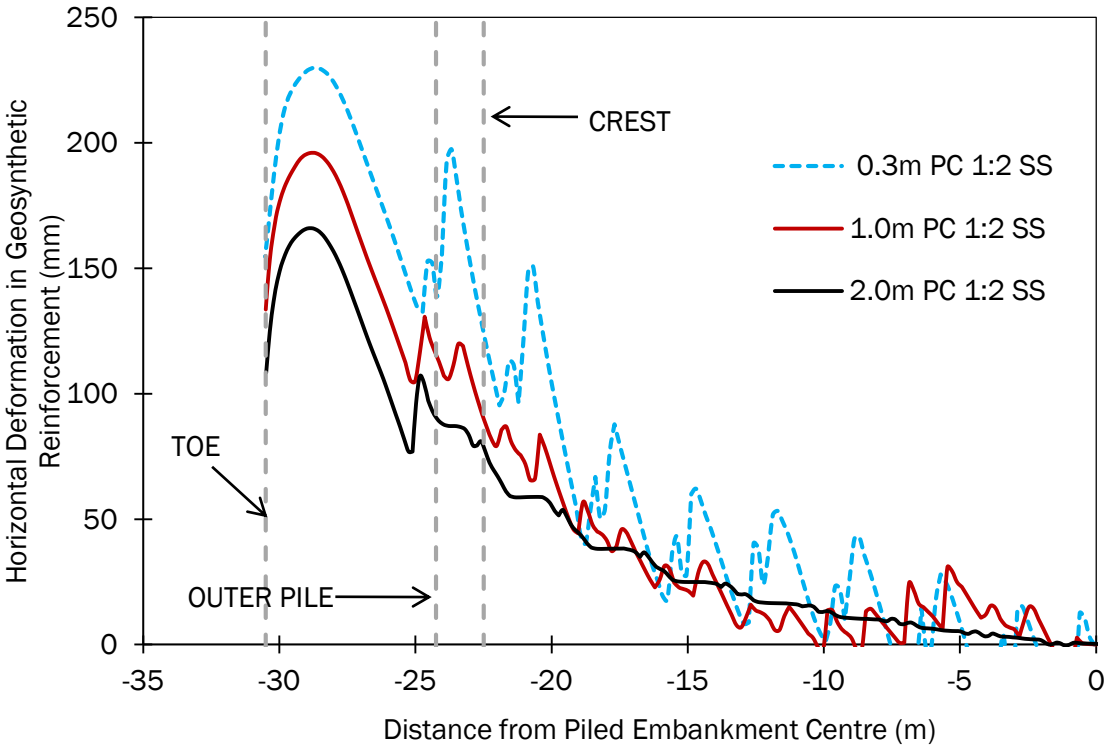

Figure 5.20 Horizontal deformation of geosynthetic reinforcement for a range of pile cap size (m) (H = 4.0m, J_{re} = 500kN/m and s = 3.0m)

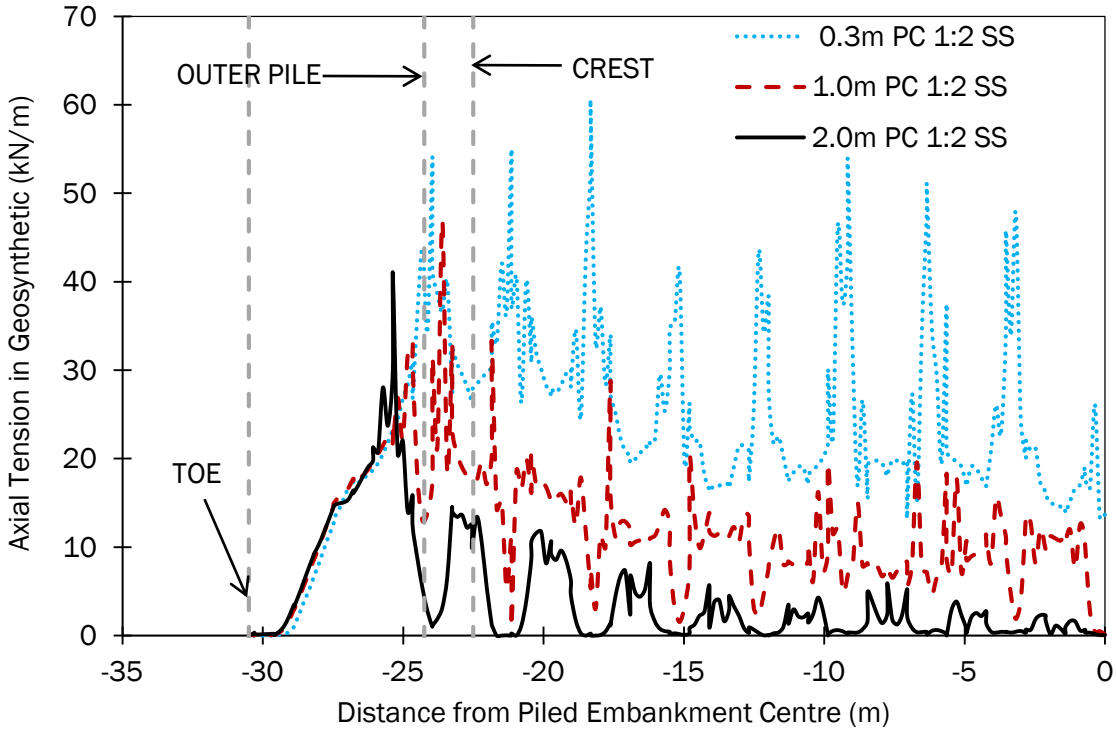

Figure 5.21 Axial tension in the reinforcement for a range of pile cap size (m) (H = 4.0m, J_{re} = 500kN/m and s = 3.0m)

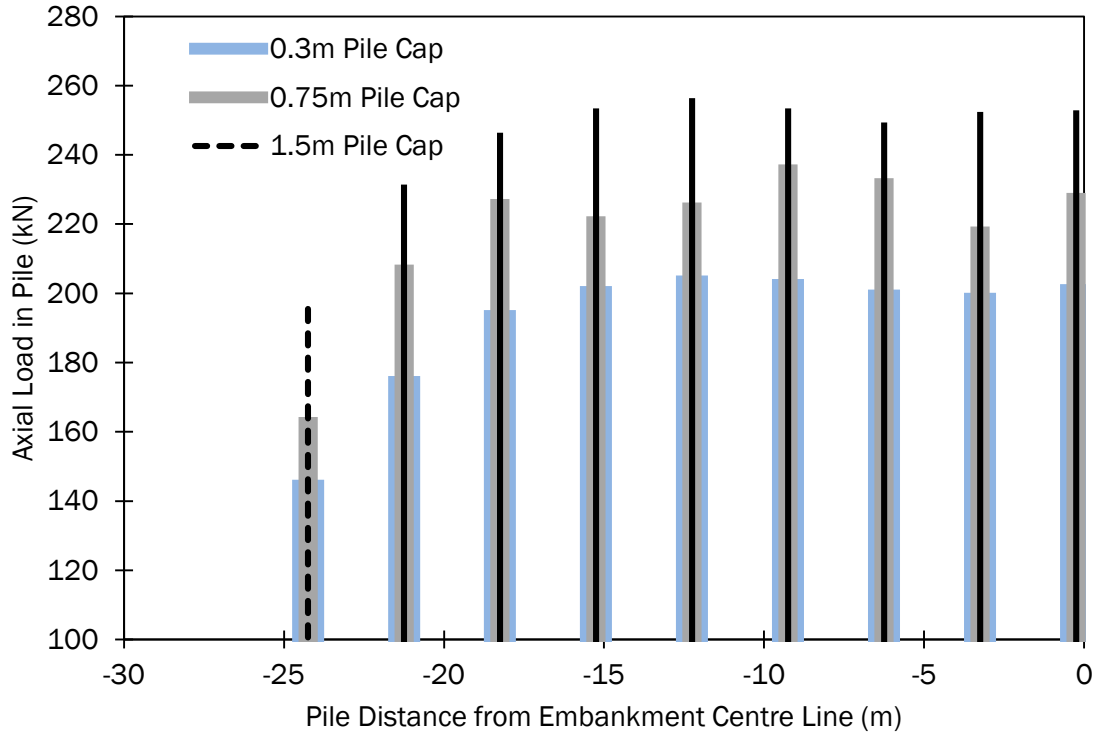

Figure 5.22 Axial loading (kN) on pile group under reinforced piled embankment for a range of pile cap size (m) (H = 4.0m, J_{re} = 500kN/m and s = 3.0m)

The deflection of the pile head within the pile group was a function of the horizontal deformation of both the geosynthetic reinforcement and the embankment fill material. Increasing the pile cap size resulted in a decrease of both the horizontal deformations of the embankment, Figures 5.16 and 5.18, and of the reinforcement, Figure 5.20. The increase of the pile cap size resulted in a decrease in the embankment deformations. An increase in embankment stability resulted in a corresponding reduction on the requirement of the pile group to resist lateral thrust from the overlying embankment structure and thus yielded lower magnitudes of deformations, Figure 5.23, and bending moments, Figure 5.24. Appendix C Figure C7 of the lateral volumetric deformation above the outer row pile suggested that an increase in the pile cap size greater than 0.75m mobilised an increase in stability of the embankment structure and the resultant decrease in lateral thrust yielded lower magnitudes of deflections and bending moments. Appendix C Figures C10 and C11 also suggest that both the lateral deformation at the pile head and the bending moments for the outer row piles decreased for an increase in the size of the pile cap. The decrease in both lateral deformation and bending moments was marginal for a pile cap size increase from 0.3m to 0.75m. A further increase (0.75m-1.5m-

2.0m) of the pile cap size resulted in an acceleration in the rate of decrease in both lateral deformation and bending moment.

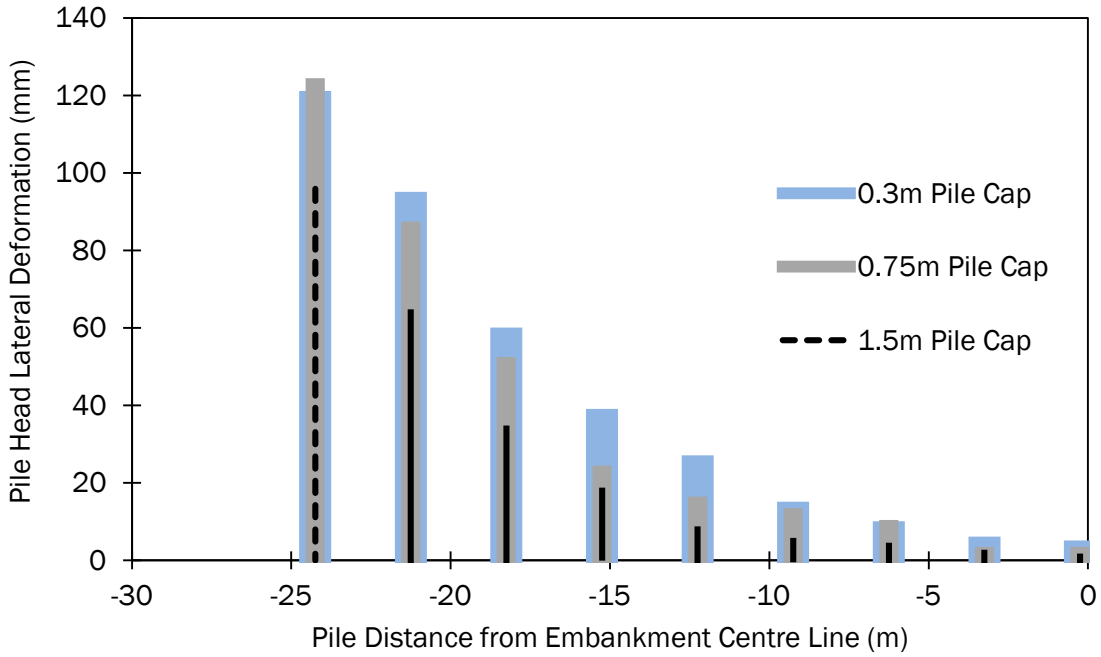

Figure 5.23 Lateral deflections (mm) at the pile head within a pile group under a reinforced piled embankment for a range of pile spacing (m) (H = 4.0m, J_{re} = 500kN/m and s = 3.0m)

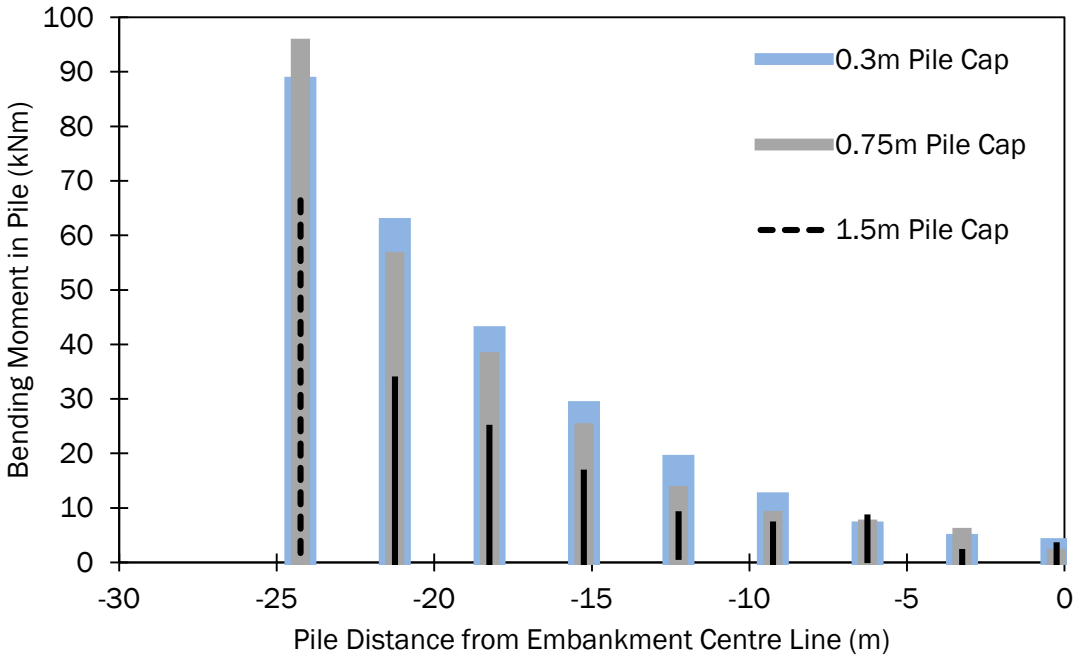

Figure 5.24 Bending moments (kNm) within a pile group for a range of pile cap size (m) (H = 4.0m, J_{re} = 500kN/m and s = 3.0m)

The pile group efficacy increased for an increase in the pile cap size, Figure 5.25. The decrease in clear span to be supported by the geosynthetic reinforcement resulted in a greater magnitude of load transferred directly onto the pile caps. As the magnitude of the loading on the piles increased, it did so in line with an increase of the pile group efficacy.

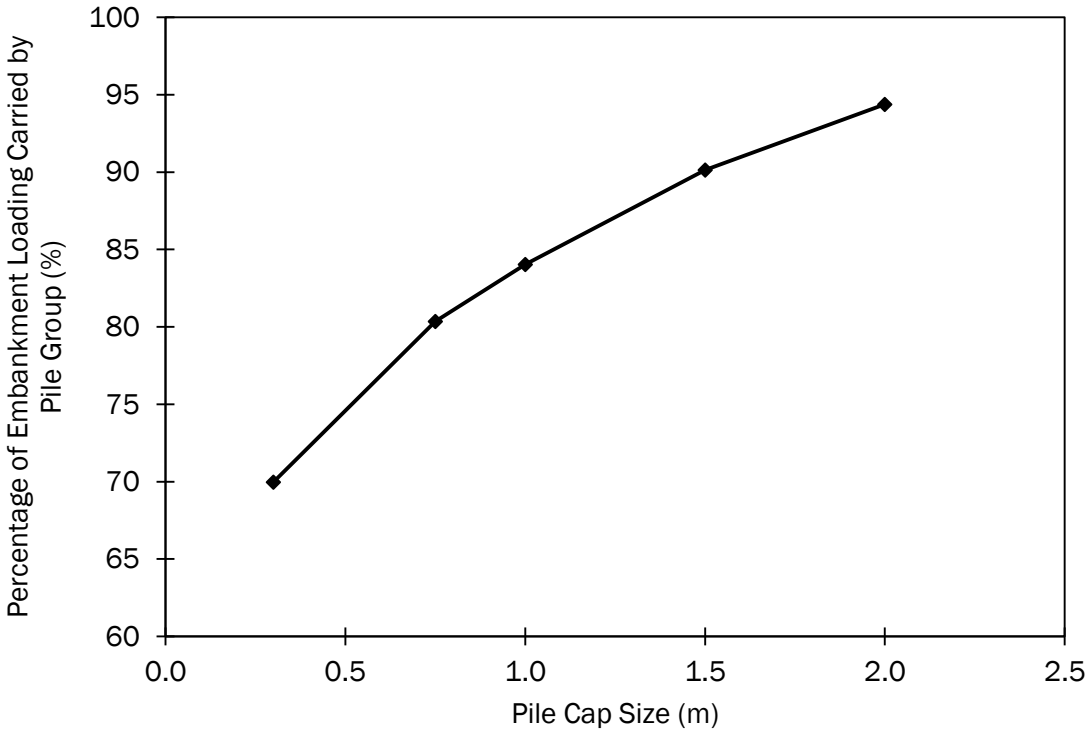

Figure 5.25 Pile group efficacy (%) for a range of pile cap size (m) (H = 4.0m, J_{re} = 500kN/m and s = 3.0m)

The strain in the reinforcement decreased as the pile cap size increased, Figure 5.26, as the clear span between the adjacent pile cap edges decreased and the resultant magnitude of load carried by the reinforcement decreased. The decrease in load yielded a reduction in strain in the geosynthetic reinforcement. The strain in the pile, which is a function of the bending moment, decreased as the pile cap size increased, Figure 5.26. An increase of the pile cap size resulted in a decrease of the embankment deformations, lower lateral deformations at the pile head and consequently, lower bending moment in the pile, Figure 5.24.

The strain in the reinforcement decreased 81% for an increase of the pile cap size from 0.3m to 2.0m (a 633% increase) and resulted in a 38.5% decrease in the

strain in the pile. The geosynthetic reinforcement yielded a greater reduction in strain in comparison to the pile, Figure 5.26. The strain compatibility ratio (SCR) increased almost linearly, approximately doubling, for an increase in the pile cap size from 0.3m to 1.0m (a 233% increase). This change in SCR suggested that as the pile cap size increased the pile group attracts a greater portion of the outward lateral thrust from the embankment in comparison to the geosynthetic reinforcement, Figure 5.26.

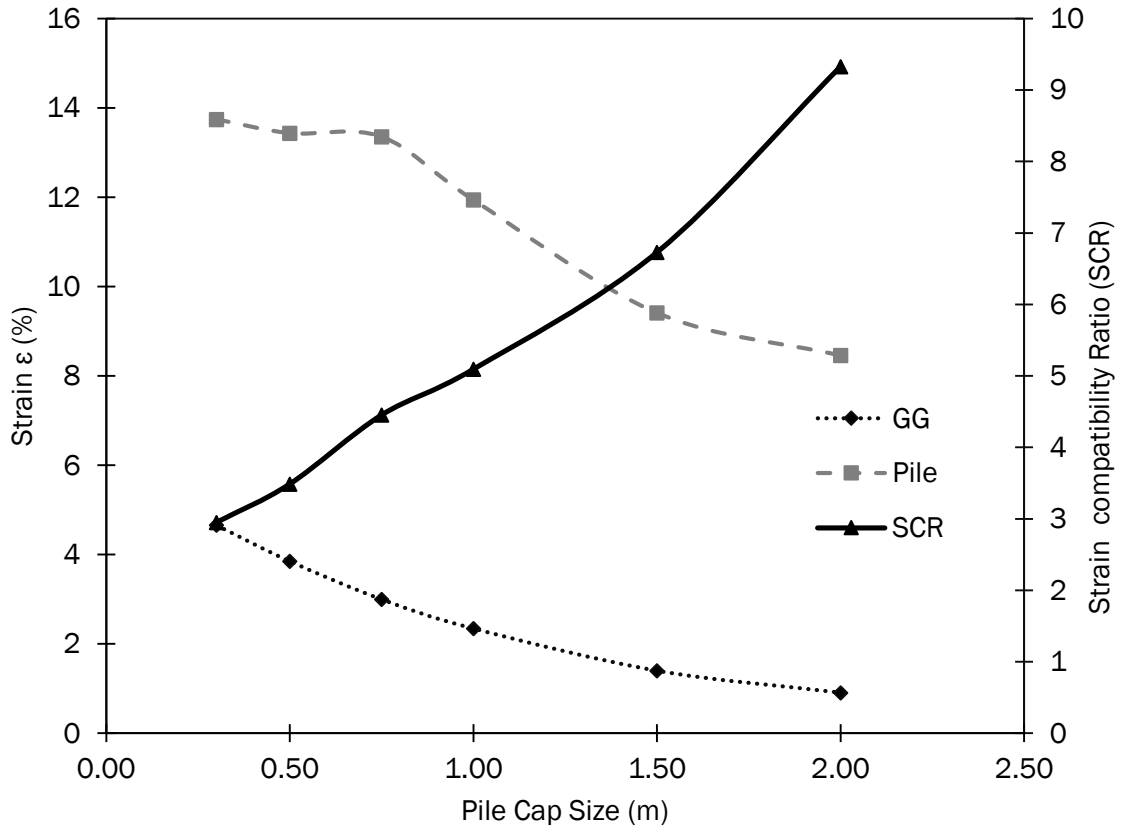

Figure 5.26 Strain in reinforcement and outer row pile and piled embankment Strain Compatibility Ratio (SCR) (%) for a range of pile cap size (m) for a 1V:2H side slope (H = 4.0m, J_{re} = 500kN/m and s = 3.0m)

Increasing the pile cap size reduced horizontal deformation of the embankment fill outwards from the embankment centre, and increased the load transferred to the pile heads, thus increasing the efficacy of the pile group, Figure 5.22. This resulted in an overall increase in stability of the GRPE, Figure 5.27.

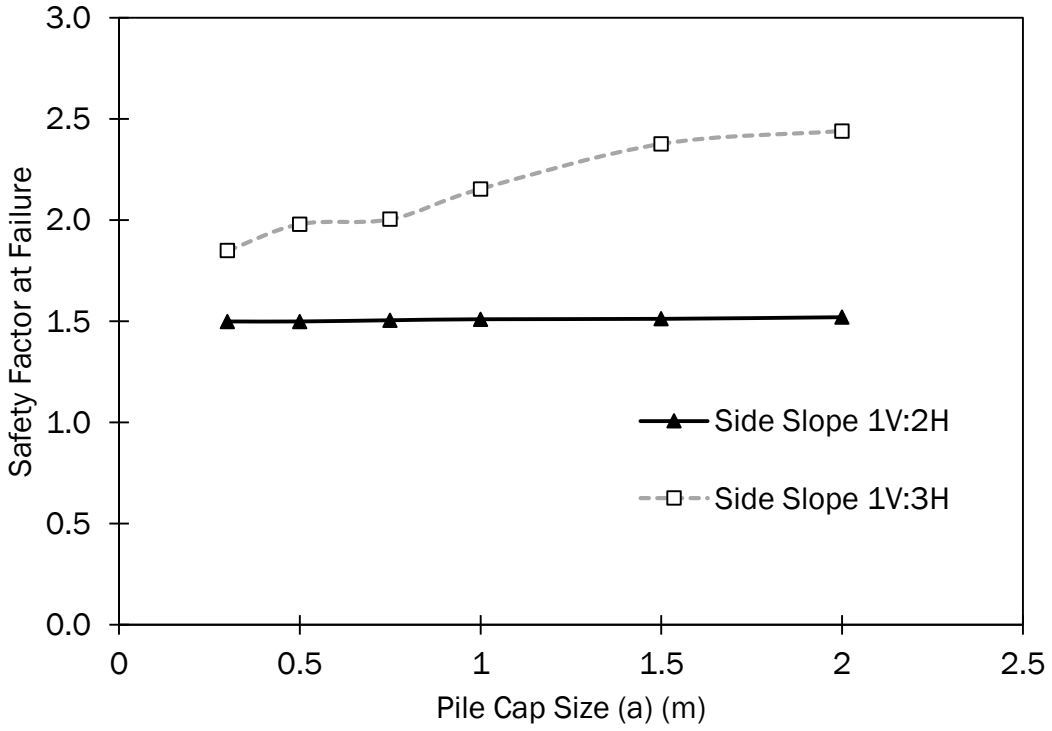

Figure 5.27 Safety factor at failure for a range of pile cap size

5.4 Influence of Outer Pile Rake

The outer pile row rake angle was varied from 0.0° to 30.0° from the vertical. An initial increase in the outer pile rake angle from 0.0° to 10.0° resulted in a minimal decrease in the vertical deformation at the embankment crest for both steepness's of side slope and a reduction of 19% (1V:2H side slope) and 18% (1V:3H side slope) in horizontal deformation, Figure 5.28. A further increase in the outer pile rake angle (greater than 10.0°) resulted in a continuation of an almost linear decrease in both horizontal and vertical deformation for an embankment side slope of 1V:2H. For a pile rake angle greater than approximately 10.0°, the raking piles had a very pronounced effect on the deformation vectors for a side slope of 1V:3H with a reversal of the initial reduction in horizontal and vertical deformations. The loading from the longer side slope (1V:3H) resulted in a significant lateral deformation of the outer pile row toward the embankment centre which destabilized the embankment fill at the crest location. The destabilization of the embankment fill within the side slope negated the earlier improvement of stability at the embankment extremities observed for low outer pile row rake angles for the 1V:3H side slope case, Figure 5.28.

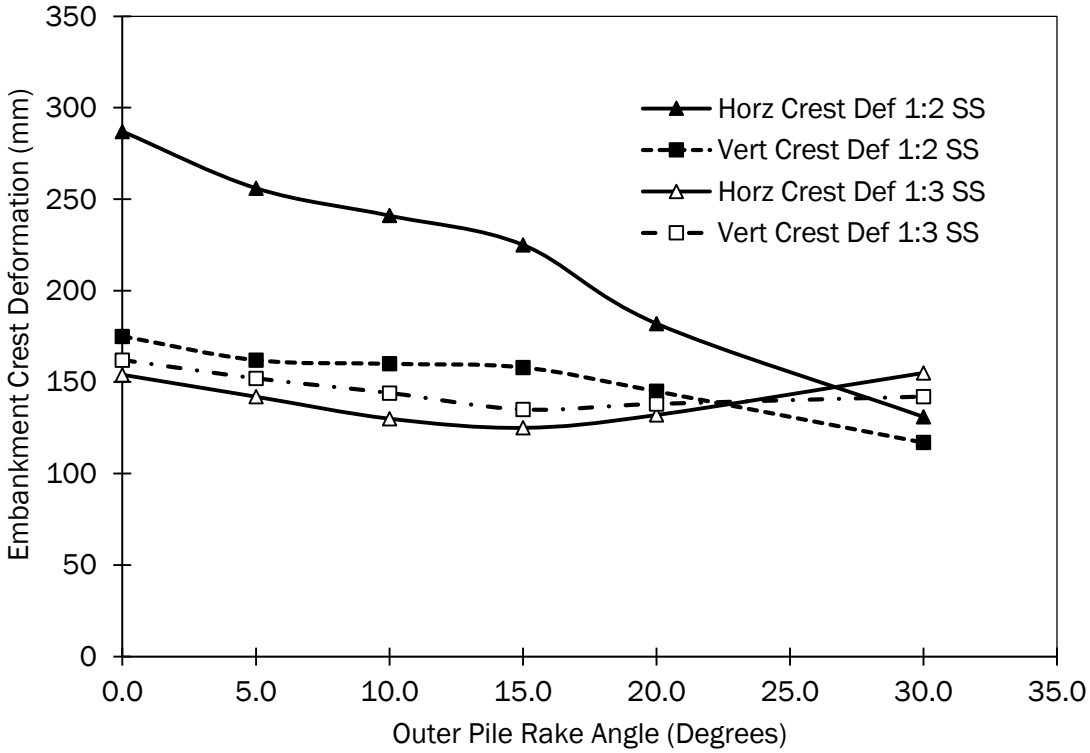

Figure 5.28 Surface deformations (mm) at the embankment crest for a range of outer pile rake angle (Degree (°)) (H = 4.0m, J_{re} = 500kN/m and s = 3.0m)

The deformation at the clear span between the toe of the embankment and the outer row pile cap edge increased marginally (5.7%) for an increase in the outer row pile rake angle across the full range of values examined for an embankment with a 1V:3H side slope, Figure 5.29. For the embankment with a 1V:2H side slope, the vertical deformation that occurred near the toe of the embankment increased 4% for an increase of the pile rake angle from 10.0° to 30.0°. Vertical deformation near the toe for both cases of side slopes steepness remained relatively consistent up to a rake angle of 20.0°. The data suggests a further increase of the pile rake angle mobilised an increase in the vertical deformations due to the outer pile row deforming laterally toward the embankment centre, Figure 5.35.

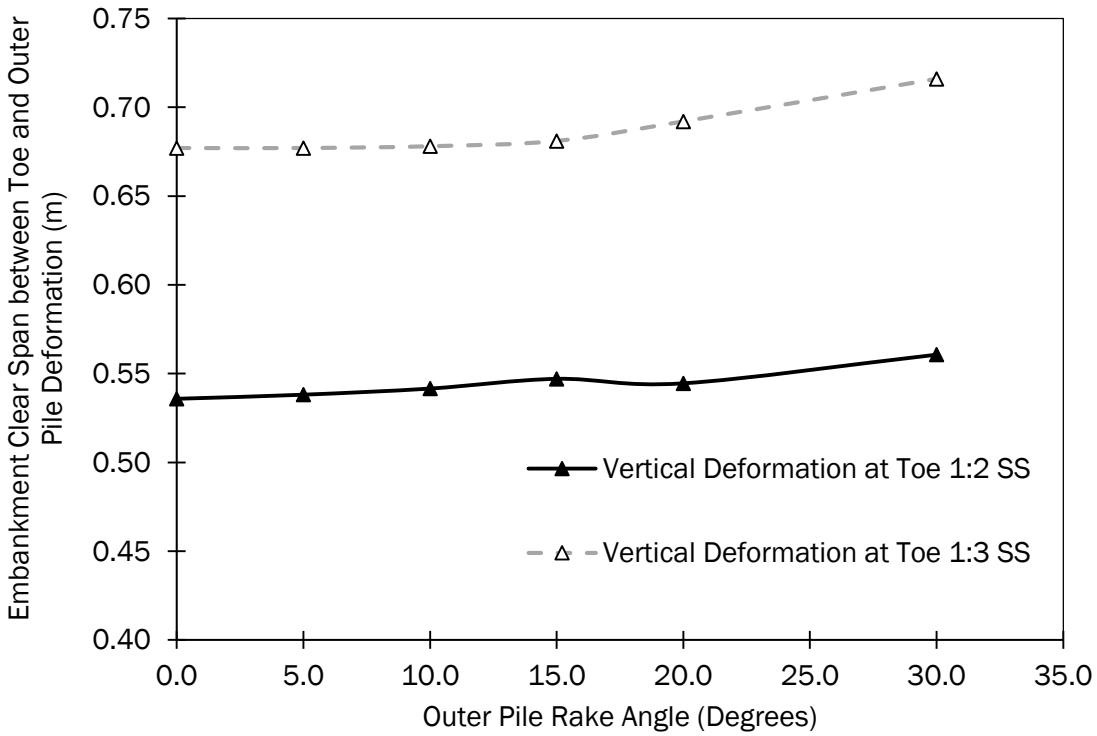

Figure 5.29 Vertical deformation (m) under the side slope between the embankment toe and outer row pile for a range of outer pile rake angle (Degree (°)) (H = 4.0m, J_{re} = 500kN/m and s = 3.0m)

The lateral deformation above the outer row pile reduced for an increase in the outer row pile rake angle with the exception of the 30° rake for the 1V:3H side slope case, Figure 5.30 (a) and (b). An increase in the outer pile row rake angle stabilized the embankment structure by providing resistance to the lateral thrust from the embankment acting outwards from the centre. Appendix C Figure C12 suggested that the lateral volumetric deformation that occurred above the outer row pile decreased (22%) in a linear fashion for a pile rake angle range from 0.0° to 15.0°. A further increase of the pile rake angle from 15.0° to 30.0° (100%) yielded an increase in the rate of reduction in the lateral volumetric deformation by 65%. Appendix C Figure C12 suggested that an increase of the pile rake angle greater than 15.0° resulted in a turning point in the rate of decrease in the LVD.

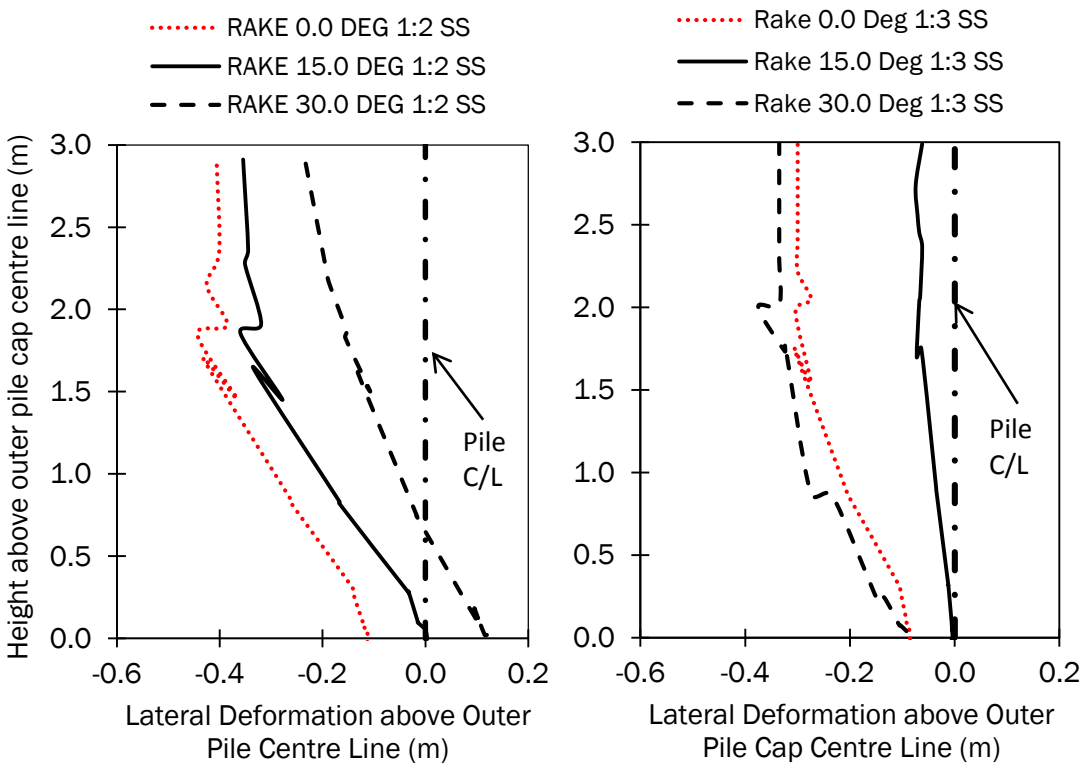

(a) *(b)*

Figure 5.30 Lateral Deformation (LD) (m) within the side slope above the outer row pile centre line for a range of outer pile rake angle (Degree (°)) for (a) a side slope of 1V:2H and (b) a side slope of 1V:3H (H = 4.0m, J_{re} = 500kN/m and s = 3.0m)

The magnitude of the vertical deformation of the reinforcement decreased for an increase of the outer pile row rake, Figure 5.31. The largest vertical deformation was located at the clear span between the toe of the embankment and the edge of the outer row pile cap for all raking piles. The differential in the magnitude of the maximum vertical deformation for a range of pile rake angles (0.0° to 30.0°) was insignificant (4%). The magnitude of the vertical deformation located within the main embankment structure itself suggested a notable influence of the pile rake angle on the vertical deformations. A pile rake angle of 30.0° consistently recorded vertical deformations between adjacent pile caps approximately 18% lower in magnitude in comparison to a pile rake of 0.0°.

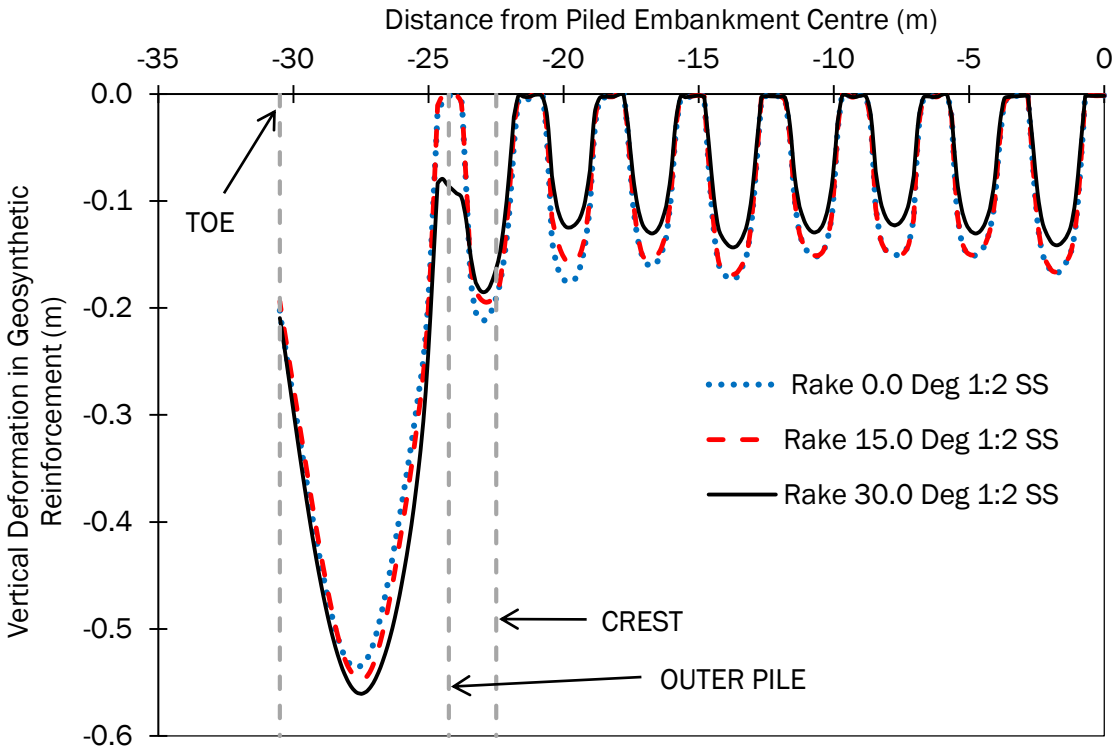

Figure 5.31 Vertical deformation of the geosynthetic reinforcement for a range of outer pile rake angle (Degree (°)) (H = 4.0m, J_{re} = 500kN/m and s = 3.0m)

The magnitude of the horizontal deformation of the reinforcement decreased for an increase of the outer pile row rake, Figure 5.32. The greater the pile rake angle, the lower the magnitude of the horizontal deformation (lateral thrust) of embankment fill material, Figures 5.28 and 5.30 and Appendix C Figure C12. An increase of the pile rake angle resulted in a reduction of both the horizontal deformation that occurred under the main embankment structure close to the centre of the embankment and also the maximum horizontal deformation located at the clear span between the embankment toe and the outer row pile cap edge.

As the outer row pile rake angle increased above approximately 20.0°, the deflection of the pile head reversed direction resulting in the pile head deflecting towards the centre of the embankment, Figure 5.32.

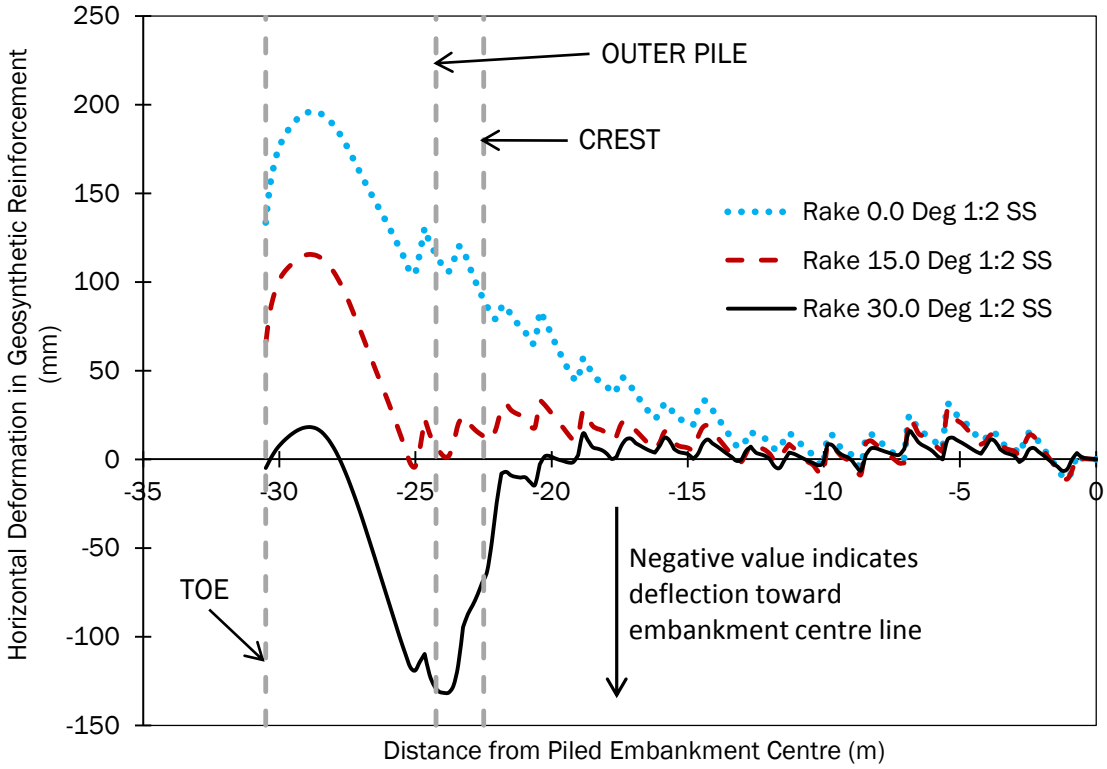

Figure 5.32 Horizontal deformations (mm) of geosynthetic reinforcement for a range of outer pile rake angle (Degree (°)) (H = 4.0m, J_{re} = 500kN/m and s = 3.0m)

The axial tension in the geosynthetic reinforcement decreased for an increase of the outer row pile rake angle, Appendix C Figure C13. The tensions developed close to the centre of the embankment structure were both relatively low in magnitude and relatively consistent for a range of pile rake angles, Figure 5.33. The tensions developed by the 0.0° and 15.0° pile rake angles were similar, a rake angle of 30.0° resulted in lower tensions developed in the reinforcement under the main embankment structure in comparison to the 0.0° and 15.0° rake angles, Figure 5.33. This was consistent with the observed vertical and horizontal deformations, Figure 5.31 and 5.32.

The axial load carried by the pie group remained relatively consistent across the width of the main embankment structure, Figure 5.34, for all pile rake angles. The axial load on the outer most pile row remained relatively consistent for all rake angles, Appendix C Figure C14.

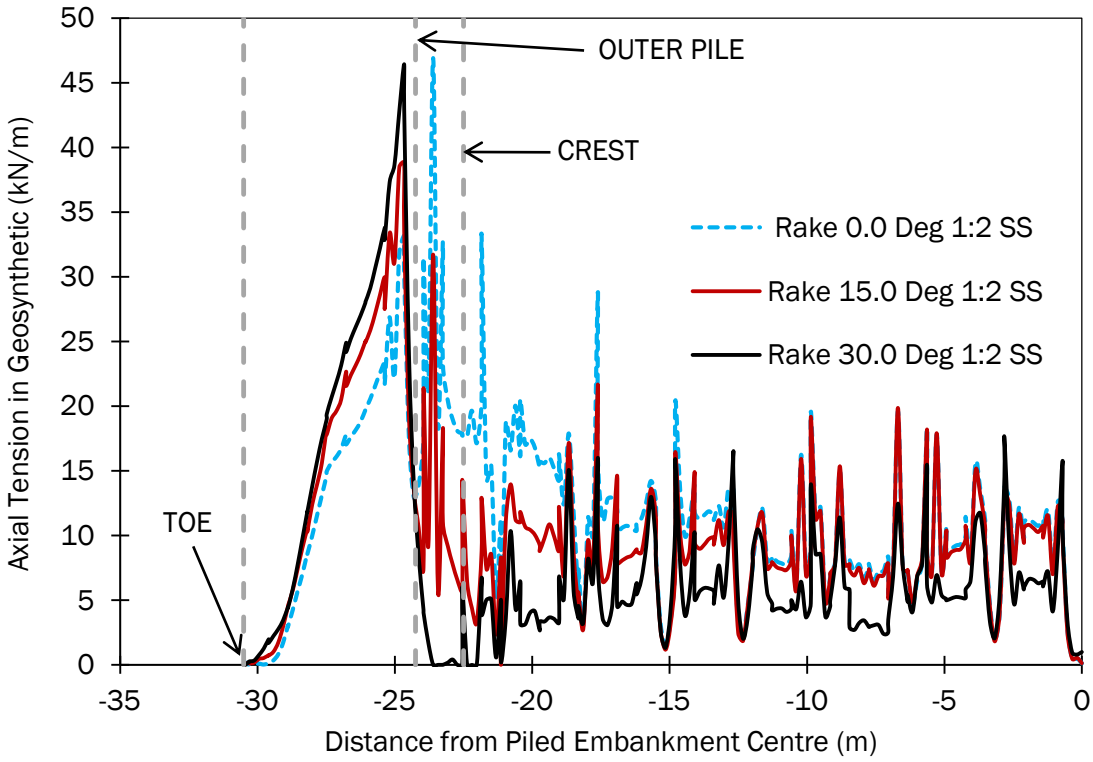

Figure 5.33 Axial tensions (kN/m) in the reinforcement for a range of outer pile rake angle (Degree (°)) (H = 4.0m, J_{re} = 500kN/m and s = 3.0m)

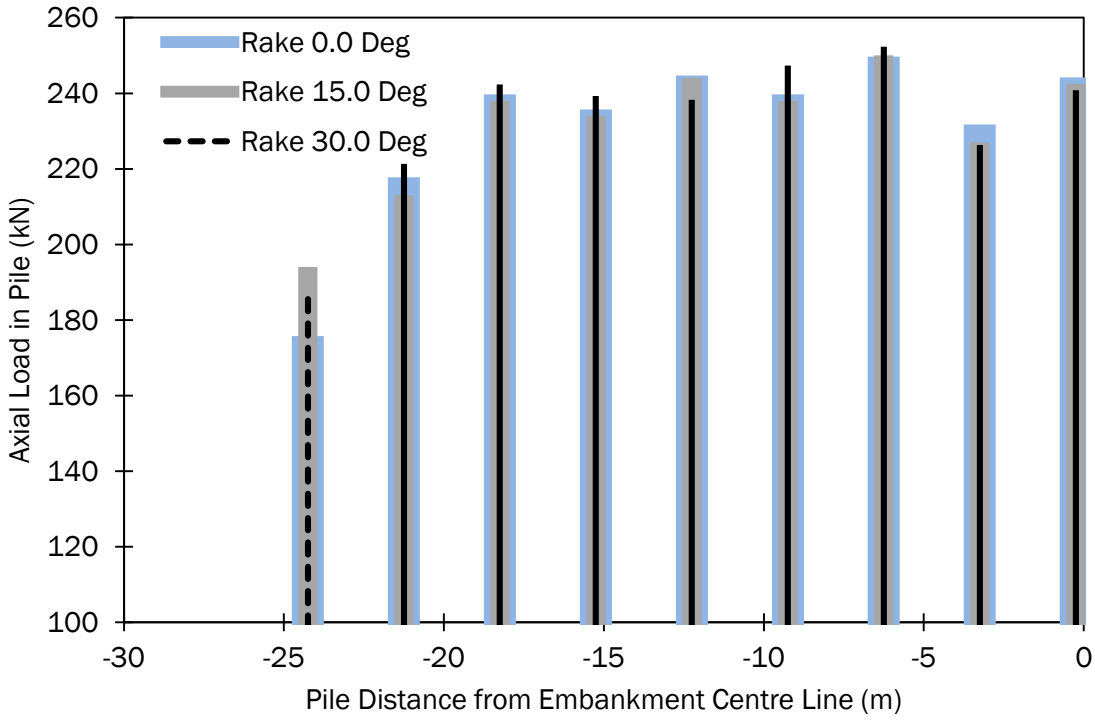

Figure 5.34 Axial loading (kN) on pile group under reinforced piled embankment for a range of outer pile rake angle (Degree (°)) (H = 4.0m, J_{re} = 500kN/m and s = 3.0m)

The lateral pile head deflection within the pile group decreased for an increase in the outer pile rake angle, Figure 5.35 and Appendix C Figure C15. An increase of the outer row pile rake angle reduced the magnitude of the lateral thrust that the vertical piles in the group were required to resist.

The bending moments in the pile group decreased almost linearly for an increase of the outer row pile rake angle from 0.0° to 15.0° for a 1V:2H side slope, Figure 5.36 and Appendix C Figure C16. The bending moment in the outer pile row increased for the 1V:2H side slope for a further increase in rake angle greater than 15.0°.

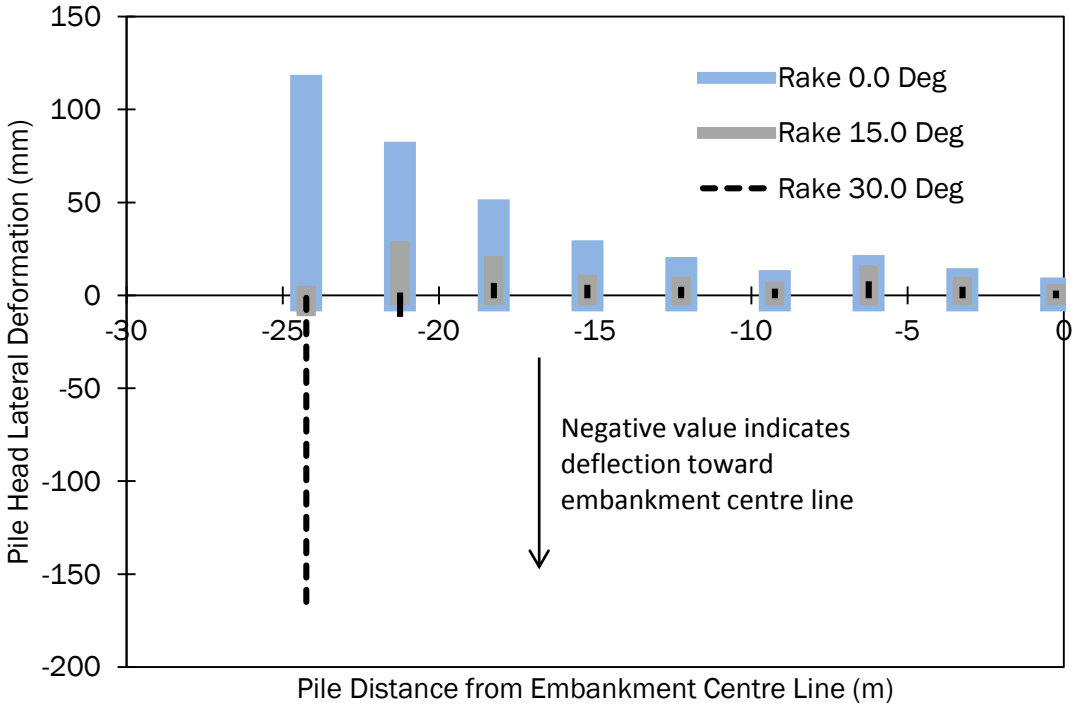

Figure 5.35 Lateral deflections (mm) at the pile head within a pile group under a reinforced piled embankment for a range of outer pile rake angle (Degree (°))

The efficacy of the pile group increased for an increase of the outer row pile rake angle, Figure 5.37. As the outer row pile rake increased, both the lateral deformation of the embankment fill and the horizontal deformation of the geosynthetic reinforcement decreased and thus transferred a greater portion of the embankment loading directly onto the piles. Although the pile group efficacy increased for an increase in the outer row pile rake from 0.0° to 30.0°, the pile group efficacy increased by a marginal 2.7%.

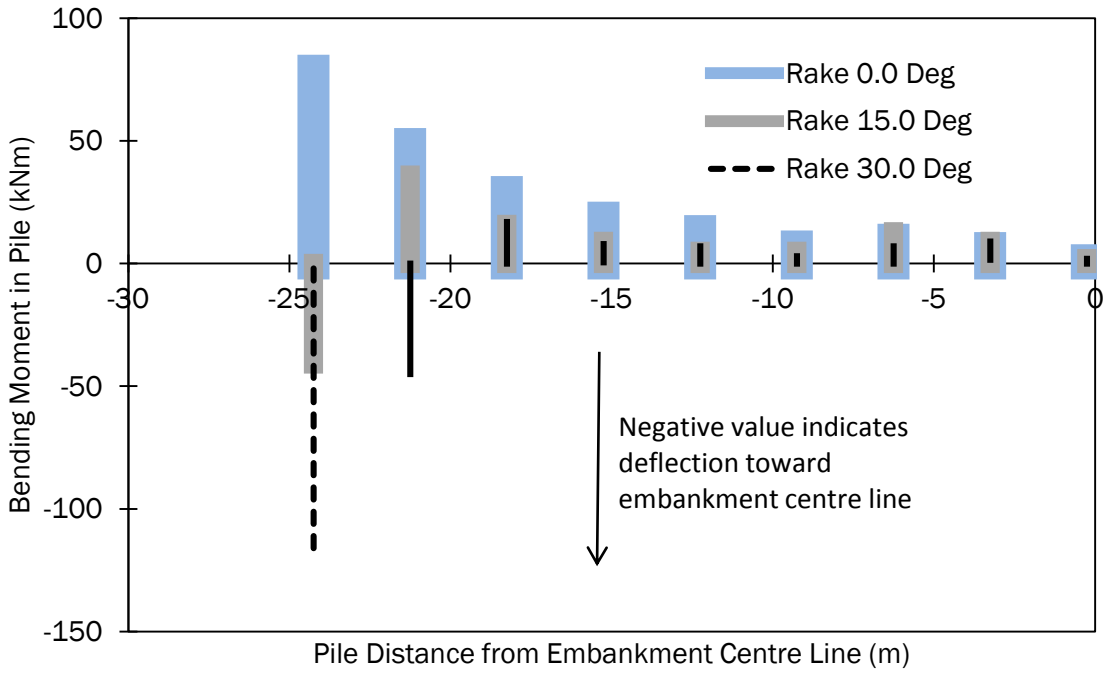

Figure 5.36 Bending moments (kNm) within a pile group for a range of outer pile rake angle (Degree (°)) (H = 4.0m, J_{re} = 500kN/m and s = 3.0m)

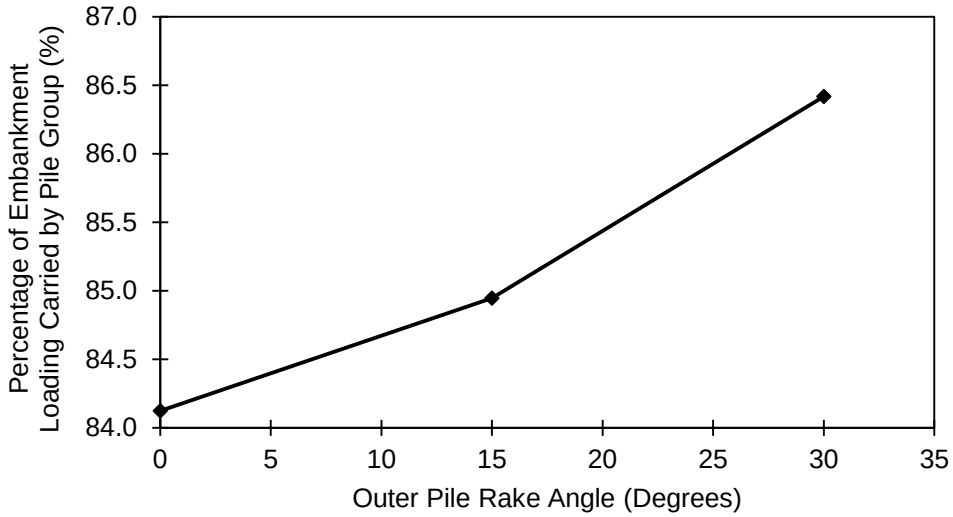

Figure 5.37 Pile group efficacy (%) for a range of outer pile rake angle (Degree (°)) (H = 4.0m, J_{re} = 500kN/m and s = 3.0m)

The strain in the geosynthetic reinforcement decreased by 8.8% for an increase of the outer row pile rake angle from 0.0° to 10.0°, a further increase of the outer pile rake angle (10.0° to 30.0°) resulted in a decrease (25.3%) of the reinforcement strain, Figure 5.38. The strain in the reinforcement decreased initially due to a reduction in tension in the reinforcement to resist the lateral thrust acting outwards

from the embankment centre. The strain in the pile decreased (76%) for an initial increase in the outer pile rake angle (0.0° to 15.0°) due to a reduction in the bending moment in the piles. A further increase of the outer pile rake angle (15.0° to 30.0°) resulted in an increase in the bending moment and pile strain (296% increase) resulting from an increase in the pile head deflection towards the embankment centre. The strain compatibility ratio (SCR) (Figure 5.38) declined linearly as the rake angle increased from 0.0° to 15.0° before increasing linearly for rake angles between 15.0° and 30.0°. This suggests that pile rake angles less than 15.0° the reinforcement was responsible for supporting an increasingly greater portion of the strain compatibility condition, while for pile rake angles greater than 15.0° the pile group was more influential in supporting the embankment loading required for equilibrium.

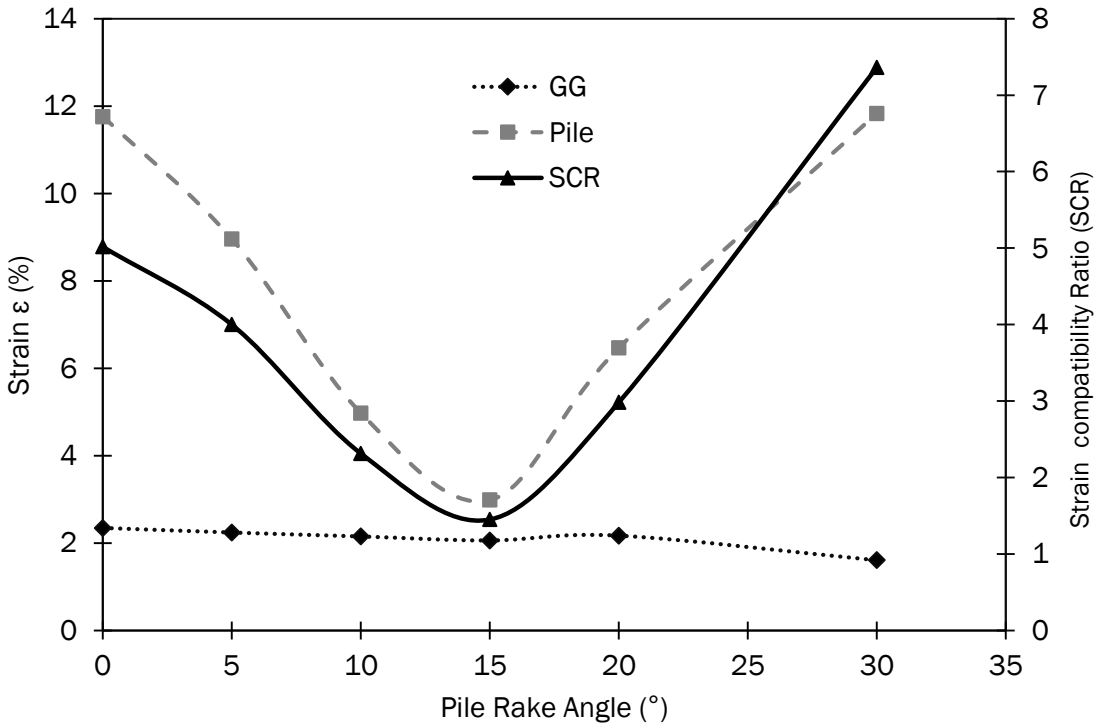

Figure 5.38 Strain in reinforcement and outer row pile and piled embankment Strain Compatibility Ratio (SCR) (%) for a range of outer pile rake angle (Degree (°)) for a 1V:2H side slope (H = 4.0m, J_{re} = 500kN/m and s = 3.0m)

An increase of the outer pile rake angle resulted in a consistent decrease of the horizontal deformation in the embankment fill, the geosynthetic reinforcement and a decrease in the pile lateral deflection and bending moments. The initial increase of the pile rake resulted in an increase of the embankment load to be supported by

the geosynthetic until the pile rake angle surpassed 15.0° and a greater portion of the embankment load was carried by the pile in comparison to the geosynthetic reinforcement.

The stability of the GRPE increased for an increase in the outer row pile rake angle, Figure 5.39. The outer row pile rake angle was varied from 0° to 30° in 5° increments. An increase of pile rake increased the piles resistance to lateral loads (a portion of lateral load converted into vertical vector and transferred axially to pile head). The data suggested that an outer row pile rake angle increase from 0° to 15° yielded the greatest reduction in the horizontal deformations of the embankment. A further increase in pile rake (greater than 15°) corresponded to a reduction in stability due to the outer row pile head deforming laterally towards the embankment centre as a result of vertical load resulting in an increase in embankment fill horizontal deformation outwards for both side slope steepness, Figure 5.39.

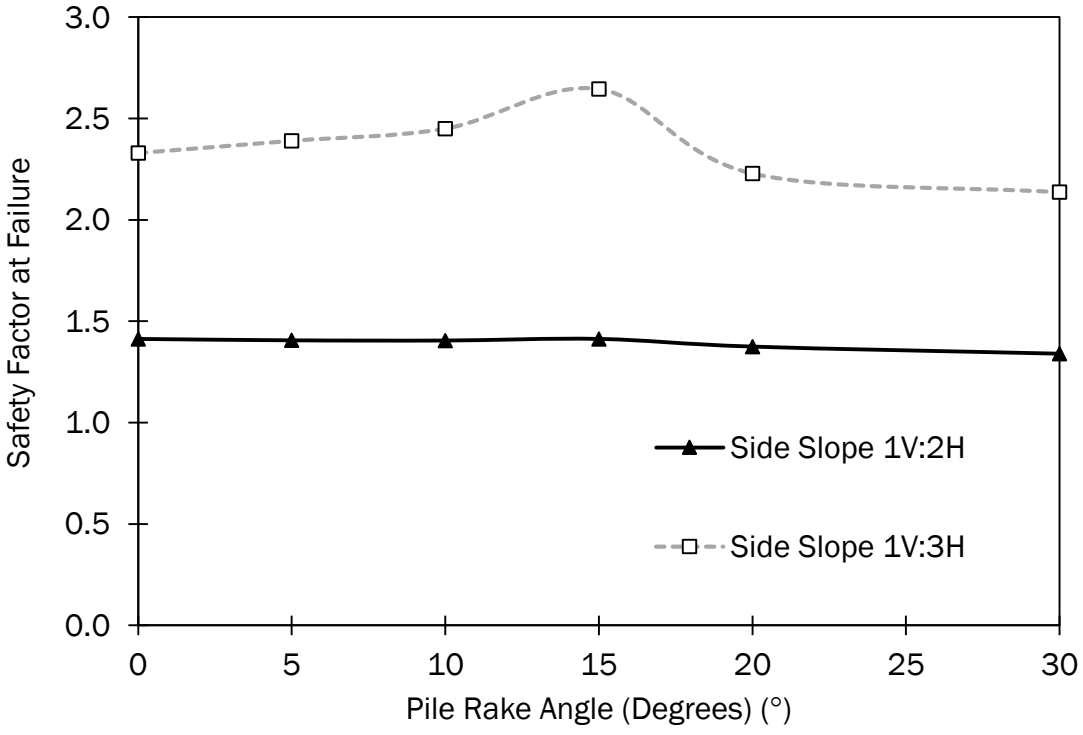

Figure 5.39 Safety factor at failure for a range of outer row pile rake angle

5.5 Influence of Geosynthetic Reinforcement Stiffness

The stiffness of the geosynthetic reinforcement (J_{re}) was ranged from 0kN/m (unreinforced case) to 4000kN/m. The horizontal and vertical deformations at the embankment crest decreased for an increase in the stiffness of the geosynthetic reinforcement, Figure 5.40. For both parameters the initial inclusion of reinforcement (0kN/m to 500kN/m) yielded the greatest rate of decrease (42% decrease in horizontal and 47% decrease in vertical) in deformations for a side slope of 1V:2H. Reinforcement stiffness's greater than 500kN/m did not have a pronounced effect on the observed deformations.

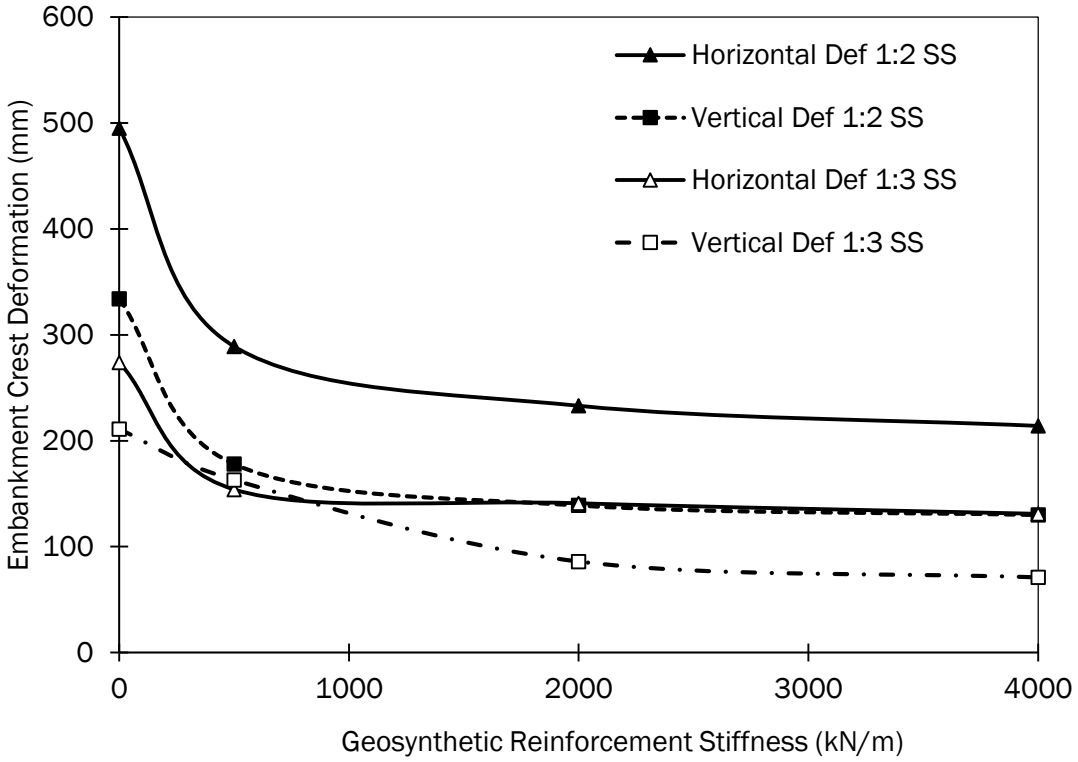

Figure 5.40 Surface deformations (mm) at the embankment crest for a range of geosynthetic reinforcement stiffness (H = 4.0m, a = 1.0m and s = 3.0m)

The deformation in the clear span under the side slope between the outer pile row edge and the embankment toe decreased for an increase in the stiffness of the geosynthetic reinforcement, Figure 5.41. Similar to the deformations at the crest of the embankment, the greatest rate of reduction in the magnitude of deformation was for an initial inclusion of reinforcement in the embankment structure. For a side slope of 1V:2H, an initial inclusion of reinforcement (0kN/m to 500kN/m) resulted

in a 25% decrease in the vertical deformation at the clear span near the toe of the embankment. A further increase in the stiffness (500kN/m to 2000kN/m) resulted in only a marginal decrease of 3% in the vertical deformations.

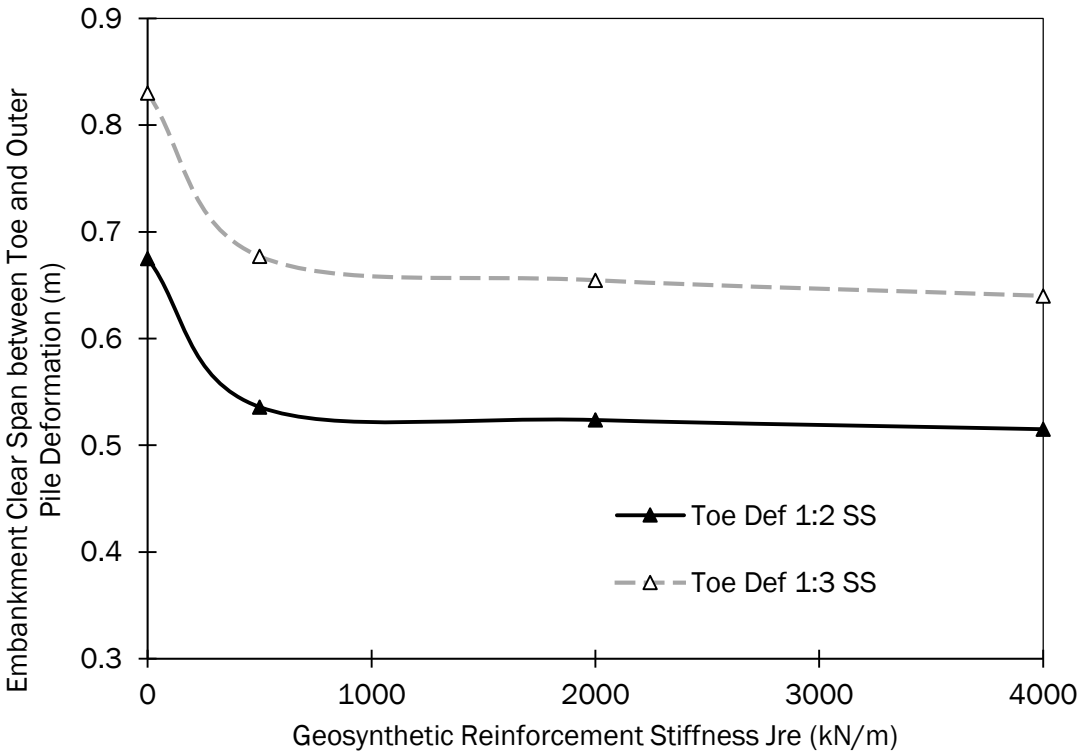

Figure 5.41 Vertical deformation (m) under the side slope between the embankment toe and outer row pile for a range of geosynthetic reinforcement stiffness (H = 4.0m, a = 1.0m and s = 3.0m)

The lateral deformation above the outer row pile decreased for an increase in the stiffness of the geosynthetic reinforcement, Figure 5.42. In both cases (Figure 5.42 (a) and (b)) the lateral deformation was significantly lower in magnitude for an initial inclusion of geosynthetic reinforcement. The embankment structure with a steeper side slope recorded greater magnitudes of lateral deformation, Figure 5.42 (a). The lateral volumetric deformation of the embankment fill material above the outer row pile decreased for an increase in the stiffness of the geosynthetic reinforcement, Appendix C Figure C17. The lateral volumetric deformation decreased (23% decrease) for the initial inclusion of geosynthetic reinforcement (0kN/m to 500kN/m). The rate of decrease in the lateral volumetric deformation reduced (17% decrease) for a further increase in the stiffness of the reinforcement.

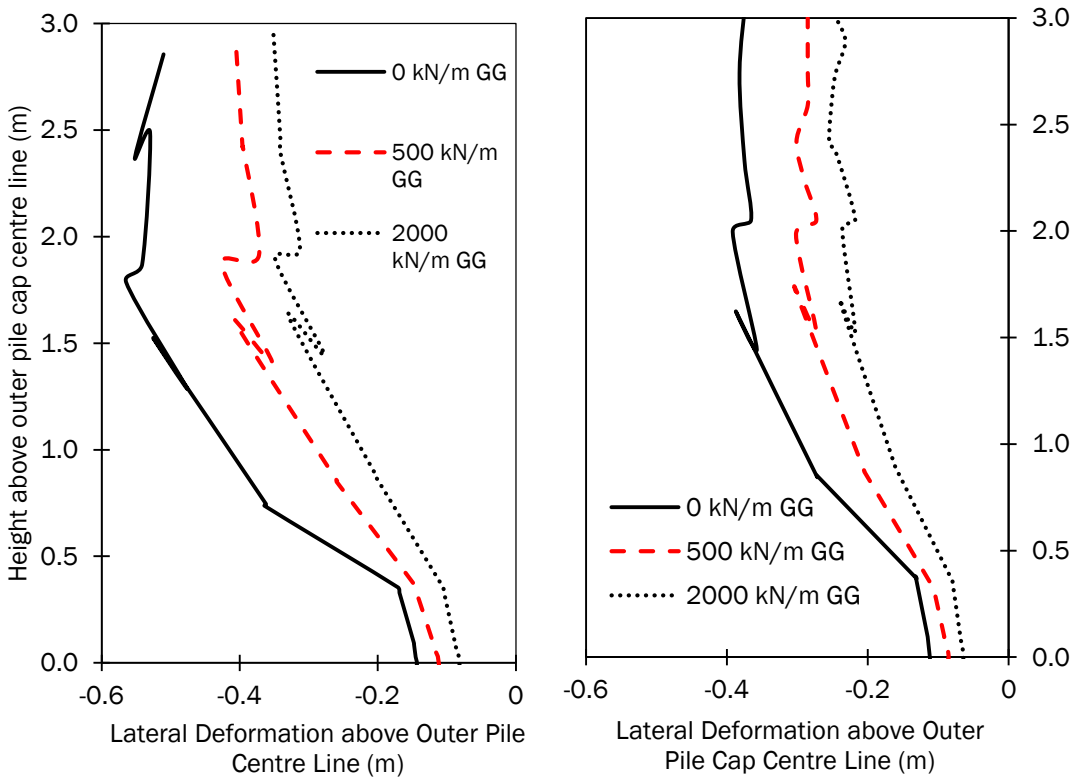

Figure 5.42 Lateral Deformation (LD) (m) within the side slope above the outer row pile centre line for a range of geosynthetic reinforcement stiffness for (a) a side slope of 1V:2H and (b) a side slope of 1V:3H (H = 4.0m, a = 1.0m and s = 3.0m)

The magnitude of the vertical deformation in the reinforcement decreased for an increase in the stiffness of the geosynthetic reinforcement, Figure 5.43. The initial increase of geosynthetic reinforcement stiffness (250kN/m to 500kN/m) reduced the magnitude of the vertical deformations seen at both the adjacent pile cap edges within the embankment structure (approximate 25% decrease) and the clear unsupported span outside of the outer row pile (approximate 13% decrease). A further increase (500kN/m to 2000kN/m) in stiffness yielded a continuation in the reduction (20% decrease between adjacent pile caps, 3% decrease in deformation near the toe) of the deformations but at a reduced rate. The magnitude of the vertical deformations between adjacent pile caps increased disproportionally near the embankment crest, Figure 5.43, corresponding to the location of the maximum lateral thrust acting within the embankment.

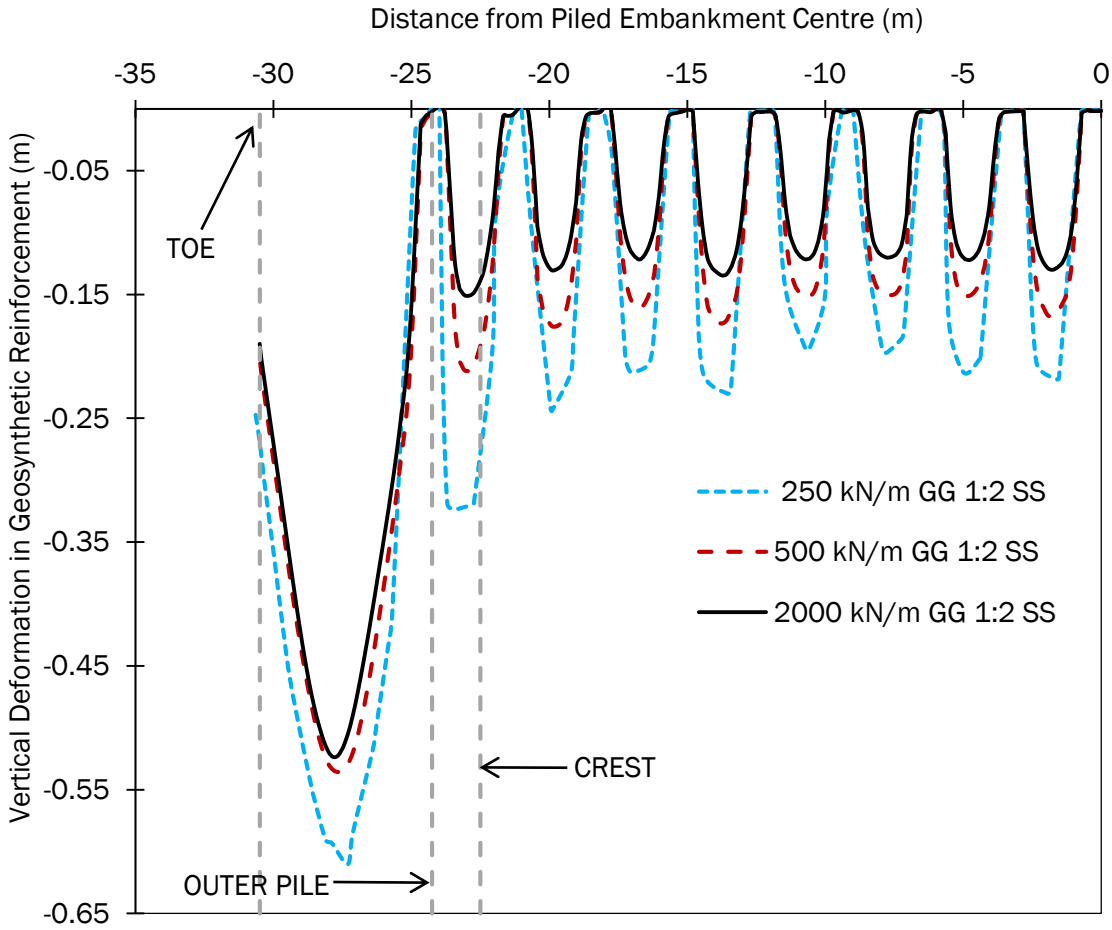

Figure 5.43 Vertical deformation of the geosynthetic reinforcement for a range of geosynthetic reinforcement stiffness (H = 4.0m, a = 1.0m and s = 3.0m)

The magnitude of horizontal deformation of the geosynthetic reinforcement decreased for an increase in the stiffness of the reinforcement, Figure 5.44. The magnitude of the horizontal deformation largely remained unaffected at or near the embankment centre, Figure 5.44. At the embankment crest, where the lateral thrust was at a maximum, the deformation of the reinforcement increased. An increase in the reinforcement stiffness (500kN/m to 2000kN/m) yielded a reduction in the maximum horizontal deformation of approximately 52% (195mm to 94mm).

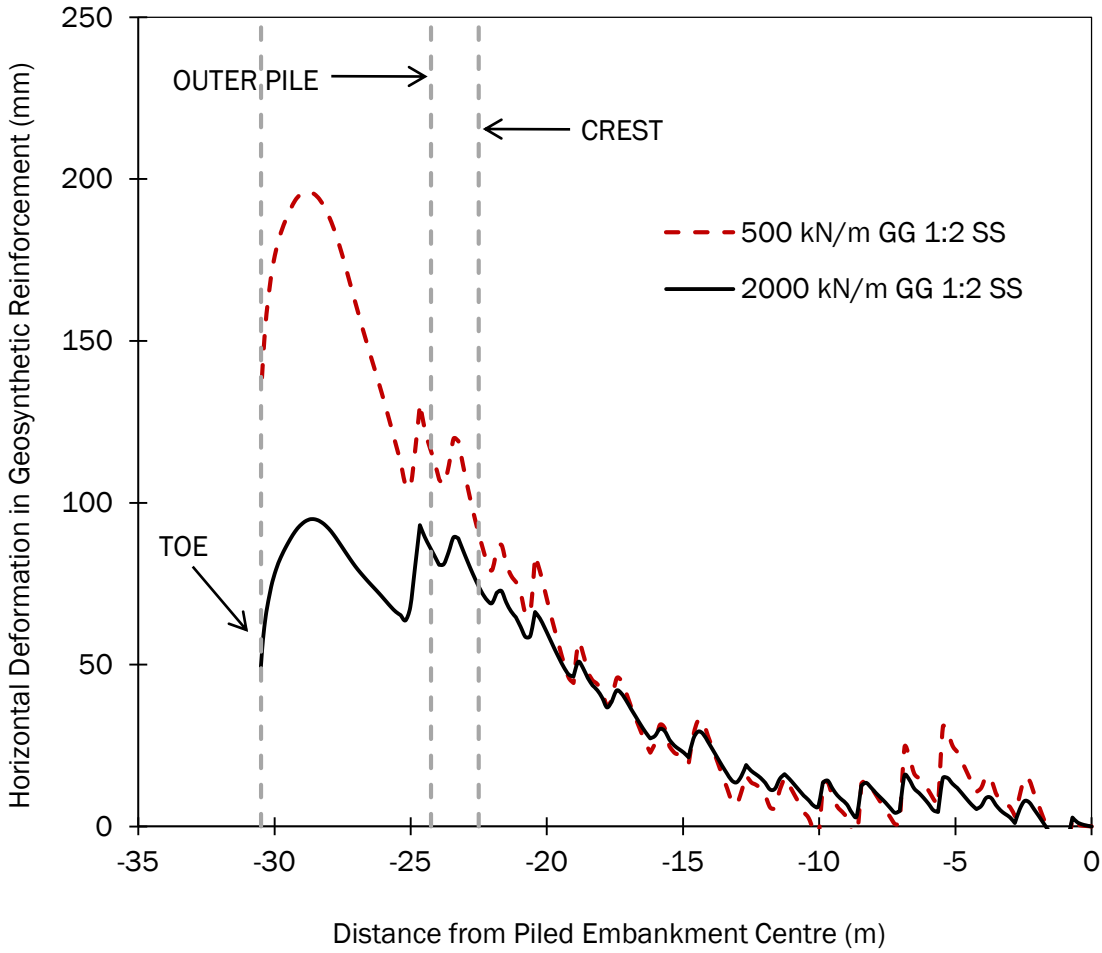

Figure 5.44 Horizontal deformations (mm) of geosynthetic reinforcement for a range of geosynthetic reinforcement stiffness (H = 4.0m, a = 1.0m and s = 3.0m)

The axial tension increased for an increase in the stiffness of the reinforcement, Figure 5.45. At or near the embankment centre, the reinforcement tensions were solely a function of the vertical deformation that occurred between the adjacent pile caps edges, Figure 5.45. The stiffer reinforcement yielded lower vertical deformations and thus higher tensions. At the outer extremities of the embankment the inclusion of stiffer reinforcement yielded greater tensions, Figure 5.45 and Appendix C Figure C18. An increase of the reinforcement stiffness resulted in an increase of 80.5% for a 1V:2H side slope case.

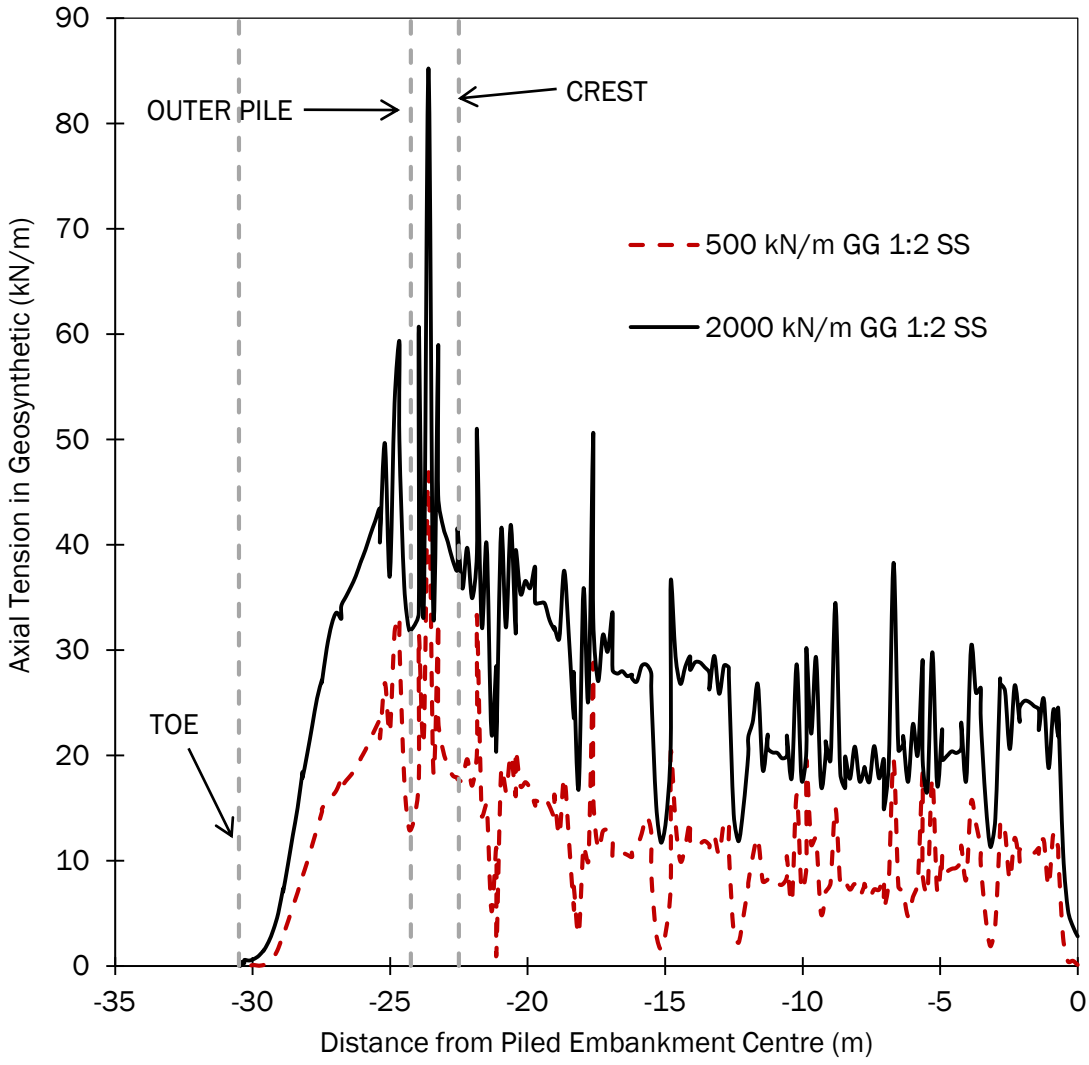

Figure 5.45 Axial tensions (kN/m) in the reinforcement for a range of geosynthetic reinforcement stiffness (H = 4.0m, a = 1.0m and s = 3.0m)

The axial load on the pile group increased marginally for an increase in the stiffness of the reinforcement, Figure 5.46. The initial inclusion of the reinforcement (0kN/m to 500kN/m) significantly altered the magnitude of the axial load on the outer pile row, Figure 5.46 and Appendix C Figure C19. The axial load increased 24% for the initial inclusion of reinforcement within the structure, a further increase of reinforcement stiffness (500kN/m to 2000kN/m) resulted in a 6.4% increase in axial pile load.

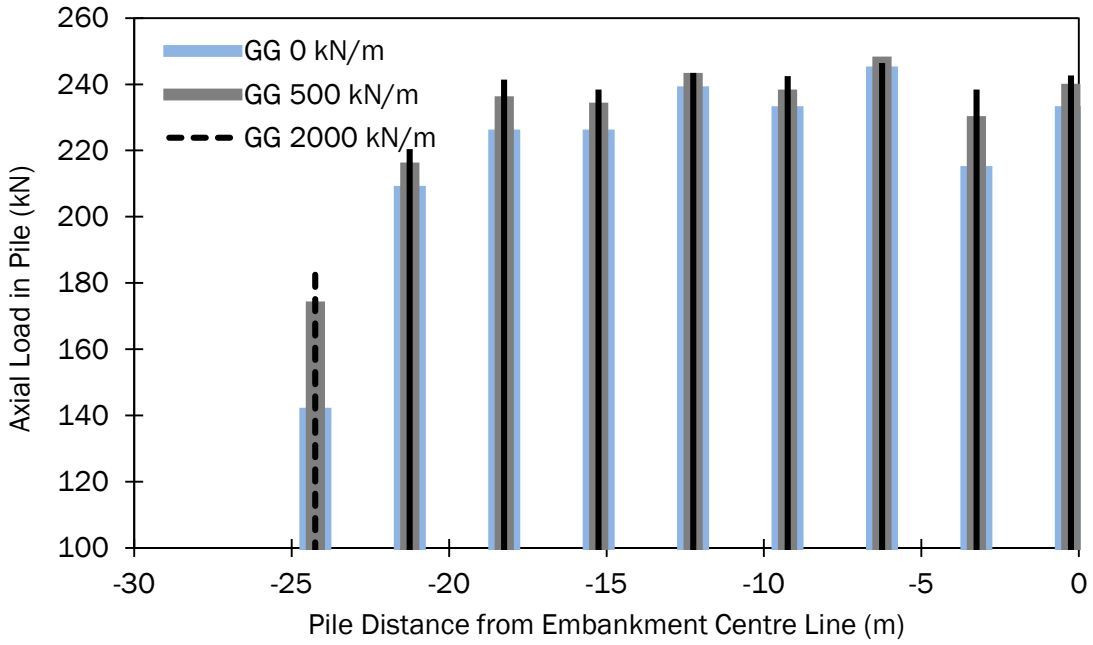

Figure 5.46 Axial loading (kN) on pile group under reinforced piled embankment for a range of geosynthetic reinforcement stiffness (H = 4.0m, a = 1.0m and s = 3.0m)

An insignificant change in the lateral deflection at the pile heads was observed as the reinforcement stiffness increased, Figure 5.47. The exception was the outer pile row which increased significantly for a decrease in the stiffness of the reinforcement. The outer row pile head deflection recorded a maximum for the unreinforced case and decreased further for an increase in the stiffness of the reinforcement. The most significant decrease in the magnitude of the pile head deflection was from the initial inclusion of the reinforcement in the structure, Appendix C Figure C20.

The bending moment at each pile within the pile group replicated the characteristic pattern of the pile head deflection, Figure 5.48. Within the confines of the pile group the magnitudes of the bending moments at each pile location decreased marginally for an increase in the stiffness of the reinforcement. Similar to the pile head deflection only the outer pile row yielded a significant differential in bending moment magnitudes for a variation of the reinforcement stiffness. The initial inclusion (0kN/m to 500kN/m) of reinforcement to the structure resulted in a decrease of the bending moment by 33%, increasing the reinforcement stiffness further yielded an additional decrease (27%) in bending moment, Appendix C Figure C21.

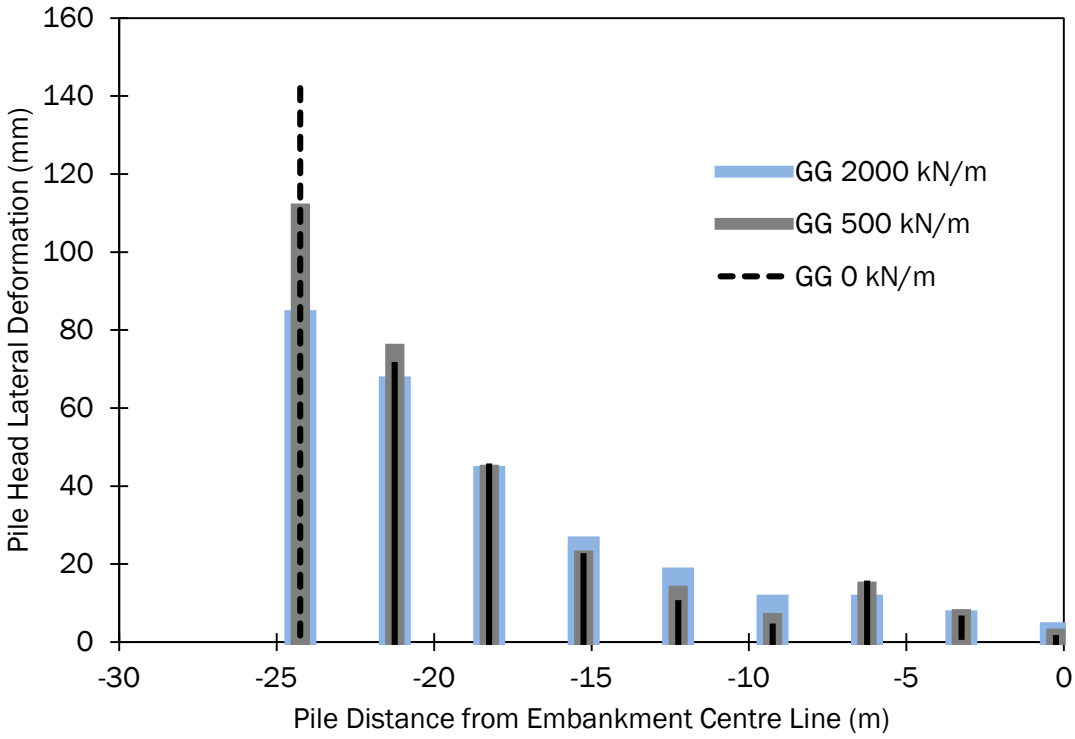

Figure 5.47 Lateral deflection (mm) at the pile head within a pile group under a reinforced piled embankment for a range of geosynthetic reinforcement stiffness (H = 4.0m, a = 1.0m and s = 3.0m)

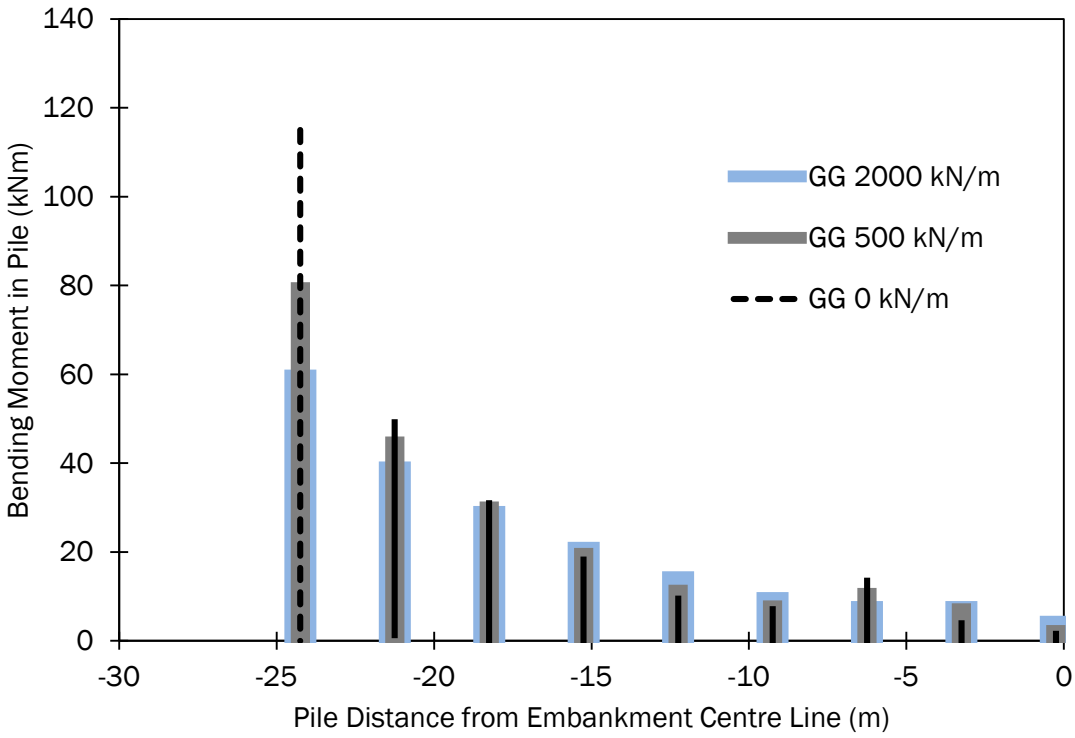

Figure 5.48 Bending moments (kNm) within a pile group for a range of geosynthetic reinforcement stiffness (H = 4.0m, a = 1.0m and s = 3.0m)

The initial inclusion of the reinforcement increased the efficacy by approximately 5%. A further increase (2.3%) in the pile group efficacy was recorded for an increase in the stiffness (500kN/m to 2000kN/m). The initial inclusion of the reinforcement to the piled embankment structure yielded the greatest improvement of load transfer efficacy to the pile, an increase of the stiffness of the reinforcement suggested a diminished rate of return with regard to an improvement of load transfer efficacy, Figure 5.49.

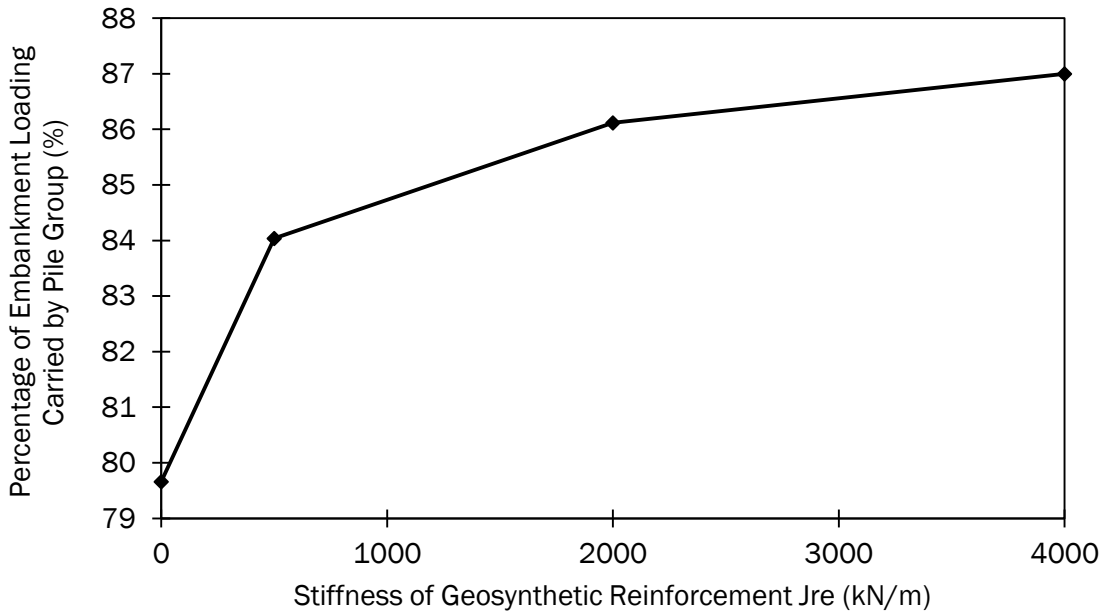

Figure 5.49 Pile group efficacy (%) for a range of geosynthetic reinforcement stiffness's (H = 4.0m, a = 1.0m and s = 3.0m)

The strain in the reinforcement decreased for an increase in the stiffness of the reinforcement, Figure 5.50. The strain in the reinforcement decreased at a rapid rate for an initial increase in the stiffness, 27% for an increase of 250kN/m to 500kN/m and a 45% decrease for a 500 – 2000kN/m increase. An increase in the stiffness from 2000kN/m to 4000kN/m resulted in a further decrease in the reinforcement strain of 35%. The rate of decrease in the strain accelerated until the stiffness of the reinforcement reached 2000kN/m.

The strain in the piles also decreased for an increase in the stiffness of the reinforcement, Figure 5.50, resulting in reduced bending moments in the pile, Figure 5.48 and Appendix C Figure C21. The strain compatibility ratio (SCR) increased for an increase in reinforcement stiffness, Figure 5.50. The increase in

the SCR suggested that as the stiffness of the reinforcement increased the pile attracted an increasingly larger portion of the strain within the structure. The initial inclusion of reinforcement and subsequent increase of the reinforcement stiffness resulted in a decrease of both the pile strain and reinforcement strain. The strain in the reinforcement decreased at a greater rate than that of the pile. This suggests that as the reinforcement platform stiffens, the pile group was required to resist a greater proportion of the lateral disturbing loads acting within the embankment structure.

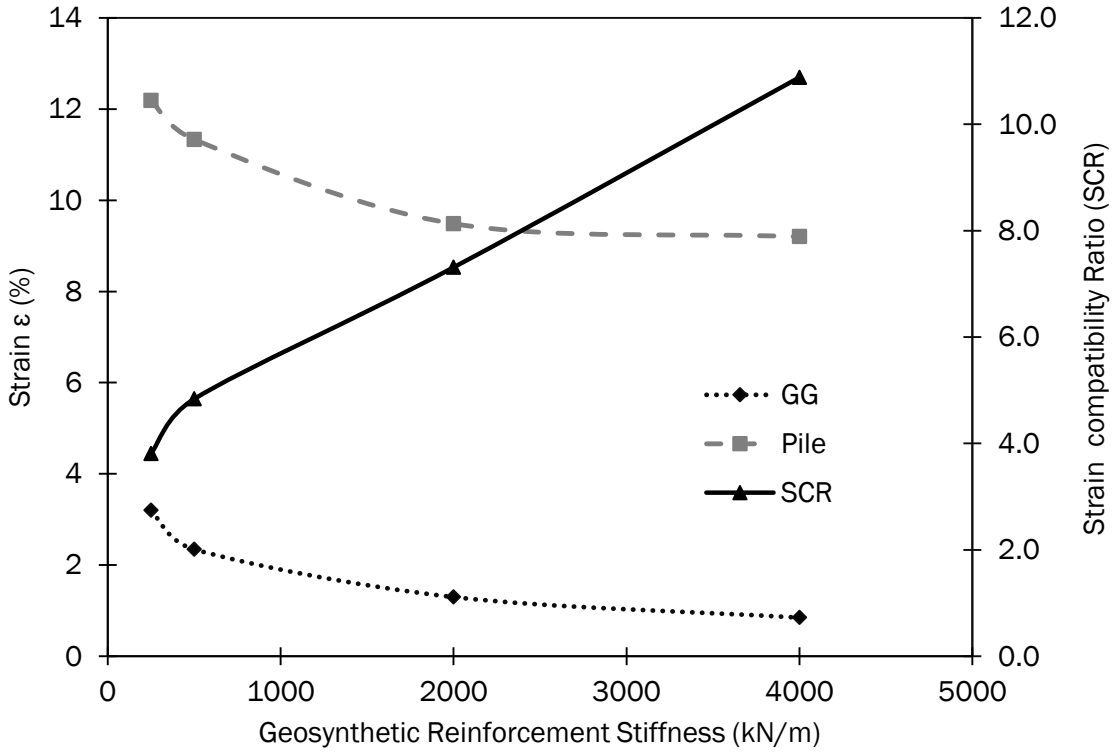

Figure 5.50 Strain in reinforcement and outer row pile and piled embankment Strain Compatibility Ratio (SCR) (%) for a range of geosynthetic reinforcement stiffness for a 1V:2H side slope (H = 4.0m, a = 1.0m and s = 3.0m)

An increase of the reinforcement stiffness decreased the magnitude of deformations in the embankment material fill, the reinforcement and the pile group. An increase in the reinforcement stiffness resulted in higher tensions as the reinforcement transferred a greater portion of vertical embankment loading to the pile group (increased the pile group efficacy) and an increase in the portion of the horizontal thrust carried by the pile group (increase of SCR, Figure 5.50).

Stability of the geosynthetic reinforced piled embankment (GRPE) structure increased for an increase in the geosynthetic reinforcement stiffness for both side slope steepness, Figure 5.51. The most significant improvement in structural stability was, again, for the initial inclusion of reinforcement to the structure, 0→500kN/m increased the factor of safety by 0.137 (1V:2H side slope) and 0.266 (1V:3H side slope), Figure 5.51. Further increases of the geosynthetic reinforcement stiffness, from 500 kN/m to 4000 kN/m, recorded a marginal increase (0.017) in the factor of safety for a 1V:2H side slope and a 0.189 increase for a 1V:3H side slope, Figure 5.51. The relationship between the factor of safety and the stiffness of the geosynthetic reinforcement was inversely correlated with the deformational response of the structure, this relationship was also observed by Han and Gabr (2002).

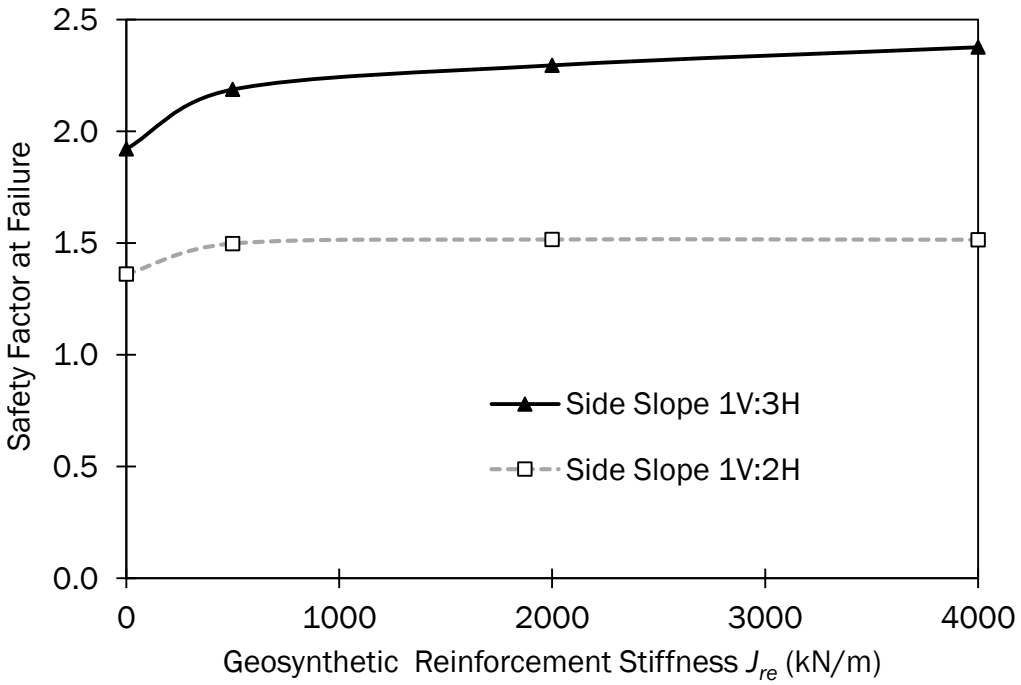

Figure 5.51 Safety factor at failure for a range of geosynthetic reinforcement stiffness (J_{re})

5.6 Influence of Depth of Soft Soil Layer

The depth of the soft soil layer was ranged from 8.0m to 15.0m. The magnitude of the deformations increased marginally for an increase in the depth of the soft soil layer underlying the piled embankment structure, Figure 5.52. The vertical deformation at the embankment crest location yielded the greatest rate of increase.

An initial increase in the depth of the soft soil layer yielded an insignificant increase in the magnitude of both vertical and horizontal deformation for both steepness's of side slopes, Figure 5.52. A further increase in the depth of the soft soil layer from 12.0m to 15.0m (25% increase) resulted in an increase in both vertical (16% increase) and horizontal deformation (9.5% increase). The embankment with a 1V:3H side slope did not have an equal magnitude of increase (in comparison to the side slope of 1V:2H) in both the horizontal and vertical deformations as the magnitude of disturbing lateral force within the embankment was not mobilised to the same extent.

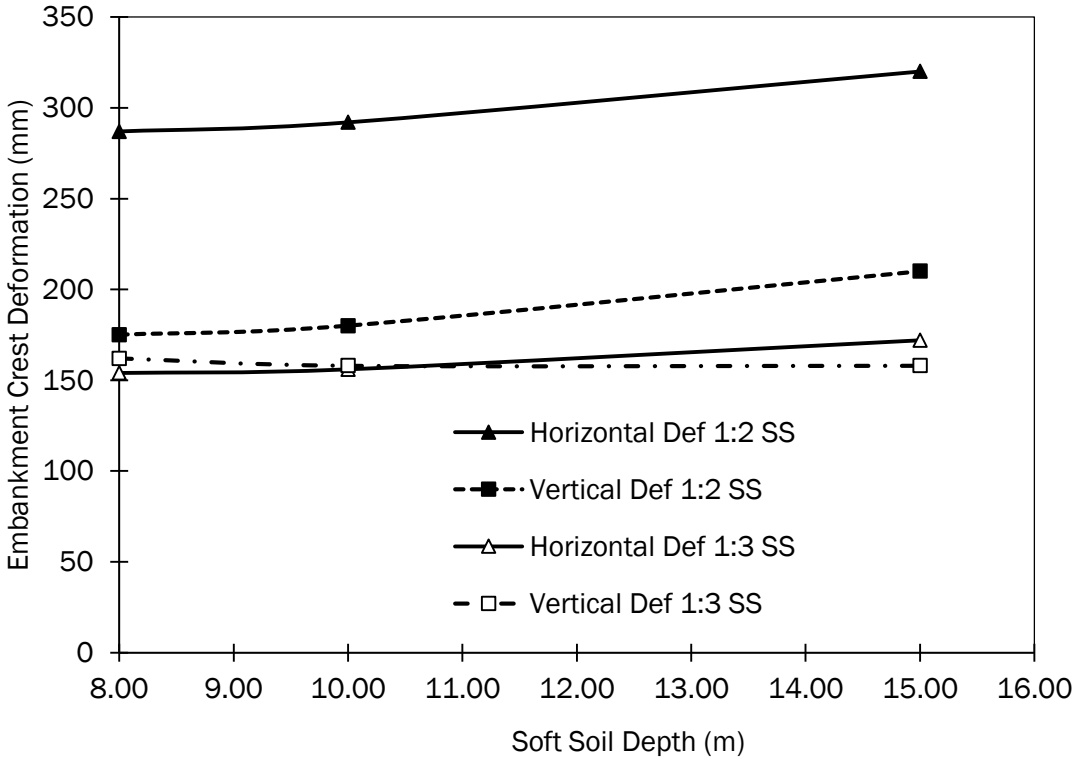

Figure 5.52 Surface deformations (mm) at the embankment crest for a range of soft soil layer depth (m) (H = 4.0m, J_{re} = 500kN/m and s = 3.0m)

The vertical deformation at the clear span between the embankment toe and the outer row pile cap edge remained constant for a range of soft soil layer depths, Figure 5.53, indicating that vertical deformations were independent of the depth of soft soil. Figures 5.52 and 5.54 suggested that the increase in depth of the soft soil layer had an insignificant effect on the lateral deformations of the embankment fill material outwards from the embankment centre towards the clear span between

the outer pile row and the toe. The result of which was that the loading on the clear span remained constant and the magnitude of the vertical deformations near the embankment toe remained constant.

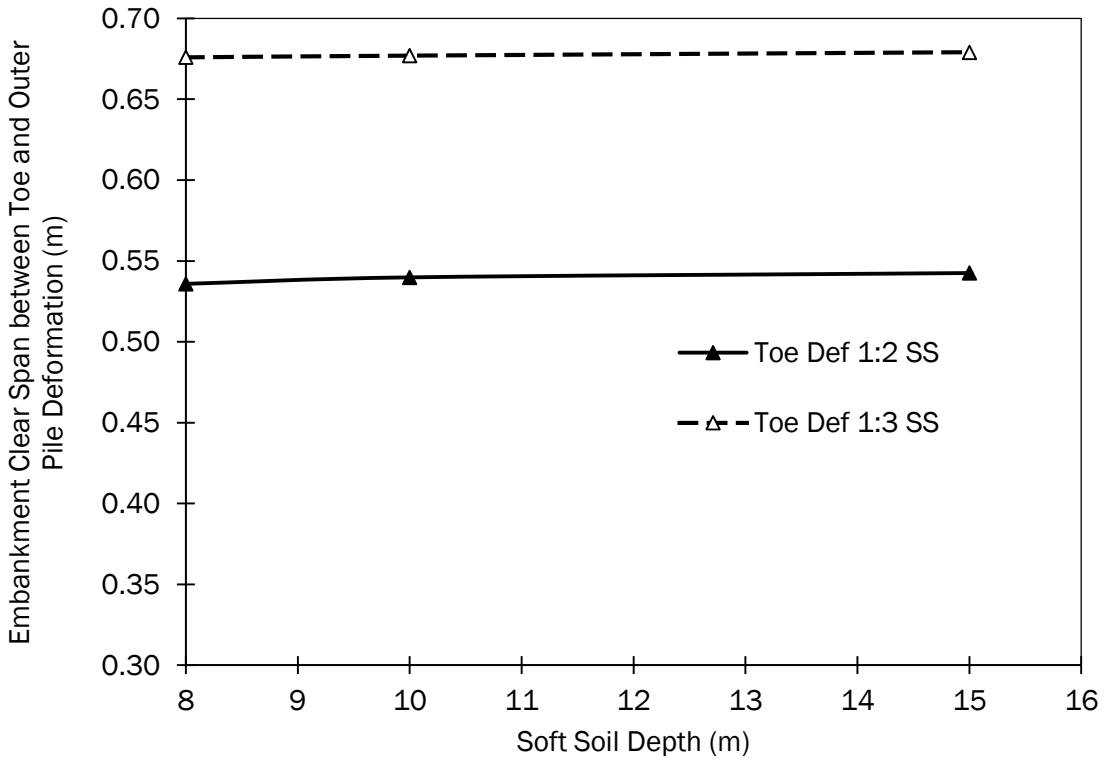

Figure 5.53 Vertical deformation (m) under the side slope between the embankment toe and outer row pile for a range of soft soil layer depth (m) (H = 4.0m, J_{re} = 500kN/m and s = 3.0m)

The magnitude of lateral deformation of the embankment fill material within the side slope of the embankment above the outer row pile was not significantly affected by a variation in the depth of the soft soil layer (Figure 5.54 (a) and (b)) for both cases of side slope steepness. The embankment model with a steeper side slope of 1V:2H, Figure 5.54 (b), recorded greater magnitudes of deformation in comparison to the embankment with a side slope of 1V:3H, Figure 5.54 (a). The lateral volumetric deformation above the outer row pile presented a similar insight into the stability of the embankment, Appendix C Figure C22.

The vertical deformation of the geosynthetic reinforcement remained reasonably constant for an increase in the depth of the soft soil layer, Figure 5.55.

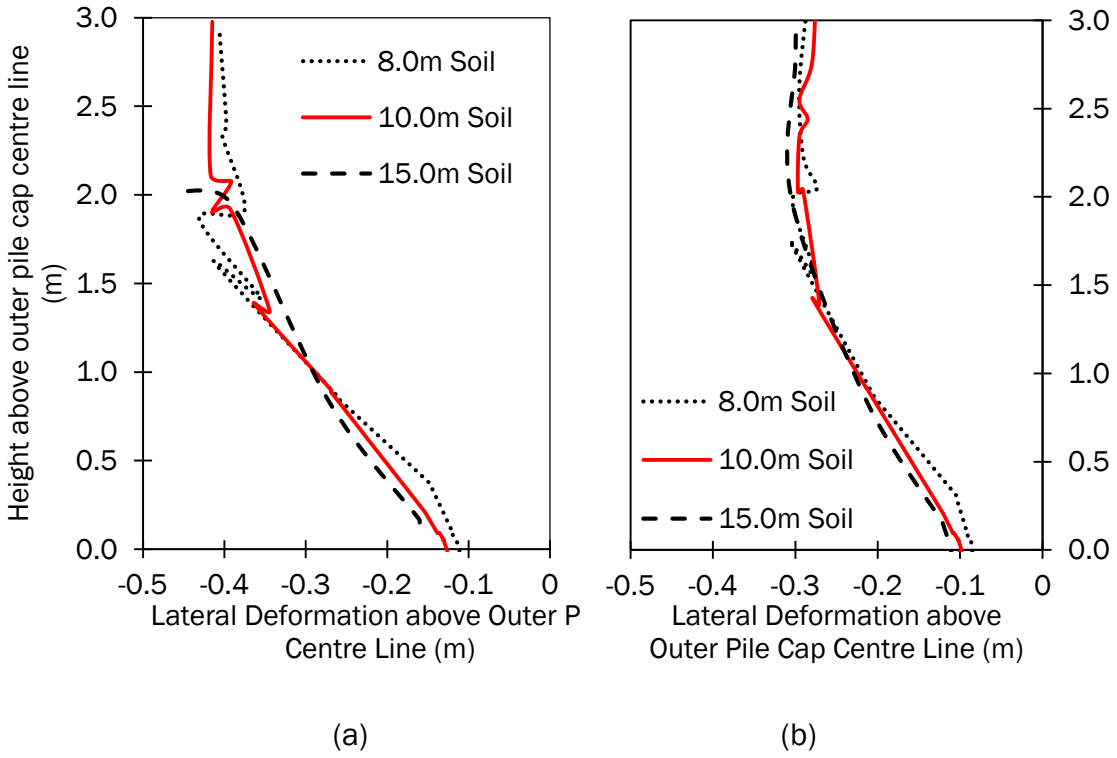

Figure 5.54 Lateral Deformation (LD) (m) within the side slope above the outer row pile centre line for a range of soft soil layer depth (m) for (a) a side slope of 1V:2H and (b) a side slope of 1V:3H (H = 4.0m, J_{re} = 500kN/m and s = 3.0m)

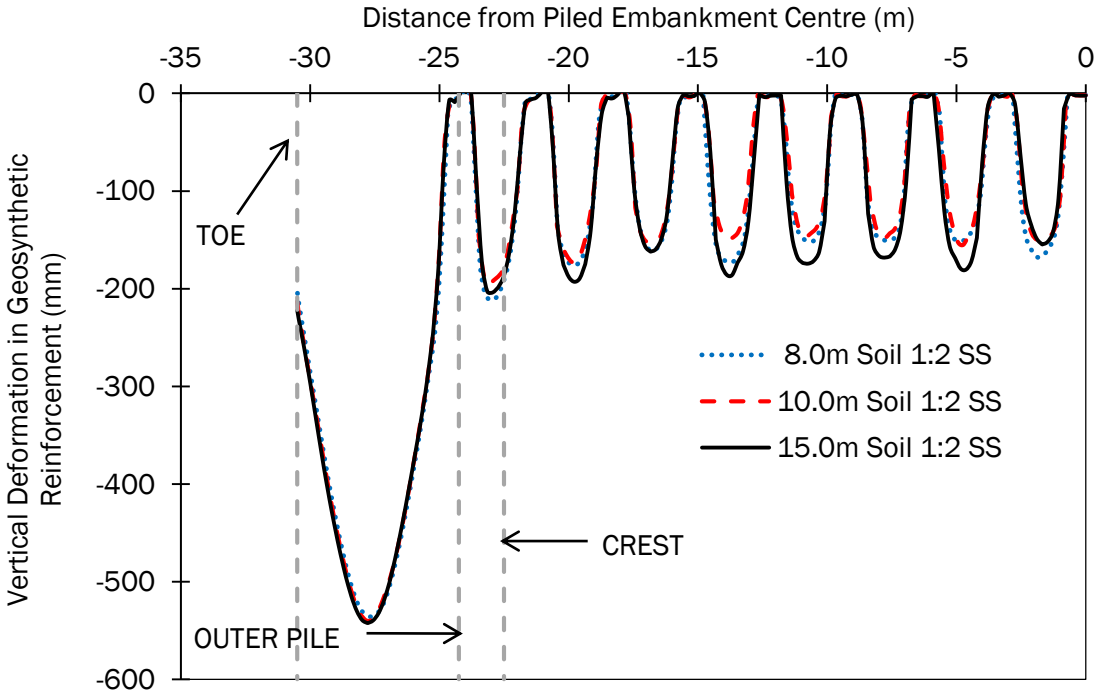

Figure 5.55 Vertical deformation of the geosynthetic reinforcement for a range of soft soil layer depth (m) (H = 4.0m, J_{re} = 500kN/m and s = 3.0m)

The horizontal deformation of the geosynthetic reinforcement showed only a slight increase as the depth of the soft soil layer increased, Figure 5.56. The axial tension in the reinforcement remained relatively constant for an increase in the depth of the soft soil, Figure 5.57. The maximum recorded axial tension in the reinforcement yielded an initial slight decrease as the depth of the soft soil layer increased (8m – 10m), the max tension remained constant for a further increase in soft soil depth (10m – 15m), Appendix C Figure C23.

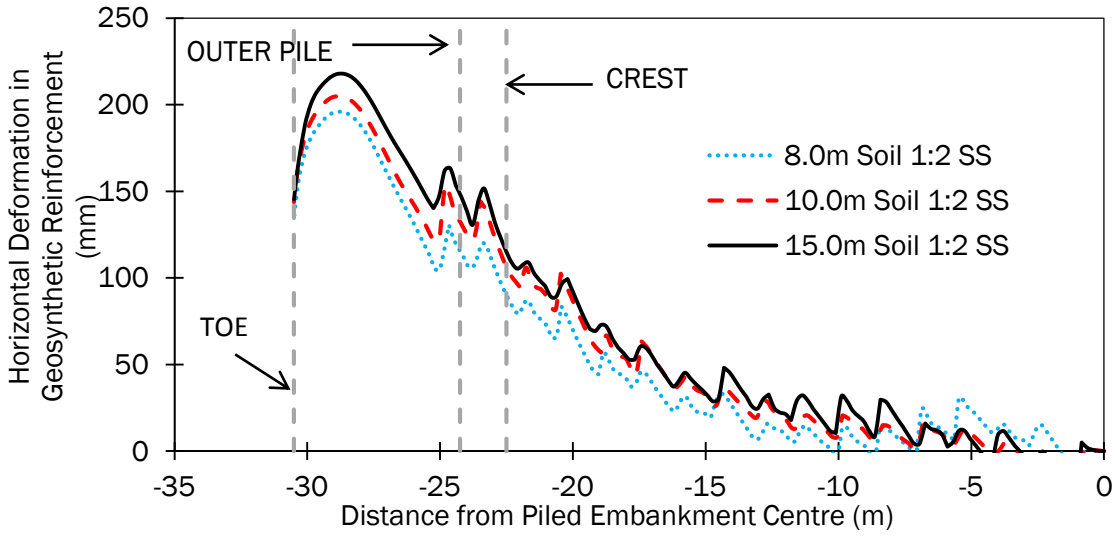

Figure 5.56 Horizontal deformations (mm) of geosynthetic reinforcement for a range of soft soil layer depth (m) (H = 4.0m, J_{re} = 500kN/m and s = 3.0m)

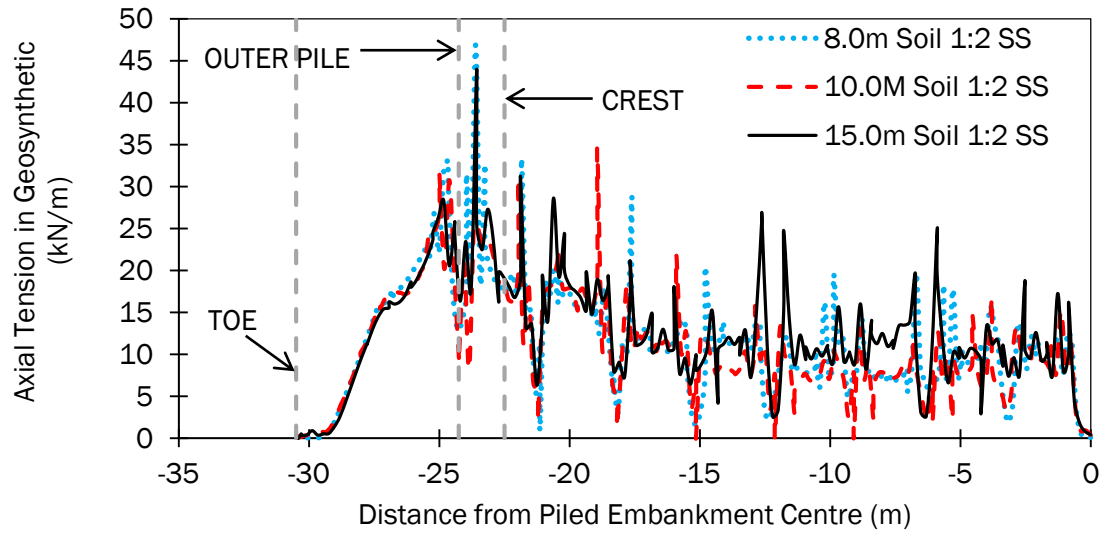

Figure 5.57 Axial tensions (kN/m) in the reinforcement for a range of soft soil layer depth (m) (H = 4.0m, J_{re} = 500kN/m and s = 3.0m)

The axial load on each pile in the pile group also increased marginally for an increase in the depth of the soft soil, Figure 5.58. As the depth of the soft soil increased, the axial load on each pile within the pile group remained relatively constant. The axial load on the outer row pile increased for an increase in the depth of the soft soil layer, Appendix C Figure C24.

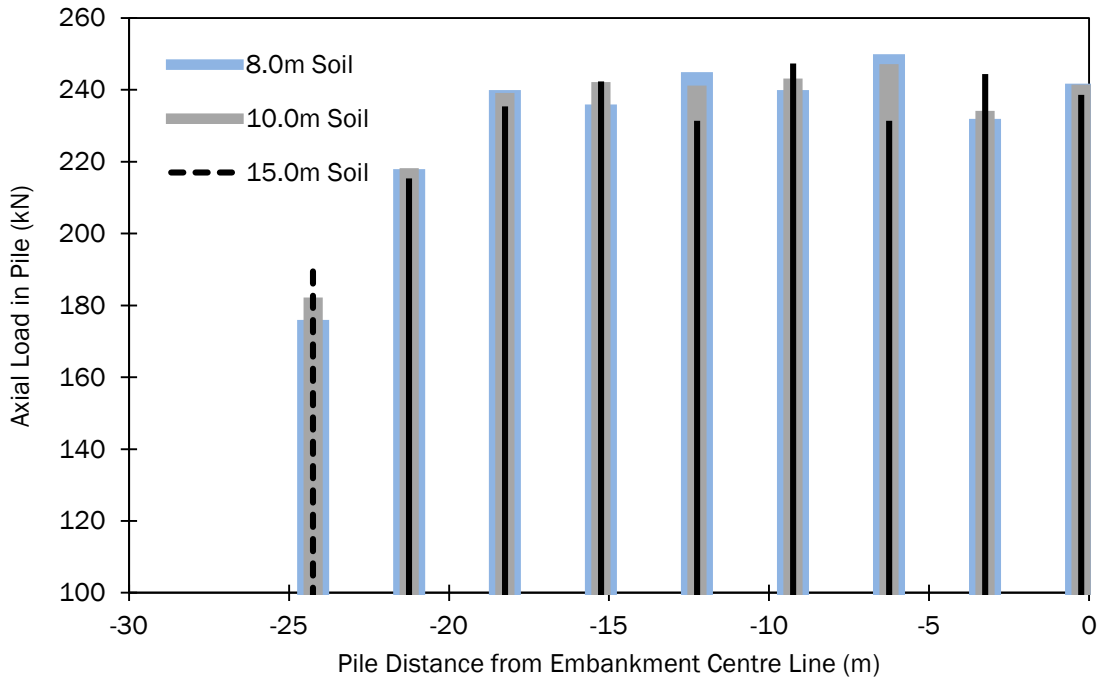

Figure 5.58 Axial loading (kN) on pile group under reinforced piled embankment for a range of soft soil layer depth (m) (H = 4.0m, J_{re} = 500kN/m and s = 3.0m)

The deflection at the pile head within the pile group increased in magnitude for an increase in the depth of the soft soil layer. As the depth of the soft soil increased, the rotational resistance of the pile decreased. For a range of soft soil depths the geometry of the embankment remained constant and as a result the maximum potential lateral thrust that could be developed remained constant. As the rotational resistance of each pile within the pile group decreased, the resultant lateral deflection at the pile head increased, Figure 5.59 and Appendix C Figure C25.

The bending moment of the piles within each pile group decreased for an increase in the depth of the soft soil layer. As the pile length increased to penetrate through the full depth of the soft soil layer the increase in the corresponding pile head deflection did not increase at the same rate and as a result the bending moment

induced in the pile for a given pile head deflection decreased. The decrease of the bending moment of the outer row pile (maximum bending moment recorded in pile group) was linear with depth, Appendix C Figure C26.

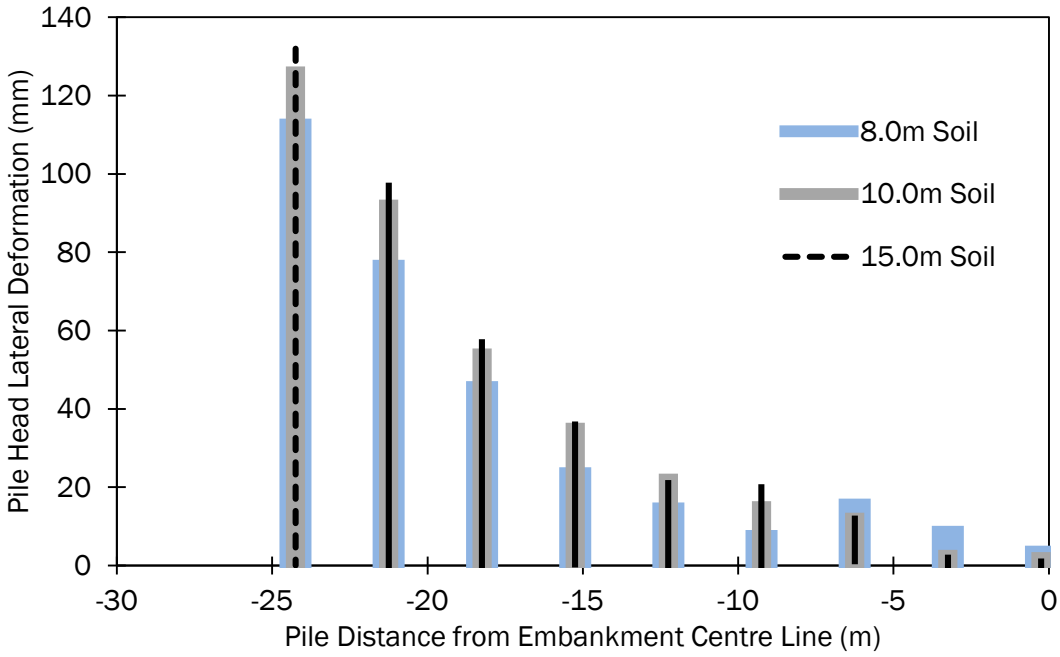

Figure 5.59 Lateral deflection (mm) at the pile head within a pile group under a reinforced piled embankment for a range of soft soil layer depth (m) (H = 4.0m, J_{re} = 500kN/m and s = 3.0m)

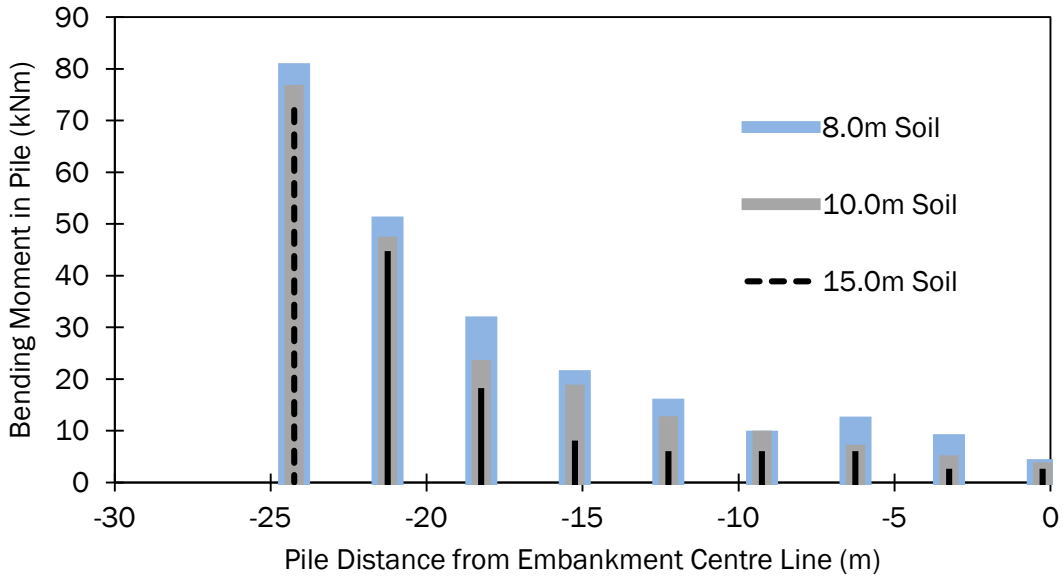

Figure 5.60 Bending moments (kNm) within a pile group for a range of soft soil layer depth (m) (H = 4.0m, J_{re} = 500kN/m and s = 3.0m)

The efficacy of the pile group increased marginally for an increase of the depth of the soft soil, Figure 5.61.

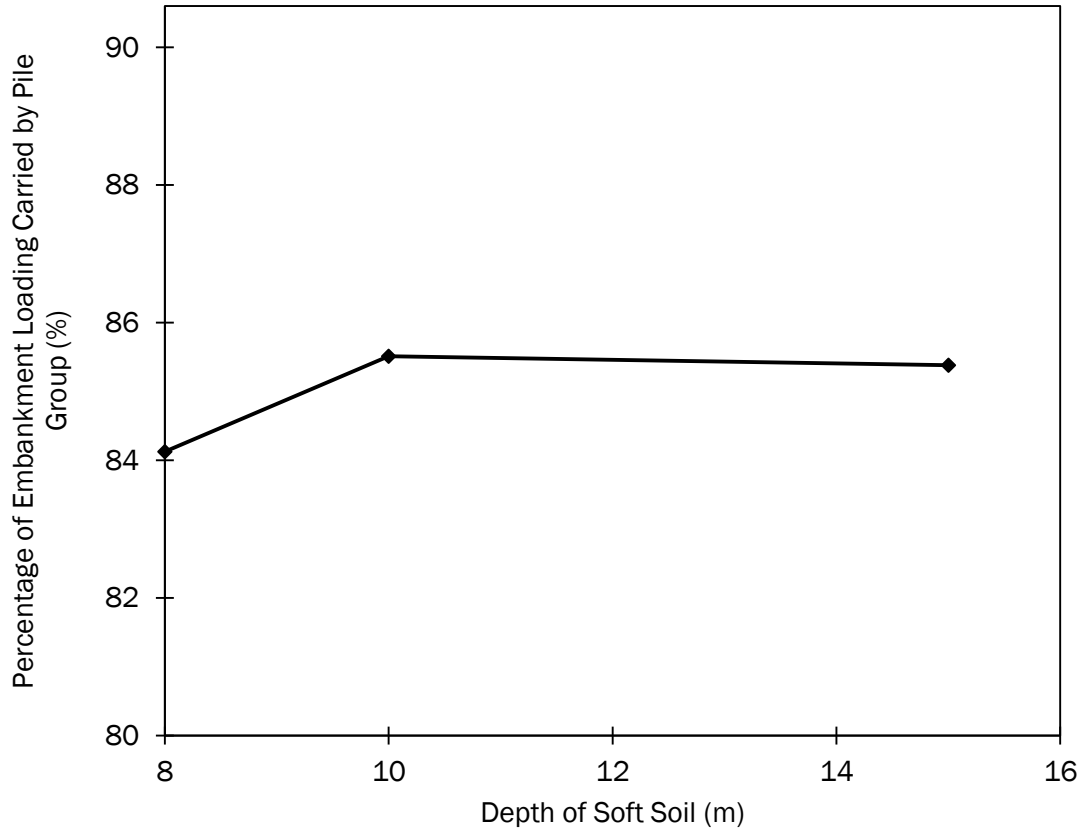

Figure 5.61 Pile group efficacy (%) for a range of soft soil layer depth (m) (H = 4.0m, J_{re} = 500kN/m and s = 3.0m)

The strain in the pile decreased marginally for an increase of the depth of the soft soil, Figure 5.62. As the bending moment in the pile decreased, Appendix C Figure C26, the strain in the pile also decreased.

The strain in the geosynthetic reinforcement also decreased marginally for an increase of the soft soil layer depth, Figure 5.62. An initial increase in the soft soil depth of 8.0m to 10.0m (25% increase) resulted in a 5% increase in the SCR (% increase of portion carried by pile to satisfy strain compatibility condition). A further increase of the soft soil depth from 10.0m to 15.0m (50% increases) yielded an insignificant increase of the SCR. The overall sensitivity of the SCR to a variation of the soft soil depth was relatively low.

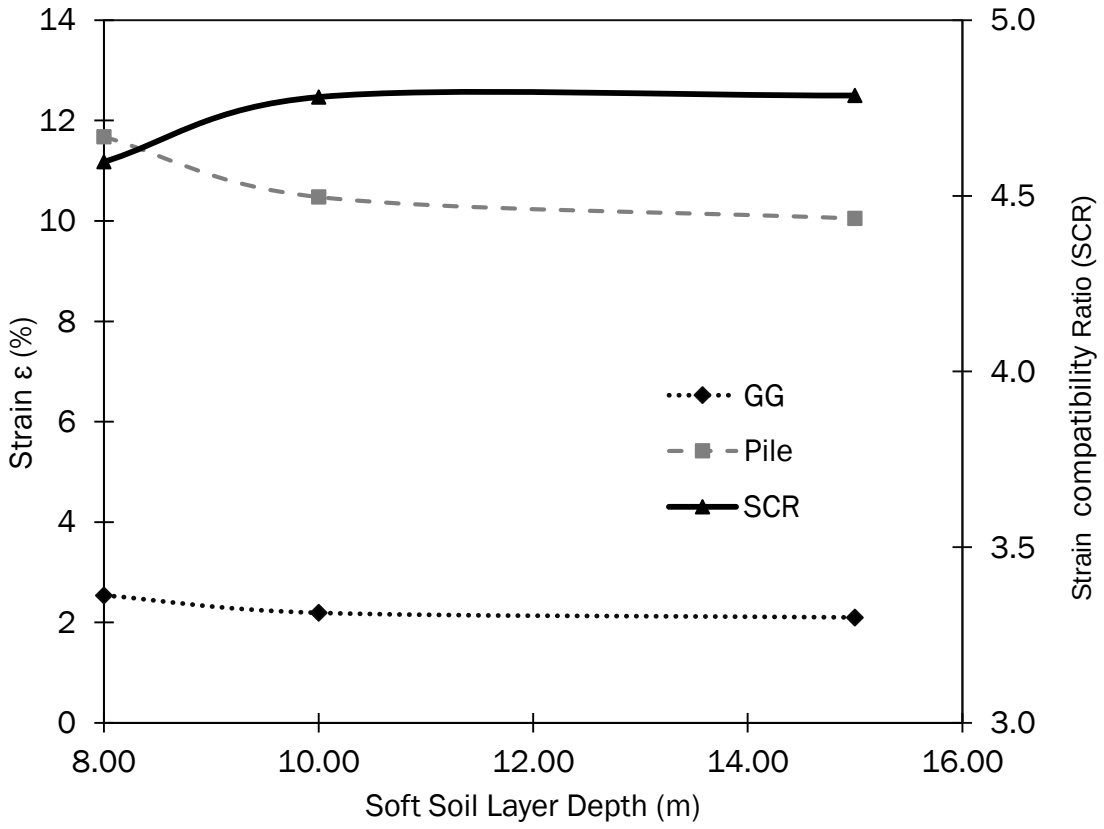

Figure 5.62 Strain in reinforcement and outer row pile and piled embankment Strain Compatibility Ratio (SCR) (%) for a range of soft soil layer depth (m) for a 1V:2H side slope (H = 4.0m, J_{re} = 500kN/m and s = 3.0m)

The depth of the soft soil layer, and consequently the length of the piles, had no effect on the overall stability of the geosynthetic reinforced piled embankment, Figure 5.63. The stability of the structure remained constant for both a range of soft soil depths and steepness of side slopes, Figure 5.63.

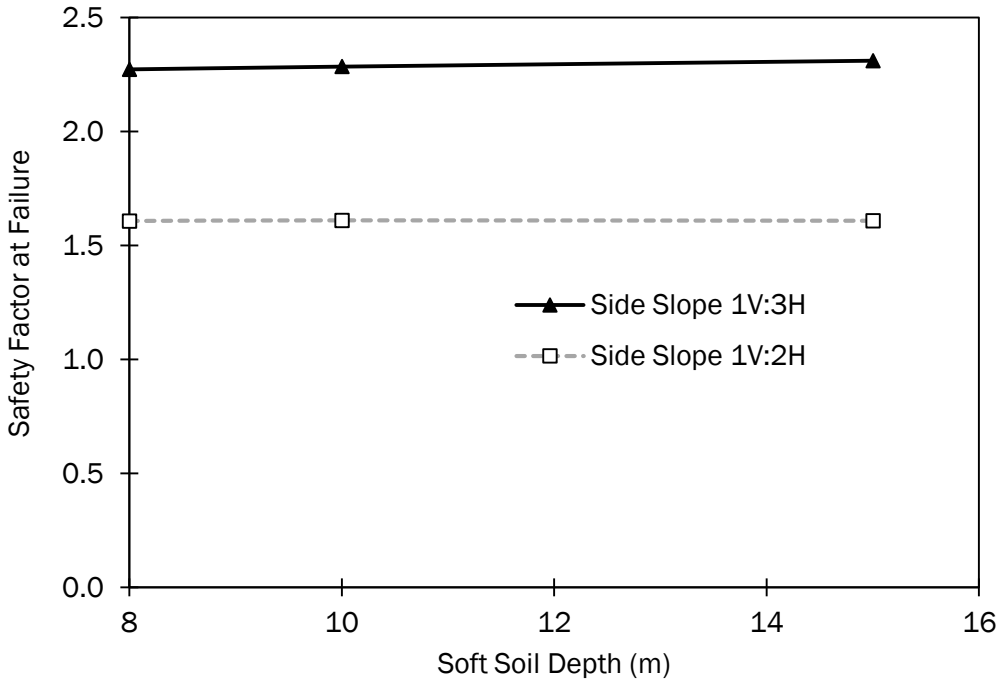

Figure 5.63 Safety factor at failure for a range of soft soil layer depth

5.7 Influence of Soft Soil Stiffness

The soft soil stiffness (Young's modulus of the soil) was ranged from 800kN/m^2 (peat) to 3333 kN/m^2 (normally consolidated clay). The magnitude of the vertical and horizontal deformations from the embankment crest origin decreased for an increase of the soft soil stiffness, Figure 5.64. The decrease in magnitude of the deformations was almost linear for all soft soil stiffness's and embankment side slope steepness's. The reduction in magnitude of the horizontal deformations recorded the greatest rate of reduction for an increase of soft soil stiffness. An increase of soft soil stiffness from 800kN/m^2 to 3333kN/m^2 resulted in a reduction of 69% and 49% in the horizontal and vertical deformations respectively. The horizontal deformations at the crest of the embankment decreased at a greater rate in comparison to the vertical deformation for all side slope steepness's. The reduction of the deformations converged as the soft soil stiffness increased, Figure 5.64, and suggested as the soil stiffness increased above approximately 3500 kN/m^2 the differential between deformational vectors and side slopes was marginal.

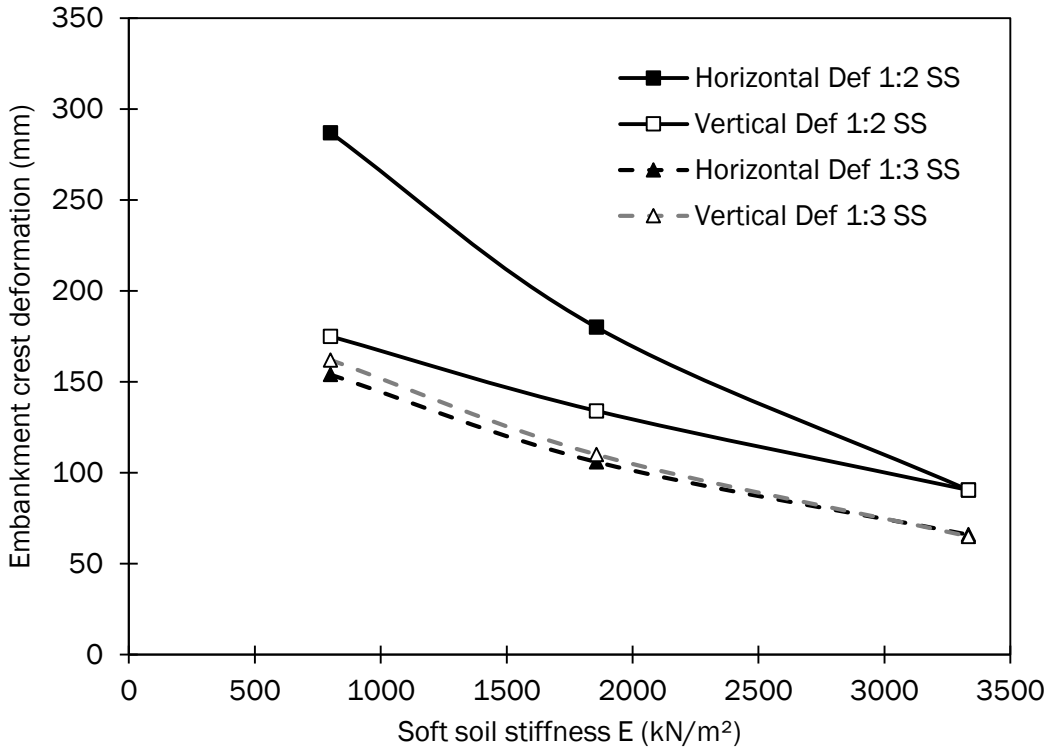

Figure 5.64 Surface deformations (mm) at the embankment crest for a range of soft soil stiffness E (kN/m²) (H = 4.0m, J_{re} = 500kN/m, s = 3.0m and a = 1.0m)

The deformation at the clear span between the toe of the embankment and the outer edge pile cap decreased for an increase of the soft soil stiffness, Figure 5.65. As the stiffness of the soft soil increased, the geosynthetic reinforcement which spanned unsupported from the embankment toe to the outer row pile cap edge underwent lower magnitude of vertical deformations. The decrease in magnitude of the vertical deformations near the toe of the embankment was almost linear.

The lateral deformation above the outer row pile cap decreased for an increase in the soil stiffness, Figure 5.66 (a) and (b). The horizontal deformations of the embankment decreased particularly within the side slope area as the deformations near the toe of the embankment reduced significantly and prevented a significant mobilization of lateral thrust within the embankment, Figure 5.65. The lateral volumetric deformation above the outer row pile within the side slope decreased for an increase of the soft soil stiffness, Appendix C Figure C27. As the stiffness of the soft soil increased, the support offered by the soil to the geosynthetic at the clear unsupported span increased. This increased the stability of the embankment side

slope and thus led to a reduction in magnitude of deformations at the clear span near the embankment toe, Figure 5.65, the embankment crest, Figure 5.64, and the above the outer row pile, Figure 5.66.

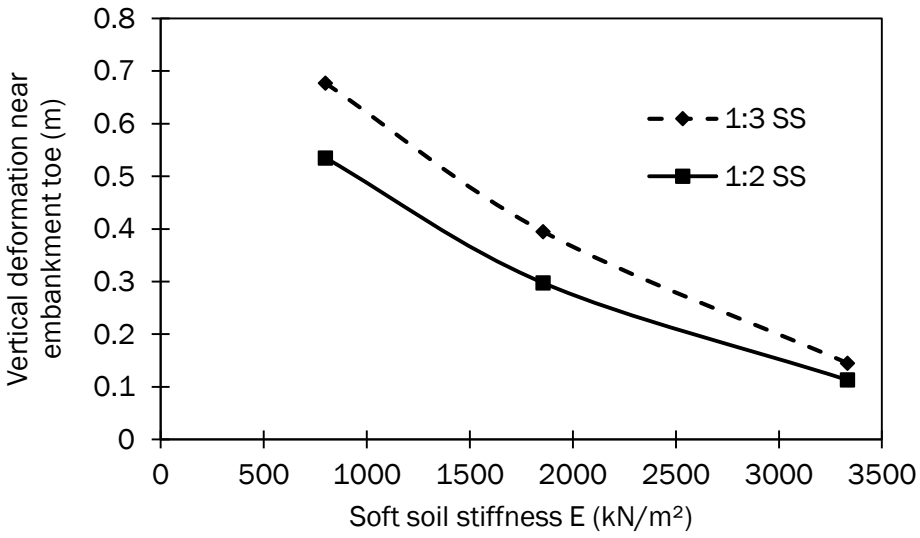

Figure 5.65 Vertical deformation (m) under the side slope between the embankment toe and outer row pile for a range of soft soil stiffness E (kN/m²) (H = 4.0m, J_{re} = 500kN/m and s = 3.0m)

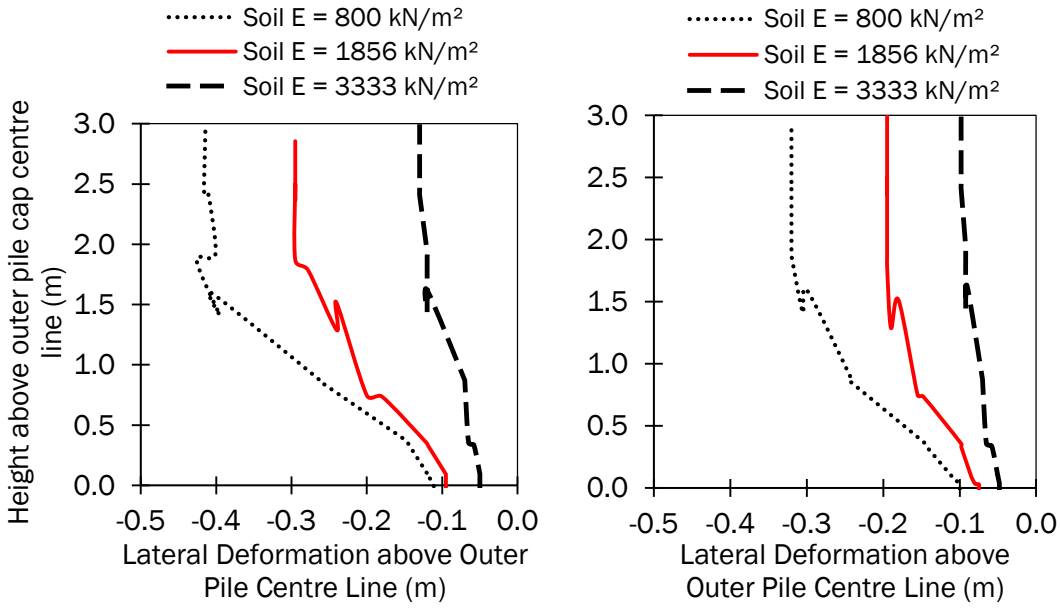

Figure 5.66 Lateral Deformation (LD) (m) within the side slope above the outer row pile centre line for a range of soft soil stiffness E (kN/m²) for (a) a side slope of 1V:2H and (b) a side slope of 1V:3H (H = 4.0m, J_{re} = 500kN/m and s = 3.0m)

The magnitude of the vertical deformations within the geosynthetic reinforcement decreased for an increase of the soft soil stiffness, Figure 5.67. At the clear span of the reinforcement between adjacent pile cap edges near the embankment centre the magnitude of the vertical deformations increased for a decrease of the soft soil stiffness. For both the 800kN/m^2 and 1856kN/m^2 soil stiffness cases, the shape of the vertical deformation of the reinforcement was parabolic in nature and suggested that the loading on the reinforcement was evenly distributed along its length. For the 3333kN/m^2 soft soil, the shape of the vertical deformation of the reinforcement near the embankment centre was not parabolic but prismoidal in shape and suggested that the reinforcement was offered considerable support from the underlying soil, Figure 5.67. An increase of soft soil stiffness from 800kN/m^2 to 1856kN/m^2 resulted in a decrease of the reinforcement vertical deformations between the adjacent pile caps of 29%, a further increase of the soft soil stiffness (1856kN/m^2 to 3333kN/m^2) resulted in a decrease in vertical deformations of 59%. The vertical deformation at the outer extremities of the embankment increased for a decrease of the soft soil stiffness, Figure 5.67 and 5.65. An increase of the soft soil stiffness increased the support offered to the unsupported length of the side slope and reduced both the embankment side slope horizontal deformations and the lateral thrust of the embankment fill.

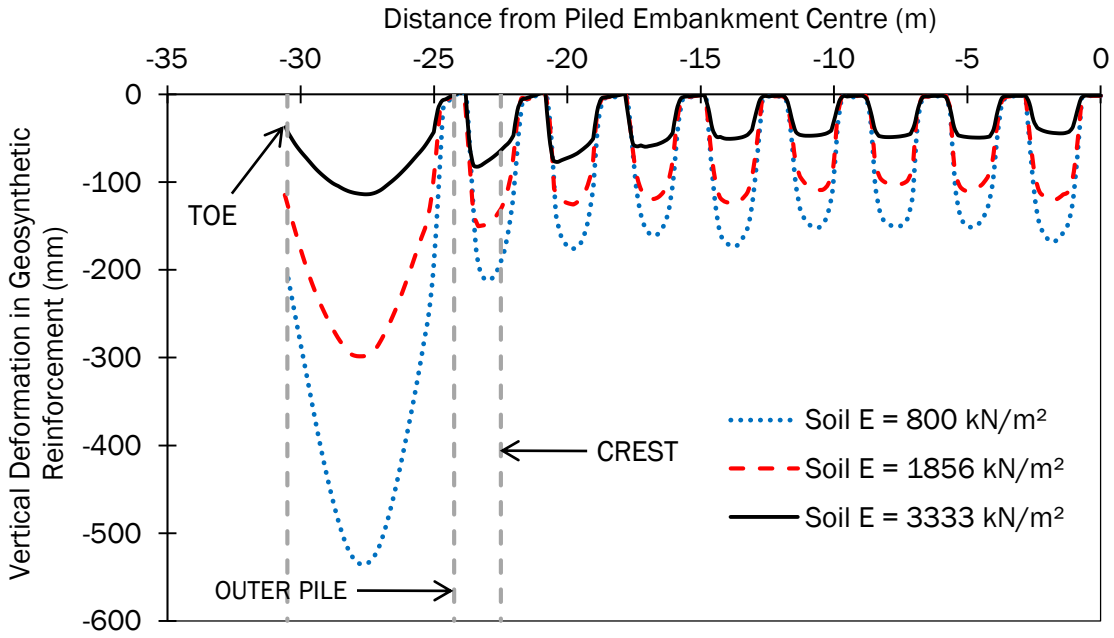

Figure 5.67 Vertical deformation of the geosynthetic reinforcement for a range of soft soil stiffness E (kN/m^2) (H = 4.0m, J_{re} = 500kN/m and s = 3.0m)

The horizontal deformation of the reinforcement increased for a decrease in the soft soil stiffness, Figure 5.68. As the stiffness of the soft soil decreased, the stability of the embankment structure decreased and resulted in the lateral thrust of the embankment mobilizing an increase in the magnitude of horizontal deformation of the embankment fill material. The maximum horizontal deformation of the geosynthetic reinforcement decreased by approximately 22% for an increase of soft soil stiffness by 132% (800kN/m^2 to 1856kN/m^2). A further increase of the soft soil stiffness of 79% (1856kN/m^2 to 3333kN/m^2) yielded a reduction in the maximum horizontal deformation of the reinforcement of 50%. As the soft soil decreased in stiffness, the vertical deformation of the reinforcement at the clear span between adjacent piles increased, Figure 5.67, an increase of the vertical deformation increased the interlocking effect of the reinforcement and the pile heads. The reinforcement deformed horizontally within the structure, the lower the stiffness of the soft soil, the greater the vertical deformations of the reinforcement in between adjacent piles, the greater the interlocking effect, the greater the jagged nature of the increase of the horizontal deformation that occurred above the pile group extent, Figure 5.68.

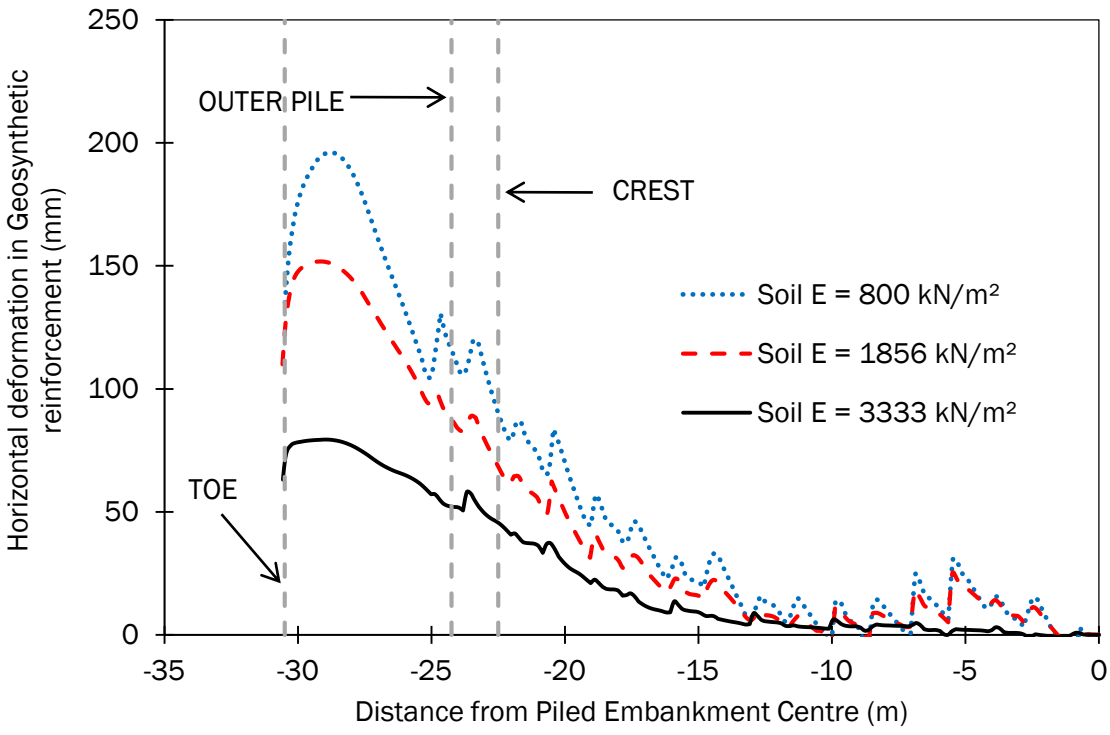

Figure 5.68 Horizontal deformations (mm) of geosynthetic reinforcement for a range of soft soil stiffness E (kN/m^2) (H = 4.0m, J_{re} = 500kN/m and s = 3.0m)

The axial tension acting in the geosynthetic reinforcement increased for a decrease of the soft soil stiffness, Figure 5.69. The maximum tension in the reinforcement increased linearly by 61% for a decrease of the soft soil stiffness (3333kN/m^2 to 800kN/m^2), Appendix C Figure C28. The axial tension in the reinforcement near the embankment centre increased for a decrease of soft soil stiffness. The lower the stiffness of the soft soil, the lower the magnitude of the support offered by the soil to the reinforcement, the greater the loading to be supported by the reinforcement, the greater the tension in the reinforcement.

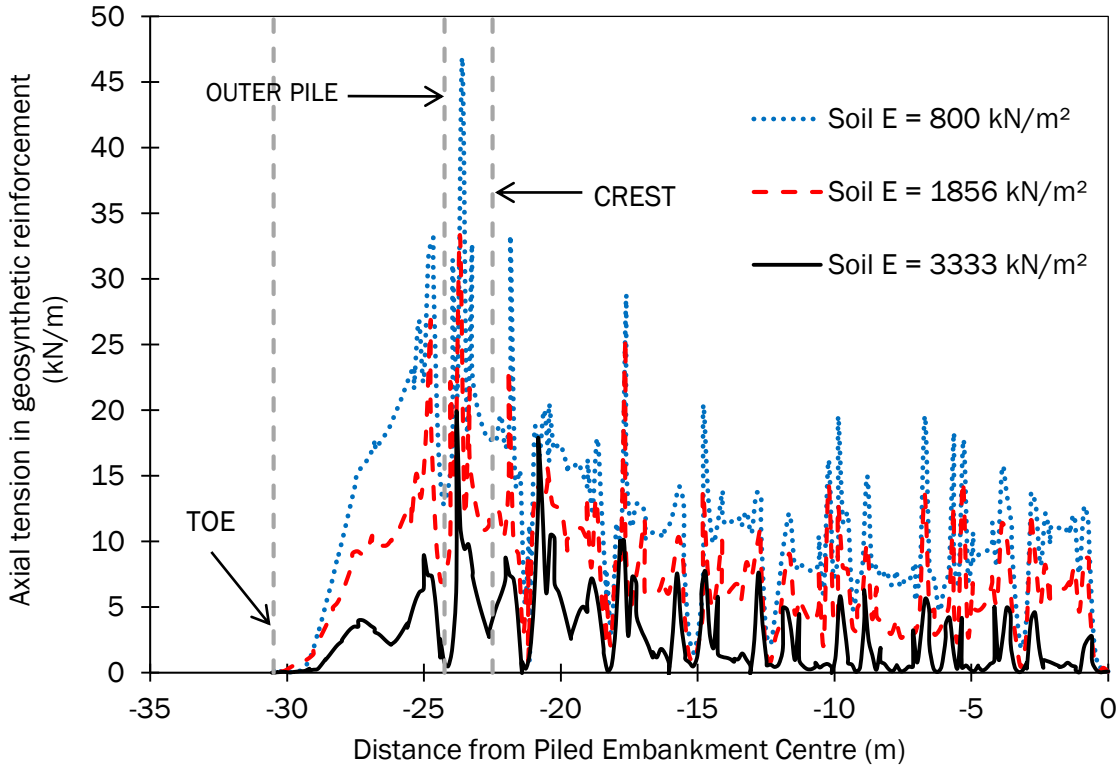

Figure 5.69 Axial tensions (kN/m) in the reinforcement for a range of soft soil stiffness E (kN/m^2) (H = 4.0m, J_{re} = 500kN/m and s = 3.0m)

The increase of axial load on the pile group for a decrease of the soil stiffness was insignificant within the pile group, Figure 5.70. The outer row pile axial loading increased for a decrease in soil stiffness, Appendix C Figure C29.

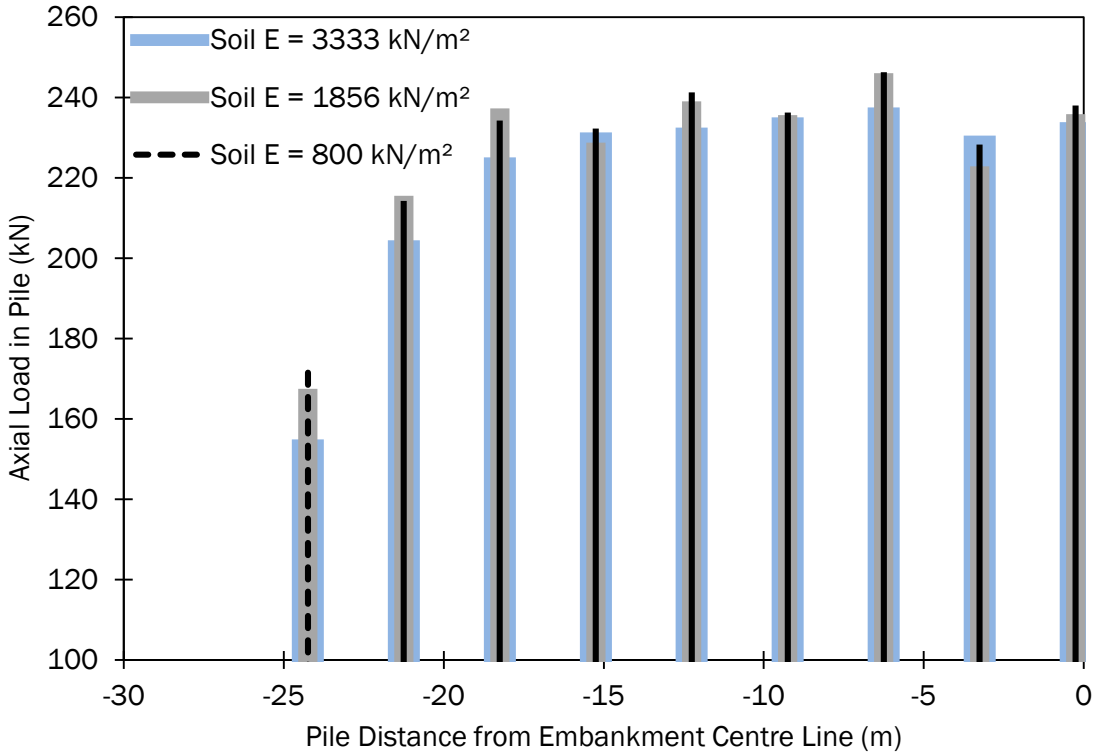

Figure 5.70 Axial loading (kN) on pile group under reinforced piled embankment for a range of soft soil stiffness E (kN/m²) (H = 4.0m, J_{re} = 500kN/m and s = 3.0m)

The lateral deformation at the pile head increased for a decrease of the soil stiffness, Figure 5.71 and Appendix B Figure B30. As the stiffness of the soil increased, the support offered by the soil along the shaft length of the pile increased, resulting in an increase of the bending stiffness of the pile soil structure and lower magnitudes of pile head deflections. As the stiffness of the soft soil decreased, the total lateral load resistance capacity of the pile group decreased and each pile within the group recorded an increase in magnitude of the pile head deflection and the maximum bending moment, Figure 5.71 and Figure 5.72. Pile head deflections and bending moments were recorded at all piles within the pile group extent. The maximum bending moments at the outer row pile increased by 51% for a 76% decrease of the soft soil stiffness, Appendix B Figure B31.

The efficacy of the pile group decreased for an increase of soft soil stiffness, Figure 5.73. As the stiffness of the soft soil increased from 800kN/m² to 3333kN/m² the pile group efficacy decreased marginally.

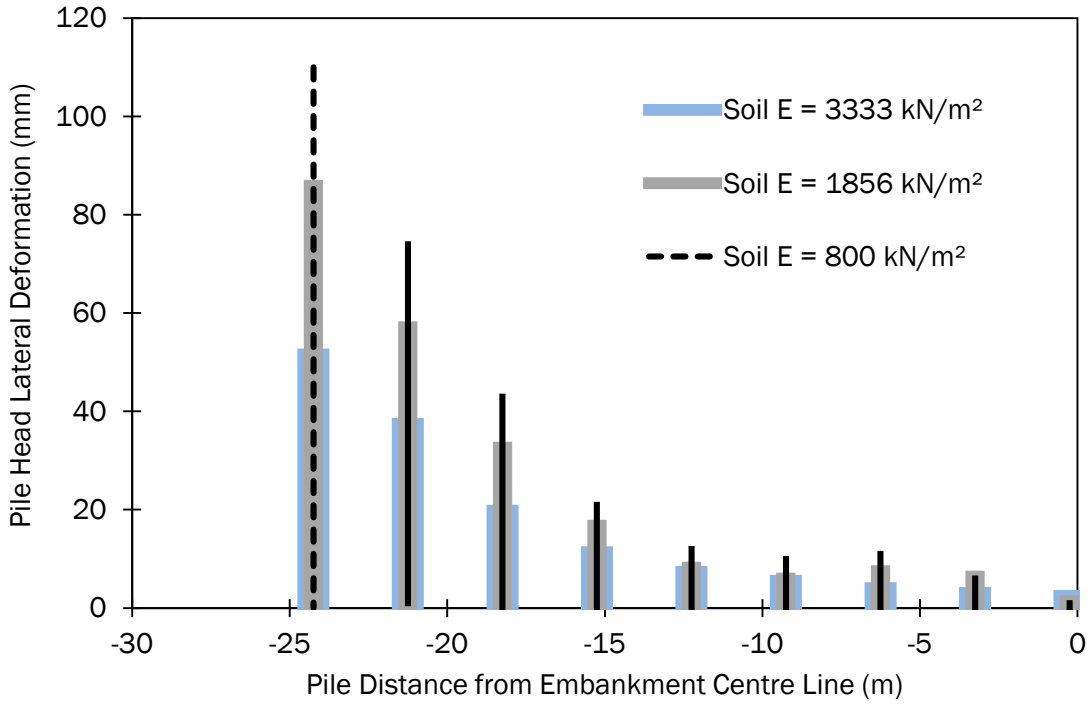

Figure 5.71 Lateral deflection (mm) at the pile head within a pile group under a reinforced piled embankment for a range of soft soil stiffness E (kN/m²) (H = 4.0m, J_{re} = 500kN/m and s = 3.0m)

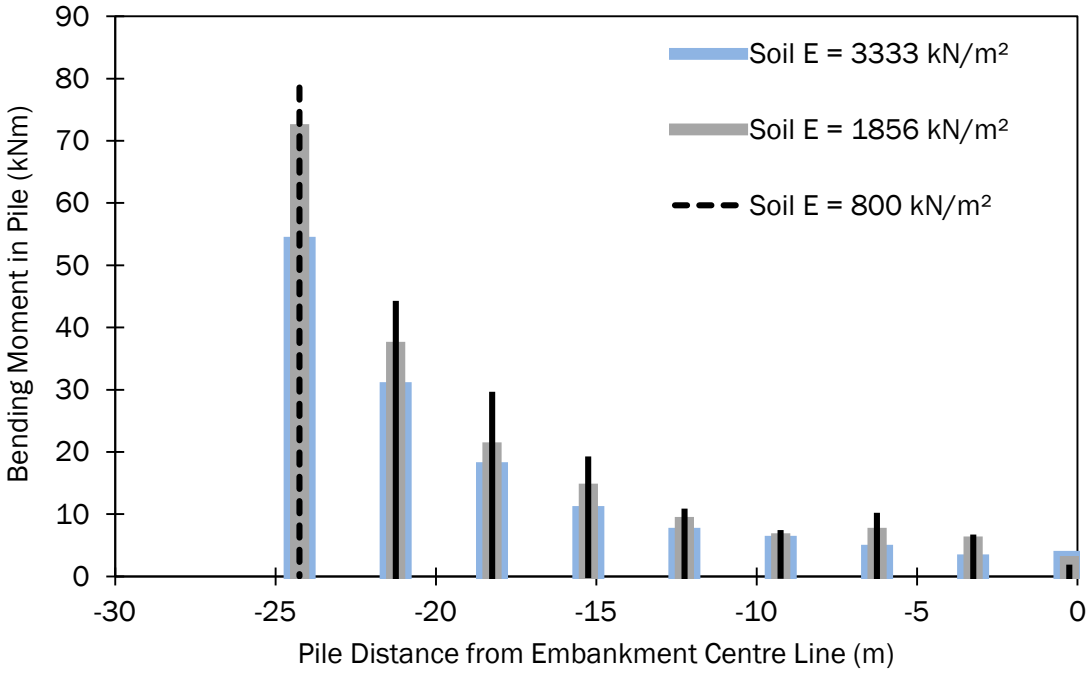

Figure 5.72 Bending moments (kNm) within a pile group for a range of soft soil stiffness E (kN/m²) (H = 4.0m, J_{re} = 500kN/m and s = 3.0m)

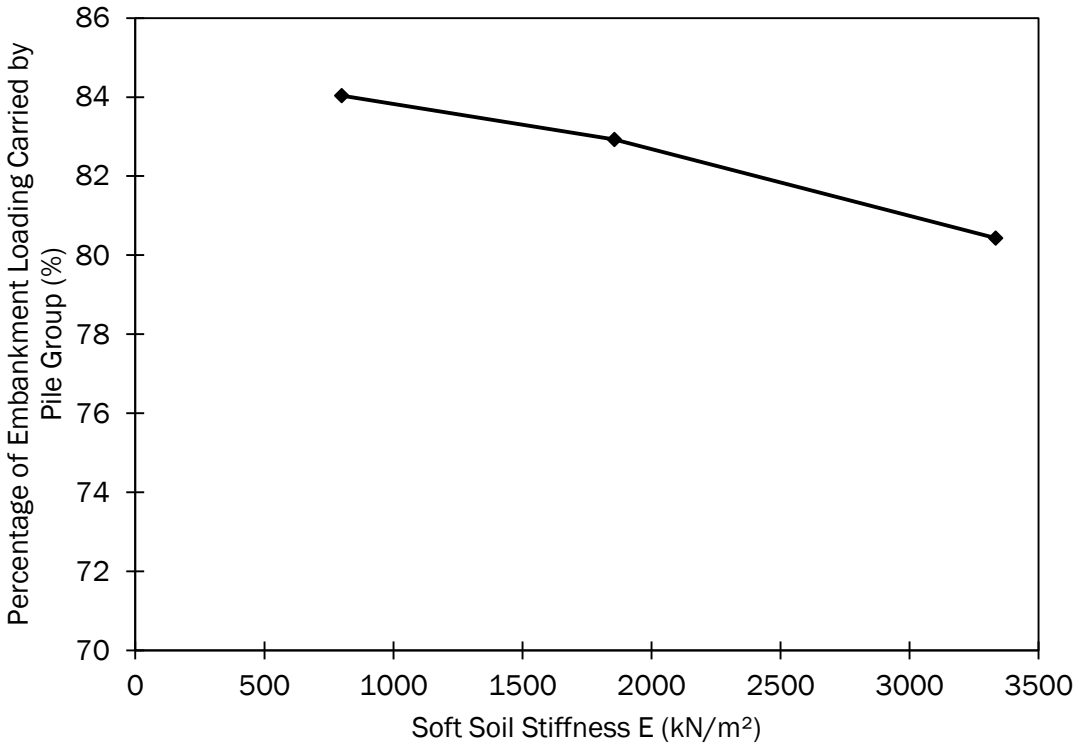

Figure 5.73 Pile group efficacy (%) for a range of soft soil stiffness E (kN/m²) (H = 4.0m, J_{re} = 500kN/m and s = 3.0m)

The strain in the reinforcement decreased for an increase of the soft soil stiffness, Figure 5.74. As the stiffness of the soft soil layer increased from 800kN/m² to 1856kN/m², the reinforcement was subjected to 41% lower magnitude of strains. As the support offered to the reinforcement by the soft soil increased and thus reduced the magnitude of the vertical and horizontal deformations and recorded lower tensions/strains in the reinforcement. The reduction of the strain in the reinforcement was almost linear for an increase of the soft soil stiffness. The strain in the pile decreased for an increase of the soft soil stiffness, Figure 5.74. As the stiffness of the soft soil increased, the combination of the pile soil interaction increased the pile group to withstand lateral deformation and thus the pile was subjected to lower magnitudes of bending moments (pile strain). An initial increase of the soft soil stiffness from 800kN/m² to 1856kN/m² resulted in a reduction of the pile strain of 19%. A further increase of the soft soil stiffness from 1856 kN/m² to 3333kN/m² resulted in a further reduction of the pile strain of 29%. The strain compatibility ratio (SCR) increased for an increase of the soft soil stiffness, Figure

5.74. As the stiffness of the soft soil increased, the support provided to the pile group by the soil underlying the embankment increased and enabled the pile group to resist the lateral thrust of the embankment structure to a greater extent. As the soft soil stiffness increased the pile group attracted a greater portion of the embankment structures lateral loading in comparison to the reinforcement.

An increase in soft soil stiffness resulted in no improvement in stability for the 1V:2H embankment and a marginal increase for the 1V:3H side slope.

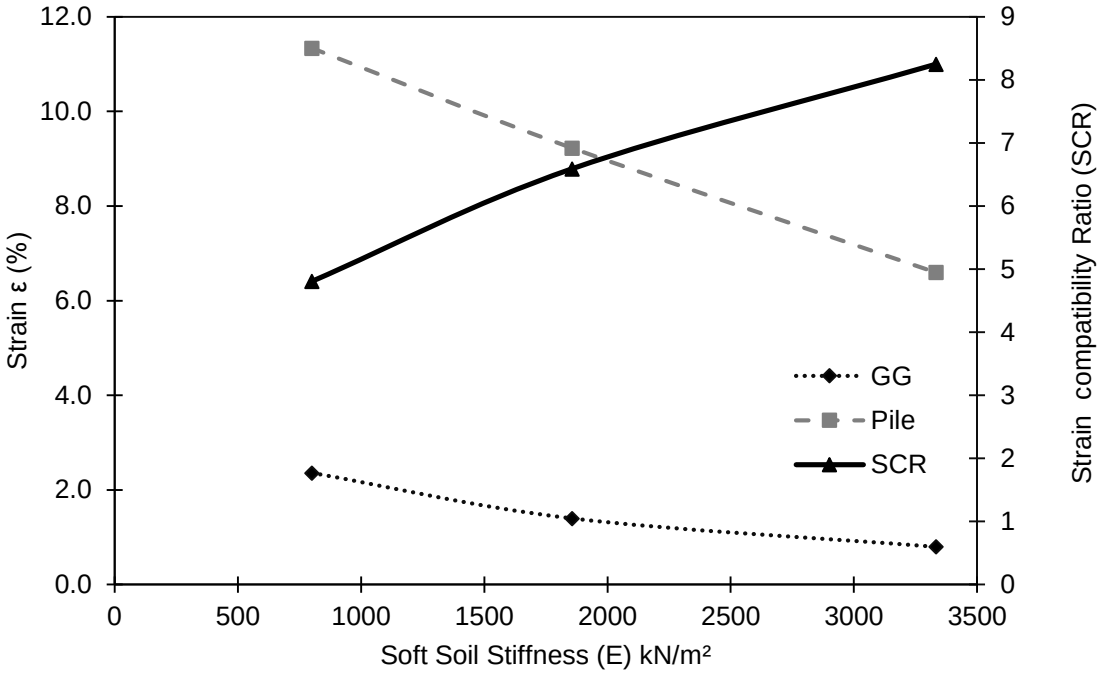

Figure 5.74 Strain in reinforcement and outer row pile and piled embankment Strain Compatibility Ratio (SCR) (%) for a range of soft soil stiffness E (kN/m²) for a 1V:2H side slope (H = 4.0m, J_{re} = 500kN/m and s = 3.0m)

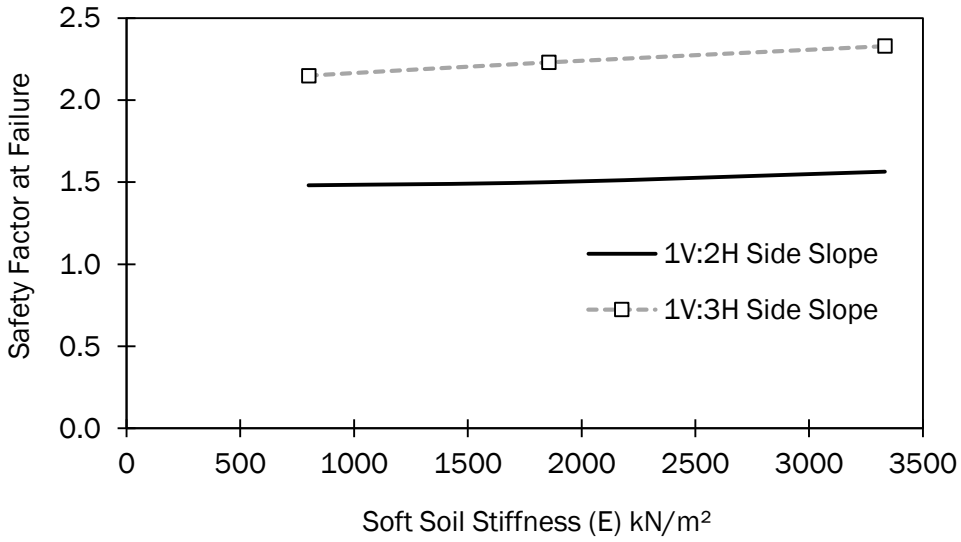

Figure 5.75 Safety factor at failure for a range of soft soil stiffness

5.8 Influence of Embankment Height

The embankment height was ranged from 2.0m to 8.0m. The magnitude of both the vertical and horizontal deformation that occurred at the embankment crest increased for an increase of the embankment height, Figure 5.76. The embankment with a side slope of 1V:2H recorded the greatest rate of increase in deformations for an increase in the embankment height. An initial increase in the embankment height from 2.0m to 4.0m resulted in a 204% increase in the horizontal deformation and a 70% increase in the vertical deformation. A further increase of the embankment height from 4.0m to 8.0m resulted in an increase in the horizontal deformation of 210% and a 337% increase in vertical deformation. The horizontal deformation for the 1V:2H side slope increased in an almost linear fashion for a linear increase of embankment height. The rate of increase in the vertical accelerated after an increase of the embankment height greater than 4.0m. The rate of increase in both deformations for the two side slope cases suggested that a divergence in the magnitudes of the deformations occurred. For a 2.0m embankment height with a 1V:2H side slope, the horizontal deformation was 100% greater in magnitude compared to the 1V:3H side slope. An increase of embankment height from 2.0m to 8.0m resulted in the 1V:2H side slope case recording an increase in differential of the horizontal deformation magnitudes from 100% to 255%.

The vertical deformation at the clear span between the embankment toe and the edge of the outer row pile cap increased with height, Figure 5.77. The vertical deformation increased at a linear rate for both cases of side slope steepness's.

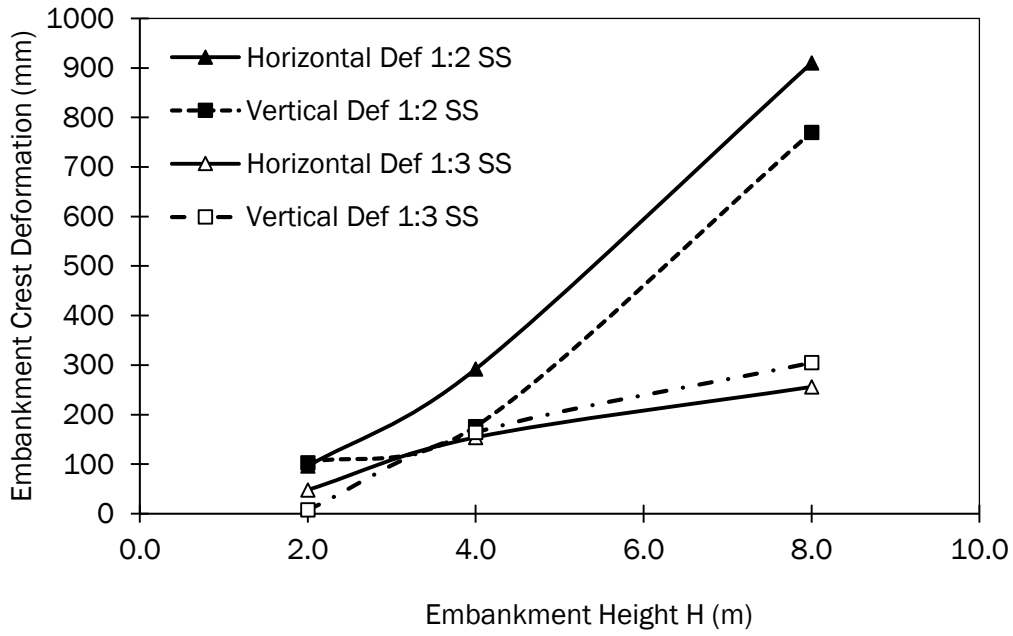

Figure 5.76 Surface deformations (mm) at the embankment crest for a range of embankment height (m) (a = 1.0m, J_{re} = 500kN/m and s = 3.0m)

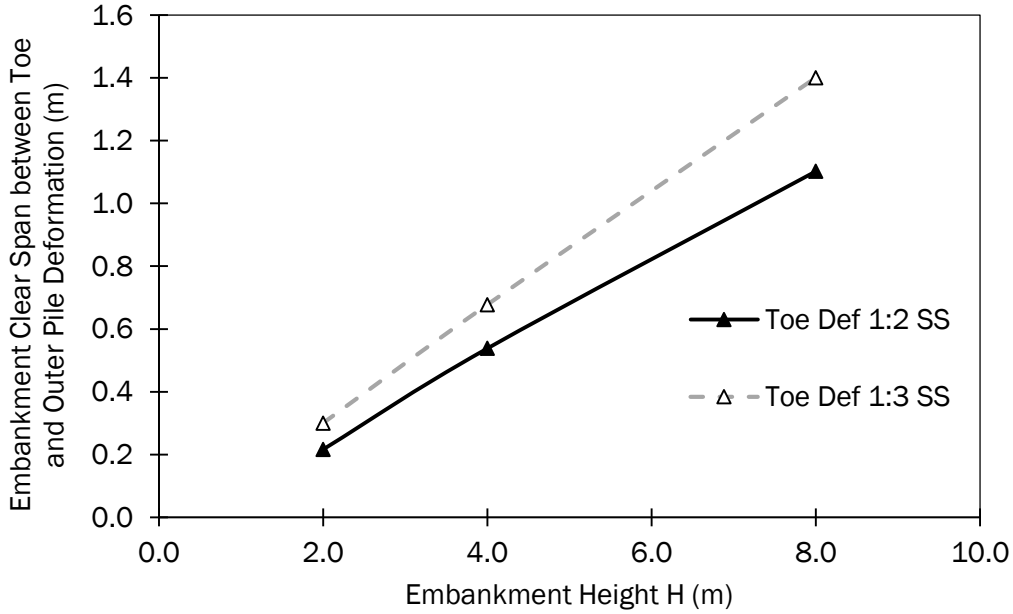

Figure 5.77 Vertical deformation (m) under the side slope between the embankment toe and outer row pile for a range of embankment height (m) (a = 1.0m, J_{re} = 500kN/m and s = 3.0m)

The lateral deformation within the side slope of the embankment above the outer row pile increased for an increase of the embankment height, Figure 5.78 (a) and (b). The lateral thrust acting outward from the centre of the embankment is directly proportional to the square of the embankment height. The magnitude of the lateral deformation increased in the same linear trend. The lateral volumetric deformation (Appendix C Figure C32) increased linearly for an increase in the embankment height. Appendix C Figure C32 suggested that the stability within the embankment side slope remained constant for an increase in the embankment height. The data from the lateral deformation above the outer row pile suggested that the height of the embankment did not reduce the stability of the embankment.

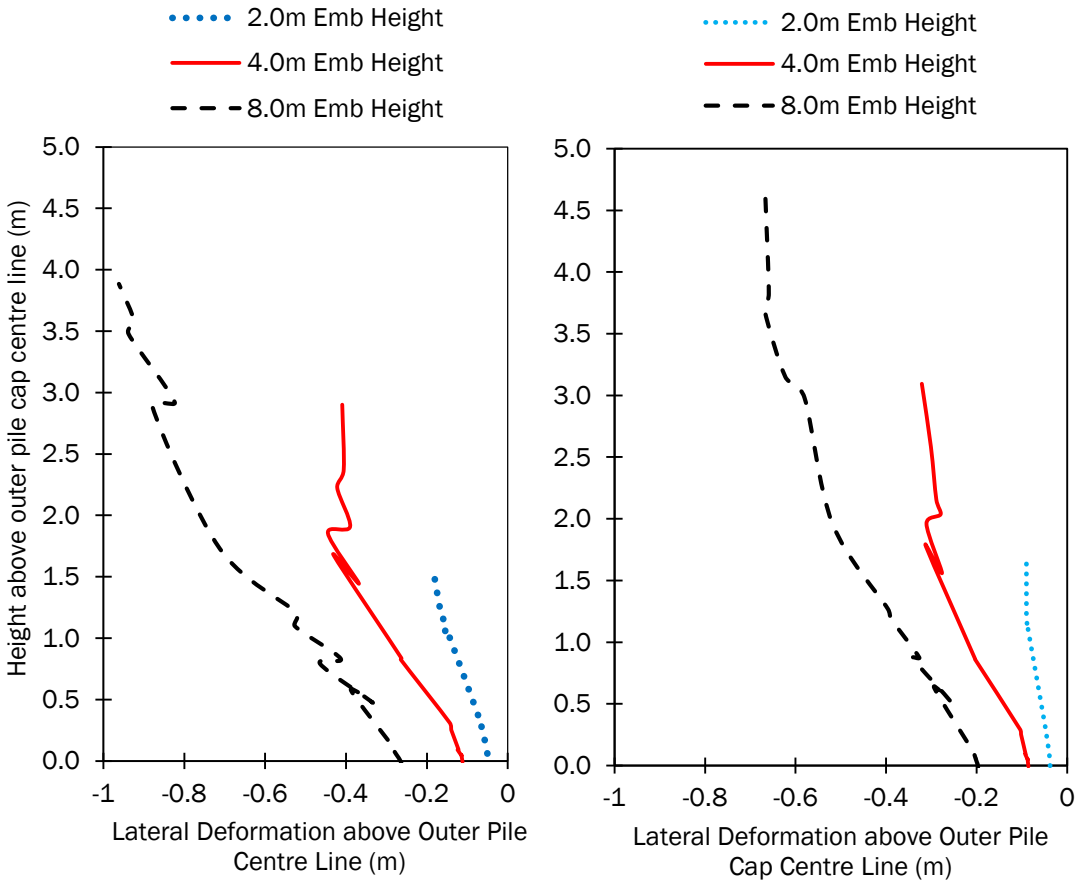

(a) (b)

Figure 5.78 Lateral Deformation (LD) (m) within the side slope above the outer row pile centre line for a range of embankment height (m) for (a) a side slope of 1V:2H and (b) a side slope of 1V:3H (a = 1.0m, J_{re} = 500kN/m and s = 3.0m)

The vertical deformations of the geosynthetic reinforcement increased for an increase in the embankment height, Figure 5.79. An increase of the embankment height from 2.0m to 8.0m resulted in an approximate 29% increase of the vertical deformation near the centre of the embankment. The vertical deformation at the clear unsupported span between the toe of the embankment and the outer row pile cap edge for an increase of the embankment height from 2.0m to 8.0m increased by 409%. The rate of increase in the vertical deformation across the width of the embankment structure for an increase in the embankment height was greatest near the toe of the embankment.

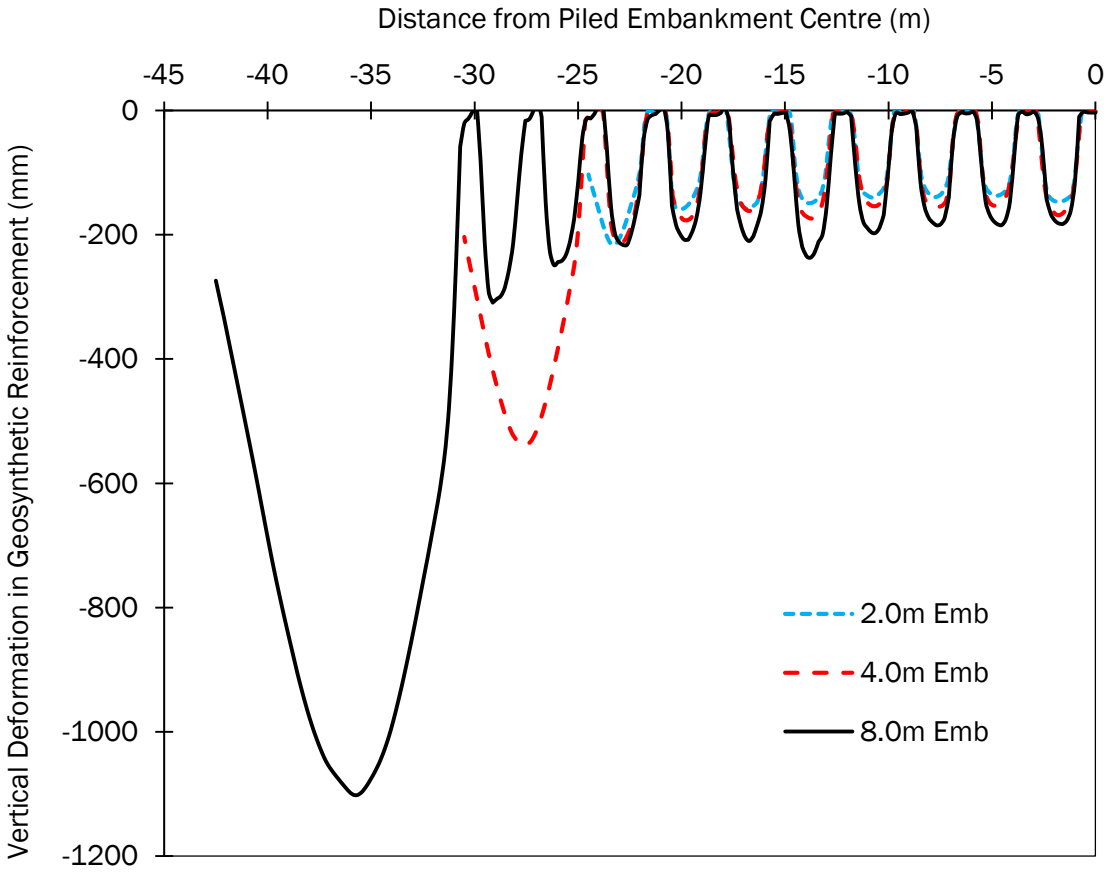

Figure 5.79 Vertical deformation of the geosynthetic reinforcement for a range of embankment height (m) (a = 1.0m, J_{re} = 500kN/m and s = 3.0m)

The horizontal deformations of the geosynthetic reinforcement increased for an increase in the embankment height (m), Figure 5.80. The magnitude of the horizontal deformation increased from zero at the embankment centre where the pullout force from the lateral thrust was insignificant. An increase of the

embankment height from 2.0m to 4.0m resulted in an increase in the maximum recorded horizontal deformation in the reinforcement of 334%. A further increase of the embankment height from 4.0m to 8.0m resulted in a further 344% increase in the magnitude of the maximum horizontal deformation. The result of which suggested that the embankment height yielded an almost perfectly linear increase in the horizontal deformation within the embankment structure. The increase in the embankment height did not mobilize a failure mechanism/functional shift in the linear trending increase of the horizontal deformation for an increase of the embankment height.

The increase of the embankment height yielded an increase in the magnitude of the horizontal deformation. As the height of the embankment increased, Figure 5.80, the location of the maximum recorded horizontal deformation moved from a location above the pile group itself (between the outer row pile and the embankment centre) to a location between the unsupported clear span from the embankment toe to the outer row pile cap edge. This suggested that as the embankment height increased, the increasing load from the side slope at the unsupported clear span between the outer pile row edge and the embankment toe resulted in significant vertical and horizontal deformation of the reinforcement.

The axial tension in the reinforcement increased for an increase of embankment height, Figure 5.81 and Appendix C Figure C33. An initial increase of the embankment height of 2.0m to 4.0m (100% increase) resulted in an increase of maximum axial tension of 123%. A further increase of embankment height from 4.0m to 8.0m yielded a further 74% increase. The axial tensions developed close to the centre of the embankment structure increased at a lesser rate than those at the outer extremities of the embankment structure. As a result of arching in the embankment fill the axial tensions are reasonably constant at the embankment centre for all embankment heights, the greater maximum axial tensions recorded near the crest location for greater embankment height was due to the increased lateral thrust from the greater embankment height, Figure 5.81.

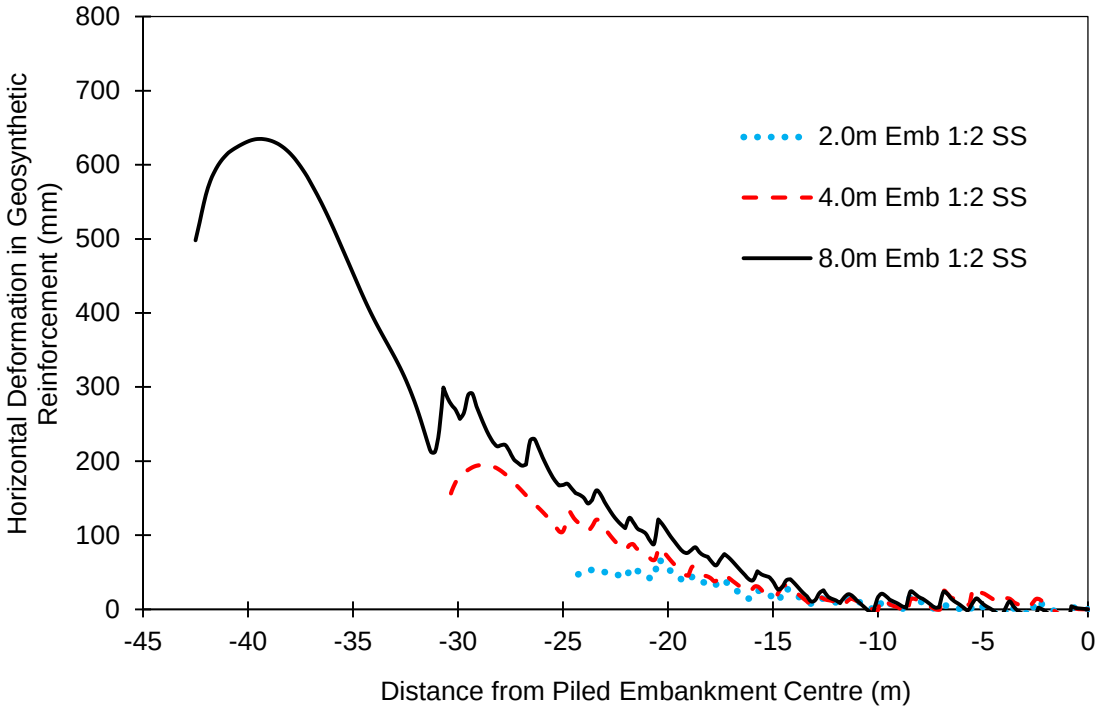

Figure 5.80 Horizontal deformations (mm) of geosynthetic reinforcement for a range of embankment height (m) (a = 1.0m, J_{re} = 500kN/m and s = 3.0m)

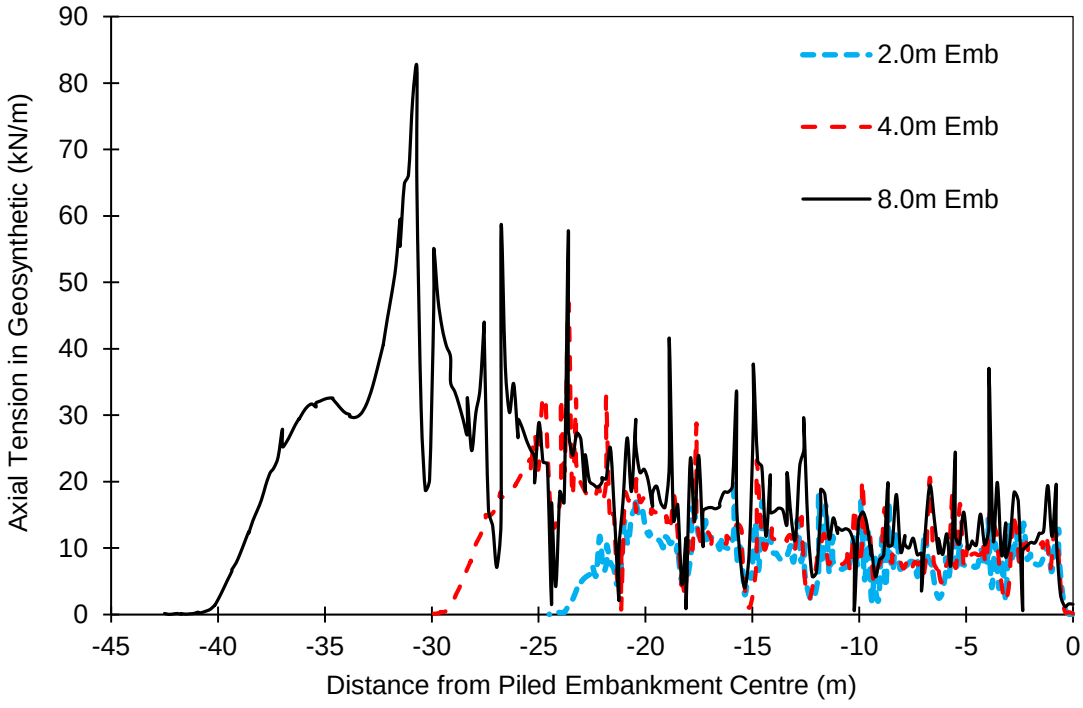

Figure 5.81 Axial tensions (kN/m) in the reinforcement for a range of embankment height (m) (a = 1.0m, J_{re} = 500kN/m and s = 3.0m)

The axial load on each pile within the pile group extent increased for an increase of the embankment height, Figure 5.82. As the height of the embankment increased, the magnitude of the axial load on the outer row pile as a percentage of the magnitude of the axial load on piles near the centre of the embankment decreased. The axial load on the outer row pile for a 2.0m embankment height was 43% lower in magnitude than a pile located near the centre of the embankment. The magnitude of the axial load for an 8.0m embankment height was 19% lower in magnitude in comparison to a pile located at or near the centre. The magnitude of the axial load on the outer row pile increased linearly for an increase of the embankment height, Appendix C Figure C34.

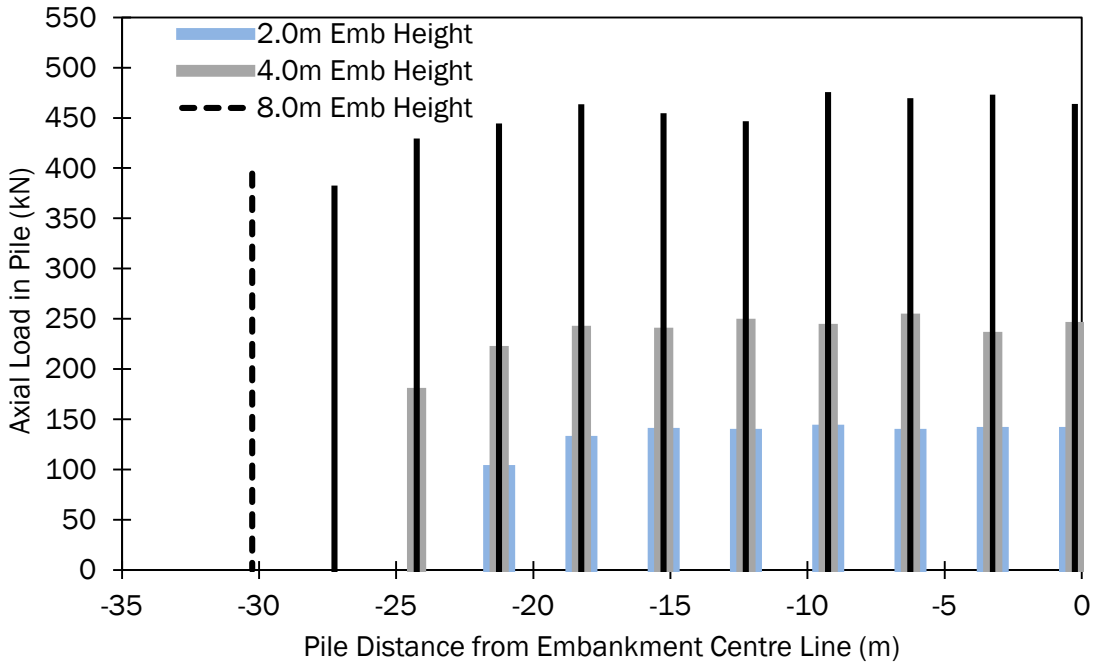

Figure 5.82 Axial loading (kN) on pile group under reinforced piled embankment for a range of embankment height (m) (a = 1.0m, J_{re} = 500kN/m and s = 3.0m)

The lateral deflection of the pile heads within the pile group increased for an increase of embankment height, Figure 5.83. The rate of increase in the lateral deflection at the outer row pile was linear, Appendix C Figure C35. As the height of the embankment increased, the lateral thrust acting outwards from the embankment centre increased exponentially with height. A 300% increase of embankment height (2.0m to 8.0m) yielded a 482% increase in the deflection of the outer row pile for a side slope of 1V:2H.

The bending moment of each pile within the pile group increased for an increase in the embankment height, Figure 5.84 and Appendix C Figure C36. The increase in magnitude of bending moment for an increase of embankment height was consistent with the lateral pile head deflection. The increase in magnitude of the bending moment at the outer row pile increased in a linear manner for an increase of embankment height, Appendix C Figure C36. An increase of the embankment height with a 1V:2H side slope from 2.0m to 8.0m yielded a 639% increase in the bending moment (28kN/m to 207kN/m) at the outer pile row.

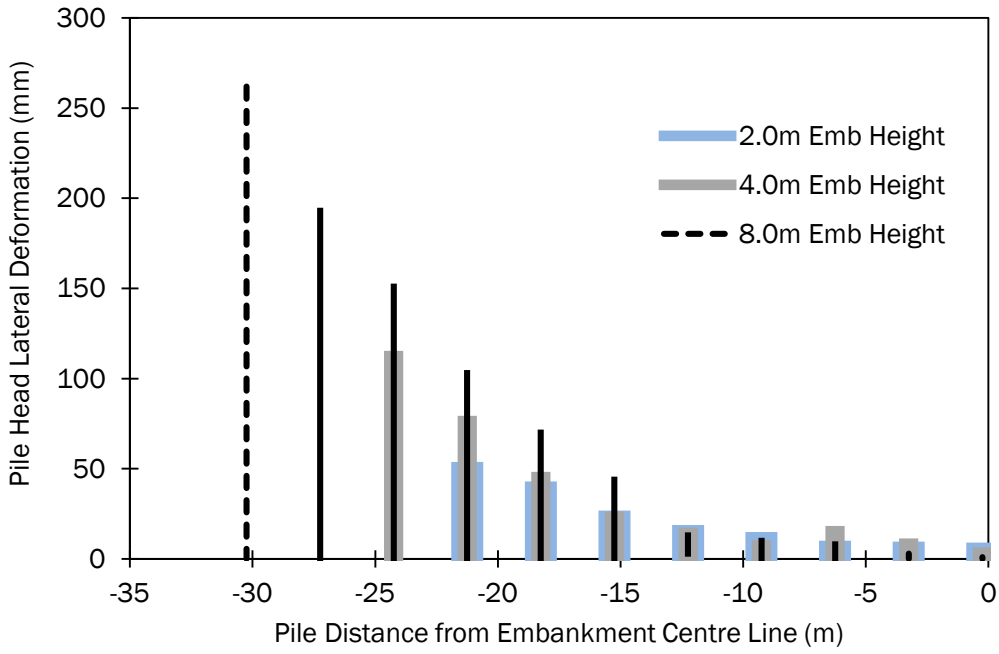

Figure 5.83 Lateral deflections (mm) at the pile head within a pile group under a reinforced piled embankment for a range of embankment height (m) (a = 1.0m, J_{re} = 500kN/m and s = 3.0m)

The efficacy of the pile group increased marginally for an increase of the embankment height, Figure 5.85. The overall increase in the pile group efficacy was 3.5% for an increase of the embankment height from 2.0m to 8.0m. Whilst an increase in height will improve arching conditions within the embankment structure, an increase of embankment height also corresponded to an increase in the magnitude of embankment fill to be supported by the soft soil near the embankment toe, Figure 5.77 and 5.79, which negated some of the improvements of load transfer efficiency due to arching, Figure 5.85.

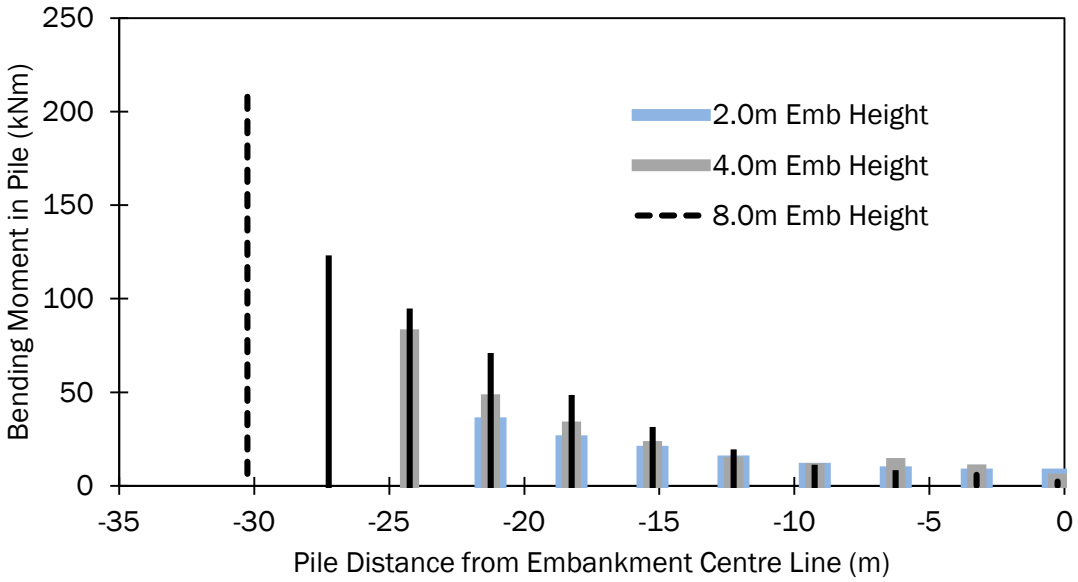

Figure 5.84 Bending moments (kNm) within a pile group for a range of embankment height (m) (a = 1.0m, J_{re} = 500kN/m and s = 3.0m)

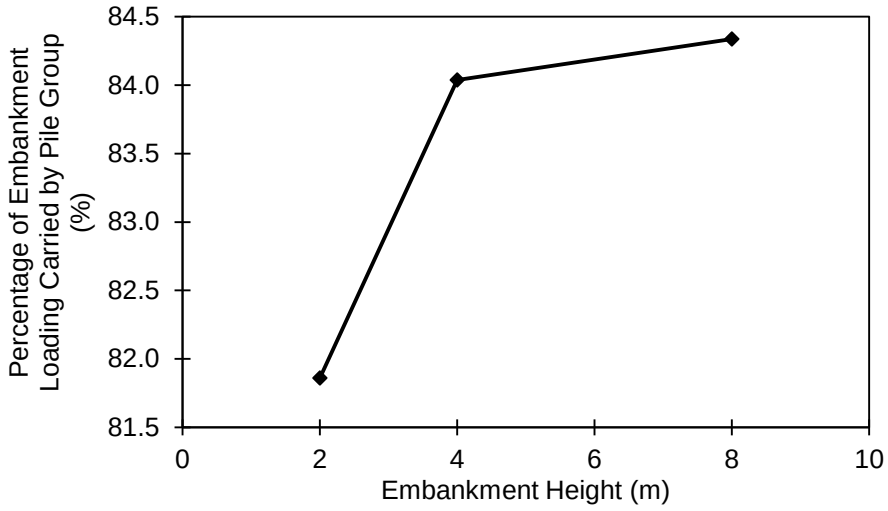

Figure 5.85 Pile group efficiencies (%) for a range of embankment height (m) (a = 1.0m, J_{re} = 500kN/m and s = 3.0m)

The strain in the reinforcement increased for an increase in the embankment height, Figure 5.86. The strain in the reinforcement was a function of both the vertical deformation of the reinforcement and the lateral thrust. An initial increase of the embankment height (1.0m to 2.0m) yielded an insignificant increase in the reinforcement strain. A further increase of the embankment height (2.0m to 4.0m) mobilised an increase of reinforcement strain. The rate of increase in reinforcement

strain slowed above a height of 4.0m due to the formation of the critical arching height within the embankment structure. The increase in reinforcement strain for a height greater than the critical height for arching was primarily due to the lateral thrust of the embankment fill. The strain in the pile group increased for an increase of embankment height, Figure 5.86. The rate of increase of the strain in the pile was almost exponential across the whole range of embankment heights. The strain in the pile was a function of the lateral thrust, which increased exponentially for an increase of the embankment height.

The strain compatibility ratio (SCR) increased rapidly for an increase of the embankment height from 1.0m to 2.0m, which was attributed to the lateral thrust mobilizing a strain in the pile and not to the same extent in the reinforcement, thus an increase in the strain compatibility required for equilibrium was carried by the pile. An increase of the embankment height from 2.0m to 4.0m resulted in both the vertical loading (critical arch formation at height at 2.8m for 1.4(s-a)) and lateral thrust increasing the strain. The acceleration in the rate of increase in magnitude of reinforcement strain negated some of the high attraction of strain in the pile, the SCR increased by 92%. An increase of the embankment height further from 4.0m to 8.0m yielded a 116% increase of SCR due to the pile attracting a greater increase of loading (greater increase of strain) than the reinforcement.

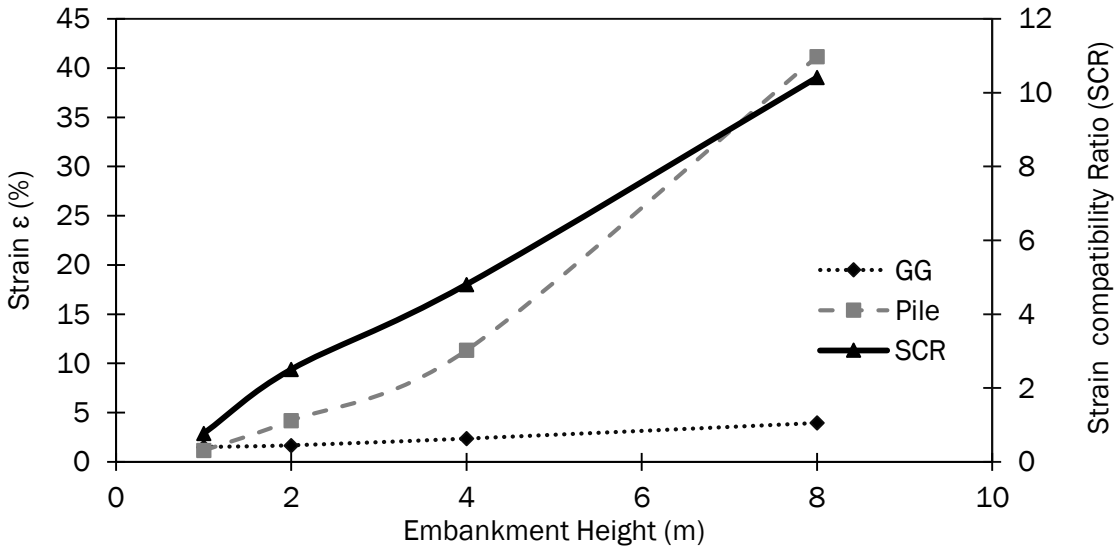

Figure 5.86 Strain in reinforcement and outer row pile and piled embankment Strain Compatibility Ratio (SCR) (%) for a range of embankment height (m) for a 1V:2H side slope (a = 1.0m, J_{re} = 500kN/m and s = 3.0m)

Stability of the GRPE decreased for an increase in embankment height, Figure 5.87, where the pile group geometric layout (pile spacing and pile cap size) remained constant. For all embankment heights, global stability was predominantly influenced by the degree of arching present and the destabilizing lateral thrust acting outwards from the embankment centre. The degree of arching present within the GRPE increased as the embankment height approached the critical height required for full arching (defined as 1.4 times the clear spacing between pile caps in BS 8006, 2010). Figure 5.87 suggests that whilst an increase in embankment height resulted in an improvement in the degree of arching, the improvement in load transfer efficiency was insignificant in comparison to the destabilizing lateral forces which resulted in an overall reduction in global stability. An increase in embankment height corresponded to an exponential increase in the lateral thrust of the embankment fill acting outwards. The increase in lateral thrust mobilised an increase in the lateral deformational response of the pile group, and resulted in a lower overall global stability for both cases of side slope steepness, Figure 5.87.

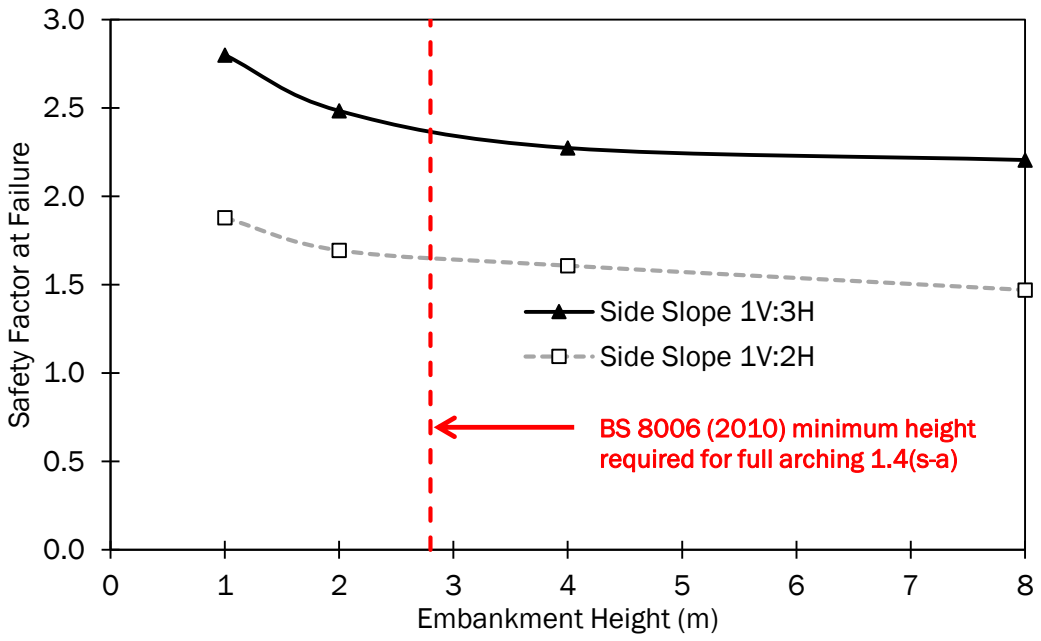

Figure 5.87 Safety factor at failure for a range of embankment height

The variation of the height of the embankment resulted in a linear increase/decrease of all deformation components (embankment structure, geosynthetic reinforcement and pile group). The majority of the strain compatibility condition was supported by the pile. The results suggested that the height of the

embankment whilst a crucial determinant in the magnitude of the deformations did not mobilize a failure mechanism within the structure.

5.9 Influence of Embankment Side Slope

The steepness of the embankment side slope was ranged from 1V:2H to 1V:4H. The embankment model with a steeper side slope (1V:2H) yielded a lower order of magnitude in vertical deformations outside the pile group extents but greater lateral deformation of the embankment fill material above the outer pile centreline, Figure 5.88, Appendix C Figure C37 and C38. The lateral volumetric deformation above the outer pile decreased significantly with a decrease of side slope steepness, Appendix C Figure C38.

The shallower the steepness of the side slope, the greater the length of side slope to be supported between the outer row pile and the toe, consequently greater magnitudes of vertical deformations were produced in comparison to side slopes of greater steepness, Figure 5.88 and Appendix C Figure C39. Vertical deformation of the geosynthetic reinforcement was a function of the clear span between the adjacent pile caps, the embankment height and the geosynthetic stiffness. The clear span and geosynthetic stiffness were held constant for the parametric variation of the embankment side slope.

The clear span between adjacent pile caps located near the centre of the embankment (Figure 5.88) recorded magnitudes of vertical deformation that was equal irrespective of side slope steepness. At locations nearer the crest of the embankment, the vertical deformation in the reinforcement became increasingly affected by the lateral thrust of the embankment, as a result of lateral deflection at the pile head.

The horizontal deformations of the reinforcement near the embankment centre increased marginally for an increase in the steepness of the embankment side slope, Figure 5.89. The steeper of the side slopes (1V:2H) yielded a maximum horizontal deformation outside the pile group extent 13% less than that of the 1V:3H side slope. The location of the maximum horizontal deformation in the reinforcement was within the clear span between the embankment toe and the outer row pile cap edge for all side slopes.

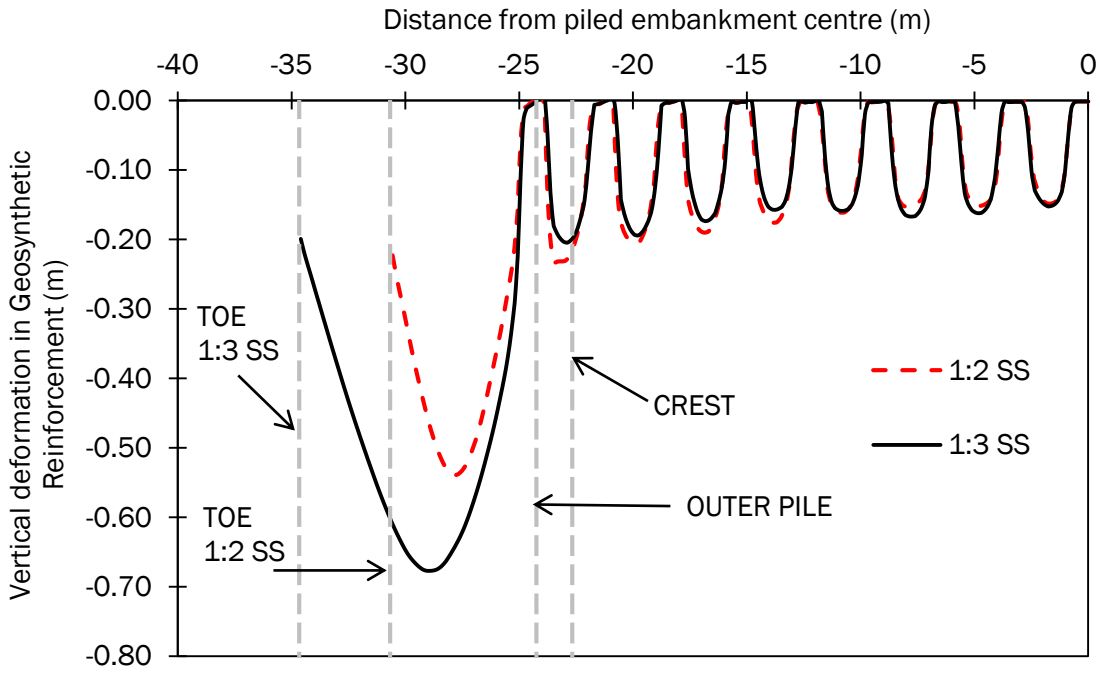

Figure 5.88 Vertical deformation of the geosynthetic reinforcement for a range of side slopes (H = 4.0m, J_{re} = 500kN/m and s = 3.0m)

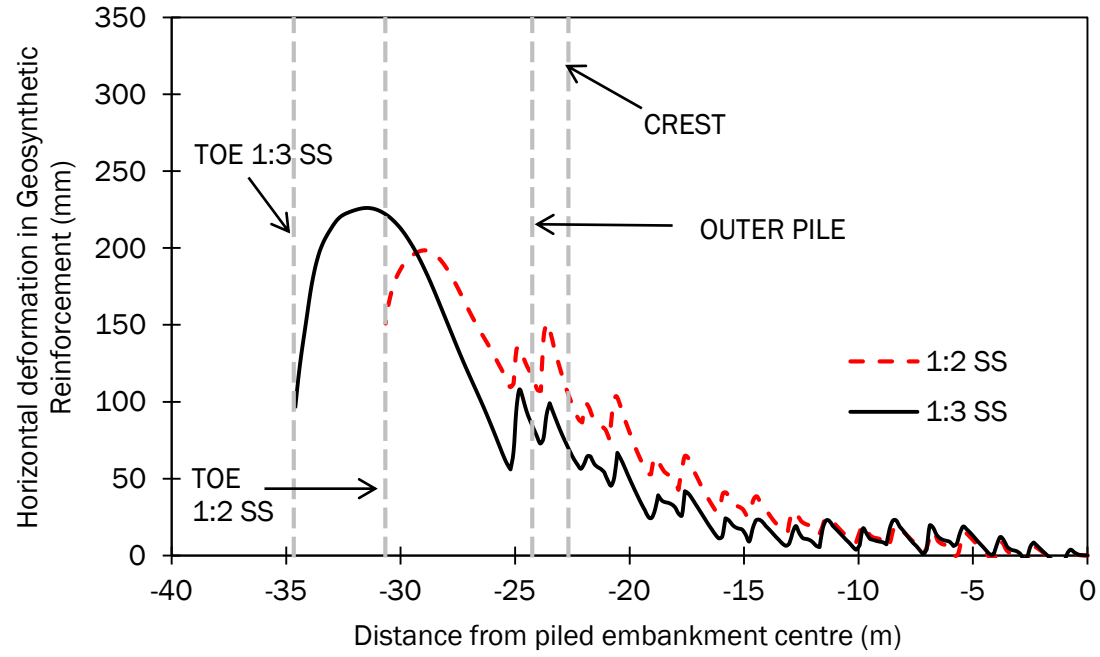

Figure 5.89 Horizontal deformations (mm) of geosynthetic reinforcement for a range of side slopes (H = 4.0m, J_{re} = 500kN/m and s = 3.0m)

The axial tension in the geosynthetic reinforcement increased slightly for an increase of the side slope steepness as the reinforcement approached the crest,

Figure 5.90. The axial tension in the reinforcement was a function of both the horizontal deformation (lateral thrust) and the vertical deformation (vertical loading on reinforcement between adjacent pile caps). The magnitude of axial tensions near the centre of the embankment remained constant for all side slope steepness's. Close to the embankment centre, the axial tension was only a function of the vertical loading from the embankment to be supported by the reinforcement. The vertical loading on the reinforcement clear span remained constant for all pile spacing locations. An increase in the magnitude of the axial tension as the reinforcement neared the embankment crest was due to the reinforcement attracting load in order to resist the lateral thrust. The maximum axial tension recorded in the Geosynthetic reinforcement increased for a reduction of the side slope steepness, Appendix C Figure C40. The lesser the steepness of the side slope, the greater the length of side slope outside of the pile group extents, the greater the magnitude of load transferred to the outer pile row pile cap by the geosynthetic reinforcement from the side slope. The result of which, was a corresponding localized maximum axial tension spike at the edge of the outer row pile cap for a reduction of side slope steepness, Appendix C Figure C40.

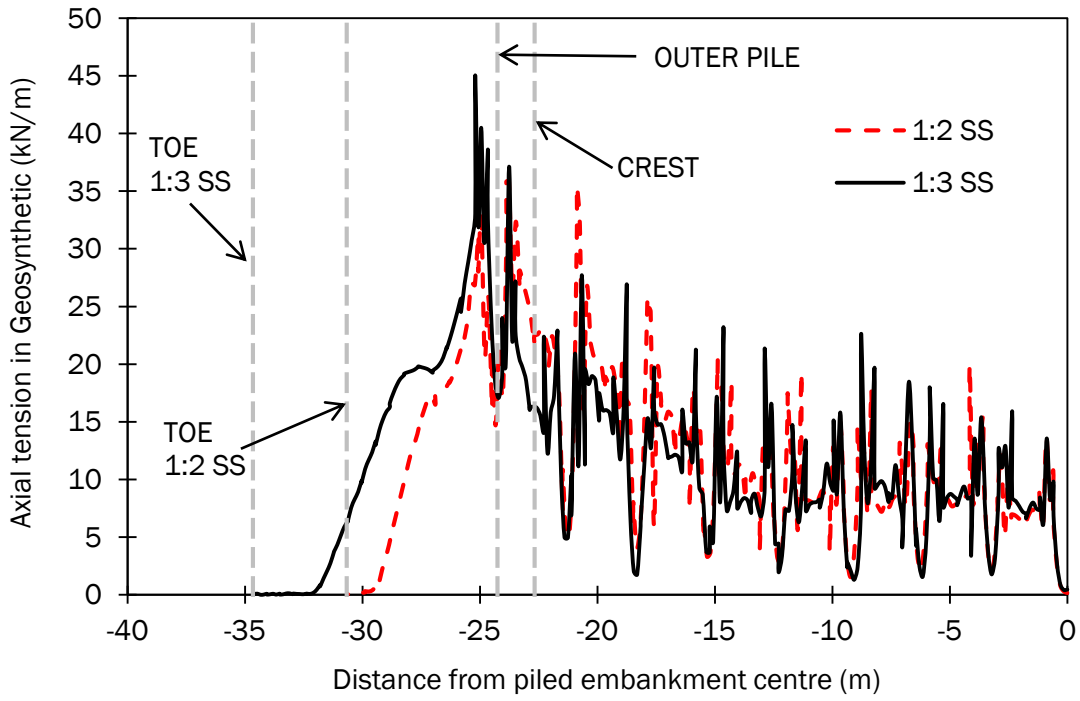

Figure 5.90 Axial tensions in the reinforcement for a range of side slopes (H = 4.0m, J_{re} = 500kN/m and s = 3.0m)

The axial loading on each individual pile near the embankment centre remained relatively constant for a variation of the side slope steepness, Figure 5.91. The axial load on the outer pile row increased for a decrease of side slope steepness. The magnitude of the axial load on the outer row pile for the side slope case of 1V:3H was approximately 16.3% greater than that of the 1V:2H side slope case. The increase in magnitude of axial load at the outer pile row was attributed to an increase in vertical loading transferred by the reinforcement to the pile head due to a greater length of side slope to be supported by the pile. The increase of axial load on the outer pile row with a decrease in side slope steepness was approximately linear, Appendix C Figure C41.

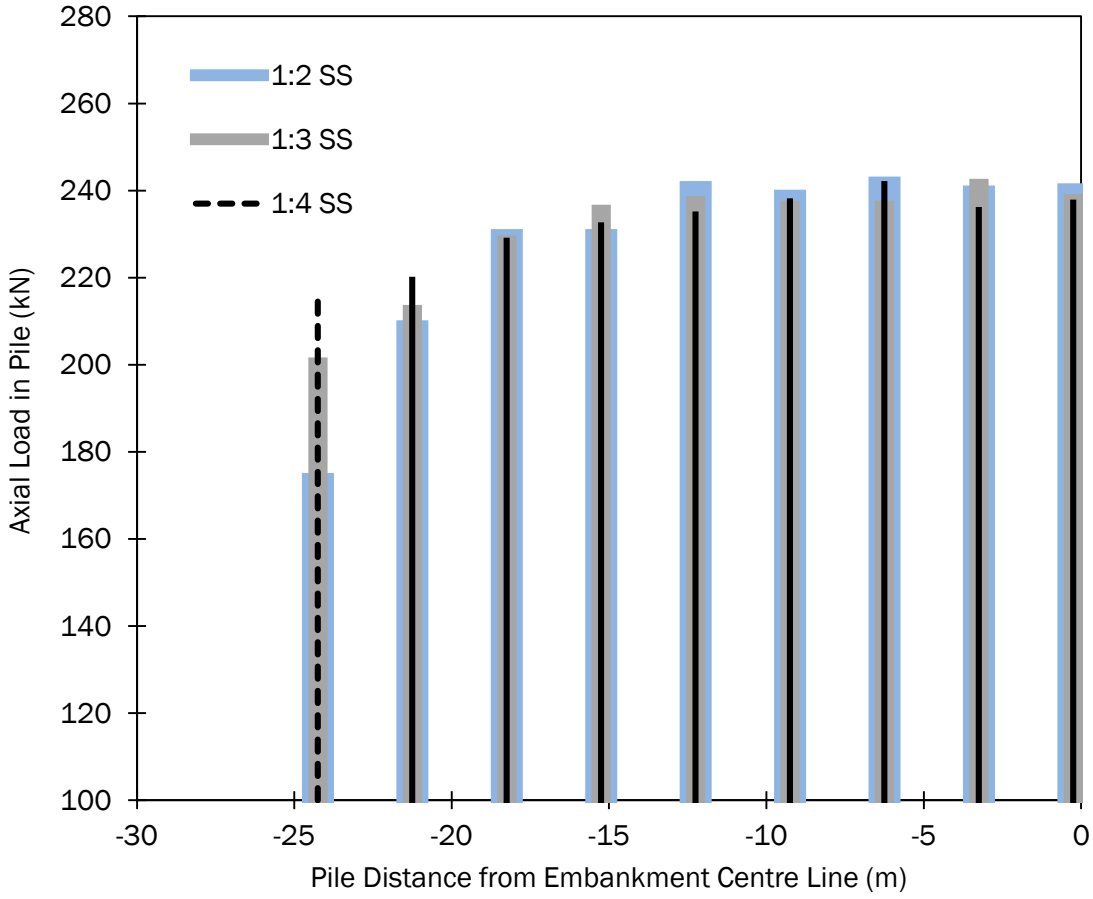

Figure 5.91 Axial loading (kN) on pile group under reinforced piled embankment for a range of side slopes (H = 4.0m, J_{re} = 500kN/m and s = 3.0m)

Figure 5.92 and Appendix C Figure C42 illustrate that the greater the side slope steepness, the greater the lateral deformation of the outer pile row. As the side slope increased, the imbalance between the lateral thrust disturbing force and the restoring force increased. The increased imbalance resulted in lateral deformation of the pile group, which was a function of the distance from the embankment crest. The closer the pile location was to the embankment crest, the greater the lateral deformation of the pile head. The 1V:2H side slope recorded a lateral deflection 38% greater than the 1V:3H side slope case. The greater the steepness of the side slope, the greater the rate of increase in lateral deformations, as the pile location moves away from the embankment centre towards the crest.

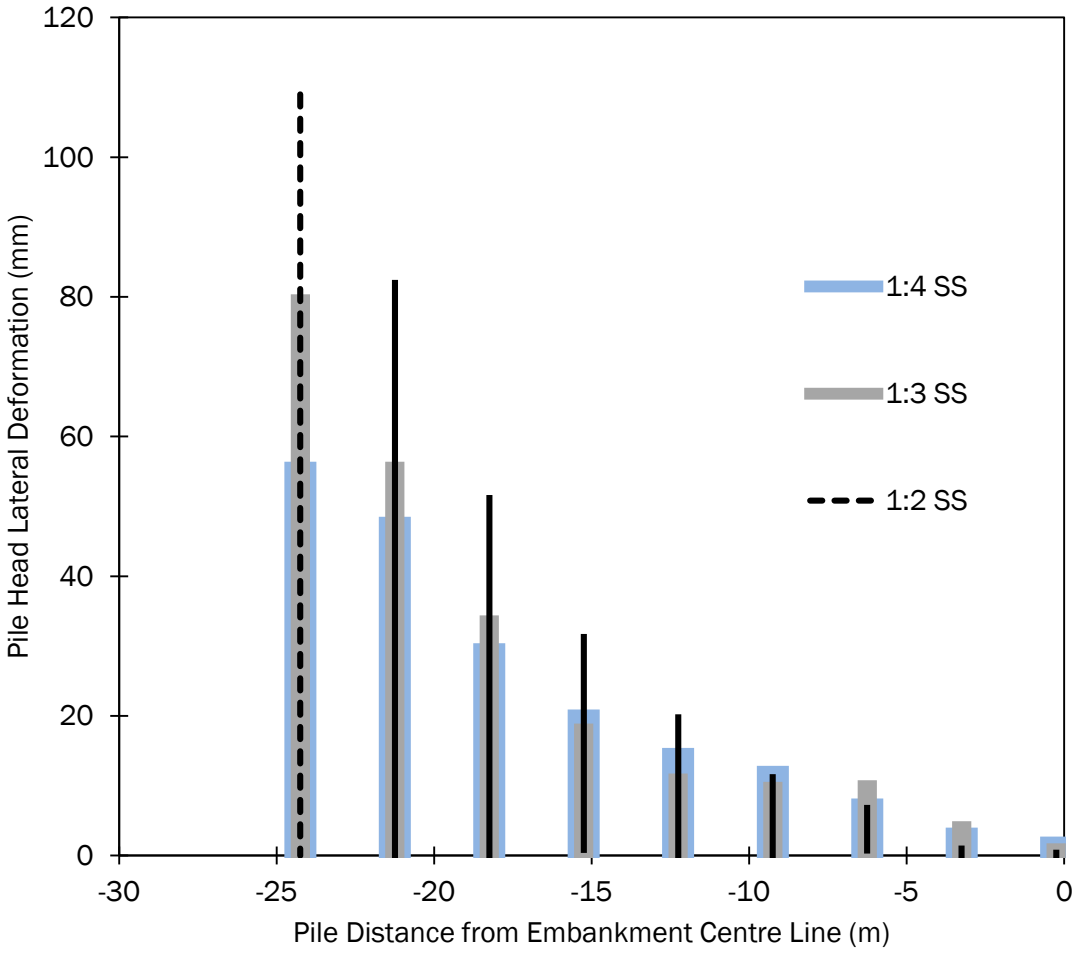

Figure 5.92 Lateral deflections (mm) at the pile head within a pile group under a reinforced piled embankment for a range of side slopes (H = 4.0m, J_{re} = 500kN/m and s = 3.0m)

The magnitude of bending moments within the pile group increased for an increase of the side slope steepness, Figure 5.93 and Appendix C Figure C43. The magnitude of the bending moment at the outer pile row was significantly higher (12%) than the 1V:3H side slope. The bending moment at the outer pile row increased linearly with an increase of side slope steepness, Appendix C Figure C43. Similar to the lateral deflections, the 1V:3H and 1V:4H side slopes recorded a lower maximum but overall the pile group was subjected to the same degree of loading at the embankment centre.

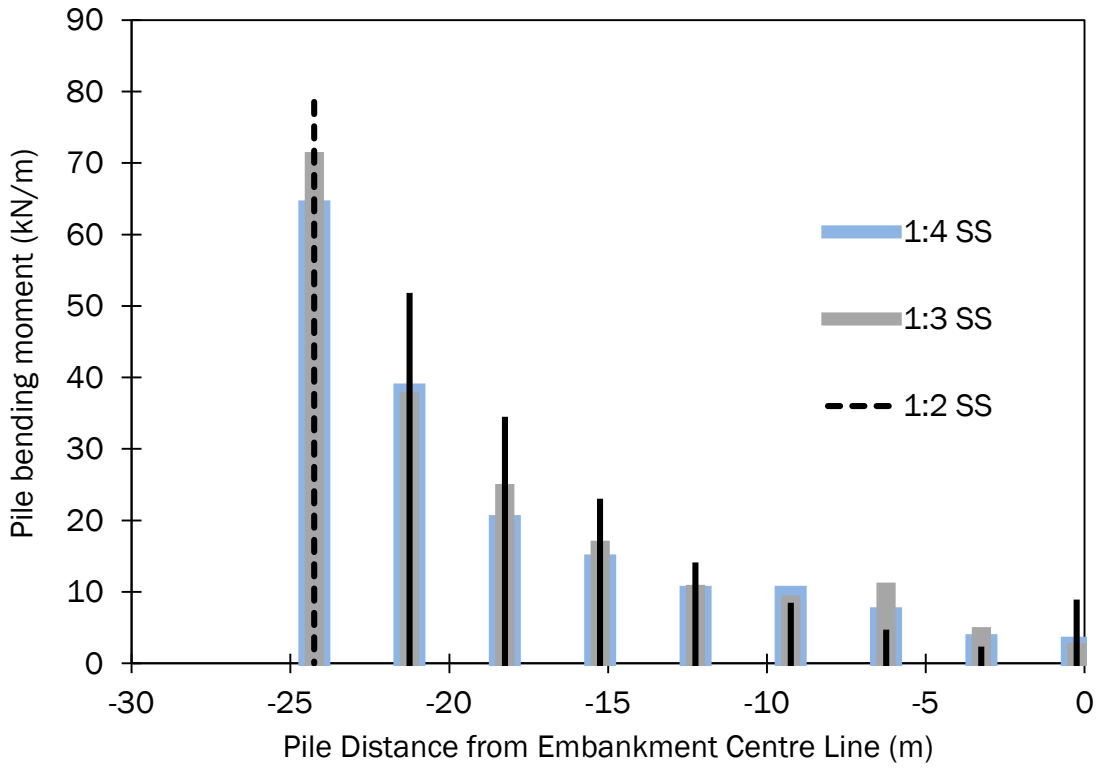

Figure 5.93 Bending moments (kNm) within a pile group for a range of side slopes (H = 4.0m, J_{re} = 500kN/m and s = 3.0m)

The efficacy of the pile group and the SCR was examined with side slope steepness's (*n*) of 1V:2H, 1V:3H and 1V:4H. The efficacy of the pile group decreased significantly for a decrease of the side slope steepness, Figure 5.94. The efficacy decreased by 10% for a decrease of the side slope from 1V:2H to 1V:4H. The efficacy of the pile group decreased as the length of the unsupported side slope of the embankment increased (for a reduction in side slope steepness) and a

greater portion of the side slope loading was transferred to the soft subsoil underneath the side slope.

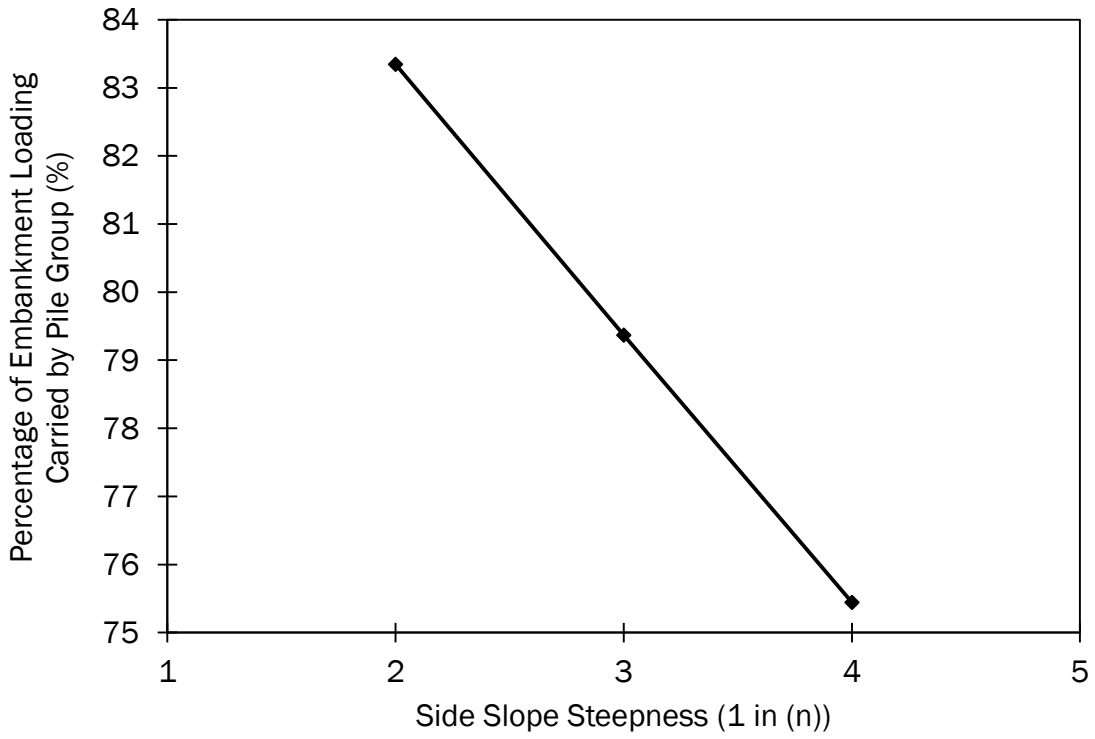

Figure 5.94 Pile group efficiencies (%) for a range of side slopes (H = 4.0m, J_{re} = 500kN/m and s = 3.0m)

The strain in the geosynthetic reinforcement decreased for a decrease of the side slope steepness, Figure 5.95. The initial decrease of the side slope steepness from 1V:2H to 1V:3H yielded a slight reduction of the reinforcement strain (7.2% decrease). A further decrease in the side slope steepness (1V:3H to 1V:4H) resulted in a further 9.7% reduction in the reinforcement strain. The pile strain decreased almost linearly with a decrease in the steepness of the side slope steepness (29% decrease). The portion of the strain compatibility carried by the pile was greater than that of the reinforcement and decreased by 14.5% for a decrease in the embankment side slope steepness from 1V:2H to 1V:3H, Figure 5.95. A further decrease of the side slope steepness from 1V:3H to 1V:4H resulted in a further marginal decrease in the portion of loading carried by the pile to satisfy the strain compatibility condition (4% decrease).

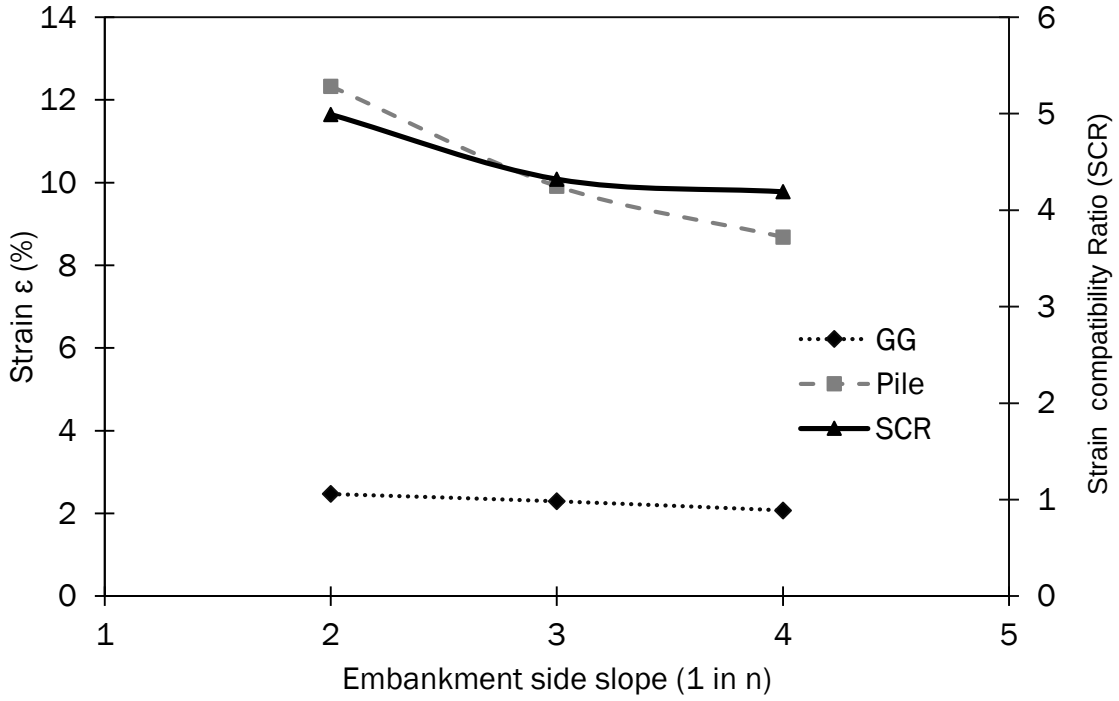

Figure 5.95 Strain in reinforcement and outer row pile and piled embankment Strain Compatibility Ratio (SCR) (%) for a range of side slopes (H = 4.0m, J_{re} = 500kN/m and s = 3.0m)

Additional analysis of the side slope steepness at n = 1, 4, 5 and 6 were conducted to capture the response of the stability of the structure. Stability of the system increased for a decrease in the steepness of the embankment side slope, Figure 5.96. As the side slope steepness increased, the differential between the passive and active earth pressure mobilised a lateral deformational response in the embankment fill outwards from the embankment centre until equilibrium was achieved. The resultant deformational response of the fill yielded deflection of the pile head and a subsequent decrease in structural stability. An increase in the steepness of side slope (1V:6H→1V:3H) resulted in only a marginal increase in structural stability, Figure 5.96. A further increase in the steepness of the side slope (1V:3H→1V:2H) significantly reduced the structural stability of the embankment. Once the side slope steepness reached approximately 1:1.25 the system became unstable (a factor of safety lower than 1.0 was recorded). The analysis suggests that there was a cut off at 1:3 and side slope shallower than that only has a marginal effect on structural stability.

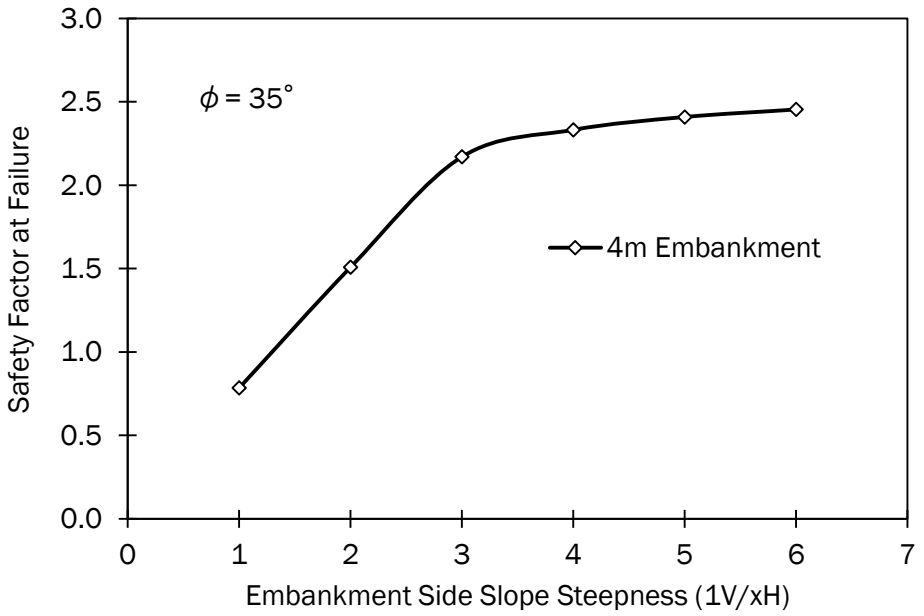

Figure 5.96 Safety factor at failure for a range of side slope steepness

An increase of the embankment side slope resulted in a decrease of the vertical deformations of the reinforcement across the width of the embankment and significantly at the outer extremities of the embankment near the embankment toe. An increase of the embankment side slope resulted in a greater rate of decrease in the axial loading on the piles within the side slope area, greater magnitude of lateral deflections and bending moments within the pile group. The steeper the side slope of the embankment, the greater the pile group efficacy and the portion of the strain compatibility condition supported by the pile group.

5.10 Influence of Outer row pile location ratio

The outer pile location ratio was ranged from 0 to 1.0. The vertical deformations of the geosynthetic reinforcement between the embankment toe and the outer row pile decreased almost linearly to zero for an increase of ORPLR for both side slopes, Figure 5.97. Reduction of the vertical deformations to zero for 1.0 ORPLR was due to the elimination of the clear span to be supported by the geosynthetic reinforcement between the toe and the outer row pile. The 1V:3H side slope case consistently recorded slightly larger magnitudes of vertical deformation in comparison to the 1V:2H side slope, Figure 5.97.

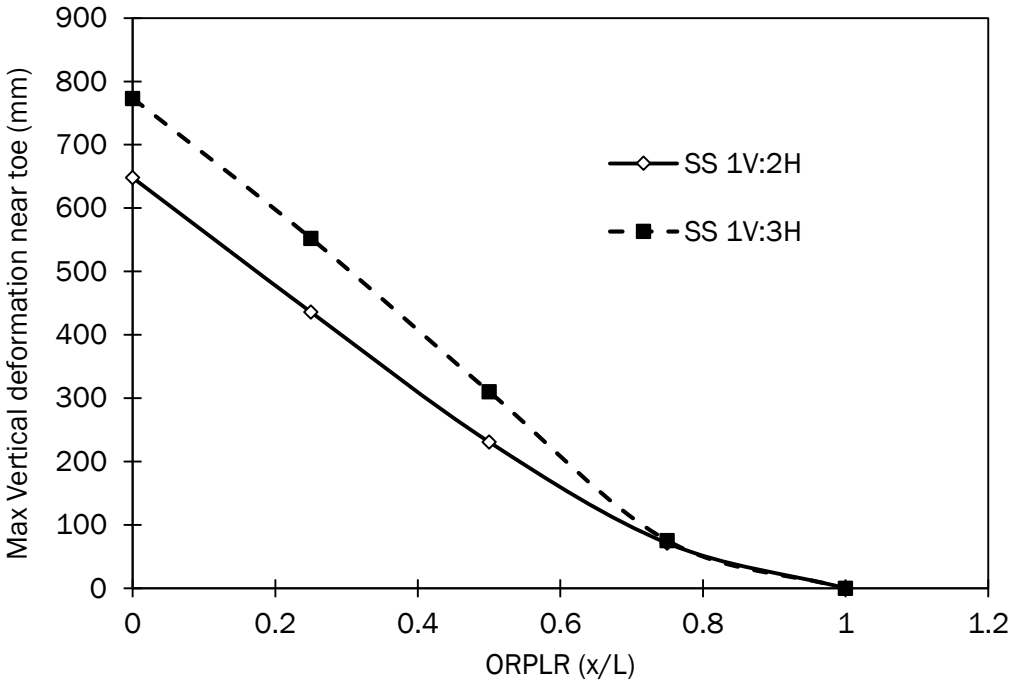

Figure 5.97 Vertical deformation (m) under the side slope between the embankment toe and outer pile row for a range of ORPLR (H = 4.0m, a = 1.0m, J_{re} = 500kN/m and s = 3.0m)

Vertical deformations of the geosynthetic reinforcement recorded an overall increase as the ORPLR decreased. The clear span between adjacent pile caps located near the centre of the embankment recorded magnitudes of vertical deformation that was equal irrespective of ORPLR, Figure 5.98. Magnitudes of vertical deformations between adjacent pile caps increased near the embankment crest as the outer pile row was located closer towards the embankment crest. The maximum vertical deformation in the geosynthetic reinforcement was localized to the clear span between the embankment toe and the outer row pile for all ORPLR case with the exception of the ORPLR 1.0 case. The ORPLR 1.0 model case recorded a vertical deformation maximum at the clear span between adjacent pile caps directly under the embankment crest, Figure 5.98. As the outer row pile was located closer to the embankment crest (ORPLR approached 0), magnitudes of vertical deformation at the unsupported span outside the outer row pile increased almost linearly, Figures 5.97 and 5.98.

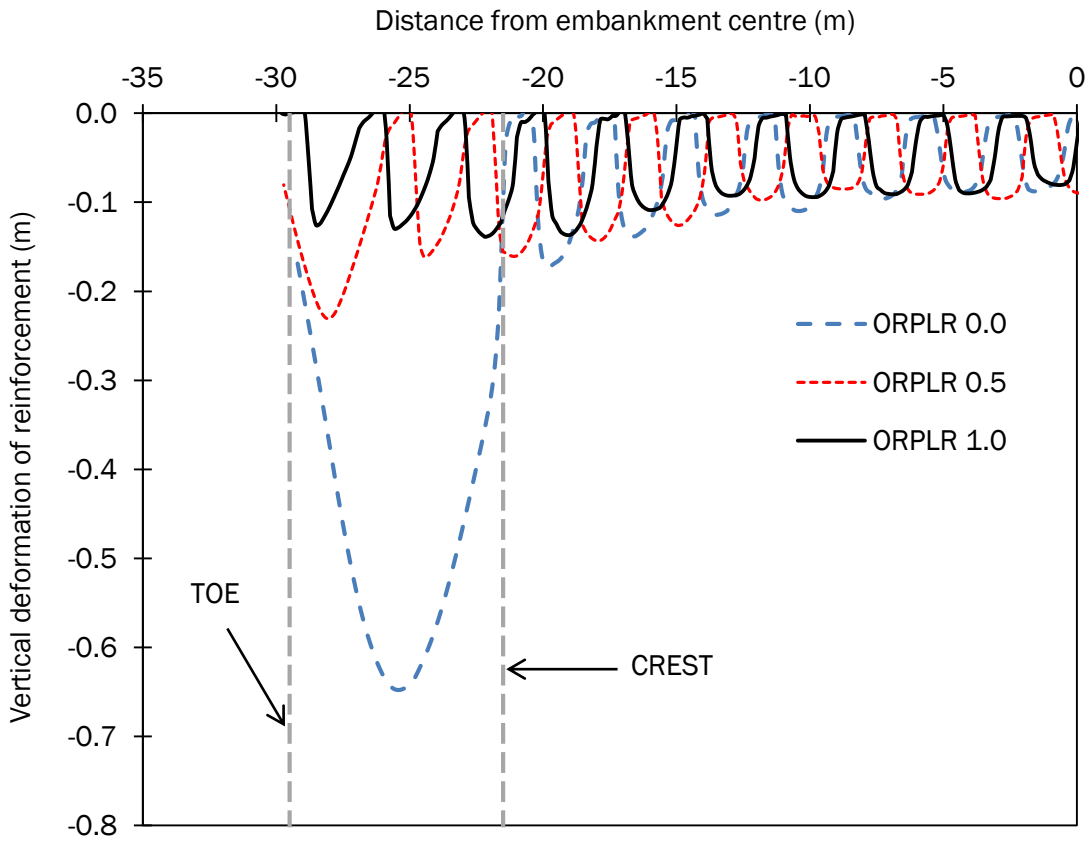

Figure 5.98 Vertical deformation of the geosynthetic reinforcement for a range of ORPLR (H = 4.0m, a = 1.0m, J_{re} = 500kN/m and s = 3.0m)

The maximum horizontal deformations of the geosynthetic reinforcement increased for a decrease of the ORPLR, Figure 5.99. The magnitude of the horizontal deformation increased from zero at the embankment centre where the pull-out force from the lateral thrust was insignificant. An increase of the ORPLR from 0 to 0.5 resulted in a decrease in the maximum recorded horizontal deformation in the reinforcement of approximately 39%. A further increase of the ORPLR from 0.5 to 1.0 (100% increase) resulted in an 18% decrease in the magnitude of the maximum horizontal deformation. The analysis suggested that an increase of the ORPLR produced a non-linear reduction in the magnitudes of horizontal response of the geosynthetic reinforcement. Magnitudes of horizontal deformation remained relatively consistent for all ORPLR case near the embankment centre.

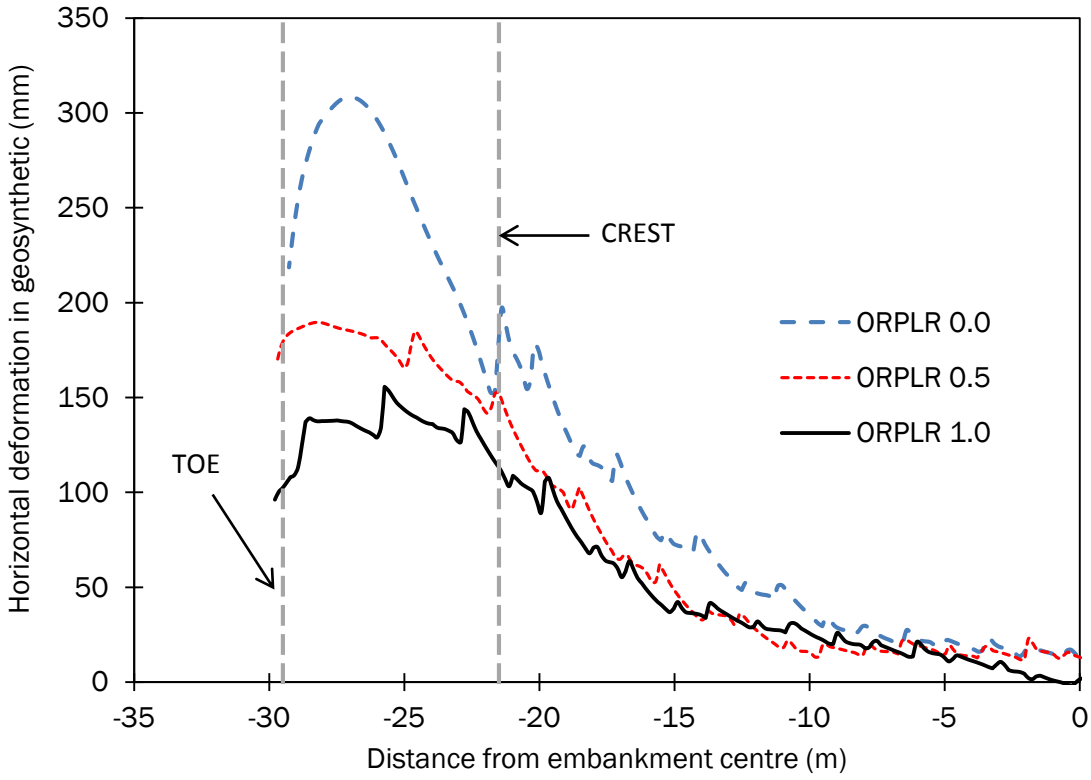

Figure 5.99 Horizontal deformations (mm) of geosynthetic reinforcement for a range of ORPLR (H = 4.0m, a = 1.0m, J_{re} = 500kN/m and s = 3.0m)

The axial tension in the geosynthetic reinforcement remained largely consistent for a decrease of the ORPLR, Figure 5.100 and Appendix C Figure C44. The ORPLR 0.0 case produced a maximum axial tension as the geosynthetic reinforcement dropped off the outer row pile. The resultant length of clear span outside the outer row pile maximum transferred a significant loading to the reinforcement which resulted in a spike of axial tensions at the outer row pile cap edge, Figure 5.100. The ORPLR 0.5 case recorded a spike in axial tension as the reinforcement dropped of the outer row pile cap edge similar to the ORPLR 0.0 case, Figure 5.100, however the ORPLR 0.5 case recorded an axial tension maximum almost directly under the embankment crest, Figure 5.100. The ORPLR 1.0 case which consists of the pile group extended all the way to the embankment toe produced a geosynthetic reinforcement axial tension maximum almost directly under the embankment crest which reduced to zero at the embankment toe.

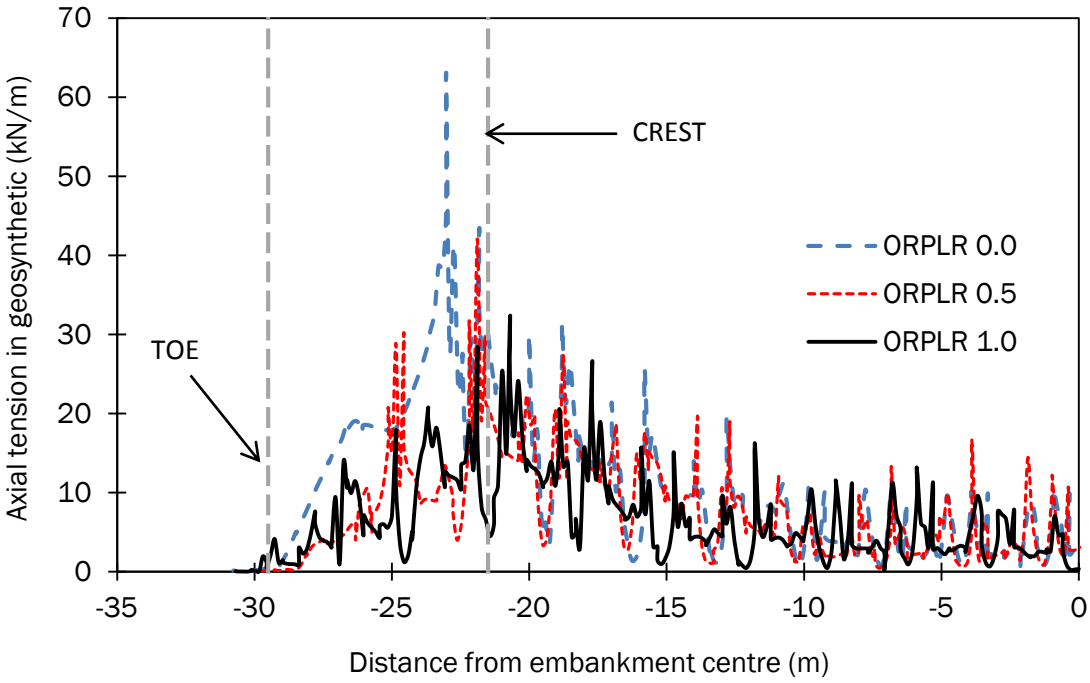

Figure 5.100 Axial tensions (kN/m) in the reinforcement for a range of ORPLR (H = 4.0m, a = 1.0m, J_{re} = 500kN/m and s = 3.0m)

Axial loads on each pile within the pile group remained relatively consistent near the embankment centre, Figure 5.101. The ORPLR 0.0 case recorded a gradual reduction in axial loads as the pile location neared the crest. The closer the pile group extent was located to the embankment toe the greater the rate of reduction in axial loading at the piles localized to the pile group extent edge, Figure 5.101.

Lateral deformations at the pile head remained relatively constant at the piles localized to the embankment center, Figure 5.102. At pile locations near the embankment crest, an increase of the ORPLR produced a reduction in magnitude of pile head lateral deformations. The lower the ORPLR, the greater the rate of increase in magnitude of lateral deformations, as the pile location approached the embankment crest. Maximum lateral deformations at the pile head and overall lateral deformations across the pile group extent decreased for an increase of ORPLR, Figure 5.102.

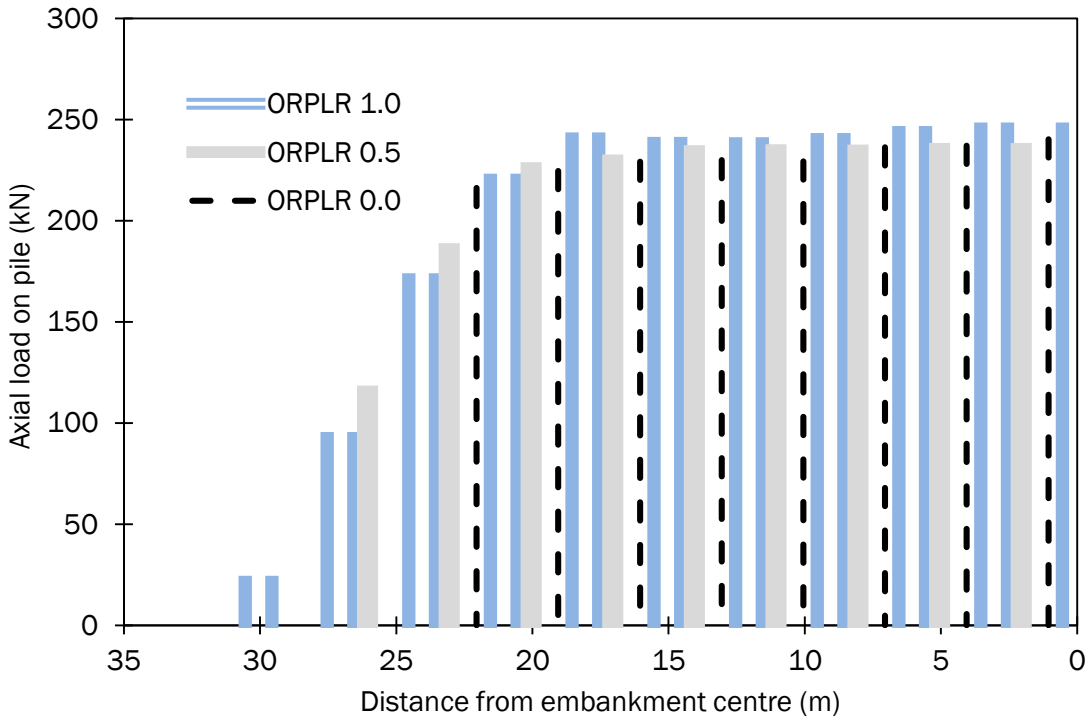

Figure 5.101 Axial loading (kN) on pile group under reinforced piled embankment for a range of ORPLR (H = 4.0m, a = 1.0m, J_{re} = 500kN/m and s = 3.0m)

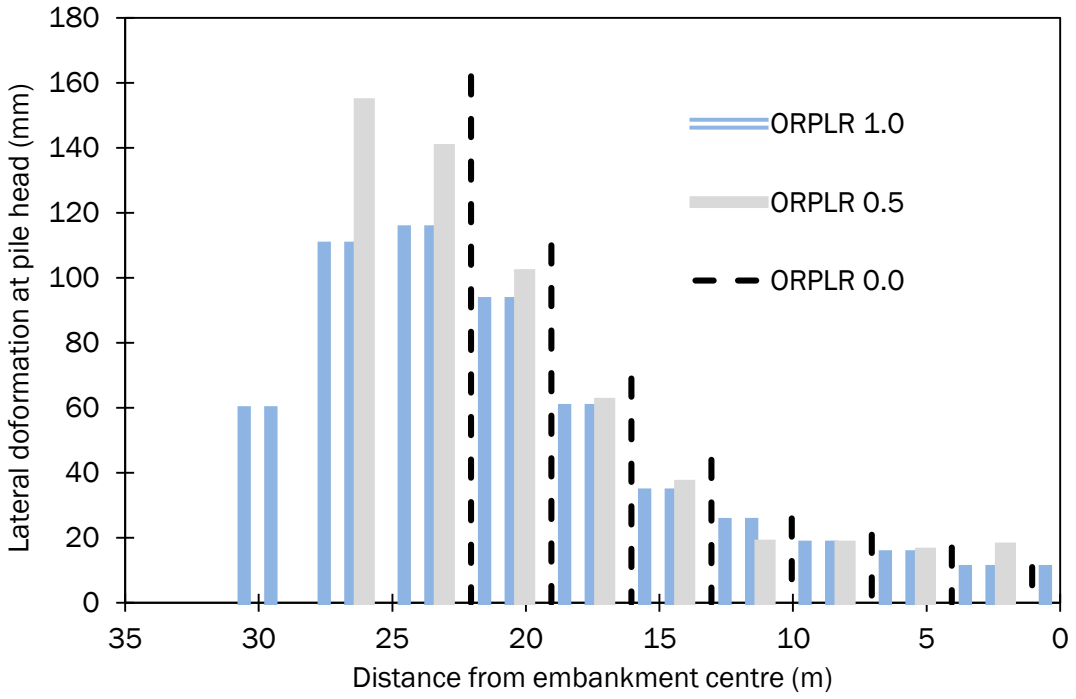

Figure 5.102 Lateral deflections (mm) at the pile head within a pile group under a reinforced piled embankment for a range of ORPLR (H = 4.0m, a = 1.0m, J_{re} = 500kN/m and s = 3.0m)

Bending moments mobilised in the piles within the pile group extent followed a similar trend to the lateral deformations. Figure 5.103 illustrates that the bending moments decreased for an increase of ORPLR. The pile group experienced an increase in the overall embankment axial loading carried by the pile group for an increase of the ORPLR, Figure 5.104. An initial increase of the ORPLR from 0 to 0.5 yielded the greatest rate of embankment loading increase, Figure 5.104. The outer pile row bending moment decreased for an increase of ORPLR, Figure 5.103 and Appendix C Figure C45.

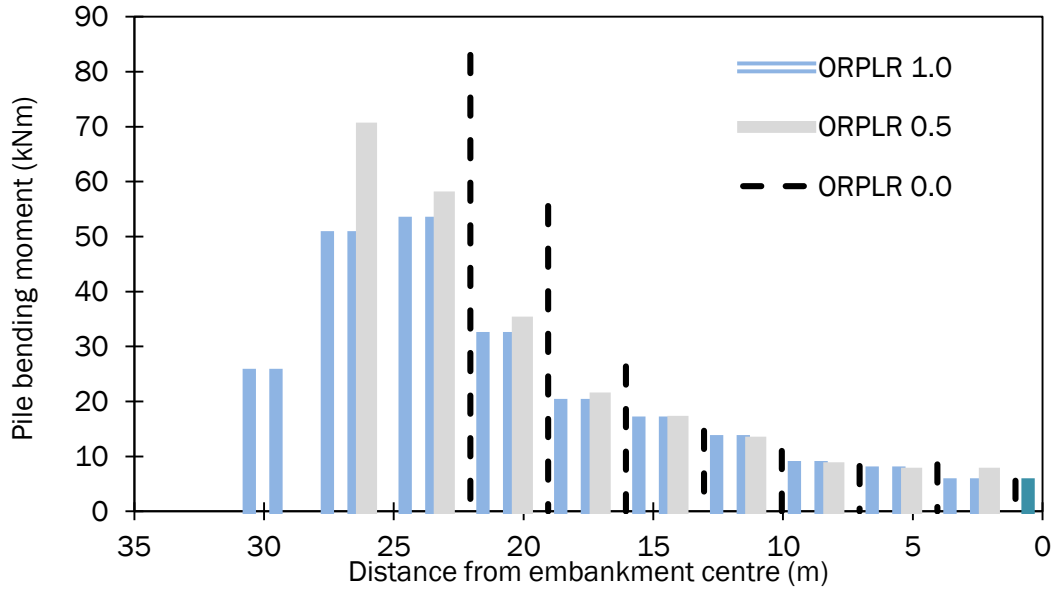

Figure 5.103 Bending moments (kNm) within a pile group for a range of embankment height (m) (H = 4.0m, a = 1.0m, J_{re} = 500kN/m and s = 3.0m)

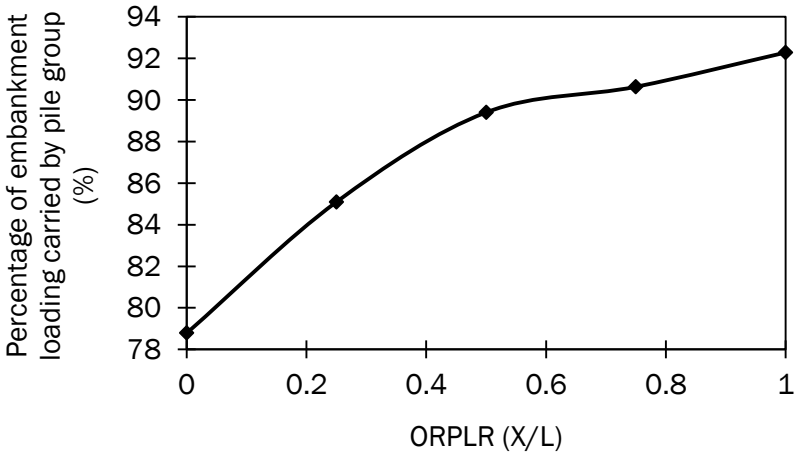

Figure 5.104 Pile group efficiencies (%) for a range of embankment height (m) (H = 4.0m, a = 1.0m, J_{re} = 500kN/m and s = 3.0m)

Both the pile group and the geosynthetic was subjected to lower magnitudes of lateral loading and axial tensions for an increase of ORPLR, Figures 5.100 and 103. Consequently the lower magnitudes of axial tension and lateral deformations at the pile head yielded an overall reduction in strain of both the pile group and the geosynthetic for an increase of ORPLR, Figure 5.105. The strain compatibility ratio suggested the pile group strain decreased at a lower rate than the geosynthetic reinforcement. The SCR suggests the lateral thrust subjected to the geosynthetic reinforcement decreased and consequently was carried by the pile group, Figure 5.105. The SCR increased by approximately 38% for an overall increase of ORPLR from 0 to 1.0, Figure 5.105.

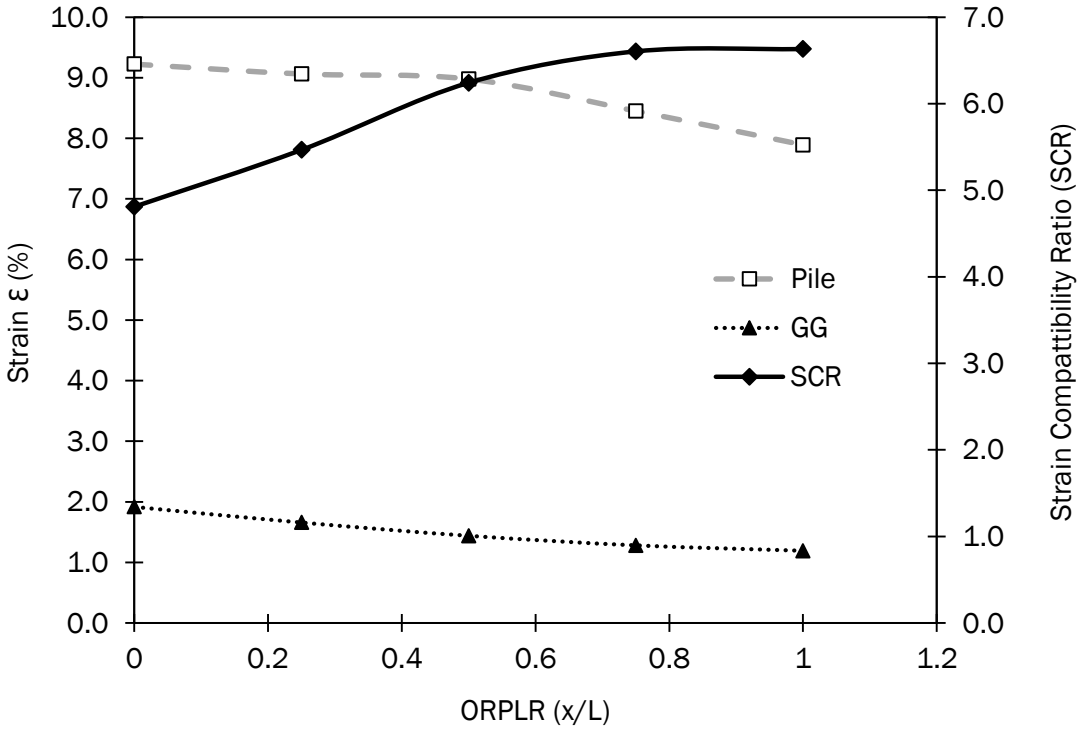

Figure 5.105 Strain in reinforcement and outer row pile and piled embankment Strain Compatibility Ratio (SCR) (%) for a range of ORPLR for a 1V:2H side slope (H = 4.0m, a = 1.0m, J_{re} = 500kN/m and s = 3.0m)

Figure 5.106 suggests the safety factor of the geosynthetic reinforced piled embankment increased for an increase of ORPLR. A marginal increase of the safety factor was observed for an increase of ORPLR from 0 to 0.25, Figure 5.106. An increase of ORPLR greater than 0.25 mobilised a significant increase in the factor

of safety, increasing almost linearly for an increase of ORPLR greater than 0.25, Figure 5.106. The increase of the safety factor at failure with ORPLR is correlated with corresponding decreases in lateral deformations at the pile heads, vertical deformations of the geosynthetic reinforcement outside the pile group near the embankment toe and axial tensions in the geosynthetic reinforcement.

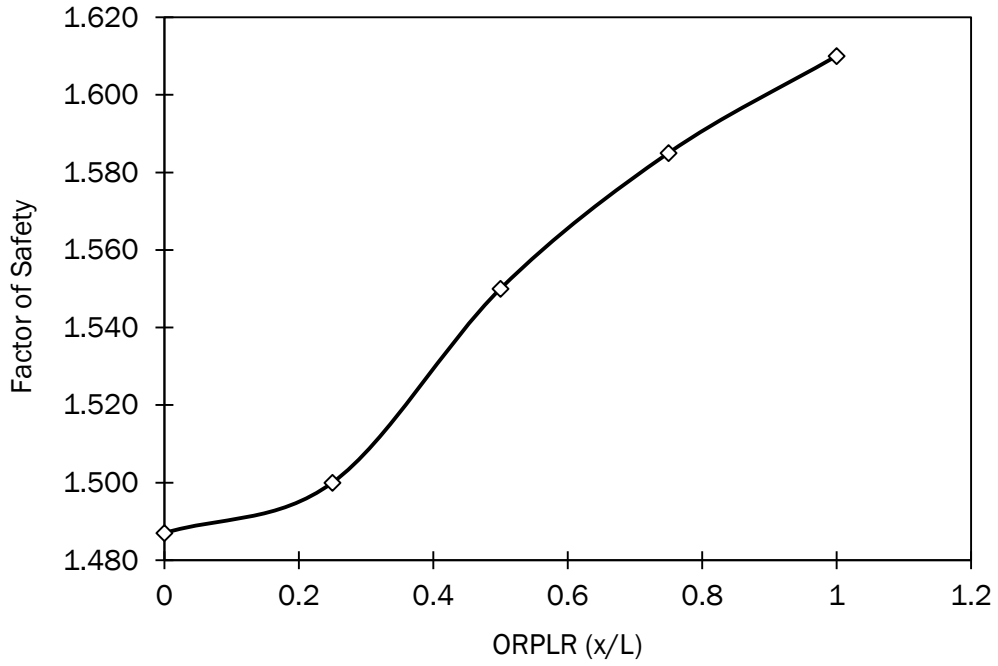

Figure 5.106 Safety factor at failure for a range of embankment height. (H = 4.0m, a = 1.0m, J_{re} = 500kN/m and s = 3.0m)

5.11 Summary

This chapter presented the results of the Plaxis 2D plane strain analysis for a range of parametric variations together with some preliminary analysis. The pile spacing, pile cap size, embankment height, outer pile row rake angle, soft soil depth, soft soil stiffness, embankment side slope steepness and the location of the outer pile row were varied during the modelling. The pile group deformations, geosynthetic reinforcement deformations/tensions and embankment surface deformations were analyzed.

Chapter 6

Discussion of Results

6.1 Introduction

The aim of this chapter is to present analysis and discussion of the results of the centrifuge and Plaxis modelling. The centrifuge model testing was divided into two test series while the Plaxis 2D analyses were divided into three test series. In both the centrifuge and Plaxis 2D Test Series 1, physical and numerical modelling was utilized to examine the response of the reinforced piled embankment to a variation of subsoil stiffness, side slope steepness and embankment height. Centrifuge and Plaxis 2D Test Series 2 consisted of modelling the outer pile row location along the side slope, with the deformational response of the structure analysed and compared. Test Series 3 conducted material and geometric parametric variations on the full scale generic model using Plaxis 2D only. The importance of these parameters, on the performance of piled embankments is assessed in this chapter.

The results from the Centrifuge and Plaxis 2D Test Series 1 and 2 were used to assess the suitability of the two-dimensional finite element program Plaxis 2D to adequately model plane strain reinforced piled embankments.

The data collected from the three test series were used to define implications for design and these are examined under the following headings:

1. Comparison of results from centrifuge and Plaxis 2D modelling (Test Series 1 & 2).
2. Plaxis 2D analysis of reinforced piled embankment (Test Series 3).
3. Implications for design.

6.2 Comparison of centrifuge modelling and Plaxis analyses

The surface and geosynthetic deformational response of a number of reinforced piled embankments was determined by means of both centrifuge and Plaxis modelling. An analysis of the results of Test Series 1 and 2 is presented with a direct comparison of the results of the centrifuge and Plaxis modelling provided under the following headings:

1. Pile group deformations
2. Geosynthetic reinforcement deformations
3. Embankment surface mean settlements

6.2.1 Pile group deformations

The results of both the centrifuge and Plaxis modelling showed considerable pile group deformations for Test Series 1. Both the centrifuge and Plaxis 2D sets of data recorded a maximum lateral pile deflection localized to the outer pile row for all parametric variations. The Plaxis 2D analysis predicted lateral pile head deformations consistently greater in magnitude with-in the pile group in comparison to the centrifuge modelling. The magnitude of the lateral deformations increased at a greater rate approaching the outer row pile in the centrifuge model than the Plaxis

2D analysis. The response of piles near the embankment centre modelled by Plaxis 2D were more sensitive to lateral loading than the centrifuge model.

Lateral deflection of the outer pile row head increased almost linearly for an increase in the H/(s-a) ratio for both data sets. Similitude conditions between the centrifuge and Plaxis 2D data existed for the characteristic trend of the lateral response of the outer row pile for an increase of embankment height (increase of embankment geometric ratio). A greater rate of increase of lateral pile deformations as the each pile location neared the embankment crest was observed in the centrifuge in comparison to the Plaxis 2D models, Figure 6.1.

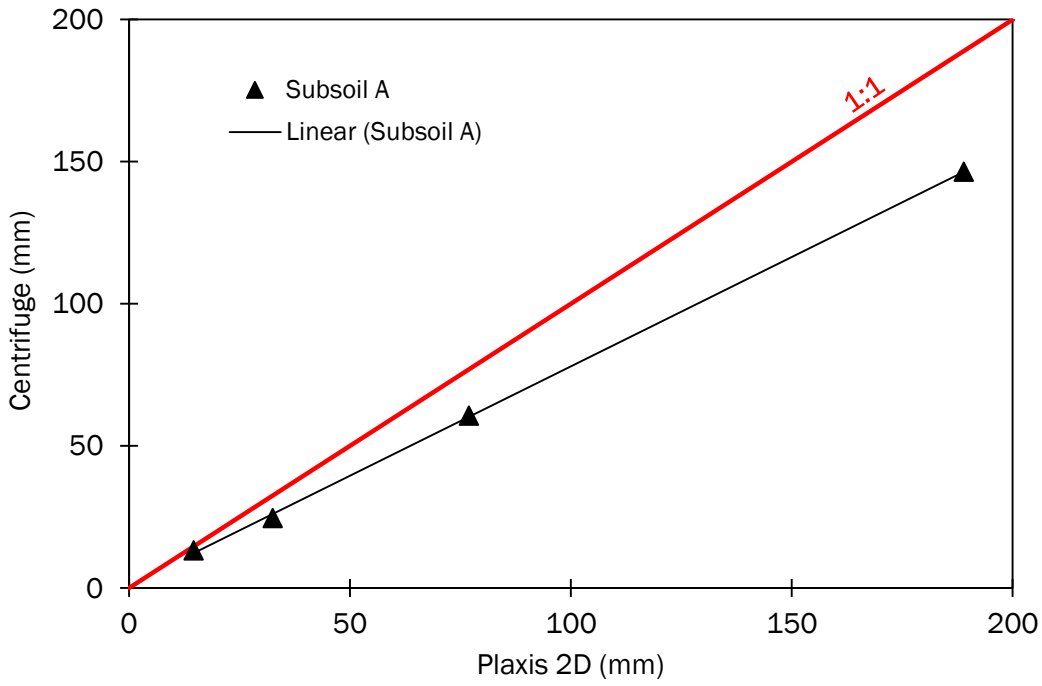

Figure 6.1 Relationship of centrifuge and Plaxis 2D modelling of the lateral deformational response of the outer pile row

Test Series 1, which varied the subsoil stiffness, produced a response in both the centrifuge and Plaxis 2D models that was in good agreement both quantitatively and qualitatively, Figure 6.2. Plaxis 2D analyses consistently predicted greater magnitudes of lateral deformations for all subsoil variations in comparison to those measured in the centrifuge.

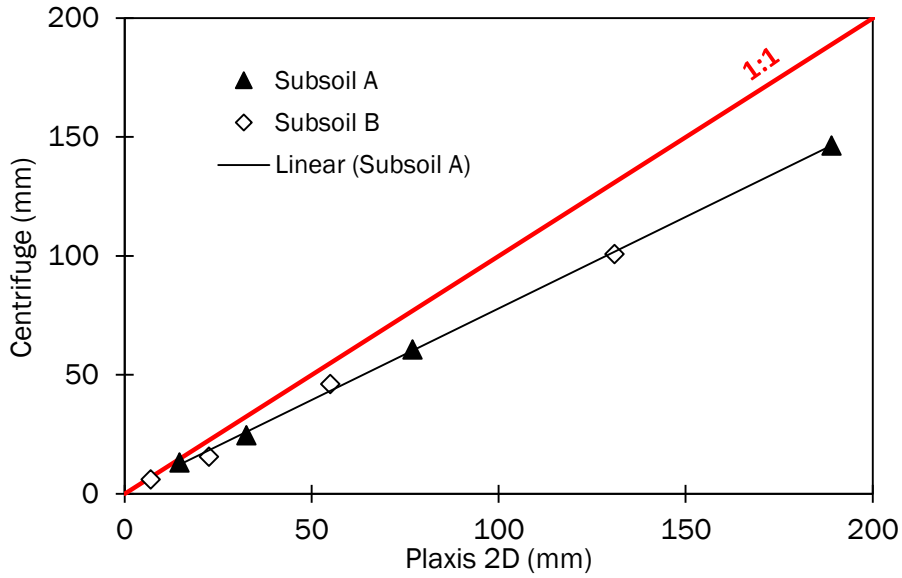

Figure 6.2 Relationship of centrifuge and Plaxis 2D modelling of the lateral deformational response of the outer pile row for both Subsoil A and B

The Plaxis 2D and centrifuge analyses recorded lateral deformations of the 1V:2H side slope steepness cases consistently greater than the 1V:3H side slopes. Both sets of data produced a linear reduction of lateral pile deformations with a reduction of embankment side slope steepness, Figure 6.3.

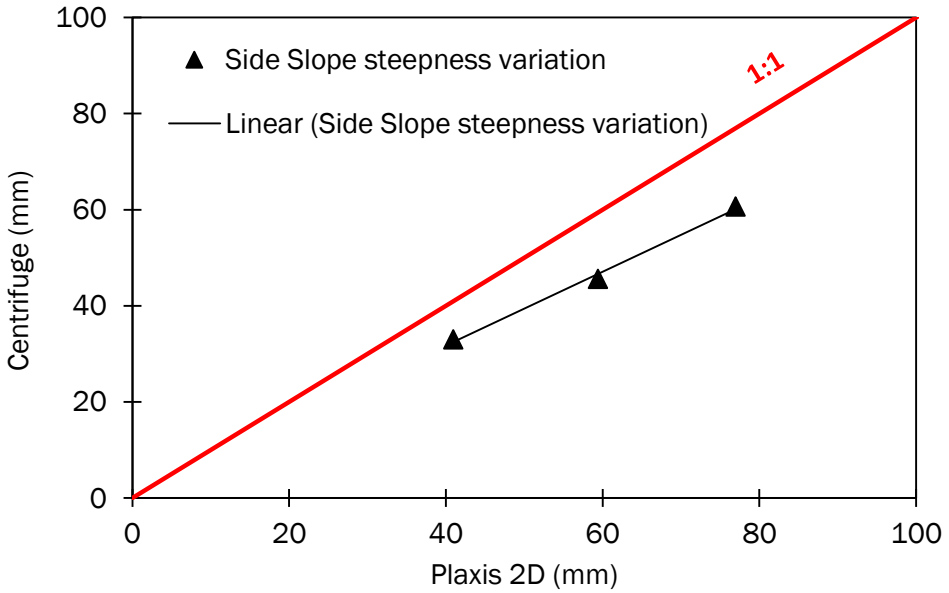

Figure 6.3 Relationship of centrifuge and Plaxis 2D modelling of the lateral deformational response of the outer pile row for a range of side slope steepness

Test Series 2 revealed that moving the location of the outer pile row closer toward the embankment toe reduced the magnitude of lateral deformations at each pile location within the pile group extent, irrespective of subsoil stiffness or embankment side slope steepness. Good qualitative agreement was observed between the centrifuge and Plaxis 2D for the deformational response of the outer pile row, Figure 6.4. Overall, the pile group strain relationship with ORPLR produced good agreement qualitatively, however, Plaxis 2D predicted deformations that were approximately 35 – 40% greater than those measured in the centrifuge. For conditions with the outer pile row close or near the crest, a greater differential between centrifuge and Plaxis 2D lateral pile deformations near the embankment centre was observed in comparison to conditions with the outer pile row closer toward the toe. The data suggests that for geometric layouts with the outer pile row near or under the crest greater magnitudes of lateral pile head deformations occurred closer toward the embankment centre in comparison to the centrifuge analyses.

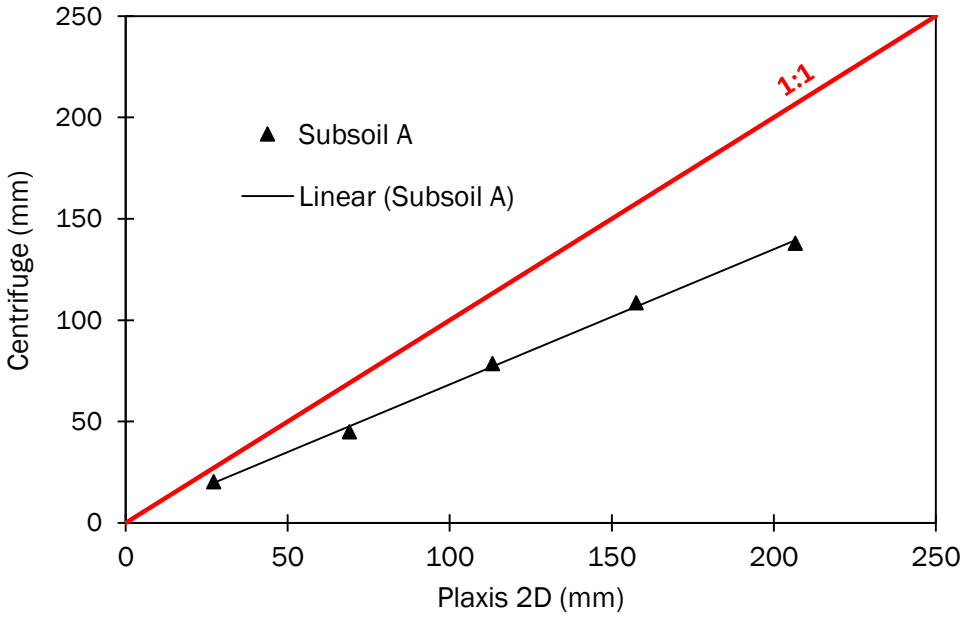

Figure 6.4 Relationship of centrifuge and Plaxis 2D modelling of the lateral deformational response of the outer pile row for a range of ORPLR

6.2.2 Geosynthetic reinforcement deformations

Considerable deformation of the geosynthetic reinforcement was observed between the toe of the embankment and the outer most piles in Test Series 1 in both the

centrifuge and Plaxis 2D analysis. Overall both modelling techniques produced a similar, catenary shape between adjacent pile caps, from the centre line of the embankment to the outer row of piles for all geometric layouts examined, Figure 4.30.

In Test Series 1 both the centrifuge and Plaxis 2D modelling produced a geosynthetic reinforcement vertical deformation maximum located outside the outer pile row near the embankment toe. Plaxis 2D consistently predicted magnitudes of vertical deformations at the midspan between adjacent pile caps that were slightly greater than comparable measured centrifuge values. However, some of this difference could be attributed to errors in measurement in the centrifuge modelling.

Vertical deformations of the geosynthetic reinforcement increased almost linearly for an increase of H/(s-a) ratio for both the centrifuge and Plaxis 2D data, Figure 6.5. Good agreement, both quantitatively and qualitatively was found between the centrifuge and Plaxis 2D modelling.

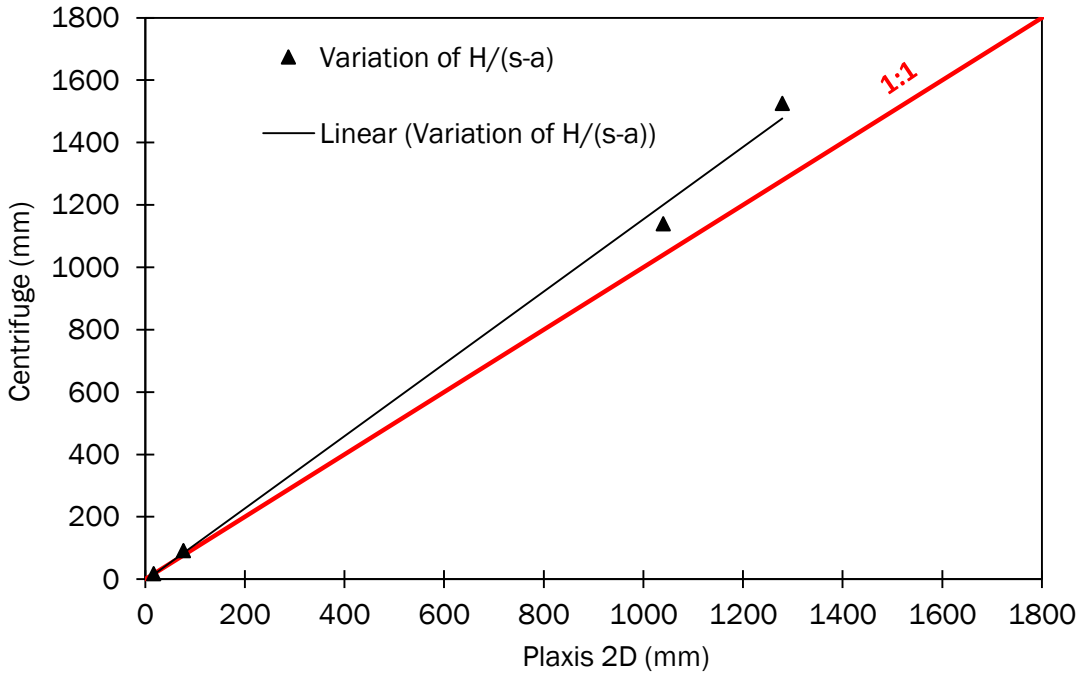

Figure 6.5 Relationship of centrifuge and Plaxis 2D modelling of the vertical deformational response of the geosynthetic reinforcement near the embankment toe

Test Series 1 showed that an initial decreased in the steepness of the side slope (1V:2H to 1V:3H) recorded a significant increase in the magnitudes of vertical deformations for both the centrifuge and Plaxis 2D data. A decrease of the side slope steepness, lower than 1V:3H, yielded an insignificant decrease in the magnitude of vertical deformations of the geosynthetic reinforcement in the centrifuge model case and a marginal increase in the Plaxis 2D case. Good agreement in both the magnitudes and the deformational response of the geosynthetic reinforcement for a variation of side slope steepness between the centrifuge and Plaxis 2D data was observed, Figure 6.6.

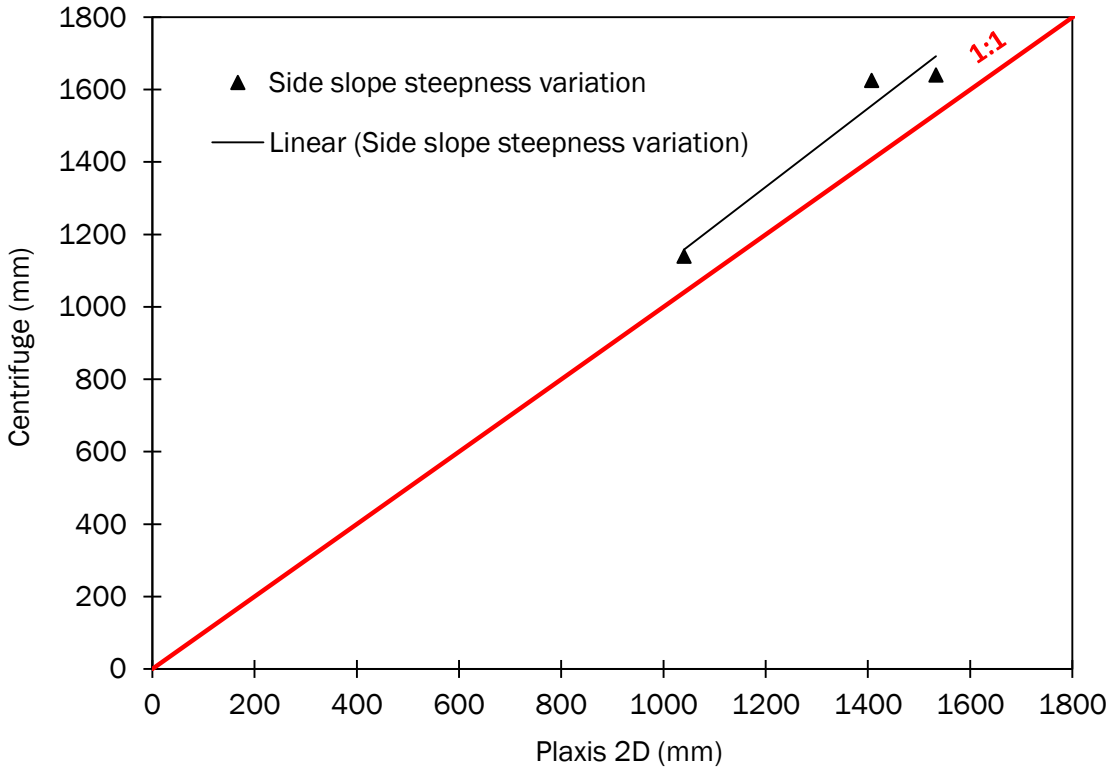

Figure 6.6 Relationship of centrifuge and Plaxis 2D modelling of the vertical deformational response of the geosynthetic reinforcement for a range of side slope steepness

The centrifuge and Plaxis 2D data showed good agreement in the measured and predicted vertical deformational response of the geosynthetic reinforcement for both subsoil stiffnesses. The centrifuge data consistently yielded greater magnitudes of vertical deformations in comparison to Plaxis 2D, Figure 6.7. The difference between the centrifuge and Plaxis 2D data recorded a slight divergence for an increase of the H/(s-a) ratio for both subsoil cases.

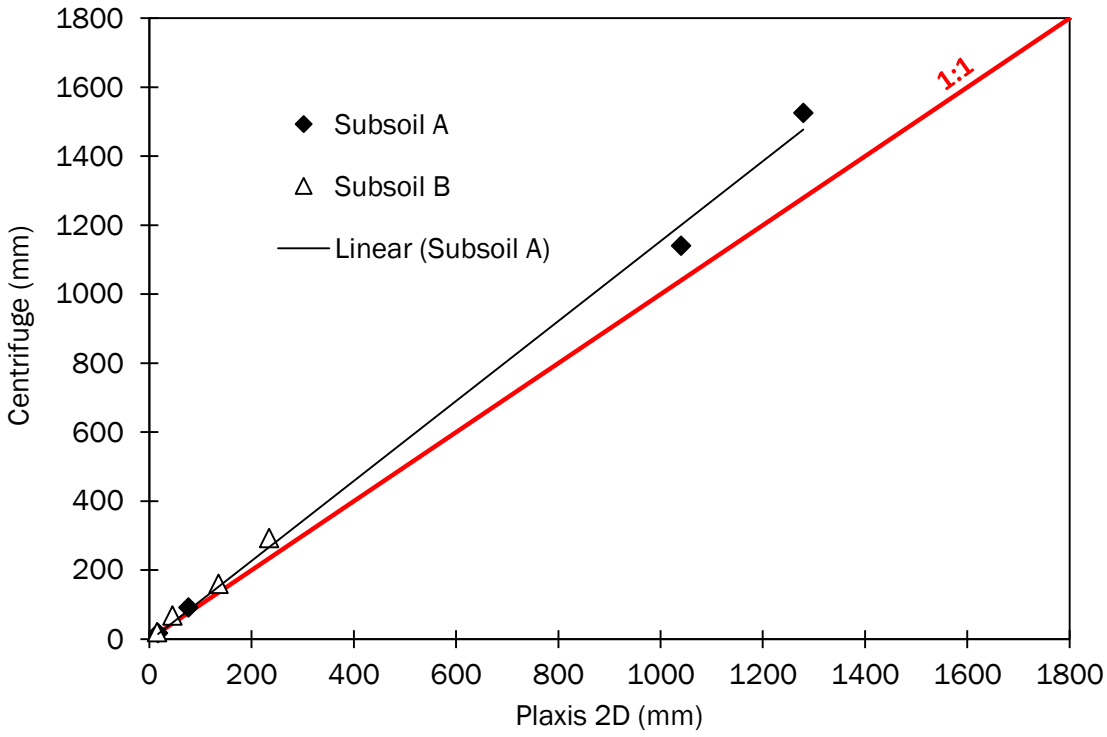

Figure 6.7 Relationship of centrifuge and Plaxis 2D modelling of the vertical deformational response of the geosynthetic reinforcement for a variation of subsoil stiffness

Test Series 2 examined the vertical deformational response of the reinforced piled embankment for a variation of the outer pile row location. Both the Plaxis 2D and the centrifuge models showed a significant reduction in vertical deformations as the outer pile row moved toward the embankment toe. Both data sets produced magnitudes of vertical deformations that reduced to zero for an extension of the pile group extents to the embankment toe. Similar conditions existed between the centrifuge and Plaxis 2D data sets in the response of the pile group to a variation of the side slope steepness.

6.2.3 Embankment mean surface deformations

Test Series 1 showed the magnitude of vertical deformation at the embankment surface increased for an increase in H/(s-a) ratio. Plaxis 2D consistently predicted lower magnitudes of embankment surface settlements than measured in comparable centrifuge models, Figure 6.8. The deformational response of the embankment fill yielded a consistent differential in magnitude between the Plaxis 2D and centrifuge models for a range of H/(s-a) ratio. The Plaxis 2D analysis was

consistently 25mm approximately lower in magnitude than the centrifuge analyses. A lower density of loose sand fill in the centrifuge embankment and densification of the embankment fill during installation of the model in the centrifuge are possible source for the difference.

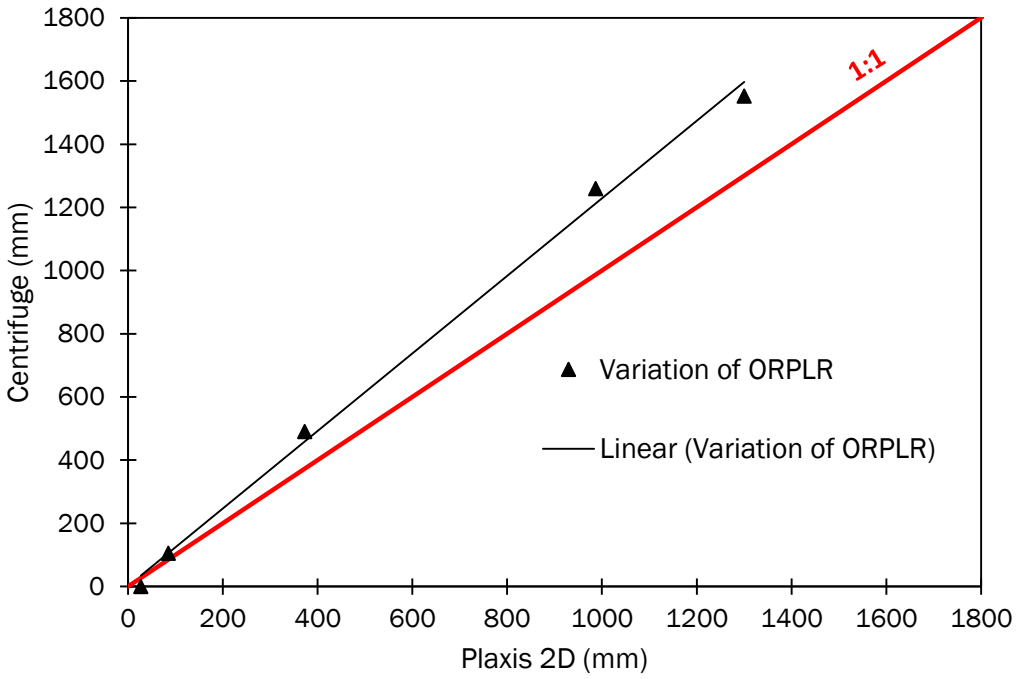

Figure 6.8 Relationship of centrifuge and Plaxis 2D modelling of the mean embankment surface deformational response of the geosynthetic reinforcement for a variation of ORPLR

Test Series 1 indicated that an increase in the steepness of the embankment side slope had a relatively insignificant influence on the overall deformation of the embankment surface. Both the Plaxis 2D and centrifuge models showed a small reduction in the magnitude of embankment surface settlement for a decrease in side slope steepness (a reduction of 5.4% and 4.9% for Plaxis 2D and the centrifuge respectively).

Test Series 1 examined the embankment mean surface deformational response of the model for a range of subsoil stiffness and H/(s-a) ratios. Embankment mean surface deformations increased for a decrease in subsoil stiffness in both the centrifuge and Plaxis models. Consistently greater magnitudes of embankment mean surface deformations were measured in the centrifuge modelling in comparison to those predicted by Plaxis 2D, Figure 6.9. Both the centrifuge and

Plaxis 2D data produced an almost linear increase of embankment mean surface deformation with H/(s-a) ratio for both subsoil stiffness's. The approximate differential of 20 – 25mm between the centrifuge and Plaxis 2D data sets in Figure 6.9 suggests possible experimental error during centrifuge modelling. Good agreement was observed between the centrifuge and Plaxis 2D both quantitatively and qualitatively for the response to subsoil stiffness, Figure 6.9.

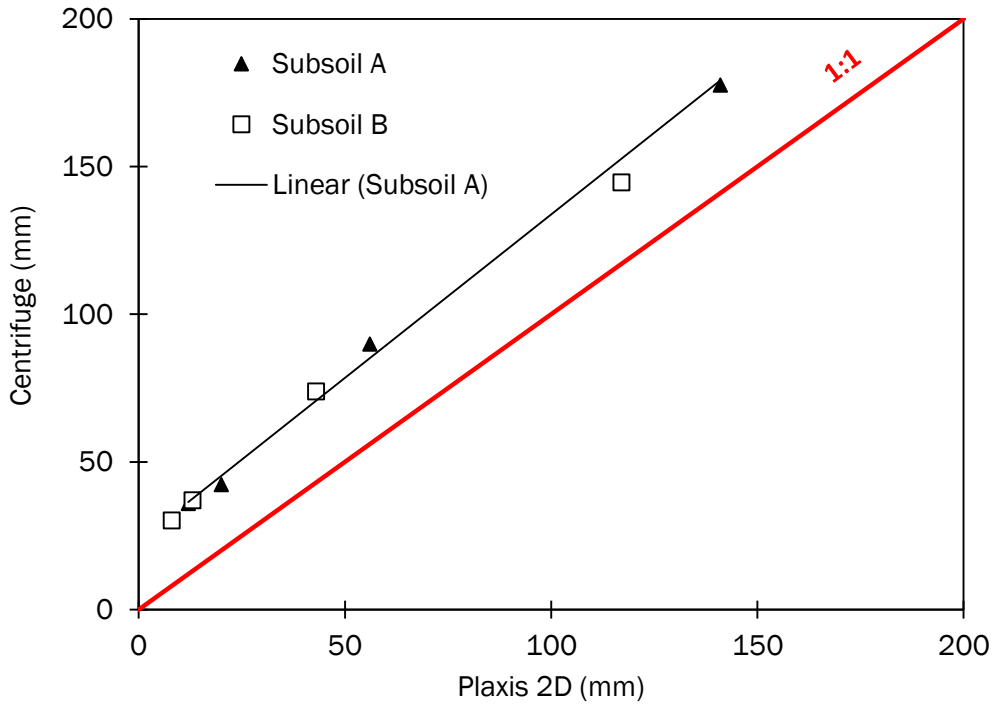

Figure 6.9 Relationship of centrifuge and Plaxis 2D modelling of the mean embankment surface deformational response of the geosynthetic reinforcement for a variation of Subsoil stiffness

The deformation at the crest of the embankment was examined in terms of its vertical and horizontal components. The ratio of improvement with regard to horizontal versus vertical deformations was linear and almost proportional for an increase in the stiffness of the geosynthetic reinforcement and a decrease in the depth of the underlying soft soil. A reduction in the steepness of the side slope yielded a notable improvement in the horizontal deformation whilst having an insignificant influence on the vertical deformation, Figure 4.37. For an increase in the embankment height, the Plaxis 2D analysis predicted a convergence of the deformational response of the two side slope steepness whilst the centrifuge data showed a consistent differential for a range of embankment heights.

Test Series 2 showed that the magnitude of mean surface deformations decreased as the outer row pile location approached the embankment toe for both modelling techniques. Agreement between Plaxis 2D and the centrifuge models in the overall characteristic response of the mean surface deformations with ORPLR was observed. The centrifuge analysis consistently yielded greater magnitudes of deformation in comparison to Plaxis 2D for both subsoils, Figure 6.10. Greater differentials between Plaxis 2D and the centrifuge models for Subsoil A in comparison to Subsoil B was observed, Figure 6.10. However, overall the centrifuge and Plaxis 2D were in good agreement both quantitatively and qualitatively, Figure 6.10.

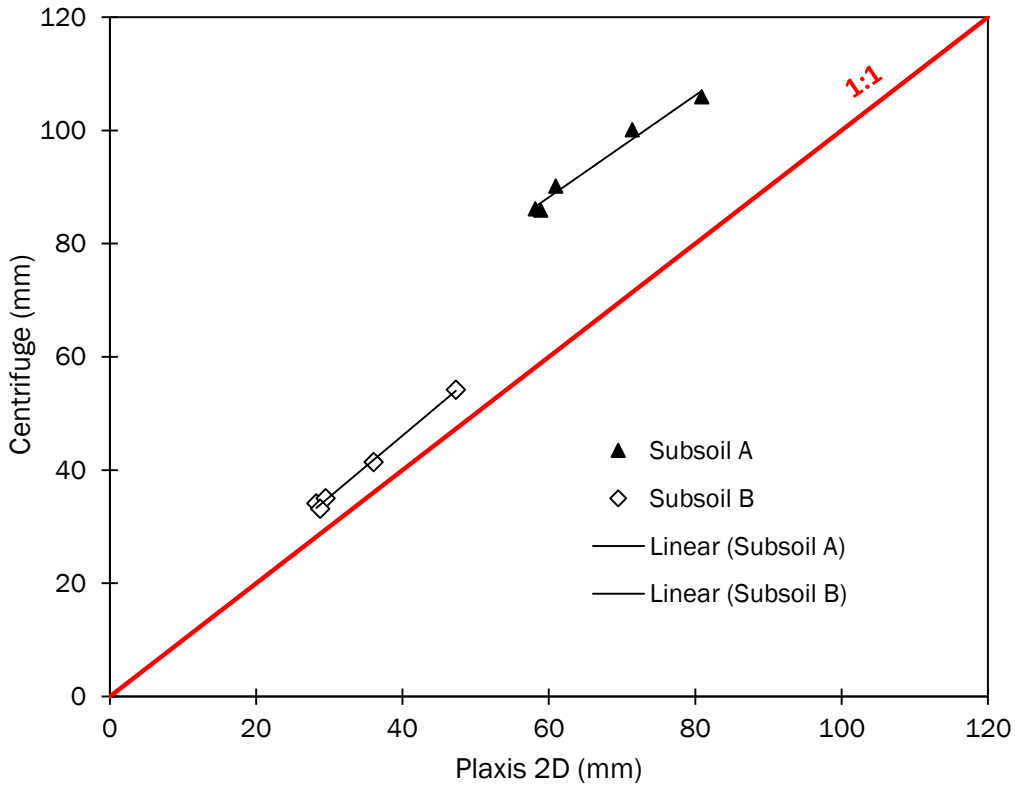

Figure 6.10 Relationship of centrifuge and Plaxis 2D modelling of the mean embankment surface deformational response of the geosynthetic reinforcement for a variation of ORPLR

6.2.4 Summary

The pile group lateral deformations, the surface settlements and geosynthetic deformations measured in the centrifuge model testing, compared reasonably well, both qualitatively and quantitatively, with those predicted in the Plaxis analyses in both Test Series 1 and 2. Plaxis 2D was therefore considered a valid numerical tool for modelling the plane strain response of reinforced piled embankment.

6.3 Finite element analysis of reinforced piled embankment

Test Series 3 consisted of a parametric variation of pertinent material, structural and geometric characteristics using Plaxis 2D.

The pile group and geosynthetic deformational response of the piled embankment was determined by Plaxis modelling. An analysis of the results of Plaxis Test Series 3 is presented with a discussion of the results under the following headings:

1. Outer pile row deformations
2. Geosynthetic reinforcement deformations
3. Geosynthetic reinforcement maximum tensions
4. Factor of safety on global stability
5. Strain compatibility ratio (SCR)

6.3.1 Outer pile row lateral deformations

The results from Plaxis Test Series 3 showed that the outer pile row was subjected to considerable magnitudes of lateral deformations for all parametric variations, Figure 6.11 and 6.12. Lateral deformations at the outer pile row head were most sensitive to a variation of embankment height and pile spacing, Figure 6.11. The lateral deflection of the pile heads within the pile group increased linearly for an increase of embankment height. The rate of increase in the lateral deflection with respect to embankment height at the outer row pile was linear.

Increasing the H/(s-a) ratio by decreasing the clear span between adjacent pile caps produced an overall decrease in lateral deformations at the outer pile row. Figure 6.11 indicated a linear decrease of the outer pile row lateral deformations for a decrease of the clear spacing between adjacent pile caps (increase in s-a). The magnitudes of lateral deformation of the outer pile row increased for a decrease in the lateral load capacity of the pile group (increase of pile spacing), Figure 6.11.

Figure 6.12 illustrates the lateral deformational response of the outer row pile for a parametric variation with the H/(s-a) ratio held constant at 2.0. The data points have been offset from the 2.0 H/(s-a) on the x-axis for greater clarity. The lateral deformation of the outer pile row was most sensitive to a variation of the pile rake angle whilst remaining relatively constant for a variation of the soft soil depth. The magnitude of lateral deformations decreased significantly as the outer pile row was located closer toward the embankment toe, Figure 6.12.

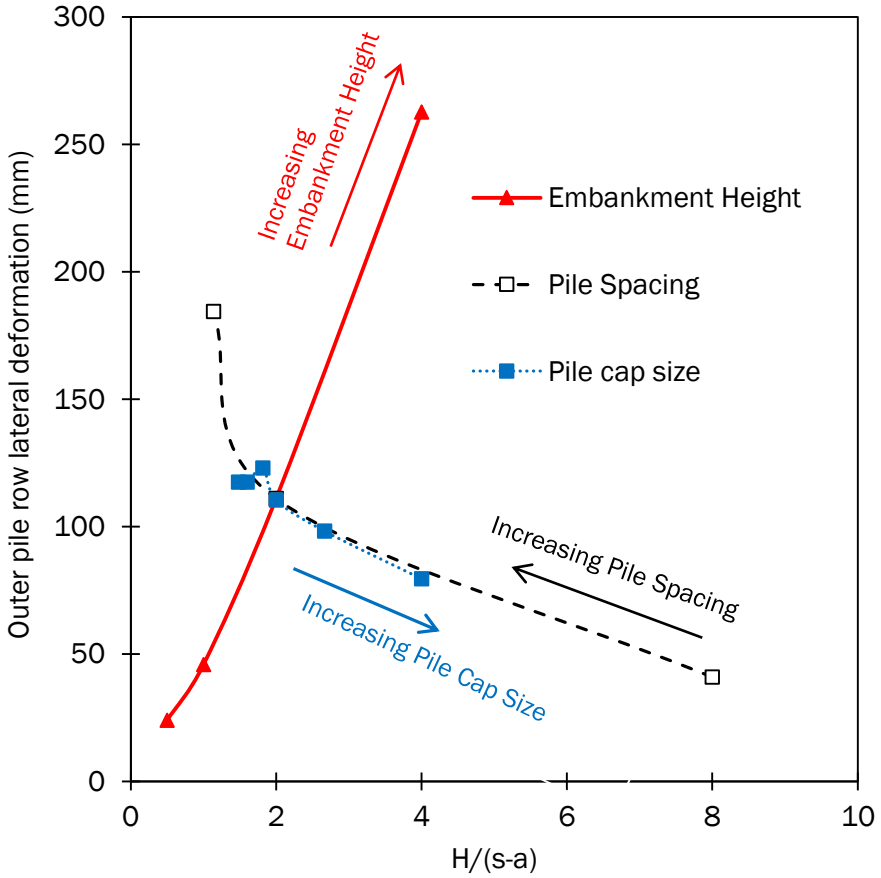

Figure 6.11 Lateral deformational response of the outer pile row for a range of parametric variations

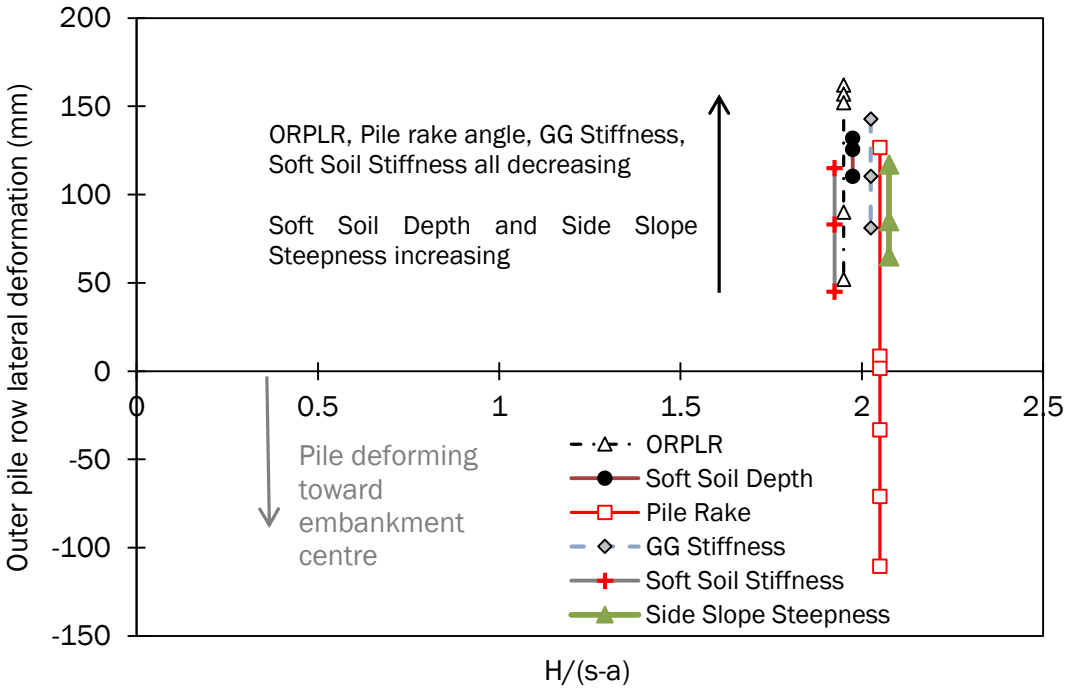

Figure 6.12 Lateral deformational response of the outer pile row for a range of parametric variations

6.3.2 Geosynthetic reinforcement vertical deformations

The vertical deformations of the geosynthetic reinforcement near the embankment toe were found to be most sensitive to the embankment height and the location of the outer pile row ORPLR, Figure 6.13 and 6.14. The magnitude of the vertical deformation at the clear span between adjacent piles, located near the embankment centre, increased linearly for an increase of the embankment height. Variation of geometric characteristics within the pile group (pile spacing and the pile cap size) had little to no effect on the vertical deformational response of the geosynthetic reinforcement near the embankment toe.

Vertical deformations of the geosynthetic reinforcement were significantly influenced by the location of the outer row pile and the stiffness of the soft soil, Figure 6.14. Geosynthetic reinforcement stiffness, outer pile row rake angle and soft soil depth had an insignificant effect on the magnitudes of vertical deformations, Figure 6.14. The vertical deformation of the geosynthetic reinforcement near the embankment toe increased for a decrease of the side slope steepness.

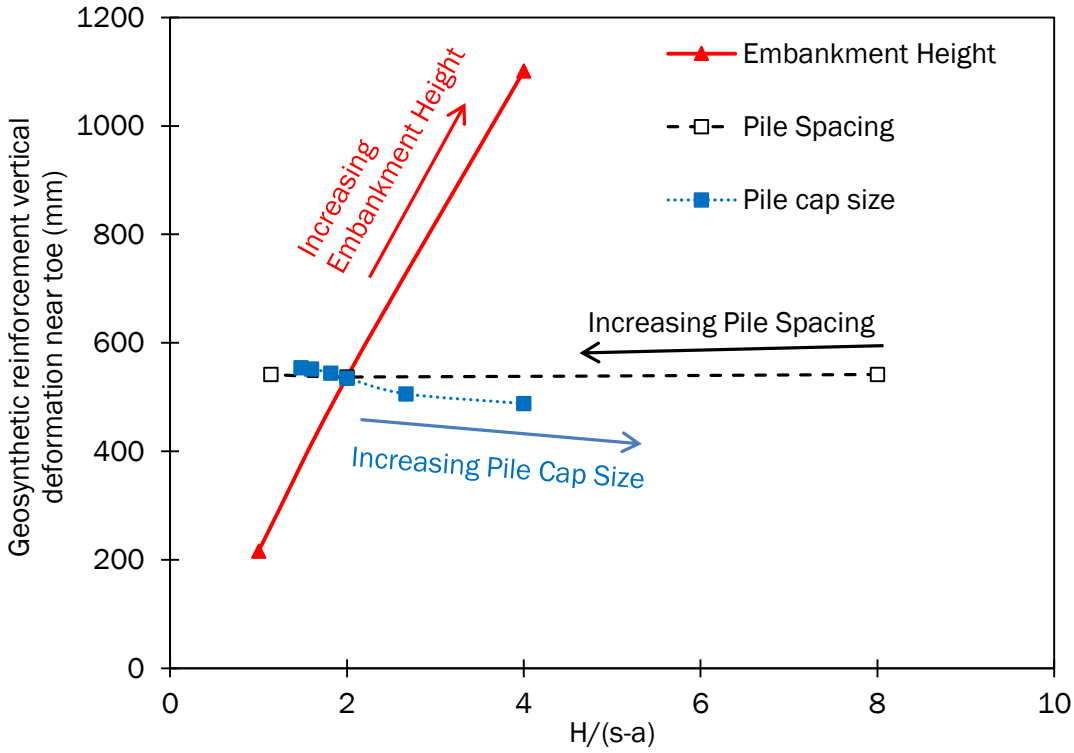

Figure 6.13 Vertical deformational response of the geosynthetic reinforcement for a range of parametric variations

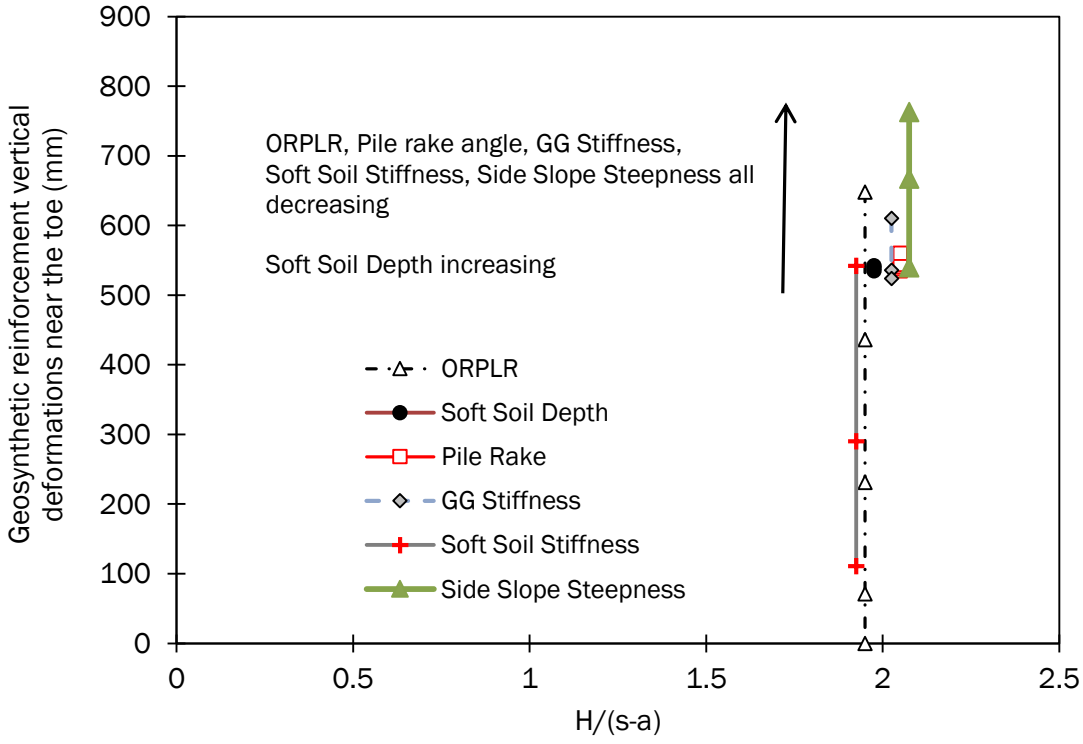

Figure 6.14 Vertical deformational response of the geosynthetic reinforcement for a range of parametric variations

6.3.3 Geosynthetic reinforcement maximum tensions

The maximum axial tension predicted in the geosynthetic reinforcement was most sensitive to a variation of the embankment height and the stiffness of the geosynthetic reinforcement, Figure 6.15 and 6.16. Increasing the embankment height produced an almost linear increase in axial tensions, Figure 6.15. Axial tensions in the reinforcement increased as the reinforcement attracted load from the lateral thrust acting outwards from the embankment centre. The reinforcement tension decreased significantly for H/(s-a) increasing from H/(s-a) = 1 to H/(s-a) = 4. Decreasing the clear spacing between the piles (s-a) lowered the critical height required for arching and stabilized the pile group behaviour, thus reducing the maximum axial tension in the geosynthetic reinforcement.

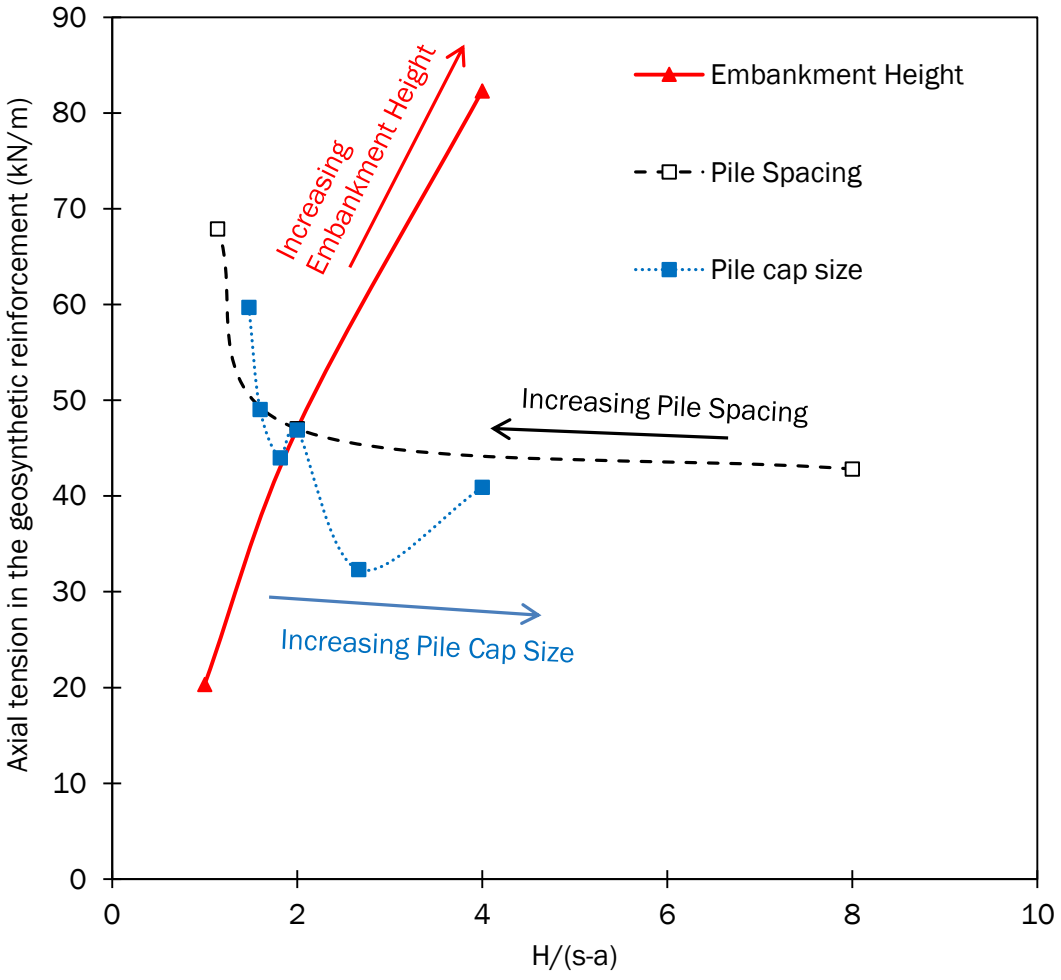

Figure 6.15 Maximum axial tension in the geosynthetic reinforcement for a range of parametric variations

Figure 6.16 illustrates the significance of the stiffness of the geosynthetic reinforcement on tension in the reinforcement. Axial tension in the geosynthetic reinforcement was not significantly affected by the side slope steepness or the soft soil depth, Figure 6.16. The axial tension acting along the reinforcement increased for an increase of the reinforcement stiffness. As the reinforcement stiffness increased, the stiffened reinforcement platform supported a greater portion of vertical loading between the adjacent pile cap edges and attracted an increased portion of the lateral thrust and resulted in an increase of axial tension in the reinforcement.

The axial tension in the geosynthetic reinforcement decreased for an increase of the ORPLR, Figure 6.16. Similar to the horizontal deformations of the geosynthetic reinforcement, magnitudes of axial tension in the reinforcement remained relatively constant at the embankment centre for a variation of ORPLR. A variation of the ORPLR had a significant effect on axial tension in the geosynthetic reinforcement under the embankment crest.

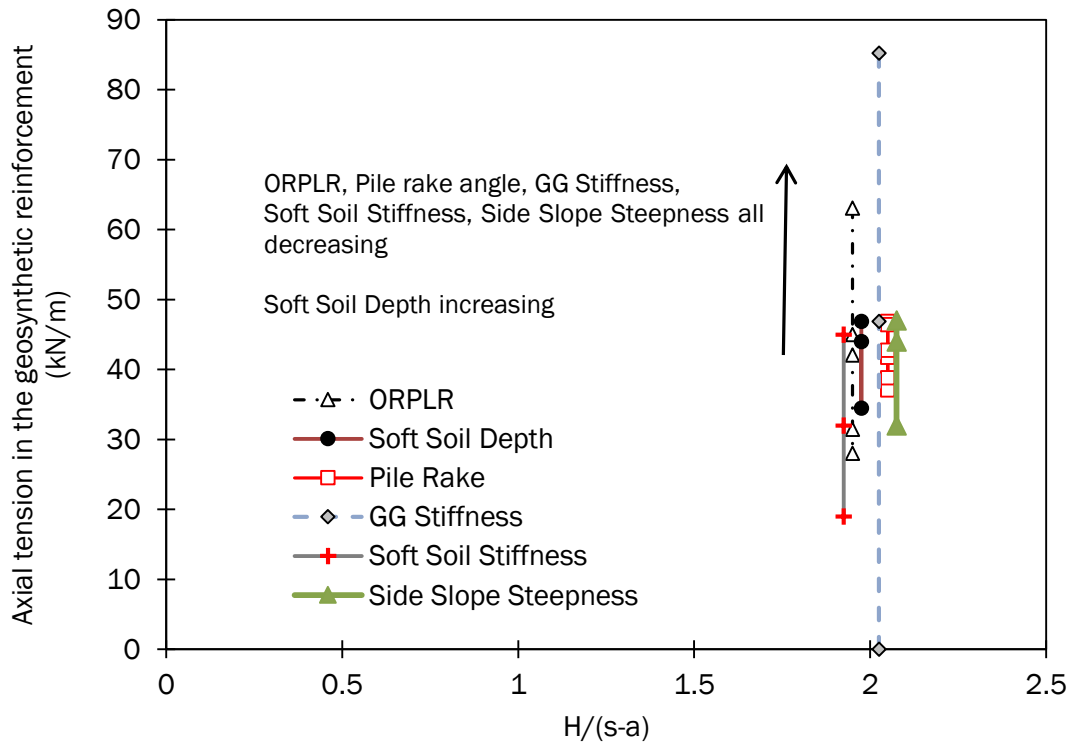

Figure 6.16 Maximum axial tension in the geosynthetic reinforcement for a range of parametric variations with H/(s-a) held constant

6.3.4 Factor of safety on global stability

Figures 6.17 and 6.18 illustrate that the factor of safety and overall stability of the geosynthetic reinforced piled embankment was most sensitive to a variation of the embankment height and the side slope steepness. Increasing the clear spacing between adjacent pile caps (s-a) produced a marginal reduction in overall stability, Figure 6.17. Increasing the embankment height required the structure to resist a greater lateral thrust and support a greater vertical loading from the embankment. Consequently, increasing the height reduced the overall structural stability. For all embankment heights, global stability was predominantly influenced by the degree of arching present and the destabilizing lateral thrust acting outwards from the embankment centre. The degree of arching present within the GRPE increased as the embankment height approached the critical height required for full arching (defined as 1.4 times the clear spacing between pile caps in BS 8006, 2010). Whilst an increase in embankment height resulted in an improvement in the degree of arching, the improvement in load transfer efficiency was insignificant in comparison to the destabilizing lateral forces which resulted in an overall reduction in global stability.

The overall stability of the GRPE structure was also sensitive to a variation of the side slope steepness. Whilst decreasing the side slope steepness significantly increased the magnitude of vertical deformation under the side slope, the overall stability of the structure increased, Figure 6.18. A decrease of the side slope steepness resulted in a decrease of the lateral thrust imbalance near the embankment crest and resulted in the pile group supporting a reduced portion of the strain compatibility condition required for equilibrium. A decrease of the embankment side slope also resulted in an increase of the overall embankment stability, Figure 6.18.

Locating the outer pile row closer toward the embankment toe increased the factor of safety of the structure, Figure 6.18. Increasing the number of piles within the side slope zone which resulted in lower magnitudes of deformations and destabilizing forces, consequently increased the stability of the structure. The greatest rate of increase of the factor of safety at failure was observed between 0.25 and 1.0 ORPLR.

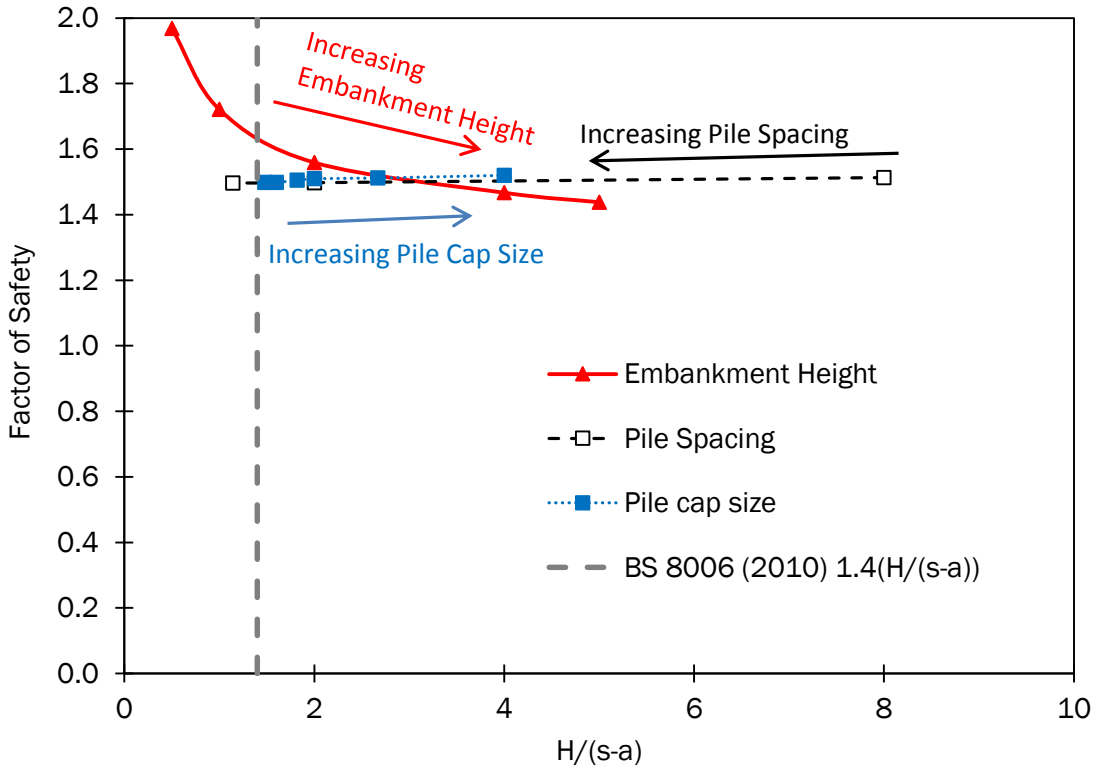

Figure 6.17 Factor of safety of the overall GRPE for a range of parametric variations with H/(s-a) held constant

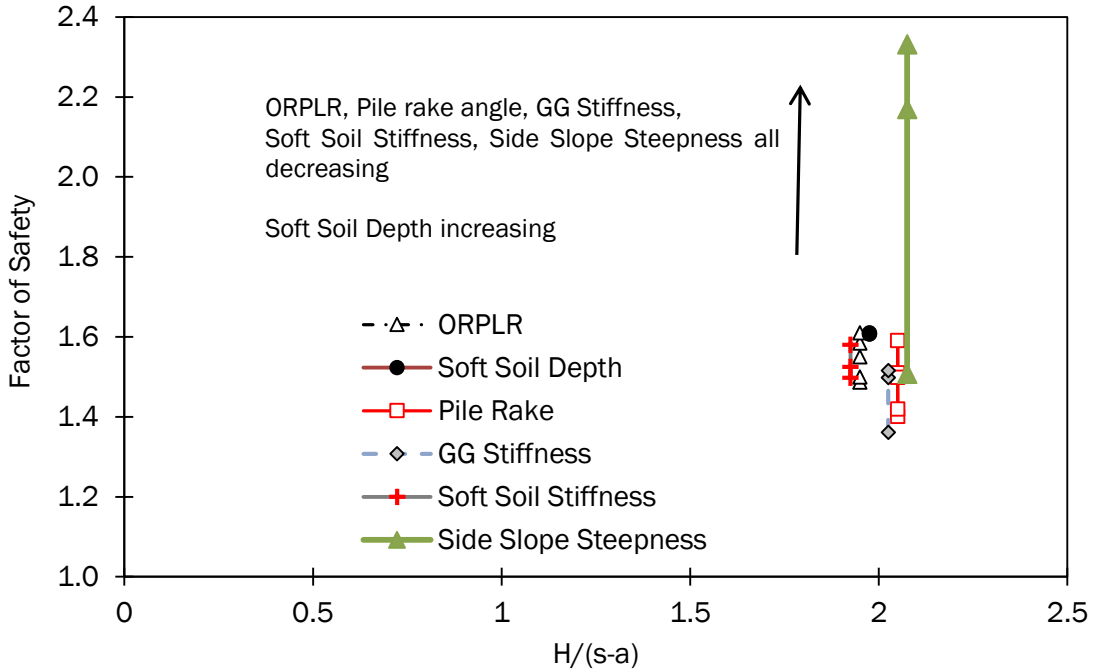

Figure 6.18 Factor of safety of the overall GRPE for a range of parametric variations with H/(s-a) held constant

6.3.5 Strain compatibility ratio (SCR)

The strain compatibility ratio was found to be most sensitive to a variation of the pile cap size and embankment height, Figure 6.19. The strain compatibility ratio increased for an increase in the pile cap size (decrease in clear span between the adjacent pile cap edges). An increase of embankment height resulted in a mobilization of lateral thrusts resisted by the pile group (increase of SCR), Figure 6.19. The strain compatibility ratio decreased for a decrease in the lateral loading capacity of the pile group (increase in pile spacing).

Figure 6.20 suggests that the geosynthetic reinforcement stiffness also had a significant influence on the SCR. The initial inclusion of geosynthetic reinforcement (0 to 500kN) in the piled embankment structure produced a significant increase in the SCR. Increasing the stiffness of the geosynthetic reinforcement further produced significant increases in the SCR. The ORPLR, soft soil depth and side slope steepness had a relatively insignificant influence on the SCR. Variation of the soft soil stiffness and the outer pile rake angle produced similar magnitude of response from the load transfer mechanism within the structure.

Whilst both the pile group and geosynthetic reinforcement were subjected to lower magnitudes of both deformations and forces, a greater rate of reduction was observed within the geosynthetic reinforcement for an increase of ORPLR, Figure 6.20. The strain compatibility ratio suggested that the pile group mobilised a significant increase (approximately 38%) in the proportion of loading carried by the pile group in comparison to the geosynthetic reinforcement as the outer pile row location approached the toe.

The strain compatibility ratio (SCR) increased for an increase in reinforcement stiffness, Figure 6.20. As the reinforcement stiffness increased, a greater portion of the strain compatibility condition necessary for equilibrium within the structure was resisted by the pile group in comparison to the geosynthetic reinforcement. The initial inclusion of reinforcement within the structure yielded the most significant reduction in deformation of the embankment structural fill material, decrease in reinforcement deformation, and an increase in magnitude of axial load, pile head deflection, bending moment and pile group efficacy. A further increase of the

reinforcement stiffness followed the same trend, but with lower magnitudes of improvement.

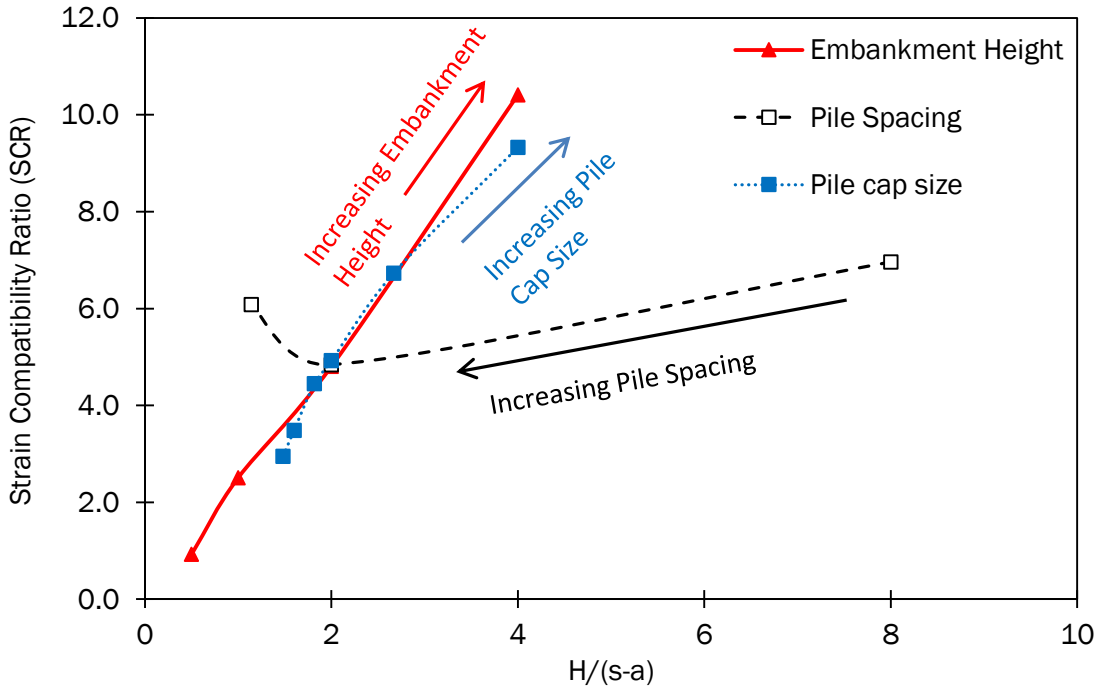

Figure 6.19 Strain Compatibility Ratio (SCR) of the overall GRPE for a variation of w H/(s-a) ratio

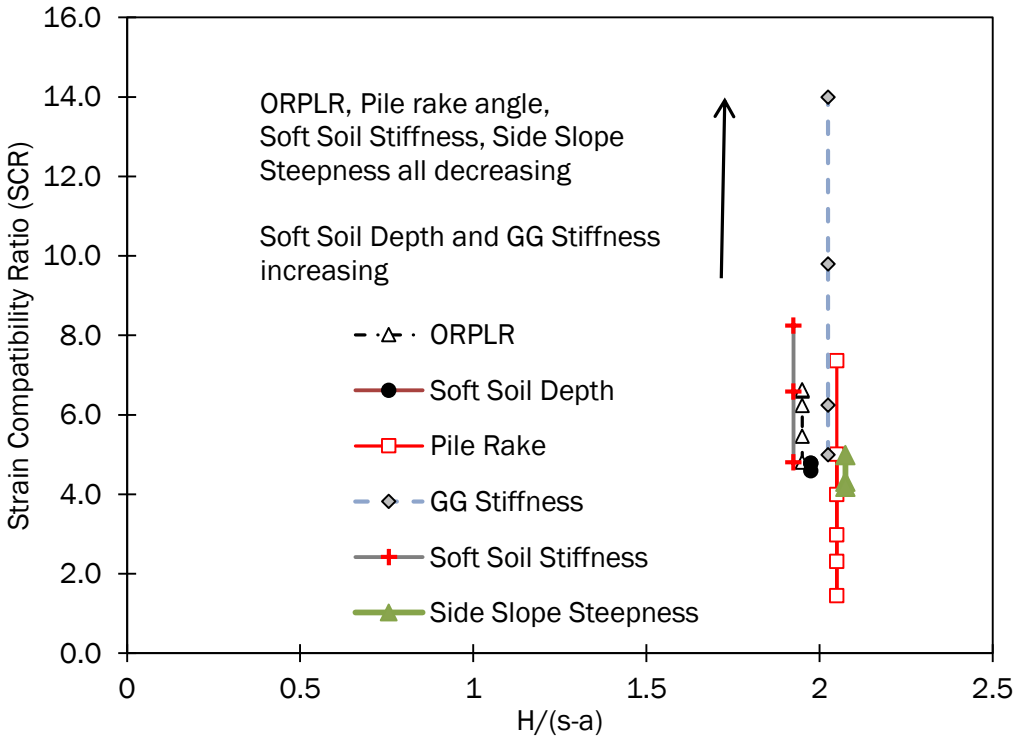

Figure 6.20 Strain Compatibility Ratio (SCR) of the overall GRPE for a range of parametric variations with H/(s-a) held constant

6.4 Implications for design

Strain compatibility must be achieved between displacement of the geosynthetic reinforcement, deformation of the pile head and the embankment fill material. Figure 6.21 illustrates the equilibrium condition for the generic case of 4.0m embankment height, pile spacing of 3.0m, pile cap size of 1.0m and geosynthetic stiffness of 500 kN/m. The horizontal deformation of the reinforcement at each location along the pile group extent was approximately equal in magnitude to the lateral deformation of each pile head. Interface elements between the geosynthetic reinforcement and the pile heads were modelled using an interface friction value in Plaxis 2D (R_{inter}) of 0.85 to enable differential sliding between the two elements. Examination of differential sliding between the pile head and reinforcement in the centrifuge tests was not possible. Further analysis is required to examine the extent of the sliding effect between the pile heads and the geosynthetic reinforcement to validate whether the lack of differential sliding between the pile head and reinforcement is consistent with full scale structures in the field or is a product of FE analyses. The tension developed in the reinforcement at the strain compatibility condition was lower than the estimated tensions T_{ds}, T_{rp} and T_{total} (= T_{rp} + T_{ds}) given in BS 8006 (2010). The BS 8006 (2010) design code was based on the assumption that the reinforcement would act as a stiffened platform and offer sufficient resistance to impede the lateral thrust and transfer only vertical loading to the pile head.

The pile group was found to offer lateral load resistance to the reinforcement and thus enabled the lateral thrust acting outward from the embankment centre to be resisted and the reinforcement attracting a lower magnitude of loading and recorded lower tensions. For all cases examined, the piles within the pile group extent were subject to lateral loads. The maximum tension in the reinforcement recorded by Plaxis 2D, increased almost linearly with embankment height, Figure 6.22. An embankment height of 2.8m, which correlated with H/(s-a) ratio of approximately 1.7 yielded a divergence in the relationship between the predicted numerical analysis tension and those estimated (T_{ds}) using the BS 8006 (2010) approach, Figure 6.22.

Figures 6.23 and 6.24 suggest the BS 8006 (2010) geosynthetic reinforcement tension predictions are much higher than the Plaxis 2D models results. The BS 8006 T_{rp} predictions are considerably higher than the equivalent Plaxis 2D results for large pile spacing (s) and small pile cap size (a). Currently, there is a lack of knowledge concerning the accuracy of the tensions predicted by BS 8006.

For a variation of the pile spacing and pile cap size, the tensions recorded by Plaxis 2D remained relatively constant in comparison to the values predicted by BS 8006. This was due to the spike in maximum tension in the reinforcement as a result of the side slope at the outer pile row pile cap edge, Figure 6.23 and 6.24.

Typically, a reinforced piled embankment will have a pile cap coverage of approximately 10 – 20% in 3D. The smallest pile cap size of 0.3m (Figure 6.24) corresponded to a pile cap coverage area of 10% in 2D but only 1% in 3D, pile cap coverage areas as low as 1% in 3D would not be encountered in the field.

The strains calculated by Plaxis 2D are generally high. The maximum tension calculated in the generic model by Plaxis 2D implies a strain of approximately 30%. In general, the BS 8006 (2010), suggests a maximum allowable strain during the design life of the structure of 6% and an additional 2% for reinforcement creep. The high strains predicted by Plaxis 2D suggests the reinforcement stiffness of 500 kN/m is generally too low. Geosynthetic reinforcement with a stiffness of 500 kN/m was modelled to ensure that the stiffness of the reinforcement was not too great for particularly low embankment heights, in order to avoid the stability of the structure being exaggerated by a stiff reinforcement platform.

The strain compatibility ratio was found to be most sensitive to a variation of the pile cap size, Figure 6.19. The strain compatibility ratio increased for an increase in the pile cap size (decrease in clear span between the adjacent pile cap edges). The strain compatibility ratio was not a function of the clear span between the adjacent pile cap edges. The strain compatibility ratio increased for a decrease in the lateral loading capacity of the pile group (increased in pile spacing).

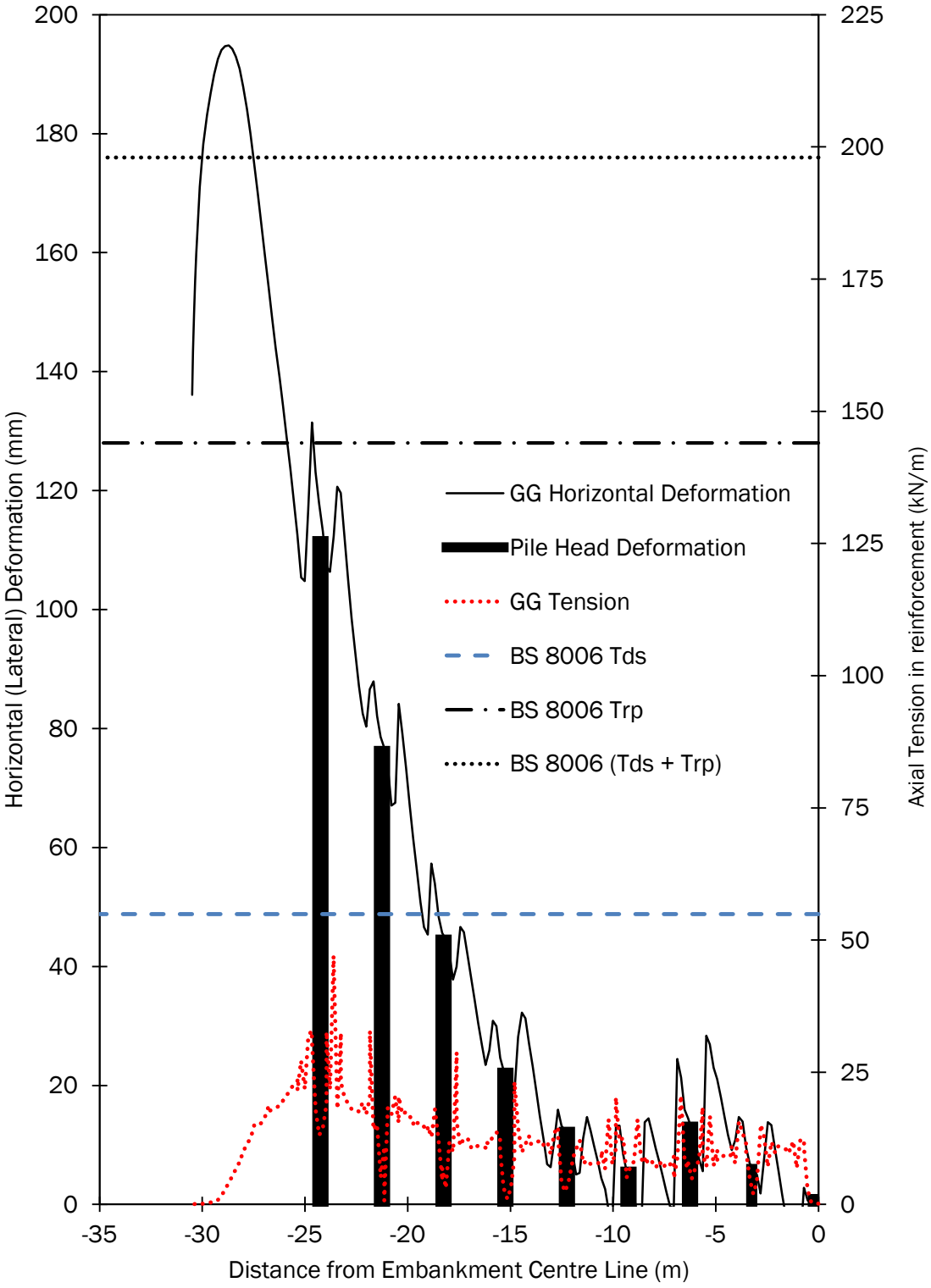

Figure 6.21 Strain Compatibility condition between reinforcement and pile group

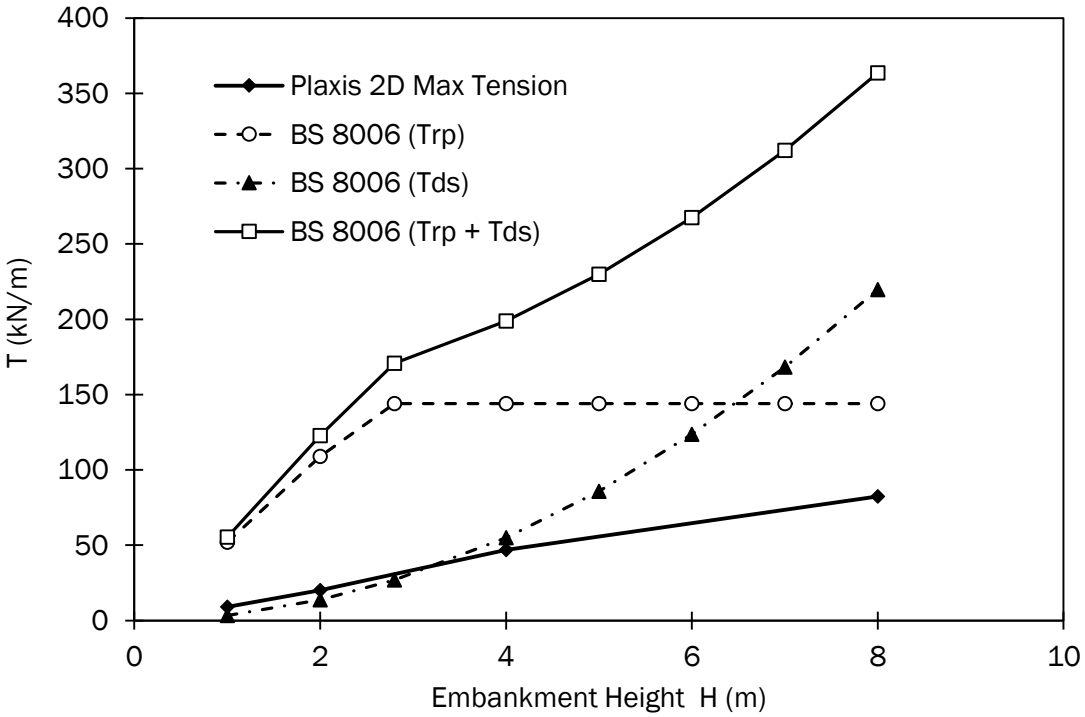

Figure 6.22 Tension developed in reinforcement for a range of embankment heights for Plaxis 2D and BS 8006 (2010) T_{ds} *&* T_{rp}

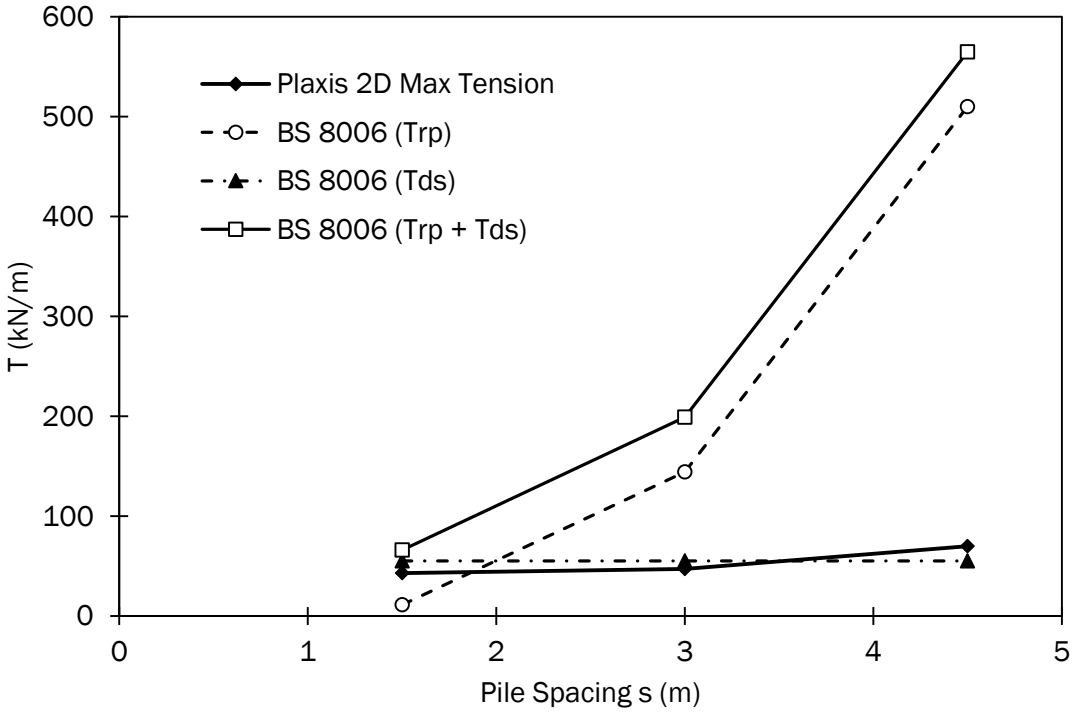

Figure 6.23 Tension developed in reinforcement for a range of pile spacing (s) for Plaxis 2D and BS 8006 (2010) T_{ds} *&* T_{rp}

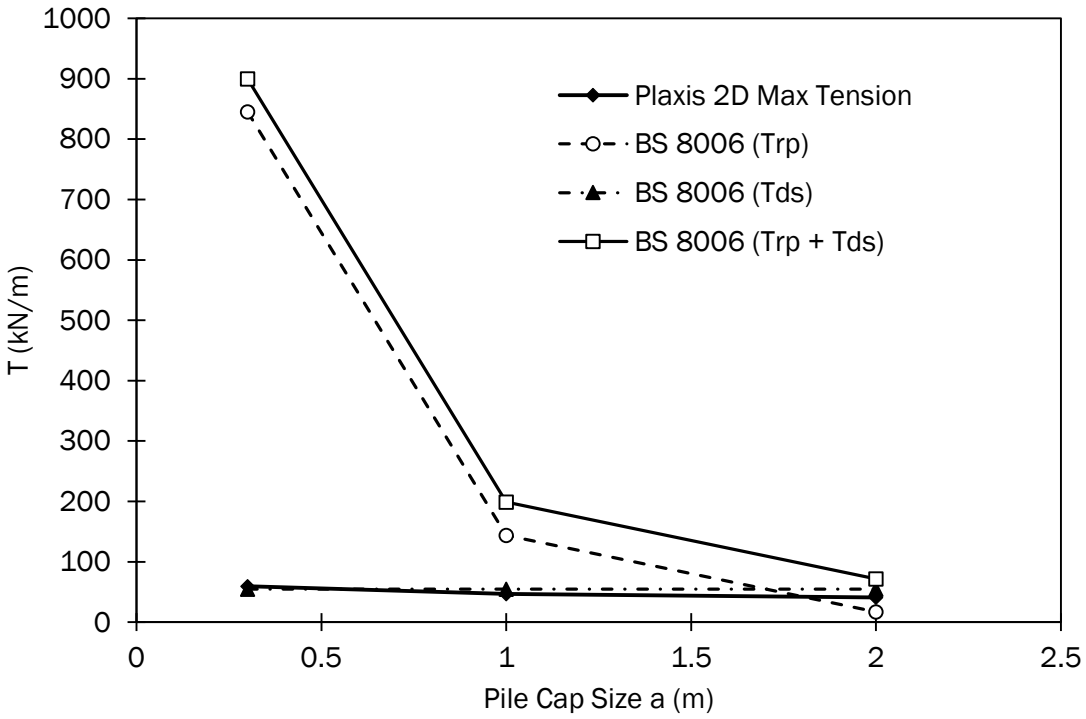

Figure 6.24 Tension developed in reinforcement for a range of pile cap size (a) for Plaxis 2D and BS 8006 (2010) T_{ds} & T_{rp}

6.5 Summary

Analysis and discussion of the results of the centrifuge and Plaxis modelling have been presented. The centrifuge testing and Plaxis analyses were divided into a number of test series. Test Series 1 and 2 consisted of centrifuge and Plaxis analysis to investigate the importance of certain design parameters, such as embankment height, side slope steepness, subsoil stiffness, and the effects of the extension of the pile group a greater distance towards the embankment toe, on the deformational performance of piled embankments. Test Series 3 consisted of Plaxis analysis to investigate the influence of embankment height, side slope steepness, pile spacing, pile cap size, geosynthetic stiffness, subsoil depth, subsoil stiffness, outer pile row rake angle and outer pile row location. The results of the centrifuge model tests were also used to validate the Plaxis analyses.

The pile group lateral deformations, the surface settlements and geosynthetic deformations measured in the centrifuge model testing, compared reasonably well,

both quantitatively and qualitatively, with those predicted by Plaxis in Test Series 1 and 2. The centrifuge model testing and Plaxis analyses indicated that embankment height to clear spacing ratio, stiffness of the subsoil, embankment side slope steepness and location of the outer pile row all had a significant effect on the piled embankment pile head lateral deformations, embankment surface settlements and geosynthetic deformations.

The relationships between the pile group lateral deformations, the vertical deformation of the reinforcement and the embankment mean surface deformations and the height to clear spacing ratio (H/(s−a)) measured in the centrifuge testing were in reasonably close agreement with those predicted by Plaxis analyses. The centrifuge testing and Plaxis suggested that H/(s−a) and subsoil stiffness had a significant influence on the pile head lateral deformation and vertical deformation of the reinforcement.

The Plaxis and centrifuge analyses from Test Series 1 both suggested significant lateral deformations occur at each pile head within the pile group extent. Both sets of analyses also suggest that the magnitude of lateral deformation of the outer pile row increased almost linearly with H/(s-a), an increase of the side slope steepness and a decrease of the subsoil stiffness.

The Plaxis and centrifuge analyses suggested significant vertical deformation of the reinforcement occurred near the embankment toe. Both sets of analyses suggested that the vertical deformation increased almost linearly with embankment height, a decrease of both side slope steepness and subsoil stiffness. The subsoil stiffness had a significant effect on both the pile group and reinforcement vertical deformations, but had a negligible effect on embankment mean surface deformations. Embankment mean surface deformations appeared to be only slightly influenced by the stiffness of the subsoil. The Plaxis analyses consistently predicted lower magnitudes of vertical deformations of both the reinforcement and the embankment mean surface deformations and greater magnitudes of pile group lateral deformations in comparison to measured centrifuge values. Good agreement, both quantitatively and qualitatively, was found between the centrifuge and Plaxis models, thus Plaxis 2D was validated for the analysis of the deformational response of a geosynthetic reinforced piled embankment.

The location of the outer pile row had a considerable effect on the lateral deformations at each pile within the pile group irrespective of the subsoil stiffness and embankment side slope steepness. Evidence of a minor reduction in the embankment surface mean settlements was observed as the outer pile row was located closer toward the embankment toe. Vertical deformation of the reinforcement outside of the pile group extent, decreased significantly as the outer row pile was located closer toward the embankment toe.

The analysis indicated that all piles within the pile group were subjected to significant deformations. Lateral deformations and pile bending moments at each pile within the pile group was influenced by the embankment height, side slope steepness, pile spacing, pile cap size and outer pile row location. The depth of the soft soil layer had a minor influence on the magnitude of pile head lateral deformations within the pile group.

The geosynthetic reinforcement was subjected to significant horizontal and vertical deformations. Horizontal deformations of the geosynthetic reinforcement were predominantly influenced by embankment height, pile spacing, pile rake angle, geosynthetic stiffness, subsoil stiffness and outer pile row location. Vertical deformation of the geosynthetic reinforcement was significantly influenced by embankment height, side slope steepness, subsoil stiffness and outer pile row location.

The axial tension in the geosynthetic reinforcement was most sensitive to H/(s-a), side slope steepness, geosynthetic stiffness and subsoil stiffness. Plaxis analyses investigating the tensile load distribution along the geosynthetic reinforcement highlighted the importance of considering subsoil support in piled embankment design. The analyses also indicated that maximum tensile loads generated in the geosynthetic reinforcement increased with H/(s−a) and the tensile stiffness of the geosynthetic.

Chapter 7

Conclusions

7.1 Introduction

This study described a detailed plane strain investigation into the lateral loading conditions on a geosynthetic reinforced piled embankment using physical (centrifuge) and numerical (Plaxis 2D) methods. The results of this study provide an improved understanding of the plane strain lateral loading mechanism within geosynthetic reinforced piled embankments and identify some of the key variables which influence the performance of piled embankments.

7.2 Project Summary

The literature review, Chapter 2, presented the piled embankment design methods and some of the key physical and numerical modelling studies which have previously been conducted on geosynthetic reinforced piled embankments. Previous studies identified the shear strength of the fill, the ratio of clear spacing to height of fill and the strength and stiffness of the geosynthetic as key parameters. The effect of the subsoil on the overall embankment response, however, was not

considered in many of these studies. The various design methods have not properly accounted for the effect of subsoil stiffness on the structures performance, but studies by Farag (2008) have suggested that significant inconsistencies exist between the various methods in relation to the reinforced piled embankment resistance to lateral loading. Currently, there is a lack of literature which examines the lateral loading conditions at the lateral extremities of reinforced piled embankments.

A detailed description of the methods used to carry out this study was presented in Chapter 3. The two-dimensional centrifuge model consisted of piles constructed from Perspex sheets (E = 1.9 GPa), subsoil modelled with synthetic sponge (E = 54 kPa) and expanded polystyrene (E = 240 kPa), geosynthetic reinforcement modelled with polyethylene sheets (J_{re} = 4.7 kN/m at 1g) and the embankment fill was modelled using a uniform slightly silty medium sand. The physical properties of these materials were determined and with centrifuge scaling factors applied, were typical of those used in piled embankments. Deformations of the in-flight model in the centrifuge were captured using photographic images.

The numerical model was developed using the finite element modelling software Plaxis 2D. A plane strain analysis of reinforced piled embankments was performed with the dimensions and material properties of the Plaxis model based on the centrifuge model subjected to a centrifugal acceleration of 60g. The embankment fill was modelled using a Mohr Coulomb model, the subsoil using a Soft Soil Model, the piles as linear elastic plates and the geosynthetic reinforcement as a geogrid.

The results of the centrifuge model testing and the Plaxis analyses were presented in Chapters 4 and 5, with analysis and discussion of the results in Chapter 6. The centrifuge model testing was divided into two test series to investigate the influence of parameters such as, embankment height to clear spacing ratio, subsoil stiffness, embankment side slope steepness and the outer pile row location on the lateral loading conditions in reinforced piled embankments. The behaviour of the system was assessed by recording the pile head lateral deformations, geosynthetic reinforcement vertical deformations spanning across the embankment structure and embankment mean surface deformations at the top of the model embankment.

The Plaxis analyses, which replicated each of the tests performed in the centrifuge, was used to further assess the surface and geosynthetic deformational response of the reinforced piled embankment, as well as the tensile force along the reinforcement, bending moments in the pile group and the factor of safety on global stability of the structure. The appropriateness of Plaxis for the analyses of piled embankments was assessed by directly comparing data from the physical and numerical models.

7.3 Results of Physical and Numerical Modelling

Generally the centrifuge model showed increased magnitudes of pile lateral deformations, geosynthetic deformations and mean surface settlements with both increased g-level and H/(s-a) ratio. Pile group deformations measured from the centrifuge models compared reasonably well, both quantitatively and qualitatively, with those predicted by Plaxis in Test Series 1. Plaxis consistently predicted greater magnitudes of pile lateral deformations within the pile group in comparison to deformations measured from the centrifuge models. The centrifuge and Plaxis modelling response of the pile group suggested that all piles within the pile group were subjected to lateral deformations at the pile head and increased almost exponentially as the pile location neared the embankment crest.

Both the centrifuge and Plaxis modelling recorded a lateral deformation maxim at the outer most pile row. The magnitude of outer pile row deformation increased almost linearly with embankment height in both Plaxis and the centrifuge and was independent of side slope steepness and subsoil stiffness. Plaxis predicted outer pile row lateral deformations from 15 to 29% greater for low to high H/(s-a) ratios in comparison to the measured values in the centrifuge. A slight divergence in lateral deformation at the outer pile two was observed between Plaxis and centrifuge data sets for an increase of embankment height for both side slopes which was independent of side slope steepness. Both analyses techniques produced a linear increase of outer pile row lateral deformation with an increase of side slope steepness. Plaxis consistently predicted outer pile row lateral deformations approximately 25% greater than those measured in the centrifuge model for a range of side slopes. The stiffness of the subsoil had a large impact on the outer pile row deformation. Outer pile row lateral deformations in the model with subsoil A

(lesser stiffness) were approximately 44 % higher than the model incorporating subsoil B, according to the Plaxis analyses, and 48 - 54 % higher, according to the centrifuge test data.

The geosynthetic vertical deformations measured in the centrifuge testing also compared reasonably well with the predicted Plaxis values. Both Plaxis and the centrifuge modelling produced vertical deformation in the geosynthetic reinforcement with a catenary type shape between adjacent pile caps, located from the centre line of the embankment to the outer row of piles, where a maxim was recorded outside the outer pile row near the embankment toe. Both the Plaxis and centrifuge modelling showed that the vertical deformation of the geosynthetic reinforcement increased almost linearly with H/(s-a) for both side slope steepnesses.

Overall, both the Plaxis and centrifuge models showed that the vertical deformations of the geosynthetic reinforcement increased with embankment height. The centrifuge model measured magnitudes of vertical deformations consistently 9 - 15% greater those predicted by the Plaxis model. The stiffness of the subsoil had a large impact on the geosynthetic deformations with the exception for low embankment heights. Geosynthetic deformations in the subsoil A (lesser stiffness) centrifuge model were approximately 10 - 20 % greater than those observed in the comparable Plaxis model and 19 – 35% greater from the stiffer subsoil B. Embankment side slope steepness had a significant effect of vertical deformations of the geosynthetic reinforcement near the toe. Increasing the embankment side slope steepness from 1V:4H to 1V:2H yielded a 47 and 43% decrease in vertical deformations near the toe in both the Plaxis and centrifuge models respectively. This reduction was attributed to a shorter length of side slope supported by the soft soil outside of the pile group. For a range of side slope steepness, centrifuge data remained consistently 9 – 15% greater than comparative Plaxis analyses.

Both the Plaxis and centrifuge modelling suggested that the embankment mean surface deformations increased almost linearly with embankment height, remained constant irrespective of side slope steepness and recorded a minor increase in magnitude for the lower stiffness subsoil A. The centrifuge consistently recorded

magnitudes of embankment mean surface deformations 25 – 30mm greater than predicted in the Plaxis model. Possible unavoidable densification of the embankment fill material layer in the centrifuge model during installation and errors in the measurement technique could explain these discrepancies.

Examination of the outer pile row location on the performance of the structure again showed good agreement between the Plaxis and centrifuge data. The data suggest that the location of the outer pile row had a considerable effect on the lateral deformations at each pile within the pile group irrespective of the subsoil stiffness and embankment side slope steepness. A decrease of 63% and 70% respectively was observed for the Plaxis and centrifuge models as the pile group extents extended from directly under the crest to the toe of the embankment. Significant reduction of vertical deformation of the geosynthetic reinforcement outside of the pile group extent as the outer row pile was located closer toward the embankment toe was observed. Both Plaxis and the centrifuge models yielded the largest decrease in geosynthetic reinforcement vertical deformations as the ORPLR approached 0.75 for both subsoil stiffnesses. Evidence of a minor decrease in the embankment surface mean settlements as the outer pile row was located closer toward the embankment toe was also observed.

Examination of the overall deformational response of the Plaxis and centrifuge models reveal good agreement between the two methods in predicting the response of the reinforced piled embankment under the side slope at the extremities of geosynthetic reinforced piled embankments.

Test Series 3 consisted of Plaxis modelling only and extended the numerical analysis to investigate other pertinent parameters. Increasing the pile spacing showed an overall increased magnitude of deformation in the system. Increasing the pile spacing within a pile group decreased the lateral load capacity of the pile group. Significant geosynthetic reinforcement vertical, horizontal and axial tensions increases along with pile group lateral deformation and bending moment increases was observed. Increasing the pile spacing decreased the pile group efficacy and the overall structural stability marginally.

Increasing the pile cap size increased the load transfer mechanisms within the structure. Vertical deformations of the geosynthetic reinforcement between

adjacent pile caps and at the clear span near the embankment toe showed a significant decrease in magnitude. Horizontal deformations and axial tension in the geosynthetic reinforcement decreased significantly along the width of the structure for an increase in pile cap size. Overall, the lateral deformations and the individual pile bending moments within the pile group decreased with an increase in pile caps size. The pile group efficacy increased significantly along with a moderate increase in structural stability for an increase of pile cap size.

Plaxis modelling showed the raking of the outer pile row decreased the overall deformations within the structure. The horizontal deformation and axial tension acting along the length of the geosynthetic reinforcement decreased for an increase of the pile rake angle. Vertical deformation of the geosynthetic near the embankment toe increased marginally with an increase of the rake angle. The outer row raked pile reduced the horizontal deformation and the axial tensions of the reinforcement not only within the side slope area of the embankment but also near the embankment centre. The pile group efficacy increased marginally for an increase of the rake angle.

Plaxis modelling also predicted decreased vertical deformations at the base of the embankment for the initial inclusion of reinforcement in the model. Further increases of geosynthetic reinforcement stiffness yielded moderate decreases in vertical and horizontal deformations and significant increases in axial tensions across the embankment width. Lateral deformations and bending moments decreased significantly at the outer pile row whilst the magnitude of lateral deformations within the pile group remained relatively constant. A slight increase of pile group efficacy and overall structural stability for an increase of geosynthetic stiffness was observed.

The depth of the subsoil layer underlying the geosynthetic reinforced piled embankment had an insignificant effect on the performance of the structure. Vertical deformations of the geosynthetic remained relatively constant whilst the horizontal deformation and axial tension increased marginally with subsoil depth. The depth of the subsoil had no effect on the magnitude of lateral pile deformations and the overall load transfer mechanisms and structural stability.

The stiffness of the subsoil had a significant effect on the structures performance. Vertical and horizontal deformations, axial tension in the geosynthetic and lateral deformation of the pile group all decreased significantly for an increase of subsoil stiffness. Whilst deformations of the pile group decreased with a stiffness increase, the pile group efficacy decreased and the factor of safety increased only marginally.

Geometric parameters, which had a significant determination as to whether the bearing capacity of the subsoil, specifically within the side slope zone, was sufficient to support the structure were the embankment height, side slope steepness and the outer pile row location.

Increasing the embankment height resulted in a greater magnitude of lateral thrust to be restrained by both the pile group and reinforcement, consequently significant horizontal deformation of the pile group and geosynthetic reinforcement combined with an increase in reinforcement axial tension was observed. Increasing the embankment height, resulted in a greater length of geosynthetic reinforcement not support by the pile group near the embankment toe. Consequently, significant increases in vertical deformations of the geosynthetic reinforcement near the toe were predicted by Plaxis.

Increasing the side slope steepness decreased the geosynthetic reinforcement span to be supported by the subsoil layer. Increasing the embankment side slope steepness yielded lower magnitudes of vertical reinforcement deformations near the toe; a minor increase in horizontal deformation and axial tension in the reinforcement within the pile group and an increase of pile group lateral deformations. Overall, increasing the side slope steepness decreased the factor of safety of the structure.

Increasing the number of piles located within the embankment side slope zone by extending the pile group closer toward the embankment toe significantly decreased lateral deformation within the pile group and vertical deformation of the geosynthetic reinforcement. Extending the outer pile row location further toward the toe also yielded a slight reduction in mean surface deformation.

Both analysis techniques indicate that significant deformation occurs under the side slope of geosynthetic reinforced piled embankments. Insufficient attention to the effects of the subsoil stiffness and the determination of the pile group extents

location along the side slope requires investigation. The SCR was a useful tool in the analysis of the response of both the pile group and geosynthetic reinforcement to achieve strain compatibility for a parametric variation.

7.4 Conclusions

This study identified the key variables and their influence on the behaviour of geosynthetic reinforced piled embankments.

The conclusions of this study were:

- The numerical Plaxis 2D model was largely validated by the results of the physical centrifuge model.
- The H/(s-a) ratio and side slope steepness are important parameters in the deformational response of geosynthetic reinforced piled embankments.
- The greater the side slope steepness, the lower the magnitude of vertical deformations of the geosynthetic reinforcement near the toe.
- The subsoil stiffness influenced pile group lateral deformations and geosynthetic reinforcement vertical deformations, both reducing with increased subsoil support.
- Increased subsoil stiffness resulted in reduced tensile loads in the geosynthetic reinforcement, particularly at the midspan between adjacent piles.
- Axial tension in the reinforcement due to lateral loading was seen to increase from near the crest of the embankment, approximately linearly, until dropping shapely to zero at the toe of the embankment.
- The tensile load distribution along the geosynthetic reinforcement indicated that the geosynthetic tensile loads spiked over the edges of the piles with significantly reduced loads occurring at the midspan between adjacent piles.
- The inclusion of raked piles at the outer row pile location significantly reduced the bending moments and pile head deflection at the outer pile row and reduced the horizontal deformations of the embankment and also the axial tensions in the geosynthetic reinforcement.
- Significant bending moments and pile head deflections in the piles together with significant deformations and axial tensions in the geosynthetic

reinforcement were observed in the Plaxis analyses. Those were a function of the embankment height, pile spacing, steepness of the side slope and stiffness of the soft soil. An increase in the pile bending moment correlates to an increase of the horizontal/vertical deformation of the geosynthetic reinforcement, greater tensions in the reinforcement, lateral volumetric deformation in the embankment side slope and a decrease in the pile group efficacy.

- The pile group should extend for a greater distance towards the toe of the embankment than that currently recommended in BS 8006 (2010).
- Extending the pile group closer toward the embankment toe would reduce lateral deformations within the pile group and vertical deformations of the geosynthetic reinforcement, with a slight reduction in mean surface deformations.
- A drained approach has been adopted in this study to examine the long term deformational response of the structure. However, undrained conditions would also be considered critical for a soft soil. Short term behaviour of the structure under undrained conditions and the time dependent consolidation analyses of the structure should be considered.
- In this study, deformations at the extremities of piled embankments was modelled in 2D plane strain. Modelling a complex 3D problem as 2D will not fully capture the complex interactions and load distributions occurring within the structure. Consequently, greater emphasis should be placed on the qualitative trends rather than the quantitative deformations presented in this study.

7.5 Recommendations for further research

The findings of this study has improved the understanding of the lateral deformational response at the side slopes of a geosynthetic reinforced piled embankment. Areas where there is scope for further research are the following:

- The plane strain centrifuge model yielded results largely validated the Plaxis 2D analyses. There remains however, a need to account for the complex three-dimensional behaviour of piled embankments. The testing of a reduced scale three-dimensional reinforced piled embankment model in a

geotechnical centrifuge and the use of Plaxis 3D would satisfy this need. The results could be used to generate conversion factors for modelling three-dimensional reinforced piled embankment problems with Plaxis 2D.

- Consideration of undrained conditions on the performance of the structure is required. The time dependent consolidation effects on the structures performance must be examined. In the case of very soft soil, the short term undrained strength of the soil could be critical.

- To define and quantify the horizontal resistance offered by the geosynthetic reinforcement, pile group and soft soil in a piled embankment. Strain compatibility must be achieved within the structure by deformation of the reinforcement, displacement of the pile head and the soft soil to achieve structural equilibrium. The individual structural capacity of each structural member is required to be quantified in terms of its lateral and vertical load capacitance and the structural components cumulative contribution in the achievement of structural equilibrium through strain compatibility.
- To develop a numerical model that can accurately represent the lateral loading mechanism in a geosynthetic reinforced piled embankment. The numerical model will enable the prediction of the deformational response of the geosynthetic reinforced piled embankment structure for a material and geometric parametric input.

- The role of geosynthetic reinforcement in piled embankments could be examined further. In addition to varying the tensile strength of the reinforcement, perhaps piled embankments reinforced with multiple layers of geosynthetic could be studied. In a three-dimensional piled embankment centrifuge study, stiffer geosynthetic reinforcement spanning the region directly between adjacent pile caps could be installed, in addition to the geosynthetic reinforcement covering the whole area.

- Validation of axial tensions developed in the Plaxis models geosynthetic reinforcement by centrifuge testing with a geosynthetic material equipped with sufficient strain gauges capable of determining the axial tension profile through the reinforcement.
- This study only investigated drained analyses with the pile group fixed at the bearing end into a stiff bearing stratum. Examination of different water

conditions, pile types, 3D pile group configurations, undrained subsoil conditions and pile group fixity conditions would enhance the understanding of the structures behaviour.

8.0 References

AASHTO (2000). *Bridge Design Specifications*, American Association of State Highway and Transportation Officials, Washington, D.C.

Abbas, J. M, Z. Chik, M. R. Taha, Q. S. M Shafiqu (2010) "Time Dependent Lateral Response of Pile Embedded in Elasto-Plastic Soil". Journal of Central South University of Technology, vol. 17(2): (in press).

Alfaro, M.C., Hayashi, S., Miura, N., Bergado, D.T., 1997. Deformation of reinforced soil wall-embankment system on soft clay foundation. Soils and Foundations 37 (4), 33–46.

Anon (2003). "*Slope Stability manual*." EM 1110-2-1902, Washington, DC: Department of the Army, Office of the Chief Engineers.

Aryal, K.P. (2006). "Slope stability evaluation by LE and FE methods." PhD thesis, Norwegian University of Science and Technology, NTNU: Electronic version: http://www.diva-portal.org/ntnu/abstract.xsql?dbid=1868.

Aryal, K.P. (2008). "Differences between LE and FE method used in slope stability evaluation." *Proc. 12th Intl. Conference of International Association for Computer Methods and Advances in Geomechanics*, India, pp 4509 – 4516.

Ashour, M., P. Pilling and G. Norris (2004) "Lateral Behaviour of Pile Groups in Layered Soils". Journal of Geotechnical and Geoenvironmental Engineering. vol.130 (6), pp. 580-592.

Auvinet, G., Gonzalez, J.L., 2000. Three-dimensional reliability analysis of earth slopes. Computers and Geotechnics 26, 247–261.

Avgherinos, P. and Schofield. 1969, *Drawdown failures of Centrifuged Models*, Proceedings, Seventh International Conference on Soil Mechanics and Foundation Engineering, Mexico, pp. 497-505.

Banerjee, P.K. and R.M.C. Driscoll (1976) Program for the analysis of pile groups of any

Banerjee, P.K. and T.G. Davies (1978). The behaviour of axially and laterally loaded single piles embedded in non-homogeneous soils, *Géotechnique*, 28(3): 309–326.

Bergado, D.T., Chai, J.C., Miura, N., 1995. FE analysis of grid reinforced embankment system on soft Bangkok clay. Computers and Geotechnics 17, 447–471.

Bergado, D.T., Teerawattanasuk, C., 2007. 2D and 3D numerical simulations of reinforced embankments on soft ground. Geotextiles and Geomembranes 26 (2008) 39–55.

Bergado, D.T., Youwai, S., Teerawattanasuk, P., Visudmedanukul, P., 2003. The interaction mechanism and behaviour of hexagonal wire mesh reinforced embankment with silty sand backfill on soft clay. Computers and Geotechnics 30, 517–534.

Bolton, M. D. 1986. The strength and dilatancy of sands. *Géotechnique*, 36(1), pp.65-78.

Briaud, J., Lim, Y., 1999. Tieback walls in sand: numerical simulation and design implications. Journal of Geotechnical and Geoenvironmental Engineering, ASCE 125 (2), 101–111.

British Standard, BS 8006. (1995)."Code of practice for strengthened/reinforced soils and other fills." *British Standard Institution*, London, 162.

British Standard, BS 8006. (2010)."Code of practice for strengthened/reinforced soils and other fills." *British Standard Institution*, London, 162.

British Standards BS8004. (1986). *"Code of practice for foundations." British Standard Institution*, London, 162.

British Standards BS8110. (1997). *"Code of practice for Structural use of concrete, Parts 1, 2 and 3."* British Standard Institution, London, 162.

Britton, E. J. & Naughton, P. J. 2008a. An experimental investigation of arching in piled embankments. *Proceedings of the 19th European Young Geotechnical Engineers' Conference,* Györ, Hungary.

Britton, E. J. & Naughton, P. J. 2008b. An experimental investigation of arching in piled embankments. *Proceedings of the 4th European Geosynthetics Conference*, Edinburgh, Scotland.

Britton, E. J. (2012). "An experimental investigation of arching in piled embankments overlying voids." Institute of Technology Sligo. Doctoral Thesis.

Brown, D.A., Morrison, C., and Resse, L.C. (1988). .Lateral load behaviour of a pile group in sand. *J. of Geotech. Engineering,* ASCE, 114(11), 1261-1276.

Brown, D.A., Resse, L.C., and O.Neill, M.W. (1987). .Cyclic lateral loading of a large-scale pile group. *J. of Geotech. Engrg.* ASCE, 113(11), 1326-1343.

BS 1377 1990. *Methods of test for Soils for civil engineering purposes.* British Standards Institute.

BS 1377-2 1990. *Methods of test for Soils for civil engineering purposes - Part 2: Classification tests*. British Standards Institute.

BS 1377-4 1990. *Methods of test for Soils for civil engineering purposes - Part 4: Compaction-related tests.* British Standards Institute.

BS 1377-7 1990. *Methods of test for Soils for civil engineering purposes - Part 7: Shear strength tests (total stress).* British Standards Institute.

BS 5930 1990**.** *Code of practice for site investigations.* British Standards Institute.

Canon Powershot S80 Digitial Camera advanced user guide.

Chai, J.C., 1992. Interaction behaviour between grid reinforcement and cohesive frictional soils and performance of reinforced wall/embankment on soft ground. Doctoral Dissertation No. GT-91-1, Asian Institute of Technology, Bangkok, Thailand.

Chai, J.C., Bergado, D.T., 1993a. Performance of reinforced embankment on Muar clay deposit. Soils and Foundations 33 (4), 1–17.

Chai, J.C., Miura, N., Bergado, D.T., Long, P.V., 1997. Finite element analysis of geotextile reinforced embankment failure on soft subsoil. Geotechnical Engineering Journal 28 (2), 249–276.

Chandrasekaran, S.S., A. Boominathan and Dodagoudar G.R. (2009) "Group Interaction Effects on Laterally Loaded Piles in Clay". J. Geotech. Geoenviron. Eng. ASCE. (in press). doi:10.1061/(ASCE)GT.1943-5606.0000245.

Chen, Y. M., Cao, W. P. & Chen, R. P. 2008a. An experimental investigation of soil arching within basal reinforced and unreinforced piled embankments. *Geotextiles and Geomembranes*, 26(2), pp. 164-174.

Chen, R. P., Chen, Y. M., Han, J. & Xu, Z. Z. 2008b. A theoretical solution for pile – supported embankments on soft soils under one – dimensional compression. *Canadian Geotechnical Journal*, 45(5), pp. 611-623.

Chenggang, B. (2005): Study on the interaction behaviour of Geosynthetics and soil in China; Ningbo Institute of Technology, Zhejiang University, China, pp. 104-115.

Chik, Z.H, Abbas, J.H, Taha, M.R. and Shafiqu, Q.S.M (2009). "Lateral behaviour of single pile in cohesionless soil subjected to both vertical and horizontal loads." *European Journal of Scientific Research*, 29(2), pp 194-205.

Corte, J.F., Editor. 1988, Proceedings, Centrifuge 88, Balkema, Rotterdam.

Cox, W.R., Dixon, D.A. & Murphy, B.S. (1984). Lateral load tests on 25.4mm diameter piles in very soft clay in side by side and in line groups. ASTM STP 835 Laterally Loaded Deep Foundation Analysis and Design, 122-139.

Craig (1983). Simulations of foundations of offshore modelling structures using centrifuge modelling. Developments in Geotechnical Engineering. Ed. P.K. Banerjee, Elsevier Applied Science, London, pp. 1-27.

Craig, R.F., 2004. Craig's Soil Mechanics, Seventh Edition.

Duncan, J.M., Evans, L.T., Jr. And Ooi, P.S.K. (1994). Lateral load analysis of single piles and drilled shafts. ASCE, Journal of Geotechnical Engineering, 120(6), 1018-1033.

Dunnavant, T.W. and M.W. O'Neill (1985). An evaluation of the behavior and analysis of laterally loaded pile groups. Report No. UNCE 85-11. Houston: University of Houston-University Park.

EBGEO (2007), Empfehlung fur den Entwurf und die Berechnung von Erdkorpern mit Bewehrung aus Geokunstoffen; Ausgabe 2007 (unveroffentlicht).

Ellis, E. & Aslam, R. 2009a. Arching in piled embankments: comparison of centrifuge tests and predictive methods – part 1. *Ground Engineering*, 42(6), pp. 34-38.

Ellis, E. & Aslam, R., 2009b. Arching in piled embankments: comparison of centrifuge tests and predictive methods - part 2. *Ground Engineering*, 42(7), pp. 28-31.

Ellis, EA & Aslam, R, 2008. Centrifuge modelling of piled embankments, *Advances in Transportation Geotechnics.* pp 363-368.

Evans, L.T., Jr and Duncan, J.M. (1982). Simplified analysis of laterally loaded piles. Rep No. UCB/GT/82-04, University of California, Berkley, California.

Fahmi Farag, GS (2008). "Lateral spreading in basal reinforced embankments supported by pile like elements." Universitat Kassel. Master's Thesis.

Federich, K., "Raked Piles." www.kurt-fredrich.de.

Fleming, W.G.K., Weltman, A.J., Randolph, M.F., Elson, W.K. (1985). Piling Engineering. Surrey University Press.

Focht, J.A. & Koch, K.J. (1973). Rational analysis of the Lateral performance of offshore pile groups. Preprints, Offshore Tech, Conf., Houston II. 701-108.

Frank, L.S. (1985). "Applied Finite Element Analysis for Engineers" Harcourt Brace Jovanovich College Publishers, Holt, Rinehart and Winston, Inc.

Gangakhedkar, R (2004). "Geosynthetic reinforced piled embankments." *Master's Thesis*. University of Florida.

Gaudin, C., Randolph, M.F. & O'Loughlin, C.D. (2006). "New insights from model tests of foundation and anchoring systems in offshore geomechanics." *Proc. 6th Int. Conf. on Physical Modelling in Geotechnics*, Hong Kong, 1, 47–62.

Geometry subjected to horizontal and vertical loads and moments, PGROUP (2.1). HECB/B/7, Department of Transport, HECB, London.

Goh, A.T.C, The, C.I., Wong, K.S. (1997). "Analysis of piles subjected to embankment induced lateral soil movements." Journal of Geotechnical and Geoenvironmental Engineering, Vol. 123, No. 9, pp. 792-801.

Griffiths, D.V, Lane, P.A. (1999). Slope Stability Analysis by Finite Elements. Geotechnique, 49(3):387-403.

Han, J. (1999). "Design and Construction of embankments on geosynthetic reinforcement platforms supported by piles" *Proc. 1999 ASCE/PaDOT Geotechnical Seminar*, Central Pennsylvania Section, ASCE and Pennsylvania Department of Transportation, Hersley, Pennsylvania, pp 66-84.

Han, J., and Gabr, M.A (2002). "Numerical analysis of geosynthetic reinforced and pile supported earth platforms over soft soil." *Journal of geotechnical and geoenvironmental engineering*, ASCE, 128(1) : 44-53.

Hinchberger, S.D., Rowe, R.K., 2003. Geosynthetic reinforced embankments on soft clay foundations: predicting reinforcement strains at failure. Geotextiles and Geomembranes 21, 151–175.

Ho, S.K. and Rowe, R.K. (1994). "Predicted behaviour of two centrifugally modelled soil walls," ASCE Journal of Geotechnical Engineering, 120(10): 1845-1873.

Ilyas, T., Leung, C.F., Chow, Y.K., and Budi, S.S., 2004. *Centrifuge Model Study of Laterally Loaded Pile Groups in Clay*, *Journal of Geotechnical and Geoenvironmental Engineering*, Vol. 130, No. 3, pp 274 – 283.

Jennings, K., Naughton, P.J. 2010. *Lateral deformation under the side slopes of piled embankments*. Proc. 9th Intl. Conference on Geosynthetics, Volume 4, Brazil: 1925-1928.

Jennings, K., Naughton, P.J. 2011. *Lateral deformation under the side slopes of piled embankments.* Proc. Geo-Frontiers, Dallas.

Jennings, K., Naughton, P.J., 2012a. *Similitude conditions modelling geosynthetic reinforced piled embankments using coupled FEM and FDM techniques*." ISRN Civil Engineering.

Jennings, K., Naughton, P.J., 2012b. *2D finite element stability analysis of a reinforced piled embankment*. Proc. Bridge and Concrete Research in Ireland, Trinity College, Dublin.

Jennings, K., Naughton, P.J., 2012c. *Comparative analysis of numerical and physical modelling of a reinforced piled embankment.* Proc. Eurogeo 5 Valencia.

John N. W. M. (1987), "Geotextiles", Blackie, Chapman and Hall, New York.

Jones, C. J. F. P., Lawson, C. R., and Ayres, D. J. (1990). "Geotextile reinforced piled embankments." *Proc, 4th International Conference on Geotextiles, Geomembranes, and Related Products*, Vol. 1, G. Den Hoedt (ed), The Hague, May - June 1990, pp. 155-160.

Kalla, S. (2010). "Modelling Studies to Assess Long Term Settlement of Light Weight Aggregate Embankment." *Master's Thesis*. University of Texas at Arlington.

Karpurapu, R., Bathurst, R.J., 1995. Behaviour of geosynthetic reinforced soil retaining walls using the finite element method. Computers and Geotechnics 17, 279–299.

Kempfert H.G., Gobel C., Alexiew D. & Heitz C. 2004. German recommendations for reinforced embankments on pile-similar elements. *Proc. 3rd European Geosynthetics Conf*, 279–284.

Kempfert, H. G., Stadel, M. and Zaeske, D. (1997). "Design of geosynthetic-reinforced bearing layers over piles". *Bautechnik,* Vol. 74, No. 12, pp. 818-825.

Kempfert, H.G., Gobel, C., Alexiew, D., & Heitz, C., 2004 "German recommendations for reinforced embankments on pile similar elements." *Proc. 3rd Eur. Conference on Geosynthetics*, Munich, Germany, pp 279-284.

Kempton, G, Russell, D, Pierpoint, ND and Jones, CJFP, 1998. "Two and Three Dimensional Numerical Analysis of the Performance of Piled Embankments," *6th International Conference on Geosynthetics*.

Kiousis, P.D, Griffiths, D.V. and Stewart, J.A (2010). "Optimization of Stabilization of Highway Embankment Slopes Using Driven Piles (Phase 1)." Colorado Department of Transportation – Research, Report No. CDOT-2010-8.

Ko, H.Y. and McLean, F.G., Editorss.1991, Proceedings, Centrifuge (91), Balkema, Rotterdam.

Krishna, N.R. (2006). "Numerical Modelling and Analysis of Pile Supported Embankments." *Master's Thesis*. University of Texas at Arlington.

Kusakabe, O. (1982). Stability of excavations in soft clay. PhD. Thesis, Cambridge University.

Laurent, Y., Simon, B., Dias, D., Kastner, R. (2003). "A 3D finite difference analysis of embankments over pile reinforced soft soil." *Proc. Intl. Workshop on Geotechnics of Soft Soils*, The Netherlands; pp 271-276.

Leung, C.F., Lee, F.H., and Tan, T.S., Editors., 1994, *Proceedings*, Centrifuge (94), Balkema, Rotterdam.

Lin, K. Q., and Wong, I.H. (1999). "Use of deep cement mixing to reduce settlements at bridge approaches." *J. Geotech. Geoenviron. Eng.*, 125(4), pp 309-320.

Love. G, & Milligan, G (2003). "Design methods for basally reinforced pile supported embankments over soft ground." *Ground Engineering*, pp 39-43.

Low B.K., Tang S.K. & Choa, V. 1994. Arching in piled embankments. *ASCE Journal of Geotechnical Engineering*, 120(11) 1917–1938.

Magnan, J. (1994) "Methods to reduce the settlement of embankments on soft clay: a review" Vertical-Horizontal Deformations of Foundations and Embankments, ASCE, Geotechnical Special Publications No. 40, pp 77-91.

Matlock, H., and Reese, L. C. (1960). "Generalized solutions for laterally loaded piles." Journal of Soil Mechanics and Foundation Division, ASCE, 86(5), 63-91.

McNulty, J. W. (1965). "An experimental study of arching in sand." *Technical Report No.* I-674, U.S. Army Engineer Waterways Experiment Station, Corps of Engineers, Vicksburg, Mississippi, pp 170

McVay, M., Zhang, L., Molnit, T., and Lai, P. (1998). .Centrifuge testing of large laterally loaded pile groups in sands,. *J. of Geotech. and Geoenviron. Engrg.*, ASCE, 124(10), 1016-1026.

Meimon, Y., Baguelin, F., and Jezequel, J.F. (1986). .Pile group behaviour under long term lateral monotonic and cyclic loading,. *Proc., Third Int'l Conf. on Numerical Methods in Offshore Piling*, Inst. Francais Du Petrole, Nantes, pp. 286-302.

Mindlin, R.D., 1936. Force at a point in the interior of a semi-infinite solid. Physics 7, 195-202.

Muir Wood, D.M. (2004). *Geotechnical Modelling* (London: SponPress).

Nag Rao (2006). Numerical modelling and analysis of pile supported embankments. University of Texas. Master's Thesis.

Naughton, P. J., Kempton, G. T. (2005). Comparison of analytical and numerical analysis design methods for piled embankment. Proc. of Geo-Frontiers, Austin, USA.

Neher, H.P., Wehnert, M. & Bonnier, P.G. (2001). “An evaluation of soft soil models based on trial embankments.” Proc. of the 10th Int. Conf. on Computer Methods and Advances in Geomechanics (IACMAG), Tuscon: 373-378. Rotterdam, A.A. Balkema.

Nunez, I.L., Phillips, R., Randolph, M.F., Wesselink, B.D. (1988). Modelling laterally loaded piles in calcareous sand. Centrifuge 88, Proc. Int. Conf. on Geotechnical Centrifuge Modelling, Paris, Ed. J.F. Corte, Balkema, pp. 371-384.

O’Loughlin, C. D., Naughton, P. J., Baker, N. & Ainsworth, A. 2010. Establishing a beam centrifuge facility at the Institute of Technology, Sligo, Ireland. *Proceedings of the 7th International Conference on Physical Modelling in Geotechnics (ICPMG 2010)*, Zurich, Switzerland.

Patra, N. R. and P. J. Pise. (2001) “Ultimate Lateral Resistance of Pile Groups in Sand”, Journal of Geotechnical and Geoenvironmental Engineering. vol.127(6), pp. 481-487.

Plaxis 2010. *Plaxis 2D Reference Manual*. Available at url: http://www.twoplussoft.com/imgUpload/2D2010-2-Reference(1).pdf

Poulos, H.G. (1971)a, Behaviour of laterally loaded piles: I – single piles, *ASCE J. Soil Mech. And Found. Div*., 97(SM5): 711–731.

Poulos, H.G. (1971)b, Behaviour of laterally loaded piles: II – pile groups, *ASCE J. Soil Mech. and Found. Div*., 97(SM5): 733–751.

Rankine, W. (1857) On the stability of loose earth. Philosophical Transactions of the Royal Society of London, Vol. 147.

Rathmayer H. (1975), "Piled embankment supported by single pile caps", In: *Istanbul conference on soil mechanics and foundation*, Istanbul, March April 1975.

Reese, L.C. and Van Impe, W.F. (2001). *Single piles and pile groups under lateral loading*, A.A. Balkema, Rotterdam, Netherlands.

Reese, L.C., Wright, S.G. & Aurora, R.P. (1984). Analysis of a pile group under lateral loading. ASTM STP 835. Lateral Loading Deep Foundation Analysis and Design, 56-71.

Reid, W.M., and Buchanan, N.W. (1984). “Bridge approach support piling.” Piling and Ground Treatment, Thomas Telford Ltd., London, pp 267-274.

Rendulic, L. (1938), Der Erddruck im StraBenbau und Bruckenbau; Forschungsarbeiten aus dem StraBenbau, Bd. 10, Berlin.

Rollins, K. M., J. D. Lane and T M. Gerber (2005) “Measured and Computed Lateral Response of a Pile Group in Sand”. Journal of Geotechnical and Geoenvironmental Engineering, ASCE. vol.131 (1), pp. 103-114.

Rollins, K. M., K. G. Olsen, D. H. Jensen, B. H. Garrett, R. J. Olsen, and J. J. Egbert (2006) “Pile Spacing Effects on Lateral Pile Group Behavior: Analysis”. Journal of Geotechnical and Geoenvironmental Engineering, ASCE. vol.132(10), pp. 1272-1283.

Rollins, K. M., Peterson, K. T., and Weaver, T. J. (1998). "Lateral load behaviour of full-scale pile group in clay," *J. of Geotech. and Geoenviron. Engrg.*, ASCE, 124(6), 468.478.

Rollins, K. M., Peterson, K. T., and Weaver, T. J. ~1998. ''Lateral load behaviour of full-scale pile group in clay.'' *J. Geotech. Geoenviron. Eng.,* 124~6!, 468–478.

Rowe, R.K. and Soderman, K.L. (1985). "An approximate method for estimating the stability of geotextile-reinforced embankments." *Canadian Geotechnical Journal.* (22), pp 392-398.

Rowe, R.K. and Soderman, K.L. (1985). "Geotextile reinforcement of embankments on peat." Geotextile and Geomembranes 2 (4), pp 277-298.

Rowe, R.K., Ho, S.K., 1998. Horizontal deformation in reinforced soil wall. Canadian Geotechnical Journal 35, 312–327.

Rowe, R.K., Li, A.L. (2002). "Geosynthetic reinforced embankments over soft foundations." *Proc. 8th Intl. Conference on Geosynthetics*, Delmas; pp 5-34.

Ruesta, P.F. and Townsend, F.C. (1997). .Evaluation of laterally loaded pile group at Roosevelt Bridge,. *J. of Geotech. and Geoenviron. Engrg.,* ASCE, 123(12) 1153-1161.

Russell, D. and Pierpoint N. (1997). "An assessment of design methods for piled embankments." *Ground Engineering*, November, pp. 39-44

Satibi, S. (2009). *Numerical analysis and design criteria of embankments on floating piles.* PhD thesis, Universität Stuttgart, Stuttgart.

Schofield, A.N. (1980). "Cambridge geotechnical centrifuge operation." Géotechnique, 30(3), 227–268.

Seaman, J.W. (1994). "A guide to accommodating or avoiding soil induced lateral loading of piled foundations for highway bridges." *Transportation Research Laboratory Project Report* 71, pp 104.

Slaats, H. (2008). *Load Transfer Platform, Bending Moments in Slender Piles.* Master thesis, Technical University Delft.

Smith, I.M., Su, N., 1997. Three-dimensional FE analysis of a nailed soil wall curved in plan. International Journal for Numerical and Analytical Methods in Geomechanics 21, 583–599.

Springman, S.M., Lateral loading on piles due to simulated embankment construction. PhD Thesis, Cambridge University.

Taylor, R.N. 1995. *Geotechnical Centrifuge Technology.* Lon-don, UK: Blackie Academic and Professional.

Terram Designing (2000), "Designing for soil reinforcement (Steep Slopes).", Terram ltd., Mamhilad, United Kingdom.

Thomas Broadbent and Sons Limited. Operating Manual for GT6/0.75 Geotechnical Beam Centrifuge H83110-OM Issue 01, © July 2009.

Tsukada, Y., Isoda, T., and Yamanouchi, T. (1993). “Geogrid subgrade reinforcement and deep foundation improvement.” *Proc., Geosynthetics Case Histories*, Int. Society for Soil Mechanics and Foundation Engineering, Committee TC9, Yono City, Japan, pp158-159.

US Army (1993). *Design of Pile Foundations,* Technical Engineering and Design Guides No. 1, U.S. Army Corps of Engineers, Washington, D.C.

van Duijnen, P.G. and, Kwast, E.A. (2003). "3D modelling of a piled embankment on soft soil." *Proc. Intl. Workshop on Geotechnics of Soft Soils*, The Netherlands; pp 589-594.

Van Eekelen, S.J.M., Bezuijen, A. (2010). "The Kyoto piled embankment: 3½ years of measurement." *Proc. 9th Intl. Conference on Geosynthetics*, Volume 4, Brazil: 1941-1944.

Viswanadham, B.V.S., Konig, D., 2004. *Studies on scaling and instrumentation of a geogrid*. Geotextiles and Geomembranes 22, pp 307-328.

Winkler, E. (1867). "Die Lehre von der Elastizitat und Festigkeit," Dominicus, Prague.

Zdravkovic, L., Potts, D.M., Hight, D.W., 2002. The effect of strength anisotropy on the behaviour of embankments on soft ground. Geotechnique 52 (6), 447–457.

Zhang H. H. and J. C. Small. (2001) “Analysis of capped pile groups subjected to horizontal and vertical loads”. Computers and Geotechnics. vol. 26, pp.1- 21.

Zhang, L., M. McVay, P. Lai. (1999) “Numerical analysis of laterally loaded 3x3 to 7x3 pile groups in sands”. Journal of Geotechnical and Geoenvironmental Eng., ASCE. vol. 125(11), pp. 936-946.

Zienkiewicz, O.C. (1977). The Finite Element Method. McGraw Hill.

APPENDIX A: Methodology analysis

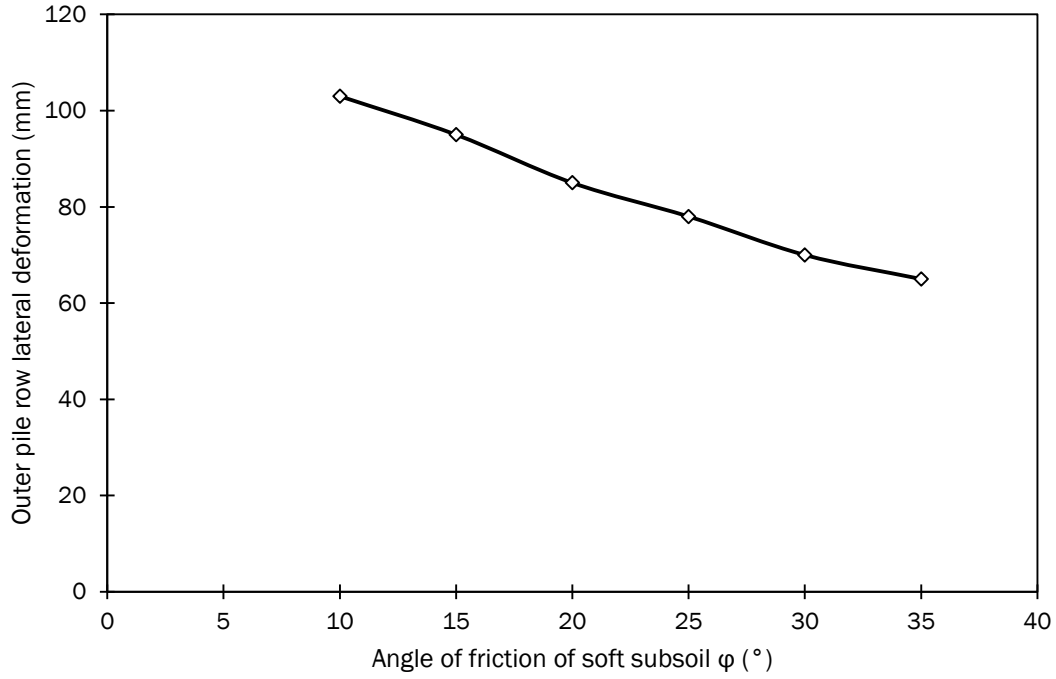

Figure A1 Outer pile row lateral deformation for a range of subsoil angle of friction φ (°)

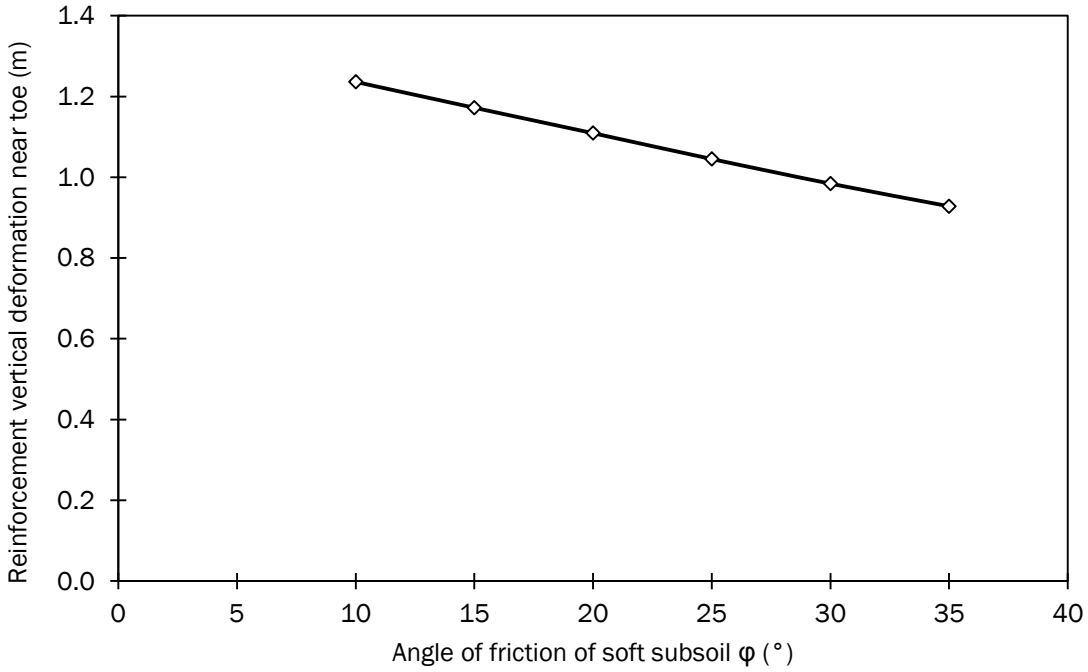

Figure A2 Vertical deformation of reinforcement near the embankment toe for a range of subsoil angle of friction φ (°)

Figure A3 Outer pile row lateral deformation for a range of subsoil angle of dilatancy Ψ (°)

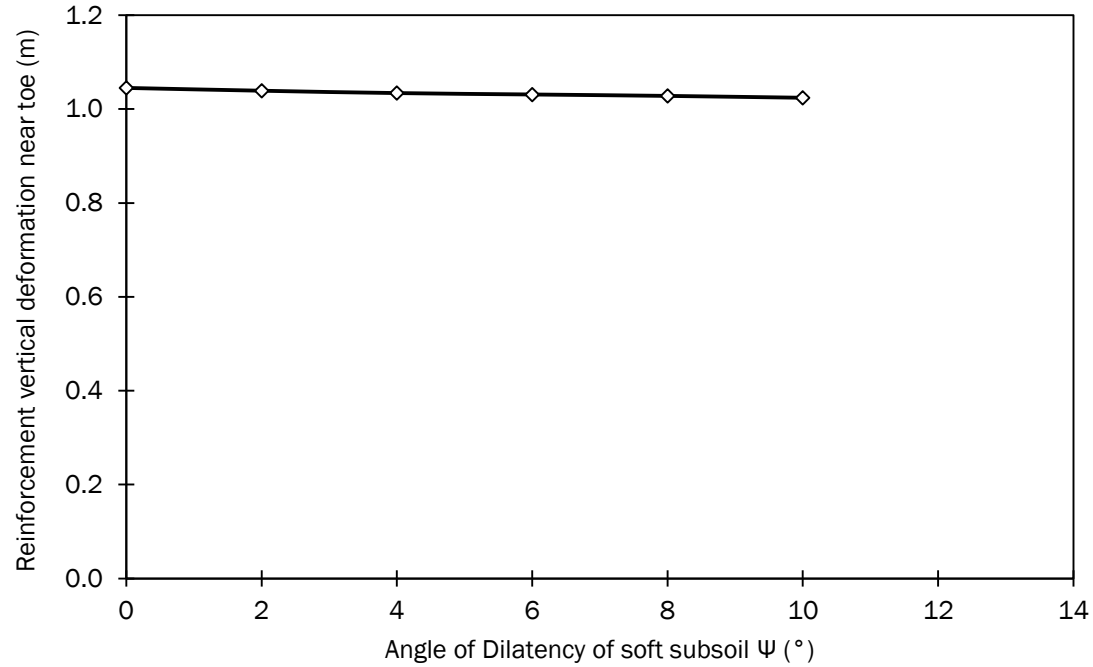

Figure A4 Vertical deformation of reinforcement near the embankment toe for a range of subsoil angle of dilatancy Ψ (°)

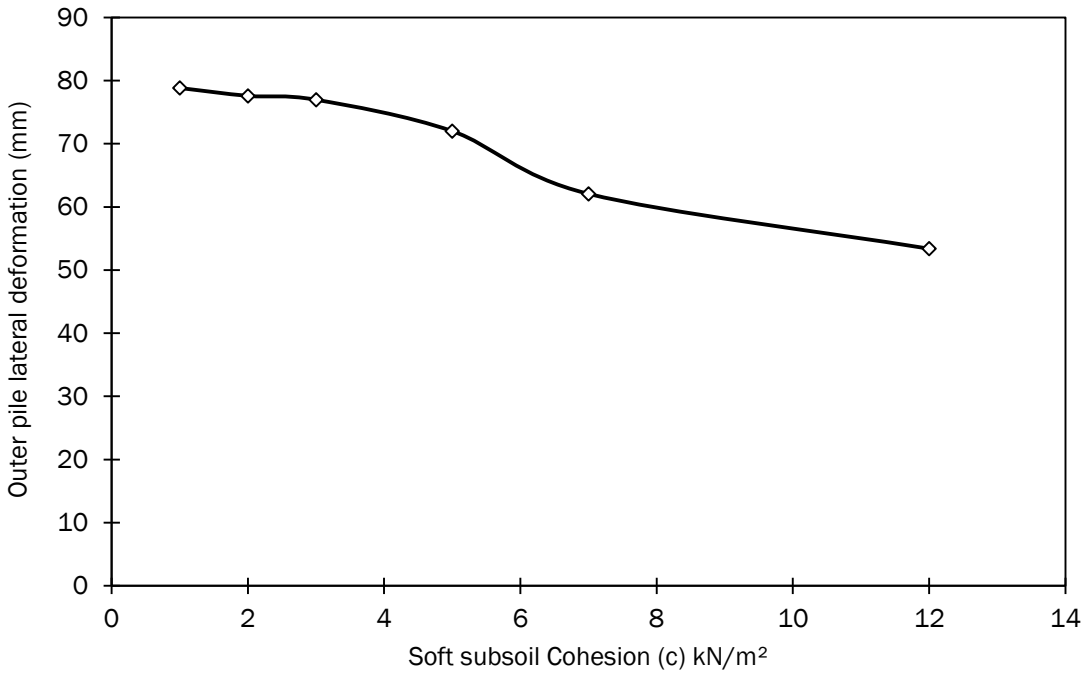

Figure A5 Outer pile row lateral deformation for a range of subsoil cohesion (c)

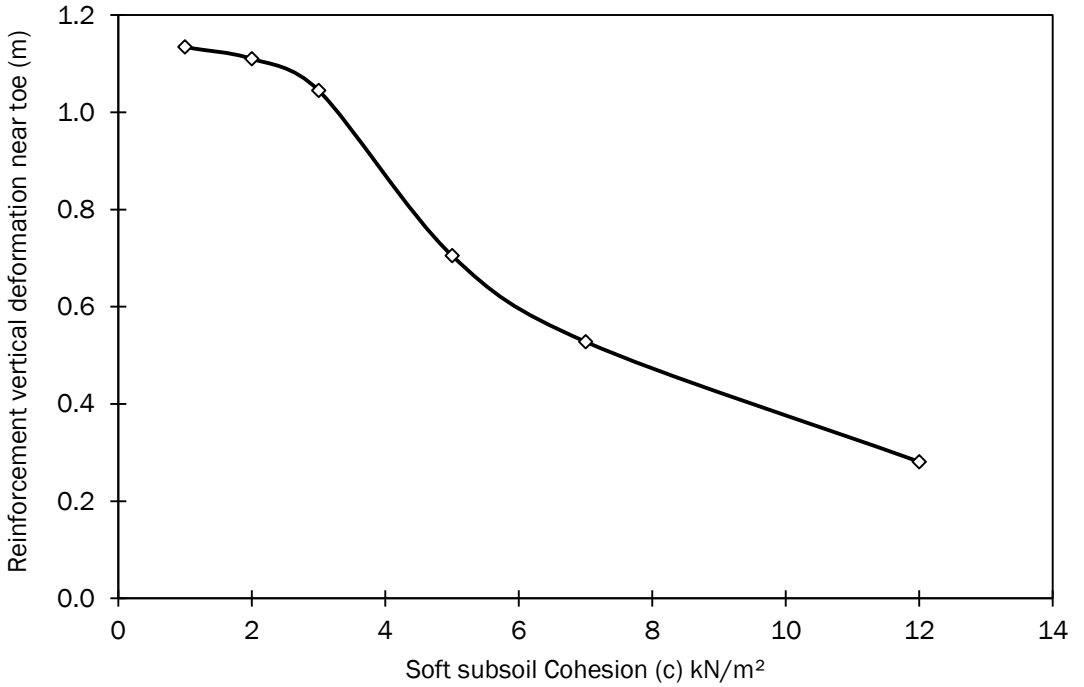

Figure A6 Vertical deformation of reinforcement near the embankment toe for a range of subsoil cohesion (c)

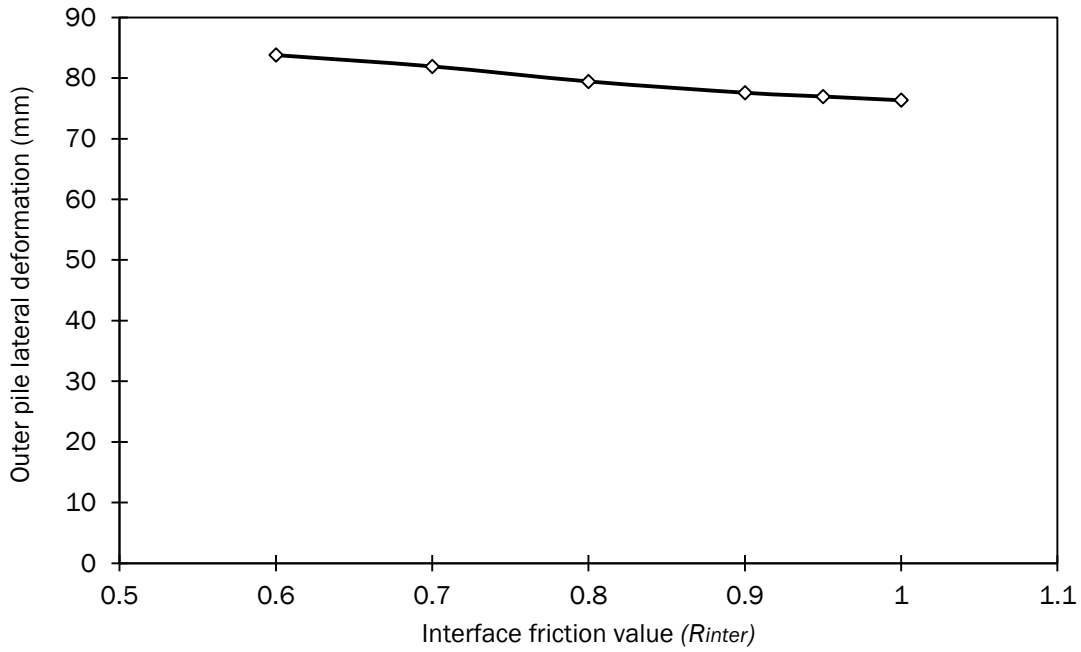

Figure A5 Outer pile row lateral deformation for a range of subsoil interface friction value (R_{inter})

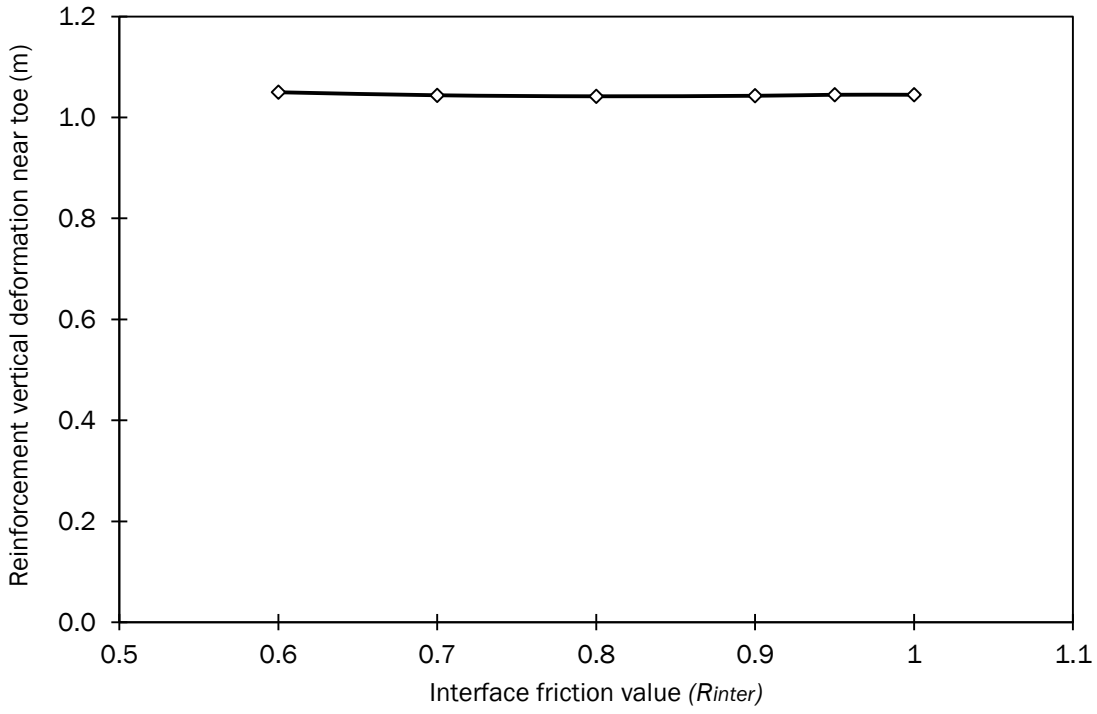

Figure A6 Vertical deformation of reinforcement near the embankment toe for a range of subsoil interface friction value (R_{inter})

Table A1 Friction coefficients for various geotextiles types, *Terram designing (2000)*

Geotextile construction	Friction (bond) coefficient *R*
Conventional geotextiles	
WOVENS	
Monofilaments	0.6 - 0.8
Multifilament	0.75 - 0.9
NONWOVENS	
Melt-bonded	0.7 - 0.8
Needle-punched	0.7 - 0.8
Resin-bonded	0.6 - 0.7
STITCH-BONDED	0.75 - 0.9
Special geotextiles	
GEOGRIDS	
Cross-laid strips	0.85 - 1.00
Punched sheets	0.85 - 1.00

APPENDIX B: Reinforced concrete pile and pile cap design

Appendix B contains the following sections:

B.1 Design of the reinforced concrete pile

B.2 Determination of the second moment of inertia (I) of the pile

B.3 Design of the reinforced concrete pile cap

B.4 Determination of the second moment of inertia (I) of the pile cap

B.1 Design of the reinforced concrete pile

One of the simplifying assumptions of the additional parametric analysis of the numerical modelling of a geosynthetic reinforced piled embankment in Chapter 5 was that a 300mm × 300mm square reinforced concrete pile was used throughout the pile group to support the structure. This required the pile to have the capacity to support a range of axial loads from low to high embankment heights and small to large pile spacing.

The piles in the basally reinforced piled embankment are installed in a square grid. BS8006 (2010) recommends that the maximum spacing between the piles is limited to:

$$s = \sqrt{\frac{Q_p}{(f_{fs}\gamma H + f_q w_s)}} \qquad \text{Equation B1}$$

where

Q_p allowable load carrying capacity of each pile in the pile group

f_{fs} partial load factor applied to the unit weight of soil

γ unit weight of the embankment fill material

H *the height of the embankment*

f_q partial load factor for the application of external loads

W_s *surcharge loading on embankment surface*

Variation of the pile spacing from 1.0m to a maximum of 4.5m yielded an increase in the allowable pile capacity from 107 kN to 2159 kN, Table B1. Variation of the embankment height (*H*) from 1.0m to a maximum of 8.0m yielded an increase in the allowable pile capacity from 328 kN to 1802 kN, Table B2.

Table B1 Effect of a variation of the pile spacing (s) on the required allowable pile capacity (Q_p)

Pile Spacing s (m)	f_{fs}	Embankment Fill unit weight γ kN/m³	Embankment Height *H* (m)	f_q	Surcharge Loading W_s kN/m	Allowable Pile Capacity Q_p kN
1.0	1.3	18	4	1.3	10	107
1.5	1.3	18	4	1.3	10	240
3.0	1.3	18	4	1.3	10	959
4.5	1.3	18	4	1.3	10	2159

Table B2 Effect of a variation of the embankment height (H) on the required allowable pile capacity (Q_p)

Embankment Height *H* (m)	f_{fs}	Embankment Fill unit weight γ kN/m³	Pile Spacing S (m)	f_q	Surcharge Loading W_s kN/m	Allowable Pile Capacity Q_P kN
1.0	1.3	18	3	1.3	10	328
2.0	1.3	18	3	1.3	10	538
4.0	1.3	18	3	1.3	10	959
6.0	1.3	18	3	1.3	10	1381
8.0	1.3	18	3	1.3	10	1802

The maximum allowable structural working load of the pile is calculated in accordance with BS 8004. The maximum working load is calculated as follows:

$$Maximum\ strutural\ working\ load = \frac{f_{cu} \times A_c}{3.65} + (f_{sc} \times A_{sc}) \quad \text{Equation B2}$$

where

f_{cu} characteristic concrete cube strength at 28 days = 30 N/mm^2

A_c area of concrete

f_{sc} characteristic strength of reinforcement = 460 N/mm^2

A_{sc} area of steel reinforcement

Based on the maximum required allowable pile capacities in Table B1 and B2, the maximum axial load capacity that the pile is to be designed was assumed as 2900 kN. To calculate the area of steel reinforcement for the 300mm square concrete pile, the above Equation B2 was used to get:

$$2900000 = \frac{30 \times (300^2)}{3.65} + (460 \times A_{sc}) \quad \text{Equation B3}$$

$$2900000 = 739726 + 460A_{sc} \quad \text{Equation B4}$$

$$2160274 = 460A_{sc} \quad \text{Equation B5}$$

$$A_{sc} = \frac{2160274}{460} \quad \text{Equation B6}$$

$$A_{sc} = 4696\ mm^2 \qquad \text{Equation B7}$$

Therefore provide 6 T 32 bars, area 4830 mm².

$$Maximum\ strutural\ working\ load = \frac{30 \times 300^2}{3.65} + (460 \times 4830) \qquad \text{Equation B8}$$

$$Maximum\ strutural\ working\ load = 2961\ kN \qquad \text{Equation B9}$$

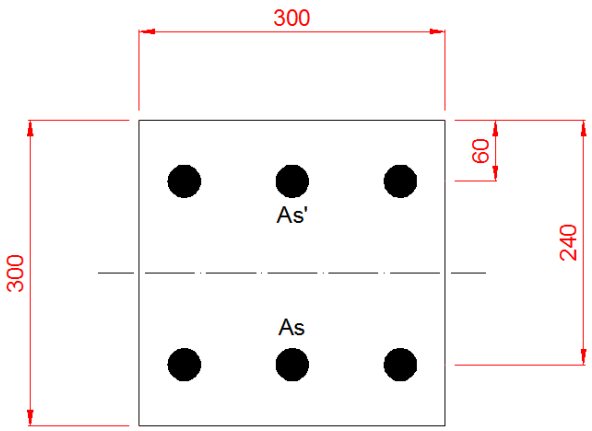

Figure B1 Reinforced concrete pile section

For the generic model case (4m embankment height and 3.0m pile spacing), the pile is required to support a 4m embankment height and a 3.0m pile spacing and an axial load of 959 kN, Table B2. The ultimate moment of resistance of the pile can be calculated using the design charts in Part 3 of BS 8110. The properties of the pile illustrated in Figure B1 are the following:

$$\frac{d}{h} = \frac{240}{300} = 0.8 \qquad \text{Equation B10}$$

f_{cu} = 30 N/mm²

f_y = 460 N/mm²

Therefore Chart No. 27 in BS 8110 Part 3 which is suitable for symmetrical sections can be used for this design case.

$$\frac{N}{bh} = \frac{956 \times 10^3}{300 \times 300} = 10.62 \qquad \text{Equation B11}$$

$$\frac{100A_{sc}}{bh} = \frac{100 \times 4830}{300 \times 300} = 5.36 \qquad \text{Equation B12}$$

From Figure B2, BS 8110, Part 3, Chart 27.

$$\frac{M}{bh^2} = 7.45 \qquad \text{Equation B13}$$

$$M = 7.45 \times 300 \times 300^2 \qquad \text{Equation B14}$$

$$M = 201.15\ kNm \qquad \text{Equation B15}$$

Therefore the reinforced concrete pile can resist a maximum bending moment for the generic numerical model case of 201 kNm.

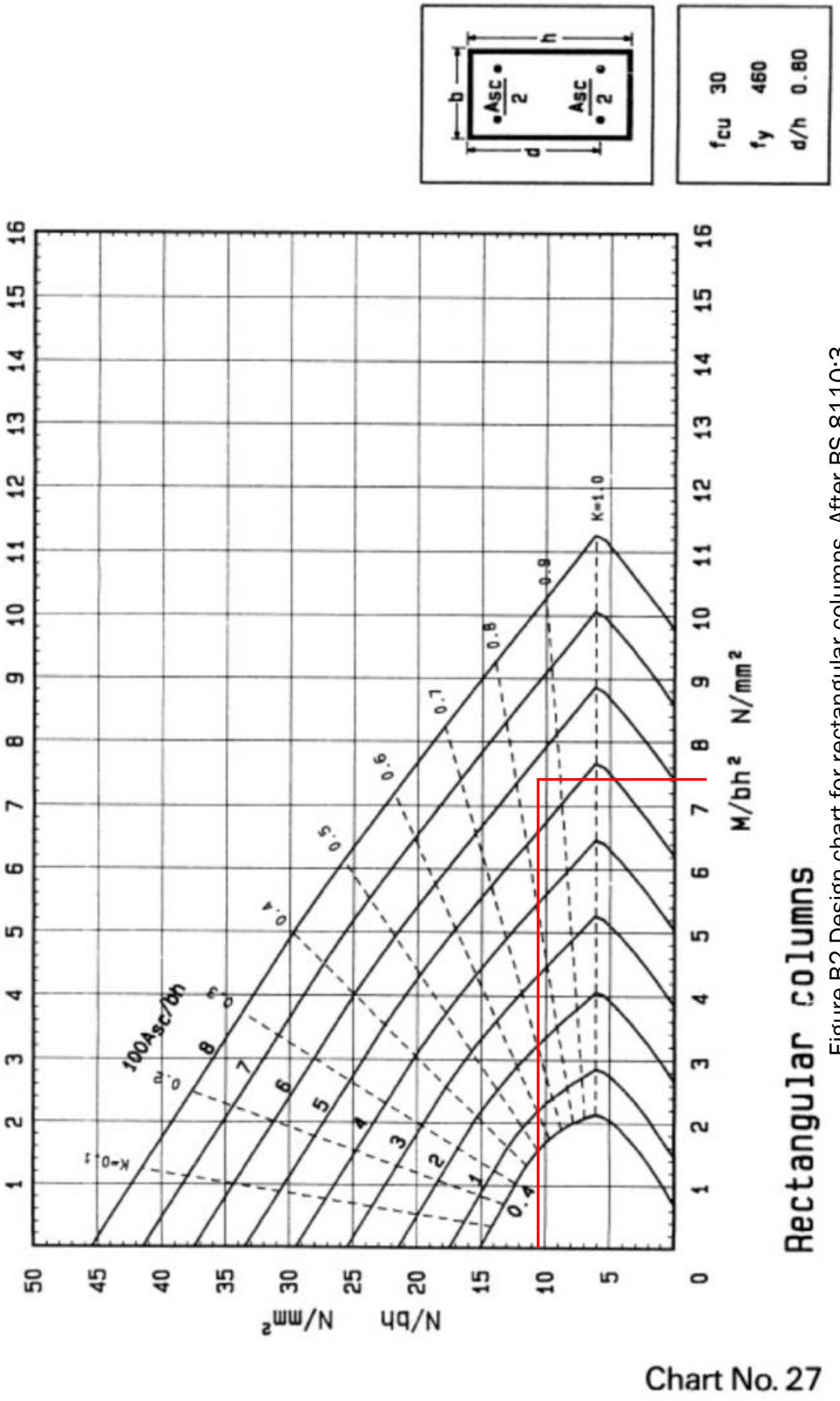

Figure B2 Design chart for rectangular columns, After BS 8110:3

The relative magnitude of the bending moment and the axial load on the reinforced concrete pile governs whether the section will fail in tension or in compression. Figure B3 illustrates the relationship between the pile working axial load and the pile bending moment capacity. A maximum bending moment of 220kNm was recorded for an axial load of 538kN. For the case where the pile is not subjected to any bending moment, a maximum pile axial load capacity of 3317kN was recorded, Figure B3.

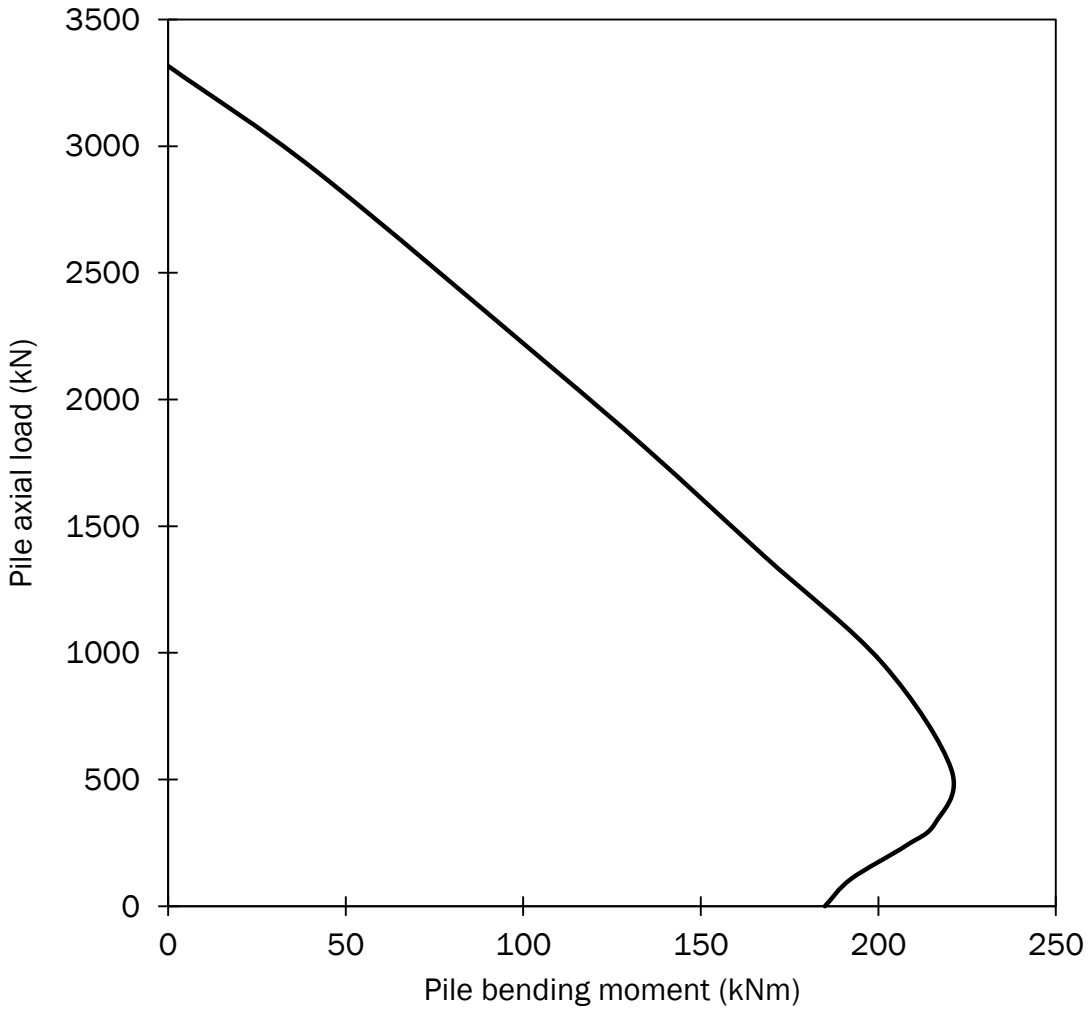

Figure B3 Bending plus axial load chart for reinforced concrete pile constructed from design chart for rectangular columns, After BS 8110:3, see Figure B2

B.2 Determination of the second moment of inertia (I) of the pile

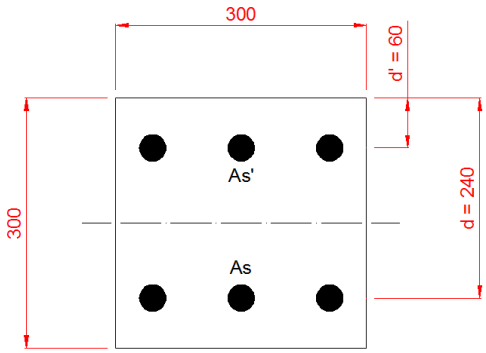

Figure B4 Section through the reinforced concrete pile

The flexural stiffness (*EI*) of the pile in Figure B4 is required to be input into the Plaxis 2D full scale modelling in Chapter 5. The second moment of inertia (*I*) of the pile is required to be determined. As the section consists of both concrete and steel, the second moment of inertia will be calculated using the transformed section method. To transform a section, the steel is transformed to an equivalent (i.e. same axial stiffness) area of concrete. This is done by multiplying the area, A_s, of each bar set by the modular ratio n ($n = E_s/E_c$). The transformed A_s is centered on the original A_s.

Some of the reinforced concrete pile section properties are the following:

$$f_c = 30 \text{ N/mm}^2$$

$$f_y = 460 \text{ N/mm}^2$$

$$E_c = 27 \text{ kN/mm}^2$$

$$E_s = 200 \text{ kN/mm}^2$$

The modular ratio (n) is defined as:

$$n = \frac{Modulus\ of\ Elasticity\ of\ Steel}{Static\ secant\ modulus\ of\ elasticity\ of\ concrete} = \frac{E_s}{E_c} \qquad \text{Equation B16}$$

$$n = \frac{200}{27} = 7.67$$ Equation B17

The area of steel reinforcement in the pile is 6 T 32 with an area of steel of 4830 mm².

$$As' = \frac{4830}{2} = 2415\ mm^2$$ Equation B18

$$As = \frac{4830}{2} = 2415\ mm^2$$ Equation B19

Table B3 Calculations for the second moment of inertia

	n	Area mm²	n × Area mm²	y_1 mm	$Y_1 \times$ n × Area mm³	I mm⁴	d mm	d² × n × Area mm⁴
As'	5.67	2415	13685	60	821100	-	-90	110848500
As	5.67	2415	13685	240	3284400	-	90	110848500
Ac	1	90000	90000	150	13500000	675000000	0	0
			117370		17605500	675000000		221697000

Note: *(n) used in the table is (n-1) to ensure that the translated area of steel is not calculated twice (i.e. 6.67 – 1 = 5.67).*

where

y1 is the depth to the centre of the area from the top of the pile section in Figure B1.

d is the distance from the neutral axis.

$$\bar{y} = \frac{\sum y1 \times n \times Area}{\sum n \times Area} = \frac{17605500}{117370} = 150\ mm$$ Equation B20

$$d = y1 - \bar{y}$$ Equation B21

$$I_{Total} = \sum I + \sum d^2 \times n \times Area$$ Equation B22

$$I_{Total} = 675{,}000{,}000 + 221{,}697{,}000 \quad \text{Equation B23}$$

$$I_{Total} = 896{,}697{,}000\ mm^4 \quad \text{Equation B24}$$

$$I_{Total} = 0.000896697\ m^4 \quad \text{Equation B25}$$

The Young's Modulus of the concrete is 30 GPa (30,000,000 kN/m²). Therefore the flexural stiffness EI can be calculated as the following:

$$EI = (30\ \times 10^6)\ \times\ 0.000896697 \quad \text{Equation B26}$$

The flexural stiffness (*EI*) of a single 300 x 300mm reinforced concrete pile is:

$$EI = 26901\ kNm^2 \quad \text{Equation B27}$$

The axial stiffness (*EA*) of a single 300 x 300mm reinforced concrete pile is calculated using the translated area (*n* × Area) from Table B3 to get:

$$EA = 30\ \times 117370 \quad \text{Equation B28}$$

$$EA = 3521100\ kN \quad \text{Equation B29}$$

$$EA = 3.521\ \times 10^6\ kN \quad \text{Equation B30}$$

B.3 Design of the reinforced concrete pile cap

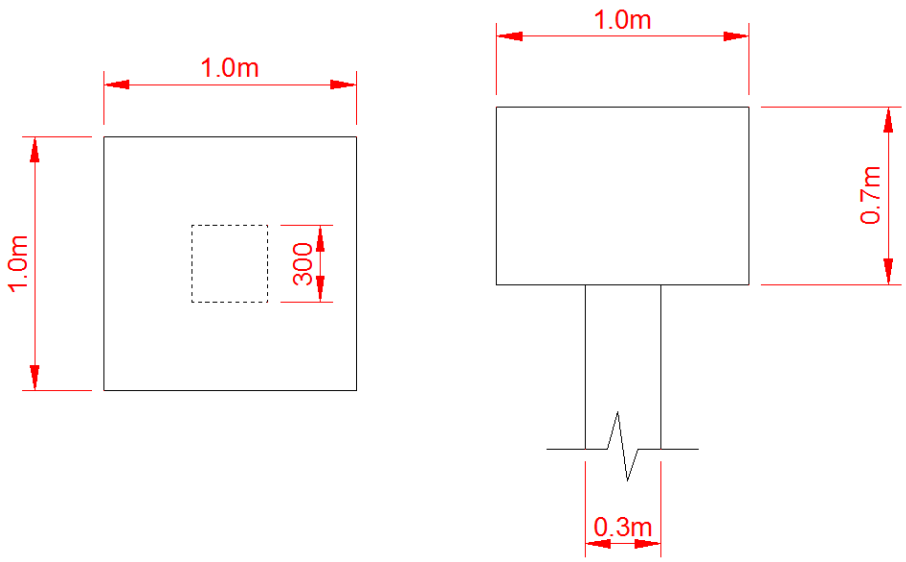

(a) (b)

Figure B5 (a) plan of pile cap (b) section through pile and pile cap

The pile cap illustrated in Figure B5 (a) & (b) is required to resist a maximum characteristic loading of 2900 kN from the embankment structure, Appendix B Section B.1. As the pile dimension is 300mm square, a pile cap of 700mm in thickness is assumed. The minimum depth of cover is 50mm. Therefore the mean effective depth is 620mm.

The uniformly distributed load from the embankment structure acting on the top of the pile cap surface is:

$$\text{Uniformly distributed loading on pile cap surface} = \frac{2900 \times 10^3}{1.0^2} \quad \text{Equation B31}$$

$$\text{UDL} = 2900 \text{ kN/m}^2 \quad \text{Equation B32}$$

B.3.1 Shear stress

At the pile head face, the shear stress, v_c is given by:

$$v_c = \frac{N}{(pile\ perimeter \times d)} \quad \text{Equation B33}$$

$$v_c = \frac{2900 \times 10^3}{(1200 \times 620)} = 3.89\ \text{N/mm}^2 \quad \text{Equation B34}$$

$$3.89\ \text{N/mm}^2 < 0.8\sqrt{f_{cu}} \quad \text{Equation B35}$$

$$3.89\ \text{N/mm}^2 < 4.38\ \text{N/mm}^2 \quad \text{Equation B36}$$

B.3.2 Punching shear check

$$\text{The critical perimeter} = \text{pile perimeter} + 8 \times 1.5d \quad \text{Equation B37}$$

$$\text{The critical perimeter} = (4 \times 300) + (8 \times 1.5\ (620)) \quad \text{Equation B38}$$

$$\text{The critical perimeter} = 8640\ \text{mm} \quad \text{Equation B39}$$

As the critical perimeter exceeds the actual perimeter (4000mm) of the pile cap no punching shear check is necessary.

B.3.3 Bending reinforcement – see Figure B6

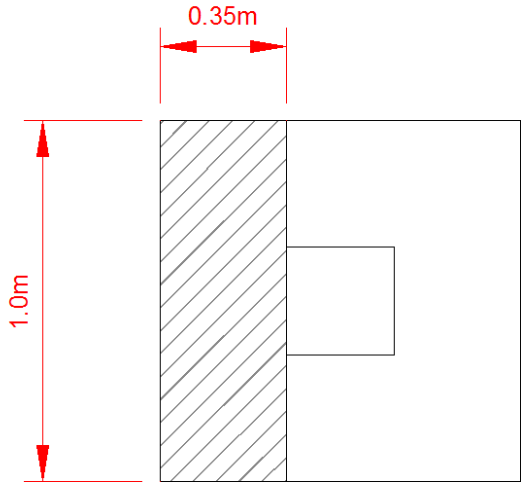

Figure B6 Area of loading of the resultant bending moment on pile cap

At the pile face which is the critical section:

$$M = 2900 \times 1.0 \times 0.35 \times \frac{0.35}{2} = 178\ kNm \qquad \text{Equation B40}$$

For the concrete

$$M_u = 0.156 f_{cu} b d^2 \qquad \text{Equation B41}$$

$$M_u = 0.156 \times 30 \times 1000 \times (620 \times 10^{-6})^2 \qquad \text{Equation B42}$$

$$M_u = 1798\ kNm > 178\ kNm \qquad \text{Equation B43}$$

$$A_s = \frac{M}{0.95 f_y z} \qquad \text{Equation B44}$$

From the lever arm curve, l_a = 0.95, therefore;

Lever arm $z = l_a \times d = 0.95 \times 620 = 589\text{mm}$ Equation B45

$$A_s = \frac{178 \times 10^6}{0.95 \times 460 \times 589}$$ Equation B46

$$A_s = 691mm^2$$ Equation B47

The minimum area of reinforcement:

$$A_s = \frac{0.13 \times 1000 \times 700}{100} = 910\text{mm}^2$$ Equation B48

The minimum reinforcement required exceeds the area required to resist the bending moment, therefore provide for the minimum area of reinforcement (910mm^2).

Provide ten T12 bars, area = 1130 mm^2, at 100mm centres in both directions.

$$A_s = \frac{100 \times 1130}{1000 \times 700} = 0.161 > 0.13 \text{ as required}$$ Equation B49

Maximum spacing = 750mm. Therefore the reinforcement provided meets the requirements specified by the code for minimum area and maximum bar spacing in a slab.

B.4 Determination of the second moment of inertia (I) of the pile cap

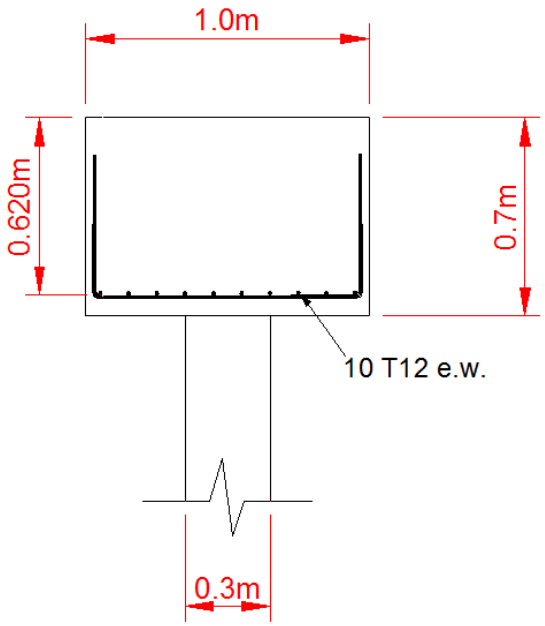

Figure B7 Section through the reinforced concrete pile cap

The second moment of inertia (*I*) of the pile cap in Figure B7 is required to be determined. As the section consists of both concrete and steel, the second moment of of inertia will be calculated using the transformed section method.

Some of the reinforced concrete pile cap section properties are the following:

f_c = 30 N/mm²

f_y = 460 N/mm²

E_c = 30 kN/mm²

E_s = 200 kN/mm²

The modular ratio (n) is defined as:

$$n = \frac{Modulus\ of\ Elasticity\ of\ Steel}{Static\ secant\ modulus\ of\ elasticity\ of\ concrete} = \frac{E_s}{E_c} \qquad \text{Equation B50}$$

$$n = \frac{200}{30} = 6.666$$ Equation B51

The area of steel reinforcement in the pile is ten T12 with an area of steel of 1130 mm².

Table B4 Calculations for the second moment of inertia of the reinforced concrete pile cap

	n	Area mm²	n × area mm²	y1 mm	Y1 × n × Area mm³	I mm⁴	d mm	d² × n × Area mm⁴
As	5.67	1130	6403.3333	620	3970066.667	-	267.6	458378499
Ac	1	700000	700000	350	245000000	28583333333	-2.4	4193072
			706403		248970066	28583333333		462571571

Note: *(n) used in the table is (n-1) to ensure that the translated area of steel is not calculated twice (i.e. 6.67 – 1 = 5.67).*

where

y1 is the depth to the centre of the area from the top of the pile cap section in Figure B1.

d is the distance from the neutral axis.

$$\bar{y} = \frac{\sum y1 \times n \times Area}{\sum n \times Area} = \frac{248970066}{706403} = 352\ mm$$ Equation B52

$$d = y1 - \bar{y}$$ Equation B53

$$I_{Total} = \sum I + \sum d^2 \times n \times Area$$ Equation B54

$$I_{Total} = 28{,}583{,}333{,}333 + 462571571$$ Equation B55

$$I_{Total} = 29{,}045{,}904{,}905\ mm^4$$ Equation B56

$$I_{Total} = 0.029045904905\ m^4$$ Equation B57

The Young's Modulus of the concrete is 30 GPa (30,000,000 kN/m²). Therefore the flexural stiffness EI of the pile cap can be calculated as the following:

$$EI = (30 \times 10^6) \times 0.029045904905 \quad \text{Equation B58}$$

The flexural stiffness (*EI*) of a single 1000 x 1000mm reinforced concrete pile cap with a thickness of 700mm is:

$$EI = 871377\ kNm^2 \quad \text{Equation B59}$$

$$EI = 871.377 \times 10^3\ kNm^2 \quad \text{Equation B60}$$

The axial stiffness (*EA*) of a single 1000 × 1000mm reinforced concrete pile cap with a thickness of 700mm is calculated using the translated area (*n* × Area) from Table B4 to get:

$$EA = 30kN/mm^2 \times 706403mm^2 \quad \text{Equation B61}$$

$$EA = 21{,}192{,}090\ kN \quad \text{Equation B62}$$

$$EA = 21.192 \times 10^6\ kN \quad \text{Equation B63}$$

APPENDIX C: Plane strain model test results

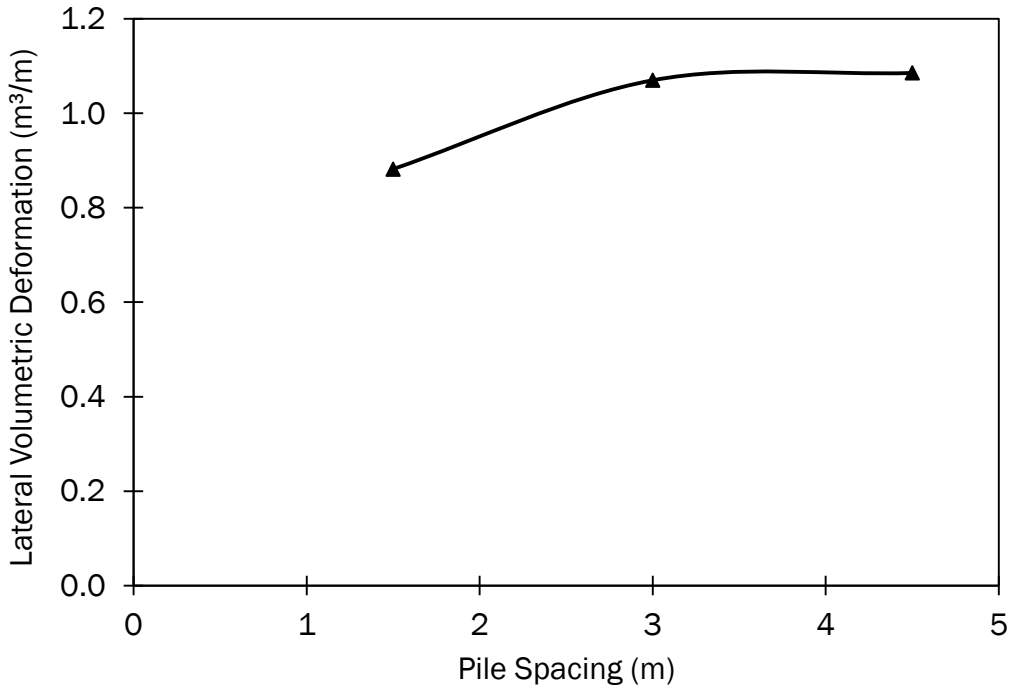

Figure C1 Lateral volumetric deformations of embankment fill above outer pile row pile cap for a range of pile spacing

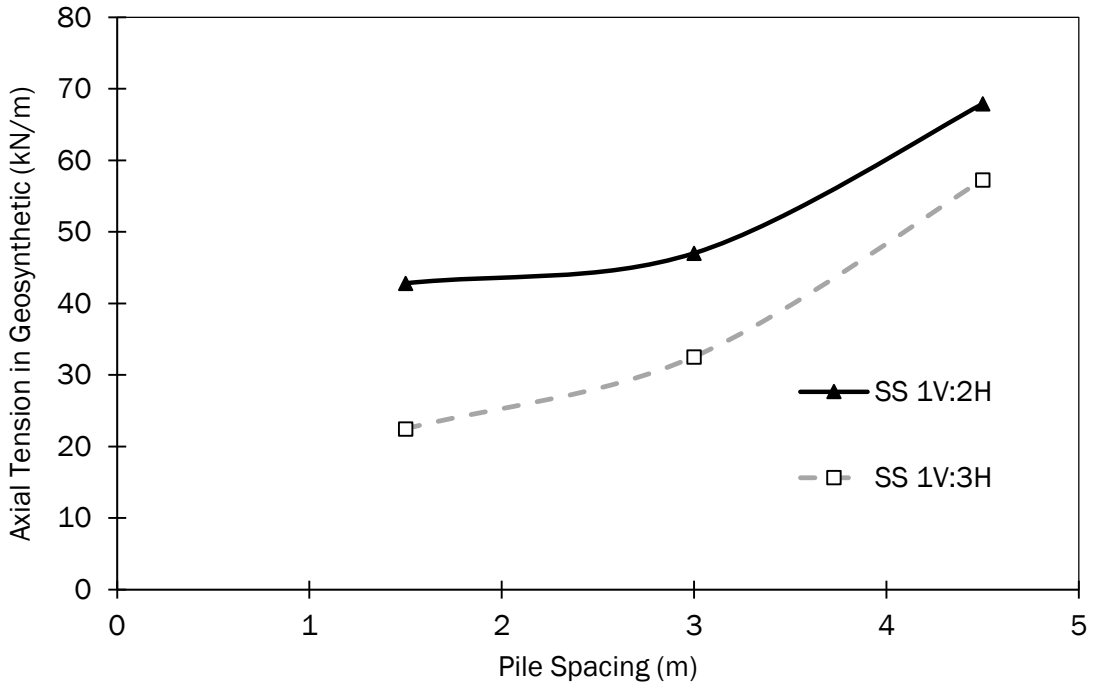

Figure C2 Maximum axial tension in geosynthetic reinforcement for a range of pile spacing

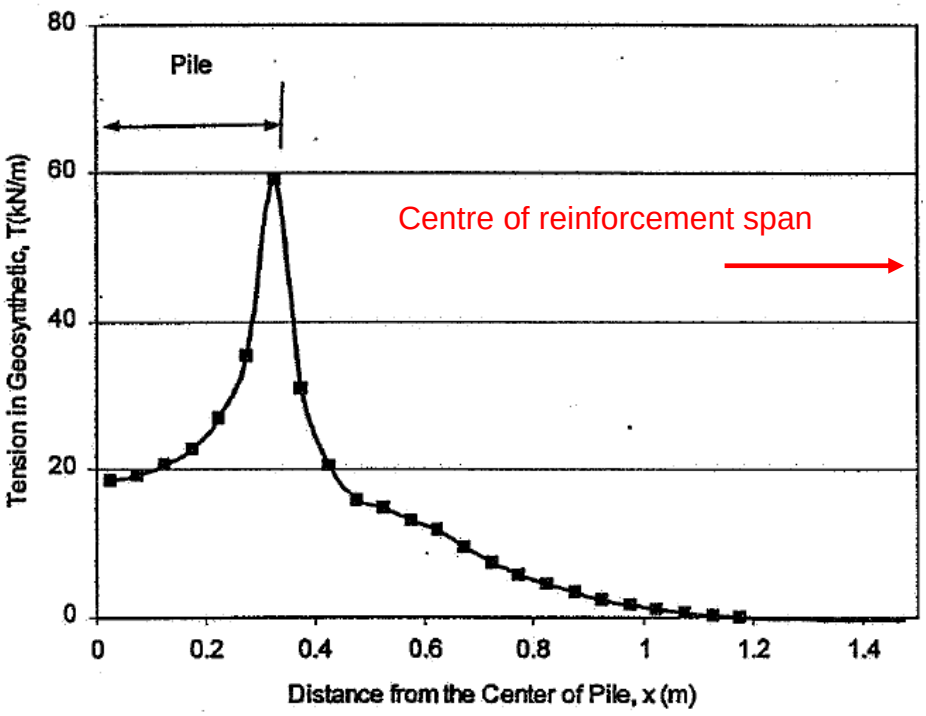

Figure C3 Distribution of axial tension in reinforcement half span (after Han & Gabr 2003) (axisymmetric analysis)

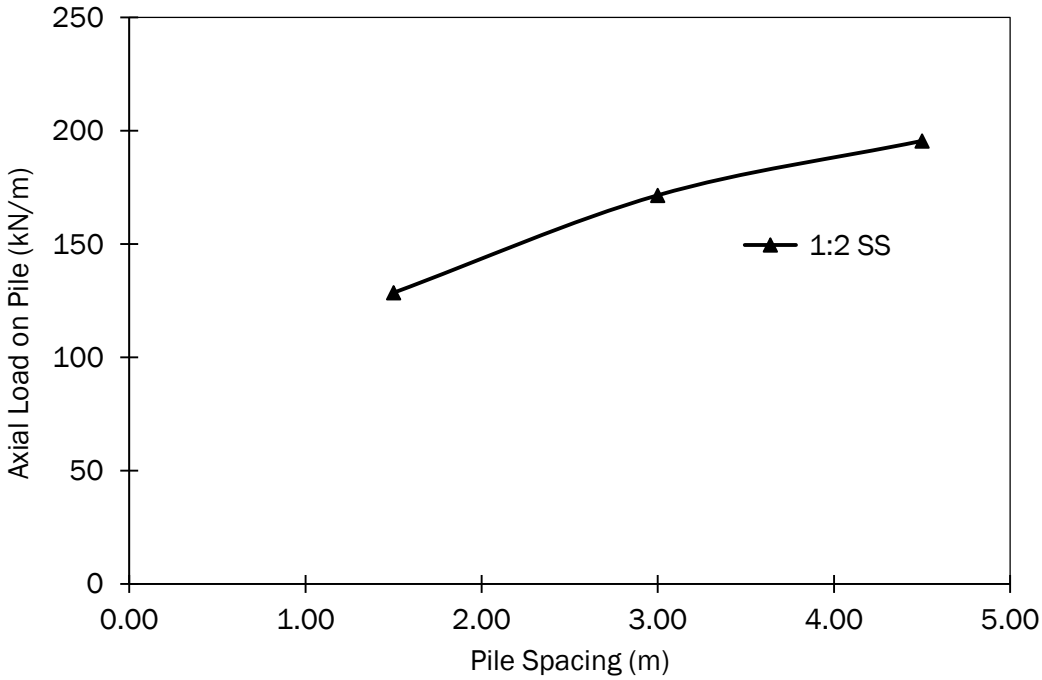

Figure C4 Axial load (kN) on outer pile for a range of pile spacing (m) (H = 4.0m, J_{re} = 500kN/m and a = 1.0m)

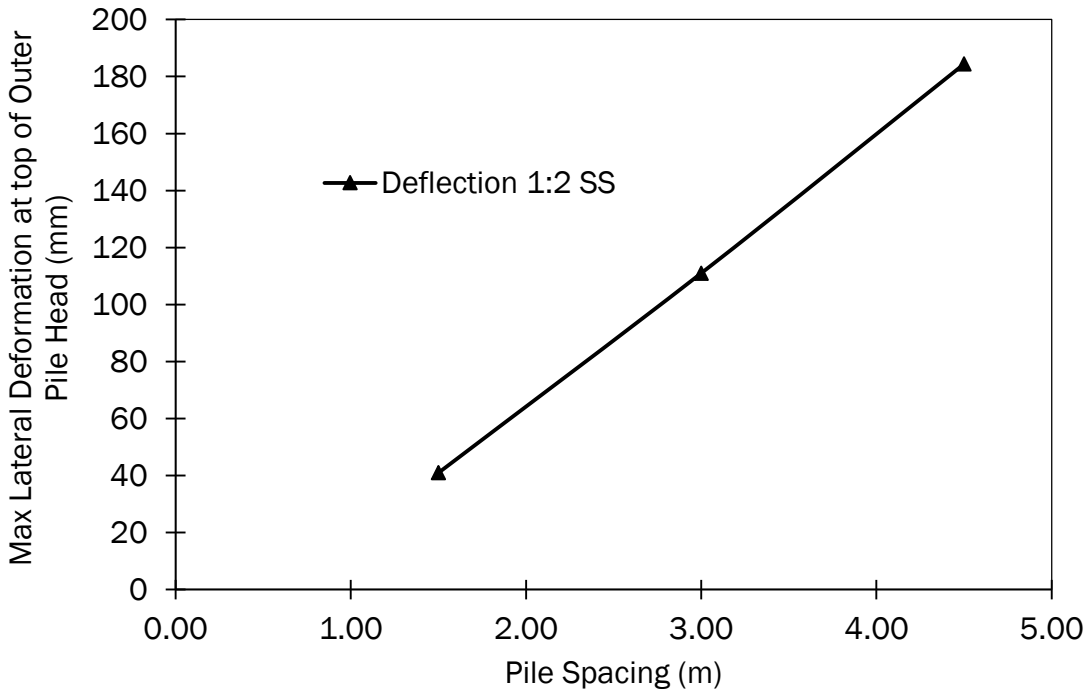

Figure C5 Lateral deformation of outer row pile head for a range of pile spacing (H = 4.0m, J_{re} = 500kN/m and a = 1.0m)

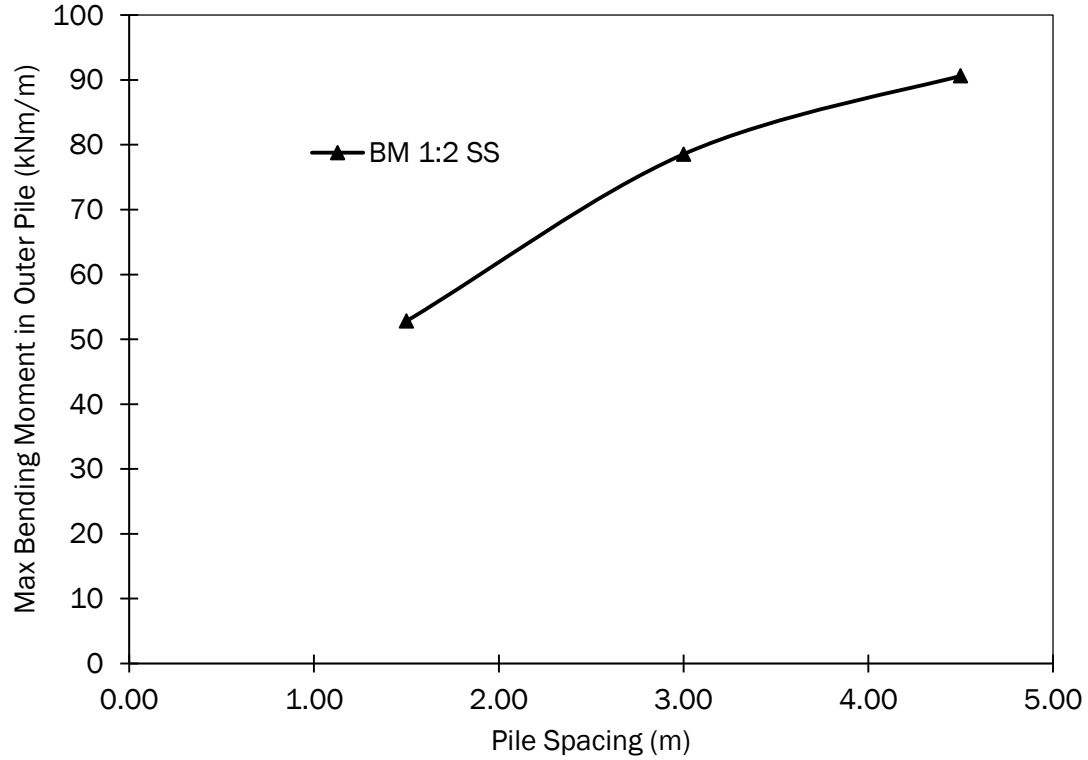

Figure C6 Outer pile row bending moments for a range of pile spacing

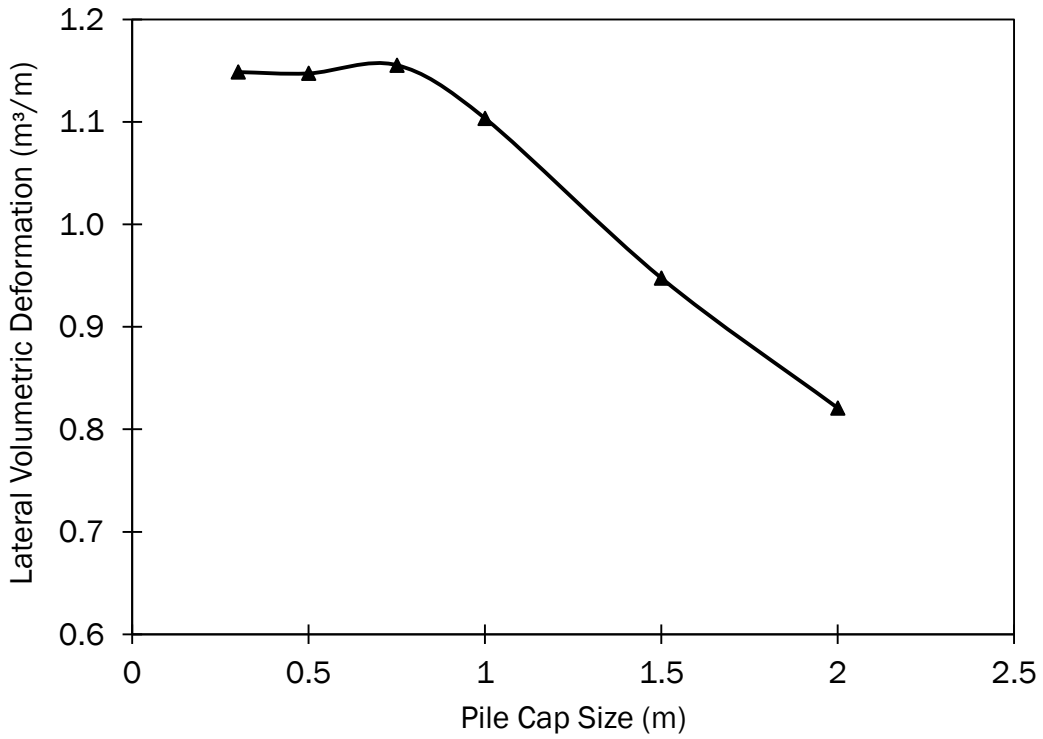

Figure C7 Lateral Volumetric Deformation (LVD) (m^3/m) above the centreline of outer row pile for a 1V:2H side slope (H = 4.0m, J_{re} = 500kN/m and s = 3.0m)

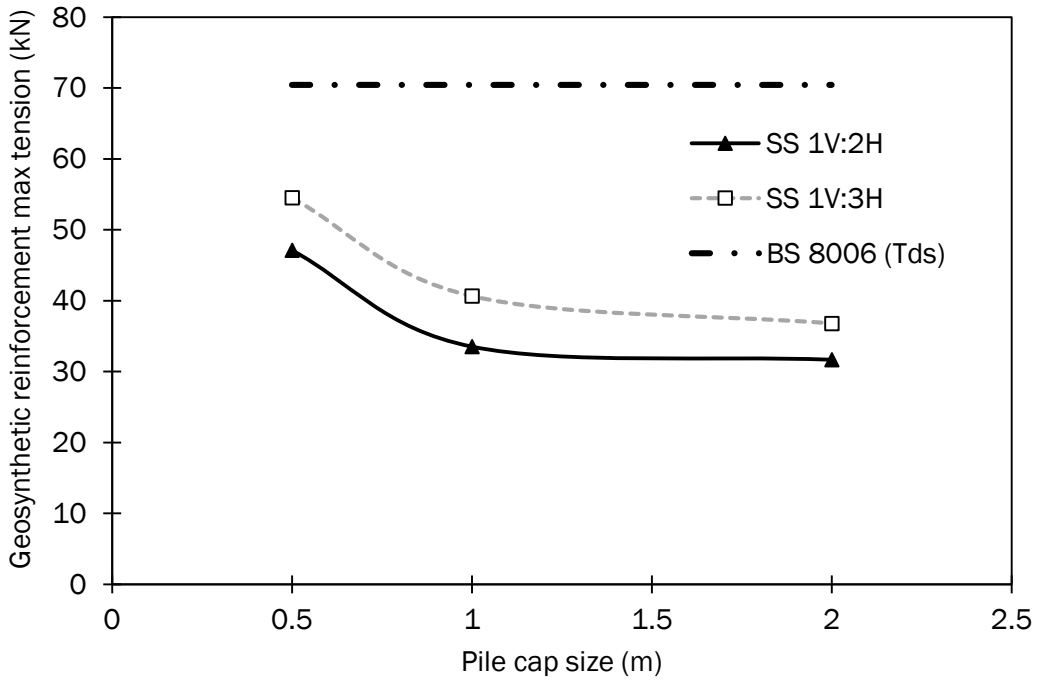

Figure C8 Maximum axial tension in geosynthetic reinforcement for a range of pile cap size

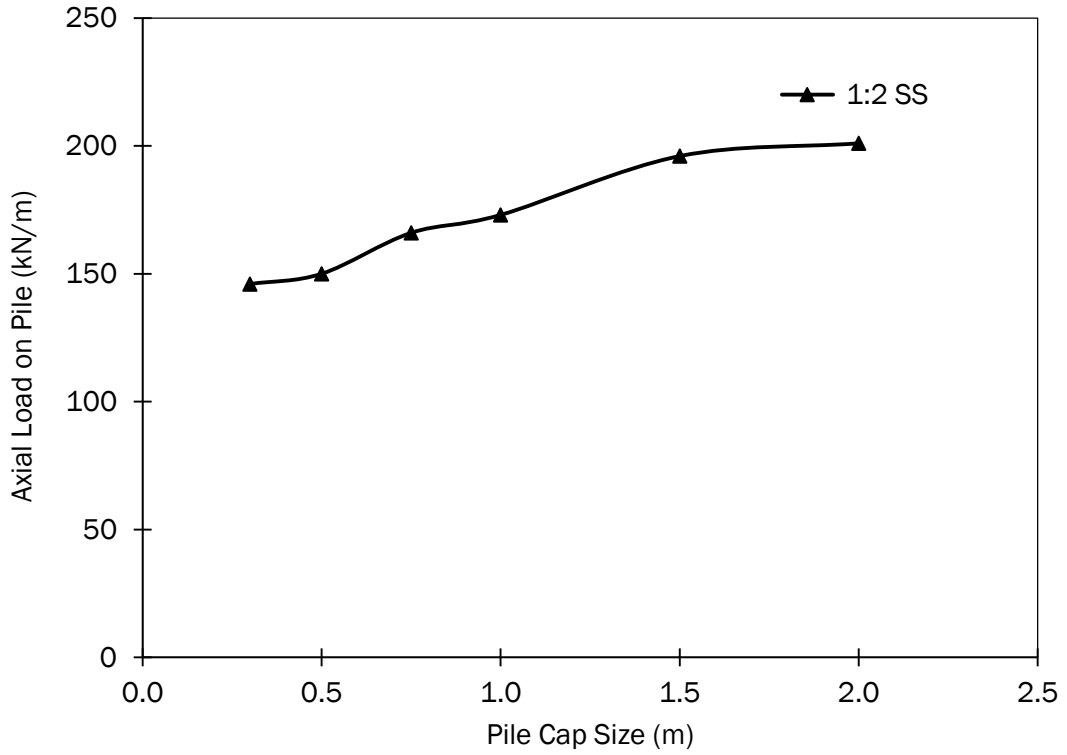

Figure C9 Axial load (kN) on outer pile for a range of pile cap size (m) (H = 4.0m, J_{re} = 500kN/m and s = 3.0m)

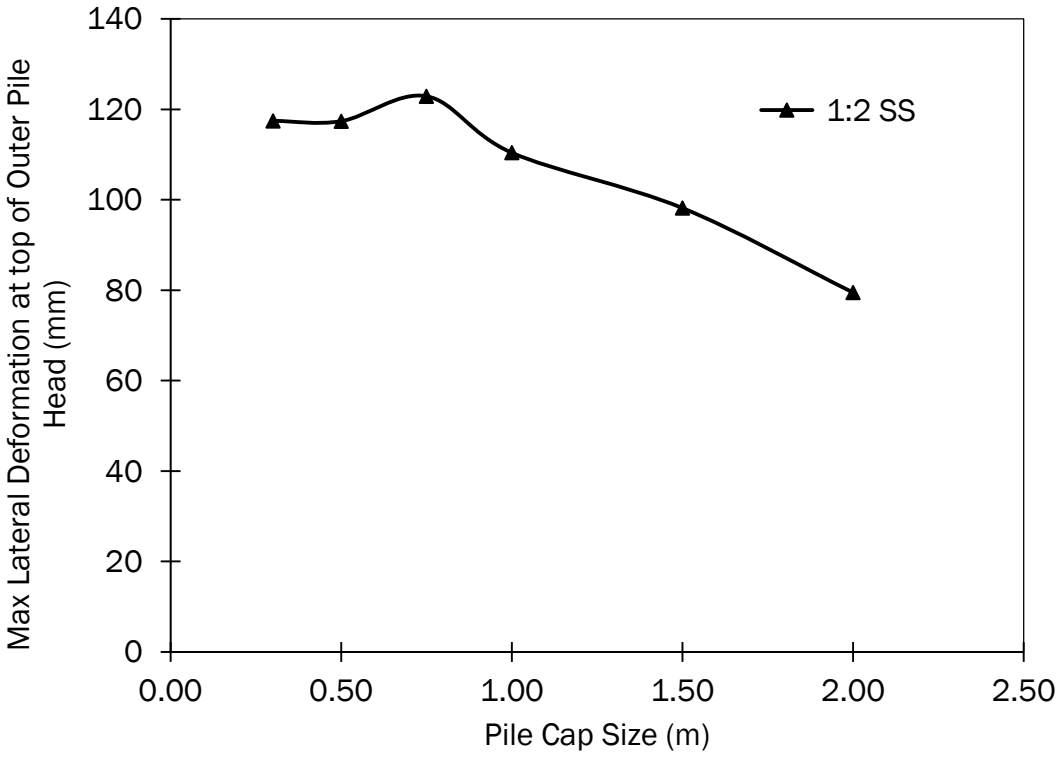

Figure C10 Deflection of outer row pile head for a range of pile cap size & side slopes (H = 4.0m, J_{re} = 500kN/m and s = 3.0m)

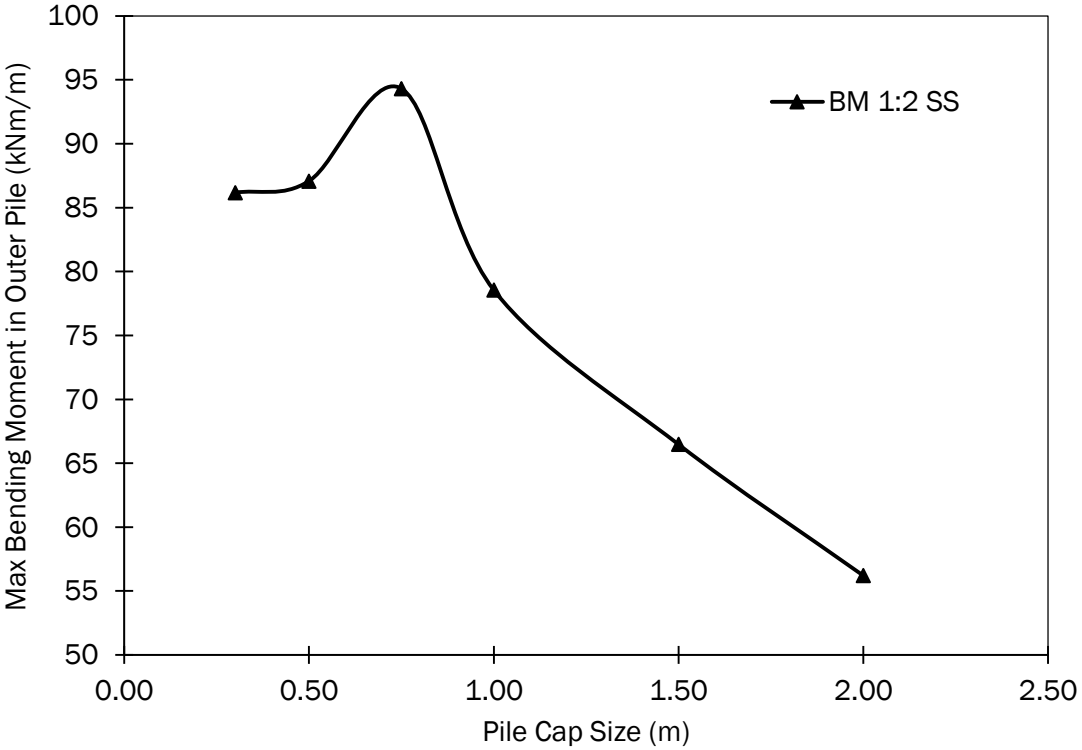

Figure C11 Outer pile row bending moments for a range of pile cap size

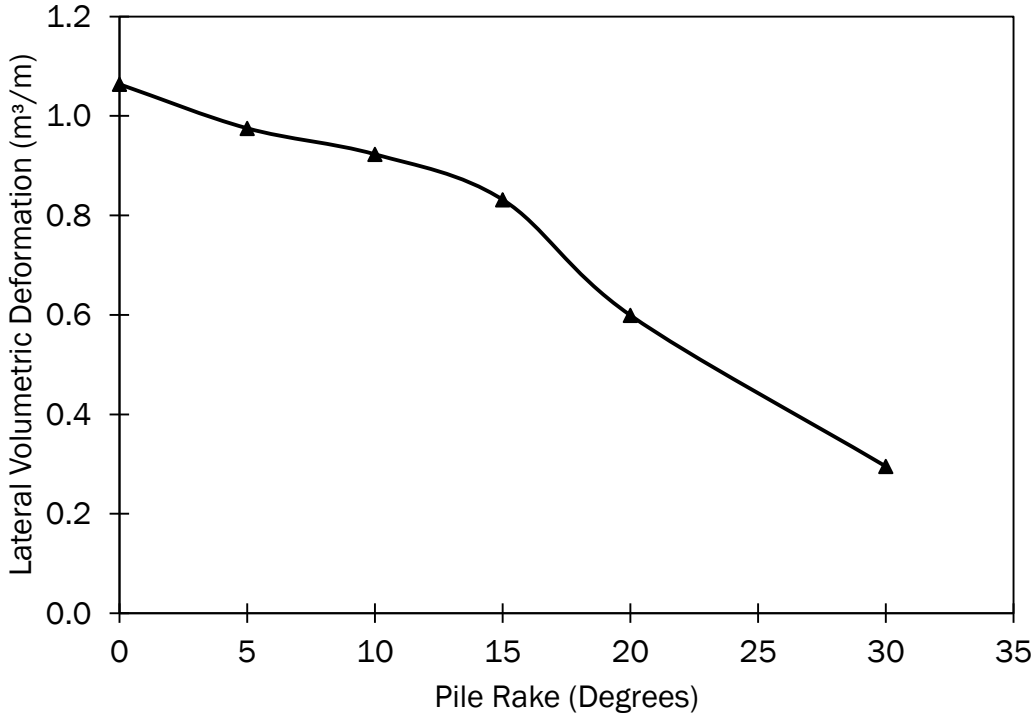

Figure C12 Lateral Volumetric Deformation (LVD) (m³/m) above the centreline of outer row pile for a 1V:2H side slope (H = 4.0m, J_{re} = 500kN/m and s = 3.0m)

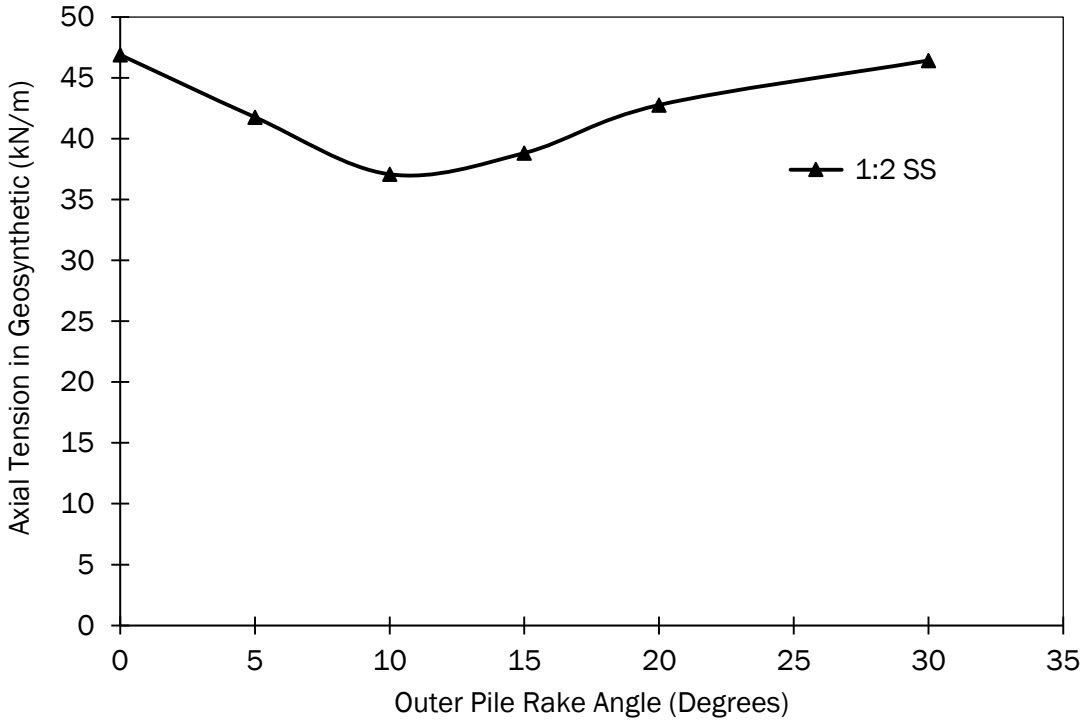

Figure C13 Max axial tension (kN/m) in reinforcement versus pile rake angle (°)(H = 4.0m, J_{re} = 500kN/m and s = 3.0m)

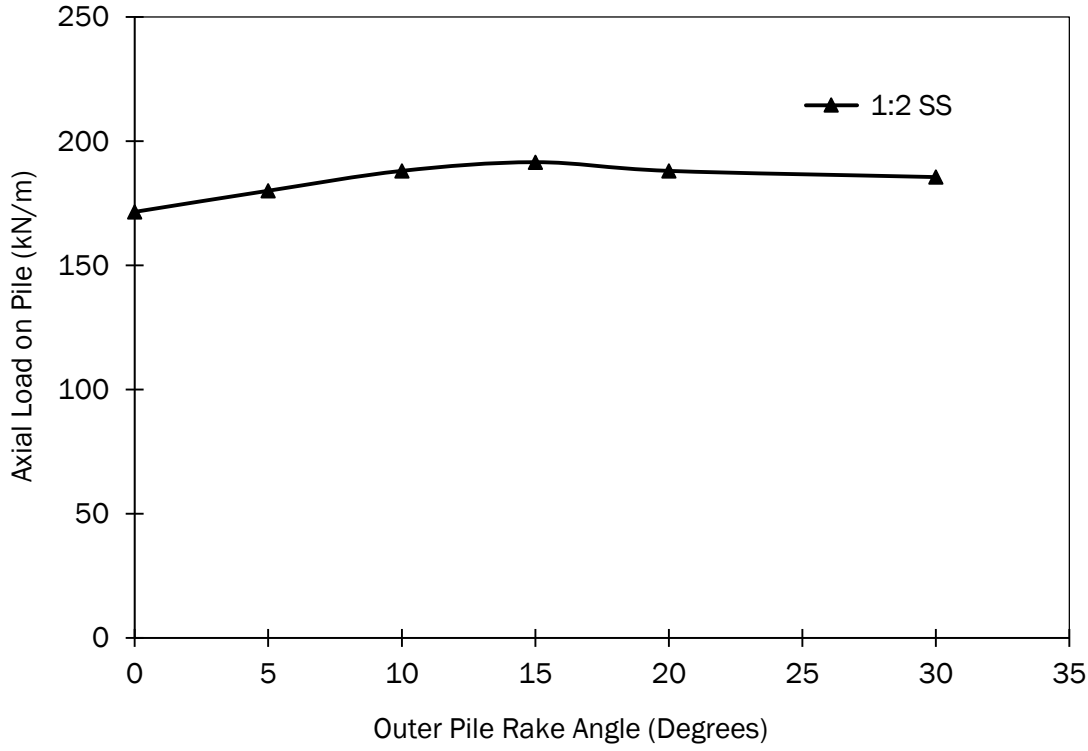

Figure C14 Axial load (kN) on outer pile for a range of pile cap size (m) (H = 4.0m, J_{re} = 500kN/m and s = 3.0m)

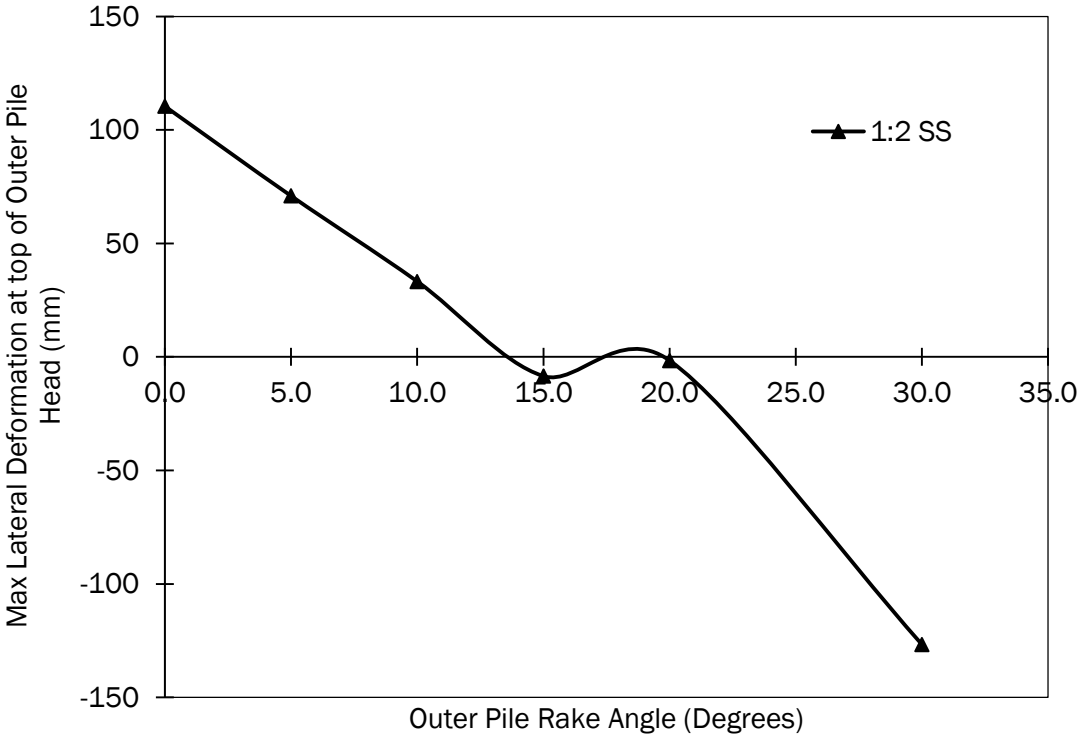

Figure C15 Deflection of outer row pile head for a range of pile rake angle (°)(H = 4.0m, J_{re} = 500kN/m and s = 3.0m)

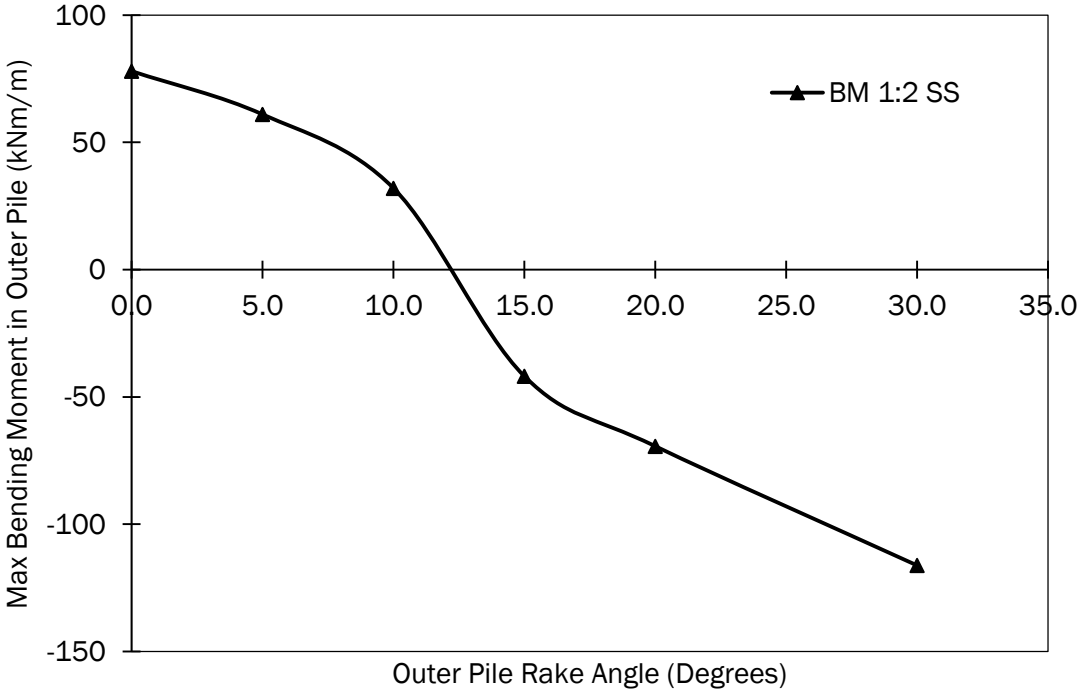

Figure C16 Max BM in outer row pile for a range of pile rake angle (°)(H = 4.0m, J_{re} = 500kN/m and s = 3.0m)

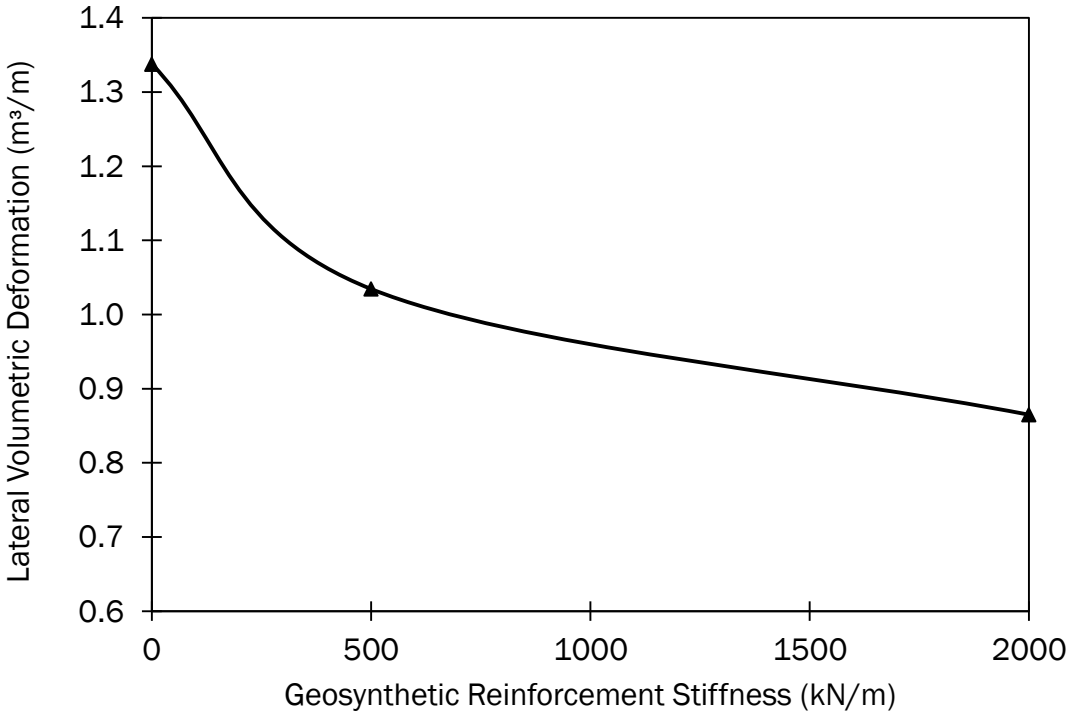

Figure C17 Lateral Volumetric Deformation (LVD) (m³/m) above the centreline of outer row pile for a 1V:2H side slope for a range of geosynthetic reinforcement stiffness (kN/m) (H = 4.0m, a=1.0m and s = 3.0m)

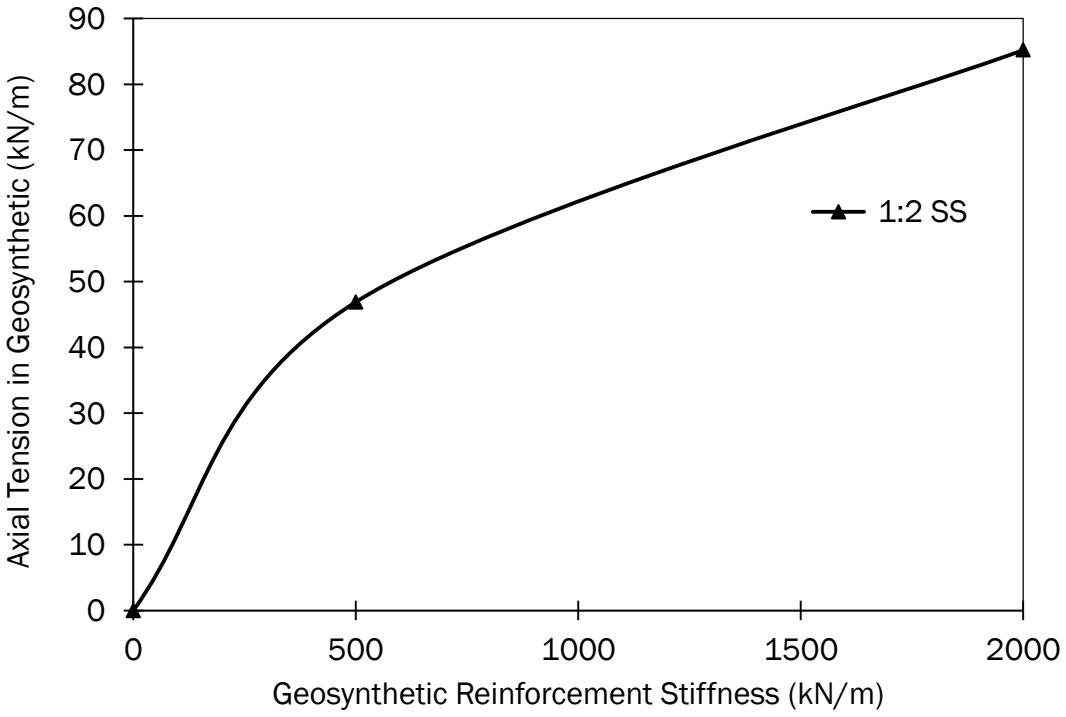

Figure C18 Max axial tension (kN/m) in reinforcement versus geosynthetic reinforcement stiffness (kN/m) (H = 4.0m, a =1.0m and s = 3.0m)

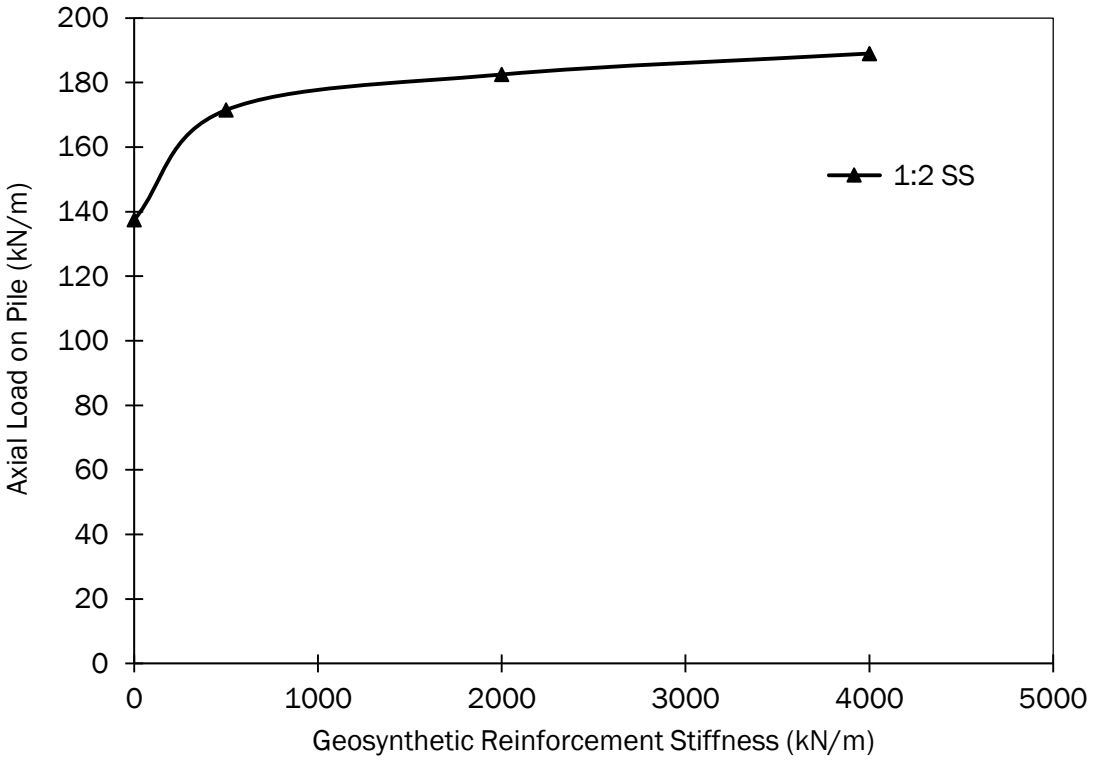

Figure C19 Axial load (kN) on outer pile for a range of geosynthetic reinforcement stiffness (kN/m) (H = 4.0m, a = 1.0m and s = 3.0m)

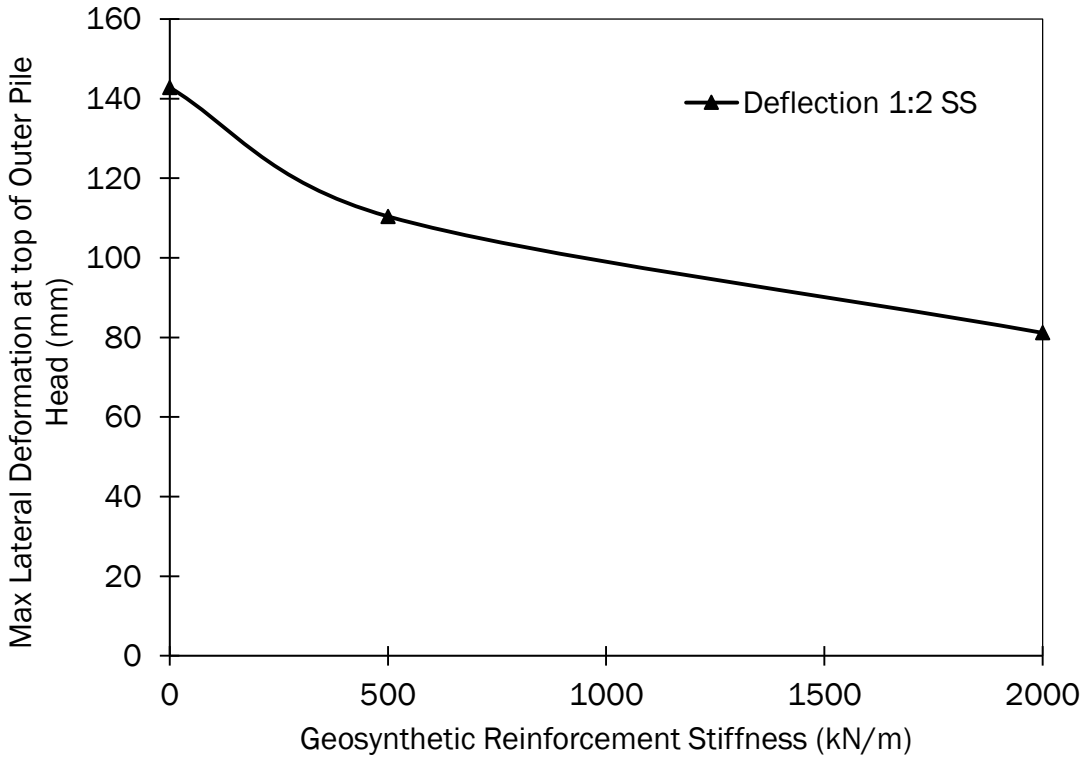

Figure C20 Deflection of outer row pile head for a range of geosynthetic reinforcement stiffness (kN/m) (H = 4.0m, a = 1.0m and s = 3.0m)

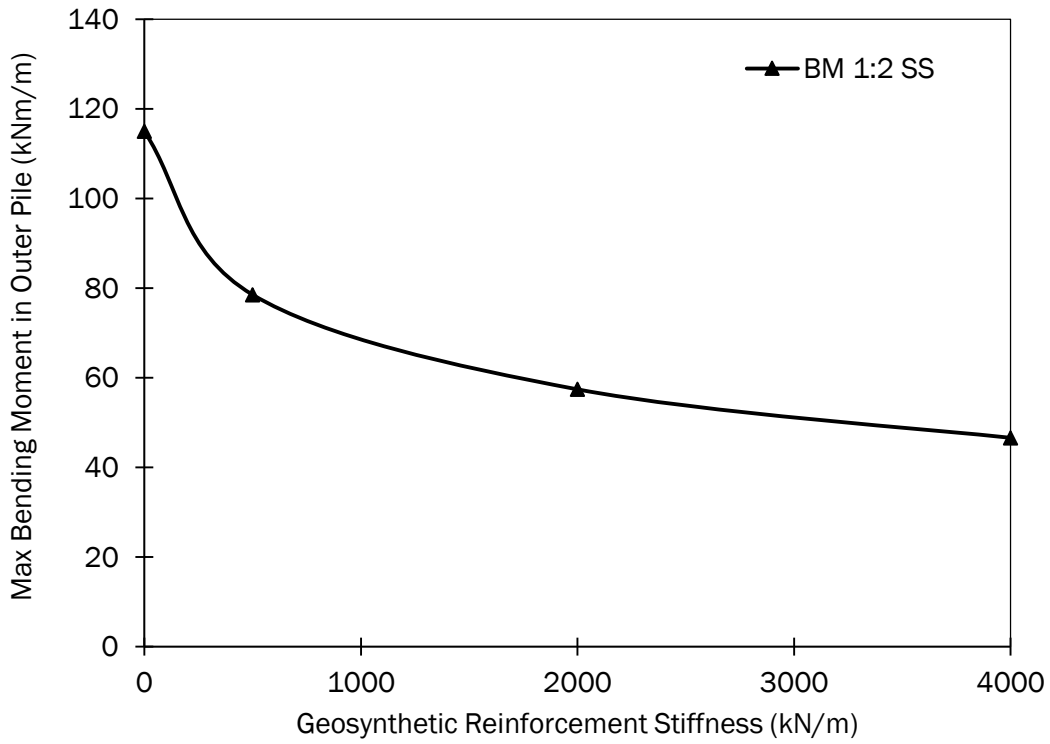

Figure C21 Max BM in outer row pile for a range of geosynthetic reinforcement stiffness (kN/m) (H = 4.0m, a = 1.0m and s = 3.0m)

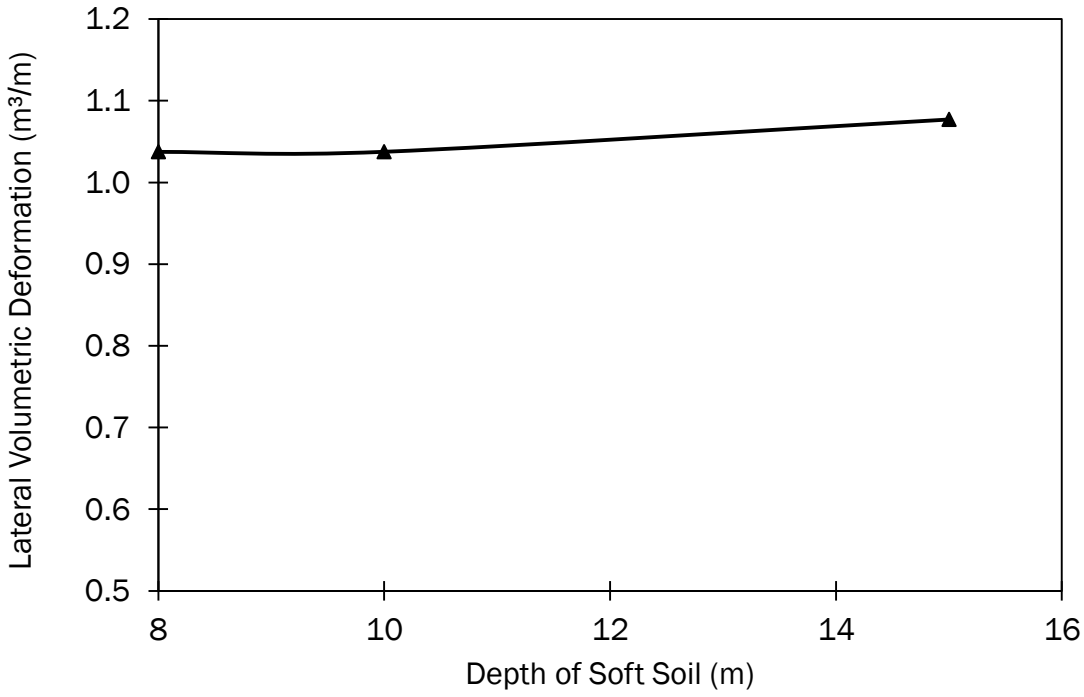

Figure C22 Lateral Volumetric Deformation (LVD) (m³/m) above the centreline of outer row pile for a 1V:2H side slope for a range of soft soil layer depth (m) (H = 4.0m, a = 1.0m and s = 3.0m J_{re} = 500kN/m)

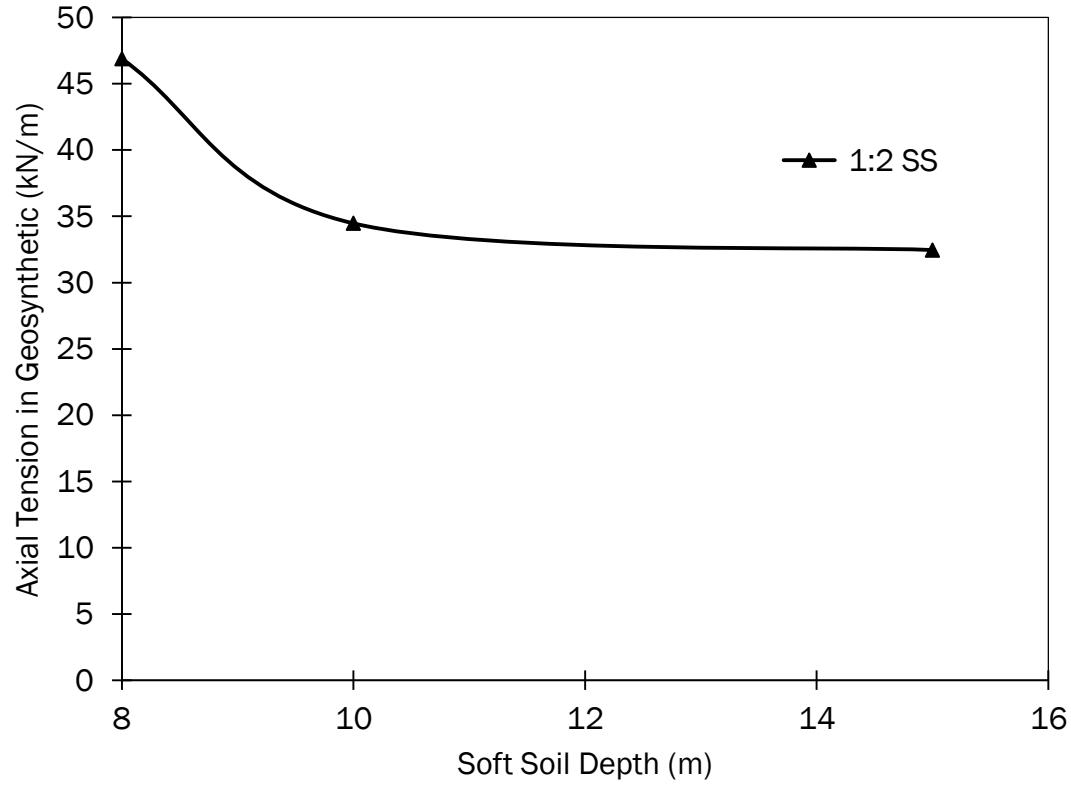

Figure C23 Max axial tension (kN/m) in reinforcement for a range of soft soil layer depth (m) (H = 4.0m, a = 1.0m and s = 3.0m J_{re} = 500kN/m)

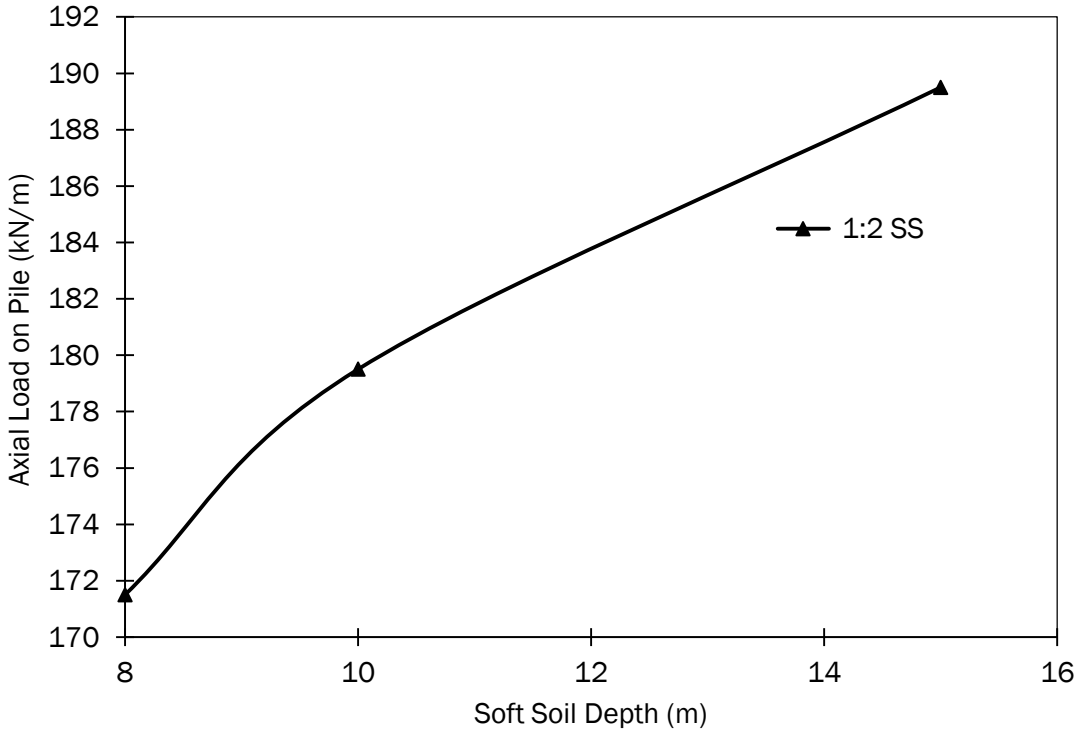

Figure C24 Axial load (kN) on outer pile for a range of soft soil layer depth (m) (H = 4.0m, a = 1.0m and s = 3.0m J_{re} = 500kN/m)

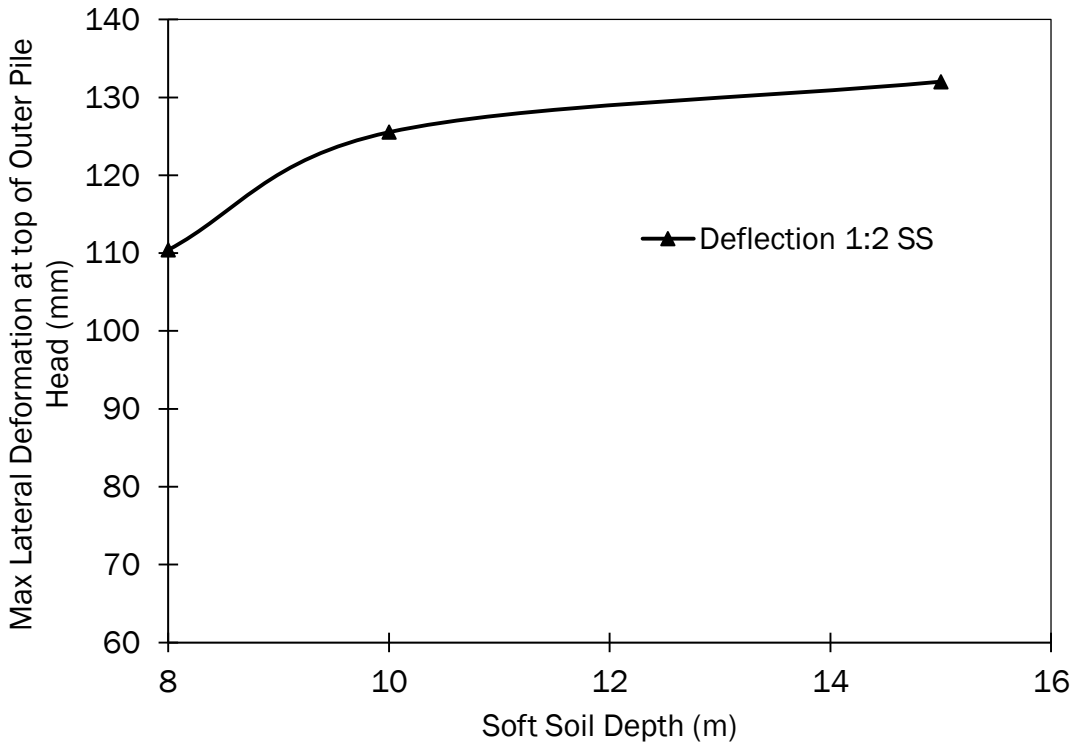

Figure C25 Deflection of outer row pile head for a range of soft soil layer depth (m) (H = 4.0m, a = 1.0m and s = 3.0m J_{re} = 500kN/m)

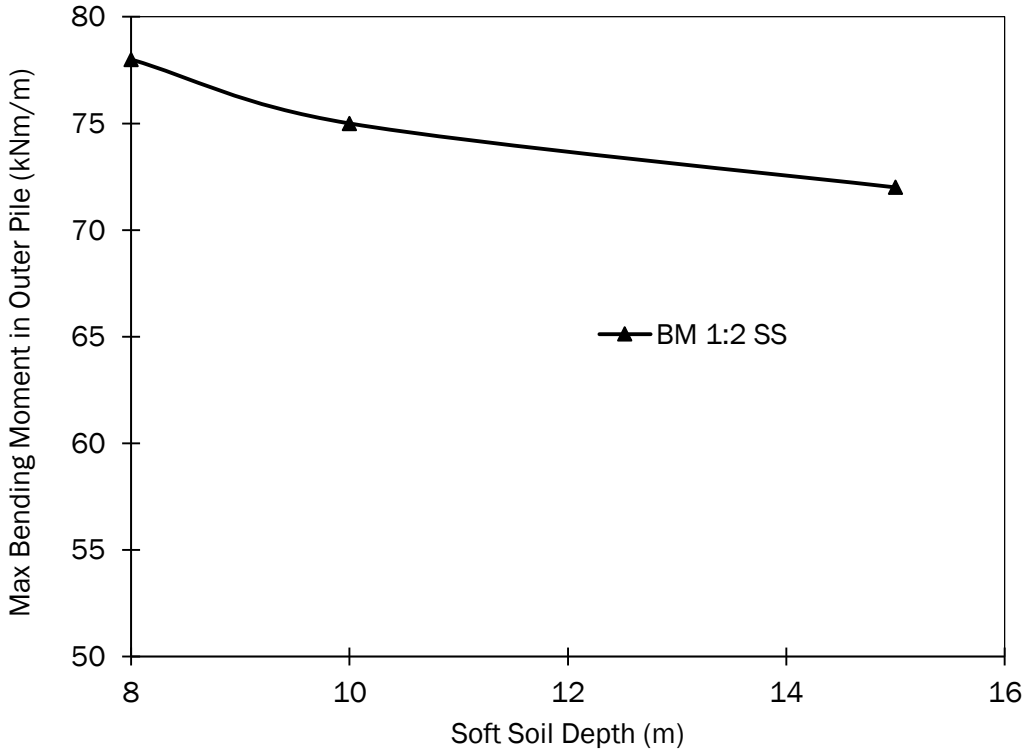

Figure C26 Max BM in outer row pile for a range of soft soil layer depth (m) (H = 4.0m, a = 1.0m and s = 3.0m J_{re} = 500kN/m)

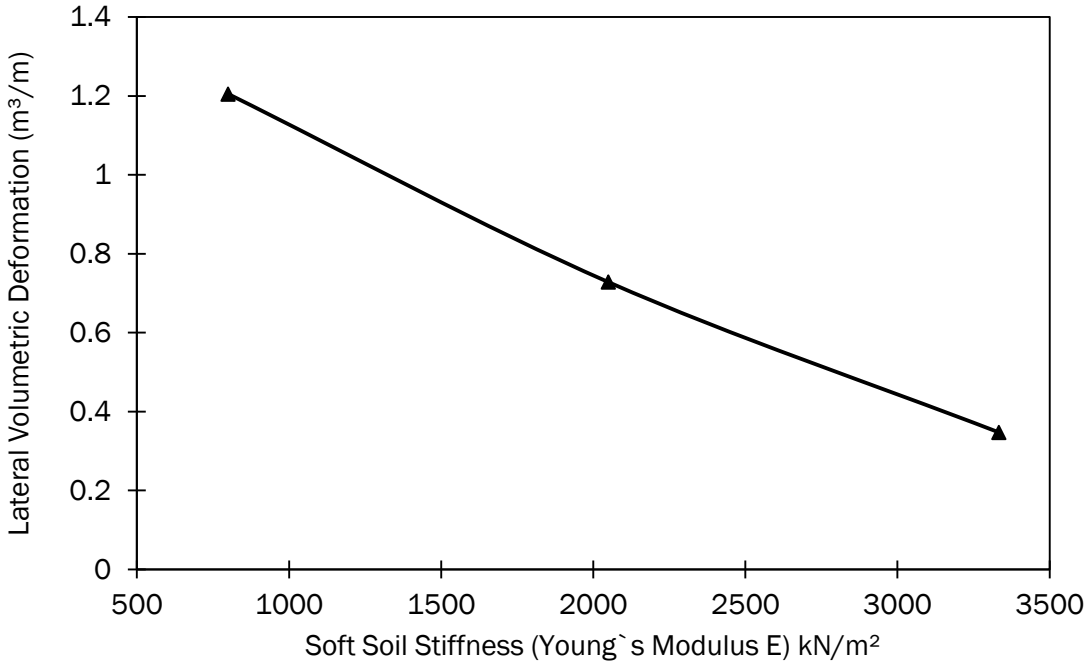

Figure C27 Lateral Volumetric Deformation (LVD) (m³/m) above the centreline of outer row pile for a 1V:2H side slope for a range of soft soil stiffness (E) (kN/m²) (H = 4.0m, a = 1.0m and s = 3.0m J_{re} = 500kN/m)

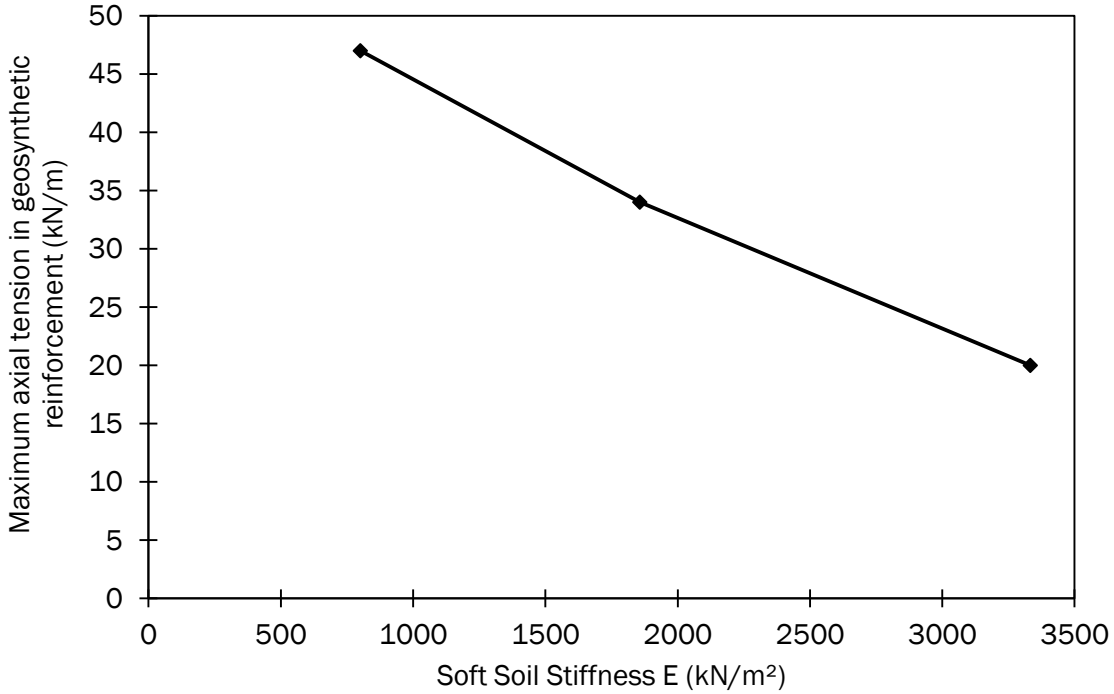

Figure C28 Max axial tension (kN/m) in reinforcement for a range of soft soil stiffness (E) (kN/m²) (H = 4.0m, a = 1.0m and s = 3.0m J_{re} = 500kN/m)

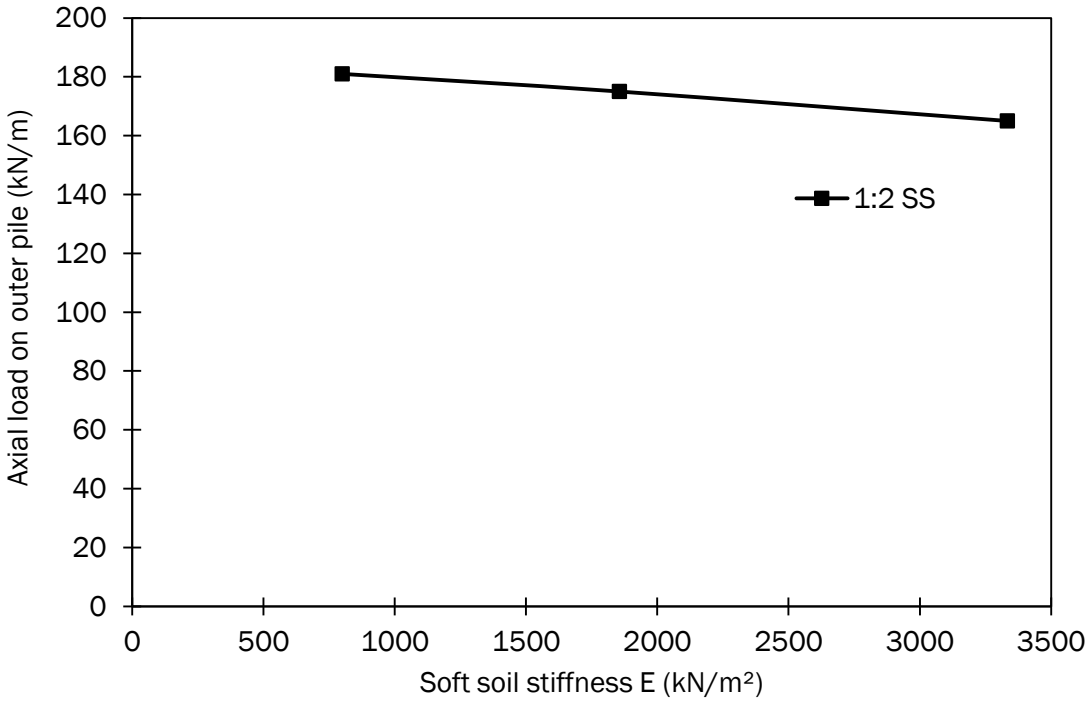

Figure C29 Axial load (kN) on outer pile for a range of soft soil stiffness (E) (kN/m²) (H = 4.0m, a = 1.0m and s = 3.0m J_{re} = 500kN/m)

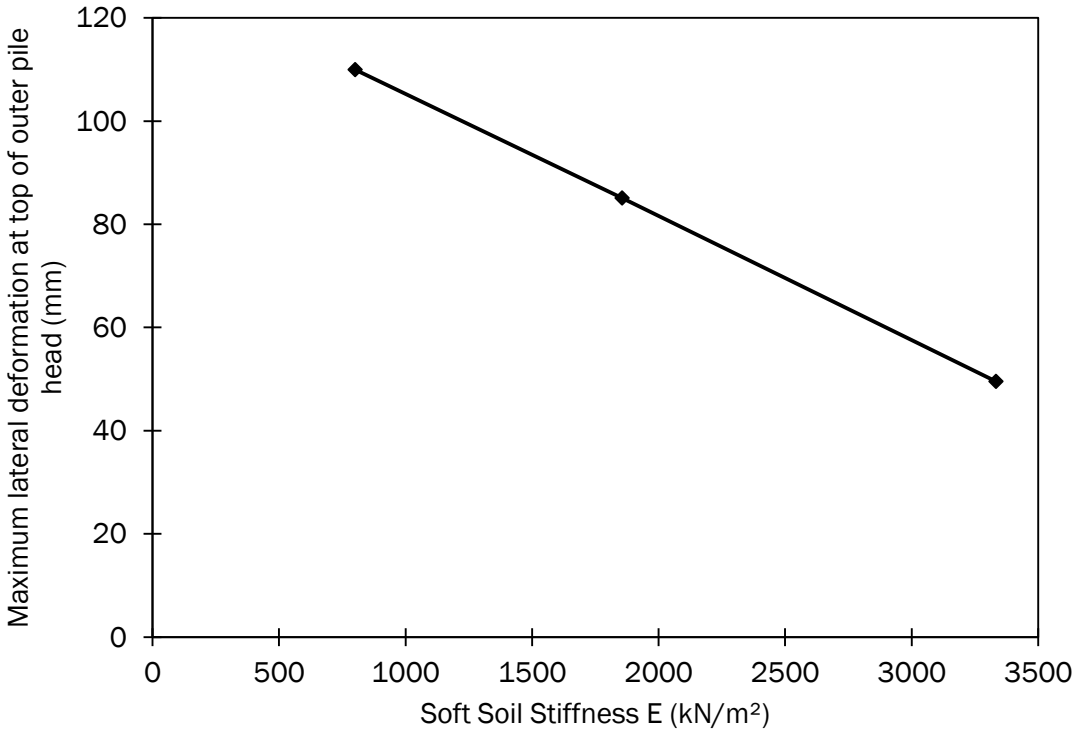

Figure C30 Deflection of outer row pile head for a range of soft soil stiffness (E) (kN/m²) (H = 4.0m, a = 1.0m and s = 3.0m J_{re} = 500kN/m)

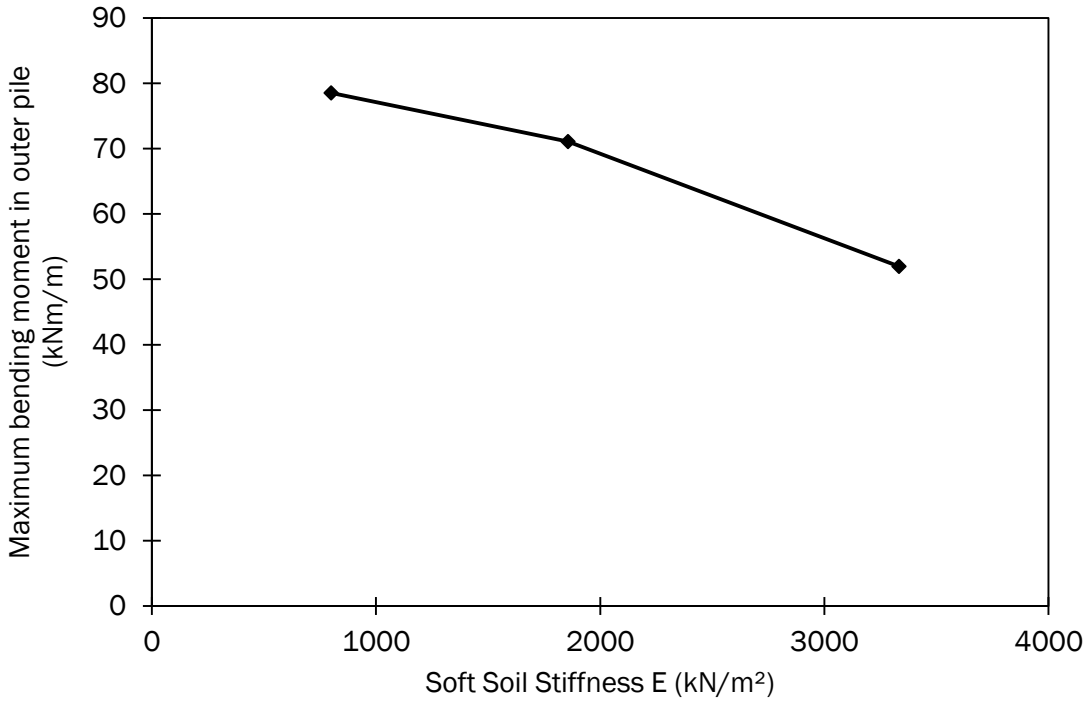

Figure C31 Max BM in outer row pile for a range of soft soil stiffness (E) (kN/m²) (H = 4.0m, a = 1.0m and s = 3.0m J_{re} = 500kN/m)

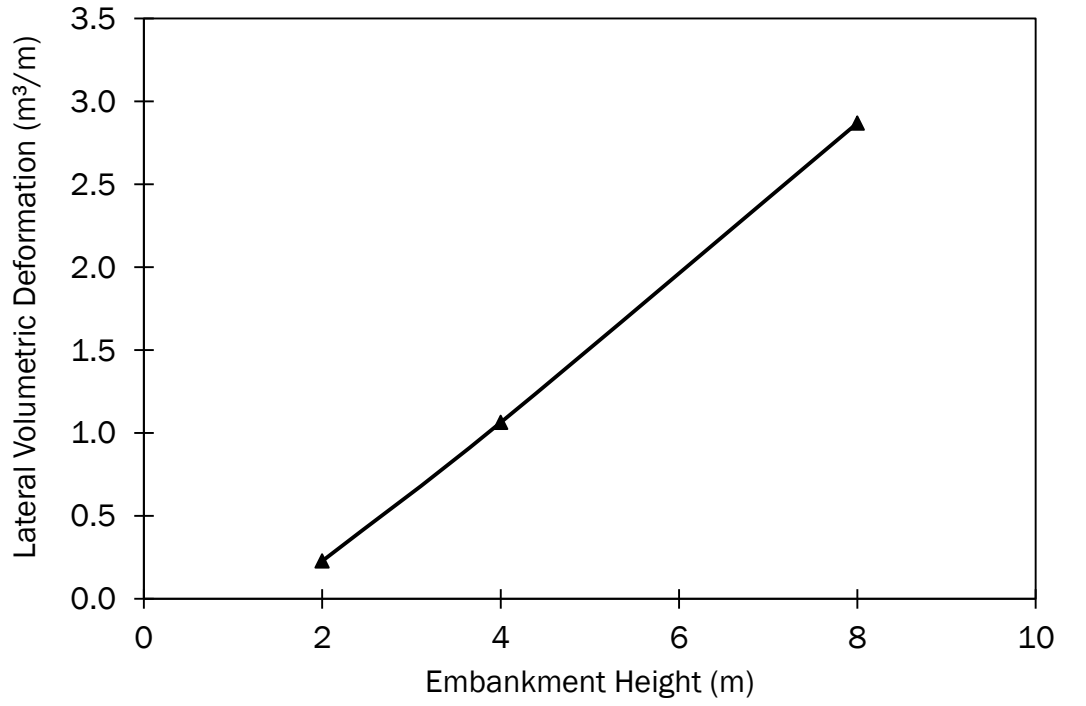

Figure C32 Lateral Volumetric Deformation (LVD) (m³/m) above the centreline of outer row pile for a 1V:2H side slope for a range of embankment height (m) (H = 4.0m, a = 1.0m and s = 3.0m J_{re} = 500kN/m)

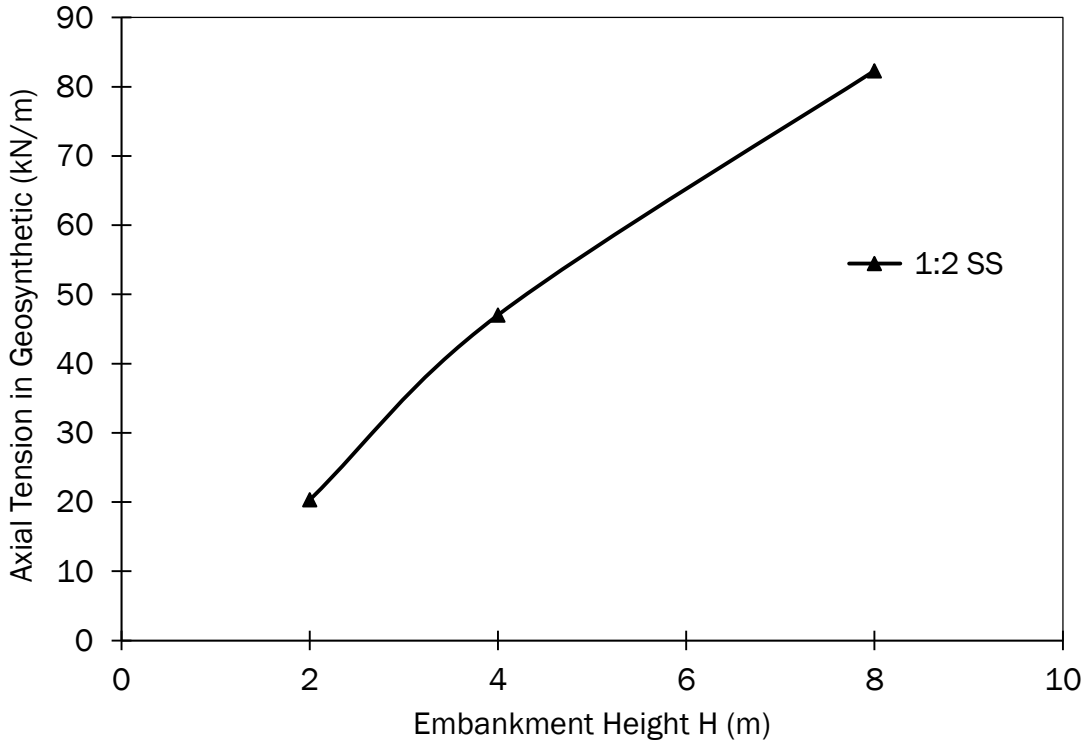

Figure C33 Max axial tension (kN/m) in reinforcement for a range of embankment height (m) (H = 4.0m, a = 1.0m and s = 3.0m J_{re} = 500kN/m)

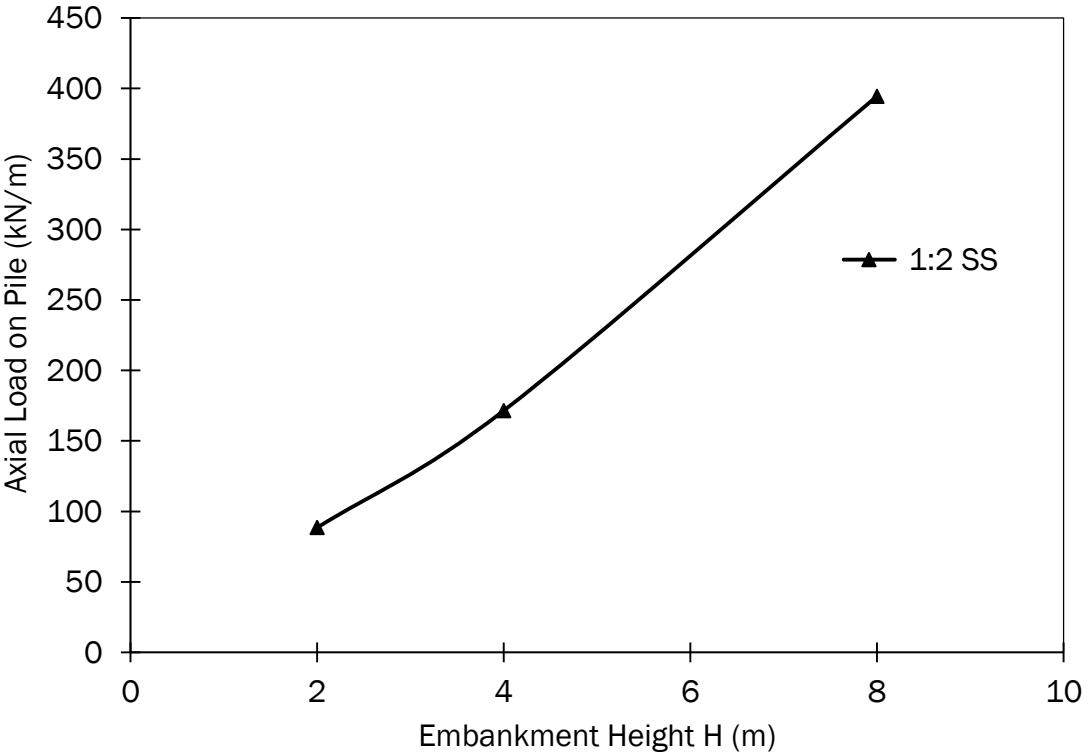

Figure C34 Axial load (kN) on outer pile for a range of embankment height (m) (H = 4.0m, a = 1.0m and s = 3.0m J_{re} = 500kN/m)

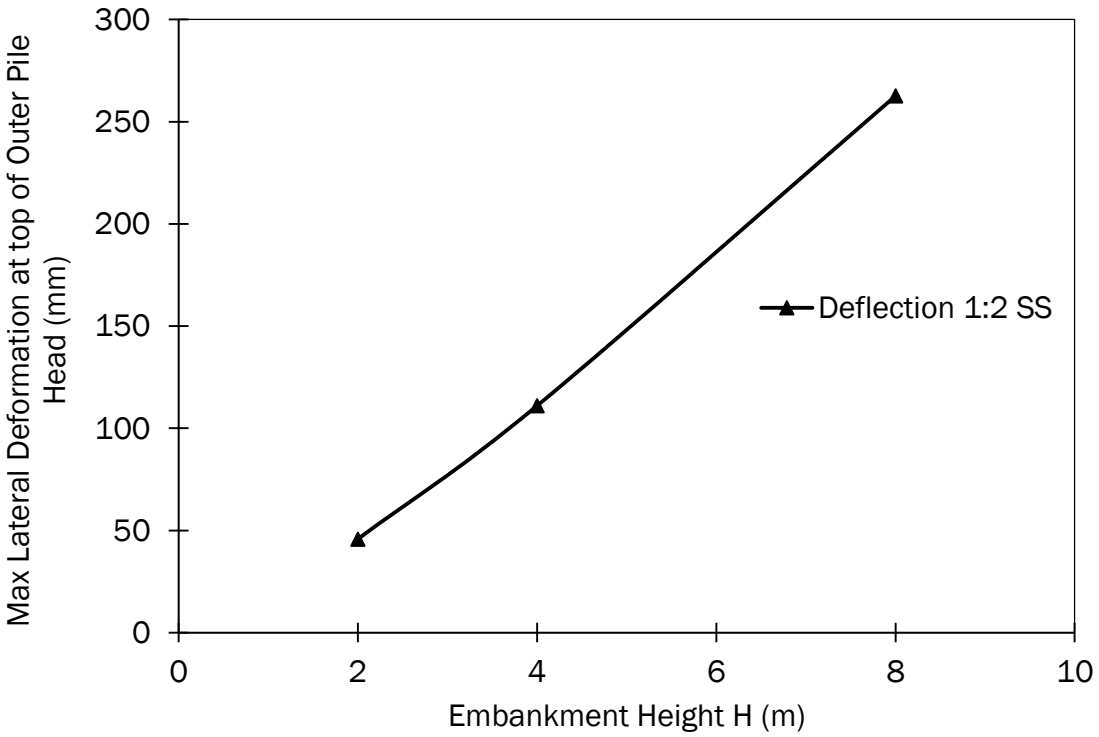

Figure C35 Deflection of outer row pile head for a range of embankment height (m) (H = 4.0m, a = 1.0m and s = 3.0m J_{re} = 500kN/m)

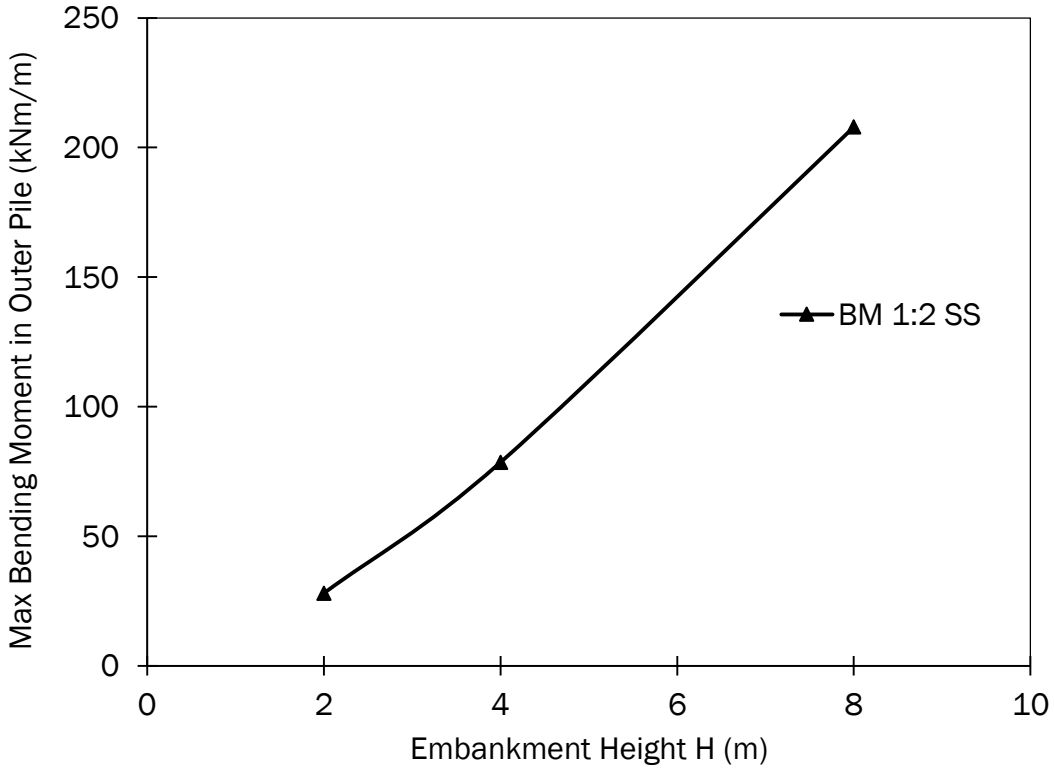

Figure C36 Max BM in outer row pile for a range of embankment height (m) (H = 4.0m, a = 1.0m and s = 3.0m J_{re} = 500kN/m)

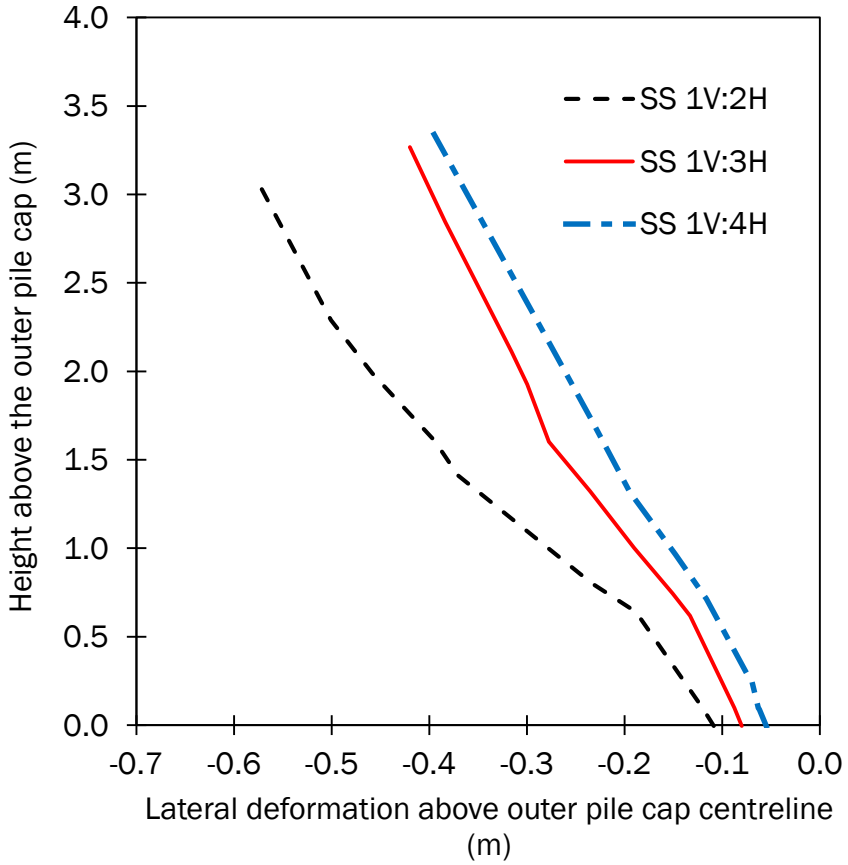

Figure C37 Lateral deformation of embankment fill material above outer pile centreline for a range of side slope steepness

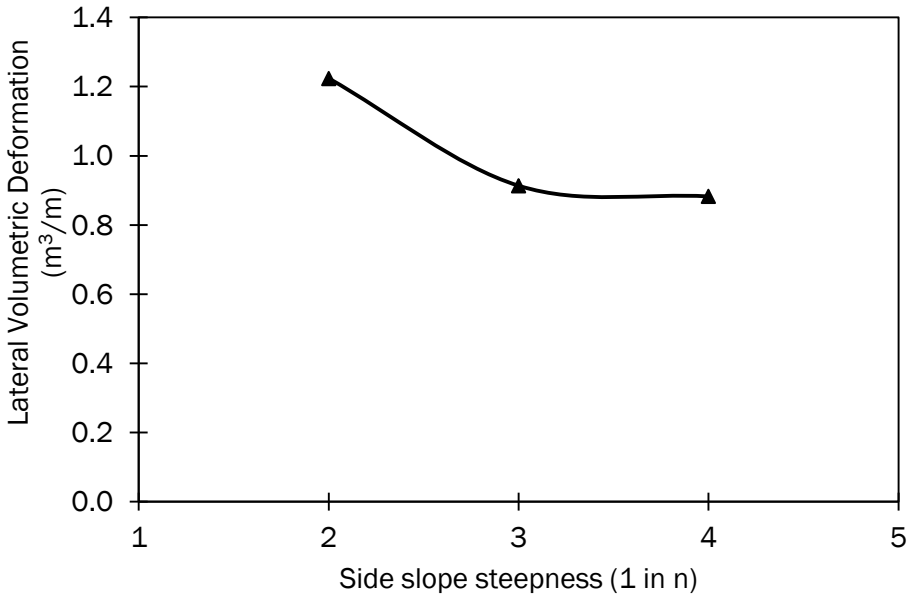

Figure C38 Lateral volumetric deformation above outer pile row for a range of side slope steepness

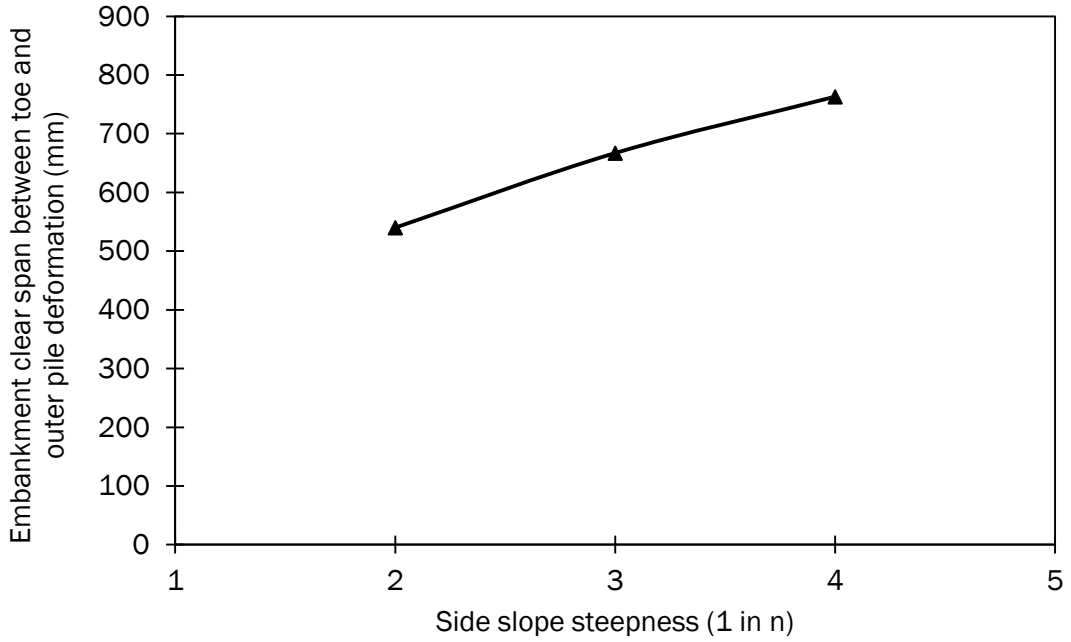

Figure C39 Geosynthetic reinforcement vertical deformation near embankment toe for a range of side slope steepness

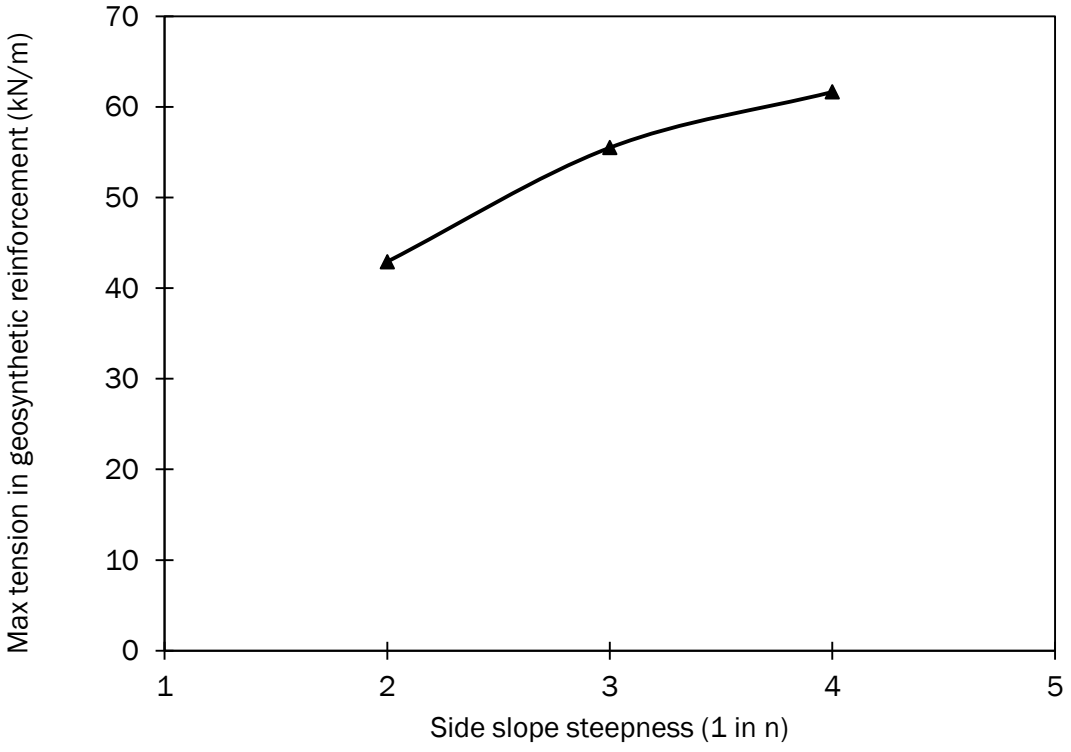

Figure C40 Geosynthetic reinforcement maximum tension for a range of side slope steepness

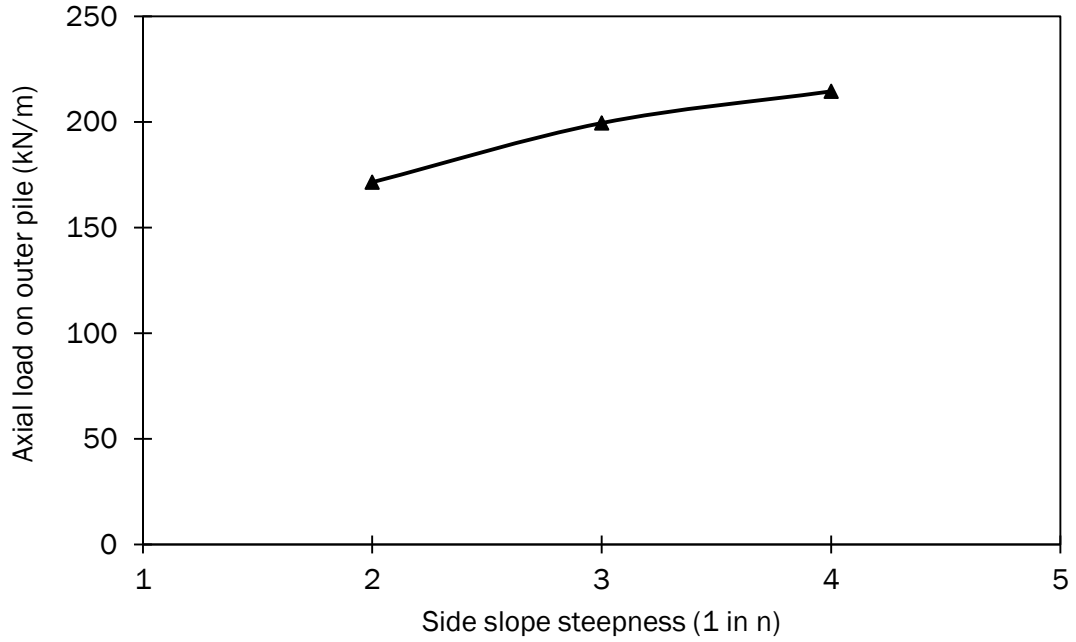

Figure C41 Axial load on outer pile row for a range of side slope steepness

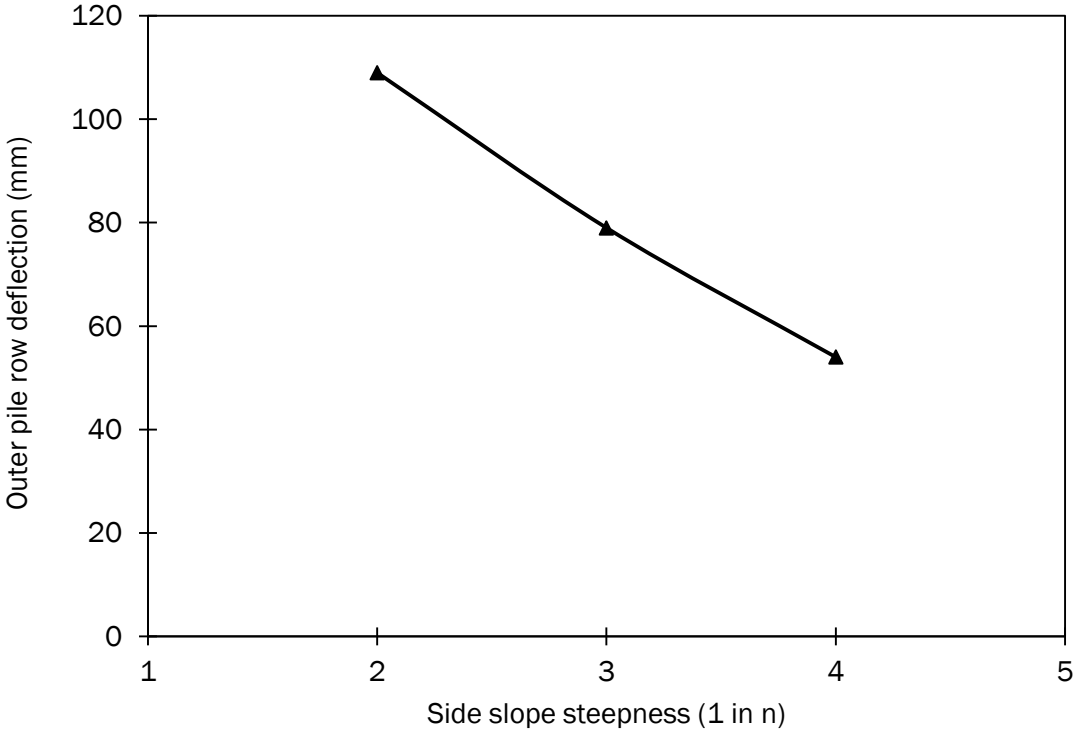

Figure C42 Outer pile row lateral deformation for a range of side slope steepness

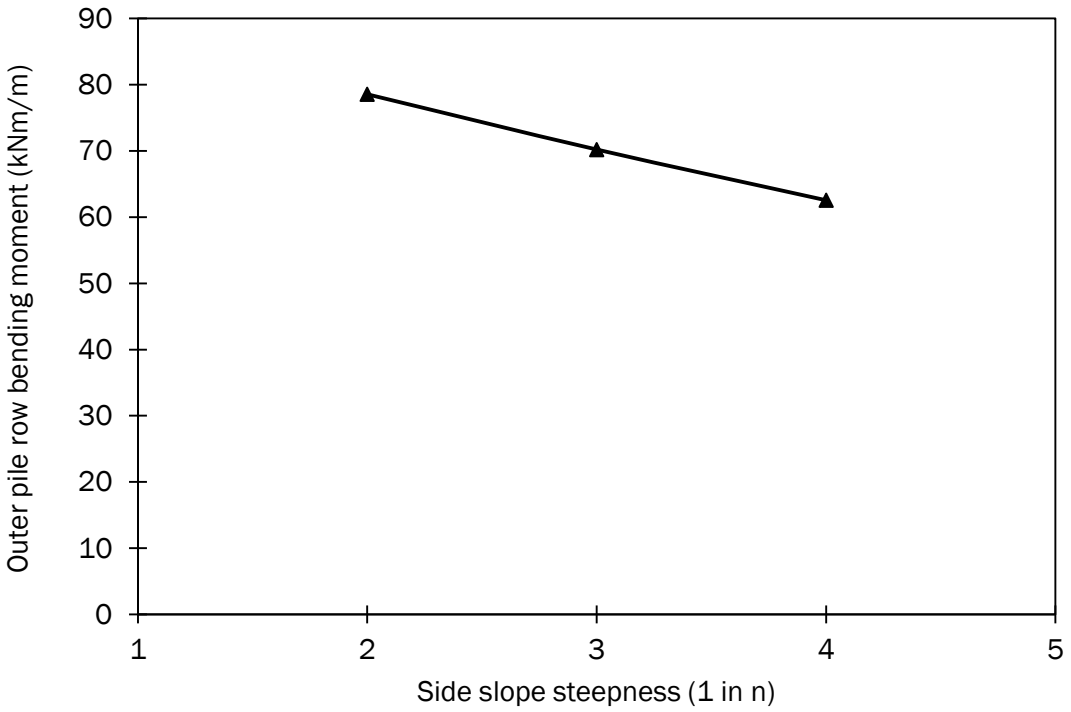

Figure C43 Outer pile row bending moments for a range of side slope steepness

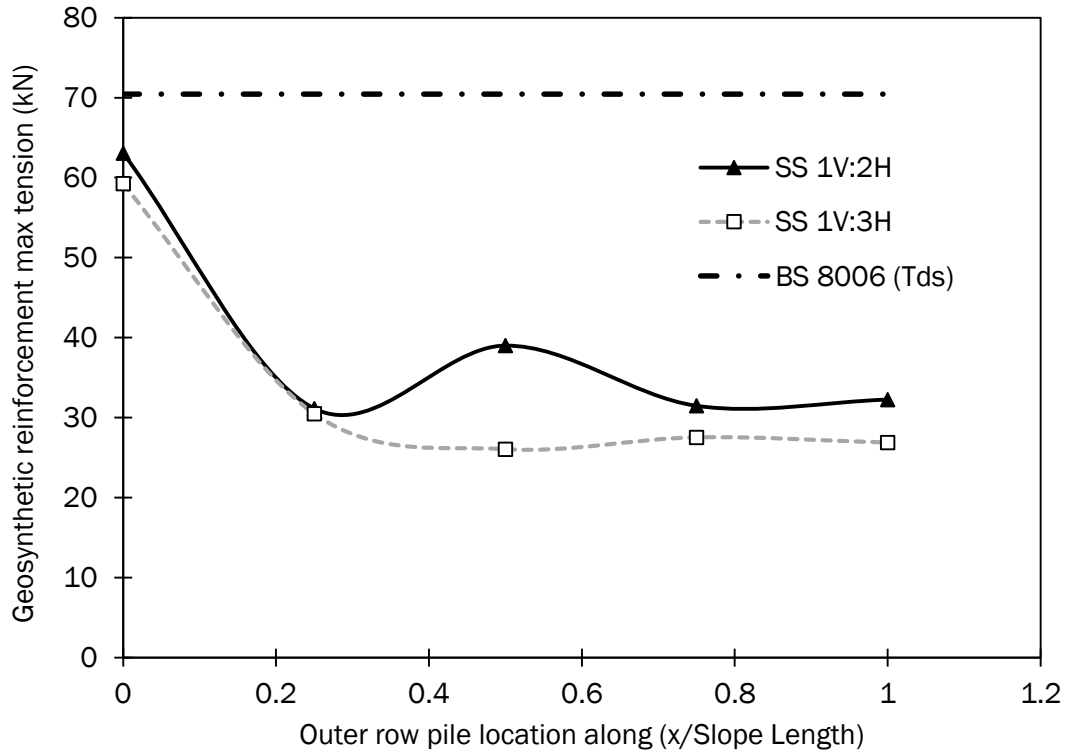

Figure C44 Geosynthetic reinforcement maximum axial tension for a range of outer pile row location

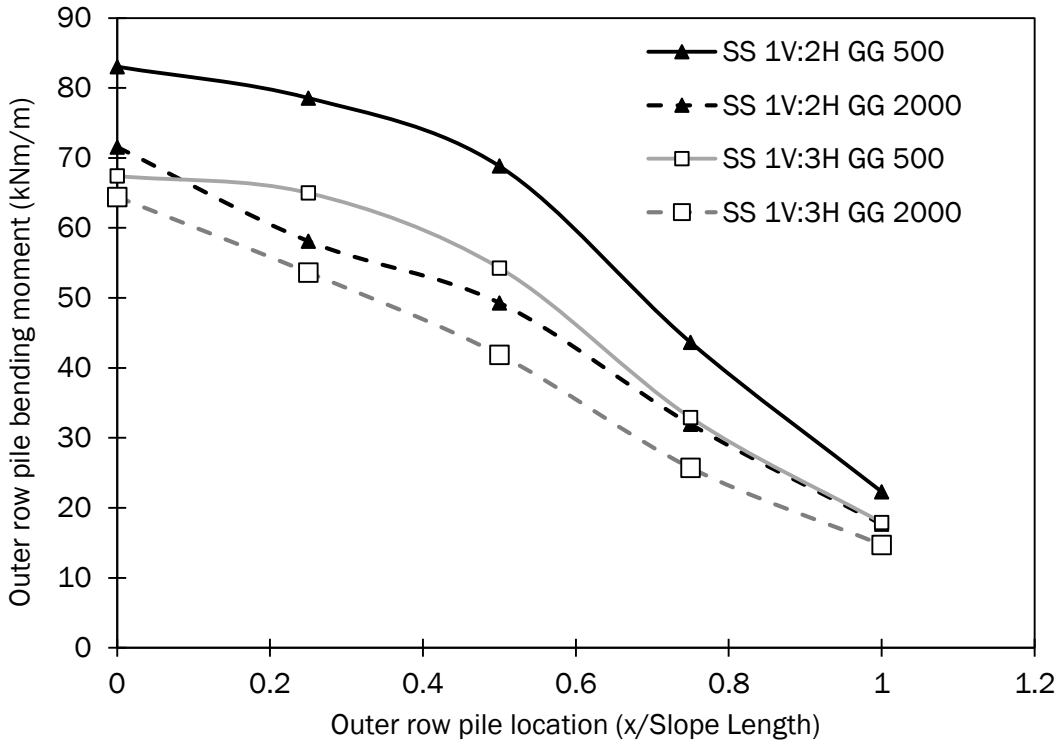

Figure C45 Outer pile row bending moments for a range of outer pile row location

APPENDIX D: Centrifuge & Plaxis 2D model

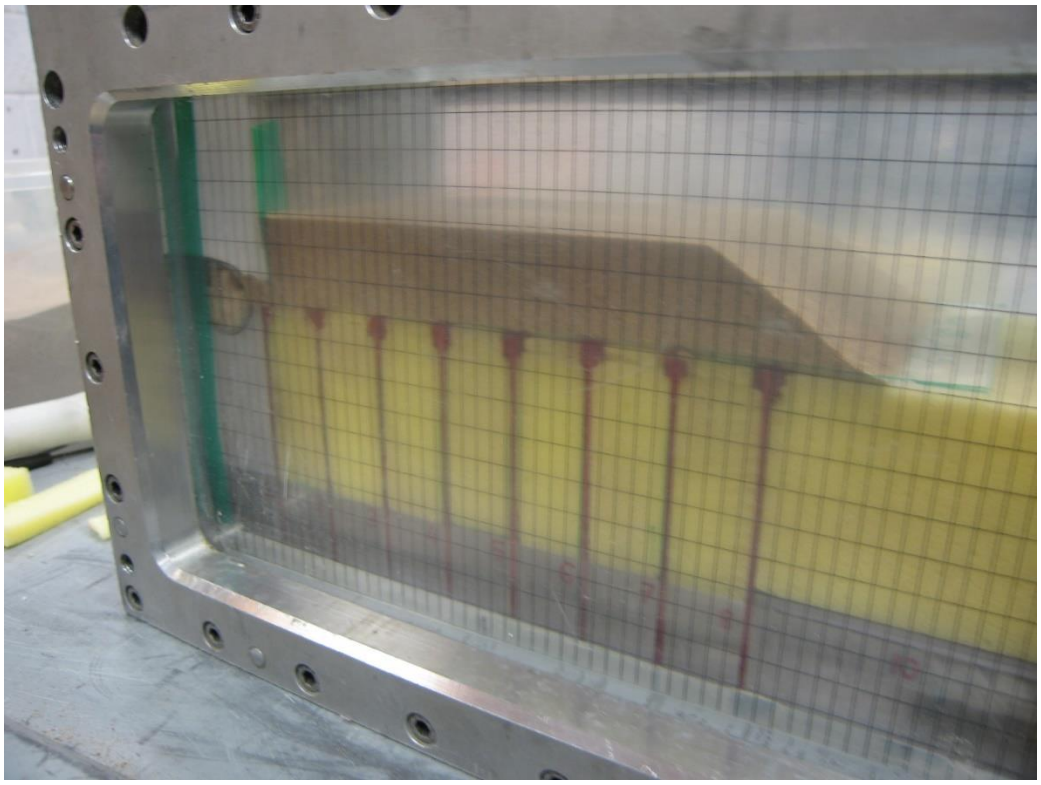

Figure D1 Centrifuge reinforced piled embankment prototype

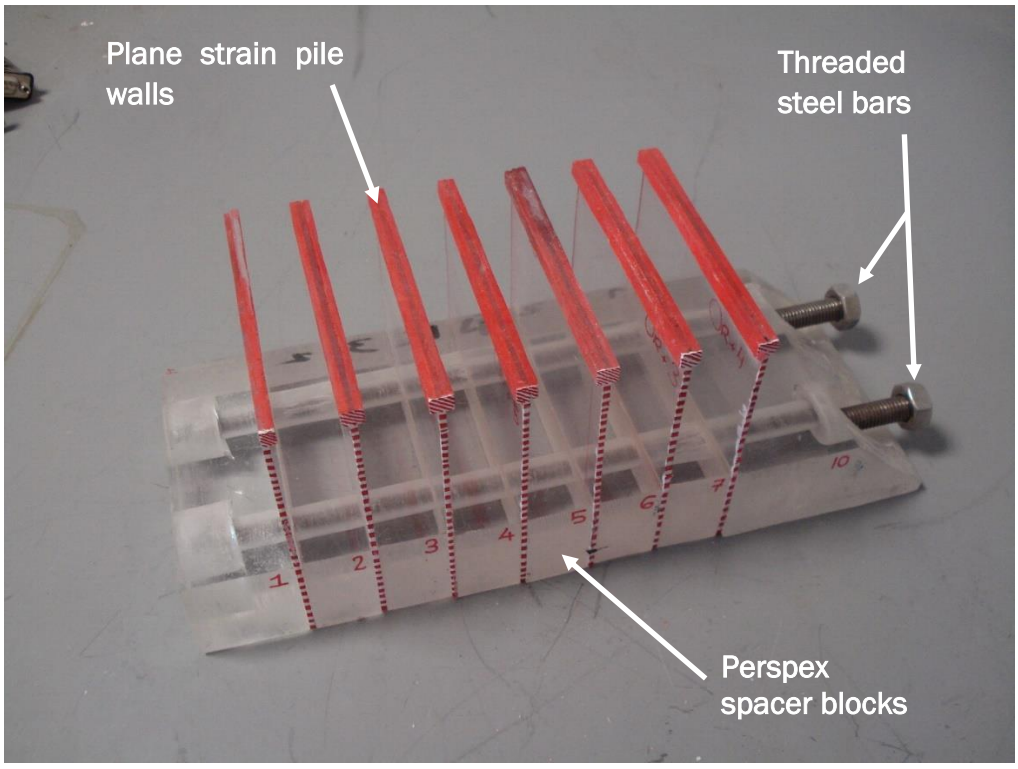

Figure D2 Pile group fixing arrangement side view

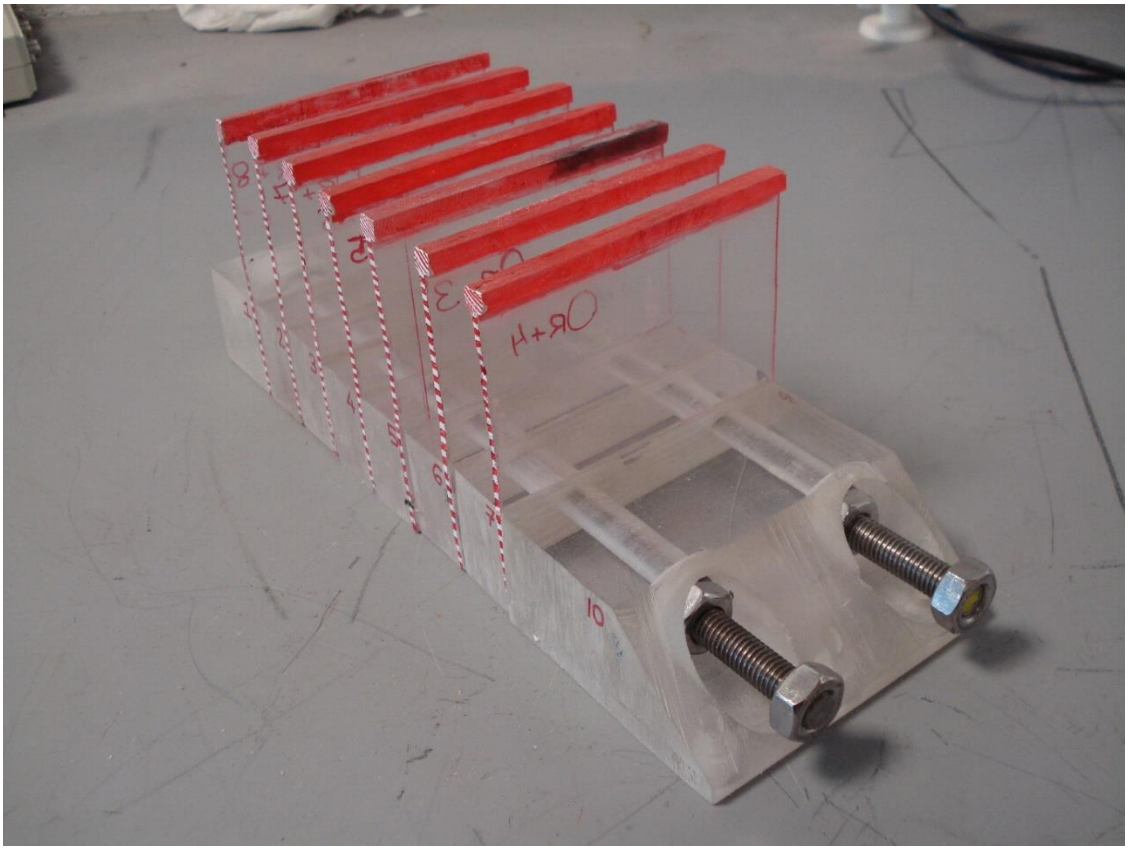

Figure D3 Pile group fixing arrangement end view

Figure D4 Centrifuge prototype geogrid restraint components

Figure D5 Centrifuge prototype geogrid restraint

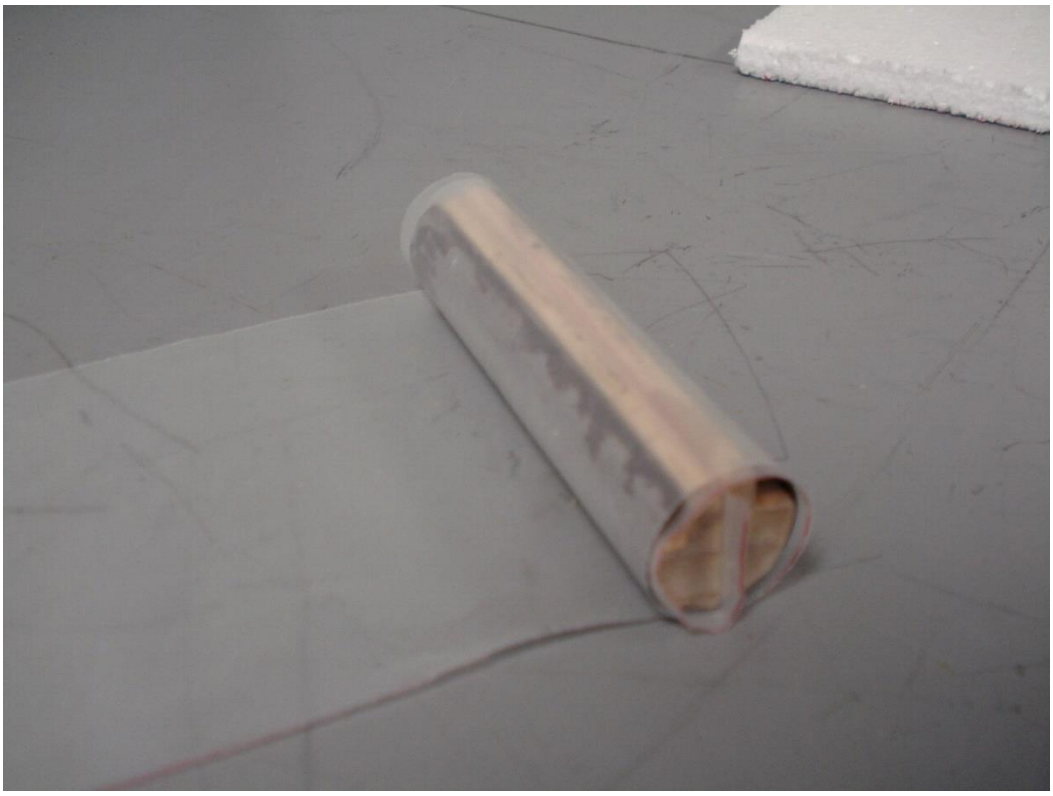

Figure D6 Centrifuge prototype geogrid restraint and geogrid

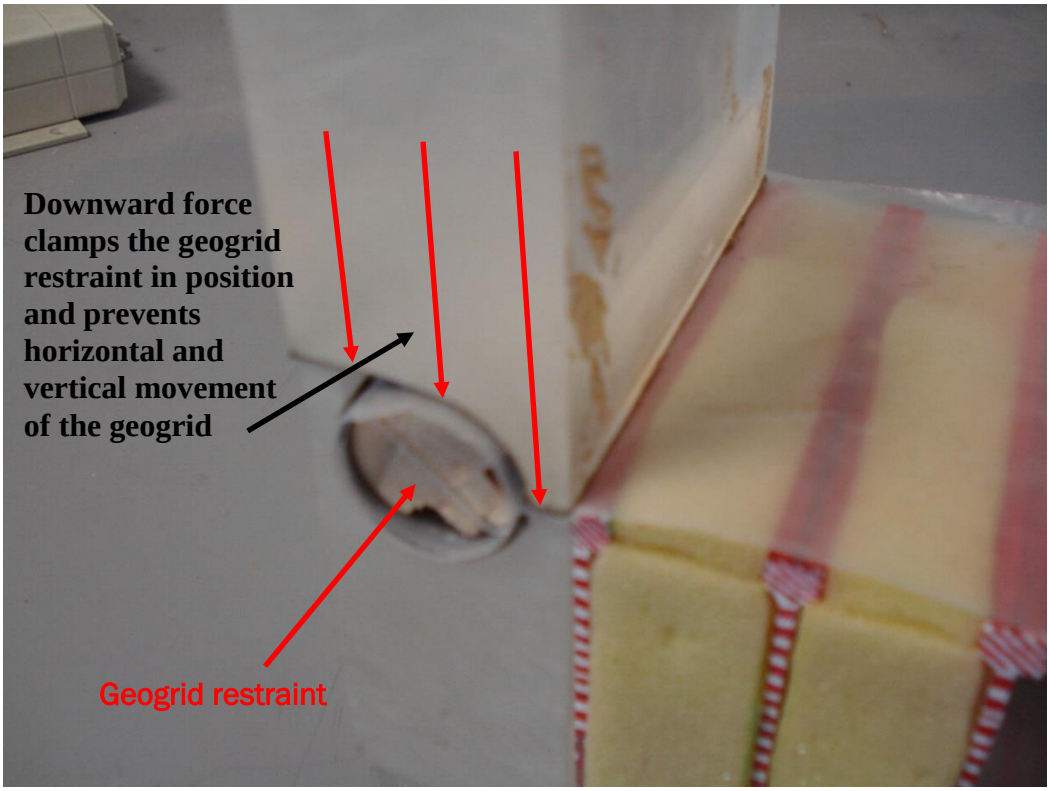

Figure D7 Centrifuge prototype geogrid restraint secured in centrifuge test box

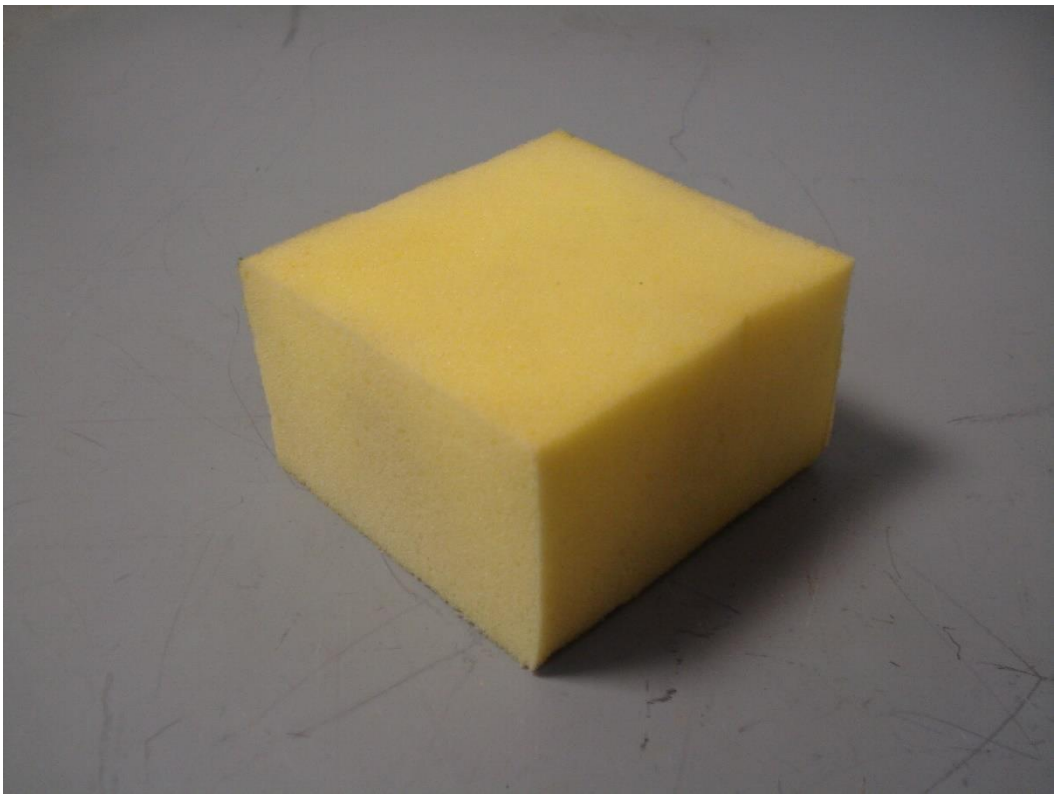

Figure D8 Centrifuge prototype Subsoil A synthetic sponge material

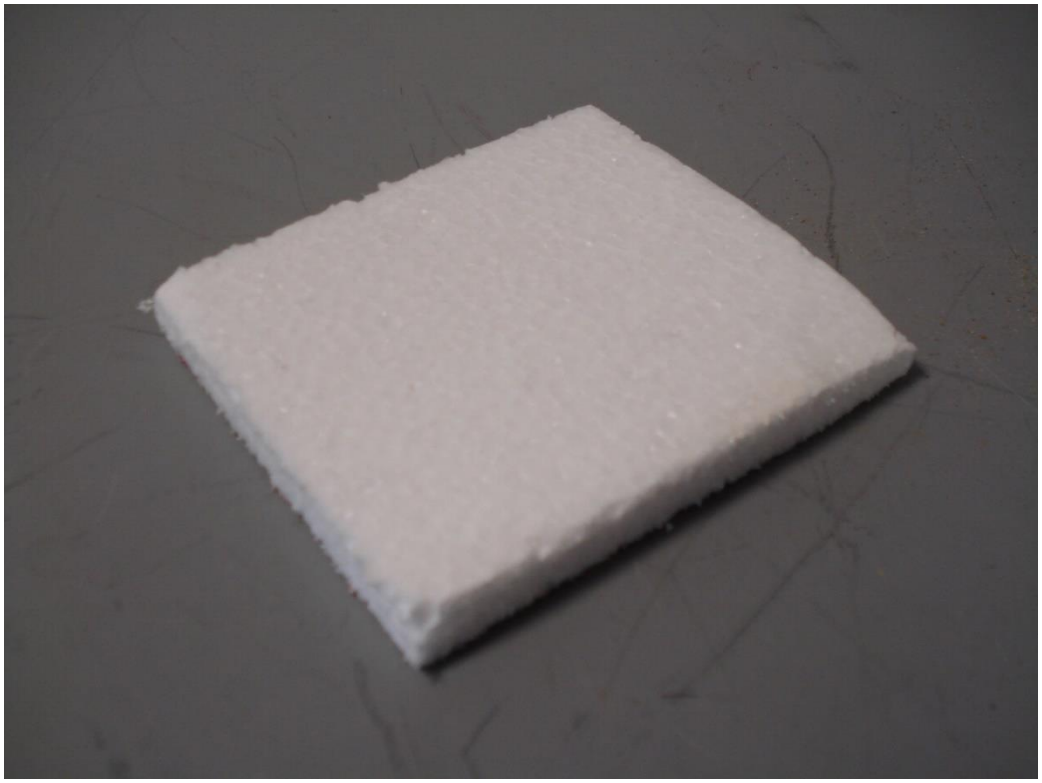

Figure D9 Centrifuge prototype Subsoil B EPS material

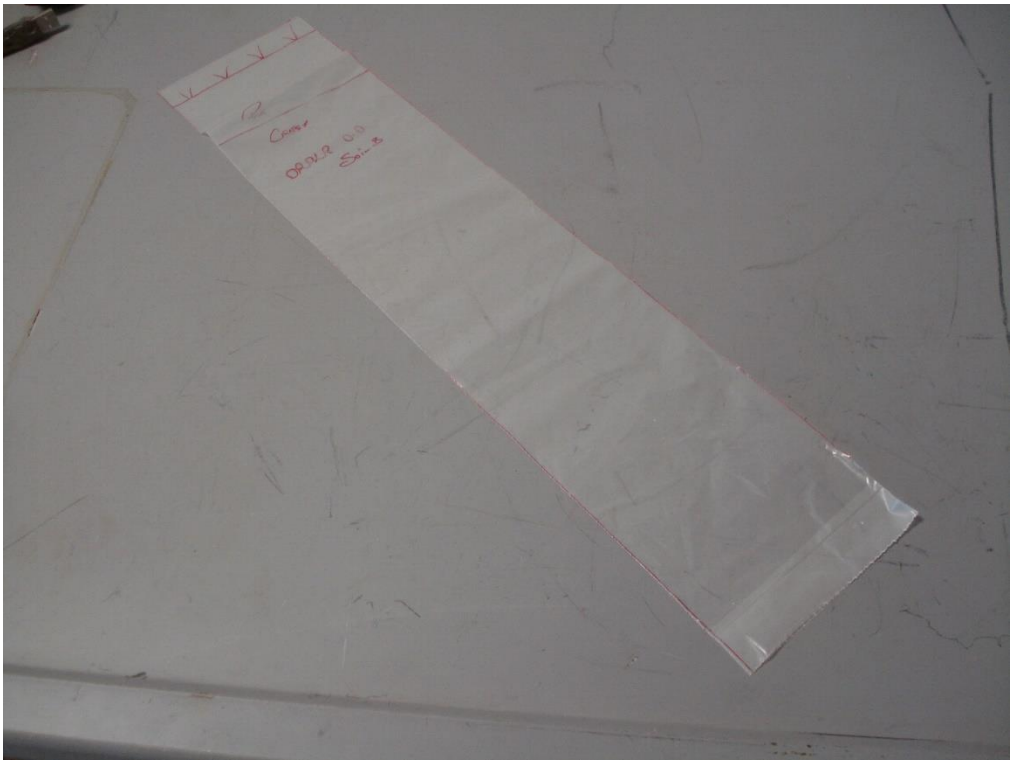

Figure D10 Centrifuge prototype 100 mm width of geogrid polyethylene material

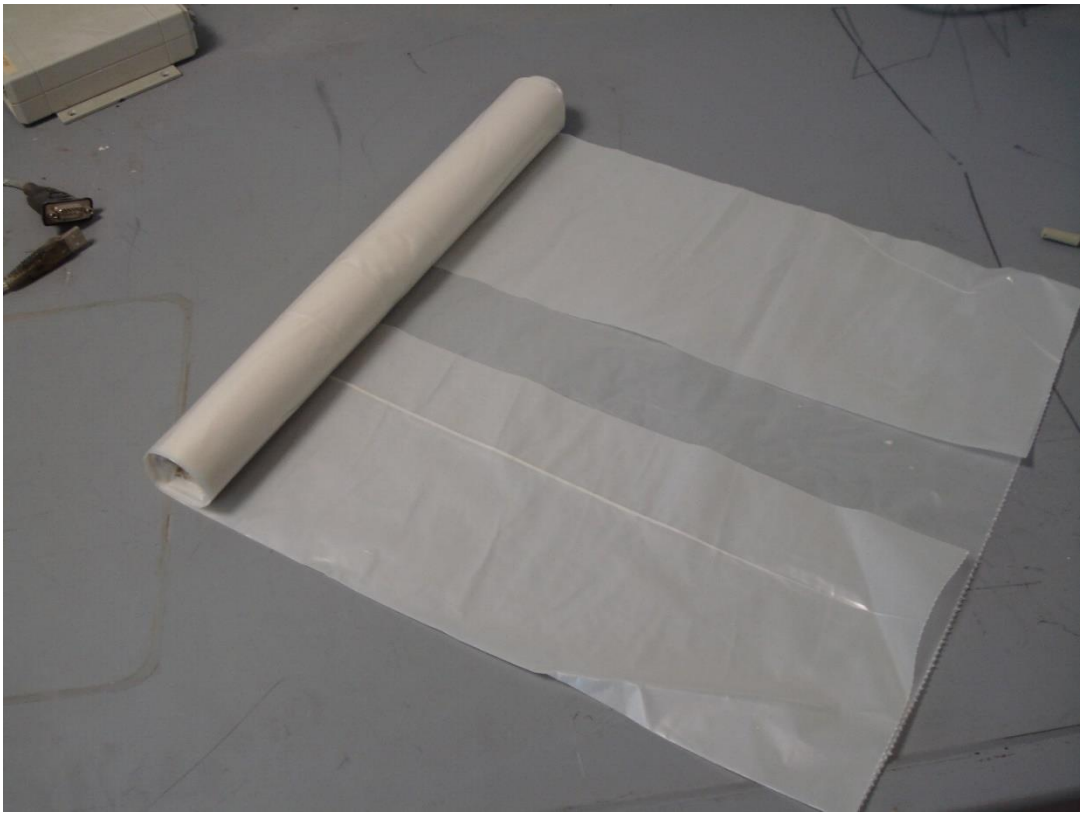

Figure D11 Centrifuge prototype geogrid polyethylene material

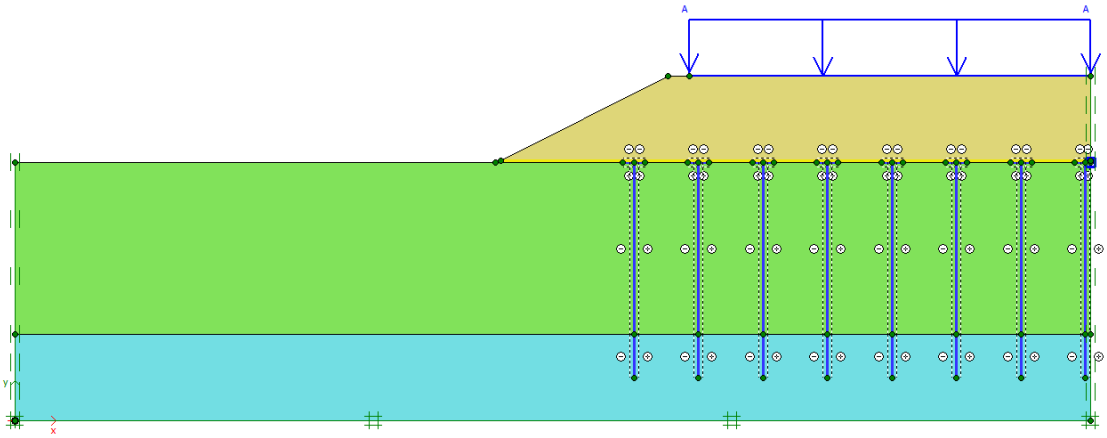

Figure D12 Plaxis 2D reinforced piled embankment typical model

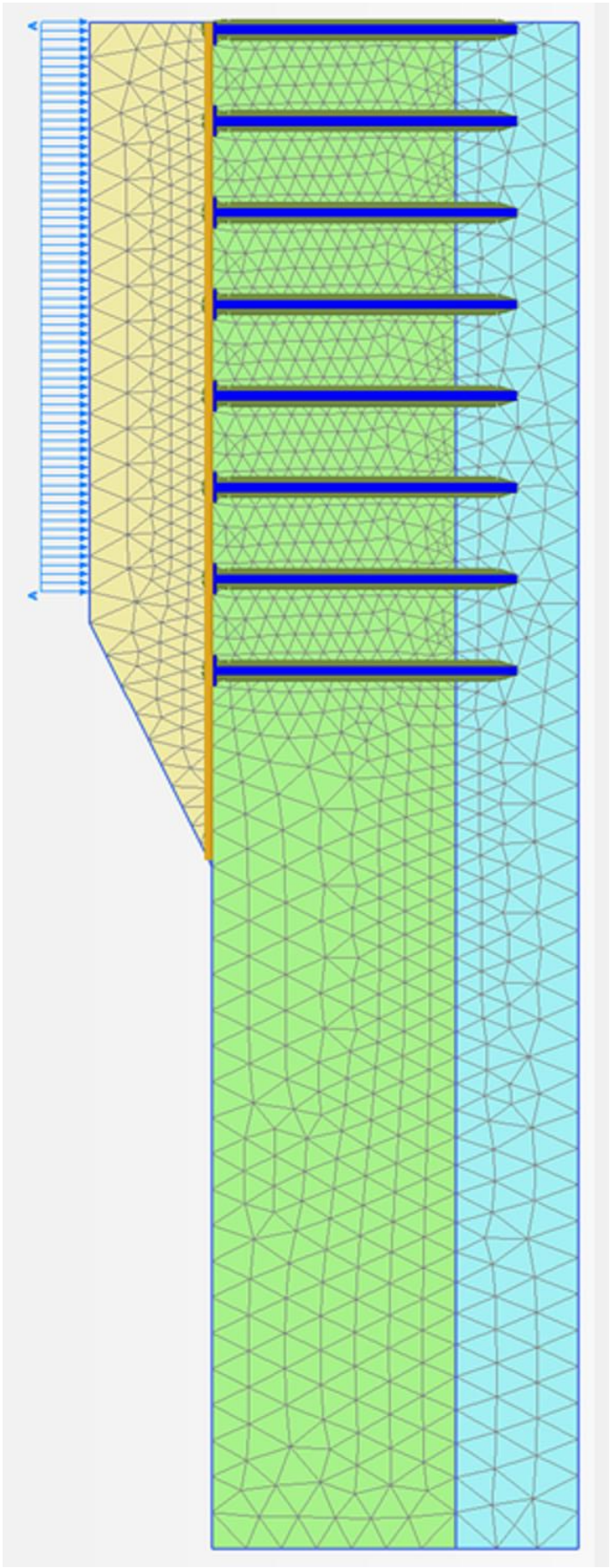

Figure D13 Plaxis 2D reinforced piled embankment typical mesh model